NUMERICAL SIMULATIONS OF REAL-GAS FLOWS WITH PHASE-EQUILIBRIUM THERMODYNAMICS

A Dissertation
Presented to
The Academic Faculty

by

Principio Tudisco

In Partial Fulfillment
of the Requirements for the Degree
Doctor of Philosophy in the
School of Aerospace Engineering

Georgia Institute of Technology
August 2020

NUMERICAL SIMULATIONS OF REAL-GAS FLOWS WITH PHASE-EQUILIBRIUM THERMODYNAMICS

Approved by:

Professor Suresh Menon,
Committee Chair
School of Aerospace Engineering
Georgia Institute of Technology

Professor Suresh Menon, Adviser
School of Aerospace Engineering
Georgia Institute of Technology

Professor Jerry Seitzman
School of Aerospace Engineering
Georgia Institute of Technology

Professor Joseph Oefelein
School of Aerospace Engineering
Georgia Institute of Technology

Professor Wenting Sun
School of Aerospace Engineering
Georgia Institute of Technology

Doctor Venkateswaran Sankaran
Air Force Office of Scientific Research
Air Force Research Laboratory

Date Approved: July 13, 2020

DEDICATION

To my wife and her incredible strength that I am still wondering where it came from

ACKNOWLEDGEMENTS

It is difficult to explain in words the feelings that I have in this moment. Reaching this stage has been definitely one of the thing that I have desired most in my life. First, I would like to thank my advisor, Prof. Menon for offering me the opportunity and support to work exactly on the type of projects I was aiming for when I applied for the PhD program at GT. As far as learning, I could not have pretended more during these 6+ years in the CCL. I can very well tell that I am definitely a better scientist and engineer than I was before and I feel that I reached the scope I had in mind when I applied: learn more about CFD, combustion and how to use them correctly in the field of rockets, which has been always my passion. Looking back at what I have produced, the skills and the knowledge that I acquired, I can say that I am proud of the choice I have pursued long time ago and that I would definitely recommend it.

I am also very grateful to Prof. Menon because of the flexibility he always showed as things happened in my life during the PhD. During the past years in fact I became father and I married my wife. Both of these things are usually quite normal, but in my case, they happened in New York City and Italy, respectively, so their management was not easy. Good amount of the present work, especially the code development was written on the plane, on the way to and from New York, where my wife had initially found her first job in the US and where I used to go at least once per month, for two years. Also, Prof. Menon always agreed to give me time off to visit my family in Italy once a year. In all these circumstances, I was deciding the amount of time to stay away and he never said no. I am grateful for this because it helped me to manage my private life at the best, and also recover from the stress of work that I was periodically accumulating in the lab. I assume I earned this privilege because I have never disappointed his expectations.

I want also to thank my thesis committee: Prof. Seitzman, Prof. Oefelein, Prof. Sun and Dr. Sankaran for the feedback I received for this work which helped to improve it.

Particularly I will always remember the afternoons spent with Prof. Seitzman and Prof. Oefelein talking about thermodynamics and combustion.

Life in the lab has not been easy. Every day I had to constantly face the fact that research is difficult, it takes (a lot of) time, and your initial plans never happen. For this reason, I want to thank Tim and Balaji for the enormous amount of knowledge they transferred to me. Both have been always kind and ready to answer my (lot of) questions. Later, I am also grateful to have met my lab mates Tim, Sai, Yogin, Jason, Achyut, Dan, Marc, Shubham, Orlando and James. With Achyut I have shared most of my research experience as the senior students left, and I always had good time in sharing thoughts and research questions. We also were providing each other support as the mood was going up and down with the research results. Same goes with Dan and I will always remember our discussions about....well everything. Marc, well... there is so much to tell about our time together that it would require another thesis. I am happy to have met him as well. Another special thank goes to the rest of the italian crew Matteo, Francesca, Andrea and Giada, with whom I shared a lot of funny moments. I also want to thank Michel Akiki for the time we spent together outside the lab.

Finally, I really want to thank the great soccer crew that I happened to meet during my last year of PhD: Walter, Luca, Kosmin, Attila, July, Lucas, Vito, Walter, Alessandro, Orlando, Francesco, Stefano and Federico for the amazing time spent together. I was waiting for our weekly match on friday like a child, and it helped me to get distracted from my research.

Earning a PhD is not easy at all. It is fundamental to have constantly support from the people who love you. For this reason, I want to thank my mom, my brother and sister and my wife's family for their support.

The most important acknowledgement however goes to my wife. I don't think I exaggerate if I say that 50% of the merit of this work goes to her. She has provided to me the support that I could not even imagine it was possible and I am so grateful for her love. With her, I feel very fortunate and I am looking forward to live all our future together with our love Vittoria.

“La costanza viene sempre premiata” A. Tudisco

(“Hard work gets always rewarded”)

Contents

DEDICATION . . . . . **iii**

ACKNOWLEDGEMENTS . . . . . **iv**

LIST OF TABLES . . . . . **xii**

LIST OF FIGURES . . . . . **xv**

LIST OF SYMBOLS OR ABBREVIATIONS . . . . . **xxxi**

SUMMARY . . . . . **xxxv**

I INTRODUCTION **1**

1.1 Scope and motivation 1

1.2 Background 3

1.2.1 Preliminaries on real gas thermodynamics 3

1.2.2 Preliminaries on VLE 12

1.3 Literature review 15

1.3.1 General observations, experimental and theoretical studies of RG mixtures 16

1.3.2 Numerical methods for real-gas simulations 24

1.3.3 Previous computational efforts with VLE 30

1.4 Objectives 33

1.5 Outline 35

II FORMULATION **37**

2.1 Governing equations for the fluid mechanics 37

2.1.1 Momentum diffusion and stress tensor 38

2.1.2 Heat and mass diffusion 39

2.1.3 Relations needed to close the problem 44

2.2 Real gas thermodynamics 46

2.2.1 Main definitions 47

2.2.2 Multi-phase equilibrium, real-gas thermodynamics 52

2.2.3 The Generic-Cubic Equation of State (GCEoS) model 63

2.3 Transport properties 80

2.3.1 Viscosity . . . 80
2.3.2 Thermal conductivity . . . 83
2.3.3 Mass diffusion coefficients . . . 85
2.3.4 Verification . . . 85
2.4 Chemistry . . . 90
2.5 Summary . . . 92

III NUMERICAL METHODS: IMPLEMENTATION AND VERIFICATION 93

3.1 Background on the numerical approach . . . 93
3.2 Spatial integration . . . 94
3.2.1 Upwind flux-difference splitting scheme . . . 94
3.2.2 The problem of pressure oscillations in conservative schemes . . . 97
3.2.3 The Double-Flux method . . . 112
3.3 An alternative way to compute cell-interface temperature . . . 124
3.4 Numerical methods for the thermodynamics . . . 128
3.4.1 Solution of the Tp problem . . . 129
3.4.2 Solution of the single-variable problems . . . 133
3.4.3 Solution of the multi-variable problems . . . 135
3.4.4 Adiabatic and isochoric mixing models . . . 139
3.4.5 Numerical computation of multi-phase thermodynamic variables . . . 140
3.5 Validation of the VLE framework . . . 143
3.5.1 TPD stability analysis method . . . 143
3.5.2 Gibbs free energy for a mixture that forms VLE . . . 147
3.5.3 Solution of the ERHO problem . . . 149
3.5.4 Solution of the PRHO and TRHO problems . . . 158
3.6 Summary . . . 160

IV RESULTS: ZERO-DIMENSIONAL (0D) THERMODYNAMICS . . . 163

4.1 Binary mixture # 1: N_2/CH_4 . . . 164
4.1.1 VLE diagram and main properties . . . 164
4.1.2 Effect of VLE on transport properties . . . 173
4.1.3 Effect of other GCEoS/MR combinations . . . 176

4.2 Binary mixture # 2: CH_4/CO_2 . . . 179
4.2.1 VLE diagram and main properties . . . 179
4.2.2 Effect of VLE on transport properties . . . 182
4.2.3 Effect of other GCEoS/MR combinations . . . 182
4.3 Ternary mixture: $CH_4/N_2/C_2H_6$ . . . 185
4.3.1 VLE diagram and main properties . . . 185
4.3.2 Effect of VLE on transport properties . . . 190
4.4 Prudhoe bay mixture . . . 191
4.4.1 VLE diagram and main properties . . . 191
4.4.2 Effect of VLE on transport properties . . . 194
4.5 Considerations on numerical vs analytical derivatives for the calculation of VLE properties . . . 195
4.6 Summary . . . 197
V RESULTS: SIMULATION OF NON-REACTING AND REACTING FLOWS . . . 199
5.1 One-dimensional (1D) advection of a multi-species contact discontinuity . . . 199
5.1.1 Case setup and results discussion . . . 200
5.1.2 Performance evaluation . . . 206
5.2 Two-dimensional (2D) shock/bubble interaction . . . 213
5.2.1 Case setup and results discussion . . . 213
5.2.2 Performance evaluation . . . 218
5.3 Three-dimensional (3D) non-reacting temporal mixing layer (TML) . . . 220
5.3.1 Case setup and results discussion . . . 220
5.3.2 Effect of the frozen VLE model and performance evaluation . . . 233
5.4 Two-dimensional (2D) non-reacting spatial mixing layer (SML) . . . 236
5.4.1 Case setup and results discussion . . . 236
5.5 Three-dimensional (3D) reacting temporal mixing layer (TML) . . . 252
5.5.1 Choice of the finite-rate kinetics . . . 253
5.5.2 VLE diagram for CH_4/O_2 . . . 260
5.5.3 Case setup and verification of the non-reacting solution . . . 261
5.5.4 Justification of the implicit integrator use for chemistry . . . 265

5.5.5 Results and discussion 268
5.6 Unsteady VLE formation in a 2D reacting spatial mixing layer (SML) . . 279
5.7 Summary 288

VI CONCLUDING REMARKS 291

6.1 Summary 291
6.2 Achievements/contributions 297
6.3 Future work 298

Appendix A — MINIMUM GIBBS CRITERION FOR COMPRESSIBILITY ROOT SELECTION 302

Appendix B — MOLE NUMBER TO MOLE FRACTION DERIVATIVE CONVERSION 304

Appendix C — PHYSICAL MEANING OF THE "FROZEN" VLE ASSUMPTION 305

Appendix D — ALGORITHMS FOR THE PRESENT THERMODYNAMIC MODEL 308

Appendix E — MAXWELL CRITERION AND ANTOINE'S EQUATION 321

Appendix F — OBTAIN C_1, C_2, C_3 AND C_4 FOR PR/MR-1 COMBINATION 324

Appendix G — ACCESSORY DERIVATIVES FOR THE DETERMINATION OF THE FUGACITY COEFFICIENT 325

Appendix H — ACCESSORY DERIVATIVES FOR THE DETERMINATION OF THE PARTIAL MOLAR QUANTITIES 328

Appendix I — FULL NEWTON METHOD FOR THE VLE PROBLEM 329

Appendix J — SOLUTION OF THE $E\rho$ PROBLEM WITH NUMERICAL JACOBIAN 333

Appendix K — MULTI-PHASE THERMODYNAMICS MATHEMATICAL DETAILS 336

Appendix L — MULTI-PHASE THERMODYNAMICS: PARTIAL MOLAR QUANTITIES 345

Appendix M — ADDITIONAL DERIVATIONS FOR THE GCEOS . . 351

M.1 Additional derivatives of the compressibility factor 351

M.2 Additional derivatives of the internal energy departure function 353
M.3 Fugacity coefficient and its derivatives 356
M.4 Partial molar quantities 370

Appendix N — EULER EQUATIONS FOR A GENERIC EOS 377

Appendix O — THERMODYNAMIC AND TRANSPORT SPECIES PROPERTIES USED IN THIS WORK 379

Appendix P — DETERMINATION OF TML DIMENSIONS 380

Appendix Q — ADDITIONAL RESULTS 382

Q.1 Results for the 1D N_2/C_6H_{14} contact advection 382
Q.2 Results for the 2D blob/shock interaction 382
Q.3 Results for the 3D non-reacting TML 385
Q.4 Results for the 2D non-reacting SML 389
Q.5 Results for the 1D diffusion flame for kinetics verification 389
Q.6 Results for the reacting 3D TML 389
Q.7 Results for the reacting 2D SML 399

Appendix R — WIDOM LINE LOCUS FOR THE GCEOS 402

REFERENCES 406

VITA 423

List of Tables

1 List of the research groups with significant work on the super-critical mixing studies. Table indicates the criteria used for the spatial, temporal discretization as well as any specific treatment that is used in the overall numerical method. The discrimination between FC and QC methods is made and the list of the EoS used is also provided. 28

2 Additional parameters for the PR-RK EoS [33] 66

3 Mixing rules for GCEoS [163, 104]. For short notation, these will be indicated as MR-X where X is the correspondig number. 68

4 Relevant parameters definitions for GCEoS 69

5 Derivatives of α_i functions for each EoS used. 70

6 Mixture-dependent c_1, c_2, c_3 and c_4 coefficients for each EoS used (except PR-RK). These are useful to recast the A_m coefficient in the form $A_m = c_1 + c_2 T^{c_4} + c_3 T$. 71

7 Mixture-dependent c_1, c_2, c_3 first derivative with respect to the generic mole fraction X_k. Here $\mathbf{X}_k = \{X_i \,|\, i = 1, \cdots, N_s, i \neq k\}$. 72

8 Mixture-dependent c_1, c_2, c_3 second derivative with respect to the generic mole fraction X_k. Here $\mathbf{X}_k = \{X_i \,|\, i = 1, \cdots, N_s, i \neq k\}$. In the derivation of all the above, the fact that $k_{kk} = 0$ has been used. 73

9 Relevant derivatives of A_m for all GCEoS except PR-RK. 74

10 Relevant derivatives of A_m for PR-RK for different mixing rules. Derivatives of $\sqrt{\alpha_i \alpha_j}$ are given in Eqs. (2.2.74)–(2.2.76). 75

11 Relevant derivatives of B_m. 76

12 Relevant derivatives of A_{ij}. The derivatives of α_i are given in Tab. 5. 76

13 Conditions at which the 1D N_2 contact discontinuity is studied. 104

14 Symbols description for the $E\rho$ and Ep multi-variable problems. 137

15 Mixture properties for CH_4 and H_2S. 143

16 Properties for (A) and (B) mixtures. 144

17 Results for (A) and (B) mixtures. 147

18 Relevant thermodynamic mixture properties for the N_2/CH_4 VLE diagram of Fig. 47 at the two reference points A and B. 150

19 Performances of the solution of the ERHO problem for point A of Fig. 47 using different parameters of the line-search method for the solution update and different dual-variable iteration algorithms. The overall algorithm tolerance is maintained constant at $\epsilon = 0.0001$. 157

20 Mixture composition in mole fractions for the Prudhoe bay gas [159]. 191

21 Comparison of computational times to calculate all the thermodynamic properties between the numerical model [139] and the analytical model (present work). Data is collected based on the mixtures considered above. 196

22 Comparison of computational times to solve Case 2 on the $N = 1024$ grid with the two different numerical schemes and by using the fully numerical and fully analytical framework for the VLE thermodynamics (top). Investigation on the use of the full Newton method (see Algorithm I) is also done for the same cases (bottom). The switch between the SSI and full Newton for VLE is chosen to $\epsilon_s = 1e{-}6$, while the overall algorithm tolerance is set to $\epsilon = 1e{-}8$. For this latter case, the additional speed up due to the use of the Newton method is also provided in parentheses with respect to the cases conducted with the SSI method only. 208

23 Comparison of computational times to solve Case 1 on different grids using different thermodynamic models (VLE and non VLE). This data refers to the PRHO problem solved numerically as in Sec. 3.4.2. For each grid resolution, the number of processors used to run the case is given in parentheses. Simulation time is given in seconds. 210

24 Comparison of computational times to solve Case 1 on different grids using different thermodynamic models (VLE and non VLE). This data refers to the PRHO problem solved analytically using the framework discussed in Sec. 3.3. For each grid resolution, the number of processors used to run the case is given in parentheses. Simulation time is given in seconds. 210

25 Comparison of computational times to solve Case 2 on different grids using different thermodynamic models (VLE and non VLE). This data refers to the PRHO problem solved numerically as in Sec. 3.4.2. For each grid resolution, the number of processors used to run the case is given in parentheses. Simulation time is given in seconds. 210

26 Comparison of computational times to solve Case 2 on different grids using different thermodynamic models (VLE and non VLE). This data refers to the PRHO problem solved analytically using the framework discussed in Sec. 3.3. For each grid resolution, the number of processors used to run the case is given in parentheses. Simulation time is given in seconds. 211

27 Comparison of computational times to solve the 2D shock/bubble interaction using different numerical/thermodynamic models. The main comparison (row) is made on the method to reconstruct the temperature at cell interface using the fully numerical approach PRHO approach of Fig. 31 or the fully analytical PRHO approach of Sec. 3.3. The second criterion (column) is the thermodynamic model ranging from the non-VLE to the frozen VLE, to the full VLE models. Investigation is also made on the use of the ERHO problem acceleration technique discussed in Sec. 3.5.3 when it is coupled with the full VLE model. Additional results for the present analyses are given in Sec. Q.2. 219

28 Conditions for Case 1 to Case 3 for the TML. Lengths values are in $\times 10^{-6}$, while vorticity thickness values are in $\times 10^{-7}$ units. Subscripts T and B refer to "TOP"and "BOTTOM", respectively. For all cases: $p = 5\,\mathrm{MPa}$, $Re_0 = 600$, $M_0 = 0.4, T_\mathrm{B} = 293.0\,\mathrm{K}$, $\rho_\mathrm{B} = 58.44\,\mathrm{kg/m^3}$, $Z_\mathrm{B} = 0.984$, $T_B/T_c = 2.32$, $p_B/p_c = 1.47$. 222

29 Time-per-step comparison of the Case 3 simulation using different thermodynamic and reconstruction models for the PRHO problem. All the simulations refer to the hybrid FC/QC scheme with switch threshold of 0.3. Numbers in parentheses report the cost increase (ratio) with respect to the non-VLE simulation. 235

30 Relevant properties used to initialize the 2D SML non-reacting setup. . . . 238

31 Operating conditions of the sub-scale rocket engine described in the work of [76]. 257

32 Forward rates used for each reaction of Eq. (5.5.1). Tuning procedure has been performed against GRI [206]. Units are in *cm*, *s*, *mol* and *cal*. 259

33 Mean and standard deviation values computed within the VLE-OX and VLE-F regions at $t = t_5$. 273

34 Mean and standard deviation values computed within the VLE region at $t = 42.5\,\mu s$. 286

35 List of species-dependent properties used in the present work: T_c critical temperature, p_c critical pressure, ω acentric factor, V_c critical volume, Σ_v Fuller parameter (used in Eq. (2.3.22)) and molecular weight. 379

36 Additional input conditions for Case 1 to Case 3 for the TML. These, along with those listed in Tab. 28 are used to determine the TML dimensions according to Eqs. (P.0.1)–(P.0.4). 381

List of Figures

1 Phase diagram of oxygen in the $p - T$ space. The black dot represents the critical point at the intersection of the long-dash lines for the critical temperature and pressure. The grey line is the pseudo-boiling line [148] or Widom line [200] and corresponds to the region of maximum specific heat at constant pressure (*cf.* Chap. R). The density is represented by the colored contours in the background. 6

2 Generalized compressibility chart. (Adapted from [182]) 7

3 Nitrogen 2D contour maps of a) density and b) specific heat at constant pressure. The same properties are showed in c) and d) at the two reference pressures indicated with the dashed lines in the 2D maps. The red dot indicates the critical point. The red dot indicates the critical point. The specific enthalpy is showed in e). These pictures have been generated using the Peng-Robinson EoS. 8

4 n-hexane 2D contour maps of a) density and b) specific heat at constant pressure. The same properties are showed in c) and d) at the two reference pressures indicated with the dashed lines in the 2D maps. The red dot indicates the critical point. The specific enthalpy is showed in e). These pictures have been generated using the Peng-Robinson EoS. 9

5 a) Sketch of the p-v diagram of a single substance. The vapor-liquid equilibrium (VLE) dome is identified at the center of the figure. In there, the thermodynamic state is in phase equilibrium, meaning that both liquid and vapor phases exist at the same time. For this reason, each point of the VLE "dome" is characterized by a *phase-fraction* (or quality [46]) that defines the thermodynamic state. b) p-X diagram for a mixture identifying the VLE dome for a given temperature. Mixture critical point is qualitatively indicated in red. 14

6 Schematics of a sub-critical, versus a super-critical jet of two distinct components in a shear coaxial type injection (From [226]). 16

7 LN_2/GHe coaxial jets under different pressure conditions (taken from [120]). 17

8 Liquid nitrogen (LN_2)/gaseous nitrogen (GN_2) jet application studied by Chehroudi *et al.* [29]. Different jet characteristics are observed as the pressure is varied from (a) sub-critical, to (b) near-critical, to (c) super-critical. 18

9 Schematics of a sub-critical, versus a super-critical interface structure for LOX-GH_2 mixture (From [36]). Liquid-gas sharp interfaces are associated with high mean free path λ, large Knudsen number Kn and surface tension σ. The interface dynamics is governed by the local molecular processes and vapor-liquid equilibrium. On the other hand, super-critical interfaces are diffused and enter the continuum regime as the local mean free path is much smaller than the interface thickness. Knudsen number is small and surface tension σ tends to zero. Vapor-liquid equilibrium no longer defines the interface thermodynamic state and therefore this state can be modeled with conventional Navier-Stokes equations with single-fluid approach. 21

10 Schematic representation of critical loci curves for mixtures of Type I and III (borrowed from [169]). 23

11 Schematic representation of a shear-coaxial injector mixing region. The flow is characterized by two streams, one in pseudo-liquid state (high p, low T) and one in pseudo-gas state (high p, high T) which produce a high- and low-density regions, respectively. When these mix, a high density gradient region forms. This is challenging to be resolved numerically. 26

12 Comparison of the compressibility and dynamic viscosity for oxygen at 300 K and 115 K for a range of pressures. In the labels, TPG denotes the classical, mixture averaged model in which the mixture viscosity is only a function of pressure and composition, RG-LowP denotes the transport model of Chung [31] without the high-pressure correction, whereas the RG-HighP indicates the same model [31] with the high-pressure correction. For reference, the NIST data is also superimposed, indicating the importance of the high-pressure correction over both models that do not employ the correction. 40

13 VLE diagram (a), mixture compressibility (b) and Gibbs free energy (c) for a nitrogen/hexane (N_2/C_6H_{16}) mixture as a function the amount of N_2 in mole fractions. The mixture pressure and temperature are maintained fixed in Fig. b) and c) at $p = 10\,\mathrm{MPa}$ and $T = 377.9\,\mathrm{K}$, respectively. For these plots, the PR EoS has been used (see also [226]). 56

14 Viscosity and thermal conductivity of the relevant single components used in the present work. The data is recorded for two reference temperature and a range of pressures and validated against the NIST database. 87

15 High-pressure thermal conductivities for mixture of argon and carbon dioxide at 298 K. 88

16 Effect of pressure, temperature and mixture solvent on the binary diffusion coefficient of the CO_2-C_2H_4 system. 89

17 Schematic representation of a) generic extrapolation of (volume-averaged) primitive variables at cell interface $i + 1/2$ and b) generic sketch of the associated Riemann problem solution. 95

18 Schematic representation of the one-dimensional N_2 contact discontinuity with a smoothed top-hat profile. 104

19 Coefficients of Eq. (3.2.20) for Case 1 using the PR EoS. 106

20 Total variation of the conservative variables according to Eq. (3.2.20) for Case 1 using the PR EoS. 106

21 Pressure variation after one time step for Case 1 using the PR EoS. The reconstructed method refers to $p_i^{n+1} = p_i^n + dp$ where dp is computed using Eq. (3.2.20), whereas the solver method refers to a pure integration using the first order MacCormack time integration (predictor step only) and the first order MUSCL spatial integration discussed in Sec. 3.2.1. 106

22 Coefficients of Eq. (3.2.20) for Case 1 using the TPG EoS. 107

23 Total variation of the conservative variables according to Eq. (3.2.20) for Case 1 using the TPG EoS. 107

24 Pressure variation after one time step for Case 1 using the TPG EoS. The reconstructed method refers to $p_i^{n+1} = p_i^n + dp$ where dp is computed using Eq. (3.2.20), whereas the solver method refers to a pure integration using the first order MacCormack time integration (predictor step only) and the first order MUSCL spatial integration discussed in Sec. 3.2.1. 107

25 Comparison of a) density, b) c_1, c) c_2, d) d_1 and e) d_2 variables defined in Eq. (3.2.21) that form the Γ coefficients in Eq. (3.2.20) using the PR EoS and TPG EoS for Case 1. 108

26 Coefficients of Eq. (3.2.20) for Case 2 using the PR EoS. 111

27 Total variation of the conservative variables according to Eq. (3.2.20) for Case 2 using the PR EoS. 111

28 Pressure variation after one time step for Case 2 using the PR EoS. The reconstructed method refers to $p_i^{n+1} = p_i^n + dp$ where dp is computed using Eq. (3.2.20), whereas the solver method refers to a pure integration using the first order MacCormack time integration (predictor step only) and the first order MUSCL spatial integration discussed in Sec. 3.2.1. 111

29 Comparison of a) density, b) c_1, c) c_2, d) d_1 and e) d_2 variables defined in Eq. (3.2.21) that form the Γ coefficients in Eq. (3.2.20) using the PR EoS and TPG EoS for Case 2. 113

30 Schematic representation of the spatial integration carried out with the DF method (adapted from [108]). 115

31 Summary of the time integration steps performed for the hybrid scheme. (a) FC scheme and (b) QC scheme. MC indicates the MacCormack integration step. (adapted from [108]). In this picture, the generic $\hat{(\cdot)}$ quantity indicates a known value, not to be confused with the HLLC interface states in Fig. 17. This helps to clarify in each stage what is given and what is the unknown. . 119

32 a) density, b) scheme switch (0 = FC, 1 = QC), c) temperature and d) pressure profiles of the 1D top-hat profile obtained with $N = 51$ grid points. 120

33 a) density, b) scheme switch (0 = FC, 1 = QC), c) temperature and d) pressure profiles of the 1D top-hat profile obtained with $N = 151$ grid points 121

34 a) density, b) scheme switch (0 = FC, 1 = QC), c) temperature and d) pressure profiles of the 1D top-hat profile obtained with $N = 201$ grid points. 121

35 a) density, b) scheme switch (0 = FC, 1 = QC), c) temperature and d) pressure profiles of the 1D top-hat profile obtained with $N = 401$ grid points. 121

36 a) density, b) scheme switch (0 = FC, 1 = QC), c) temperature and d) pressure profiles of the 1D "smoothed" top-hat profile obtained with $N = 51$ grid points. 122

37 a) density, b) scheme switch (0 = FC, 1 = QC), c) temperature and d) pressure profiles of the 1D "smoothed" top-hat profile obtained with $N = 151$ grid points. 122

38 a) density, b) scheme switch (0 = FC, 1 = QC), c) temperature and d) pressure profiles of the 1D "smoothed" top-hat profile obtained with $N = 201$ grid points. 122

39 a) density, b) scheme switch (0 = FC, 1 = QC), c) temperature and d) pressure profiles of the 1D "smoothed" top-hat profile obtained with $N = 401$ grid points. 122

40 Schematic representation of the 2D N_2/n-$C_{12}H_{26}$ advection testcase (figure borrowed from [108]). 123

41 a) Density and b) n-dodecane profiles taken along the y direction after one period of simulation corresponding to $t = 0.02$ ms. The expected exact solution and the results reported by [108] are superimposed for comparison. 124

42 Collection of the scheme switch field and the corresponding pressure field obtained for different values of the ξ parameter, as well as the pure DF scheme. In the switch pictures, the red color indicates where the QC scheme is activated only, whereas the blue color indicates the regions where the FC scheme is activated only. The pressure colormap is in [Pa] units. 125

43 Basic algorithm of the VLE problem solution. 129

44 Speed-up mechanism for the ERHO problem. 138

45 TPD analysis for the CH_4/H_2S mixture. a) TPD function for $\mathbf{X} = [0.5, 0.5]$ composition, b) Normalized Gibbs energy variation as the mixture composition is varied, c) same as b) with some reference lines to help the discussion in the text and d) trend of the phase fraction β. 145

46 a) VLE diagram of the $N_2C_6H_{14}$ mixture for various iso-therms at different pressures. Reference dotted data is taken from [45]. Horizontal black dashed line indicates the iso-baric reference line at 10 MPa. b) Compressibility factor plotted along the iso-baric line of 10 MPa as a function of the nitrogen mole fraction. The result is showed with and without the VLE model. c) Mixture Gibbs free energy as function of the compressibility factor along the same iso-baric reference line of 10 MPa computed with and without the VLE model. d) Phase fraction (β) colormap diagram of the mixture VLE loci at 377 K. 148

47 VLE diagram of N_2/CH_4 at fixed temperature of 150 K for a range of pressures and amount of nitrogen in the mixture. 150

48 a) Internal energy and b) density residuals 3D trajectories in the thermodynamic space as the ERHO algorithm advances iterations using different models for point A. 151

49 a) Internal energy and b) density residuals as a function of the number of iterations for the different models for point A. 151

50 a) Internal energy and b) density residuals 3D trajectories in the thermodynamic space as the ERHO algorithm advances iterations using the dual-variable algorithm for point A when the non-VLE model is forced to work. 152

51 a) Internal energy and b) density residuals as a function of the number of iterations using the dual-variable algorithm for point A when the non-VLE model is forced to work. 152

52 a) Internal energy and b) density residuals 3D trajectories in the thermodynamic space as the ERHO algorithm advances iterations using different models for point B. 154

53 a) Internal energy and b) density residuals as a function of the number of iterations for the different models for point B. 154

54 (a) Solid lines: isothermal VLE diagram for the present mixture for a range of pressures as a function of the N_2 mole fraction. Dots (•): comparison taken from [45, 164]. Colored domes indicate the regions where mixture forms VLE, while outside the domes, single phase is found (either vapor or liquid). (b) $T\rho$ problem for N_2 with and without VLE information, which is provided using Antoine's equation (see Appendix E) [46]. 160

55 (a) Constant temperature-density and (b) constant pressure-density diagrams for $\mathbf{X} = \mathbf{X}^* = [0.5, 0.5]$. Solid lines (—) in the legend indicate the reference solution extracted from Fig. 54. Dashed lines (- -) indicate the non-VLE solution, while symbol (▲) indicate the VLE solution. 161

56 (a) Constant temperature-density and (b) constant pressure-density diagrams for $\mathbf{X} = \mathbf{X}^{**} = [0.95, 0.05]$. Solid lines (—) in the legend indicate the reference solution extracted from Fig. 54. Dashed lines (- -) indicate the non-VLE solution, while symbol (▲) indicate the VLE solution. 161

57 a) 3D VLE diagram for the N_2/CH_4 mixture. The three iso-thermal VLE domes are the same represented also in (b) where dots represent data taken from [24]. Dashed and dotted lines indicate the iso-composition and the iso-baric conditions along with data is analyzed further. 165

58 Iso-composition results for the N_2/CH_4 mixture. Variables are organized column-wise with respect to the fixed amount of N_2 mole fraction. Variables labeled as $(\cdot) \times 10^x$ indicate that the represented data is multiplied by the factor 10^x. 167

59 Iso-baric results for the N_2/CH_4 mixture. Variables: β, Z and $d\beta/dp$. . . . 169

60 Iso-baric results for the N_2/CH_4 mixture. Variables: $d\beta/dT$, $dp/d\rho$ and c_p. 169

61 Iso-baric results for the N_2/CH_4 mixture. Variables: c, α_p and γ. 170

62 Partial molar volume (top row), enthalpy (mid row) and liquid-phase partial molar volume (bottom row) computed along iso-composition line $X_{N_2} = 0.5$ using the three different thermodynamic models. 171

63 Partial molar volume (top row), enthalpy (bottom row) and vapor-phase partial molar volume (bottom row) computed along the iso-baric line $p =$ 4 MPa using the three different thermodynamic models. 172

64 Dynamic viscosity μ, thermal conductivity λ and binary mass diffusion coefficient $\mathcal{D}_{N_2,CH_4}$ computed along the three iso-composition lines of Fig. 57(b) using the three different thermodynamic models. Data is organized column-wise with the labels (a), (b) and (c) indicating the column of the relative composition. 174

65 Dynamic viscosity μ, thermal conductivity λ and binary mass diffusion coefficient $\mathcal{D}_{N_2,CH_4}$ computed along the three iso-baric lines of Fig. 57(b) using the three different thermodynamic models. Data is organized column-wise with the labels (a) and (b) indicating the column of the relative pressure. . 175

66 (a) VLE diagram, (b) density profiles and (c) speed of sound profiles obtained with the VDW EoS for the iso-composition $X_{N_2} = 0.2$ case. Dotted data is taken from [24]. 177

67 (a) VLE diagram, (b) density profiles and (c) speed of sound profiles obtained with the RK EoS for the iso-composition $X_{N_2} = 0.2$ case. Dotted data is taken from [24]. 178

68 (a) VLE diagram, (b) density profiles and (c) speed of sound profiles obtained with the SRK EoS for the iso-composition $X_{N_2} = 0.2$ case. Dotted data is taken from [24]. 178

69 (a) VLE diagram, (b) density profiles and (c) speed of sound profiles obtained with the PR-RK EoS for the iso-composition $X_{N_2} = 0.2$ case. Dotted data is taken from [24]. 178

70 a) Iso-thermal and b) iso-baric VLE diagrams for CH_4/CO_2 mixture. 179

71 Iso-composition (left column) and iso-thermal (right column) results set # 1 (ρ, β, c_v. $\partial p/\partial \rho$ and $\partial \beta/\partial T$) for the CH_4/CO_2 mixture. 180

72 Iso-composition (left column) and iso-thermal (right column) results set # 2 (c_p, γ, $\partial p/\partial T$, κ_S and c) for the CH_4/CO_2 mixture. 180

73 Partial molar volume (top row) and enthalpy (bottom row) computed along iso-composition line $X_{CH_4} = 0.1$ using the three different thermodynamic models. 181

74 Liquid phase partial molar volume (top row) and vapor phase partial molar volume (bottom row) computed along iso-composition line $X_{CH_4} = 0.1$ using the three different thermodynamic models. 182

75 a) dynamic viscosity b) thermal conductivity and c) binary mass diffusivity for the CH_4/CO_2 mixture at $X_{CH_4} = 0.1$ using the three different thermodynamic models. 183

76 a) dynamic viscosity b) thermal conductivity and c) binary mass diffusivity for the CH_4/CO_2 mixture at $T = 220$ K using the three different thermodynamic models. 183

77 (a) VLE diagram, (b) density profiles and (c) speed of sound profiles obtained with the VDW EoS for the iso-thermal $T = 220$ K case. Dotted data is taken from [240]. The binary interaction parameters used in this case are $k_{ij} = [0.0, 0.135, 0.135, 0.0]$. 184

78 (a) VLE diagram, (b) density profiles and (c) speed of sound profiles obtained with the RK EoS for the iso-thermal $T = 220$ K case. Dotted data is taken from [240]. The binary interaction parameters used in this case are $k_{ij} = [0.0, 0.125, 0.125, 0.0]$. 185

79 (a) VLE diagram, (b) density profiles and (c) speed of sound profiles obtained with the SRK EoS for the iso-thermal $T = 220$ K case. Dotted data is taken from [240]. The binary interaction parameters used in this case are $k_{ij} = [0.0, 0.048, 0.048, 0.0]$. 185

80 (a) VLE diagram, (b) density profiles and (c) speed of sound profiles obtained with the PR-RK EoS for the iso-thermal $T = 220$ K case. Dotted data is taken from [240]. The binary interaction parameters used in this case are $k_{ij} = [0.0, 0.015, 0.015, 0.0]$. 186

81 Ternary VLE diagrams for $CH_4/N_2/C_2H_6$ mixture at different pressures and temperatures. Solid blue and dashed red lines indicate the dew and bubble point contours. Symbols are taken from [222]. 187

82 Ternary mixture relevant properties set # 1 (ρ, β and $\partial \beta/\partial T$) analyzed along the test line # 3 of Fig. 81 for $p = 4$ MPa and varying the temperature: $T = 140$ K (left column) and $T = 200$ K (right column). These correspond to the test line # 3 of Fig. 81(d) and Fig. 81(f) respectively. 188

83 Ternary mixture relevant properties set # 2 (c_p, γ and c) analyzed along the test line # 3 of Fig. 81 for $p = 4$ MPa and varying the temperature: $T = 140$ K (left column) and $T = 200$ K (right column). These correspond to the test line # 3 of Fig. 81(d) and Fig. 81(f) respectively. 188

84 Partial molar volume (top row) and enthalpy (bottom row) computed along test line # 3 of Fig. 81(d) ($T = 140$ K, $p = 4$ MPa) and Fig. 81(f) ($T = 200$ K, $p = 4$ MPa). 189

85 Investigation about the behavior of the phases densities for the $T = 200$ K, $p = 4$ MPa case of Fig. 82f. 189

86 a) dynamic viscosity b) thermal conductivity and c)-d)-e) mass diffusivity coefficients (in Hirschfelder-Curtiss form) for the $T = 140$ K, $p = 4$ MPa case, corresponding to Fig. 81(d) 190

87 a) dynamic viscosity b) thermal conductivity and c)-d)-e) mass diffusivity coefficients (in Hirschfelder-Curtiss form) for the $T = 200$ K, $p = 4$ MPa case, corresponding to Fig. 81(f) 191

88 a) VLE diagram of the Prudhoe gas at fixed composition (dotted data taken from [159]), b) speed of sound comparison along $p = 1$ MPa with different models: (—) VLE, (– –) no VLE, (...) frozen VLE, c) Iso-baric enthalpy (cfr. Fig. 88(a)), d) speed of sound along iso-baric lines (Fig. 88(a), dotted data taken from [159]), e) isentropic compressibility along iso-baric lines (Fig. 88(a), dotted data taken from [139]), f) specific heat and constant pressure (cfr. Fig. 88(a)). In b) and d) solutions are as follows: (—) VLE, (...) frozen VLE, (– –) Wood's equation [242]. In c) and f) solutions are as follows: (—) VLE, (...) frozen VLE, no VLE (– –). 192

89 a) Dynamic viscosity and b) thermal conductivity for the iso-thermal condition at $T = 200$. 194

90 a) Dynamic viscosity and b) thermal conductivity for the iso-baric condition at $p = 5$ MPa. 195

91 Adiabatic (H) and isochoric (V) mixing lines with and without VLE thermodynamics at $p = 5$ MPa conducted for (a) case 1 and (b) case 2. VLE dome is also superimposed with blue, dotted/dashed lines to indicate the bubble and dew curves, respectively. 201

92 Sequence of pressure p, phase fraction β, reduced temperature T^*, nitrogen mass fraction Y_{N_2}, mixing temperature T, density ρ, speed of sound c and specific heat at constant volume c_v for case 1. Sensitivity analysis on numerical scheme, thermodynamics and resolution is shown. 203

93 Sequence of pressure p, phase fraction β, reduced temperature T^*, nitrogen mass fraction Y_{N_2}, mixing temperature T, density ρ, speed of sound c and specific heat at constant volume c_v for case 2. Sensitivity analysis on numerical scheme, thermodynamics and resolution is shown. 205

94 Solution comparison of the 1D advection for Case 2 of Tab. 22. Results are carried out using the FC (MUSCL) scheme only with VLE thermodynamics. The different lines pertain to the different algorithms used to solve for VLE thermodynamics: (−) Fully analytical VLE model, (−) fully analytical VLE model with the use of the Newton method, (•) fully numerical VLE model, (▲) fully numerical VLE model with Newton method. Results show (a) the pressure field, (b) the phase fraction field and (c) the temperature field. . . 208

95 Solution comparison of the 1D advection for Case 2 of Tab. 22. Results are carried out using the QC (DF) scheme only with VLE thermodynamics. The different lines pertain to the different algorithms used to solve for VLE thermodynamics: (−) Fully analytical VLE model, (−) fully analytical VLE model with the use of the Newton method, (•) fully numerical VLE model, (▲) fully numerical VLE model with Newton method. Results show (a) the pressure field, (b) the phase fraction field and (c) the temperature field. Both PRHO and ERHO problems have fixed tolerances of $1e-5$ with $\lambda_0 = 0.9$, $\Delta T_{max} = 100$ K and $\Delta p_{max} = 0.5$ MPa. 209

96 Performances comparison on the simulations of Case 1 and Case 2 with all schemes, thermodynamic model and PRHO solution combinations. Pictures refer to the data reported in Tab. 23–Tab. 26. 211

97 Schematic of the 2D shock-droplet interaction with (a) relevant dimensions and (b) shock qualitative position at which data is analyzed. Top and bottom outlets, as well as the inflow are treated as subsonic conditions, whereas the right outlet is treated with the supersonic condition. 214

98 Representation of the bubble interface thermodynamic state during the four time instants analyzed. Symbols correspond to the different times and they are colored based on the local value of the phase fraction β. VLE domes at $T = 310.93$ K and $T = 488.4$ K are directly taken from Fig. 54. Symbols are scattered from the initial raw data with an interval of 7 to improve picture readability. This data is obtained by using the fully numerical PRHO problem solution for the temperature interface reconstruction for the VLE problem. 215

99 Time sequence contour snapshots of phase fraction β, pressure p and temperature T. This data is obtained by using the fully numerical PRHO problem solution for the temperature interface reconstruction for VLE. 216

100 From top to bottom: density, speed of sound, temperature and specific heat at constant pressure sequence conditional averages (with shaded) standard deviations for the four time instants. The results are for the VLE, non-VLE and frozen VLE models. 217

101 Illustration of the grid setup used for TML with relevant dimensions. Top stream is filled with C_6H_{14}, while bottom stream is filled with N_2. 222

102 Comparison of the normalized momentum thickness for all cases for different resolutions of the TML box: 32^3, 64^3 and 128^3. For these simulations VLE thermodynamics is always used. 223

103 Comparison of the normalized momentum thickness for the 64^3 cases with and without VLE. 223

104 Instantaneous contour plots of relevant quantities at $\tau = 10$ for (a)-(b) Case 1, (c)-(d) Case 2 and (e)-(f) Case 3. Figures refer to the hybrid, VLE simulations at 64^3 resolution for all cases. For the hybrid switch, only discrete values must be considered: white (zero) FC scheme activated, black (one) QC scheme activated. 224

105 Hybrid 64^3 real mixing curves for all three cases with and without VLE. . . 226

106 Effect of the resolution and VLE thermodynamics with pure FC scheme. . . 226

107 Effect of the resolution and VLE thermodynamics with pure QC scheme. . 227

108 Density contours for the (a) QC and (b) FC scheme at $\tau = 5$. 227

109 Pressure contours for the (a) QC and (b) FC scheme at $\tau = 5$. 227

110 Relevant properties computed along the mixing lines for the hybrid 64^3 case of Fig. 105 with and without VLE. (a) Density, (b) specific heat at constant volume, (c) specific heat at constant pressure, (d) speed of sound, (e) phase fraction, (f) dynamic viscosity, (g) thermal conductivity. Note that the triangles symbols for $\beta \in (0, 1)$ obtained for the non-VLE case are artificially obtained through the conditional average operation and indicates the fact that some points switch between pure liquid ($\beta = 0$) or pure gas ($\beta = 0$), such that their time- and conditional-averaged value is $0 < \beta < 1$. 230

111 Gibbs energy variation computed along the mixing lines for the hybrid 64^3 case of Fig. 105 with and without VLE. 231

112 Relevant properties computed along the mixing lines for the hybrid 64^3 case 3 of Fig. 105 with different combinations of VLE model, VLE derivatives model and PRHO model for temperature reconstruction. Mixture properties are showed along the mixing line. 233

113 Sketch of the generic spatial mixing layer (SML) setup. Main dimensions are indicated along with the boundary conditions. 237

114 Computational domain discretization: (a) broad view and (b) near splitter-plate zoomed view. 239

115 Time sequence for the VLE 2D SML. Snapshots show the density, phase fraction and speed of sound at the five time instants starting from the initial condition (top row). 240

116 Time sequence for the non-VLE 2D SML. Snapshots show the density, phase fraction and speed of sound at the five time instants starting from the initial condition (top row). Note that the phase fraction field has been intentionally left in the cell-center based solution in order to not artificially produce $\beta \in [0, 1]$ during the post-processing. 241

117 Time sequence of the five snapshots of the vorticity z component for the VLE (left column) and non-VLE (right column). Micro-mixing generated by the non-linear coupling between VLE thermodynamics and fluid-mechanics enhances vortex breakdown. This is accompanied by a vorticity field that is both positive and negative along the vortex edge. 243

118 First set of properties collected across the reference abscissa s at the vortex leading edge (*cf.* Fig. 161) for both simulations: (a) C_6H_{14} mass diffusion coefficient, (b) N_2 mass diffusion coefficient, (c) dynamic viscosity, (d) density, (c) speed of sound and (d) thermal conductivity. Colors refer to the time instant (indicated on the axis). Solid lines indicate the VLE solution, while dashed lines indicate the non-VLE solution. 244

119 Second set of properties collected across the reference abscissa s at the vortex leading edge (*cf.* Fig. 161) for both simulations: (a) temperature vs N_2 mass fraction (mixing line), (b) temperature, (c) temperature gradient, (d) phase fraction, (c) C_6H_{14} distribution (d) C_6H_{14} gradient. Colors refer to the time instant (indicated on the axis). Solid lines indicate the VLE solution, while dashed lines indicate the non-VLE solution. 245

120 Joint PDF between (a) n-hexane mass fraction and temperature and (b) speed of sound and temperature. Data refers to the line segment extracted for the VLE simulation at vortex leading edge. 246

121 Joint PDF between (a) n-hexane mass fraction and temperature and (b) speed of sound and temperature. Data refers to the line segment extracted for the non-VLE simulation at vortex trailing edge. 246

122 Speed of sound versus temperature for different amounts of hexane in the mixture. Symbols are also colored by the phase fraction to indicate the presence or absence of VLE. For clarity, the injection point for C_6H_{14} is also indicated. 247

123 Lewis number calculated across the reference abscissa s at the vortex leading edge (*cf.* Fig. 161). 249

124 Time-averaged density fields for the (a) VLE and (b) non-VLE case. 251

125 Time-averaged temperature fields for the (a) VLE and (b) non-VLE case. . 251

126 (a) Density contour lines extracted from the time-averaged field at the values of $\rho_{\min} = 120\,kg/m^3$ (N_2 side - bottom) and $\rho_{\max} = 380\,kg/m^3$ (C_6H_{14} side - top), (a) temperature contour lines extracted from the time-averaged field at the values of $T_{\min} = 320\,K$ (N_2 side - bottom) and $T_{\max} = 450\,kg/m^3$ (C_6H_{14} side - top), (c) N_2 mass fraction contour lines extracted from the time-averaged field at the value of 0.5. 252

127 Tree diagram of the main differences between the class of detailed/skeletal mechanism and the quasi-global/global. 255

128 Relevant results collected for the comparison between the WD [239] global mechanism and the GRI [206] detailed mechanism at 13.3 MPa. Results include: (a) adiabatic flame temperature, (b) ignition delay versus mixture initial temperature for $\phi = 1$, (c) temperature history for ignition delay at $T_0 = 1300$ K, (d) temperature history for ignition delay at $T_0 = 1700$ K, (e) temperature distribution within the 1D diffusion flame for strain rate of 500 s^{-1}, (f) temperature distribution within the 1D diffusion flame for strain rate of 15000 s^{-1}, (g) species distribution within the 1D diffusion flame for strain rate of 500 s^{-1}, (h) species distribution within the 1D diffusion flame for strain rate of 15000 s^{-1}. 258

129 VLE diagram for the CH_4/O_2 combination. Dashed black line indicates the operating condition for the present TML case. 261

130 Initial conditions used for the 3D TML: velocity component fields. 263

131 Initial conditions used for the 3D TML: burnt solution. 263

132 Non-reacting fields: XY plane. (a) Temeprature, (b) compressibility factor and (c) phase-fraction. 264

133 Non-reacting fields: XZ plane. (a) Temeprature, (b) compressibility factor and (c) phase-fraction. 264

134 Non-reacting field: scatter plot of the temperature data. 265

135 Methane (a) and carbon dioxide (b) reaction rates computed with explicit time integration. 266

136 Methane (a) and carbon dioxide (b) reaction rates computed with implicit time integration using DVODE [20]. 266

137 Characteristic chemical time scales associated with each reaction step listed in Eq. (5.5.1). 267

138 Relevant field variables obtained for the VLE (top) and non-VLE (bottom) solutions on plane YZ at time $t_1 = 0.21\,\mu$s 269

139 Relevant field variables obtained for the VLE (top) and non-VLE (bottom) solutions on plane YZ at time $t_2 = 10.18\,\mu$s 269

140 Relevant field variables obtained for the VLE (top) and non-VLE (bottom) solutions on plane YZ at time $t_3 = 19.30\,\mu$s 270

141 Relevant field variables obtained for the VLE (top) and non-VLE (bottom) solutions on plane YZ at time $t_4 = 28.22\,\mu$s 270

142 Relevant field variables obtained for the VLE (top) and non-VLE (bottom) solutions on plane YZ at time $t_5 = 37.09\,\mu$s 271

143 Relevant field variables plotted along the TML centerline for the same time instants indicated in Figs. (138)–(142). Vorticity plot in Fig. (f) is limited to the first and last time instants in order to achieve a better picture quality. Variables are: (a) density, (b) temperature, (c) speed of sound, (d) thermal conductivity, (e) phase fraction, (f) vorticity x component. 272

144 3D TML domain subdivision in sectors. 273

145 Sector-averaged variables as function of time. Only sectors number 3, 8 and 9 are showed in order to improve the picture clarity. Other sector-averages showed similar behavior. Variables are: (a) density, (b) temperature, (c) speed of sound, (d) thermal conductivity, (e) dynamic viscosity, (f) velocity y component. 274

146 Temperature-Oxygen mole fraction diagram for the top side of the TML for $Y_{CO_2} = 0.0012$. The color map refers to the phase fraction field as the amount of oxygen and temperature are varied. Dew line is represented with a white dashed line at approximately constant $X_{O_2} = 0.00379$. Bubble line is represented with a green dashed curve on the right side of the picture (*cf.* the value of the β field). Blue and black lines indicate the isochoric and adiabatic mixing models. Specifically: blue line (. . .) indicates the isochoric mixing with $T_{H_2O} = T_{CO_2} = 2000$ K, black line (. . .) indicates the adiabatic mixing with $T_{H_2O} = T_{CO_2} = 2000$ K, blue line (.-) indicates the isochoric mixing with $T_{H_2O} = T_{CO_2} = 2500$ K, black line (.-) indicates the adiabatic mixing with $T_{H_2O} = T_{CO_2} = 2500$ K. In all cases the initial oxygen temperature is set to 115 K. Squared blue symbols refer to the data directly extracted from the TML. 275

147 Temperature-methane mole fraction diagram for the bottom side of the TML. The mixture is considered binary with water only. The color map refers to the phase fraction field as the amount of methane and temperature are varied. Dew line is represented with a white dashed line at approximately constant $X_{CH_4} = 0.00753$. Bubble line is represented with a green dashed curve on the right side of the picture (*cf.* the value of the β field). Blue and black lines indicate the isochoric and adiabatic mixing models. Specifically: blue line (. . .) indicates the isochoric mixing with $T_{H_2O} = 2000$ K, black line (. . .) indicates the adiabatic mixing with $T_{H_2O} = 2000$ K, blue line (.-) indicates the isochoric mixing with $T_{H_2O} = 2500$ K, black line (.-) indicates the adiabatic mixing with $T_{H_2O} = 2500$ K. In all cases the initial methane temperature is set to 263 K. Squared blue symbols refer to the data directly extracted from the TML. 276

148 Relevant flow field properties computed at the evolved non-reacting solution, before the ignition. The phase fraction field (a) shows no VLE formation, in agreement with both 0D thermodynamics of Fig. 129 and the TML results of Figs. (132)–(134). 279

149 Field variables extracted from the VLE simulation at three different time instants after which the flame was extinguished. 282

150 Field variables extracted from the non-VLE simulation at three different time instants after which the flame was extinguished. 283

151 Phase fraction, density and mixture fraction fields at $t = 51\,\mu s$ for the VLE (top) and non-VLE (bottom) models. 284

152 Iso-density (top) at 700 kg/m^2 and iso-mixture fraction (bottom) at stoichiometric value of 0.2 comparison between the two thermodynamic models at two different time instants. 285

153 Ternary VLE diagrams between $CH_4/O_2/H_2O$ at $p = 13.0$ MPa for $Y_{CO_2} = 0.002$. Simulation data is superimposed with blue triangles. 287

154 Illustration of the Maxwell method through the "equal area" rule. (a) Three different isotherms shown for N_2: sub-critical, critical and super-critical. (b) sub-critical isotherm sliced at the corresponding saturation pressure $p_s(T)$ to create two equal areas in the VLE region. 322

155 Sequence of pressure p, phase fraction β, reduced temperature T*, nitrogen mass fraction Y_{N_2}, mixing temperature T, speed of sound c and specific heat at constant volume c_v for case 1 obtained with the fully-analytical PRHO model for the temperature interface reconstruction. Sensitivity analysis on numerical scheme, thermodynamics and resolution is shown. 383

156 Sequence of pressure p, phase fraction β, reduced temperature T*, nitrogen mass fraction Y_{N_2}, mixing temperature T, speed of sound c and specific heat at constant volume c_v for case 2 obtained with the fully-analytical PRHO model for the temperature interface reconstruction. Sensitivity analysis on numerical scheme, thermodynamics and resolution is shown. 384

157 Representation of the bubble interface thermodynamic state during the four time instants analyzed. Symbols correspond to the different times and they are colored based on the local value of the phase fraction β. VLE domes at $T = 310.93$ K and $T = 488.4$ K are directly taken from Fig. 54. Symbols are scattered from the initial raw data with an interval of 7 to improve picture readability. This picture refers to the simulation run with the fully analytical PRHO model for temperature interface reconstruction. 385

158 Time sequence contour snapshots of phase fraction β, pressure p and temperature T. This picture refers to the simulation run with the fully analytical PRHO model for temperature interface reconstruction. 386

159 From top to bottom: density, speed of sound, temperature and specific heat at constant pressure sequence conditional averages (with shaded) standard deviations for the four time instants. The results are for the VLE, non-VLE and frozen VLE models. This picture refers to the simulation run with the fully analytical PRHO model for temperature interface reconstruction. . . . 387

160 Relevant properties computed along the mixing lines for the hybrid 64^3 case 3 of Fig. 105 with the non-VLE model and different PRHO model for temperature reconstruction. Mixture properties are showed along the mixing line. Similarly to what explained for Fig. 110, the $\beta \in (0, 1)$ values are artificially obtained because of the time- and conditional-average operation. 388

161 Identification of the reference line taken to study the vortex leading edge. . 390

162 Identification of the reference line taken to study the vortex trailing edge. . 391

163 First set of properties collected across the reference abscissa s at the vortex trailing edge (*cf.* Fig. 162) for both simulations: (a) C_6H_{14} mass diffusion coefficient, (b) N_2 mass diffusion coefficient, (c) dynamic viscosity, (d) density, (c) speed of sound and (d) thermal conductivity. Colors refer to the time instant (indicated on the axis). Solid lines indicate the VLE solution, while dashed lines indicate the non-VLE solution. 392

164 Second set of properties collected across the reference abscissa s at the vortex trailing edge (*cf.* Fig. 162) for both simulations: (a) temperature vs N_2 mass fraction (mixing line), (b) temperature, (c) temperature gradient, (d) phase fraction, (c) C_6H_{14} distribution (d) C_6H_{14} gradient. Colors refer to the time instant (indicated on the axis). Solid lines indicate the VLE solution, while dashed lines indicate the non-VLE solution. 393

165 Joint PDF between (a) n-hexane mass fraction and temperature and (b) speed of sound and temperature. Data refers to the line segment extracted for the VLE simulation at vortex trailing edge. 394

166 Joint PDF between (a) n-hexane mass fraction and temperature and (b) speed of sound and temperature. Data refers to the line segment extracted for the non-VLE simulation at vortex trailing edge. 394

167 Lewis number calculated across the reference abscissa s at the vortex trailing edge (*cf.* Fig. 162). 394

168 N_2 mass fractions profiles extracted at several x locations downstream the SML. 395

169 Speed of sound profiles extracted at several x locations downstream the SML. 395

170 Density profiles extracted at several x locations downstream the SML. . . . 395

171 Temperature profiles extracted at several x locations downstream the SML. 395

172 Dynamic viscosity profiles extracted at several x locations downstream the SML. 396

173 One-dimensional laminar diffusion flame at 13.3 MPa between CH_4 and O_2 for a strain rate of $\xi = 50\ s^{-1}$. (a) Temperature and (b) major species distribution across the flame width. 396

174 Relevant field variables obtained for the VLE (top) and non-VLE (bottom) solutions on plane XZ at time $t_1 = 0.21\,\mu s$ 397

175 Relevant field variables obtained for the VLE (top) and non-VLE (bottom) solutions on plane XZ at time $t_2 = 10.18\,\mu$s 397

176 Relevant field variables obtained for the VLE (top) and non-VLE (bottom) solutions on plane XZ at time $t_3 = 19.30\,\mu$s 398

177 Relevant field variables obtained for the VLE (top) and non-VLE (bottom) solutions on plane XZ at time $t_4 = 28.22\,\mu$s 398

178 Relevant field variables obtained for the VLE (top) and non-VLE (bottom) solutions on plane XZ at time $t_5 = 37.09\,\mu$s 399

179 Temperature-Oxygen mole fraction diagram for the top side of the TML for (a) $Y_{CO_2} = 0.0001$, (b) $Y_{CO_2} = 0.0024$ and (c) $Y_{CO_2} = 0.0036$. The color map refers to the phase fraction field as the amount of oxygen and temperature are varied. Dew line is represented with a white dashed line at approximately constant $X_{O_2} = 0.00379$. Bubble line is represented with a green dashed curve on the right side of the picture (*cf.* the value of the β field). Blue and black lines indicate the isochoric and adiabatic mixing models. Specifically: blue line (. . .) indicates the isochoric mixing with $T_{H_2O} = T_{CO_2} = 2000$ K, black line (. . .) indicates the adiabatic mixing with $T_{H_2O} = T_{CO_2} = 2000$ K, blue line (.-) indicates the isochoric mixing with $T_{H_2O} = T_{CO_2} = 2500$ K, black line (.-) indicates the adiabatic mixing with $T_{H_2O} = T_{CO_2} = 2500$ K. In all cases the initial oxygen temperature is set to 115 K. Squared blue symbols refer to the data directly extracted from the TML. 400

180 Iso-density (top) at 350 kg/m^2 comparison between the two thermodynamic models at two different time instants. 401

181 Two dimensional density color maps for (a) N_2, (b) O_2 and (c) CH_4 displaying the Widom line in dashed white color departing from the species critical point (red dot). 404

LIST OF SYMBOLS OR ABBREVIATIONS

CFD Computational Fluid Dynamics.

CPG Calorically Perfect Gas.

CSP Corresponding States Principle.

DF Double-Flux.

DNS Direct Numerical Simulation.

EoS Equation of State.

ERHO Thermodynamic problem that involves the calculation of temperature and pressure out of internal energy, density and composition (also indicated as $E\rho$ problem).

FC Fully conservative scheme.

FDS Flux-Difference Splitting.

GCEoS Generalized-Cubic Equation of State.

HLLC Harten-Lax-van Leer with Contact.

IG Ideal Gas.

IK Irving-Kirkwood.

LOX Liquid Oxygen.

MR Mixing rule.

MUSCL Monotone Upstream-centered Schemes for Conservation Laws.

NIST National Institute of Standards and Technology.

PR EoS Peng-Robinson Equation of State.

PRHO Thermodynamic problem that involves the calculation of temperature out of pressure, density and composition (also indicated as $p\rho$ problem).

QC Quasi conservative scheme.

RG Real Gas.

RK EoS Redlich-Kwong Equation of State.

SRK EoS Soave-Redlich-Kwong Equation of State.

TML Temporal Mixing Layer.

TPG Thermally Perfect Gas.

TRHO	Thermodynamic problem that involves the calculation of pressure out of temperature, density and composition (also indicated as $T\rho$ problem).
TVD	Total Variation Diminishing.
VLE	Vapor-Liquid Equilibrium.
k_B	Boltzmann's Constant, 1.38065×10^{-23} J.K^{-1}.
R_u	Universal Gas Constant, 8.31451 J.mol^{-1}.K^{-1}.
α_p	$\frac{1}{v}\left(\frac{\partial v}{\partial T}\right)_p = -\frac{1}{\rho}\left(\frac{\partial \rho}{\partial T}\right)_p$: Isobaric expansivity, K^{-1}.
β	Phase fraction, dimensionless.
$\boldsymbol{\zeta}$	Generic phase composition vector: $\mathbf{x}$ for liquid and $\mathbf{y}$ for vapor, dimensionless.
μ^{dp}	Dipole moment, debyes.
η	Generic phase index: L for liquid and V for vapor, dimensionless.
κ_s	Isentropic compressibility, Pa^{-1}.
κ_T	$-\frac{1}{v}\left(\frac{\partial v}{\partial p}\right)_T = \frac{1}{\rho}\left(\frac{\partial \rho}{\partial p}\right)_T$: Isothermal compressibility, Pa^{-1}.
λ	Thermal conductivity, W.(m.K)$^{-1}$.
μ	Dynamic viscosity, kg.m^{-1}.s^{-1} or chemical potential, J.mol^{-1}.
ω	Acentric factor, dimensionless.
ϕ_i	Fugacity coefficient of the i-th component in the mixture, dimensionless.
ρ	Density, kg.m^{-3}.
τ	Viscous stress, Pa.
i	Species i specific quantity/index.
k	Species k specific quantity/index.
0	Low-pressure quantity.
A	Mixture molar Helmholtz free energy, J.mol^{-1}.
c_p	Specific heat at constant pressure, J.kg^{-1}.K^{-1}.
C_p	Molar heat at constant pressure, J.mol^{-1}.K^{-1}.
C_v	Molar specific heat at constant volume, J.mol^{-1}.K^{-1}.
c_v	Specific heat capacity at constant volume, J.kg^{-1}.K^{-1}.
$\mathcal{D}_{A,B}$	Binary diffusion coefficient between species A and B, m^2.s^{-1}.
$\mathcal{D}_{k,m}$	Pseudo binary diffusion coefficient between species k and the mixture, m^2.s^{-1}.

E	Internal energy, J.mol^{-1}.
e	Massic internal energy, J.kg^{-1}.
e_T	Massic total energy = massic internal energy + massic kinetic energy, J.kg^{-1}.
E^V	Molar internal energy in the vapor phase, J.mol^{-1}.
f_i	Fugacity of the i-th component in the mixture, Pa.
G	Mixture molar Gibbs free energy, J.mol^{-1}.
γ	Specific heats ratio, dimensionless.
H	Mixture molar enthalpy, J.mol^{-1}.
H_k	Partial molar enthalpy of species k, J.mol^{-1}.
h_k	Partial massic enthalpy of formation of species k, J.kg^{-1}.
j_k	Mass diffusion flux for species k, W.m^{-2}.
M	Mixture Molar Weight, kg.mol^{-1}.
Ma	Mach number, dimensionless.
$\overline{M}$	Mass, kg.
M^L	Mixture Molar Weight in the liquid phase, kg.mol^{-1}.
M^V	Mixture Molar Weight in the vapor phase, kg.mol^{-1}.
MW	Mixture Molecular Weight, g.mol^{-1} or kg.kmol^{-1}.
N	Mixture total number of moles, mol.
N_i **or** N_k	i-th (or k-th) species mole number, mol.
N^L	Mixture number of moles in the liquid phase, mol.
N_R	Number of reactions in the system, dimensionless.
N_s	Number of species in the system, dimensionless.
ν'_{ik}	Stoichiometric coefficient in the reaction i for the species k in the forward direction, mol.
ν''_{ik}	Stoichiometric coefficient in the reaction i for the species k in the reverse direction, mol.
N^V	Mixture number of moles in the vapor phase, mol.
p	Pressure, Pa.
p_r	Reduced pressure, dimensionless.
Ψ	Generic molar-based intensive property.

$\overline{\Psi}$	Generic extensive property corresponding to Ψ.
q	Heat diffusion flux, W.m^{-2}.
S	Mixture molar entropy, J.K^{-1}.mol^{-1}.
T	Temperature, K.
u	Velocity, m.s^{-1}.
V	Molar volume, m^3.mol^{-1}.
$\overline{V}$	Volume, m^3.
$\mathcal{V}_{i,k}$	Diffusion velocity of species k in the direction i, m.s^{-1}.
$[X]_k$	Concentration of species k, mol.m^{-3}.
X_i	Mole fraction of species i, dimensionless.
x_i	Mole fraction of species i in the liquid phase, dimensionless.
Y_i	Mass fraction of species i, dimensionless.
y_i	Mole fraction of species i in the vapor phase, dimensionless.
Y_k	Mass fraction of species k, dimensionless.
Z	Compressibility factor, dimensionless.

SUMMARY

Motivated by the complex physics of multi-component mixtures in strongly non-ideal, real-gas (RG) conditions reported in the field of chemical engineering, this work aims to address the behavior of multi-phase thermodynamics from a broader point of view. The focus is to evaluate the differences, as well as the possible sources of errors that would arise in a computational fluid-dynamics (CFD) simulation when conventional single-phase and multi-phase equilibrium RG thermodynamics are employed: an area of research that despite the active interest in many communities (especially CFD), has not been completely understood.

Knowledge of the effects that multi-phase RG thermodynamics with the assumption of vapor-liquid equilibrium (VLE) can have on a flow dynamics is important because it establishes the relevance of the fully coupled CFD-VLE solver. In fact, this relevance may go beyond the stand-alone calculation of a multi-phase state, providing important insights about the physics that may not be captured if the single-phase assumption is invoked.

This work provides an extensive study of RG mixtures from a physical and numerical point of view. The difficulties associated with their modeling are discussed in detail and solutions are provided accordingly. Emphasis is given to the occurrence and suppression of numerical noise in form of pressure oscillations that can pollute the simulation to the point that it cannot be performed. Extension of existing models to eliminate such problem is achieved by incorporating the effects of VLE thermodynamics in a consistent manner, ultimately forming a new and robust tool to investigate the physics further.

The resulting model is applied to non-reacting and reacting flows in canonical setups where emphasis is devoted to the discussion of the differences and sources of errors that would occur if this multi-phase behavior is not taken into account. Results show that the different thermodynamic states reached by this advanced model can have an impact on the flow physics, especially in a non-reacting (or more in general cold) regime. In particular,

the strong non-linear coupling between the VLE thermodynamics and the transport properties is identified as a key element of difference with respect to the single-phase model counterpart. These differences manifest into the occurrence of localized changes in the fluid properties (such as density) that affect the flow-field in their vicinity, causing visible discrepancies even when time-averaging is performed.

Concurrently, results obtained on the reacting side and carried out (for the first time) with finite-rate kinetics suggest that any VLE formation between the products and the reactants may be considered of minor importance. The latter conclusion is supported by the analysis conducted on the multi-phase field which appears to be largely composed of the vapor solution, as expected, hence limiting the analogous effect observed the non-reacting system where a broader range of phase-separation appears instead.

Chapter I

INTRODUCTION

1.1 Scope and motivation

Real-gas (RG) thermodynamics represents one of the most important topics in computational physics. Evidence of this can be found in many examples of published works ranging from the CO_2 processing [6, 18, 100], to heat exchanger design and cooling [203, 71, 199, 161, 241], to Earth and planetary exploration [21, 217], to pharmaceutical studies [198] and to fluid mechanics and combustion applications [134, 125, 89, 192, 229, 245, 226].

RG thermodynamics is so important because of the operating conditions usually found in the aforementioned fields. These are very far from ideal in terms of both pressure and temperature therefore their thermodynamic representation cannot be accurately achieved by the common ideal-gas (IG) model.

For instance, power generation cycles based on super-critical CO_2 constitute a significant area of research in the energy community. Super-critical carbon dioxide contains the concrete potential to replace the commonly used steam-based generators because of its higher density obtained with high-pressure and moderately high-temperature conditions ($\sim$ 30 MPa or above, 700° C) that can be translated into a volume reduction of many plant hardware components (such as turbines) [16], ultimately reducing the cost and theoretically improve the production efficiency by roughly 50% [210]. Other important applications of super-critical CO_2 systems include its recycling through oxy-fuel combustion that can drastically reduce emissions [74].

The important role of RG thermodynamics has been also highlighted in the context of engine design and optimization, including diesel engines [169, 89], gas-turbines engines [172] and rockets [125, 116, 229] because of their range of operating conditions. All of these applications operate at high (20-50 bar for gas turbines, 50-250 bar for rockets)[60, 213] or very high (1000-2000 bar for diesel engines) [68] pressures to achieve higher machine

performances: high compression ratio in the case of diesel engines and high efficiency/specific impulse in the case of gas turbines and rockets. Likewise, chemical processes involving separation, precipitation and storage require the use of more sophisticated thermodynamic and transport models [49].

Since the improvements of large computing systems, computational fluid dynamics (CFD) has represented an important portion of the research in the field of RG mixing and combustion, where the role of non-ideal thermodynamics and transport has been constantly highlighted to overcome the limitations of the IG counterpart through the study of single- and multi-component jet configurations [192, 136, 89] or more canonical applications [146, 82, 245]. Despite the fact that RG, super-critical thermodynamic models have been developed for three decades and the need of RG thermodynamics has been clearly established by the comparison with the IG model, less attention has been dedicated to the differences between single- and multi-phase states within the RG model itself. As a result, a major aspect has not been extensively incorporated so far: the role of multi-phase conditions in RG systems.

The importance of such complex thermodynamic states occurring at non-ideal conditions has been already identified in many of the applications cited above. Diesel engines are likely to show this behavior due to the combination of high-pressure, ambient (low) temperature and multi-component mixing characterized by heavy hydrocarbons at the injection [170, 169]. Chemical processes involving bio-diesel [198, 190], oil processing [58], refrigeration systems [88] and CO_2 separation through absorption [8] for current and future power plants are only few additional examples in which multi-phase RG thermodynamics has a strong impact on the physics. Even more interesting, the role of multi-phase conditions has been proposed in a recent work [98] as a possible explanation of the Venus' atmosphere temperature profile measured by the VeGa-2 probe in 1985. Regarding rockets and gas turbines, there is no clear evidence of this multi-phase phenomenon however the non-ideal conditions at which they operate (high pressure, low temperature at injection) and the fact that they are characterized by multi-component mixing prior to combustion, also suggests the potential occurrence of this multi-phase behavior. These applications clearly pose

fundamental questions in the physics of RG mixtures, immediately followed by modeling challenges associated with the simulation of such systems when fluid-mechanics with or without combustion are also taken into account. Are there any differences between the single-phase and the multi-phase RG thermodynamics from a microscopic and macroscopic point of view and what are the valid mathematical and numerical models that can represent these systems under these conditions?

This evidently broad range of applications of RG thermodynamics with multi-phase effects therefore poses interesting challenges from both a scientific and an engineering point of views: correct understanding of the physics behind this problem can help the development of the numerical and computational tools to perform high-fidelity simulations with the ultimate goal to improve the design process and the system performances. Because of these reasons, the present work aims to advance this topic by leveraging the current state-of-the art information on RG thermodynamics, with a more in-depth analysis and development of new theoretical and numerical tools and their coupling with CFD. The latter part has been found particularly lacking in the literature and therefore it forms an important contribution of this work.

1.2 Background

The following two sub-sections introduce the thesis work by providing definitions and descriptions of the topic, highlighting the main questions that will be expanded later through the literature review and the objectives statement. Each of the physical and numerical concepts introduced here is addressed in depth in the following chapters.

1.2.1 Preliminaries on real gas thermodynamics

The definition of a "real-gas" (RG) can denote different meanings in gas dynamics. Generally speaking, it represents a thermodynamic state that is far from an "ideal-gas" (IG) case. This IG case presents the following peculiar characteristics: molecules have zero volume and do not exert interaction forces among them with the exception of conservative elastic forces occurring during their collisions [87].

Using these two main assumptions, the following state relations describing the link among the main thermodynamic variables can be obtained: Eq. (1.2.1) which represents the "standard" equation of state (EoS) and Eq. (1.2.2) which represents the "thermal" EoS:

$$pV = R_u T \tag{1.2.1}$$

$$E = C_v T \tag{1.2.2}$$

where p is the pressure, V is the molar volume, R_u is the universal gas constant, T is the temperature, E is the molar internal energy, C_v is the molar heat capacity at constant volume and is assumed constant. In Eq. (1.2.2), the reference energy is taken to zero at the absolute zero, for convenience. The above assumptions are typically used to denote a gas as "thermally" and "calorically" perfect.

When RG thermodynamic effects are investigated in the context of high-temperatures, more advanced description of the specific heat at constant volume C_v is required in the thermal EoS, particularly in the case when the molecule shape and structure are more complex than a simple "point mass". In this case, even though the standard equation of state remains that of Eq. (1.2.1), the different description of C_v through the inclusion of rotational and vibrational (and more) modes to store energy, modifies Eq. (1.2.2) only. Some of these modes are usually taken into account by employing temperature-dependent functions of C_v[1] in form of polynomials [123, 80], whereas more rigorous and complete approaches are available by employing the partition function concept [87]. As a result, this type of RG behavior is taken into account even when the IG EoS in the form of Eq. (1.2.1) is used.

However, in this work, the RG definition takes one step forward that includes the above. Inter-molecular forces exerted among molecules are considered beyond elastic collisions and the volume occupied by the molecule at a given pressure and temperature is considered finite (hence the point-mass assumption is no longer used).

These two improvements on the molecules physical representation have an impact on both the standard and the thermal EoS. Specifically, the fact that the molecules must have a different (realistic) volume at a given pressure and temperature modifies the standard EoS,

[1]Typically electronic modes are neglected

whereas the fact that inter-molecular forces are now accounted have a result on the work done by one molecule on another, hence affecting the mutual energy transfer. This has an impact on the form of the thermal EoS.

Depending on the magnitude of these inter-molecular forces, the fluid may assume different phases: the liquid, the vapor/gas or the so-called super-critical. These are schematically represented in Fig. 1, where the density phase diagram of a single component (oxygen) is represented as a function of pressure and temperature (p-T diagram). For each species, the *critical point* can be identified with the corresponding critical values of pressure p_c and temperature T_c (red dot in Fig. 1). The sub-critical regime occurs at pressures $p < p_c$ and is characterized by the liquid and vapor/gas phase. On the other hand the super-critical regime occurs at pressures $p > p_c$ and is characterized by a single phase called "super-critical" phase. This, depending on the value of the temperature, is commonly split into two "pseudo-phases" called *compressibile liquid* for $T < T_c$ and super-critical fluid for $T > T_c$. The important thing to underline is the presence of a sharp transition between the liquid and the vapor/gas phase at the sub-critical regime, whereas a smooth transition, called pseudo-boiling line [148] occurs at the super-critical state. This difference has an enormous impact on the modeling and numerical aspects of the problem which are going to be discussed later.

During an injection process, depending on the values of pressure and temperature, "super-critical injection" and "sub-critical injection" can be also used to denote the thermodynamic state at which the species (or the mixture) are injected. A "trans-critical injection" instead denotes the transformation that a fluid, initially in its compressible liquid state, becomes super-critical by crossing the pseudo-boiling line [243, 142]. From the density color-map showed in Fig. 1 it is apparent that properties can vary significantly depending on the thermodynamic regime, thus it is important to correctly represent them.

Early experimental work in 1820 of Cagniard de la Tour [41] begun to establish the foundations regarding the definition of a "fluid" beyond those of liquid and gas that were common from the direct experience. Thanks to his work [41], an enormous amount of experiments

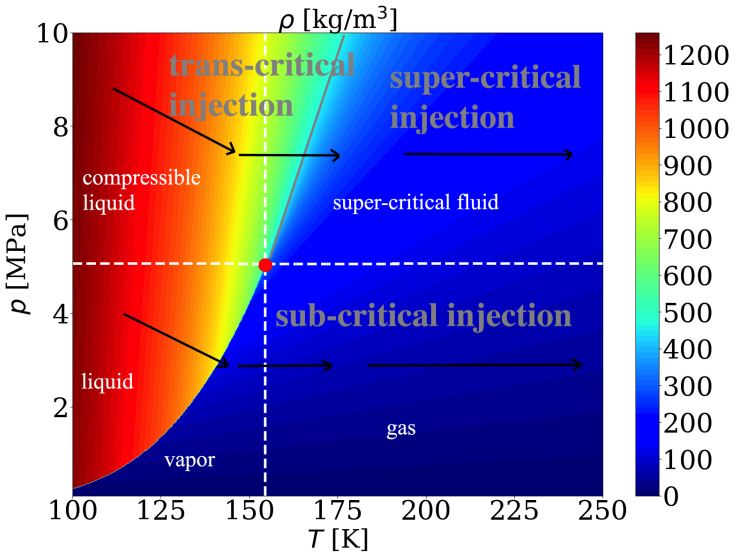

Figure 1: Phase diagram of oxygen in the $p-T$ space. The black dot represents the critical point at the intersection of the long-dash lines for the critical temperature and pressure. The grey line is the pseudo-boiling line [148] or Widom line [200] and corresponds to the region of maximum specific heat at constant pressure (*cf.* Chap. R). The density is represented by the colored contours in the background.

were followed for nearly 50 years, recently reported in the work of Berche *et al.* [14], that effectively outlined the definition of what we commonly indicate as "phase diagram" today, that is the domain of existence of different states (or phases) of a pure component (such as that illustrated in Fig. 1).

Later, this work was used by Van der Waals in 1873 when he introduced the concept of the compressibility factor Z [230] along with the concept of the *Corresponding States Principle* (CSP), stating that when pressure p and temperature T are normalized by their corresponding critical values, the resulting compressibility factor Z shows a sort of universal trend, no matter the selected species.

This concept is shown in Fig. 2 for some pure substances, underlining the fact that a generalized compressibility chart can be outlined based on experimental values of only few species. This knowledge was particularly useful in the past, where some strongly non-ideal conditions were not possible to be reached in the experiments with the available technology. Additional experiments showed that, although this CSP was a powerful tool to investigate

pure substances in non-ideal conditions, some of them did not show such self-similar behavior, but additional non-linear dependencies of the compressibility factor were required to be modeled as the molecule "complexity" was increased, especially near the critical point. This led to the introduction of an additional constant named the *acentric factor* ω by Pitzer [160] in 1955 which provides a measure of the non-sphericity of the molecules. With

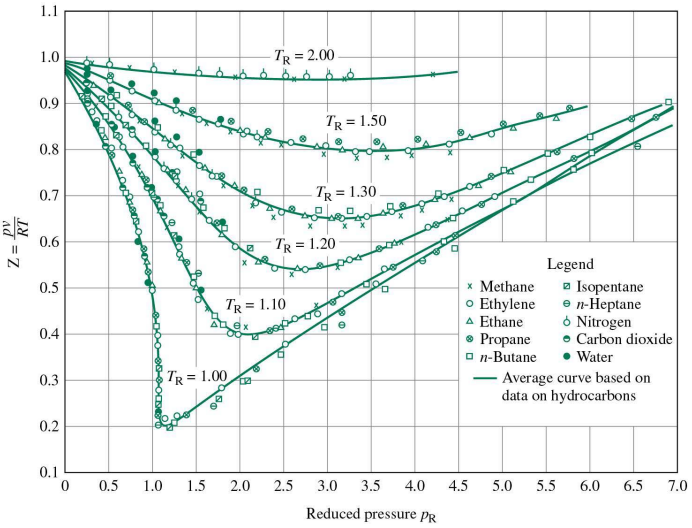

Figure 2: Generalized compressibility chart. (Adapted from [182])

the species-dependent, critical quantities properly defined, a more rigorous discussion of the pure component phase diagram is introduced next. Figures 3 and 4 show relevant 2D contour maps and corresponding isobaric lines at different temperatures for N_2 and C_6H_{14}, respectively. These two species are used in Chap. 5. The two-dimensional maps show the densities and the specific heat capacities, where two different isobaric lines are conventionally taken to show the different behavior of the pure component properties as the pressure and temperature are varied. The critical point is indicated by the red dot in both diagrams. With reference to the nomenclature introduced in Fig. 1, one can observe that in the subcritical regime, the classical liquid and gas/vapor phases are observed. These are separated by the boiling line, which consists of a subset of points in the thermodynamic space where all the properties undergo to a sharp jump. This jump physically corresponds to the energy

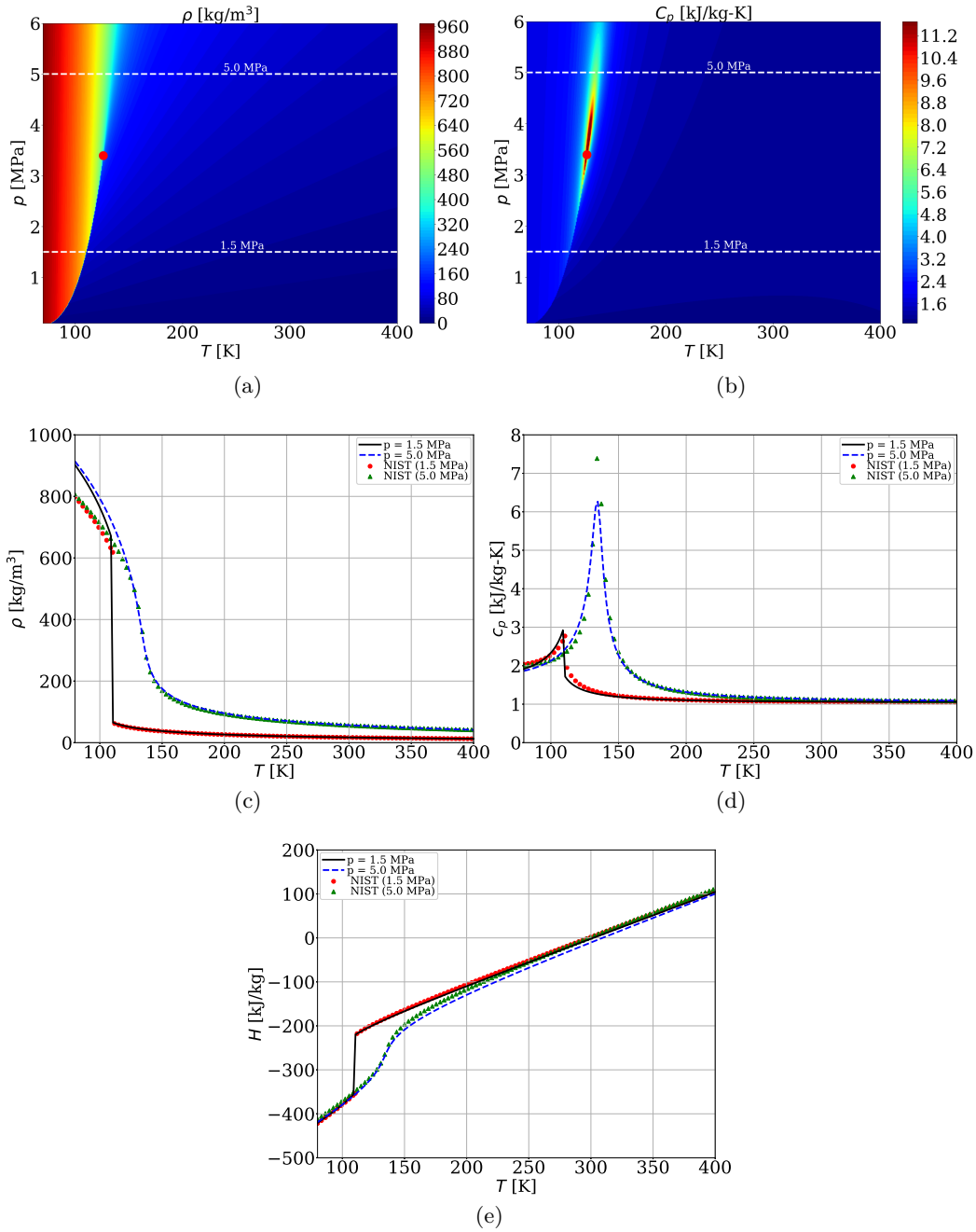

Figure 3: Nitrogen 2D contour maps of a) density and b) specific heat at constant pressure. The same properties are showed in c) and d) at the two reference pressures indicated with the dashed lines in the 2D maps. The red dot indicates the critical point. The red dot indicates the critical point. The specific enthalpy is showed in e). These pictures have been generated using the Peng-Robinson EoS.

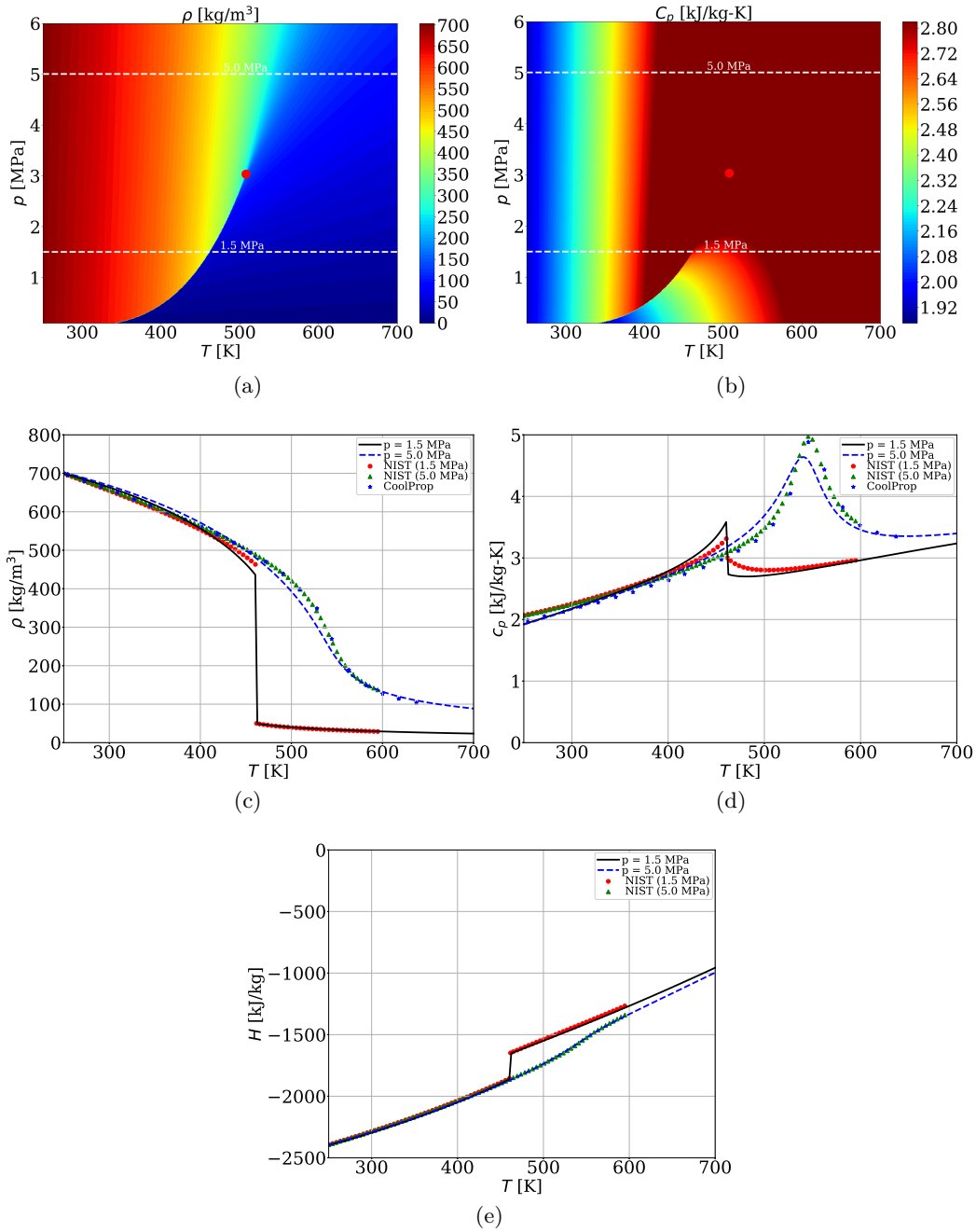

Figure 4: n-hexane 2D contour maps of a) density and b) specific heat at constant pressure. The same properties are showed in c) and d) at the two reference pressures indicated with the dashed lines in the 2D maps. The red dot indicates the critical point. The specific enthalpy is showed in e). These pictures have been generated using the Peng-Robinson EoS.

associated to the phase change, called the *heat of vaporization*. For example in the nitrogen case of Fig. 3a, if one imagines to move along the isobaric line of 1.5 MPa, as temperature increases, the transition from the liquid phase to the gaseous phase is experienced. Given the endothermic nature of this phase transition, the gas enthalpy variation is identical to the heat of vaporization, which is a constant for a given pressure. As a result, the nitrogen enthalpy suddenly increases as showed in Fig. 3e (and similarly in Fig. 4e) and a sudden decrease in the specific heat at constant pressure is accompanied (*cf.* Fig. 3d and Fig. 4d). On the other hand as the pressure is elevated above the species' critical value, the thermodynamic state enters into the *super-critical* regime. Here, properties show different trends as temperature is increased and in particular they do not show any sudden change anymore. The fluid transitions from a "liquid-like" state (high density) to a "gas-like" state (low density) in a smooth manner. The distinction between the two "pseudo phases" is no longer sharp and the fluid seems rather to behave as a "single-phase" not a pure liquid, nor a pure gas and both together, all at the same time. This is clear by looking at the profiles of Figs. (3)–(4) of density, enthalpy and specific heat at constant pressure: abrupt changes of the properties are not observed. One important point to observe is the peak of C_p during the transition between the liquid-like to the gas-like state (*cf.* trans-critical transition of Fig. 1). This peak seems to define the transition (although not sharp) between the two pseudo phases and moves as pressure is changed, becoming sharper (but not a discontinuity) as the pressure is lowered close to the critical value. For this reason, the envelope of the C_p maxima has been defined as *pseudo-boiling line* or Widom line [124, 200] in analogy with the sub-critical boiling line. For a trans-critical injection (see Fig. 1), the fluid goes from a compressible liquid ($T < T_c$, $p > p_c$) condition to a super-critical fluid ($T > T_c$, $p > p_c$) condition, and the Widom line cross-over mimics the action of a super-critical heat of vaporization release, that is instead released in a continuous manner. The characterization of the Widom line has recently attracted a lot of attention. For example Banuti [10] discusses the concept of heat of vaporization in the super-critical regime and provides an equation to quantify it. In addition, the shift of the Widom line towards higher

temperatures as pressure is increased is described with a simple algebraic equations validated against some pure components. In another work [11], Banuti discusses the similarity between the actual sub-critical evaporation and the presence of a Widom line and provides another simple model to re-scale the phase diagram for a simple component beyond the use of the classical reduced temperature $T_r = T/T_c$ and pressure $p_r = p/p_c$ by introducing a new scaled reduced pressure p_r^* that is only a function of the acentric factor ω showing that the phase diagram will now "look" the same for a set of different species and effectively extending the principle of corresponding states. Following this work, Lapenna *et al.* [96] studied the effect of the pseudo-boiling transition of nitrogen using DNS simulations of a TML by defining a pseudo-boiling ratio and decomposing it into two parts. On the other hand, analytical efforts have been made in order to uniquely define the Widom line locus. In addition to the aforementioned works which attempted to extend past algebraic correlations, the work of Lamorgese *et al.* [95] tackles the calculation of the Widom line using the SRK EoS using the concept of zero temperature derivative of the specific heat at constant pressure. Following the same approach, his work [95] is further extended and although not being the primary goal of the present investigation, a generic approach to calculate the Widom line for the generic cubic equation of state (GCEoS) model is provided in Appendix R along with some quantitative analysis.

All the works discussed so far refer to the single component state diagram, which no matter the scaling laws, it can be uniquely defined by the species critical point, meaning that also the thermodynamic states are "readily" available once the temperature and pressure are known. However, what happens in case of mixtures? State diagrams are hardly uniquely definable in the form of Fig. 3a and Fig. 4a mainly because the critical point is no longer a constant but a function of the mixture composition itself (this is discussed later). A shift from single- to multi-phase behavior can also have an impact on transport properties and chemical reactions that must be taken into account accordingly. These arguments introduce to the problem of a multi-phase condition in RG mixtures, which is discussed next.

1.2.2 Preliminaries on VLE

Definition of the thermodynamic regime, *i.e.*, sub-critical or super-critical, is relatively easy for a single component based on the information provided in the previous section. The knowledge of the species' critical point is enough to compare to the actual state and determine where it falls in the phase diagram. However what happens for mixtures? How is the mixture's critical point defined? Can the single species' critical point be directly used to determine the information on the mixture? All these are important questions that need to be addressed not only for the scientific importance, but also because of the following reason: if the mixture properties follow similar variations as those displayed in Fig. 1 for a single component, it becomes extremely important to determine in which state the mixture falls as failure to do so may return erroneous state properties.

It is already known [163] that the mixture critical point can be much higher than the components' individual values and it is obviously a function of the amount of each component in the mixture[2]. Concurrently, the existence of Widom lines have been identified for binary mixtures using molecular dynamics [174] with a physical meaning that seems to resemble that of a single component.

As a result, even if super-critical pressures are chosen with respect to one or more components according to the diagram of Fig. 1, it is not certain that the mixture will enter the same thermodynamic state. Therefore, the mixture can enter in a multi-phase, sub-critical (with respect to the mixture) condition, meaning that more than one phase can co-exist at the same point. A-priori knowledge of the mixture critical locus (*i.e.*, the envelope of the temperature, pressure and composition states defining the local critical point) is certainly an important aspect of the problem. It can be used in fact before the actual simulation to identify whether the desired operating conditions would fall in any multi-phase region or not, helping the proper choice of the associated numerical tool (single- or multi-phase). Different simplified approaches have been suggested to compute the mixture critical point. All

[2]The critical locus may exhibit very complex behaviors as indicated in the work of [231]. It can be extremely difficult to predict the critical line from the information of the individual components' critical points.

of them use the so-called group contribution method, where a sort of averaging procedure is applied on each component's individual critical properties [167, 30]. These can provide a rough estimate of the critical locus, however significant departures can be observed depending on the mixture and the conditions [163]. The most rigorous method to compute the critical locus is that of Heidemann and Khalil [67]. This method is directly derived from thermodynamic considerations by imposing the constraint that the second and third derivatives of the Helmholtz free energy A with respect to any component number of moles in the system at constant pressure and volume has to be zero.

Once the occurrence of a multi-phase condition is established, another aspect to be considered is the time-scale associated to the transition from single- to multi-phase. An exhaustive theory regarding the rates at which phase-change is achieved in this context does not seem to be well established and considerable amount of research is expected to align into this direction. Characteristic relaxation times between phases have been proposed by [42, 2] using the concept of homogeneous nucleation theory. This concept was later used by Qiu *et al.* [168] to justify the hypothesis of phase equilibrium in a numerical calculation. However these phase non-equilibrium models are still far to be fully incorporated into a CFD calculation and identification of these is considered out of the scope of the present work[3]. As a consequence, the hypothesis of phase-equilibrium is invoked throughout the rest of the present work.

Furthermore, if the analysis is restricted to the liquid and the vapor phases only, the problem becomes similar to that of the vapor-liquid equilibrium (VLE) "dome" that is formed for a single component in the common p-v diagram as represented in Fig. 5(a), where the thermodynamic state is a function of the amount of each phase that is formed[4]. However, in the case of a mixture, finding a *phase-fraction*, *i.e.*, the right amount of liquid and vapor

[3]Incorporation of a phase non-equilibrium model can be potentially achieved by adding another transport equation for the phase-fraction variable β. The challenge here will most likely be associated to the development of a reliable source term, similar to a reaction rate in case of a reacting mixture that would properly predict the transition from a single-phase to a multi-phase state, given an arbitrary initial condition.

[4]Note that complex mixtures may actually exhibit an even more complex phase behavior, involving more than two phases. This will be discussed in Sec. 1.3.1.

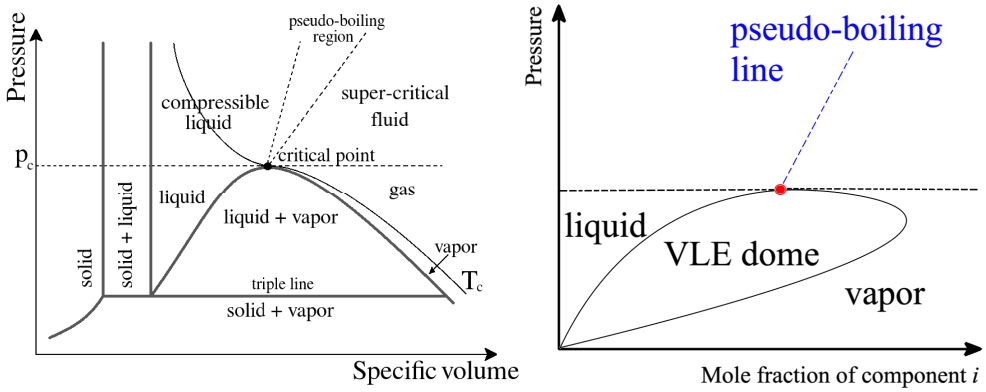

(a) p-v diagram - single component (b) p-X diagram - mixture

Figure 5: a) Sketch of the p-v diagram of a single substance. The vapor-liquid equilibrium (VLE) dome is identified at the center of the figure. In there, the thermodynamic state is in phase equilibrium, meaning that both liquid and vapor phases exist at the same time. For this reason, each point of the VLE "dome" is characterized by a *phase-fraction* (or quality [46]) that defines the thermodynamic state. b) p-X diagram for a mixture identifying the VLE dome for a given temperature. Mixture critical point is qualitatively indicated in red.

phase formed at equilibrium is inevitably a composition-dependent problem as schematically depicted in Fig. 5(b). One way to illustrate the presence of VLE in a multi-component mixture is through the pressure-composition p-X diagram, where X refers to the mole (or mass, alternatively) fraction of one component in the (binary) mixture. In this diagram, temperature is typically maintained constant and existence of the VLE dome is explored by varying the pressure and the composition. The VLE dome interior represents the thermodynamic states ensemble where both liquid and vapor coexist. For a mixture, this means that each component has some liquid and some vapor contribution at the same time. Outside the dome, single phase states exist, either liquid or vapor. These are connected through a similar pseudo-boiling line that departs from the mixture's critical point (at the given isotherm) and effectively defines the mixture's super-critical state, where the distinction between the original liquid and vapor phases no longer exists.

The important analogy between the two VLE domes is that they define a thermodynamic state that is in equilibrium, that is the two phases are assumed to be completely "blended" or in other words there is no net interface between the two. This thermodynamic state occurs at a particular condition in nature dictated by the minimum of the Gibbs free energy [129],

which is a direct consequence of the application of the 2^{nd} law of thermodynamics. Therefore, given that a particular thermodynamic state must be unique, it means that for a given set of p, T and X values, the (equilibrium) state is either single-phase or multi-phase: other possibilities do not exist. As a result, the fundamental questions arise: a) since even at "super-critical" conditions in one (or more) components, multi-phase conditions can occur, and given that the latter is the most stable state that exists (therefore the most likely to occur), shouldn't it be the VLE[5] model the most correct approach to use, compared to the single-phase counterpart, when dealing in general with RG mixtures? b) is there currently available a comprehensive VLE thermodynamic model and associated numerical tools that can be consistently incorporated into a CFD solver? c) once VLE is consistently taken into account, are there any substantial effects that can corroborate its use, compared to the single-phase model, when dealing with RG mixtures? This work aims to answer these questions.

One last thing has to be underlined. Since the VLE condition is a direct consequence of the 2^{nd} law of thermodynamics, its imposition is necessary and sufficient to find it. That is, EoS models are not enough to find VLE states, as the minimum Gibbs free energy condition needs to be imposed at the top of the procedure. This and other related details are going to be discussed in Sec. 2.2.

1.3 Literature review

In this section, the literature review that supports the scope and leads to the objectives of the present work is presented. In order to provide a cohesive reading path, general observations and theoretical studies on super-critical mixtures and RG thermodynamics are given first. Next, the numerical challenges associated with the simulation of super-critical flows are discussed. Finally, past efforts related to simulation with VLE are presented.

[5]Once again, it is emphasized that any non-equilibrium model may be important in the transition between a single- and a multi-phase state.

(a) $p < p_c$ (b) $p > p_c$

Figure 6: Schematics of a sub-critical, versus a super-critical jet of two distinct components in a shear coaxial type injection (From [226]).

1.3.1 General observations, experimental and theoretical studies of RG mixtures

Extensive experimental research conducted over the past thirty years [122, 120, 121, 29, 148] has proven through the use of many different imaging techniques that there is a clear distinction between mixing at sub-critical versus super-critical conditions.

As schematically illustrated in Fig. 6, the process that typically characterizes classical two-phase atomization (spray) in the sub-critical state with droplet formation, atomization and evaporation (Fig. 6(a)) [202] appears substantially different from a diffusion-dominated mixing that on the other hand takes place at super-critical pressures (Fig. 6(b)). In the sub-critical regime, first the jet breaks into irregular ligament shapes (primary breakup) surrounded by the gaseous environment that eventually further decompose into droplets of smaller size where the evaporation process becomes important. Mass and energy transfer between the liquid phase and the surrounding gas phase occurs through the evaporation process which ultimately leads to combustion for a reacting mixture. The interface between the liquid and the gas appears regular and distinct as a clear discontinuity, where shear and surface tension promote the liquid breakup and subsequent atomization. On the other hand when a jet develops in super-critical conditions, the interface between the liquid and the gas are no longer distinguishable and the mixing seems more dominated by diffusion processes. Surface tension and heat of vaporization are also absent because there are no phases to be distinguished.

Early experimental works conducted by Meyer *et al.* [122, 120, 121] highlighted this

process by visualizing liquid oxygen (LOX)/gaseous hydrogen (GH_2) and liquid nitrogen (LN_2)/gaseous helium (GHe) shear coaxial jets. The results, as illustrated in Figs. 7(a) and (b), respectively for a sub-critical and a super-critical LN_2/GHe jet, show the behavior described. While the liquid ligaments and droplets formation were clearly visible in the left picture, they were absent in the right picture.

Similar experiments were carried out by Chehroudi et *al.* [29] and Oshwald et *al.* [148]. In

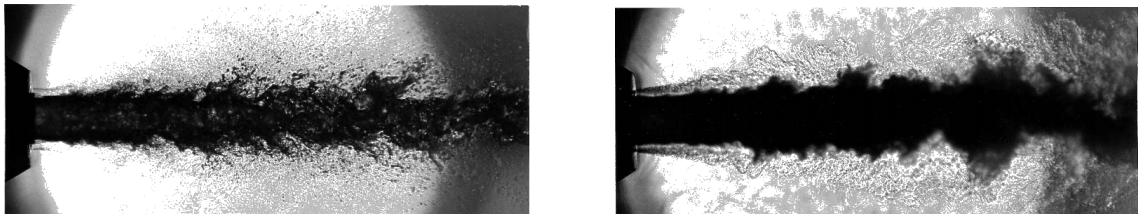

(a) $p = 1$ MPa (b) $p = 6$ MPa

Figure 7: LN_2/GHe coaxial jets under different pressure conditions (taken from [120]).

the first study [29], liquid nitrogen (LN_2) at sub-critical temperatures between 90 K and 110 K was injected into gaseous nitrogen (GN_2) at fixed super-critical temperature of 300 K, while the pressure was systematically varied from sub-critical to super-critical in order to investigate both operating regimes. In either cases, the same observations regarding the different jet breakup mechanism were reported. This is illustrated in Fig. 8. In addition, an extensive discussion was made regarding the jet growth rate and mean axial profile: the conclusion of this study was that when the jet is at its purely super-critical, pseudo-gaseous state, it behaves more like an incompressible gas with stratified density characteristics and in fact, typical scaling laws developed in such context for jet growth rate and axial profiles in the self-similar domain were observed to successfully match the experimental measurements.

In the work of Oshwald et *al.* [148], two different laboratories (AFRL and DLR) performed analogous experiments with the aim to further validate the experimental approach and confirm the earlier observations. Both studies agreed on the manifestation of two different breakup regimes, one more characterized by classical spray behavior at pressures lower than the critical value and one characterized by a gas-like behavior, where droplet formation was

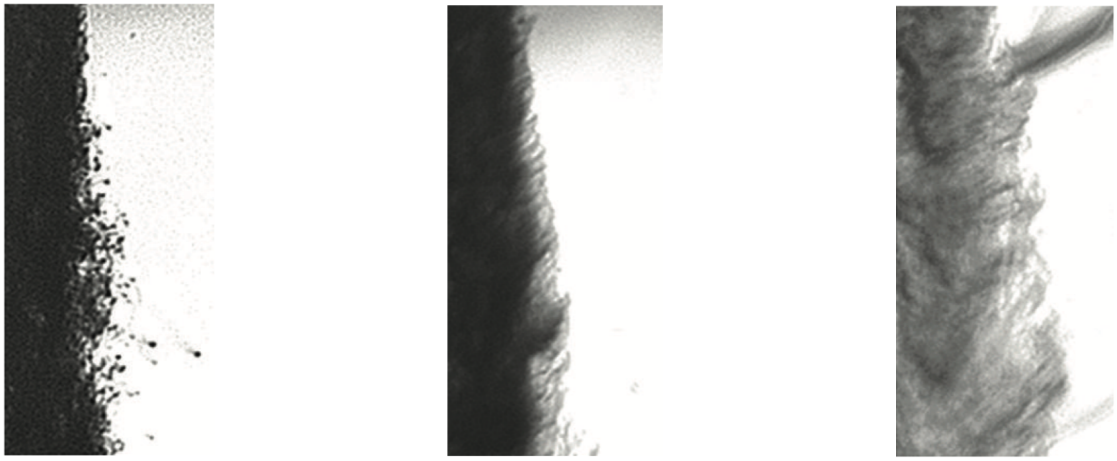

(a) (b) (c)

Figure 8: Liquid nitrogen (LN_2)/gaseous nitrogen (GN_2) jet application studied by Chehroudi *et al.* [29]. Different jet characteristics are observed as the pressure is varied from (a) sub-critical, to (b) near-critical, to (c) super-critical.

not reported. Disagreement was instead reported in the measurement of the jet potential core length obtained with different techniques. These observations were denoted irrespective of i) the type of species, ii) the use of external acoustic forcing (which showed less impact on the super-critical jet) and iii) the fact that the mixture was ignited as discussed in the H_2/O_2 case.

Additionally, both of these studies [29, 148] pointed out the drastic differences in the jet shape and mixing not only when the pressure ranges from sub-critical to super-critical regimes, but also when the temperature was continuously varied across its pseudo-boiling value (T_{pb}) for a fixed super-critical pressure (where the pseudo-boiling temperature was defined as the temperature where the specific heat at constant pressure reaches its maximum). They noticed that the jet spreading for $T < T_{pb}$ was smaller compared to the case when $T > T_{pb}$, confirming the fact that characteristic mixing time and length scales are significantly affected by the thermodynamic regime. Experimental work of Candel *et al.* [23] reported the study liquid-oxygen (LOX) with methane and hydrogen at various pressure conditions based on the early work of Singla *et al.* [201]. According to the visualization,

they reported substantially different flame behavior as the pressure was increased from sub-critical to super-critical with respect to the oxygen critical pressure. On the one hand, the sub-critical condition showed a "shell"-shaped flame structure surrounded by a cloud of LOX droplets. On the other hand, the super-critical regime showed a different flame shape where its self-sustaining mechanism was identified to be mixing-dominated rather than vaporization-dominating as in the sub-critical counterpart, hence leading to the important conclusions that mixing, rather than vaporization, should drive combustor design at such high pressures.

Another important study is that of Manin *et al.* [113] because it treated hydrocarbons, specifically n-dodecane at conditions that are typically employed in diesel engines. In this work [113], different injections conditions were analyzed by varying the injection pressure and temperature and the near-field jet region was closely observed to study the effect of those thermodynamic parameters on the breakup mechanism. The n-dodecane was injected into a nitrogen environment. They reported that surface tension effects, such as droplets and primary breakup instabilities, were observed even when the operating pressure was raised above the fuel's critical value, while absence of such phenomena was progressively observed as the pressure was raised even more. A similar note was made by Chehroudi in another work [28], where the role of multi-component mixing even at high pressures was clearly indicated as a critical aspect of the mixtures under RG regime, indicating that multi-phase conditions may occur even when the pressure is raised above a reference super-critical value (based for example on one of the components).

Analogous conclusions can be found in many other experimental works [28, 147, 61, 103, 187, 196, 186, 183] and references therein. More recently, Baab *et al.* [7] explored the characterization of an n-hexane under-expanded jet into a super-critical nitrogen environment and focused on the mean speed of sound profiles measurements along the axial and radial dimensions as the jet evolved into the chamber. This work was later numerically investigated by [224] who reported qualitative agreement of the simulation with the jet vapor and liquid phase distribution in the chamber, thus confirming that phase-separation (VLE) can occur at "super-critical" pressures (based on one component).

It is clear from these experimental works that i) as the pressure is varied in both non-reacting and reacting systems, macroscopic differences in the jet, micro-mixing and/or flame shapes arise, ii) these differences are mainly driven by the disappearance of droplets and typical primary breakup instability mechanisms, substituted by diffusion-driven mechanisms as the pressure is increased. Finally, iii) there seems to be a third portion of the picture, in which super-critical, multi-component mixing can produce local multi-phase conditions. These are difficult to predict in advance and cannot be avoided by simply setting the pressure at an arbitrarily "high" value. This behavior is characterized by a multi-phase, multi-component RG characteristics that add on top of the single-phase ones. As a result, it is a strong function of the species being used in addition to the values of pressure and temperature. Unfortunately not many experimental data are available for this particular regime, supporting the fact that additional investigations are required in order to quantify the effect of multi-phase conditions in RG flows. These aspects need further understanding and modeling.

A novel theoretical work that attempts to explain the change in behavior of mixing in super-critical regime has been proposed by Dahms [36] and Dahms and Oefelein [37, 38] by combining the use of linear and non-linear gradient theory with a complex RG equation of state such as the Benedict-Webb-Rubin or Helmholtz. The linear gradient theory was developed by Van der Waals in 1893 [230] and later revisited by Cahn and Hilliard in 1958 [22] to describe the microscopic inter-facial behavior of two phase fluids. This theory says that the difference in the mixing process from a sharp to a diffused liquid/gas interface is a result of three different combined effects [37]: 1) the broadening of the interface thickness, 2) the reduced mean free path of molecules relative to the interface thickness, and 3) the reduction of surface tension. In a sharp gas/liquid interface, the thickness is smaller than the mean free path, thus the interface dynamics is governed by the local molecular processes (i.e., continuum equations are no longer valid across the interface) and the interface temperature reaches the equilibrium value dictated by the VLE conditions [37, 38]. On the other hand, a diffused interface is thicker by at least one order of magnitude of the mean free path. In this case, the interface dynamics enter the continuum regime where diffusive

(Fickian) processes dominate and the interface temperature does not reach an equilibrium value (dictated by the VLE), rather is composed of a continuous temperature profile going from the gas-like to the liquid-like respective (far-field) temperatures.

This theory was applied to the adiabatic mixing between n-dodecane and N_2 and as shown in

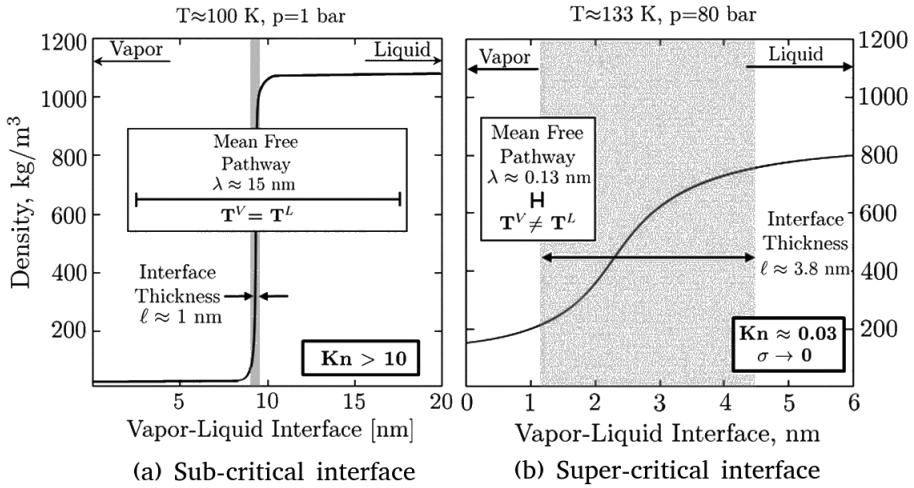

Figure 9: Schematics of a sub-critical, versus a super-critical interface structure for LOX-GH_2 mixture (From [36]). Liquid-gas sharp interfaces are associated with high mean free path λ, large Knudsen number Kn and surface tension σ. The interface dynamics is governed by the local molecular processes and vapor-liquid equilibrium. On the other hand, super-critical interfaces are diffused and enter the continuum regime as the local mean free path is much smaller than the interface thickness. Knudsen number is small and surface tension σ tends to zero. Vapor-liquid equilibrium no longer defines the interface thermodynamic state and therefore this state can be modeled with conventional Navier-Stokes equations with single-fluid approach.

Fig. 9 [37], sharp interfaces are associated with a high Knudsen number (the ratio between the mean free molecular path and the interface thickness), where the continuum hypothesis is not valid and a rigorous VLE calculation is needed to determine the interface temperature. Conversely in a diffused interface, a lower value of the Knudsen number is obtained and the approach where a unique phase, *i.e.*, the super-critical phase, exists (single fluid or phase approach) becomes valid.

This theory provides a theoretical foundation about the interface dynamics of two different macroscopic observations, however it does not contemplate the fact that multi-component mixtures can form VLE even at high pressures because the mixture critical point can reach

much larger values than the corresponding value of each component. If VLE establishes at a given point in space and time, the equation of state convexity is lost, that is a thermodynamic state becomes no longer unique, unless an energy criterion (*i.e.*, 2^{nd} thermodynamic law) is employed which brings back the solution uniqueness. Furthermore, even within the region of vapor-liquid equilibrium where no interface occurs, the thermodynamic properties of the mixture cannot be calculated with a single equation of state because it does contain any information about how much liquid or vapor are at a given point and forcing the solution to behave as a "single fluid" (one phase, either liquid or vapor) may lead to large errors in the prediction of the thermodynamic states or even non-physical states as shown later in this work.

In another work, Poursadegh *et al.* [165] investigated theoretically and experimentally the injection of n-propane into nitrogen, again with relevance to internal combustion engines. In their work [165], they proposed a model to distinguish the time scale related to the droplet evaporation to the time scale related to the droplet formation as the primary jet entered the combustion chamber with the ultimate goal to provide an understanding about the conditions under which the droplet formation can be effectively neglected and the flow treated with the single-fluid model.

All the above remarkable works contributed to the fundamental understanding of the differences that occur when mixing (with or without combustion) of one or multiple components is operated at elevated pressures. By doing so, most of the times, the aforementioned multi-phase effects that may occur at the same conditions are neglected, with the effect one may ignore the physics related to them. Additionally, while the calculation of phase equilibrium from a given state represents a well-established tool in the field of chemical engineering, the associated thermodynamic properties (necessary for a CFD calculation) are not so well-established. For instance, Fig. 10 shows a piece of the classifications of RG mixtures collected in the work of Van Konynenburg *et al.* [231] where, depending on the shape of their VLE (phase) diagram, binary mixtures were categorized in "Types". In this picture, Type I and Type III mixtures are discussed. When dealing with Type I mixtures, only one critical locus line, that is the mixture critical point envelope as the amount of one

component is varied (for fixed temperature), exists. This line departs from the critical point of one component taken alone and continuously propagates up to the critical point of the other component. Conversely, when dealing with Type III mixtures, two distinct critical curves can be observed: one that departs from the component with relatively high critical temperature and propagates up to infinite pressures and a second critical line that departs from the component with relatively low critical temperature and matches the critical point of the mixture 3-phase (vapor-liquid-liquid) region. The first behavior is typically observed in combinations of low molecular weight hydrocarbons with non-hydrocarbons, such as nitrogen, whereas the Type III behavior is observed in heavier hydrocarbon mixtures [169]. A more detailed discussion of mixture phase diagrams can be found in [189, 152].

Once established that RG mixtures can represent (very complex) phase behavior even at

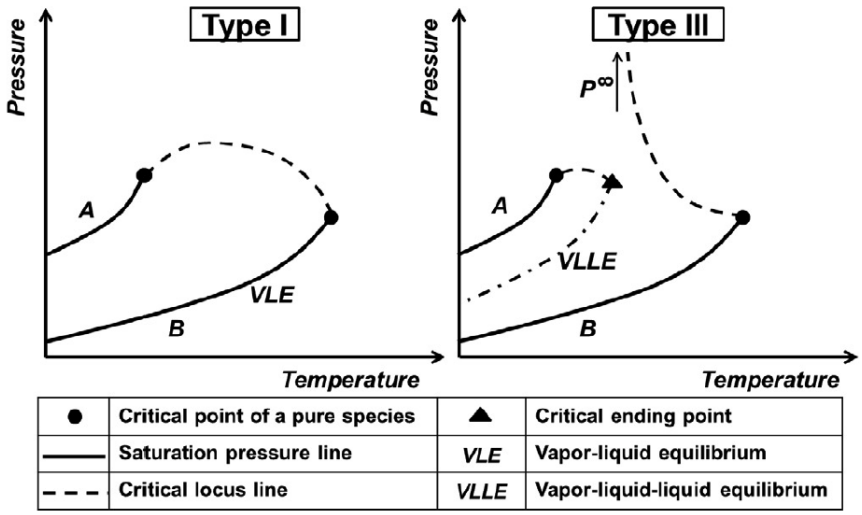

Figure 10: Schematic representation of critical loci curves for mixtures of Type I and III (borrowed from [169]).

high-pressures, the next question is how to carry the existing RG mathematical and numerical models one step forward in order to be fully compatible with the conservation equations for fluid mechanics so that a comprehensive simulation tool becomes available to study the effects of these conditions, even if initially applied to relatively simplistic configurations. To do so, a review of the numerical methods used so far in the RG community is an essential

part of the research problem. This is discussed next.

1.3.2 Numerical methods for real-gas simulations

Inspired by the experimental observations and theoretical models, the computational fluid dynamics (CFD) community has produced an enormous amount of research on all kinds of applications of RG flows, from canonical to more complex. Whenever the assumption of pure single-phase, super-critical fluid (hereafter also called single-fluid approach) was invoked throughout the calculation, the choice between pseudo phases was made at most, usually based on the one that provides the minimum Gibbs free energy when the EoS of the cubic family was employed (see Appendix A).

This approach to the problem solution is quite intuitive: since the operating conditions are purely super-critical, whether a single or a multi-component mixture is being used, the interface between the two pseudo-phases is dominated by Fickian diffusion and it is thick enough that it is directly resolved by the computational grid. All the inter-facial phenomena occur at the continuum scales, therefore conventional Navier-Stokes equations coupled with a more accurate EoS that is capable to correctly represent the thermodynamic states in this regime represent a complete and physically correct model to study the problem. Even assuming that this is the case all the time, this approach carries uncertainties from physical and numerical points of view that need to be addressed separately. This is confirmed by the fact that each of these following topics represents an active area of research in different communities. In this section, the difficulties related to the solution of RG flows (even when the single-fluid approach is used) are described with particular emphasis on the numerical methods.

Simulations of RG flows require additional physical and numerical efforts that are of less importance in IG conditions [12]. Typically, transport properties, as dynamic viscosity μ, thermal conductivity λ and binary mass diffusion coefficient D_{ij} require models that are representative of molecular processes happening at scales smaller than the continuum. These models need to be augmented with high-pressure and/or high-density corrections to capture their deviations with respect to the ideal condition. For dynamic viscosity and

thermal conductivity, usually the models of Chung [31] and Reid et *al.* [163] are used with reasonable accuracy, whereas for the binary mass diffusion coefficients either the model of Takahashi [214] or Fuller/Riazi [52, 178] have been reported in the literature. If complex multi-component transport models are used, additional coefficients are required [12]. On the other hand, EoS require non-linear mixing rules that in turn are expressed with the inclusion of binary interaction parameters k_{ij}, usually tuned for specific mixtures to achieve superior accuracy in the prediction of certain properties in particular regimes [163]. These parameters can be constant or temperature-dependent, producing an even stronger non-linearity in the equations, as well as non-trivial complexity in the derivation of mixture properties such as departure functions, fugacity coefficients and their derivatives [46].

Various models have been proposed over the years for these parameters [104], however the lack of experimental data and the fact that interactions occurring at molecular scales are strong functions of the species forming the mixture makes it difficult to formulate them in a generalized form, ultimately producing an additional model uncertainty that was recently found to play a non-negligible role in the development of turbulent structures of binary mixtures [9].

As a consequence, experimental and numerical techniques have not reached the stage of a well-established framework, and considerable amount of work is still expected to be done in order to answer questions from a more fundamental perspective, for example, those related to the pseudo-boiling understanding and characterization [200, 10], to multi-component transport modeling and relevance [181, 57, 244, 12], to multi-phase occurrence [169, 224, 226, 227](primarily addressed in this work) or to unified modeling for computing transport properties in all regimes [163]. Concurrently, similar efforts are expected to be made on the numerical techniques front, for example, related to the modeling (and ultimately understand the importance of) closure models for EoS sub-grid terms in the context of Large-Eddy Simulations (LES) [221, 197, 19, 96, 180, 235], or the improvement of thermodynamic/transport properties tabulation for acceleration purposes [157, 130].

On top of all the aforementioned challenges, one major issue related to the simulation of super-critical mixtures remains the suppression of numerical pressure waves that form when

fully conservative schemes are employed. In such cases, in fact, the numerical errors accumulated by the spatial and temporal discretization can be amplified by the EoS non-linearity. Typically, this phenomenon happens for two main reasons:

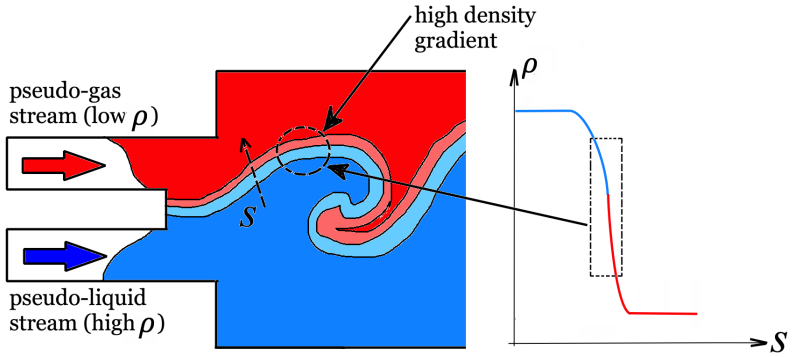

Figure 11: Schematic representation of a shear-coaxial injector mixing region. The flow is characterized by two streams, one in pseudo-liquid state (high p, low T) and one in pseudo-gas state (high p, high T) which produce a high- and low-density regions, respectively. When these mix, a high density gradient region forms. This is challenging to be resolved numerically.

- the flow is characterized by large density gradients. This is typical of non-reacting and reacting flows that are formed by at least two streams of different fluids, different thermodynamic conditions or both. One example is the shear-coaxial injector configuration where a fuel and an oxidizer are injected into a confined environment. This is schematically represented in Fig. 11. The differences in the species and/or injection conditions in terms of pressure and temperature can produce a drastic difference in the densities of two steams (up to three orders of magnitude), ultimately producing a region of large density gradients where these two streams merge;

- one or both of the aforementioned streams may incur a trans-critical injection (see Fig. 1) across which the EoS expresses very large non-linear effects and thermodynamic properties have very large gradients. As a consequence, a small perturbation of a given thermodynamic state, (say) in temperature or internal energy, can produce a significant departure of a derived thermodynamic property, for example the pressure.

This problem is quantitatively explained in Sec. 3.2.2, in a different way than reported in

other works [108, 216, 188], hence constituting another contribution of this work.

As previously stated, the amount of research performed by the CFD community on this topic has been tremendous. For the purpose to categorize these by the use of the numerical scheme to suppress the problem described earlier, Tab. 1 reports some major groups with their most relevant works. As immediately observable, each group adopts different techniques to address the problem of non-physical oscillations. The most practical solution would be to refine the grid in the regions of high density gradients, however, this can become difficult to apply to a complex system. Certainly, use of filtering [132, 134, 146, 144, 145] or artificial dissipation schemes [116, 125, 248, 236, 194, 193, 229, 191, 158, 157, 179, 188] are popular choices, along with the use of hybrid schemes that couple an higher-order method to spatially resolve the (convective) fluxes away from those high-density gradients regions and a lower-order method, usually of the family of the upwind schemes, to resolve the gradients in those critical regions [115, 59, 90, 89, 91]. However it is important to note that reducing the spatial discretization order may not be enough to solve the problem as the accuracy of the cell-interface states can be reduced, hence increasing even more the error fed to the EoS when reversed thermodynamic problem solutions are sought (see Sec. 3.2.2).

All these solve the governing equations in their fully conservative (FC) form. Another class of methods is that of quasi-conservative (QC) family, which instead treat the energy equation non conservatively. One approach is that of Terashima *et al.* [216, 79] who proposed to solve directly for the energy equation written in form of pressure, later used by Matheis *et al.* [118]. In this way, pressure becomes a transported quantity and it does not need to be calculated from the total energy and density, thus avoiding magnifying their errors due to poor resolution in the region of high-density gradients. However, this approach (and other non-conservative approaches) come with their own limitations in the sense that even though the pressure oscillations are eliminated, the corresponding temperature field has an error because its value does not correspond to that obtained if the energy equation is solved for (unless grid refinement is adopted [118]).

Another QC approach is that recently introduced by Pantano [151] or Lacaze *et al.* [92]

Table 1: List of the research groups with significant work on the super-critical mixing studies. Table indicates the criteria used for the spatial, temporal discretization as well as any specific treatment that is used in the overall numerical method. The discrimination between FC and QC methods is made and the list of the EoS used is also provided.

Research group (Code)	**Spatial discretization**[a]	**Temporal discretization**	**Specific treatment**	**Form**	**Equation of State**
JPL [132, 134, 146, 144, 145]	6^{th} or 8^{th} order central, finite difference	4^{th} order RK[b]	filtering	FC[c]	PR
Georgia Tech #1 (LESLIE) [116, 115, 59, 226]	4^{th} order predictor-corrector or hybrid 3^{rd} ord. MUSCL with 2^{nd} ord. pred.-corr. or Double-Flux	2^{nd} ord. pred.-corr.	2^{nd} and 4^{th} order AD[e] or hybrid switch	FC/QC[d]	PR, VLE
Georgia Tech #2 [125, 248, 236]	4^{th} order with AD	2^{nd} order backward (explicit time) 4^{th} order RK (pseudo-time)	Preconditioning with dual-time stepping	FC/QC	SRK
Georgia Tech #3 [92]	2^{nd} order QUICK	4^{th} order RK	staggered grid plus 1^{st} order upwind with switch	FC/QC	PR
BOSCH (CharLES) [83]	2^{nd} order central ENO with 1^{st} order upwind with sensor switch	3^{rd} order RK	constant specific heats	FC	PR with modified p_{sat}
Pantano et *al.* [151]	1^{st} order with modified HLLC Riemann solver	1^{st} order explicit Euler	Additional transport equation	QC	VDW
CERFACS (AVBP) [194, 193, 229, 191]	2^{nd} order TTG4A	4^{th} order RK	artificial dissipation	FC/QC	SRK/PR
Sandia (RAPTOR) [90, 89, 91, 188]	3^{rd} order QUICK combined with 1^{st} order upwind	3^{rd} order RK (explicit time) 4^{th} order RK (pseudo time)	Preconditioning with dual-time stepping, staggered grid, hybrid switch	FC	PR
Terashima and Kawai [216, 79]	6^{th} order compact, finite difference	3^{rd} order RK	artificial dissipation	QC	PR, tabulated
VCU [185]	5^{th} order WENO with Double-Flux	3^{rd} order RK	hybrid sensor	QC	PC-SAFT
TUM (INCA) [136, 137, 224, 117, 118]	2^{nd} order TVD	3^{rd} order RK	immersed boundary adaptive mesh	FC	PR, VT-PR, VLE
Stanford (CharLES[x]) [108, 109]	2^{nd} order ENO	3^{rd} order SSP-RK	entropy-stable flux	QC	PR
CNRS (SitCom-B) [158, 157, 179]	4^{th} order skew-symmetric like	4^{th} order RK	artificial dissipation	FC	PR, SRK, tabulated
DIMA [96, 97]	Spectral Element Method (SEM)	3^{rd} order implicit	Low-Mach formulation	QC	tabulated NIST
IFPEN [245]	Quasi-Second-Order-Upwind (QSOU)+SIMPLE	-	single-fluid fluxes	FC	PR-VLE

a This refers to the way inviscid fluxes are integrated. Viscous fluxes are found to be always integrated with central derivatives due to their parabolic nature.
b Runge-Kutta.
c Fully-Conservative.
d Quasi-Conservative.
e Artificial Dissipation.

which use an additional transport equation, in the first case, for a group that is a function of the specific heat ratio γ [151] and, in the second case, for the mechanical pressure [92] to obtain directly the pressure field and avoid the conversion from energy to temperature. Another method is that of the Double-Flux (DF) [108], which extended its original application to TPG EoS [1, 15] and has been proven to be an effective and low-cost method to resolve single-phase transcritical flows [108]. Given its simplicity, this method has been chosen for this work and extended to include VLE thermodynamics (discussed in Sec. 3.2.3), which constitutes another contribution to this work.

Another source of uncertainty in the simulation of RG flows is carried by the EoS model itself. The amount of EoS presented in the literature is vast [163] however, if one restricts the attention to the CFD field, the class of the *cubic* EoS are largely used because they provide the best compromise between accuracy and cost. Among these, the Peng-Robinson (PR EoS) [154], the Soave-Redlich-Kwong (SRK EoS) [207], the Redlich-Kwong (RK EoS) [177] are widely used and will be used in this work too. It is however important to underline that these EoS are models that may work better in some regimes than in others and for certain categories of species [104, 163]. More accurate EoS are available such as the *volume-translated* PR, [3] which adds a correction to the calculated volume (density), improving the prediction accuracy in the liquid/compressible liquid regimes. Another choice is the Benedict-Webb-Rubin EoS [13] (later further modified by other works [75, 247]), which consists of a sum of different terms (up to 32), each coming with an associated constant for each species. Nevertheless, the most accurate model is the Helmholtz EoS [163], (which would require up to 42 constants for each species to be completely defined). Some works in the CFD community have successfully carried out simulations with these more accurate EoS [119, 161, 141], however, much higher computational costs with respect to the cubic EoS family was reported. For this reason, these are avoided in this work, however, as will be discussed in Sec. 2.2.2, the VLE analytical framework developed in this work is EoS independent [227]; therefore, it can potentially be associated with the aforementioned EoS.

1.3.3 Previous computational efforts with VLE

As stated in the previous section, working with the single-fluid assumption relies on the fact, that for some (undefined) high-pressure threshold, the mixture forms one phase at most, even in the case of multi-component. However, local multi-phase conditions can occur as pointed out in many chemical engineering resources (see [46, 49, 170, 168, 169] and references therein), as well as recent works in the field of fluid-mechanics [44, 208, 118, 224, 245, 226]. In fact, as initially discussed in the works of [44, 208], the EoS do not have the capability to predict properties of both single- and multi-component mixtures within their VLE regions. Thus, non-physical properties may lead to complex eigenvalues for the Euler Jacobian matrix that becomes non hyperbolic or in other words the EoS convexity is lost. This was confirmed by a later study conducted by Qiu et *al.* [171], where regular and retrograde condensation of a single component was studied in presence of shocks. In order to account for multi-phase phenomena, they all [44, 208, 171] employed an homogeneous phase equilibrium (VLE) solver for which an additional variable indicating the *phase-fraction* was computed. This has a big impact on all the thermodynamic relations that get modified accordingly, effectively producing a multi-phase model in contrast to the single-phase strategy commonly used. This leads to the next problem: what are the thermodynamic properties in the VLE region? In a numerical simulation, the VLE problem itself, *i.e.*, finding the amount of liquid/gas at given T, p and X is a known procedure [126, 127, 170, 129], continuously updated for robustness, convergence and range of application [49, 138, 77, 205, 48]. However, not so established is the determination of all the rest of mixture properties that follow. This aspect becomes very important when a CFD solver needs to be coupled: how to compute the specific heats, speed of sound, fluid compressibilities and partial molar properties? It is clear that, if VLE forms, correct determination of all the thermodynamic properties is essential to aim for that correct physics representation that is missing in the single-fluid approach. Even in the case those properties do not differ too much from those predicted with the single-fluid approach (and this is not the case as proven in Chap. 4), having established their correct form is preparatory to the development and use of corresponding reduced-order/simplified models because the latter can be validated and justified

against the exact values.

The main challenge embedded in the determination of VLE thermodynamic properties is the fact that the VLE problem is a function of pressure and temperature (at fixed composition). That is, when all the typical thermodynamic properties are sought as derivatives of primary variables with respect to temperature and pressure at fixed composition, if the original state is a VLE state, then its derivatives must be taken into account accordingly and cannot be ignored. To put in perspective, for fixed composition, say mole fractions X, variation of pressure and/or temperature varies the amount of liquid and vapor composition, including the phase fraction. This aspect was not found extensively covered in the literature.

One example is the work of [56] who reported the use of VLE with highly accurate EoS such as Helmholtz. In this work [56], the VLE problem was addressed and the importance of the accuracy embedded with the EoS was provided as well, however VLE thermodynamic properties are not discussed. Other works instead [219, 218] tackle the issue by providing thermodynamic relationships [219] and expressing the derivatives of the VLE by exploiting their dependency on specific volume and enthalpy. However, how to actually compute these quantities is not provided for multi-component mixtures [218].

VLE-coupled CFD works have been recently reported by Matheis *et al.* [118], Yi *et al.* [245] and Pelletier *et al.* [153]. However, Matheis *et al.* [118] do not discuss how the thermodynamic properties are computed in the VLE region. The approach of Yi *et al.* [245] uses the mixture properties computed with VLE, such as density, to calculate the other thermodynamic properties using the single-fluid formulation where in addition, a frozen, single phase approach was reported to be used during the inviscid fluxes reconstruction, while retaining the multi-phase VLE approach at the conversion between conservatives to primitives stage. This approach contains inherent inconsistencies from a thermodynamic point of view because mixed single- and multi-phase strategies are used together. Pelletier *et al.* [153] assume that the VLE composition between the liquid and vapor phases is the same throughout the simulation with the purpose to save computational time. Unfortunately, the amount of liquid and vapor phases are determinant in the evaluation of thermodynamic

properties as discussed in Chap. 4 and keeping them equal may result in an approximation. In another work, Qiu *et al.* [169] have reported the application of a simple linear blending rule between the liquid (L) and the vapor (V) phase for the mixture specific heat at constant pressure C_p in the VLE region, computed as $C_p = \beta C_p^V + (1-\beta)C_p^L$ [169], where the phase fraction β indicates the mole fraction of the vapor phase in the mixture. This approach may lead to significant departures from the actual solution as showed in Chap. 4, as well as further discussed in Appendix C.

Another important point to raise is that the differences between the single-fluid approach and the VLE model are not extensively reported either. For example, the ECN spray A jet configuration has been studied by using different models: the single-fluid approach [140, 32], the VLE model [118, 184] and the Lagrangian particle tracking model for the liquid phase [238]. All studies show good agreement of the liquid jet penetration length and spreading rate with experimental data. Therefore another motivation of this work is: what is the effect of VLE compared to the single-phase approach? It is in-fact obvious that if no effect is found and indeed the only purpose is to understand how much liquid and how much vapor phase is found in the multi-component region, then VLE can be only be used as a post-processing tool, with online calculations performed with the single-fluid approach only, which also turns out to be computationally much faster. Other works [245, 184] use an approximate formula to compute the speed of sound in the two phase region based on the method of Wood [242].

In the works of Traxinger and Tudisco [224, 223, 226], the correct model based on the numerical differentiation proposed by Nichita [139] was used, however this model carries its own limitations, particularly related to the order of accuracy of the numerical derivatives and their associated computational cost which is discussed in this work in Chap. 4. Works of [49, 26], devoted substantial efforts to the calculation of thermodynamic properties in two phase systems, however their focus is limited to some variables only, particularly the speed of sound and the compressibilities. This lack of information, simplified approaches or limitations of the pre-existing models motivated the present work to enhance this particular field.

Finally, it is important to mention the relevance that molecular dynamics (MD) simulations are expected to provide to macroscopic models, such as that developed in this work. Molecular dynamics simulations treat the thermodynamic system as an ensemble of particles at the molecular scale from which macroscopic properties can be extracted [62]. Enormous amount of research has been performed in the past decade on this thanks to the development of large-scale computing systems and works of Mills *et al.* [135] and Raju *et al.* [175] are only examples of the application of such methods to obtain physical properties of materials or more in general thermodynamic systems. Recently, efforts have been devoted to the investigation of super-critical and sub-critical properties of single- and multi-component systems using MD. Examples are the calculation of Widom lines in binary mixtures [174], or VLE diagrams in multi-component mixtures [237, 234, 173]. The latter are currently limited to provide the equilibrium density across the VLE interface, while a larger number of variables is required for a CFD simulation as discussed.

1.4 Objectives

As seen in the previous sections, simulation of RG flows involves a considerably broad range of physical and numerical models development and application. In order to provide a contribution to the current existing framework and understanding of the underlying physics of these complex mixtures, the following objectives are identified for this work:

- **Develop a multi-phase equilibrium real-gas thermodynamic library that is consistent with thermodynamic laws and investigate the differences with pre-existing models both from a physical and computational point of view.**

  This first objective is an essential portion of the overall thesis goal. A thermodynamically consistent multi-phase RG model is necessary to develop first and validate against currently available models. This includes to develop a VLE solver (T, p, X) first and then augment it with the solution of all the thermodynamic properties that are correctly computed in the VLE region. Differences of this model with other pre-existing models are studied. Zero-dimensional (0D) thermodynamics is initially sufficient to investigate these differences and it is applied on different mixtures with

different level of complexity. This first step should provide a clear answer between the differences in the thermodynamic properties among all the models. The same investigation needs to be conducted on the transport properties, for which a proper model within the VLE region has not been proposed yet. Within this study, different equations of states of the cubic family and associated mixing rules are going to be explored in order to identify what is the best compromise for the subsequent CFD simulations;

- **Couple the VLE solver with the CFD solver by taking into account consistency with all the numerics and study the mutual effects of VLE thermodynamics, numerical scheme and grid resolution.**

  With the developed stand-alone VLE model, the next step is to attach it to a CFD solver that is capable to treat both non-reacting and reacting flows. To do so, all the direct and inverse thermodynamic problems encountered by the CFD solver need to be extended to include the effect of VLE. That is, the algorithm that treats the solution of T, p and X will likely be not enough and reversed problems, such as conversion between internal energy and density to temperature and pressure will be required. Moreover, the inclusion of a stable numerical scheme to treat large density gradients discontinuity needs to be incorporated and adapted consistently to VLE. This requires first to understand the source(s) or errors in numerical simulations that involve flows with high-density gradients, and then adapt the corresponding numerical algorithms to the multi-phase RG thermodynamics. Furthermore, the following questions will be investigated: does resolution have any effect on VLE? What is the relationship between the error produced by the spurious oscillations and VLE (if any)? To answer these questions, simple 1D and 2D test cases will be considered.

- **Analyze the effects that VLE thermodynamics has on non-reacting and purely reacting flows, identifying (if any) the key sources of such differences compared to the single-fluid approach.**

  Once the CFD solver is properly coupled with VLE, the next objective is to understand

what is its effect on the flow field compared to the single-fluid model. This will help to establish its relevance since no specific works have addressed this comparison so far. For this purpose, canonical configurations, including temporal mixing layers (TML) or spatial mixing layers (SML) are going to be used. Depending on the simulation cost, the setup will be chosen between a 2D or a 3D format, however in both cases, systematic anlayses between the VLE and the non-VLE (single-fluid) models will be carried out. For the non-reacting cases, a mixture already validated in objective 1 will be used, while for the reacting cases, the focus will be a methane-oxygen based mixture because of its relevance in the aerospace field (discussed later) and the fact that it is not completely clear what is its behavior from a VLE perspective. In this context, a purely reacting flow is meant to be a thermodynamic condition where the reactants do not form VLE by themselves (as this is going to be investigated in the non-reacting case), rather where VLE is potentially formed only by the products, if it occurs.

1.5 Outline

This first chapter was dedicated first to background information on RG thermodynamics, introducing the basic key concepts and terminology that were necessary to explain the problem, the past studies and the proposed work. Next, emphasis on the literature, past works and relevant questions that have not been extensively answered yet have been discussed. All this brought to the formulation of the present work objectives. The rest of this thesis is organized as follows:

Chapter 2 details the analytical formulation used in this work. This includes the governing equations and all the sub-models. In this part, the novel analytical VLE framework to compute thermodynamic properties is discussed along with its use with the cubic EoS and adaptation to the pre-existing transport models. Chapter 3 discusses the numerical methods used for both the fluid mechanics and the thermodynamics. In this chapter, the details regarding how to solve the VLE problems and associated issues are extensively reported, as well as the problem of the pressure oscillations in conservative schemes and the extension

of the Double-Flux model to incorporate VLE effects. In Chapter 4, zero-dimensional thermodynamics is applied to various mixtures to address the different outcomes with different thermodynamic models, EoS and mixing rules. Chapter 5 applies all the theoretical/numerical framework to both reacting and non-reacting canonical configurations and provides broad discussion regarding the relevance of VLE from different point of views. Chapter 6 finally provides the conclusions were thesis contributions are delineated and future work applications are also suggested.

Chapter II

FORMULATION

In this chapter the equations for the generic multi-component, compressible, reacting mixture's fluid-mechanics are discussed. Where applicable, the assumptions that are considered for the present study are introduced and justified accordingly. Next, a specific section is dedicated to the RG thermodynamics, introducing to the VLE problem for a generic EoS first and then the specific equations for the GCEoS model are provided. Next, the transport model is discussed and validation is shown accordingly. Finally, the general formulation of the chemical kinetics are detailed.

2.1 Governing equations for the fluid mechanics

The Navier-Stokes equations are considered in the present work. They describe the motion of an unsteady, compressible, reacting, multi-species fluid through the conservation of mass, momentum, total energy and species. By invoking the continuum assumption and neglecting the effect of buoyancy, using the Einstein summation convention, the governing equations read:

$$\frac{\partial \rho}{\partial t} + \frac{\partial \rho u_i}{\partial x_i} = 0\,, \tag{2.1.1}$$

$$\frac{\partial \rho u_i}{\partial t} + \frac{\partial}{\partial x_j}\left(\rho u_i u_j + p\delta_{ij} - \tau_{ij}\right) = 0\,, \tag{2.1.2}$$

$$\frac{\partial \rho e_T}{\partial t} + \frac{\partial}{\partial x_i}\left(\left(\rho e_T + p\right) u_i + q_i^{\mathrm{IK}} - u_j \tau_{ij}\right) = 0\,, \tag{2.1.3}$$

$$\frac{\partial \rho Y_k}{\partial t} + \frac{\partial}{\partial x_i}\left(\rho Y_k u_i + j_{i,k}\right) = \dot{\omega}_k \quad k = 1, \cdots, N_s\,. \tag{2.1.4}$$

In the above equations, ρ is the density, u_i is the velocity component along the $i = 1, 2, 3$ direction of a Cartesian reference frame, p is the pressure, τ is the viscous stress tensor, e_T is the total massic energy defined as the sum of the internal energy e plus the kinetic energy $u_i u_i/2$:

$$e_T = e + \frac{u_i u_i}{2}\,. \tag{2.1.5}$$

q^{IK} is the heat diffusion flux in its "Irving-Kirkwood" form including the enthalpy flux by mass diffusion, Y_k is the mass fraction for species k (or i where applicable) and j_k is the mass diffusion flux for species k , k varying between 1 and N_s, the number of species considered in the mixture. Finally, $\dot{\omega}_k$ is the rate of production/destruction of species k in the mixture. The δ_{ij} indicates the Kronecker delta.

2.1.1 Momentum diffusion and stress tensor

Within the assumption of Newtonian fluid, the relationship between the shear stress tensor and the strain rate is linear and writes as follows:

$$\tau_{ij} = \mu \left(\frac{\partial u_i}{\partial x_j} + \frac{\partial u_j}{\partial x_i} \right) + \lambda \frac{\partial u_k}{\partial x_k} \delta_{ij} \, . \tag{2.1.6}$$

Similarly to all other state functions, the dynamic viscosity μ depends on two state variables, such as the temperature T and/or the pressure p, as well as the mixture composition. It is important to underline that even under conditions where thermodynamic departures from ideal gas (such as the compressibility values) are small, transport properties such as dynamic viscosity can display quite significant departures. To illustrate this point, Fig. 12 shows the comparison between oxygen IG and RG compressibility factor Z and dynamic viscosity μ for two different temperatures and for a range of pressures. Real-gas calculations to compute the compressibility are performed with an advanced EoS (the PR EoS) which can capture non-ideal thermodynamic states (more discussion follows in Sec. 2.2), whereas transport properties calculations are performed either with the classical mixture-averaged model, typically used for TPG mixtures, as well as with a different transport model of Chung [31] that can employ corrections for high-pressure (high-density) situations. From these pictures, it can be observed that even at relatively "high" temperatures of 300 K, while the departure of the compressibility factor for the RG case with respect to the IG case is less than 5%, the corresponding departure for the dynamic viscosity reaches values above 10%. This is even more pronounced in the 115 K case (Fig. 12(c) and (d)), where the oxygen crosses its vapor-liquid "dome" transforming its thermodynamic state from vapor to sub-critical liquid to super-critical, compressible liquid (*cf.* Fig. 1). In this case, the sudden jump in the compressibility is accompanied by a huge jump in dynamic viscosity,

that shows departures of the order of one order of magnitude. Although the sub-critical state is not of interest in the present work, one can recognize that in both cases, beyond the critical pressure value for O_2 ($p_c = 5.04$ MPa), the difference in the transport property is significant compared the corresponding prediction provided by the TPG model or the Chung [31] model without high-pressure correction, thus making important the use of such model. More details and validation are provided in Sec. 2.3. The second viscosity coefficient in Eq. (2.1.6) is the volume viscosity. According to the Stokes' hypothesis [47], the coefficient of bulk viscosity, expressed as $\left(\lambda + \frac{2}{3}\mu\right)$, must be zero because the stress tensor should be traceless. An analysis of this hypothesis for real gas flows was given in [114], where nearly zero effects were showed on λ on the main flow features. For this reason, the Stokes' assumption is still employed in this work and the stress tensor can simply be written as:

$$\tau_{ij} = 2\mu \left(S_{ij} - \frac{1}{3} S_{kk} \delta_{ij} \right) , \tag{2.1.7}$$

where S_{ij} is the local rate of strain tensor:

$$S_{ij} = \frac{1}{2} \left(\frac{\partial u_i}{\partial x_j} + \frac{\partial u_j}{\partial x_i} \right) . \tag{2.1.8}$$

2.1.2 Heat and mass diffusion

2.1.2.1 General multi-component formulation

For a complete description of the molecular and heat diffusion fluxes, one can refer to the Keizer's [81] fluctuation-dissipation theory and non-equilibrium thermodynamics. In his work [81] the generic form of these vectors are shown here in the so-called Irving-Kirkwood (IK) form:

$$\boldsymbol{J_k} = L_{kq} \nabla \left(\frac{1}{R_u T} \right) - \sum_{l=1}^{N_S} L_{kl} \nabla \left(\frac{\mu_l}{R_u T} \right) , \tag{2.1.9}$$

$$\boldsymbol{Q}^{\mathrm{IK}} = L_{qq} \nabla \left(\frac{1}{R_u T} \right) - \sum_{l=1}^{N_S} L_{ql} \nabla \left(\frac{\mu_l}{R_u T} \right) , \tag{2.1.10}$$

where $\boldsymbol{J_k}$ is the partial molar flux for species k, $\boldsymbol{Q}^{\mathrm{IK}}$ is the Irving-Kirkwood form of the heat flux, μ_l is the chemical potential of species l in the mixture and R_u is the universal gas constant. Once written in this form, the diffusion coefficients can be immediately recognized:

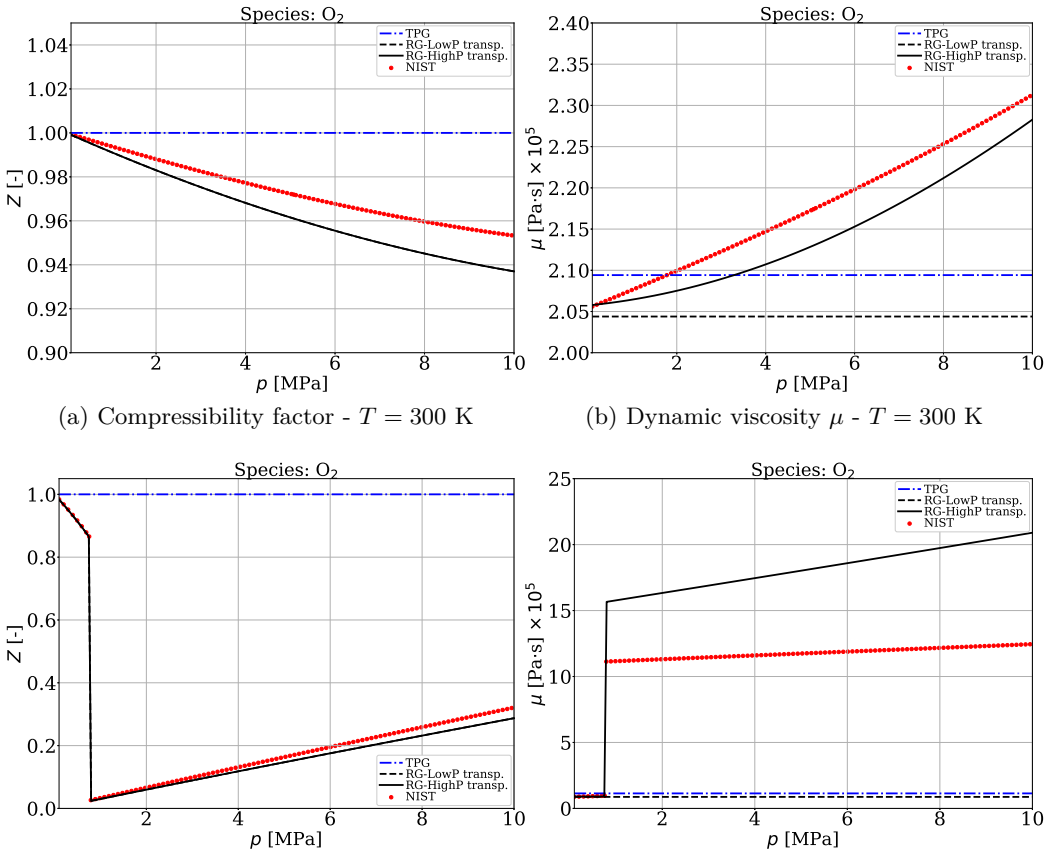

(a) Compressibility factor - $T = 300$ K

(b) Dynamic viscosity μ - $T = 300$ K

(c) Compressibility factor - $T = 115$ K

(d) Dynamic viscosity μ - $T = 115$ K

Figure 12: Comparison of the compressibility and dynamic viscosity for oxygen at 300 K and 115 K for a range of pressures. In the labels, TPG denotes the classical, mixture averaged model in which the mixture viscosity is only a function of pressure and composition, RG-LowP denotes the transport model of Chung [31] without the high-pressure correction, whereas the RG-HighP indicates the same model [31] with the high-pressure correction. For reference, the NIST data is also superimposed, indicating the importance of the high-pressure correction over both models that do not employ the correction.

- L_{kq} are the Soret diffusion elements.
- L_{kl} are the Fick diffusion elements.
- L_{qq} is the Fourier diffusion element.
- L_{ql} are the Dufour diffusion elements.

However, for a fluid mechanics/CFD application, it is more convenient to recast these diffusion fluxes with respect to the gradients of primitive variables such as T, p or X_k. After lengthy derivations one can prove that it is possible to write the overall diffusion fluxes as the sum of contributions caused by temperature, pressure and species gradients [81]:

$$J_k = A_{j,k}\nabla T + B_{j,k}\nabla p + \sum_{\substack{l=1 \\ l\neq k}}^{N_S} C_{j,kl}\nabla X_l \,, \tag{2.1.11}$$

$$Q = A_q\nabla T + B_q\nabla p + \sum_{\substack{l=1 \\ l\neq k}}^{N_S} C_{ql}\nabla X_l \,, \tag{2.1.12}$$

In the above, the mass diffusion caused by species gradients and the heat diffusion caused by temperature gradients constitute the Fick's and Fourier's type of diffusion, respectively. The additional terms appearing are instead cross diffusion effects since the diffusion of a certain property is caused by the gradients of another property. The rigorous derivation of the $A_{j,k}$, $B_{j,k}$, $C_{j,kl}$, A_q, B_q and C_{ql} coefficients is beyond the scope of the present work. The reader is referred to the works of Bird [17], Palle [149] and Giovangigli et al. [57] for detailed discussions on how to link the above diffusion terms of Eq. (2.1.12) to the fundamental diffusivity coefficients, depending on whether they are approached from a statistical mechanics, a statistical thermodynamics or a macroscopic point of view.

For the scope of the current work, this approach is discarded for the following reasons: first the inclusion of the Soret and Dufour effects are still controversial for RG mixtures at super-critical conditions even (ed especially) without phase-equilibrium [131, 105, 144, 149, 150, 233, 181, 27]. Pioneering work of Miller *et al.* [131] investigated the role of these two effects using compressible mixing layers and concluding that the Soret effect had an important effect on the shear layer growth when the pressure gradients where aligned

with the species gradients, which would occur at the edge of strong vortices. Simplified one-dimensional analyses of Palle [149] and Ribert *et al.* [181] found that these two effects were of minor and negligible effects on H_2/O_2 flames due to the large reaction rates, respectively. Analogous results were reported by [93] on oxygen droplet evaporation at high pressures. Similar results were also discussed by Giovangigli *et al.* [57] who found that while the Soret diffusion had an appreciable effect on the species diffusion fluxes, the flame structure was not significantly altered. In the work of Mahle *et al.* [112] Soret contribution was presented to significantly contribute to instantaneous differences observed in TML configurations using H_2/O_2, however differences on the order of 10% or less were identified in time-averaged properties. More recently, Kim *et al.* [82] and Traxinger *et al.* [225] explored the LOX-Kerosene and LOX-H_2 / LOX-CH_4 laminar diffusion flames using parametric EoS [82] and different propellant conditions [225] with the flamelet model and the unitary Lewis number diffusion model (therefore ignoring the multi-component diffusion model). In the first case [82], good agreement with a chemical equilibrium solver was reported, whereas in the second study [225] no specific comparison was reported for the one-dimensional flames since the focus was on the investigations of phase-separation occurrence in reacting systems (here discussed in Chap. 5). More importantly Yao *et al.* [244] recently suggested that the full multi-component mass diffusion model does not have a significant impact on the phase stability locus of relevant mixtures. This study [244] along with [225] seem to agree on the fact that Soret and Dufour effects, along with complex multi-component diffusion models of Eq. (2.1.12) do not have a major impact on the effect of VLE occurrence, thus it is possible for the present study to use simplified diffusion models which would still take into account for non-ideal transport, as briefly outlined in Fig. 12, while retaining the reduction of the computational cost that is of crucial importance for the present study.

Another important reason related to the use of the simplified diffusion model is in fact related to the high cost of the calculation of phase-equilibrium thermodynamics, thus inclusion of the above diffusion model would make the overall calculations unfeasible, even for the relatively simple 3D cases treated here (especially for those treated with implicit chemistry integration as discussed in Chap. 5). Furthermore, the effects of phase-equilibrium

thermodynamics are already relatively unexplored as far as their impact on the numerical scheme and the overall physics of the problem being studied. Since the major goal of this work is to isolate the effect that VLE has on RG mixtures without any additional perturbation included by either a physical or numerical aspect, the simplified approach for diffusive fluxes is chosen here, which is discussed in Sec. 2.1.2.2.

2.1.2.2 Simplified diffusion model

After discarding the Soret and Dufour effects, the heat and mass diffusion fluxes become based on Fick's and Fourier's type of diffusion and they can be expressed as follows :

$$j_{i,k} = \rho Y_k \mathcal{V}_{i,k} = -\rho Y_k \frac{1}{X_k} \mathcal{D}_{k,m} \frac{\partial X_k}{\partial x_i} \,, \tag{2.1.13}$$

$$q_i^{\mathrm{IK}} = -\lambda \frac{\partial T}{\partial x_i} + \sum_{k=1}^{N_S} j_{i,k} h_k \,, \tag{2.1.14}$$

Here $\mathcal{V}_{i,k}$ is the diffusion velocity for species k in the i-th direction, X_k is the mole fraction for species k, λ is the thermal conductivity and h_k is the partial massic enthalpy of species k. For completeness, the corresponding partial molar enthalpy H_k is defined, which can be obtained from the massic one using the following relationship:

$$H_k = h_k M_k \,, \tag{2.1.15}$$

where M_k is the molar mass of the component k in the mixture. $\mathcal{D}_{k,m}$ is the pseudo binary diffusion coefficient between the species k and the mixture and allows for a simpler representation of the species diffusive fluxes by neglecting multi-component diffusion (also known as Hirschfelder-Curtiss approximation [70]):

$$\mathcal{D}_{k,m} = \frac{1 - Y_k}{\sum_{j \neq k} \frac{X_j}{\mathcal{D}_{k,j}}} \,. \tag{2.1.16}$$

where $\mathcal{D}_{A,B}$ is the generic binary diffusion coefficient of species "A" into species "B". Despite these assumptions, exact mass conservation is not mathematically enforced in Eq. (2.1.13) as the net species diffusion flux $\sum_{k=1}^{N_S} \mathcal{V}_{i,k} Y_k$ is not necessarily zero. For this reason, a correction velocity needs to be included to the diffusion velocities so that the net diffusion results zero:

$$\mathcal{V}_i^{\mathrm{cor}} = -\sum_{k=1}^{N_S} Y_k \left(\frac{\mathcal{D}_{k,m}}{X_k} \frac{\partial X_k}{\partial x_i} \right) \,. \tag{2.1.17}$$

The final expression for the mass diffusion flux is therefore:

$$j_{i,k} = \rho Y_k \left(\mathcal{V}_{i,k} + \mathcal{V}_i^{\text{cor}} \right) . \tag{2.1.18}$$

2.1.3 Relations needed to close the problem

With all the equations discussed so far in Sec. 2.1, all the state relations are missing in order to close the problem. In general, for a compressible solver in its fully conservative form, the massic internal energy e, the density ρ and the composition Y_k are directly obtained from the integration of the governing equations Eqs. (2.1.1)–(2.1.4), from which pressure, temperature and the associated transport properties need to be computed. Without loss of generality the following state relations can be declared:

$$\begin{aligned} &p = p(\rho, T, Y_k) , && e = e(\rho, T, Y_k) , && \mu = \mu(\rho, T, Y_k) , \\ &\lambda = \lambda(\rho, T, Y_k) , && D_{A,B} = D_{A,B}(\rho, T, Y_k) . \end{aligned} \tag{2.1.19}$$

In all the above, specific thermodynamic and transport models are to be defined. Concerning the thermodynamics, an EoS needs to be specified. In this work the thermodynamic equilibrium is assumed, therefore an algebraic EoS is going to be used (in other words time does not play a role here). The EoS defines the links between pressure, temperature, density, internal energy and composition, plus additional relationships between other state variables, where required. Depending on the complexity of the EoS, the p and e relationships of Eq. (2.1.19) can be very complicate, involving non-trivial mathematical steps for derivation and specific numerical treatments for their solutions as already discussed in [114]. In addition, the functional dependency of p and e of Eq. (2.1.19) can evolve further, in case VLE is taken into account. Specifically, *all* the state relations of Eq. (2.1.19), plus all other thermodynamic variables that are directly or indirectly related to them through exact thermodynamic relations, need to be further corrected to account for the *phase-equilibrium*, which is an additional assumption invoked in the present work on top of the thermodynamic equilibrium.

In such case, another state variable: the *phase-fraction* β needs to be defined. As more rigorously discussed in Sec. 2.2.2, β is the ratio between the mixture number of moles in the

vapor phase, over the total number of moles in the mixture. At equilibrium, $\beta = \beta(T, p, Y_k)$ is not an independent variable of the system as it can be uniquely defined by the system temperature, pressure and composition, however its inclusion drastically changes the functional form of most of the relations written in Eq. (2.1.19) (plus all other derived relations), which therefore need to be adjusted accordingly to ensure thermodynamic consistency and correctness. This aspect will be extensively discussed in Sec. 2.2.2.

On the other hand, the transport properties of Eq. (2.1.19) will be computed using the model of Chung [31] and employing the high-pressure correction. This model is presented in Sec. 2.3. In case VLE occurs, the functional dependency of μ, λ and $D_{A,B}$ does not change, and the thermodynamic properties (such as ρ) coming from the VLE are going to be used instead. To further explain this point, if μ is the dynamic viscosity in a mixture that forms VLE, it is avoided here to compute $\mu = \beta\mu^V + (1-\beta)\mu^L$ where μ^V and μ^L are be the viscosities of the vapor and the liquid phases only, but the original *single-phase* functional form of Chung [31] is still used, generally expressed in Eq. (2.1.19), where ρ is corrected for the VLE. The reason behind this choice is motivated by the following discussion: the model of Chung [31] is already capable to deal with both phases, either liquid or vapor at both sub-critical or super-critical conditions, hence it is already adapted to deal with two phases, though not occurring at the same point together. The VLE method discussed in Sec. 2.2.2 essentially blends already some properties between the two phases: one of these is the density. As a result, with a blended value of density that is already representative of the whole mixture in the VLE state, there is no reason to blend the viscosities of the two phases computed separately. First, viscosity is not an extensive variable, for which a "mass" or "volume" (or β) based average would physically make sense, and secondly by imposing a linear blend rule, some non-linearities between the two phases will be intrinsically destroyed. As demonstrated in Appendix C, simplifications of non-linear relationships can lead to significant errors in the predictions of some thermodynamic variables, therefore it is preferred to not use the linear blend rule for the viscosity and proceed with original functional dependencies of all transport properties of Eq. (2.1.19) and directly use VLE-based state variables, where needed. Same discussion follows for the mixture thermal conductivity

in presence of VLE.

2.2 Real gas thermodynamics

In this section, the entire thermodynamic module is discussed both from a single-phase and VLE perspective. The generic definitions that hold for either the single- and the multi-phase states are provided, followed by an extensive mathematical description of the VLE model. Particular emphasis is given to the calculation of the mixture thermodynamic properties in presence of VLE that although well established for single-phase systems, they are not for multi-phase equilibrium systems. This is one major contribution of the present work. Finally, the formulation of the single-phase RG thermodynamics is given in form of a Generalized Cubic EoS (GCEoS), where all the combinations of EoS and mixing rules (MR) are introduced. As discussed in Sec. 1.3.2, many different EoS models are available. Usually an higher model accuracy is accompanied by a corresponding higher computational expense to compute the properties. As a result, an EoS of the "cubic" family has been chosen for the present study because it compromises the accuracy with cost. One main advantage of the GCEoS is the fact that analytic forms of some thermodynamic problems are available at least within the single-phase region. These are discussed further in Sec. 2.2.3.
The generic form of a cubic EoS is made of two terms as illustrated below:

$$p = \frac{R_u T}{V - b} - \frac{\Theta}{V^2 + \delta V + \varepsilon}\,. \tag{2.2.1}$$

By varying the form of the coefficients Θ, δ and ϵ different models can be obtained [163]. This form illustrates the physics modeled by cubic EoSs. Recall that this form of EoS differs from the ideal law because it takes into account some inter-molecular forces:

- The first term is $\frac{R_u T}{V-b}$ instead of $\frac{R_u T}{V}$ and models the repulsive force that molecules exert on each other at short distance. The b term is proportional to the actual volume of the molecule, that is a correction to the molecule volume occupied at a given pressure and temperature is applied.

- The second term $\frac{\Theta}{V^2+\delta V+\varepsilon}$ models the long-range attractive forces between the molecules such as electrostatics forces, polarization or London dispersion forces. These forces

are responsible in maintaining gas molecules together and that allow for the liquid state to exist. They decrease the pressure caused by the fluid on the walls of a vessel, hence the negative sign for this term.

Once again it is important to understand that any EoS model is independent of the VLE model which comes from pure thermodynamic concepts related to the second law. Theoretically any EoS (or group of EoSs) can be adapted to VLE as long as one has the ability to achieve enough mathematical description of two or more phases in which one is interested. For instance, it is possible to have two different EoS models, one that predicts the gaseous phase only and one that predicts the liquid phase only. Both can be concurrently used as sub-models for the VLE as long as the problem solution follows the same steps detailed in Sec. 2.2.2. For the present GCEoS case, this problem does not exist because the GCEoS can predict both the gaseous and the liquid phase.

In the next three sections, the generic main definitions for a N_s component, real-gas mixture are given, followed by the description of the VLE model and the GCEoS model. The idea is that the first two sections are EoS-free and can be theoretically applied to any EoS model. The division of these three subsections is intentional in order to emphasize the fact that the GCEoS model is auxiliary to both the generic (single-phase) RG model, as well as the VLE model but the opposite does not hold.

2.2.1 Main definitions

Let p, T, ρ the pressure, the temperature and the density of a multi-component mixture with N_s species, each having mole fraction X_i, a corresponding mass fraction Y_i, molecular weight MW_i and molar mass $M_i = MW_i/1000$, $i = 1, \cdots, N_s$. Without loss of generality, the link between the above state variables can be expressed (as in Eq. (2.1.19)) through a general form of EoS that is explicit in pressure:

$$p = p(T, \rho, \mathbf{X}) \,, \tag{2.2.2}$$

where $\mathbf{X} = \{X_i \,|\, i = 1, \cdots, N_s\}$ and $\mathbf{Y} = \{Y_i \,|\, i = 1, \cdots, N_s\}$ are the sets of mole and mass fractions, respectively. Using its definition, the compressibility factor Z is given:

$$Z = \frac{pV}{R_u T} = \frac{pM}{\rho R_u T}\,, \tag{2.2.3}$$

where R_u= 8.31451 J/mol-K is the universal gas constant, M is the mixture molar mass (or weight) and V= M/ρ is the mixture molar volume. In the following sections, partial derivatives will be in general expressed as $(\partial(\cdot)/\partial(\circ))_x$ notation, where x, represents the variable or the set of variables that is considered constant during the derivation process and will be specified accordingly. Finally, variables denoted with over bars, such as $\overline{\Psi}$ represent the extensive quantity corresponding to the intensive quantity Ψ. For a mole-based intensive quantity, the relationship $\overline{\Psi} = N\Psi$ holds, where N= $\sum_{i=1}^{N_s} N_i$ is the sum of the number of moles for each species N_i or N_k in the mixture. Additional definitions, useful throughout the subsequent discussion are given below:

$$\rho = \frac{\overline{M}}{\overline{V}} \ \text{ in kg.m}^{-3} \tag{2.2.4}$$

$$v = \frac{\overline{V}}{\overline{M}} \ \text{ in m}^3\text{.kg}^{-1} \tag{2.2.5}$$

$$V = vM \ \text{ in m}^3\text{.mol}^{-1} \tag{2.2.6}$$

$$\rho = \frac{1}{v} = \frac{M}{V} = 10^{-3}\frac{MW}{V}\,, \tag{2.2.7}$$

where the system extensive mass $\overline{M}$ and volume $\overline{V}$ have been introduced alongside the specific volume v. Additional important relations are the conversions between mole fractions X_i and mass fractions Y_i and the different possible computations of the mixture molecular weight MW or molar weight M:

$$X_i = Y_i\frac{MW}{MW_i} = Y_i\frac{M}{M_i} \tag{2.2.8}$$

$$Y_i = X_i\frac{MW_i}{MW} = X_i\frac{M_i}{M} \tag{2.2.9}$$

$$MW = \frac{1}{\sum_i^{N_s}\frac{Y_i}{MW_i}} = \sum_i^{N_s} X_i MW_i \tag{2.2.10}$$

$$M = \frac{1}{\sum_i^{N_s}\frac{Y_i}{M_i}} = \sum_i^{N_s} X_i M_i\,. \tag{2.2.11}$$

Departure functions are constructed from the principle of corresponding states [46] and define the deviations that the actual real-gas property has compared to the corresponding ideal-gas value. Indicating as $\Delta\Phi = \Phi - \Phi^{ig}$ the departure function of a generic thermodynamic, mole-based, intensive variable Φ with respect to its corresponding ideal gas value Φ^{ig}, the (intensive) internal energy E, enthalpy H, entropy S, Gibbs energy $G = H - TS$ and Helmholtz energy $A = G - pV$ departure functions can be written as:

$$\frac{\Delta E}{R_u T} = -\int_0^{\rho} T \left(\frac{\partial Z}{\partial T}\right)_{\rho,\mathbf{X}} \frac{d\rho}{\rho}\,, \tag{2.2.12}$$

$$\frac{\Delta H}{R_u T} = \frac{\Delta E}{R_u T} + (Z-1)\,, \tag{2.2.13}$$

$$\frac{\Delta S}{R_u} = \int_0^{\rho} \left[-T\left(\frac{\partial Z}{\partial T}\right)_{\rho,\mathbf{X}} - (Z-1)\right]\frac{d\rho}{\rho} + \ln Z = \frac{\Delta E}{R_u T} - \int_0^{\rho}(Z-1)\frac{d\rho}{\rho} + \ln Z\,, \tag{2.2.14}$$

$$\frac{\Delta G}{R_u T} = \int_0^{\rho}\left(\frac{Z-1}{\rho}\right)d\rho + (Z-1) - \ln Z = \frac{\Delta H}{R_u T} - \frac{\Delta S}{R_u}\,, \tag{2.2.15}$$

$$\frac{\Delta A}{R_u T} = \int_0^{\rho}\left(\frac{Z-1}{\rho}\right)d\rho - \ln Z = \frac{\Delta G}{R_u T} - (Z-1)\,. \tag{2.2.16}$$

The above departure functions are obtained when T, p and $\mathbf{X}$ are maintained constant [46]. Another definition, useful for later purposes is the Helmholtz energy departure function obtained when T and V are maintained constant:

$$\frac{\Delta A_{TV}}{R_u T} = \int_0^{\rho}\left(\frac{Z-1}{\rho}\right)d\rho\,. \tag{2.2.17}$$

Regarding the corresponding IG value Φ^{ig}, the general form can be expressed as $\Phi^{ig} = \sum_{i=1}^{N_s} X_i \psi_i^{ig}$, where ψ_i^{ig} is the $i-$th species, mole-based, IG property that can be obtained, for example, using the NASA 9-coefficients [123] or CHEMKIN 7-coefficients [80] polynomials. Note that in case of entropy, ψ_i^{ig} is also a function of pressure, therefore the result obtained from the polynomials must be added to the pressure term $-R_u \ln(p/1bar)$. Moreover, when ideal-gas mixture entropy is computed, the additional mixing term $-R_u \sum_{i=1}^{N_s} X_i \ln X_i$ needs to be added to Φ^{ig} [43]. These additional terms have also an impact on the calculation of the Gibbs and Helmholtz energies according to their definitions.

Similarly, one can compute the molar specific heats departure functions starting from their

definition:

$$\Delta C_v = \left(\frac{\partial \Delta E}{\partial T}\right)_{\rho,\mathbf{X}} , \tag{2.2.18}$$

$$\Delta C_p = \left(\frac{\partial \Delta H}{\partial T}\right)_{p,\mathbf{X}} = \Delta C_v + \frac{TM}{\rho^2}\frac{\left(\frac{\partial p}{\partial T}\right)^2_{\rho,\mathbf{X}}}{\left(\frac{\partial p}{\partial \rho}\right)_{T,\mathbf{X}}} - R_u \, . \tag{2.2.19}$$

On the other hand, the isentropic speed of sound is provided by [139]:

$$c^2 = \left(\frac{\partial p}{\partial \rho}\right)_{S,\mathbf{X}} = \gamma \left(\frac{\partial p}{\partial \rho}\right)_{T,\mathbf{X}} , \tag{2.2.20}$$

where $\gamma = C_p/C_v = c_p \, / \, c_v$ is the specific heats ratio. Finally, introducing the definition of the isobaric expansivity α_p and isothermal compressibility κ_T [43]:

$$\alpha_p = -\frac{1}{\rho}\left(\frac{\partial \rho}{\partial T}\right)_{p,\mathbf{X}} \underset{\text{using } \left(\frac{\partial \rho}{\partial T}\right)_{p,\mathbf{X}} \left(\frac{\partial T}{\partial p}\right)_{\rho,\mathbf{X}} \left(\frac{\partial p}{\partial \rho}\right)_{T,\mathbf{X}} = -1}{=} \frac{1}{\rho}\frac{\left(\frac{\partial p}{\partial T}\right)_{\rho,\mathbf{X}}}{\left(\frac{\partial p}{\partial \rho}\right)_{T,\mathbf{X}}} , \qquad \kappa_T = \frac{1}{\rho\left(\frac{\partial p}{\partial \rho}\right)_{T,\mathbf{X}}} , \tag{2.2.21}$$

we can define another important quantity: the isentropic compressibility κ_s as [163]:

$$\kappa_s = \kappa_T - \frac{T\alpha_p^2}{\rho c_p} \, . \tag{2.2.22}$$

In this way, a different definition of the speed of sound can be obtained, which will result useful for later discussion:

$$c^2 = \frac{1}{\kappa_s \rho} \, . \tag{2.2.23}$$

Using the definition of κ_T from Eq. (2.2.21) into Eq. (2.2.20) and compare the result with Eq. (2.2.23) it is also possible to obtain the following relationship:

$$\frac{\kappa_T}{\kappa_s} = \gamma \, . \tag{2.2.24}$$

Another important relationship between c_p, c_v and α_p is given by [43]:

$$C_p - C_v = \frac{TM}{\rho^2}\left(\frac{\partial p}{\partial T}\right)_{\rho,\mathbf{X}}\left(\frac{\partial \rho}{\partial T}\right)_{p,\mathbf{X}} = T\frac{M}{\rho}\frac{\alpha_p^2}{\kappa_T} \, . \tag{2.2.25}$$

At this stage, the derivatives $(\partial p/\partial T)_{\rho,\mathbf{X}}$, $(\partial \rho/\partial T)_{p,\mathbf{X}}$ and $(\partial p/\partial \rho)_{T,\mathbf{X}}$ are assumed to be known with the analytical expression of the EoS in Eq. (2.2.2).

The partial molar quantity of a generic intensive mixture property Ψ is defined for each species i as [43]:

$$\Psi_i = \left(\frac{\partial \overline{\Psi}}{\partial N_i}\right)_{T,p,\mathbf{N}_i} = \left(\frac{\partial N\Psi}{\partial N_i}\right)_{T,p,\mathbf{N}_i}, \qquad i = 1,\ldots,N_s \tag{2.2.26}$$

where $\mathbf{N}_i = \{N_j \,|\, j = 1,\cdots,N_s,\, j \neq i\}$. The set of partial molar quantities has the unique property to satisfy the following relationship:

$$\Psi = \sum_{i=1}^{N_s} \Psi_i X_i \,. \tag{2.2.27}$$

For an IG , the relationship simplifies to $\Psi_i = \psi_i^{ig}$ because $\Psi \equiv \Phi^{ig}$ (defined earlier)

Partial molar volume and partial molar enthalpy are also of interest, both particularly useful for example in the determination of mass and energy diffusion terms as indicated in Eq. (2.1.14) as well as in [195]:

$$V_i = \left(\frac{\partial \overline{V}}{\partial N_i}\right)_{T,p,\mathbf{N}_i} = \left(\frac{\partial NV}{\partial N_i}\right)_{T,p,\mathbf{N}_i}, \quad H_i = \left(\frac{\partial \overline{H}}{\partial N_i}\right)_{T,p,\mathbf{N}_i} = \left(\frac{\partial NH}{\partial N_i}\right)_{T,p,\mathbf{N}_i}. \tag{2.2.28}$$

The fugacity f_i of the i-th species in a non-ideal mixture is used in place of the pressure to describe RG behaviors of the species alone, as well as in the mixture. One way to look at it, is to define the chemical potential of the i-th species in an ideal μ_i^{ig} and a non-ideal μ_i case [43]:

$$\mu_i(T,p,\mathbf{X}) = \mu_i^{\circ}(T,p_0) + R_u T \ln\left(\frac{f_i(T,p,\mathbf{X})}{p_0}\right), \qquad \mu_i^{ig}(T,p,\mathbf{X}) = \mu_i^{\circ}(T,p_0) + R_u T \ln\left(\frac{pX_i}{p_0}\right),$$

where $\mu_i^{\circ}(T,p_0)$ is the reference chemical potential of the i-th species at the reference pressure p_0. By taking the difference of both quantities one obtains:

$$\mu_i(T,p,\mathbf{X}) - \mu_i^{ig}(T,p,\mathbf{X}) = R_u T \ln\left(\frac{f_i(T,p,\mathbf{X})}{pX_i}\right) = R_u T \ln\phi_i(T,p,\mathbf{X}), \tag{2.2.29}$$

where the fugacity coefficient $\phi_i(T,p,\mathbf{X}) = f_i(T,p,\mathbf{X})/pX_i$ has been defined. Clearly, the fugacity defines the departure function of the species chemical potentials, in fact if $f_i = pX_i$, as in the ideal case, one recovers $\mu_i = \mu_i^{ig}$. Equation (2.2.29) also represents the

mathematical definition of the fugacity and the fugacity coefficient. Given the fact that the chemical potential is the partial molar Gibbs free energy of species i in the mixture, one obtains [46]:

$$\mu_i - \mu_i^{ig} = \left(\frac{\partial(\overline{G} - \overline{G}^{ig})}{\partial N_i}\right)_{T,p,\mathbf{N}_i} = \left(\frac{\partial(\overline{A} - \overline{A}^{ig})_{T,V}}{\partial N_i}\right)_{T,\overline{V},\mathbf{N}_i} - \ln Z = \\ = \left(\frac{\partial \Delta\overline{A}_{T,V}}{\partial N_i}\right)_{T,\overline{V},\mathbf{N}_i} - R_u T \ln Z\,,$$

where the interchange between Gibbs and Helmholtz energies in the above step is simply an additional manipulation that makes the actual calculation easier once an EoS model is chosen [46]. Therefore the final definition of the i-th fugacity coefficient can be written as:

$$\ln\phi_i(T,p,\mathbf{X}) = \frac{\mu_i - \mu_i^{ig}}{R_u T} = \frac{1}{R_u T}\left(\frac{\partial \Delta\overline{A}_{T,V}}{\partial N_i}\right)_{T,\overline{V},\mathbf{N}_i} - \ln Z = \frac{1}{R_u T}\left(\frac{\partial N \Delta A_{T,V}}{\partial N_i}\right)_{T,\overline{V},\mathbf{N}_i} - \ln Z\,, \tag{2.2.30}$$

where $\Delta A_{T,V}$ is computed from Eq. (2.2.17).

2.2.2 Multi-phase equilibrium, real-gas thermodynamics

In this section, the known concept of VLE applied for a generic, multi-component mixture at given temperature, T, pressure p and composition $\mathbf{X}$ is introduced first. Next, all the multi-phase, thermodynamic properties in presence of VLE are derived, which constitutes a key contribution of this work.

2.2.2.1 The VLE problem

To represent multi-phase behavior of multi-component mixtures, the assumption of phase equilibrium (VLE) is invoked throughout the calculations. This assumption imposes equality of pressure, temperature and fugacity of both the liquid (L) and the vapor (V) phase such that [46]:

$$p_L = p_V = p; \quad T_L = T_V = T; \quad f_i^L = f_i^V \qquad i = 1, \ldots, N_s\,. \tag{2.2.31}$$

Note that this method assumes two or more components in the system. For single component one can use other methods such as Clausius-Clapeyron equation discussed in classical

thermodynamic books, or Maxwell's method or Antoine's equation as discussed in Appendix E. An additional unknown β is introduced, which indicates the ratio between the mixture number of moles in the vapor phase over the total number of moles. Then, mass conservation imposes [49]: $X_i = \beta y_i + (1-\beta)x_i$, where x_i and y_i correspond to the mole fractions of species i in the liquid and the vapor phase, respectively. Both x_i and y_i satisfy the condition: $\sum_{i=1}^{N_s} x_i = 1$ and $\sum_{i=1}^{N_s} y_i = 1$. For each phase taken separately, still all the formulas discussed in Sec. 2.2.1 hold, provided that the substitution $x_i \leftarrow X_i$ and $y_i \leftarrow X_i$ is made for the liquid and the vapor phase, respectively, wherever mole fractions are used, including the calculation of the phase molar mass with Eq. (2.2.11).

However, additional *blend rules* for the phase properties are required in order to define the properties of the whole mixture and close the problem. Two extensive properties are required to be blended. In this work, similarly to other works [118, 168], the extensive volume and the extensive internal energy are blended, however other approaches are possible were volume and enthalpy are blended [44]:

$$\overline{V} = \overline{V}^V + \overline{V}^L \;\rightarrow\; NV = N^V V^V + N^L V^L \;\rightarrow V = \frac{M}{\rho} = \frac{N^V}{N}\frac{M^V}{\rho^V} + \frac{N^L}{N}\frac{M^L}{\rho^L}\,, \quad (2.2.32)$$

$$\overline{E} = \overline{E}^V + \overline{E}^L \;\rightarrow\; NE = N^V E^V + N^L E^L \;\rightarrow E = \frac{N^V}{N}E^V + \frac{N^L}{N}E^L\,, \quad (2.2.33)$$

where N, N^L and N^V are the total number of moles of the mixture, liquid and vapor phase respectively. Therefore, by using the definition $\beta = N^V/N$ and observing that $N = N^L + N^V$ for continuity, the accessory state relations for the multi-phase equilibrium thermodynamics become:

$$\frac{M}{\rho} = \beta\frac{M^V}{\rho^V} + (1-\beta)\frac{M^L}{\rho^L} \quad (2.2.34)$$

$$E = \beta E^V + (1-\beta)E^L\,. \quad (2.2.35)$$

In the above, for example the vapor molar mass $M^V = M^V(\mathbf{y})$ and the vapor phase internal energy is $E^V = E^V(T, p, \mathbf{y})$, with $\mathbf{y} = \{y_i \,|\, i = 1, \cdots, N_s\}$ (and similarly M^L and E^V for the liquid phase). Both can be computed using the single phase thermodynamics formulas however $\mathbf{y}$ is unknown and needs to be computed along with $\mathbf{x} = \{x_i \,|\, i = 1, \cdots, N_s\}$ and β. Also note that Eqs. (2.2.34)–(2.2.35) naturally collapse to the single phase ones in case a

pure liquid ($\beta = 0$, $\mathbf{x} = \mathbf{X}$) or a pure vapor ($\beta = 1$, $\mathbf{y} = \mathbf{X}$) exist. The latter conditions may happen either in a sub-critical (pure liquid or pure gas/vapor) or super-critical (compressible liquid or super-critical fluid) state.

To find the unknowns, the fugacity equalities of Eq. (2.2.31) are recast in form of fugacity coefficient and defining the vapor to liquid phase mole fractions ratio for each i-th component $K_i = y_i/x_i$ one obtains a set of N_s non-linear algebraic equations, to which an additional constraint $\sum_{i=1}^{N_s} x_i - \sum_{i=1}^{N_s} y_i = 0$ needs to be added. This latter constraint can be further manipulated using the definition of K_i and $X_i = \beta y_i + (1-\beta)x_i$ to obtain the Rachford-Rice equation [46]. Therefore, the non-linear system of $N_s + 1$ equations in the unknowns K_i and β becomes:

$$\frac{y_i}{x_i} = \frac{\phi_i^L}{\phi_i^V}\frac{p^L}{p^V} \qquad \rightarrow \qquad \ln K_i - \ln\phi_i^L + \ln\phi_i^V = 0\,, \qquad i = 1, \ldots, N_s \tag{2.2.36}$$

$$\sum_{i=1}^{N_s} \frac{X_i(K_i - 1)}{1 + \beta(K_i - 1)} = 0\,. \tag{2.2.37}$$

The system of Eqs. (2.2.36)–(2.2.37) is solved for given mixture temperature T, pressure p and composition $\mathbf{X}$ (hereafter called Tp problem). It is very important to keep in mind the temperature, pressure and composition dependency of the unknowns: $\beta = \beta(T, p, \mathbf{X})$, $\mathbf{y} = \mathbf{y}(T, p, \mathbf{X})$, $\mathbf{x} = \mathbf{x}(T, p, \mathbf{X})$.

Fugacity coefficients in each phase are determined using Eq. (2.2.30), where proper phase mole fractions are used as specified above. It is emphasized the fact that in Eq. (2.2.36), the assumption of $p^V = p^L = p$ has been used. Accounting for mechanical non-equilibrium would provide a model for the pressures ratio, which involves capillarity effects [49, 106]. In addition, Eq. (2.2.36) has been written in logarithmic form in order to improve numerical convergence. Solution of Eqs. (2.2.36)–(2.2.37) is also known as VLE problem [127] and its solution is discussed in Sec. 3.4.1.

Once these basic variables are known, mixture compressibility Z is obtained using its definition in Eq. (2.2.3) and $H = E + pV = E + pM/\rho$, where ρ and E are now calculated through Eq. (2.2.34) and Eq. (2.2.35). Similarly $G = \beta G^V + (1-\beta)G^L$, $S = (H - G)/T$ and $A = G - pM/\rho$ follow their definitions too (for the Gibbs energy, the same approach

of Eq. (2.2.33) is used, however S and A follow their definitions, for thermodynamic consistency). Other phase-related quantities are also available such as the ρ^η, M^η, Z^η, where $\eta = L$ or V. For example $\rho^L = \rho^L(T, p, \mathbf{x})$ is obtained by inversion of Eq. (2.2.2) once $\mathbf{x}$ is known. Typically for the family of cubic EoS, such as the Peng-Robinson EoS [154], this means to obtain $Z^L = Z^L(T, p, \mathbf{x})$ first through a cubic, algebraic equation (see Appendix A), and then compute $\rho^L = pM^L/(Z^L R_u T)$. If during the solution of the cubic equation in Z^L multiple real roots arise, that is $\mathbf{Z}^L = [Z_1, Z_2, Z_3]^T$ with $Z_1 < Z_2 < Z_3$, the choice is now correctly based on the phase, which is known upfront. For instance if Z^L is sought, then $Z^L = Z_1$. On the contrary, if the vapor phase is being sought, the same procedure applies and $Z^V = Z_3$.

Note that the solution $\mathbf{Z}^L = [Z_1, Z_2, Z_3]^T$ would be different if one approaches the problem in the form $Z = Z(T, p, \mathbf{X})$ because $\mathbf{x} \neq \mathbf{X}$ in the VLE region. In other words, solving for $Z = Z(T, p, \mathbf{X})$, meaning solving the problem assuming "single-fluid" provides a different (erroneous) solution, and in addition, the choice that one would make on the value of Z in case multiple real roots occur, would be, at the best, based on the minimum Gibbs energy criterion (see Appendix A), if not arbitrary. The minimum Gibbs criterion (which boils down to the Maxwell's criterion for a single component mixture), simply computes the Gibbs energies of the "presumed" pseudo phases corresponding to a lower and upper value of the $\mathbf{Z}$ vector, and the pseudo phase corresponding to the minimum Gibbs energy is chosen because it is considered more stable.

However, the application of VLE imposes Eq. (2.2.31) and guarantees the true Gibbs energy minimum [126]. That is the same as saying that VLE ensures to reach a *fourth* value of the mixture compressibility factor such that the system is at an even lower value of the Gibbs energy, not reachable with the $Z = Z(T, p, \mathbf{X})$ (single fluid) approach.

For example, Fig. 13(b) shows the variation of the N_2/C_6H_{16} mixture compressibility as a function of the nitrogen mole fraction, for $p = 10\,\text{MPa}$ and $T = 377.9\,\text{K}$. This mixture is known to form VLE for a range of values of pressure and temperature [45, 164] for which the VLE diagram is represented in Fig. 13(a) along with the chosen $p = 10\,\text{MPa}$ isobaric line. The two curves agree identically at the extremes, where the single phases occur, whereas

substantial variations can be observed in the center values of compressibility where VLE forms. Figure 13(c) shows the mixture Gibbs energy as a function of the mixture compressibility (essentially G is plotted along the Z curves of Fig. 13(b)) for the two approaches. While the two values of G match in the single phase regions, the value computed with VLE is always smaller than the minimum Gibbs approach in the center region, where VLE occurs, confirming the fact that the mixture tends to spontaneously form a multi-phase system that needs to be taken into account correctly.

Because of the above statements, even when the $Z = Z(T, p, \mathbf{X})$ problem returns one real

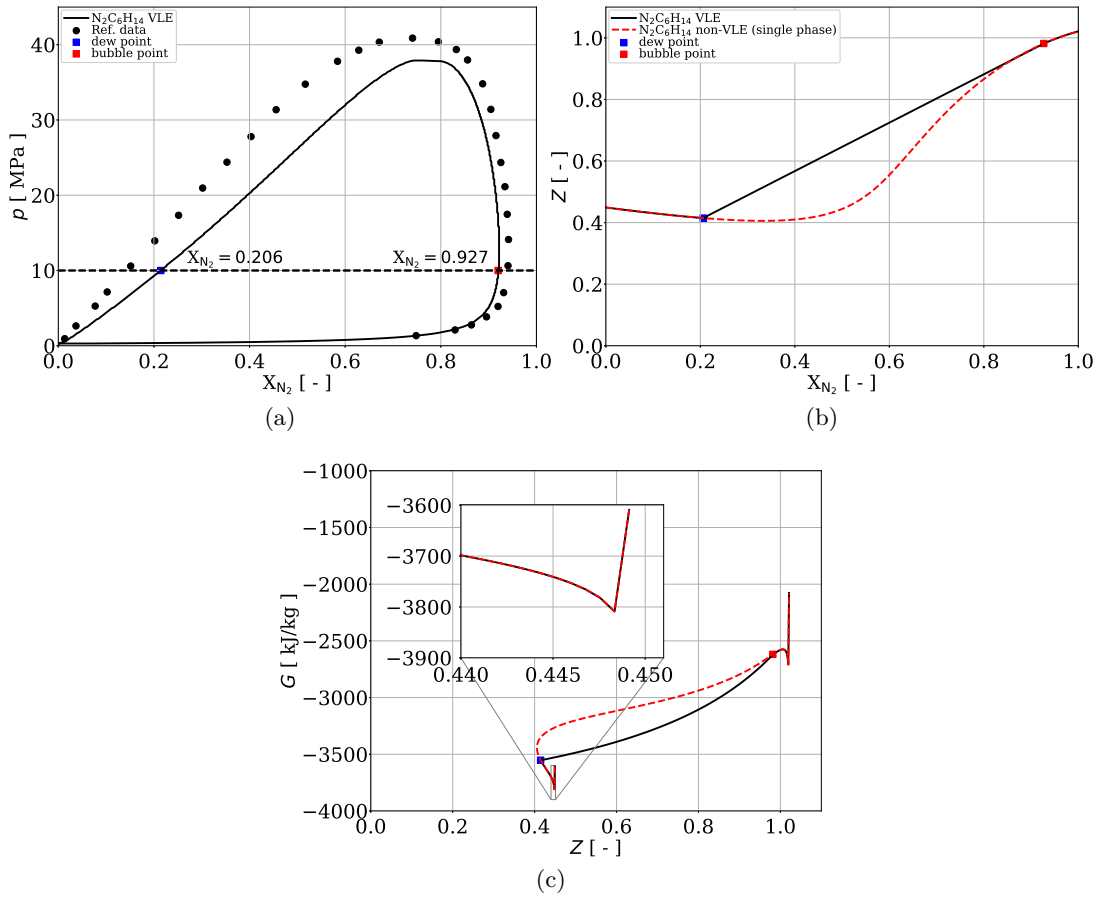

Figure 13: VLE diagram (a), mixture compressibility (b) and Gibbs free energy (c) for a nitrogen/hexane (N_2/C_6H_{16}) mixture as a function the amount of N_2 in mole fractions. The mixture pressure and temperature are maintained fixed in Fig. b) and c) at $p = 10\,\mathrm{MPa}$ and $T = 377.9\,\mathrm{K}$, respectively. For these plots, the PR EoS has been used (see also [226]).

value of Z, it cannot be said that VLE does not form. Instead the whole procedure based

on Eq. (2.2.31) must be followed and only in the case the result of $\beta = 0$ or $\beta = 1$ is obtained, one can conclude that only one phase exists, and therefore the single fluid/phase approach theory discussed in Sec. 2.2.1 is perfectly valid [129]. Algorithm 1 in Appendix D summarizes the steps to perform in order to compute the phase quantities described above once the VLE problem is solved (description on how to solve the VLE problem is addressed in Sec. 3.4.1 but extensive details are given in [129]). Algorithm 2 instead summarizes the steps to compute some basic mixture quantities. Once again, if VLE does not occur, the well-known single phase RG thermodynamics applies and phases/mixture values become identical.

2.2.2.2 Real gas - VLE thermodynamics: main derivatives

The information provided in the previous section are in general enough for a calculation that requires only minimal output, such as mixture density, compressibility or internal energy. However, in general all the quantities defined in Sec. 2.2.2.1 are needed. Calculation of higher order thermodynamic variables in the VLE region requires the knowledge of the derivatives of the VLE variables. This can be seen immediately if one considers the calculation of C_p. Its definition must be the one dictated by thermodynamics. This involves H, which involves E and ρ obtained using Eqs. (2.2.34)–(2.2.35). That is:

$$C_p = \left(\frac{\partial H}{\partial T}\right)_{p,\mathbf{X}} = \left(\frac{\partial \left(E + \dfrac{pM}{\rho}\right)}{\partial T}\right)_{p,\mathbf{X}} \overset{\text{using Eq. (2.2.35) for } E}{\downarrow =}$$
$$= \beta \left(\frac{\partial E^V}{\partial T}\right)_{p,\mathbf{X}} + (1-\beta)\left(\frac{\partial E^L}{\partial T}\right)_{p,\mathbf{X}} + \left(\frac{\partial \beta}{\partial T}\right)_{p,\mathbf{X}} (E^V - E^L) - \frac{pM}{\rho^2}\left(\frac{\partial \rho}{\partial T}\right)_{p,\mathbf{X}}, \tag{2.2.38}$$

which is substantially different from a simple blend between phase quantities in the form $C_p = \beta C_p^V + (1-\beta) C_p^L$ used by [169] (refer to Appendix C for more insights). Note that $E^V = E^V(T, p, \mathbf{y})$, $E^L = E^L(T, p, \mathbf{x})$, meaning that both $\mathbf{y}$ and $\mathbf{x}$ dependency on T need to be taken into account with the derivative. The same applies to the last term for the density derivative with respect to temperature. In fact, whenever a temperature/pressure

derivative appears, even with fixed mixture "global" composition $\mathbf{X}$, phase compositions $\mathbf{x}$ and $\mathbf{y}$ vary accordingly, because β varies as well. For this reason, the following quantities:

$$\left(\frac{\partial\beta}{\partial T}\right)_{p,\mathbf{X}}, \quad \left(\frac{\partial\beta}{\partial p}\right)_{T,\mathbf{X}}, \quad \left(\frac{\partial\mathbf{x}}{\partial T}\right)_{p,\mathbf{X}}, \quad \left(\frac{\partial\mathbf{y}}{\partial T}\right)_{p,\mathbf{X}}, \quad \left(\frac{\partial\mathbf{x}}{\partial p}\right)_{T,\mathbf{X}}, \quad \left(\frac{\partial\mathbf{y}}{\partial p}\right)_{T,\mathbf{X}}, \tag{2.2.39}$$

are required to construct all the VLE thermodynamic variables. The last four are vectors of dimension N_s.

The approach requires to impose Eq. (2.2.31). First, the following change in variables is made:

$$v_i = \beta y_i\,, \qquad l_i = (1-\beta)x_i \qquad i = 1,\cdots,N_s \tag{2.2.40}$$

such that one can write $\mathbf{X} = \mathbf{v}+\mathbf{l}$, with $\mathbf{v} = \{v_i \,|\, i = 1,\cdots,N_s\}$ and $\mathbf{l} = \{l_i \,|\, i = 1,\cdots,N_s\}$. In this way, the following identity can be applied since $\sum_{i=1}^{N_s} y_i = \sum_{i=1}^{N_s} x_i = 1$:

$$\beta = \sum_{i=1}^{N_s} v_i\,. \tag{2.2.41}$$

The variables $\mathbf{v}$, T and p are now the independent variables. Determination of all the quantities in Eq. (2.2.39) essentially requires the knowledge of both temperature and pressure derivatives of the v_i quantities. The step-by-step derivations are given in Appendix K. In the following the final result is directly provided, which is given by the solution of two linear systems:

$$\boldsymbol{\mathcal{A}}\boldsymbol{\chi}_T = \boldsymbol{b}_T\,, \tag{2.2.42}$$

$$\boldsymbol{\mathcal{A}}\boldsymbol{\chi}_p = \boldsymbol{b}_p\,, \tag{2.2.43}$$

where:

$$\mathcal{A}_{ik} = \left(1-\delta_{ki}\frac{X_k}{y_k x_k}\right) + \\ + \beta(1-\beta)\sum_{j=1}^{N_s}\left[\frac{y_j}{\beta}\left(\frac{\partial \ln\phi_i^V}{\partial y_j}\right)_{T,p,\mathbf{X},\mathbf{y}_j}\left(1-\frac{\delta_{kj}}{y_j}\right) + \frac{x_j}{1-\beta}\left(\frac{\partial \ln\phi_i^L}{\partial x_j}\right)_{T,p,\mathbf{X},\mathbf{x}_j}\left(1-\frac{\delta_{jk}}{x_j}\right)\right], \tag{2.2.44}$$

$$b_{T,i} = \beta(1-\beta)\left[\left(\frac{\partial \ln\phi_i^V}{\partial T}\right)_{p,\mathbf{X},\mathbf{y}} - \left(\frac{\partial \ln\phi_i^L}{\partial T}\right)_{p,\mathbf{X},\mathbf{x}}\right], \tag{2.2.45}$$

$$b_{p,i} = \beta(1-\beta)\left[\left(\frac{\partial \ln\phi_i^V}{\partial p}\right)_{T,\mathbf{X},\mathbf{y}} - \left(\frac{\partial \ln\phi_i^L}{\partial p}\right)_{T,\mathbf{X},\mathbf{x}}\right], \tag{2.2.46}$$

$$\chi_{T,k} = \left(\frac{\partial v_k}{\partial T}\right)_{p,\mathbf{X}}, \tag{2.2.47}$$

$$\chi_{p,k} = \left(\frac{\partial v_k}{\partial p}\right)_{T,\mathbf{X}}, \tag{2.2.48}$$

with $i, k = 1, \cdots, N_s$ and δ_{ij} the Kronecker delta.

Note that $\mathcal{A}$ is the same for both systems and thus it can be assembled/inverted only once. All the fugacity coefficients (frozen) derivatives appearing in Eqs. (K.0.23)–(K.0.25) can be easily computed using an EoS model (see Sec. M.3), thus the above formulation can be applied to any EoS that is capable to provide the fugacity coefficient and its derivatives. It is interesting to underline the fact that the v_k derivatives lead to a linear system. This is due to the effect that all species-related properties are not independent but they are linked to each other. Additional important formulas are the phase molar masses derivatives with respect to pressure and temperature: $\left(\frac{\partial M^V}{\partial T}\right)_{p,\mathbf{X}}$, $\left(\frac{\partial M^V}{\partial p}\right)_{T,\mathbf{X}}$, $\left(\frac{\partial M^L}{\partial T}\right)_{p,\mathbf{X}}$ and $\left(\frac{\partial M^L}{\partial p}\right)_{T,\mathbf{X}}$. These are also provided in Appendix K. Algorithm 3 in Appendix D summarizes the steps that are required to compute all the quantities of Eq. (2.2.39). Note, this requires that VLE exists and it is known in terms of β, $\mathbf{x}$, $\mathbf{y}$.

2.2.2.3 Real gas - VLE thermodynamics: mixture and phase derivatives

With the above formulas, many additional properties for the mixture, as well as the phases separately, can be constructed. Here only some relevant quantities are discussed, for brevity. Additional details are given in Appendix K. The mixture density and internal energy derivatives with respect to temperature and pressure are given below:

$$\left(\frac{\partial \rho}{\partial T}\right)_{p,\mathbf{X}} \overset{\text{Using Eq. (2.2.34)}}{\downarrow} = -\frac{\rho^2}{M}\left\{\left(\frac{\partial \beta}{\partial T}\right)_{p,\mathbf{X}}\left(\frac{M^V}{\rho^V}-\frac{M^L}{\rho^L}\right)+\frac{\beta}{\rho^{V^2}}\left[\rho^V\left(\frac{\partial M^V}{\partial T}\right)_{p,\mathbf{X}}-M^V\left(\frac{\partial \rho^V}{\partial T}\right)_{p,\mathbf{X}}\right]+\right.$$
$$\left.+\frac{1-\beta}{\rho^{L^2}}\left[\rho^L\left(\frac{\partial M^L}{\partial T}\right)_{p,\mathbf{X}}-M^L\left(\frac{\partial \rho^L}{\partial T}\right)_{p,\mathbf{X}}\right]\right\}. \tag{2.2.49}$$

$$\left(\frac{\partial \rho}{\partial p}\right)_{T,\mathbf{X}} = -\frac{\rho^2}{M}\left\{\left(\frac{\partial \beta}{\partial p}\right)_{T,\mathbf{X}}\left(\frac{M^V}{\rho^V}-\frac{M^L}{\rho^L}\right)+\frac{\beta}{\rho^{V^2}}\left[\rho^V\left(\frac{\partial M^V}{\partial p}\right)_{T,\mathbf{X}}-M^V\left(\frac{\partial \rho^V}{\partial p}\right)_{T,\mathbf{X}}\right]+\right.$$
$$\left.+\frac{1-\beta}{\rho^{L^2}}\left[\rho^L\left(\frac{\partial M^L}{\partial p}\right)_{T,\mathbf{X}}-M^L\left(\frac{\partial \rho^L}{\partial p}\right)_{T,\mathbf{X}}\right]\right\}. \tag{2.2.50}$$

$$\left(\frac{\partial E}{\partial T}\right)_{p,\mathbf{X}} = \left(\frac{\partial \beta}{\partial T}\right)_{p,\mathbf{X}} (E^V - E^L) + \beta \left(\frac{\partial E^V}{\partial T}\right)_{p,\mathbf{X}} + (1-\beta)\left(\frac{\partial E^L}{\partial T}\right)_{p,\mathbf{X}}, \tag{2.2.51}$$

$$\left(\frac{\partial E}{\partial p}\right)_{T,\mathbf{X}} = \left(\frac{\partial \beta}{\partial p}\right)_{T,\mathbf{X}} (E^V - E^L) + \beta \left(\frac{\partial E^V}{\partial p}\right)_{T,\mathbf{X}} + (1-\beta)\left(\frac{\partial E^L}{\partial p}\right)_{T,\mathbf{X}}. \tag{2.2.52}$$

All of above require the knowledge of the VLE derivatives of Eq. (2.2.39), as well as specific, phase-related derivatives, such as $(\partial \rho^L/\partial p)_{T,\mathbf{X}}$ or $(\partial E^L/\partial T)_{p,\mathbf{X}}$ and similar. The latter are derived in Appendix K. Note that these derivatives do not correspond to the ones directly derived from the EoS and the departure functions because the variation of VLE quantities is also involved and must be taken into account using the total differential concept (see Appendix K). For example $(\partial \rho^L/\partial p)_{T,\mathbf{X}}$ is not equal to $(\partial \rho^L/\partial p)_{T,\mathbf{X},\mathbf{x}}$, which is the one (easily) computed from the EoS and their difference is related to the existence of all the Eq. (2.2.39) in the VLE region (see Eq. (K.0.35) for this specific example). Algorithm 5 provides the necessary steps to compute the derivatives in each phase, while Algorithm 4 provides the final steps to compute additional derivatives for the VLE mixture, up to specific heats, isothermal compressibility, isobaric expansivity and speed of sound. The last quantities to compute are the partial molar volume and enthalpy in the VLE region. These are discussed in the next section.

2.2.2.4 Real gas - VLE thermodynamics: partial molar quantities

The starting point is the definition of partial molar volume of Eq. (2.2.28). Using Eq. (2.2.32) for the definition of the total volume one gets:

$$V_i = \left(\frac{\partial \overline{V}}{\partial N_i}\right)_{T,p,\mathbf{N}_i} = \left(\frac{\partial \overline{V}^V}{\partial N_i}\right)_{T,p,\mathbf{N}_i} + \left(\frac{\partial \overline{V}^L}{\partial N_i}\right)_{T,p,\mathbf{N}_i} \qquad i = 1, \cdots, N_s\,. \tag{2.2.53}$$

Since $\overline{V}^\eta = \overline{V}^\eta(T, p, \boldsymbol{\sigma})$, where:

$$\boldsymbol{\sigma} = \{\sigma_i \,|\, i = 1, \cdots, N_s\} = \begin{cases} \mathbf{N}^L = \{N_i^L \,|\, i = 1, \cdots, N_s\} & \text{if } \eta = L \\ \mathbf{N}^V = \{N_i^V \,|\, i = 1, \cdots, N_s\} & \text{if } \eta = V \end{cases}, \tag{2.2.54}$$

$$\sigma = \begin{cases} N^L = \sum_{i=1}^{N_s} N_i^L & \text{if } \eta = L \\ N^V = \sum_{i=1}^{N_s} N_i^V & \text{if } \eta = V \end{cases}, \tag{2.2.55}$$

and N_i^L, N_i^V are the number of moles of species i in each phase. The total differential of the extensive volume in the generic phase η writes:

$$d\overline{V}^{\eta} = \left(\frac{\partial \overline{V}^{\eta}}{\partial T}\right)_{p,\boldsymbol{\sigma}} dT + \left(\frac{\partial \overline{V}^{\eta}}{\partial p}\right)_{T,\boldsymbol{\sigma}} dp + \sum_{k=1}^{N_s} \left(\frac{\partial \overline{V}^{\eta}}{\partial \sigma_k}\right)_{T,p,\boldsymbol{\sigma}_k} d\sigma_k \,, \tag{2.2.56}$$

where $\boldsymbol{\sigma}_k = \{\sigma_i \,|\, i = 1, \cdots, N_s, i \neq k\}$ has been defined to make it consistent with the previous notation. Because the partial molar quantities are by definition taken at constant temperature and pressure, the first two terms in Eq. (2.2.56) vanish. Next, by evaluating the variation of Eq. (2.2.56) with respect to the generic N_i, one gets immediately for both phases:

$$\left(\frac{\partial \overline{V}^{V}}{\partial N_i}\right)_{T,p,\mathbf{N}_i} = \sum_{k=1}^{N_s} \left(\frac{\partial \overline{V}^{V}}{\partial N_k^V}\right)_{T,p,\mathbf{N}_k^V} \left(\frac{\partial N_k^V}{\partial N_i}\right)_{T,p,\mathbf{N}_k^V,\mathbf{N}_i} \qquad i = 1, \cdots, N_s \,, \tag{2.2.57}$$

$$\left(\frac{\partial \overline{V}^{L}}{\partial N_i}\right)_{T,p,\mathbf{N}_i} = \sum_{k=1}^{N_s} \left(\frac{\partial \overline{V}^{L}}{\partial N_k^L}\right)_{T,p,\mathbf{N}_k^L} \left(\frac{\partial N_k^L}{\partial N_i}\right)_{T,p,\mathbf{N}_k^L,\mathbf{N}_i} \qquad i = 1, \cdots, N_s. \tag{2.2.58}$$

In both phases, the summation term contains the product between two quantities: $(\partial \overline{V}^{\eta}/\partial \sigma_k)_{T,p,\boldsymbol{\sigma}_k}$ which describes how the phase extensive volume changes with an infinitesimal addition of moles of species k in the phase η, and the term $(\partial \sigma_k/\partial N_i)_{T,p,\boldsymbol{\sigma}_k,\mathbf{N}_i}$, which describes how much the number of moles of species k in the phase η changes for an infinitesimal addition of number of "total" moles of species i in the mixture. This is the most challenging term to compute and it is going to be the subject of the next discussion.

Given the number of crucial steps involved, the step-by-step derivation is reported in Appendix L and only the final result is shown here, for brevity. The vapor contribution $(\partial N_k^V/\partial N_i)_{T,p,\mathbf{N}_k^V,\mathbf{N}_i}$ of Eq. (2.2.57) is obtained by solving N_s times the following linear system in the unknown vector $\boldsymbol{\chi}_N^{(i)}$:

$$\boldsymbol{\mathcal{C}}\boldsymbol{\chi}_N^{(i)} = \mathbf{b}_N^{(i)} \qquad i = 1, \cdots, N_s \,, \tag{2.2.59}$$

where:

$$\mathcal{C}_{kj} = \sum_{s=1}^{N_s} \left[\left(\frac{\partial \ln \phi_k^L}{\partial x_s}\right)_{T,p,\mathbf{x}_s} \left(\frac{\delta_{sj} - x_s}{1-\beta}\right) + \left(\frac{\partial \ln \phi_k^V}{\partial y_s}\right)_{T,p,\mathbf{y}_s} \left(\frac{\delta_{sj} - y_s}{\beta}\right) \right] + \frac{1}{x_k}\frac{\delta_{kj} - x_k}{1-\beta} + \frac{1}{y_k}\frac{\delta_{kj} - y_k}{\beta} \,, \tag{2.2.60}$$

$$b_{N,k}^{(i)} = \sum_{j=1}^{N_s} \delta_{ji} \left\{ \sum_{s=1}^{N_s} \left[\left(\frac{\partial \ln \phi_k^L}{\partial x_s} \right)_{T,p,\mathbf{x}_s} \left(\frac{\delta_{sj} - x_s}{1-\beta} \right) \right] + \frac{\delta_{ji}}{x_k} \left(\frac{\delta_{kj} - x_k}{1-\beta} \right) \right\} , \tag{2.2.61}$$

$$\chi_{N,j}^{(i)} = \left(\frac{\partial N_j^V}{\partial N_i} \right)_{T,p,\mathbf{N}_j^V,\mathbf{N}_i} . \tag{2.2.62}$$

However, given the fact that the matrix $\boldsymbol{\mathcal{C}}$ does not depend on i, the matrix inversion itself must be done only once for all the unknowns. On the other hand, the liquid contribution $(\partial N_k^L/\partial N_i)_{T,p,\mathbf{N}_k^V,\mathbf{N}_i}$ of Eq. (2.2.57) is easily obtained from the vapor contribution by exploiting mass continuity (see Appendix L). Algorithm 6 in Appendix D summarizes the steps to compute the partial molar volume for each species in the mixture, in case VLE occurs. If VLE does not occur, the single phase formula applies.

Next, the formula to compute the partial molar enthalpy in the VLE region is derived. Starting from the definition of Eq. (2.2.28) and use the definition of enthalpy, one gets:

$$H_i = \left(\frac{\partial \overline{H}}{\partial N_i} \right)_{T,p,\mathbf{N}_i} = \left(\frac{\partial NH}{\partial N_i} \right)_{T,p,\mathbf{N}_i} = \left(\frac{\partial N \left(E + \dfrac{pM}{\rho} \right)}{\partial N_i} \right)_{T,p,\mathbf{N}_i} \overset{\overline{V} = NV = NM/\rho}{=} \left(\frac{\partial \left(\overline{E} + p\overline{V} \right)}{\partial N_i} \right)_{T,p,\mathbf{N}_i} =$$

$$= p \left(\frac{\partial \overline{V}}{\partial N_i} \right)_{T,p,\mathbf{N}_i} + \left(\frac{\partial \overline{E}^V}{\partial N_i} \right)_{T,p,\mathbf{N}_i} + \left(\frac{\partial \overline{E}^L}{\partial N_i} \right)_{T,p,\mathbf{N}_i} \qquad i = 1, \cdots, N_s ,$$

$$\downarrow$$

$$\overline{E} = N[\beta E^V + (1-\beta) E^L] = N^V E^V + N^L E^L = \overline{E}^V + \overline{E}^L$$

which leads to:

$$H_i = pV_i + \left(\frac{\partial \overline{E}^V}{\partial N_i} \right)_{T,p,\mathbf{N}_i} + \left(\frac{\partial \overline{E}^L}{\partial N_i} \right)_{T,p,\mathbf{N}_i} \qquad i = 1, \cdots, N_s . \tag{2.2.63}$$

Finally, an approximate method to compute partial molar quantities is proposed and will be used later in Chap. 4. Given that one can compute the respective phase-related molar volume and enthalpy V_i^η and H_i^η using Eq. (2.2.28), and given the fact that:

$$V^V = \sum_{i=1}^{N_s} V_i^V y_i , \qquad V^L = \sum_{i=1}^{N_s} V_i^L x_i , \qquad H^V = \sum_{i=1}^{N_s} H_i^V y_i , \qquad H^L = \sum_{i=1}^{N_s} H_i^L x_i , \tag{2.2.64}$$

must be satisfied, the mixture approximate two-phase partial molar quantities are computed as:

$$V_i = \frac{\beta y_i V_i^V + (1-\beta) x_i V_i^L}{X_i}\,, \qquad i = 1, \cdots, N_s \tag{2.2.65}$$

$$H_i = \frac{\beta y_i H_i^V + (1-\beta) x_i H_i^L}{X_i}\,, \qquad i = 1, \cdots, N_s\,, \tag{2.2.66}$$

which can be easily proven to satisfy the required condition that $V = \sum_{i=1}^{N_s} V_i X_i$ and $H = \sum_{i=1}^{N_s} H_i X_i$.

2.2.3 The Generic-Cubic Equation of State (GCEoS) model

In Sec. 2.2.2, an EoS-free theoretical framework was provided under the following assumptions: a) equilibrium as per Eq. (2.2.31) and b) two phases exist at most. Inclusion of a three phase equilibrium can be easily derived following the same steps and taking into account another value of β for the equilibrium between the second and the third phase [66, 101, 102] (equilibrium between the first and the third follows as a consequence). Additionally, the inclusion of capillarity effects is also possible [49], provided that a generic and robust model for surface tension is available. This would imply additional terms appearing in all derivation of Sec. 2.2.2.

Under these assumptions, the remaining task is to provide an EoS model for all the specific derivatives that are required. In the present work, the focus is on the family of the 3-parameters *cubic* EoS which have been widely used in the context of fluid flows [125, 248, 158, 157, 116, 59, 90, 136, 89, 188, 193, 108, 109, 110, 64, 143] as well as reservoir simulations [49, 168] because of their good compromise between accuracy and simplicity. Some derivatives have been already provided for a specific EoS, as for example in the works of [125, 116, 143, 82], however an extension of these works is made here by providing all the derivatives that are necessary for Sec. 2.2.1 and Sec. 2.2.2 for a class of EoS models, from now on denoted as generic cubic EoS model (GCEoS). Additionally, four different kinds of mixing rules are investigated.

2.2.3.1 General definitions and main properties

The GCEoS model has a generic formula that is explicit in pressure. It has the following form:

$$p = \frac{\rho R_u T}{M - B_m \rho} - \frac{\rho^2 A_m}{(M + \delta_1 B_m \rho)(M + \delta_2 B_m \rho)}\,, \tag{2.2.67}$$

where $A_m = A_m(T, \mathbf{X})$ and $B_m = B_m(\mathbf{X})$ are mixture-dependent parameters that require additional modeling, called *mixing rules*. In this work, four types listed in Tab. 3 are analyzed. By varying the coefficients δ_1 and δ_2, different EoS models can be obtained as provided in Tab. 4: Peng-Robinson (PR), Redlich-Kwong (RK), Soave-Redlich-Kwong (SRK), Van der Waals (VDW) and blended PR-RK. Additional information are provided below:

- $p_{c,i}$, $T_{c,i}$ and ω_i are the main species-dependent, constant parameters (from which the "3-parameters" label is obtained);
- additional useful constant, species-dependent parameters are the critical compressibility $Z_{c,i}$ and the critical molar volume $V_{c,i} = Z_{c,i} R_u T_{c,i}/p_{c,i}$. All these need to be stored in a species database;
- the VDW EoS is a degenerate 3-parameters EoS since it requires two and not three parameters (ω_i is not used);
- for the PR-RK EoS the value of δ_1 is species-dependent and is obtained through the non-linear equation reported in Tab. 3, for which additional constants are given in Tab. 2. After it is known for each species, the corresponding value of δ_2 is computed. For this reason, an additional mixing rule needs to be defined in order to compute the mixture values. In this work, the following are used:

  $$\delta_1 = \sum_{i=1}^{N_s} X_i \delta_{1,i} \qquad \delta_2 = \sum_{i=1}^{N_s} X_i \delta_{2,i}\,. \tag{2.2.68}$$

  where $\delta_{1,i}$ and $\delta_{2,i}$, $i = 1, \cdots, N_s$ are those obtained from the formulas in Tab. 4;

- A_i, B_i, are species-dependent, EoS-dependent constants, while $\alpha_i(T, \omega_i)$ is another EoS-dependent and species-dependent value, that has also a non-linear dependency on the temperature T;

- in all cases, k_{ij} represent the *interaction parameters*, which are empirical constants meant to improve accuracy for specific mixtures. Generally, they are tuned against experimental data, however some analytical models have also been proposed for them. Clearly $k_{ii} = 0$ and $k_{ij} = k_{ji}$ by definition. A good list of these is given in [212];

- special care is needed for the Okong'o/Miller mixing rule (MR-3) where A^* is effectively a symmetric matrix built with mixed species properties that are pre-computed before hand (see Tab. 3):

$$\begin{aligned} A^*_{ij} &= A(T_{c,ij}, p_{c,ij})\,, & T_{c,ij} &= \sqrt{T_{c,i}T_{c,j}}(1 - k_{ij}) \\ p_{c,ij} &= Z_{c,ij}\frac{R_u T_{c,ij}}{V_{c,ij}}\,, & V_{c,ij} &= \frac{1}{8}\left(V_{c,i}^{1/3}V_{c,j}^{1/3}\right)^3 \\ \omega_{ij} &= \frac{1}{2}(\omega_i + \omega_j)\,, & Z_{c,ij} &= \frac{1}{2}(Z_{c,i} + Z_{c,j})\,, \end{aligned} \tag{2.2.69}$$

  and similarly $\alpha_{ij} = \alpha_{ij}(T, \omega_{ij})$, $f_{ij} = f_{ij}(\omega_{ij}, Z_{c,ij})$ according to the formulas of Tab. 4 for each EoS;

- for all the following discussion, the "global" mixture conditions are considered, that is if a derivative of a generic function ψ: e.g. $(\partial\psi/\partial p)_{T,\mathbf{X}}$ is provided, the same identical analytical formula holds to compute the same quantity in each phase, provided that the substitutions $\mathbf{x} \leftarrow \mathbf{X}$ and $\mathbf{y} \leftarrow \mathbf{X}$ are applied for the liquid and the vapor phase, respectively. This means to recompute in a systematic manner all the phase related properties as per Algorithm 1 and 5 in Appendix D. Additionally, no referring to a multi-phase condition is made to any of the following mixture properties. All the following discussion pertains to a single-phase system.

First, the compressibility equation is provided. Using Eq. (2.2.2) into Eq. (2.2.67) to eliminate the density and rearranging, the following cubic, algebraic equation is obtained:

$$a_1 Z^3 + a_2 Z^2 + a_3 Z + a_4 = 0\,, \tag{2.2.70}$$

Table 2: Additional parameters for the PR-RK EoS [33]

parameters for $\delta_{1,i}$		parameters for $f_i(\omega_i)$	
d_1	0.428363	$\mathcal{A}_1$	-2.4407
d_2	18.496215	$\mathcal{A}_0$	0.0017
d_3	0.338426	$\mathcal{B}_1$	7.4513
d_4	0.660000	$\mathcal{B}_0$	1.9681
d_5	789.723105	$\mathcal{C}_1$	12.5040
d_6	2.512392	$\mathcal{C}_0$	-2.7238

where:

$$
\begin{aligned}
a_1 &= \frac{R_u^3 T^3}{p^3}\,, \\
a_2 &= \frac{R_u^3 T^3}{p^3}\left[\frac{p}{R_u T} B_m((\delta_1+\delta_2)-1)-1\right], \\
a_3 &= \frac{R_u T B_m^2}{p}\left(\delta_1\delta_2-(\delta_1+\delta_2)\right)-(\delta_1+\delta_2)\frac{R_u^2 T^2 B_m}{p^2}+A_m\frac{R_u T}{p^2}\,, \\
a_4 &= -\delta_1\delta_2 R_u T\frac{B_m^2}{p}-\frac{A_m B_m}{p}-\delta_1\delta_2 B_m^3\,.
\end{aligned}
\tag{2.2.71}
$$

Solution of Eq. (2.2.70) for given T, p and $\mathbf{X}$ involves the selection of the real root in case multiple real values occur as discussed in Sec. 2.2.2.1. The minimum Gibbs energy criterion discussed in Appendix A cannot provide any VLE solution but only single phase solutions are allowed. Hence, in case an additional VLE problem is investigated according to Eq. (2.2.31), the root selected with the minimum Gibbs energy can be used as initial condition for the VLE problem (see Sec. 3.4.1). Another useful formula involving the compressibility factor, is the one obtained when density and temperature are known. By eliminating the pressure in Eq. (2.2.67) using Eq. (2.2.3) the following formula is obtained:

$$
Z=\frac{M}{M-B_m\rho}-\frac{\rho M}{R_u T}\frac{A_m}{(M+\delta_1 B_m\rho)(M+\delta_2 B_m\rho)}\,,
\tag{2.2.72}
$$

from which the derivative with respect to temperature at constant density and composition (useful for Eqs. (2.2.12)–(2.2.14)) is readily obtained:

$$
\left(\frac{\partial Z}{\partial T}\right)_{\rho,\mathbf{X}}=-\frac{\rho M}{R_u T}\frac{1}{(M+\delta_1 B_m\rho)(M+\delta_2 B_m\rho)}\left[\left(\frac{\partial A_m}{\partial T}\right)_{\mathbf{X}}-\frac{A_m}{T}\right].
\tag{2.2.73}
$$

In Eq. (2.2.73), the derivative of A_m with respect to temperature appears. Before contin-

uing the discussion about the EoS derivatives, some ancillary derivatives of A_m, B_m and α_i are required. These steps are easy, although very tedious and involve the derivation of terms appearing in Tab. 3 and Tab. 4, which are EoS and mixing rule dependent. First, the derivatives of α_i appearing in Tab. 4 are given in Tab. 5 for each EoS. Additionally, more useful derivatives of the quantity $\sqrt{\alpha_i \alpha_j}$ are provided in Eqs. (2.2.74)–(2.2.76), which will be used later.

Next, the form of A_m coefficient of Tab. 3 is recast in the form: $A_m = c_1 + c_2 T^{c_4} + c_3 T$, where c_1, c_2 and c_3 are temperature-independent and are functions of the mixture only, while c_4 is an EoS-dependent constant. These are obtained by unrolling completely the sums of Tab. 3 and group together the terms containing no dependency on T, dependency on T^{c_4} (through which c_4 is identified) and T, respectively. An example is given in Appendix F for PR/MR-1 while Tab. 6 summarizes these quantities for each mixing rule. Note that this form is not possible to be obtained for the PR-RK EoS due to the power dependency of T in the α_i function (see Tab. 4). Next, the derivatives of c_1, c_2 and c_3 coefficients can be computed. These are listed in Tab. 7 and Tab. 8. In this way, the derivatives of A_m coefficients can be easily expressed as reported in Tab. 9. For the PR-RK EoS the derivatives are computed explicitly and are listed in Tab. 10. Similarly, derivatives of the mixture-dependent coefficient B_m can be defined. These do not depend on the temperature and therefore depend only on the type of the mixing rule chosen and not on the EoS. These are given in Tab. 11. Additional useful derivatives are those of the single A_{ij} elements of Tab. 3, such that A_m can be written in the generic form: $A_m = \sum_{i=1}^{N_s} \sum_{j=1}^{N_s} X_i X_j A_{ij}$. These are reported in Tab. 12.

$$\frac{\partial(\sqrt{\alpha_i \alpha_j})}{\partial T} = \frac{1}{2} (\alpha_i \alpha_j)^{-1/2} \left[\alpha_i \frac{\partial \alpha_j}{\partial T} + \alpha_j \frac{\partial \alpha_i}{\partial T} \right], \tag{2.2.74}$$

$$\frac{\partial^2(\sqrt{\alpha_i \alpha_j})}{\partial T^2} = \frac{\alpha_i \dfrac{\partial^2 \alpha_j}{\partial T^2} + \alpha_j \dfrac{\partial^2 \alpha_i}{\partial T^2} + 2 \dfrac{\partial \alpha_i}{\partial T} \dfrac{\partial \alpha_j}{\partial T}}{2\sqrt{\alpha_i \alpha_j}} - \frac{1}{4} (\alpha_i \alpha_j)^{3/2} \left(\alpha_i \frac{\partial \alpha_j}{\partial T} + \alpha_j \frac{\partial \alpha_i}{\partial T} \right)^2, \tag{2.2.75}$$

Table 3: Mixing rules for GCEoS [163, 104]. For short notation, these will be indicated as MR-X where X is the correspondig number.

Mixing rule (MR)	A_m	B_m
1) Van der Waals (VDW)	$\sum_{i=1}^{N_s}\sum_{j=1}^{N_s} X_i X_j \sqrt{A_i A_j \alpha_i \alpha_j}(1-k_{ij})$	$\sum_{i=1}^{N_s} X_i B_i$
2) Arithmetic	$\sum_{i=1}^{N_s}\sum_{j=1}^{N_s} X_i X_j \frac{A_i\alpha_i + A_j\alpha_j}{2}(1-k_{ij})$	$\sum_{i=1}^{N_s} X_i B_i$
3) Okong'o/Miller	$\sum_{i=1}^{N_s}\sum_{j=1}^{N_s} X_i X_j A^*_{ij}\alpha_{ij}$	$\sum_{i=1}^{N_s} X_i B_i$
4) Hirschfelder	$\sum_{i=1}^{N_s}\sum_{j=1}^{N_s} X_i X_j \sqrt{A_i A_j \alpha_i \alpha_j}(1-k_{ij})$	$\sum_{i=1}^{N_s}\sum_{j=1}^{N_s} X_i X_j \left[\frac{1}{2}\left(B_i^{1/3}+B_j^{1/3}\right)\right]^3$

$$
\begin{aligned}
\frac{\partial^3(\sqrt{\alpha_i\alpha_j})}{\partial T^3} =& \frac{\alpha_i\frac{\partial^3\alpha_i}{\partial T^3} + 3\frac{\partial\alpha_i}{\partial T}\frac{\partial^2\alpha_j}{\partial T^2} + 3\frac{\partial\alpha_j}{\partial T}\frac{\partial^2\alpha_i}{\partial T^2} + \alpha_j\frac{\partial^3\alpha_j}{\partial T^3}}{2(\alpha_i\alpha_j)^{1/2}} + \\
&- \frac{1}{2}\left[\left(\alpha_i\frac{\partial\alpha_j}{\partial T} + \alpha_j\frac{\partial\alpha_i}{\partial T}\right)\left(\frac{1}{2}\alpha_i\frac{\partial^2\alpha_j}{\partial T^2} + \frac{1}{2}\alpha_j\frac{\partial^2\alpha_i}{\partial T^2} + \frac{\partial\alpha_i}{\partial T}\frac{\partial\alpha_j}{\partial T}\right)\right] + \\
&- \frac{1}{4}\left[\left(\alpha_i\frac{\partial\alpha_j}{\partial T} + \alpha_j\frac{\partial\alpha_i}{\partial T}\right)\left(\frac{\alpha_i\frac{\partial^2\alpha_j}{\partial T^2} + \alpha_j\frac{\partial^2\alpha_i}{\partial T^2} + 2\frac{\partial\alpha_i}{\partial T}\frac{\partial\alpha_j}{\partial T}}{(\alpha_i\alpha_j)^{3/2}} - \frac{3\left(\alpha_i\frac{\partial\alpha_j}{\partial T} + \alpha_j\frac{\partial\alpha_i}{\partial T}\right)^2}{2(\alpha_i\alpha_j)^{5/2}}\right)\right] + \\
&- \frac{\left(\alpha_i\frac{\partial\alpha_j}{\partial T} + \alpha_j\frac{\partial\alpha_i}{\partial T}\right)\left(\alpha_i\frac{\partial^2\alpha_j}{\partial T^2} + \alpha_j\frac{\partial^2\alpha_i}{\partial T^2} + 2\frac{\partial\alpha_i}{\partial T}\frac{\partial\alpha_j}{\partial T}\right)}{4(\alpha_i\alpha_j)^{3/2}}\,. \qquad (2.2.76)
\end{aligned}
$$

2.2.3.2 Departure functions and derivatives of main state variables

The internal energy departure function for GCEoS is obtained directly through the application of Eq. (2.2.12). After substituting Eq. (2.2.73) inside the integral and rearranging one obtains:

$$
\frac{\Delta E}{R_u T} = \frac{M}{R_u}\left[\left(\frac{\partial A_m}{\partial T}\right)_{\mathbf{X}} - \frac{A_m}{T}\right]\int_0^\rho \frac{d\rho}{M^2 + (\delta_1+\delta_2)B_m\rho M + \delta_1\delta_2 B_m^2\rho^2}\,, \qquad (2.2.77)
$$

Table 4: Relevant parameters definitions for GCEoS

EoS	δ_1	δ_2	$A_i \times p_{c,i}/(R_u T_{c,i})^2$	$B_i \times p_{c,i}/(R_u T_{c,i})$	$\alpha_i(T;\omega_i)$	$f_i(\omega_i)$
VDW [230]	0	0	27/64	1/8	1	0
RK [177]	1	0	0.457236	0.0778	$\frac{1}{\sqrt{T_{c,i}/T}}$	1
SRK [207]	1	0	0.42748	0.08644	$[1+f_i(\omega_i)(1-\sqrt{T/T_{c,i}})]^2$	0.48508+ 1.55171ω_i− 0.15613ω_i^2
PR [154]	$1+\sqrt{2}$	$1-\sqrt{2}$	0.457236	0.07780	$[1+f_i(\omega_i)(1-\sqrt{T/T_{c,i}})]^2$	0.37464+ 1.54226ω_i− 0.26992ω_i^2
PR-RK [33]	$d_1+d_2(d_3-1.168Z_{c,i})^{d_4}+$ $d_5(d_3-1.168Z_{c,i})^{d_6}$	$\frac{(1-\delta_1)}{(1+\delta_1)}$	$\frac{3y^2+3dy+d^2+d-1}{(3y+d+1)^2}$ $y=1+[2(1+\delta_1)]^{1/3}+\left(\frac{4}{1+\delta_1}\right)^{1/3}$ $d=\frac{1+\delta_1^2}{1+\delta_1}$	$\frac{1}{3y+d-1}$	$\left(\frac{3}{2+T/T_{c,i}}\right)^{f(\omega_i)}$	$(1.168Z_{c,i}\mathcal{A}_1+\mathcal{A}_0)\omega_i^2+$ $(1.168Z_{c,i}B_1+B_0)\omega_i+$ $(1.168Z_{c,i}\mathcal{C}_1+\mathcal{C}_0)$

Table 5: Derivatives of α_i functions for each EoS used.

	Equation of state			
	VDW	RK	SRK/PR	PR-RK
$\frac{d\alpha_i}{dT}$	0	$-\frac{1}{2}\sqrt{T_{c,i}}T^{-3/2}$	$-\frac{f_i}{\sqrt{T_{c,i}T}}\left[1+f_i\left(1-\sqrt{\frac{T}{T_{c,i}}}\right)\right]$	$-\frac{f_i 3^{f_i}}{T_{c,i}\left(2+\frac{T}{T_{c,i}}\right)^{f_i+1}}$
$\frac{d^2\alpha_i}{dT^2}$	0	$\frac{3}{4}\sqrt{T_{c,i}}T^{-5/2}$	$\frac{f_i^2}{2TT_{c,i}}+\frac{f_i}{2\sqrt{T^3T_{c,i}}}\left[1+f_i\left(1-\sqrt{\frac{T}{T_{c,i}}}\right)\right]$	$\frac{f_i(f_i+1)3^{f_i}}{T_{c,i}^2\left(2+\frac{T}{T_{c,i}}\right)^{f_i+2}}$
$\frac{d^3\alpha_i}{dT^3}$	0	$-\frac{15}{8}\sqrt{T_{c,i}}T^{-7/2}$	$-\frac{3}{4}\frac{f_i^2}{T^2T_{c,i}}-\frac{3}{4}\frac{f_i}{T^3}\sqrt{\frac{T}{T_{c,i}}}\left[1+f_i\left(1-\sqrt{\frac{T}{T_{c,i}}}\right)\right]$	$-\frac{f_i(f_i+1)(f_i+2)3^{f_i}}{T_{c,i}^3\left(2+\frac{T}{T_{c,i}}\right)^{(3+f_i)}}$

Table 6: Mixture-dependent c_1, c_2, c_3 and c_4 coefficients for each EoS used (except PR-RK). These are useful to recast the A_m coefficient in the form $A_m = c_1 + c_2 T^{c_4} + c_3 T$.

	MR-1 and MR-4		
	VDW	RK	SRK/PR
c_1	$\sum_{i=1}^{N_s}\sum_{j=1}^{N_s} X_i X_j (1-k_{ij})\sqrt{A_i A_j}$	0	$\sum_{i=1}^{N_s}\sum_{j=1}^{N_s} X_i X_j (1-k_{ij})\sqrt{A_i A_j}(1+f_i+f_j+f_i f_j)$
c_2	0	$\sum_{i=1}^{N_s}\sum_{j=1}^{N_s} X_i X_j (1-k_{ij})\sqrt{A_i A_j}(T_{c,i}T_{c,j})^{1/4}$	$-\sum_{i=1}^{N_s}\sum_{j=1}^{N_s} X_i X_j (1-k_{ij})\sqrt{A_i A_j}\left(\dfrac{f_j(1+f_i)}{\sqrt{T_{c,j}}}+\dfrac{f_i(1+f_j)}{\sqrt{T_{c,i}}}\right)$
c_3	0	0	$\sum_{i=1}^{N_s}\sum_{j=1}^{N_s} X_i X_j (1-k_{ij})\sqrt{A_i A_j}\dfrac{f_i f_j}{\sqrt{T_{c,i}T_{c,j}}}$
c_4	N/A	$-1/2$	1/2
	MR-2		
	VDW	RK	SRK/PR
c_1	$\sum_{i=1}^{N_s}\sum_{j=1}^{N_s} X_i X_j (1-k_{ij})\dfrac{A_i+A_j}{2}$	0	$\dfrac{1}{2}\sum_{i=1}^{N_s}\sum_{j=1}^{N_s} X_i X_j (1-k_{ij})\left[A_i(1+f_i^2+2f_i)+A_j(1+f_j^2+2f_j)\right]$
c_2	0	$\dfrac{1}{2}\sum_{i=1}^{N_s}\sum_{j=1}^{N_s} X_i X_j (1-k_{ij})\left(A_i\sqrt{T_{c,i}}+A_j\sqrt{T_{c,j}}\right)$	$-\sum_{i=1}^{N_s}\sum_{j=1}^{N_s} X_i X_j (1-k_{ij})\left[f_i A_i\dfrac{1+f_i}{\sqrt{T_{c,i}}}+f_j A_j\dfrac{1+f_j}{\sqrt{T_{c,j}}}\right]$
c_3	0	0	$\dfrac{1}{2}\sum_{i=1}^{N_s}\sum_{j=1}^{N_s} X_i X_j (1-k_{ij})\left(A_i\dfrac{f_i^2}{T_{c,i}}+A_j\dfrac{f_j^2}{T_{c,j}}\right)$
c_4	N/A	$-1/2$	1/2
	MR-3		
	VDW	RK	SRK/PR
c_1	$\sum_{i=1}^{N_s}\sum_{j=1}^{N_s} X_i X_j (1-k_{ij})A_{ij}^*$	0	$\sum_{i=1}^{N_s}\sum_{j=1}^{N_s} X_i X_j (1-k_{ij})A_{ij}^*(1+f_{ij})^2$
c_2	0	$\sum_{i=1}^{N_s}\sum_{j=1}^{N_s} X_i X_j (1-k_{ij})A_{ij}^*\sqrt{T_{c,ij}}$	$-2\sum_{i=1}^{N_s}\sum_{j=1}^{N_s} X_i X_j (1-k_{ij})A_{ij}^*\dfrac{f_{ij}(1+f_{ij})}{\sqrt{T_{c,ij}}}$
c_3	0	0	$\sum_{i=1}^{N_s}\sum_{j=1}^{N_s} X_i X_j (1-k_{ij})A_{ij}^*\dfrac{f_{ij}^2}{T_{c,ij}}$
c_4	N/A	$-1/2$	1/2

Table 7: Mixture-dependent c_1, c_2, c_3 first derivative with respect to the generic mole fraction X_k. Here $\mathbf{X}_k = \{X_i \,|\, i = 1, \cdots, N_s, i \neq k\}$.

	MR-1 and MR-4		
	VDW	RK	SRK/PR
$\left(\frac{\partial c_1}{\partial X_k}\right)_{\mathbf{X}_k}$	$2\sum_{i=1}^{N_s} X_i(1-k_{ik})\sqrt{A_iA_k}$	0	$2\sum_{i=1}^{N_s} X_i(1-k_{ik})\sqrt{A_iA_k}(1+f_i+f_k+f_if_k)$
$\left(\frac{\partial c_2}{\partial X_k}\right)_{\mathbf{X}_k}$	0	$2\sum_{i=1}^{N_s} X_i(1-k_{ik})\sqrt{A_iA_k}(T_{c,i}T_{c,k})^{1/4}$	$-2\sum_{i=1}^{N_s} X_i(1-k_{ik})\sqrt{A_iA_k}\left(\frac{f_k(1+f_i)}{\sqrt{T_{c,k}}}+\frac{f_i(1+f_k)}{\sqrt{T_{c,i}}}\right)$
$\left(\frac{\partial c_3}{\partial X_k}\right)_{\mathbf{X}_k}$	0	0	$2\sum_{i=1}^{N_s} X_i(1-k_{ik})\sqrt{A_iA_k}\frac{f_if_k}{\sqrt{T_{c,i}T_{c,k}}}$
	MR-2		
	VDW	RK	SRK/PR
$\left(\frac{\partial c_1}{\partial X_k}\right)_{\mathbf{X}_k}$	$\sum_{i=1}^{N_s} X_i(1-k_{ik})(A_i+A_k)$	0	$\sum_{i=1}^{N_s} X_i(1-k_{ik})\left[A_i(1+f_i^2+2f_i)+A_k(1+f_k^2+2f_k)\right]$
$\left(\frac{\partial c_2}{\partial X_k}\right)_{\mathbf{X}_k}$	0	$\sum_{i=1}^{N_s} X_i(1-k_{ik})\left(A_i\sqrt{T_{c,i}}+A_k\sqrt{T_{c,k}}\right)$	$-2\sum_{i=1}^{N_s} X_i(1-k_{ik})\left[A_i\frac{f_i(1+f_i)}{\sqrt{T_{c,i}}}+A_k\frac{f_k(1+f_k)}{\sqrt{T_{c,k}}}\right]$
$\left(\frac{\partial c_3}{\partial X_k}\right)_{\mathbf{X}_k}$	0	0	$\sum_{i=1}^{N_s} X_i(1-k_{ik})\left(A_i\frac{f_i^2}{T_{c,i}}+A_k\frac{f_k^2}{T_{c,k}}\right)$
	MR-3		
	VDW	RK	SRK/PR
$\left(\frac{\partial c_1}{\partial X_k}\right)_{\mathbf{X}_k}$	$2\sum_{i=1}^{N_s} X_i(1-k_{ik})A_{ik}^*$	0	$2\sum_{i=1}^{N_s} X_i(1-k_{ik})A_{ik}^*(1+f_{ik})^2$
$\left(\frac{\partial c_2}{\partial X_k}\right)_{\mathbf{X}_k}$	0	$2\sum_{i=1}^{N_s} X_i(1-k_{ik})\sqrt{T_{c,ik}}$	$-4\sum_{i=1}^{N_s} X_i(1-k_{ik})A_{ik}^*\frac{f_{ik}(1+f_{ik})}{\sqrt{T_{c,ik}}}$
$\left(\frac{\partial c_3}{\partial X_k}\right)_{\mathbf{X}_k}$	0	0	$2\sum_{i=1}^{N_s} X_i(1-k_{ik})A_{ik}^*\frac{f_{ik}^2}{T_{c,ik}}$

Table 8: Mixture-dependent c_1, c_2, c_3 second derivative with respect to the generic mole fraction X_k. Here $\mathbf{X}_k = \{X_i \,|\, i = 1, \cdots, N_s, i \neq k\}$. In the derivation of all the above, the fact that $k_{kk} = 0$ has been used.

	MR-1 and MR-4		
	VDW	RK	SRK/PR
$\left(\frac{\partial^2 c_1}{\partial X_k^2}\right)_{\mathbf{X}_k}$	$2A_k$	0	$2A_k(1 + 2f_k + f_k^2)$
$\left(\frac{\partial^2 c_2}{\partial X_k^2}\right)_{\mathbf{X}_k}$	0	$2A_k\sqrt{T_{c,k}}$	$-4A_k\frac{f_k(1+f_k)}{\sqrt{T_{c,k}}}$
$\left(\frac{\partial^2 c_3}{\partial X_k^2}\right)_{\mathbf{X}_k}$	0	0	$2A_k\frac{f_k^2}{T_{c,k}}$
	MR-2		
	VDW	RK	SRK/PR
$\left(\frac{\partial^2 c_1}{\partial X_k^2}\right)_{\mathbf{X}_k}$	$2A_k$	0	$2(1 + 2f_k + f_k^2)$
$\left(\frac{\partial^2 c_2}{\partial X_k^2}\right)_{\mathbf{X}_k}$	0	$2A_k\sqrt{T_{c,k}}$	$-4\left(f_k A_k\frac{1+f_k}{\sqrt{T_{c,k}}}\right)$
$\left(\frac{\partial^2 c_3}{\partial X_k^2}\right)_{\mathbf{X}_k}$	0	0	$2A_k\frac{f_k^2}{T_{c,k}}$
	MR-3		
	VDW	RK	SRK/PR
$\left(\frac{\partial^2 c_1}{\partial X_k^2}\right)_{\mathbf{X}_k}$	$2A^*_{kk}$	0	$2A^*_{kk}(1 + f_{kk})^2$
$\left(\frac{\partial^2 c_2}{\partial X_k^2}\right)_{\mathbf{X}_k}$	0	$2A^*_{kk}\sqrt{T_{c,kk}}$	$-4A^*_{kk}\frac{f_{kk}(1+f_{kk})}{\sqrt{T_{c,kk}}}$
$\left(\frac{\partial^2 c_3}{\partial X_k^2}\right)_{\mathbf{X}_k}$	0	0	$2A_{kk}\frac{f_{kk}^2}{T_{c,kk}}$

Table 9: Relevant derivatives of A_m for all GCEoS except PR-RK.

	Derivatives of $A_m(T, \mathbf{X})$		
	VDW	RK	SRK/PR
$\left(\frac{\partial A_m}{\partial T}\right)_{\mathbf{X}}$	0	$-\frac{c_2}{2}T^{-3/2}$	$\frac{1}{2\sqrt{T}}c_2 + c_3$
$\left(\frac{\partial^2 A_m}{\partial T^2}\right)_{\mathbf{X}}$	0	$\frac{3c_2}{4}T^{-5/2}$	$-\frac{c_2}{4T\sqrt{T}}$
$\left(\frac{\partial^3 A_m}{\partial T^3}\right)_{\mathbf{X}}$	0	$-\frac{15c_2}{8}T^{-7/2}$	$\frac{3c_2}{8T^2\sqrt{T}}$
$\left(\frac{\partial A_m}{\partial X_k}\right)_T$	$\left(\frac{\partial c_1}{\partial X_k}\right)_{\mathbf{X}_k}$	$\frac{1}{\sqrt{T}}\left(\frac{\partial c_2}{\partial X_k}\right)_{\mathbf{X}_k}$	$\left(\frac{\partial c_1}{\partial X_k}\right)_{\mathbf{X}_k} + \sqrt{T}\left(\frac{\partial c_2}{\partial X_k}\right)_{\mathbf{X}_k} + T\left(\frac{\partial c_3}{\partial X_k}\right)_{\mathbf{X}_k}$
$\left(\frac{\partial^2 A_m}{\partial X_k^2}\right)_T$	$\left(\frac{\partial^2 c_1}{\partial X_k^2}\right)_{\mathbf{X}_k}$	$\frac{1}{\sqrt{T}}\left(\frac{\partial^2 c_2}{\partial X_k^2}\right)_{\mathbf{X}_k}$	$\left(\frac{\partial^2 c_1}{\partial X_k^2}\right)_{\mathbf{X}_k} + \sqrt{T}\left(\frac{\partial^2 c_2}{\partial X_k^2}\right)_{\mathbf{X}_k} + T\left(\frac{\partial^2 c_3}{\partial X_k^2}\right)_{\mathbf{X}_k}$
$\left(\frac{\partial^2 A_m}{\partial X_k \partial T}\right)$	0	$-\frac{1}{2}T^{-3/2}\left(\frac{\partial c_2}{\partial X_k}\right)_{\mathbf{X}_k}$	$\frac{1}{2\sqrt{T}}\left(\frac{\partial c_2}{\partial X_k}\right)_{\mathbf{X}_k} + \left(\frac{\partial c_3}{\partial X_k}\right)_{\mathbf{X}_k}$
$\left(\frac{\partial^3 A_m}{\partial X_k \partial^2 T}\right)$	0	$\frac{3}{4}T^{-5/2}\left(\frac{\partial c_2}{\partial X_k}\right)_{\mathbf{X}_k}$	$-\frac{1}{4}T^{-3/2}\left(\frac{\partial c_2}{\partial X_k}\right)_{\mathbf{X}_k}$

Table 10: Relevant derivatives of A_m for PR-RK for different mixing rules. Derivatives of $\sqrt{\alpha_i \alpha_j}$ are given in Eqs. (2.2.74)–(2.2.76).

	Derivatives of $A_m(T, \mathbf{X})$ for PR-RK		
	MR-1 and MR-4	MR-2	MR-3
$\left(\frac{\partial A_m}{\partial T}\right)_{\mathbf{X}}$	$\sum_{i=1}^{N_s}\sum_{j=1}^{N_s} X_i X_j (1-k_{ij})\sqrt{A_i A_j}\frac{d\left(\sqrt{\alpha_i \alpha_j}\right)}{dT}$	$\frac{1}{2}\sum_{i=1}^{N_s}\sum_{j=1}^{N_s} X_i X_j (1-k_{ij})\left(A_i\frac{d\alpha_i}{dT} + A_j\frac{d\alpha_j}{dT}\right)$	$\sum_{i=1}^{N_s}\sum_{j=1}^{N_s} X_i X_j (1-k_{ij}) A^*_{ij}\frac{d\alpha_{ij}}{dT}$
$\left(\frac{\partial^2 A_m}{\partial T^2}\right)_{\mathbf{X}}$	$\sum_{i=1}^{N_s}\sum_{j=1}^{N_s} X_i X_j (1-k_{ij})\sqrt{A_i A_j}\frac{d^2\left(\sqrt{\alpha_i \alpha_j}\right)}{dT^2}$	$\frac{1}{2}\sum_{i=1}^{N_s}\sum_{j=1}^{N_s} X_i X_j (1-k_{ij})\left(A_i\frac{d^2\alpha_i}{dT^2} + A_j\frac{d^2\alpha_j}{dT^2}\right)$	$\sum_{i=1}^{N_s}\sum_{j=1}^{N_s} X_i X_j (1-k_{ij}) A^*_{ij}\frac{d^2\alpha_{ij}}{dT^2}$
$\left(\frac{\partial^3 A_m}{\partial T^3}\right)_{\mathbf{X}}$	$\sum_{i=1}^{N_s}\sum_{j=1}^{N_s} X_i X_j (1-k_{ij})\sqrt{A_i A_j}\frac{d^3\left(\sqrt{\alpha_i \alpha_j}\right)}{dT^3}$	$\frac{1}{2}\sum_{i=1}^{N_s}\sum_{j=1}^{N_s} X_i X_j (1-k_{ij})\left(A_i\frac{d^3\alpha_i}{dT^3} + A_j\frac{d^3\alpha_j}{dT^3}\right)$	$\sum_{i=1}^{N_s}\sum_{j=1}^{N_s} X_i X_j (1-k_{ij}) A^*_{ij}\frac{d^3\alpha_{ij}}{dT^3}$
$\left(\frac{\partial A_m}{\partial X_k}\right)_T$	$2\sum_{i=1}^{N_s} X_i (1-k_{ij})\sqrt{A_i A_k}\left(\sqrt{\alpha_i \alpha_k}\right)$	$\sum_{i=1}^{N_s} X_i (1-k_{ik})\left(A_i\alpha_i + A_k\alpha_k\right)$	$2\sum_{i=1}^{N_s} X_i (1-k_{ij}) A^*_{ik}\alpha_{ik}$
$\left(\frac{\partial^2 A_m}{\partial X_k^2}\right)_T$	$2A_k\alpha_k$	$2A_k\alpha_k$	$2A^*_{kk}\alpha_{kk}$
$\left(\frac{\partial^2 A_m}{\partial X_k \partial T}\right)$	$2\sum_{i=1}^{N_s} X_i (1-k_{ik})\sqrt{A_i A_k}\frac{d\left(\sqrt{\alpha_i \alpha_k}\right)}{dT}$	$\sum_{i=1}^{N_s} X_i (1-k_{ik})\left(A_i\frac{d\alpha_i}{dT} + A_k\frac{d\alpha_k}{dT}\right)$	$2\sum_{i=1}^{N_s} X_i A^*_{ik}(1-k_{ik})\frac{d\alpha_{ik}}{dT}$
$\left(\frac{\partial^3 A_m}{\partial X_k \partial^2 T}\right)$	$2\sum_{i=1}^{N_s} X_i (1-k_{ik})\sqrt{A_i A_k}\frac{d^2\left(\sqrt{\alpha_i \alpha_k}\right)}{dT^2}$	$\sum_{i=1}^{N_s} X_i (1-k_{ik})\left(A_i\frac{d^2\alpha_i}{dT^2} + A_k\frac{d^2\alpha_k}{dT^2}\right)$	$2\sum_{i=1}^{N_s} X_i A^*_{ik}(1-k_{ik})\frac{d^2\alpha_{ik}}{dT^2}$

Table 11: Relevant derivatives of B_m.

	Derivatives of $B_m(\mathbf{X})$	
	MR-1, MR-2 and MR-3	MR-4
$\left(\frac{\partial B_m}{\partial X_k}\right)_{\mathbf{X}_k}$	B_k	$2\sum_{i=1}^{N_s} X_i \left[\frac{1}{2}\left(B_i^{1/3}+B_k^{1/3}\right)\right]^3$
$\left(\frac{\partial^2 B_m}{\partial X_k^2}\right)_{\mathbf{X}_k}$	0	$2B_k$

Table 12: Relevant derivatives of A_{ij}. The derivatives of α_i are given in Tab. 5.

	Derivatives of $A_{ij}(T)$		
	MR-1 and MR-4	MR-2	MR-3
$A_{ij}(T)$	$\sqrt{A_i A_j}\sqrt{\alpha_i(T)\alpha_j(T)}(1-k_{ij})$	$\frac{A_i\alpha_i(T)+A_j\alpha_j(T)}{2}(1-k_{ij})$	$A^*_{ij}\alpha_{ij}(T)$
$\frac{dA_{ij}(T)}{dT}$	$\frac{(1-k_{ij})\sqrt{A_iA_j}}{2\sqrt{\alpha_1\alpha_j}}\left(\alpha_j\frac{d\alpha_i}{dT}+\alpha_i\frac{d\alpha_j}{dT}\right)$	$\frac{1}{2}(1-k_{ij})\left(A_i\frac{d\alpha_i}{dT}+A_j\frac{d\alpha_j}{dT}\right)$	$A^*_{ij}\frac{d\alpha_{ij}}{dT}$

using the following trivial result:

$$\int_0^\rho \frac{d\rho}{M^2+(\delta_1+\delta_2)B_m\rho M+\delta_1\delta_2 B_m^2\rho^2} = \begin{cases} \frac{1}{(\delta_1-\delta_2)B_m M}\ln\left(\frac{\delta_1 B_m\rho+M}{\delta_2 B_m\rho+M}\right) & \text{if } \delta_1,\delta_2\neq 0 \\ & \text{(for all GCEoS except VDW)} \\ \frac{\rho}{M^2} & \text{if } \delta_1=\delta_2=0 \\ & \text{(for VDW EoS only)} \end{cases} \tag{2.2.78}$$

the internal energy departure function is readily obtained:

$$\Delta E = \begin{cases} \frac{1}{(\delta_1-\delta_2)B_m}\left[T\left(\frac{\partial A_m}{\partial T}\right)_{\mathbf{X}}-A_m\right]\ln\left(\frac{\delta_1 B_m\rho+M}{\delta_2 B_m\rho+M}\right) & \text{if } \delta_1,\delta_2\neq 0 \\ \frac{\rho}{M}\left[T\left(\frac{\partial A_m}{\partial T}\right)_{\mathbf{X}}-A_m\right] & \text{if } \delta_1=\delta_2=0\,. \end{cases} \tag{2.2.79}$$

Next, the following integral is computed:

$$
\begin{aligned}
-\int_0^\rho (Z-1)\frac{d\rho}{\rho} &\overset{\text{Using Eq. (2.2.72) for } Z}{=} \int_0^\rho \left[\frac{M}{M-B_m\rho} - \frac{\rho A_m M}{R_u T}\frac{1}{M^2+(\delta_1+\delta_2)B_m M\rho+\delta_1\delta_2 B_m^2\rho^2} - 1\right]\frac{d\rho}{\rho} = \\
&= -\int_0^\rho \frac{B_m}{M-B_m\rho}d\rho + \frac{MA_m}{R_u T}\int_0^\rho \frac{d\rho}{M^2+(\delta_1+\delta_2)B_m\rho M+\delta_1\delta_2 B_m^2\rho^2} = \\
&= -\ln\left(\frac{M-B_m\rho}{M}\right) + \frac{MA_m}{R_u T}\int_0^\rho \frac{d\rho}{M^2+(\delta_1+\delta_2)B_m\rho M+\delta_1\delta_2 B_m^2\rho^2} = \\
&= \ln(Z-\tilde{B}_m) - \ln Z + \frac{MA_m}{R_u T}\int_0^\rho \frac{d\rho}{M^2+(\delta_1+\delta_2)B_m\rho M+\delta_1\delta_2 B_m^2\rho^2}\,, \\
&\qquad\qquad \downarrow \text{Use } \rho = pM/(ZR_uT)
\end{aligned}
\tag{2.2.80}
$$

where $\tilde{B}_m = B_m p/(R_u T)$ has been defined. Thus, following Eq. (2.2.14) the entropy departure function can be constructed:

$$
\begin{aligned}
\Delta S &= \frac{\Delta E}{T} - R_u\int_0^\rho (Z-1)\frac{d\rho}{\rho} + R_u \ln Z = \\
&\overset{\text{Using Eq. (2.2.78), Eq. (2.2.79) and Eq. (2.2.80)}}{=} \begin{cases} R_u\ln(Z-\tilde{B}_m) + \dfrac{1}{(\delta_1-\delta_2)B_m}\left(\dfrac{\partial A_m}{\partial T}\right)_{\mathbf{X}} \ln\left(\dfrac{\delta_1 B_m\rho + M}{\delta_2 B_m\rho + M}\right) & \text{if } \delta_1,\delta_2 \neq 0 \\ R_u\ln(Z-\tilde{B}_m) + \dfrac{\rho}{M}\left(\dfrac{\partial A_m}{\partial T}\right)_{\mathbf{X}} & \text{if } \delta_1 = \delta_2 = 0\,. \end{cases}
\end{aligned}
\tag{2.2.81}
$$

For later purpose, Eq. (2.2.79) and Eq. (2.2.81) can be further manipulated in order to recast the logarithm term in such a way Z and $\tilde{B}_m$ appear (using $\rho = pM/(ZR_uT)$):

$$
\Delta E = \begin{cases} \dfrac{1}{(\delta_1-\delta_2)B_m}\left[T\left(\dfrac{\partial A_m}{\partial T}\right)_{\mathbf{X}} - A_m\right]\ln\left(\dfrac{\delta_1\tilde{B}_m + Z}{\delta_2\tilde{B}_m + Z}\right) & \text{if } \delta_1,\delta_2 \neq 0 \\ \dfrac{p}{ZR_u}\left[\left(\dfrac{\partial A_m}{\partial T}\right)_{\mathbf{X}} - \dfrac{A_m}{T}\right] & \text{if } \delta_1 = \delta_2 = 0\,. \end{cases}
\tag{2.2.82}
$$

$$\Delta S = \begin{cases} R_u \ln(Z - \tilde{B}_m) + \dfrac{1}{(\delta_1 - \delta_2) B_m} \left(\dfrac{\partial A_m}{\partial T} \right)_{\mathbf{X}} \ln \left(\dfrac{\delta_1 \tilde{B}_m + Z}{\delta_2 \tilde{B}_m + Z} \right) & \text{if } \delta_1, \delta_2 \neq 0 \\ \\ R_u \ln(Z - \tilde{B}_m) + \dfrac{p}{Z R_u T} \left(\dfrac{\partial A_m}{\partial T} \right)_{\mathbf{X}} & \text{if } \delta_1 = \delta_2 = 0 \,. \end{cases} \tag{2.2.83}$$

With available ΔE and ΔS all other departure functions can be constructed by applying Eqs. (2.2.12)–(2.2.16). Particularly, the departure function of Helmholtz energy at constant V and T is important because it is used later for the determination of the fugacity coefficient. According to Eq. (2.2.17), using the result of Eq. (2.2.80) one obtains:

$$\frac{\Delta A_{TV}}{R_u T} = \begin{cases} -\ln \left(\dfrac{M - B_m \rho}{M} \right) - \dfrac{A_m}{R_u T B_m (\delta_2 - \delta_1)} \ln \left(\dfrac{\delta_2 B_m \rho + M}{\delta_1 B_m \rho + M} \right) & \text{if } \delta_1, \delta_2 \neq 0 \\ \\ -\ln \left(\dfrac{M - B_m \rho}{M} \right) - \dfrac{A_m \rho}{M R_u T} & \text{if } \delta_1 = \delta_2 = 0 \,. \end{cases} \tag{2.2.84}$$

Next, the specific heat at constant volume departure function can be obtained by applying Eq. (2.2.18):

$$\Delta C_v = \left(\frac{\partial \Delta E}{\partial T} \right)_{\rho, \mathbf{X}} \underset{\text{Using Eq. (2.2.79)}}{=\!=\!=} \begin{cases} \dfrac{T}{(\delta_1 - \delta_2) B_m} \left(\dfrac{\partial^2 A_m}{\partial T^2} \right)_{\mathbf{X}} \ln \left(\dfrac{\delta_1 B_m \rho + M}{\delta_2 B_m \rho + M} \right) & \text{if } \delta_1, \delta_2 \neq 0 \\ \\ \dfrac{\rho}{M} T \left(\dfrac{\partial^2 A_m}{\partial T^2} \right)_{\mathbf{X}} & \text{if } \delta_1 = \delta_2 = 0 \,. \end{cases} \tag{2.2.85}$$

And the specific heat at constant pressure departure function is readily computed using Eq. (2.2.19), where $(\partial p / \partial T)_{\rho, \mathbf{X}}$ and $(\partial p / \partial \rho)_{T, \mathbf{X}}$ are obtained by differentiating Eq. (2.2.67)

accordingly:

$$\left(\frac{\partial p}{\partial T}\right)_{\rho,\mathbf{X}} = \frac{\rho R_u}{M - B_m\rho} - \frac{\rho^2 \left(\frac{\partial A_m}{\partial T}\right)_{\mathbf{X}}}{(M + \delta_1 B_m\rho)(M + \delta_2 B_m\rho)}\,, \tag{2.2.86}$$

$$\left(\frac{\partial p}{\partial \rho}\right)_{T,\mathbf{X}} = \frac{M R_u T}{(M - B_m\rho)^2} - \frac{A_m\rho M\left[2M + (\delta_1 + \delta_2)B_m\rho\right]}{(M + \delta_1 B_m\rho)^2(M + \delta_2 B_m\rho)^2}\,, \tag{2.2.87}$$

while $(\partial\rho/\partial T)_{p,\mathbf{X}}$ is obtained by inversion of Eq. (K.0.32). Equations (2.2.86) and (2.2.87) hold for all GCEoS/MR combinations, provided that A_m, B_m and $(\partial A_m/\partial T)_{\mathbf{X}}$ are properly supplied. In addition, Eqs. (2.2.86)–(2.2.87) allow to compute the single-phase isentropic speed of sound, the isobaric expansivity and the isothermal compressibility using Eq. (2.2.20), and Eq. (2.2.21), respectively.

Given the considerable amount of formulas involved, it is preferred once again to point the reader to Appendix M for step-by-step derivations of all the other quantities that are left. These include the derivatives of the compressibility factor (Sec. M.1), additional derivatives of the departure functions (Sec. M.2), definition of fugacity coefficient and its derivatives (Sec. M.3) and definitions of partial molar quantities (Sec. M.4).

2.3 Transport properties

With the simplifying assumptions invoked in Sec. 2.1.2.2 the transport properties are discussed in this section according to Eq. (2.1.19): the viscosity μ, the thermal conductivity λ and binary diffusion coefficients $\mathcal{D}_{k,m}$. Regarding the calculation of viscosity and thermal conductivity in non-ideal conditions, the method of Chung [31] has been chosen, as done by Masquelet [114], Ma [107] and many other works [163, 34]. This model is based on the Corresponding State Principle (CSP) and it represents a compromise between cost and prediction of RG transport properties of various species, as well as mixtures. Another advantage is related to the fact that this method mostly requires similar species-dependent properties that are shared with the GCEoS model, therefore minimal additional coding effort is required.

On the other hand, the method of Fuller *et al.* [52] is chosen to compute the mixture pseudo binary diffusion coefficients. This method requires some additional constants that are readily available in common resources [163], and it is relatively computationally inexpensive compared to alternatives. Regarding the calculation of its high-pressure correction, the method of Riazi *et al.* [178] is chosen instead of the other common option represented by the Takahashi method [214] because it is fully analytical and its main shortcoming (wrong asymptotic behavior at low pressures) is irrelevant for the current work. It is important to highlight the fact that the thermodynamic and transport models are distinct and do not require each other from an implementation point of view. In other words, one could use the TPG model for thermodynamics with the Chung [31] and Riazi *et al.* [178] models for transport. Of course this (and any other) inconsistent choice, although possible, may come with erroneous outcomes, therefore consistent selection of the whole RG modules is always advised.

2.3.1 Viscosity

The calculation of molecular viscosity is treated in this section. The expression proposed by Chung [31] is:

$$\mu = \mu^* \frac{36.344 \times 10^{-7} \sqrt{MW_m T_{c,m}}}{V_{c,m}^{2/3}}\,, \tag{2.3.1}$$

where μ is the mixture viscosity in N.s.m^{-2} (or Pa.s) and $V_{c,m}$ is a critical volume of the mixture computed as $V_{c,m} = (\sigma_m/0.809)^3$ in cm^3.mol^{-1}. For consistency, it is recommended that the Lennard-Jones parameter σ is determined from the critical volume of each component in the mixture rather than arbitrarily defined using some different constant [163]

$$\sigma_m^3 = \sum_i \sum_j X_i X_j \sigma_{ij}^3 \,, \tag{2.3.2}$$

$$\sigma_{ij} = \xi_{ij} \sqrt{\sigma_i \sigma_j} \,, \tag{2.3.3}$$

$$\sigma_i = 0.809 V_{c,i}^{1/3} \,. \tag{2.3.4}$$

Also, the mixture critical temperature is defined as:

$$T_{c,m} = 1.2593 \left(\frac{\varepsilon_m}{k_B} \right)^{-1} \,. \tag{2.3.5}$$

Note that in the expression for σ_{ij} (Eq. 2.3.3) an interaction parameter xi_{ij} can also be specified. However, due to the lack of data or associated predictive models, these are often set to unity.

The value of μ^* in Eq. (2.3.1) is defined as:

$$\mu^* = \frac{\sqrt{T_m^*}}{\Omega_v} \,, \left(F_{c,m} \left[G_2^{-1} + E_6 y \right] \right) + \mu^{**} \,, \tag{2.3.6}$$

The dimensionless temperature T^*, the other Lennard-Jones parameter $\frac{\varepsilon}{k_B}$ and the collision integral Ω_v are related by:

$$T_m^* = T/T_{c,m} \,, \tag{2.3.7}$$

$$\frac{\varepsilon_m}{k_B} = \frac{\sum_i \sum_j X_i X_j \frac{\varepsilon_{ij}}{k_B} \sigma_{ij}^3}{\sigma_m^3} \,, \tag{2.3.8}$$

$$\frac{\varepsilon_{ij}}{k_B} = \sqrt{\frac{\varepsilon_i}{k_B} \frac{\varepsilon_j}{k_B}} \,, \tag{2.3.9}$$

$$\frac{\varepsilon_i}{k_B} = \zeta_{ij} \frac{T_{c,i}}{1.2593} \,, \tag{2.3.10}$$

$$\Omega_v = A(T^*)^{-B} + C e^{-DT^*} + E e^{-FT^*} \,, \tag{2.3.11}$$

where k_B is the Boltzmann constant, while the other parameters that appear are defines as [70]:

$$A = 1.16145 \qquad B = 0.14874$$

$$C = 0.52487 \qquad D = 0.77320$$

$$E = 2.16178 \qquad F = 2.43787$$

Note also that the expression for $\frac{\varepsilon_{ij}}{k_B}$ (Eq. 2.3.9) may include a binary interaction parameter ζ_{ij} which is also set to one usually, unless specific data/models are available for it.
The function $F_{c,m}$ accounts for the shape and polarity of the molecules through its dependencies on the acentric factor ω, the dimensionless dipole moment μ_r and the association factor κ:

$$F_{c,m} = 1 - 0.2756\omega_m + 0.059035\mu_{r,m}^4 + \kappa_m$$

The additional mixing rules required for these mixture quantities are given below:

$$MW_m = \left(\frac{\sum_i \sum_j X_i X_j \frac{\varepsilon_{ij}}{k} \sigma_{ij}^2 \sqrt{MW_{ij}}}{\frac{\varepsilon_m}{k} \sigma_m^2} \right)^2 \tag{2.3.12}$$

$$MW_{ij} = \frac{2}{\frac{1}{MW_i} + \frac{1}{MW_j}} \tag{2.3.13}$$

$$\omega_m = \frac{\sum_i \sum_j X_i X_j \omega_{ij} \sigma_{ij}^3}{\sigma_m^3} \tag{2.3.14}$$

$$\omega_{ij} = \frac{\omega_i + \omega_j}{2} \tag{2.3.15}$$

The reduced dipole moment is computed from the physical dipole moment μ^{dp} in debyes:

$$\mu_{r,m} = 0.1313 \frac{\mu_m^{dp}}{\sqrt{V_c T_c}} \tag{2.3.16}$$

$$\left(\mu_m^{dp}\right)^4 = \sigma_m^3 \sum_i \sum_j \left(\frac{X_i X_j (\mu_i^{dp})^2 (\mu_j^{dp})^2}{\sigma_{ij}^3} \right) \tag{2.3.17}$$

$$\kappa_m = \sum_i \sum_j X_i X_j \kappa_{ij} \tag{2.3.18}$$

$$\kappa_{ij} = \sqrt{\kappa_i \kappa_j} \tag{2.3.19}$$

Table 35 summarizes the non-zero values of these coefficients for the species considered in this work.

Finally, the high-pressure/high-density correction terms are provided as follows:

$$
\begin{aligned}
y &= \frac{v_c}{6v} \\
G_1 &= \frac{1-0.5y}{(1-y)^3} \\
G_2 &= \frac{E_1\left[\left(1-e^{-E_4 y}\right)/y\right] + E_2 G_1 e^{E_5 y} + E_3 G_1}{E_1 E_4 + E_2 + E_3} \\
\mu^{**} &= E_7 y^2 G_2 e^{E_8 + \frac{E_9}{T^*} + \frac{E_{10}}{(T^*)^2}}
\end{aligned}
$$

Clearly, the low-pressure viscosity: μ^0 is immediately available by setting y to zero. This step is particularly useful for the computation of the thermal conductivity as discussed in the next subsection. In the above, the parameters E_1 to E_{10} are a linear functions of the acentric factor ω of the mixture:

$$
\begin{aligned}
E_1 &= 6.324 + 50.412\omega_m & E_2 &= 0.00121 - 0.001154\omega_m \\
E_3 &= 5.283 + 254.209\omega_m & E_4 &= 6.623 + 38.096\omega_m \\
E_5 &= 19.745 + 7.630\omega_m & E_6 &= -1.9 - 12.537\omega_m \\
E_7 &= 24.275 + 3.45\omega_m & E_8 &= 0.7972 - 1.117\omega_m \\
E_9 &= -0.2382 + 0.06770\omega_m & E_{10} &= 0.06863 + 0.3479\omega_m
\end{aligned}
$$

One flaw of Chung's method is that it does not allow to recover the single component viscosities asymptotically as already pointed out by [114, 107]. In addition, as discussed by Masquelet [114] this method also suffers when species with negative acentric factor (such as H_2) are considered.

2.3.2 Thermal conductivity

Viscosity and thermal conductivity are related

$$
\lambda = \frac{31200\mu^0\Psi}{MW_m}\left(\frac{1}{G_2} + B_6 y\right) + qB_7 y^2 \sqrt{T_{r,m}} G_2 \tag{2.3.20}
$$

where λ is the thermal conductivity in W.(m.K)$^{-1}$, the superscript 0 in μ^0 denotes the low-pressure viscosity mentioned earlier and q is defined as:

$$
q = 3.586 \times 10^{-3} \sqrt{\frac{T_{c,m}}{MW_m V_{c,m}^{4/3}}}
$$

and Ψ is a function of the molar heat capacity at constant volume C_v, the acentric factor ω and the reduced temperature T_r:

$$\Psi = 1 + \alpha \frac{0.215 + 0.28288\alpha - 1.061\beta + 0.26665Z}{0.6366 + \beta Z + 1.061\alpha\beta} \tag{2.3.21}$$

with:

$$\alpha = \frac{C_v}{R_u} - \frac{3}{2}$$

$$\beta = 0.7862 - 0.7109\omega_m + 1.3168\omega_m^2$$

$$Z = 2.0 + 10.5(T_m^*)^2$$

The other parameters are very similar to the ones used for the viscosity, allowing an easy implementation:

$$y = \frac{V_c}{6v}$$

$$G_1 = \frac{1 - 0.5y}{(1-y)^3}$$

$$G_2 = \frac{B_1\left[\left(1 - e^{-B_4 y}\right)/y\right] + B_2 G_1 e^{B_5 y} + B_3 G_1}{B_1 B_4 + B_2 + B_3}$$

$$B_1 = 2.4166 + 0.74824\omega_m$$

$$B_2 = -0.50924 - 1.5094\omega_m$$

$$B_3 = 6.6107 + 5.6207\omega_m$$

$$B_4 = 14.543 - 8.9139\omega_m$$

$$B_5 = 0.79274 + 0.82019\omega_m$$

$$B_6 = -5.8634 + 12.801\omega_m$$

$$B_7 = 91.089 + 128.11\omega_m$$

The mixing rules used to compute the mixture properties are also the same ones than for the viscosity computation.

2.3.3 Mass diffusion coefficients

The method of Fuller et al. [52] modifies the classical expression from Chapman and Enskog that was derived from the Boltzmann equation and kinetic theory:

$$\mathcal{D}_{ij} = \frac{C_D T^{1.75}}{p\sqrt{MW_{ij}}\left((\Sigma_v)_i^{1/3} + (\Sigma_v)_j^{1/3}\right)^2}, \tag{2.3.22}$$

The pressure dependency satisfies the phenomenological law that $p\mathcal{D}$ or $\rho\mathcal{D}$ is essentially constant at low pressures. The atomic diffusion volumes Σ_v represent the additional input to the model compared to the original theory, however they improve the results, avoid the expensive computation of the collision integrals and can be easily estimated using a group contribution method (see Table 11-1 from Poling [163]). The factor C_D is a constant and it is equal to 0.00143 for a diffusion coefficient in cm^2/s and the pressure p in bar. The averaged molecular weight is computed through a geometric mean $MW_{ij} = \frac{2}{\frac{1}{MW_i}+\frac{1}{MW_j}}$. For high-pressure regimes where the density is large enough, the assumption of $p\mathcal{D}$ or $\rho\mathcal{D}$ being constant with increasing pressure is no longer valid. Instead, these quantities decrease with either increasing pressure or increase density. Very few models exist because of the scarcity of experimental data and the one chosen for this work is the one by Riazi and Whitson [178] similarly to what has been done by [114]:

$$\frac{\rho\mathcal{D}_{ij}}{(\rho\mathcal{D}_{ij})^o} = 1.07\left(\frac{\mu}{\mu^o}\right)^{(-0.27-0.38\omega-(0.05+0.1\omega)p_r)}. \tag{2.3.23}$$

Where p_r is the reduced pressure. Other possible models for high-pressure mass diffusion coefficients include the empirical correlation by Takahashi [214] and the more fundamental work by Harstad and Bellan [63].

2.3.4 Verification

Verification of the transport model is carried out in this subsection. First, the viscosities and thermal conductivities of relevant species considered in non-ideal conditions in the present work are presented. Figure 14 shows the viscosity and the thermal conductivity for O_2, N_2, CH_4 and C_6H_{14} which are mainly used in the next sections. The properties are plotted as a function of pressure for two relevant temperatures, both meaningful for the results that are

going to be discussed later in Chap. 5. Data is verified against NIST values. In this case, the low pressure model of Chung without high-pressure/high-density correction is turned off to improve the picture quality. The absence of that was in fact already highlighted in Fig. 12 for O_2, therefore its repetition is avoided in this case. In all cases, the Chung model performs very well with the reference data. In general, one can observe that as temperature increases, the non-ideal effects reduce, even if pressure increases, indicating that temperature has a more important effect, as far as non-ideal conditions, than pressure. Next, the calculation of the thermal conductivity for mixtures is considered here. The experimental work of Yorizane et al. [246] is taken as reference which considers high-pressure binary mixtures of argon and carbon dioxide at 298 K. Figure 15 shows the predictions of the mixture thermal conductivity as the amount of CO_2 is varied and by varying the pressure too (from 11 bar to 71 bar). Dashed curves correspond to the empirical curvefits taken from the work of Stiel and Thodos [211]. Some disagreement is observed between the model and the reference data especially at higher pressures. This represents one level of uncertainty that is considered acceptable for the present work as it seems limited between 5% and 7%. Finally, in order to validate the current implementation for the calculation of the binary mass diffusion coefficients, the experimental work of Takahashi *et al.* [215] is considered here. In his work [215], the mass diffusion coefficients of the CO_2-C_2H_4 system are measured for different temperatures and pressures by varying the amount of one species into the mixture. Particularly the amount of CO_2 is varied such that the mixture presents "traces" of CO_2 into a bath of C_2H_4 or viceversa. The actual amount of the species in the mixture is not exactly specified in the paper [215], therefore a reference "trace" amount in the present work is considered of 1% by mass in the present work. Additional tests performed in the vicinity of such reference values did not bring any different conclusions so they are omitted here. The model of Eq. (2.3.22) augmented with the high-pressure correction of Eq. (2.3.23) is the model tested here. It is compared against the corresponding "low-pressure" model which employs only Eq. (2.3.22) without any correction, as well as the experimental data of [215]. This comparison is shown in Fig. 16. In this figure, one may

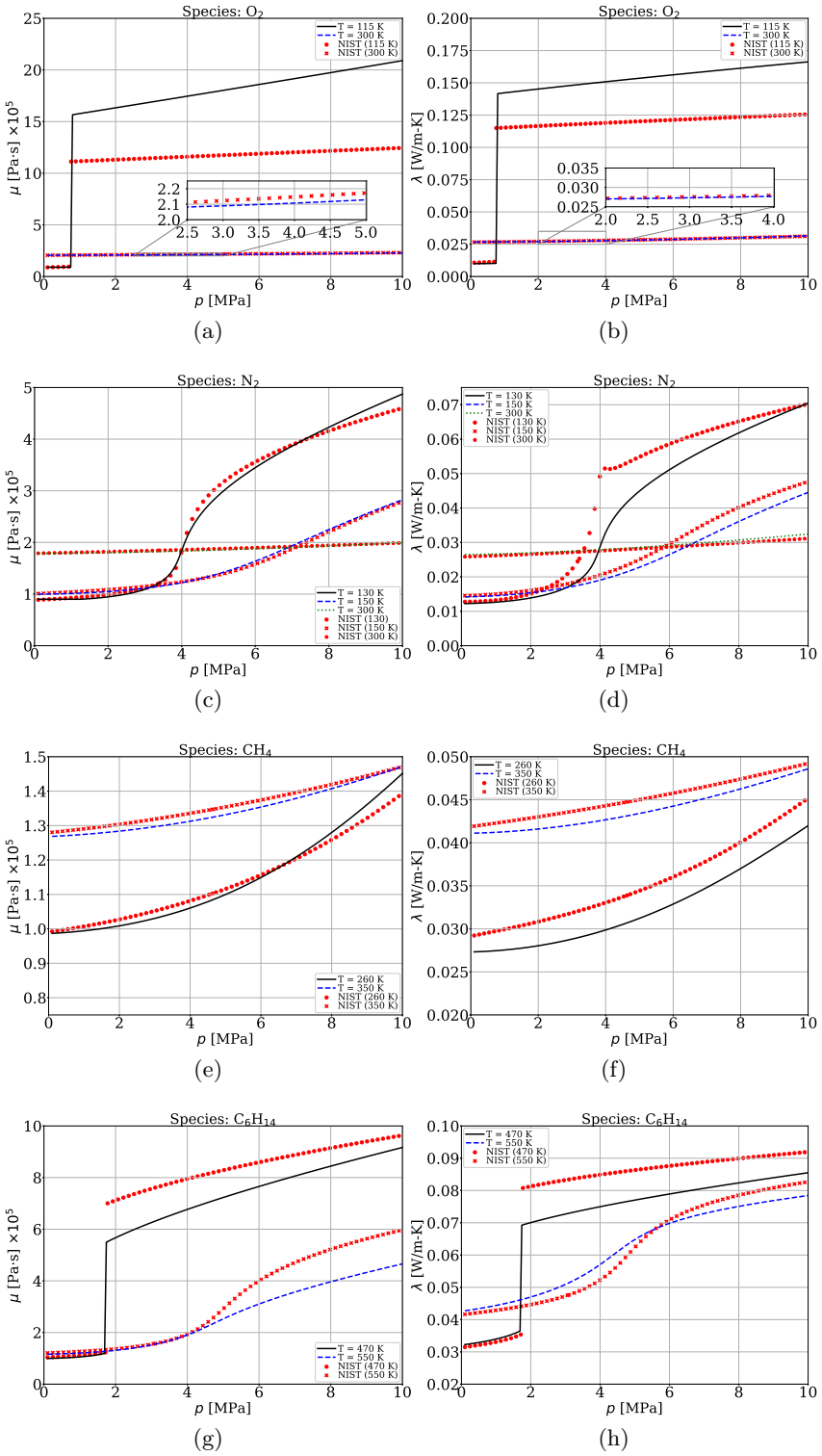

Figure 14: Viscosity and thermal conductivity of the relevant single components used in the present work. The data is recorded for two reference temperature and a range of pressures and validated against the NIST database.

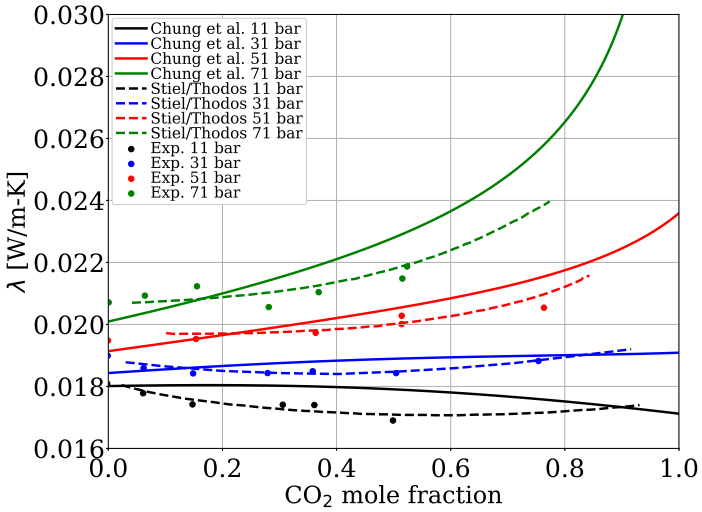

Figure 15: High-pressure thermal conductivities for mixture of argon and carbon dioxide at 298 K.

observe that at low pressures all the data agree. Particularly there is an overlap between the low-pressure model and the corrected model indicating that the correction does not have any impact, as expected. As pressure increases, the correction is shown to have some effects that according to the experimental data, reduce the coefficients, while the low-pressure model would predict a higher value. The effect of the mixture solvent is not particularly clear, both in the analytical model, as well as from the experimental data since experimental dots seem to follow an overlapped trend, similarly to what predicted by the Fuller/Riazi model. Overall, given the absence of a more accurate model with comparable computational speed, the present model is considered satisfactory, which overall shows consistent trends with experimental data, although the mass diffusivity seems to be over-predicted in magnitude.

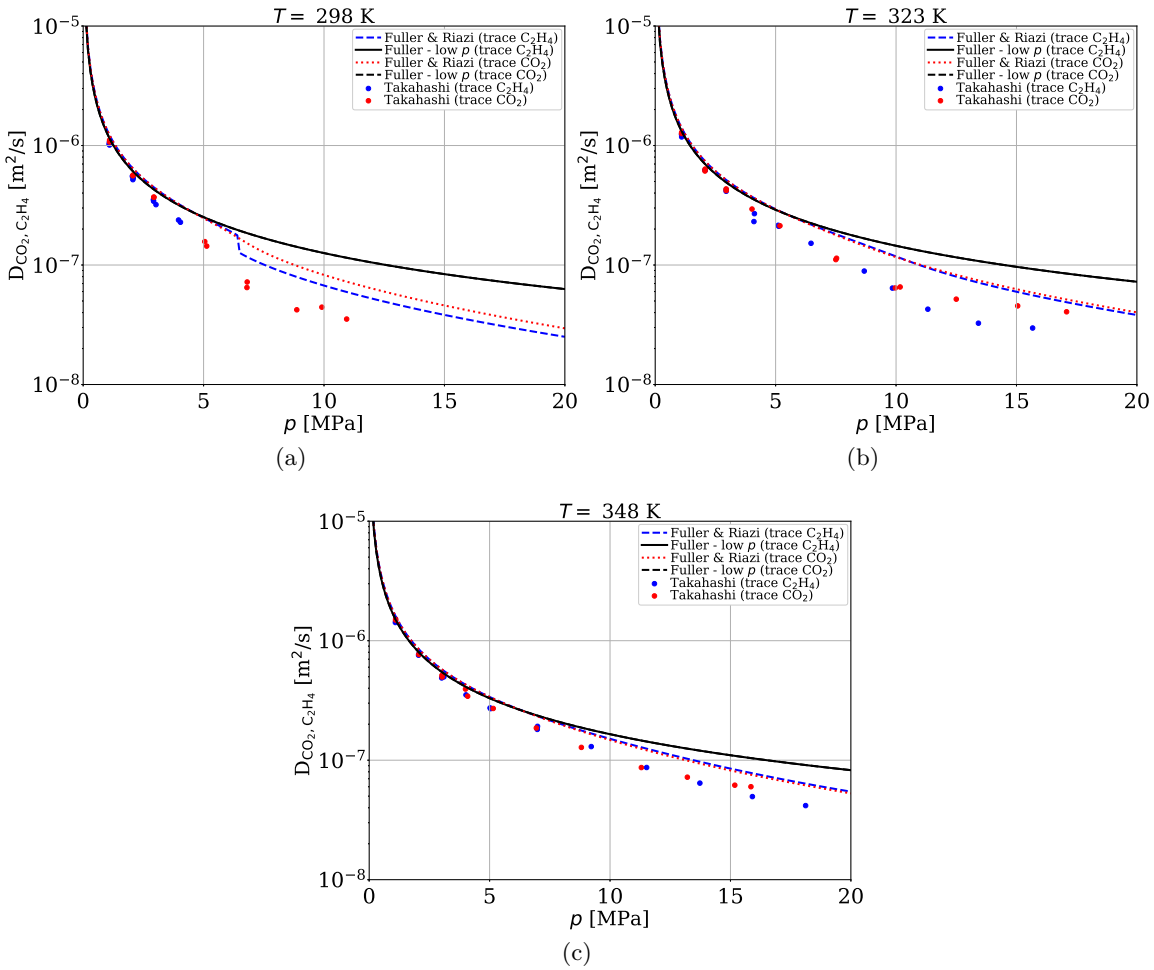

Figure 16: Effect of pressure, temperature and mixture solvent on the binary diffusion coefficient of the CO_2-C_2H_4 system.

2.4 Chemistry

A brief discussion on how to compute the reaction rate $\dot{\omega}_k$ in Eq. (2.1.4) is given in this section. For a reacting system composed of N_s components and employing N_R reactions in the form [162]:

$$\sum_{k=1}^{N_s} \nu'_{ki} \mathcal{M}_k \rightleftharpoons \sum_{k=1}^{N_s} \nu''_{ki} \mathcal{M}_k \,, \tag{2.4.1}$$

we seek to determine the reaction rate of each species in the mixture $\dot{\omega}_k$. In the above, $i = 1, \cdots, N_R$ is the index of the reaction step, $k = 1, \cdots, N_s$ is the species index in the mixture and $\mathcal{M}_k$ is the generic symbol to indicate the species k in the mixture. The stoichiometric coefficients ν'_{ik} and ν''_{ik} are those referring to the reaction step i and species k in the forward and reverse direction, respectively. Enforcing mass conservation, *i.e.*the fact that total mass between reactants and products should not be altered at any time, one gets:

$$\sum_{k=1}^{N_s} \nu'_{ki} M_k \rightleftharpoons \sum_{k=1}^{N_s} \nu''_{ki} M_k \quad \rightarrow \quad \sum_{k=1}^{N_s} \nu_{ki} M_k = 0 \,, \quad i = 1, \cdots, N_R \,, \tag{2.4.2}$$

where $\nu_{ki} = \nu''_{ki} - \nu'_{ki}$. By definition, the reaction rate for each species k is the sum of the reaction rates of every step in which the production/destruction of that species occur:

$$\dot{\omega}_k = \sum_{i=1}^{N_R} \dot{\omega}_{ki} = M_k \sum_{i=1}^{N_R} \nu_{ki} \mathcal{Q}_i \,, \tag{2.4.3}$$

where:

$$\mathcal{Q}_i = k_{f,i} \prod_{k=1}^{N_s} [X_k]^{\nu'_{ki}} - k_{b,i} \prod_{k=1}^{N_s} [X_k]^{\nu''_{ki}} \quad i = 1, \cdots, N_R \,. \tag{2.4.4}$$

The concentration of $[X]_k$ of each species k is defined as:

$$[X_k] = \frac{\rho Y_k}{M_k} \,, \tag{2.4.5}$$

and can be further manipulated by employing the generic EoS form of Eq. (2.2.3):

$$[X_k] = \frac{\rho Y_k}{M_k} = \frac{p}{Z R_u T} \frac{M Y_k}{M_k} = \frac{p}{Z R_u T} X_k \,, \tag{2.4.6}$$

where Eq. (2.2.11) has been also used in the last step. The latter represents a generic way to formulate Eq. (2.4.4) for any EoS because of the compressibility factor appearing in the

scaling law that defines the concentration. However, in this work the assumption of an IG behavior from a kinetic point of view is made, meaning that Z is set to 1 in Eq. (2.4.6). The reason is once again related to the fact that low temperature thermodynamics that is supposed to be the regime where VLE forms is essentially a cold-flow region. As soon as the temperature overcomes values that are already considered "low" from a kinetics point of view (such as 500-600 K), VLE disappears as discussed in Chap. 4 and the mixture has already the tendency to behave towards the ideal gas regime. Of course, this assumption may have a strong impact in other contexts, such as ignition delays computations as discussed in the work of [84], however this is not the case of the present work. Nevertheless future outlooks may look into this effect as well.

The *forward* reaction rate $k_{f,i}$ for each reaction is typically specified using the Arrhenius form:

$$k_{f,i} = A_{f,i} T^{b_i} \exp\left(-\frac{\mathrm{E_a}}{\mathrm{R_u T}}\right), \tag{2.4.7}$$

where $A_{f,i}$ is the pre-exponential factor, b_i is the temperature power coefficient and E_a is the activation energy specified in the units consistent with R_u and T. The knowledge of these parameters require sophisticated, ad-hoc studies that go beyond the scope of the current work [176], however the tuning procedure used in this work with the scope of investigating the role of species production near the flame on the VLE formation is addressed in Sec. 5.5.1. Regarding the calculation of the *backwrd* reaction rate $k_{b,i}$, the relationship between the forward one and the *equilibrium* constant $k_{eq,i}$ is typically used [162]:

$$k_{b,i} = \frac{k_{f,i}}{k_{eq,i}}, \tag{2.4.8}$$

where:

$$k_{eq,i} = \left(\frac{p^0}{R_u T}\right)^{\nu_i} \exp\left(\frac{\Delta \mathrm{S_i^0}}{\mathrm{R_u}} - \frac{\Delta \mathrm{H_i^0}}{\mathrm{R_u T}}\right), \tag{2.4.9}$$

is the equilibrium constant of the i-th reaction in the mechanism. In Eq. (2.4.9), p^0 is the standard-state pressure of 1 bar, ΔS_i^0 and ΔH_i^0 represent the change in entropy and

enthalpy of the i-th reaction:

$$\Delta S_i^0(T) = \sum_{k=1}^{N_s} \nu_{ki} S_{k,f}^0(T)\,, \tag{2.4.10}$$

$$\Delta H_i^0(T) = \sum_{k=1}^{N_s} \nu_{ki} H_{k,f}^0(T)\,. \tag{2.4.11}$$

and $S_{k,f}^0(T)$, $H_{k,f}^0(T)$ represent the entropy and enthalpy of formation of the species k (in the step i) obtained from its formation reaction at the standard state, respectively [228]. Typically both of these quantities can be computed using curvefit polynomials taken from either the CHEMKIN [80] or NASA [123] version. Lastly, the ν_i quantity in Eq. (2.4.9) is defined as:

$$\nu_i = \sum_{k=1}^{N_s} \nu_{ki}\,. \tag{2.4.12}$$

2.5 Summary

In this chapter, a detailed description of the analytic tools used throughout the rest of the work are provided and emphasis is given to the various assumptions employed along with their justification. The main contribution to this work is the development of a consistent thermodynamic model with VLE [227] previously non-existent in the literature. This effort partly addresses the content of **Objective 1**. In addition, thermodynamic relations are provided for the GCEoS model, which were also not extensively found, especially in conjunction with several mixing rules. The material presented in this chapter is the subject of more extensive discussions from both numerical and physical perspectives covered in the next chapters.

Chapter III

NUMERICAL METHODS: IMPLEMENTATION AND VERIFICATION

This chapter presents the numerical methods used to solve the analytic problems formulated in Chap. 2. Well-established methods are not discussed here for brevity and the reader is referred to the literature, cited accordingly. The present discussion mainly focuses on the development of robust tools to simulate RG flows in high-density gradients conditions without and with VLE. In parallel, the solutions the thermodynamic problems that involve VLE are discussed and their impact on erroneous choice of the thermodynamic condition emphasized.

3.1 Background on the numerical approach

The Navier-Stokes equations written in Sec. 2.1 are discretized using the conventional finite-volume method [220, 111]. Advection fluxes are solved for using an upwind-based spatial discretization that employs the MUSCL [5] interpolation at cell-faces from cell-centered values (discussed later). Time integration is carried out using the second-order accurate method of MacCormack [111, 5]. Regarding the viscous fluxes, these are computed using second-order accurate finite-difference derivatives based on the cell-centered properties. The time-step determination is based on the well-known Courant-Friedrich-Levy (CFL) condition which is also adjusted to take into account the local restrictions imposed by the diffusive time scales [5]. These tools are considered well-established and therefore the reader is referred to the cited literature. More emphasis is given here regarding the spatial integration. This, although it is known too, it is considered preparatory to the discussion of the quasi-conservative (QC) treatment, as well as their extension to VLE thermodynamics which is another contribution of this work.

3.2 Spatial integration

3.2.1 Upwind flux-difference splitting scheme

The baseline spatial integration scheme is based on a flux-difference splitting (FDS) scheme, which was already applied to trans-critical flows [116, 114] and validated against more canonical conditions [55]. The interface states are reconstructed using the Monotone Upstream Centered Scheme for Conservation Laws (MUSCL) technique, which deals with the inviscid part of the fluxes. This technique evaluates the left and right states at each cell interface, setting up the resolution of a Riemann problem. For this study, an approximate Riemann solver of type HLLC is chosen [220] as exact Riemann solvers are too expensive, even for a TPG EoS. With reference to Fig. 17 and the nomenclature introduced in Sec. 3.1, following the MUSCL approach from van Leer [232], the left and right states at a cell interface in direction i can be expressed in the most general way as:

$$\overline{U}^L_{i+\frac{1}{2}} = \overline{U}_i + \frac{(1-\xi_i)}{4}\left[(1-\kappa)\,\phi\left(r^+_{i-\frac{1}{2}}\right) + (1+\kappa)\,\phi\left(\frac{1}{r^+_{i-\frac{1}{2}}}\right)\phi\left(r^+_{i-\frac{1}{2}}\right)\right]\left(\overline{U}_i - \overline{U}_{i-1}\right) \tag{3.2.1}$$

$$\overline{U}^R_{i+\frac{1}{2}} = \overline{U}_{i+1} - \frac{(1-\xi_{i+1})}{4}\left[(1-\kappa)\,\phi\left(r^-_{i+\frac{3}{2}}\right) + (1+\kappa)\,\phi\left(\frac{1}{r^-_{i+\frac{3}{2}}}\right)\phi\left(r^-_{i+\frac{3}{2}}\right)\right]\left(\overline{U}_{i+2} - \overline{U}_{i+1}\right), \tag{3.2.2}$$

where $\overline{U}_i$ is the volume-averaged vector of primitive variables stored at the cell center i, whereas Eq. (3.2.1) and Eq. (3.2.2) define the left and right interface state (in the form of a vector of primitive variables), respectively. Here, the function ϕ represents the Total Variation Diminishing (TVD) limiter. The TVD condition states that the total variation $\sum_i |U_{i+1} - U_i|$ decreases for each iteration [65] and ensures the monotonicity of the reconstructed state at the interface as extrapolated stated should not create local maxima in the primitive variables with respect to the adjacent cell-centers. The variable r is defined as:

$$r^+_{i+\frac{1}{2}} = \frac{\overline{U}_{i+2} - \overline{U}_{i+1}}{\overline{U}_{i+1} - \overline{U}_i} \tag{3.2.3}$$

$$r^-_{i+\frac{1}{2}} = \frac{\overline{U}_i - \overline{U}_{i-1}}{\overline{U}_{i+1} - \overline{U}_i} = \frac{1}{r^+_{i-\frac{1}{2}}} \tag{3.2.4}$$

Equations (3.2.1) and (3.2.2) may be modified depending on the local flow conditions. In particular, by modifying the *flow-limiters* ξ_i, one can turn on and off the higher order extrapolation. If all the ξ_i are set to one, the first order extrapolation is achieved, otherwise if they are set to zero, higher order extrapolation can be achieved depending on the coefficient κ with possible values of -1 (second-order upwind), 1 (second-order central) and $\frac{1}{3}$ (third-order upwind biased). However, depending on the limiter ϕ that is used, this dependency on κ can disappear. The flow limiter ξ_i can be a function of space (that is why the dependency on i and $i+1$), making it useful if particular flow sensors are needed, such as in the vicinity of shocks or large discontinuities. In this work, it is set to zero since large gradient regions (particular density jumps) are treated with the Double-Flux (DF) model. In this way, third order extrapolation is achieved away from zones that require this special treatment.

For this work, the TVD limiter is chosen to be the minmod (MM) among others [220, 111, 5] because it was found to be the most stable one:

$$\phi_{mm}(r) = \max[0; \min(r; 1)]\,. \tag{3.2.5}$$

Also, for the present work, the reconstruction technique is applied to the set of primitive variables (ρ, u_i, p, Y_k). While the reconstruction technique described above ensures the monotonicity property for each of these primitive variables alone, attention must be given to ensure the TVD property over all variables and especially that the gradient does not change sign at the interface. The latter is enforced by checking the sign of $(\overline{U}_{i+1} - \overline{U}_i)(\overline{U}^R_{i+\frac{1}{2}} - \overline{U}^L_{i+\frac{1}{2}})$. If it becomes negative, the MUSCL reconstruction is over-written by the following

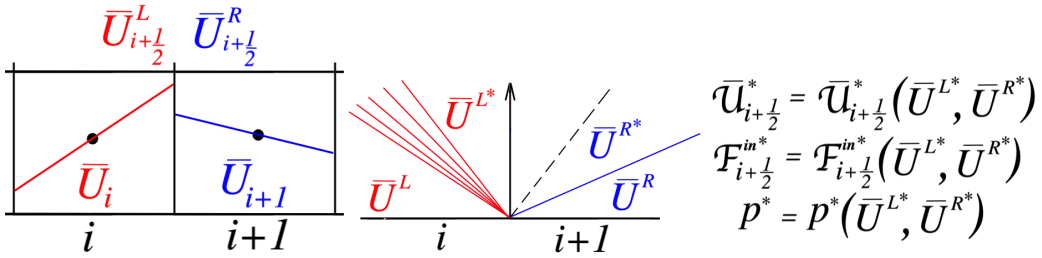

(a) (b)

Figure 17: Schematic representation of a) generic extrapolation of (volume-averaged) primitive variables at cell interface $i + 1/2$ and b) generic sketch of the associated Riemann problem solution.

expressions [54]:

$$\overline{U}_{i+\frac{1}{2}}^{L,\text{new}} = \frac{1}{2}\left(\overline{U}_{i+\frac{1}{2}}^{L,\text{old}} + \overline{U}_{i+\frac{1}{2}}^{R,\text{old}}\right) = \overline{U}_{i+\frac{1}{2}}^{R,\text{new}} \tag{3.2.6}$$

Similarly, the monotonicity of temperature, which is used in the Riemann solver described next, the following kind of relationship needs to be verified:

$$\max(T_i, T_{i+1}) \geq T_{i+\frac{1}{2}}^{L} \geq \min(T_i, T_{i+1}) \tag{3.2.7}$$

If it is not the case, one of density or pressure interpolated values needs to be recomputed accordingly. Following the work of Masquelet [114] density is recomputed out of new temperature $T_{i+\frac{1}{2}}^{L}$.

Since pressure, density and species are the extrapolated primitive quantities at the interface, temperature needs to be computed accordingly. This step involves the solution of the PRHO problem which, depending on whether the VLE model is included or not, it can have two different ways to be solved as it will be discussed in Sec. 3.4.2. Once the extrapolated primitive vectors are known at left and right interface, the Riemann problem can be solved. Essentially the Riemann problem solves for the evolution of the initial state discontinuity (provided by $\overline{U}^{L}$ and $\overline{U}^{L}$) and detects what is the interface state with respect to the waves that form as schematically illustrated in Fig. 17(b). In other words, the unknowns states $\overline{U}^{L,*}$ and $\overline{U}^{R,*}$ are found and depending on the wave speeds it is determined whether the interface pertains to the $\overline{U}^{L}$, $\overline{U}^{L,*}$, $\overline{U}^{R}$ or $\overline{U}^{R,*}$ condition (in the sketch of Fig. 17(b), the interface pertains to $\overline{U}^{L,*}$). Next, using the interface state, the vector of the conservatives $\overline{\mathcal{U}^{*}}$ is updated, which is used to compute the inviscid flux $\mathcal{F}^{in,*}$.

3.2.1.1 Approximate Riemann solver

The Riemann problem represents the solution of a conservation equation that has a discontinuity as initial condition. With reference to the earlier terminology this can be summarized as:

$$\overline{U}(x, t=0) = \begin{cases} \overline{U}^{L} & \text{for } x < 0 \\ \overline{U}^{R} & \text{for } x >= 0 \end{cases} \tag{3.2.8}$$

Physically, this can be imagined as the evolution of the wave system that results from the interaction of two gases, initially separated by a seal, at different states (which can be

translated into different values of the conservative vector $\overline{\mathcal{U}}$). As the seal is removed, a system of waves establishes to satisfy the limiting initial states forming an intermediate two states separated by a contact discontinuity. Determination of the fluid properties in these intermediate states represents the actual solution of the problem. For simple gases, this solution can be carried out in an exact fashion by employing an iterative process, however this is usually too expensive and in practice never used in CFD problems. For this reason, approximate solvers are available which compute the intermediate states in an approximate manner, however using explicit formulas and thus avoiding expensive iterations. For this study, the HLLC modification by Toro [220] of the original HLL approximate solver by Harten et al. [65] is selected. One important feature of this model is that the pressure and the velocity of the intermediate states (indicated with the $(*)$ superscript in Fig. 17(b)) are readily available [220]. For this reason, the interface temperature is again found by solving for another PRHO problem (again this may or may not involve VLE). If one does not have pressure available directly from the approximate Riemann solver, then internal energy and density are available, meaning that an ERHO problem needs to be solved instead. The approximation of the method comes into the estimation of the wave speeds that forms from the initial discontinuity. For these, additional sub-models can be used. For this study, the approach of Davis [40] is used for its simplicity and robustness already used in other relevant studies [114]. It should be underlined that the generic formulation of the HLLC Riemann solver is EoS independent [220] and thus it does not get modified in the presence of VLE as well. The inclusion of the VLE effects come in the determination of the wave speed approximation that requires the speed of sound. As a result, the mixture speed of sound can be computed by taking into account VLE or not by following the procedure discussed in Sec. 2.2.2. For additional details regarding the HLLC Riemann solver, the reader is referred to [220].

3.2.2 The problem of pressure oscillations in conservative schemes

The MUSCL scheme discussed in Sec. 3.2.1, like any other scheme that integrates the governing equations in their conservative form presents an issue related to the calculation

of the fluid thermodynamic properties from the conservative variables. In general, the combination of the MUSCL scheme with the MacCormack time integration was sufficient to obtain satisfactory results in the RG regime similarly to what done in past as well [114], however this does not seem to be always the case since different RG conditions, along with different grid resolutions can present the problem mentioned above. So what is the relationship between the scheme, the RG condition and the grid resolution? To illustrate this point, there is no need to investigate on a complex case, rather a simple case is good enough. This is the purpose of this section.

When the governing equations are solved in a conservative form, at the end of each sub-time step all the conservative quantities are known through the vector $\overline{\mathcal{U}}$. As a result, temperature and pressure are computed using the information of density, internal energy (obtained from total energy minus the kinetic energy) and species mass fractions. In other words, an ERHO problem needs to be solved. When the pressure is computed, nonphysical states can be obtained in terms of large amplitude fluctuations that can even reach negative values within a single temporal integration step. This issue is not related to the lack of convergence of the ERHO problem algorithm as instead can happen when VLE is used (discussed in Sec. 3.5.3). The thermodynamic problem is most likely showing perfect convergence from a mathematical point of view, however it results to converge to an impossible state. Before going to the explanation of the problem and the root cause of it, the steps required are summarized in the following bullets:

- density, ρ, internal energy E and species compositions $\mathbf{Y}$ (or $\mathbf{X}$) are known at the end of the time integration step;
- if internal energy is written as $E = E(\rho, T, \mathbf{X}) = E^{ig}(T, \mathbf{X}) + \Delta E(\rho.T, \mathbf{X})$, where ΔE is, for example given in Eq. (2.2.77), no matter the complexity, T can be found iteratively using any non-linear equation solution algorithm;
- once T is found, pressure p can be found using Eq. (2.2.67).

Note the above pseudo-algorithm does not involve VLE necessarily. In fact, for the present section it is assumed that one phase occurs at most at a given point with the ultimate goal

to highlight the fact that the pressure-oscillation problem does not depend on the use of VLE.

When Eq. (2.2.67) is applied, a corresponding state is found, therefore there is no convergence problem "as such" (of course the non-linear equation $E = E(\rho, T, \mathbf{Y})$ is assumed to have converged here, which it does). So if a corresponding erroneous value of pressure is found, why that happens? The only possible explanation is hidden in the error that is carried by the inputs of Eq. (2.2.67), that is, density, temperature, species and therefore internal energy and all the rest of the conservatives. For example the value of density ρ that is taken from the conservatives after the time integration, for instance, must be interpreted as $\rho = \rho^* + \rho^\epsilon$ where ρ^* is the (unknown) true value, whereas ρ^ϵ is its corresponding error associated to the spatial and temporal discretization accuracy that comes from the numerical scheme. Same holds for internal energy and species. When these values are introduced into the thermodynamic state relations, both the true value and the error are given as inputs. As a result, the output, say the temperature, is going to be affected by an error too: $T = T^* + T^\epsilon$ and similarly the pressure when the last step is performed.

The next question is: what is the relationship between the initial error that comes from the conservatives and the final error, say in the pressure value? The answer is again hidden in the EoS and specifically in the mutual derivatives of the state variables. To explain it simply, imagine to have an imaginary EoS where pressure is only a function of internal energy through a coefficient: $p = kE$ and assume for simplicity that $k = 1$. Then if an error of 1% on E that comes from the spatial and numerical integration is introduced, the same percentage of error will be propagated in p because $p = kE = k(E^* + E^\epsilon) = kE^* + kE^\epsilon = p^* + p^\epsilon$ due to the fact that the relationship is linear. However, if more in general, $k = \partial p/\partial E$ is not a constant, the relationship becomes non-linear. This means that if k is large enough (and this can happen for example near material jumps or discontinuities in general), a 1% error in E can be quickly amplified into a nonphysical value of p. This is what happens with super-critical flows with governing equations solved in their conservative form. The coupling between the spatial/numerical integration error and the EoS strong non-linearities

near density jumps causes a formidable combination that drives (even) the small error produced by the numerical integration to a non-physical state. The same issue happens with the TPG EoS, with the difference that TPG EoS is much less non-linear in the dependency of state variables, therefore it does not amplify the initial error, to the point that it seems that no error is created at all.

What is the source of the numerical/spatial integration error? For a given numerical scheme it comes from the grid resolution. As a result, the problem of non-physical pressure fluctuations is directly tied to the spatial and temporal resolution of the flow gradients. This concept is now going to be illustrated and proven from a more rigorous point of view, and examples will be also given for clarity.

Consider the dependency of the pressure and temperature from the conservative variables in the way listed above: $T = T(\rho, e, \mathbf{Y})$, $p = p(\rho, T, \mathbf{Y})$, where now $e = E/M$ is the internal energy per unit mass. The total differential of both the above quantities write as follows:

$$dT = \left(\frac{\partial T}{\partial \rho}\right)_{e,\mathbf{Y}} d\rho + \left(\frac{\partial T}{\partial e}\right)_{\rho,\mathbf{Y}} de + \sum_{i=1}^{N_s} \left(\frac{\partial T}{\partial Y_i}\right)_{e,\mathbf{Y}_i} dY_i \tag{3.2.9}$$

$$dp = \left(\frac{\partial p}{\partial \rho}\right)_{T,\mathbf{Y}} d\rho + \left(\frac{\partial p}{\partial T}\right)_{\rho,\mathbf{Y}} de + \sum_{i=1}^{N_s} \left(\frac{\partial p}{\partial Y_i}\right)_{\rho,\mathbf{Y}_i} dY_i \,. \tag{3.2.10}$$

In the above, all the notation is consistent with that introduced in Sec. 2.2.2. Substitution of Eq. (3.2.9) into Eq. (3.2.10) and rearranging provides an immediate dependency of the change in pressure as density, internal energy and individual species mass fractions are changed:

$$\begin{aligned} dp = &\left[\left(\frac{\partial p}{\partial \rho}\right)_{T,\mathbf{Y}} + \left(\frac{\partial p}{\partial T}\right)_{\rho,\mathbf{Y}} \left(\frac{\partial T}{\partial \rho}\right)_{e,\mathbf{Y}}\right] d\rho + \left[\left(\frac{\partial p}{\partial T}\right)_{\rho,\mathbf{Y}} \left(\frac{\partial T}{\partial e}\right)_{\rho,\mathbf{Y}}\right] de + \\ &+ \sum_{i=1}^{N_s} \left[\left(\frac{\partial p}{\partial Y_i}\right)_{\rho,T,\mathbf{Y}_i} + \left(\frac{\partial p}{\partial T}\right)_{\rho,\mathbf{Y}} \left(\frac{\partial T}{\partial Y_i}\right)_{\rho,e,\mathbf{Y}_i}\right] dY_i \,. \end{aligned} \tag{3.2.11}$$

Using the Maxwell relations and the inverse property, one can write:

$$\left(\frac{\partial T}{\partial \rho}\right)_{e,\mathbf{Y}} = -\frac{1}{\left(\frac{\partial \rho}{\partial e}\right)_{T,\mathbf{Y}} \left(\frac{\partial e}{\partial T}\right)_{\rho,\mathbf{Y}}} = -\frac{\left(\frac{\partial e}{\partial \rho}\right)_{T,\mathbf{Y}}}{\left(\frac{\partial e}{\partial T}\right)_{\rho,\mathbf{Y}}} \,, \tag{3.2.12}$$

$$\left(\frac{\partial T}{\partial e}\right)_{\rho,\mathbf{Y}} = \frac{1}{\left(\frac{\partial e}{\partial T}\right)_{\rho,\mathbf{Y}}} \,. \tag{3.2.13}$$

Substituting Eq. (3.2.12) and Eq. (3.2.13) into Eq. (3.2.11) one gets the final form of the total variation of pressure with density, internal energy and species:

$$dp = \left[\left(\frac{\partial p}{\partial \rho}\right)_{T,\mathbf{Y}} - \frac{\left(\frac{\partial p}{\partial T}\right)_{\rho,\mathbf{Y}}\left(\frac{\partial e}{\partial \rho}\right)_{T,\mathbf{Y}}}{\left(\frac{\partial e}{\partial T}\right)_{\rho,\mathbf{Y}}}\right] d\rho + \left[\frac{\left(\frac{\partial p}{\partial T}\right)_{\rho,\mathbf{Y}}}{\left(\frac{\partial e}{\partial T}\right)_{\rho,\mathbf{Y}}}\right] de + \\ + \sum_{i=1}^{N_s}\left[\left(\frac{\partial p}{\partial Y_i}\right)_{\rho,T,\mathbf{Y}_i} + \left(\frac{\partial p}{\partial T}\right)_{\rho,\mathbf{Y}}\left(\frac{\partial T}{\partial Y_i}\right)_{\rho,e,\mathbf{Y}_i}\right] dY_i \,. \tag{3.2.14}$$

For the purpose of demonstration in this section, the simplification of single component is employed. This reduces Eq. (3.2.14) to the following form:

$$dp = \left[\left(\frac{\partial p}{\partial \rho}\right)_{T,\mathbf{Y}} - \frac{\left(\frac{\partial p}{\partial T}\right)_{\rho,\mathbf{Y}}\left(\frac{\partial e}{\partial \rho}\right)_{T,\mathbf{Y}}}{\left(\frac{\partial e}{\partial T}\right)_{\rho,\mathbf{Y}}}\right] d\rho + \left[\frac{\left(\frac{\partial p}{\partial T}\right)_{\rho,\mathbf{Y}}}{\left(\frac{\partial e}{\partial T}\right)_{\rho,\mathbf{Y}}}\right] de \,. \tag{3.2.15}$$

Note that this assumption does not alter the conclusions, instead the dependency on multi-component derivatives can be an additional augmenting factor for the error which can be included in future studies as a further refinement of the present description.

Next, the total differential of the internal energy de of Eq. (3.2.15) needs to be related to the differential of the total energy, which is the quantity that is integrated directly in conservative schemes. The starting point is the one-dimensional Euler equations written in conservative form:

$$\frac{\partial \rho}{\partial t} + \frac{\partial \rho u}{\partial x} = 0 \,, \tag{3.2.16}$$

$$\frac{\partial \rho u_i}{\partial t} + \frac{\partial}{\partial x}\left[\rho u^2 + p\right] = 0 \,, \tag{3.2.17}$$

$$\frac{\partial \rho e_T}{\partial t} + \frac{\partial}{\partial x}\left[\left(\rho e_T + p\right) u\right] = 0 \,. \tag{3.2.18}$$

Since $e_T = e + 1/2u^2 = e + k$ (sum of internal and kinetic energy), the differential of e is: $de = de_T - dk$. Using the following steps:

$$\begin{aligned}
de_T =& d\left(\frac{\rho e_T}{\rho}\right) = \frac{1}{\rho}\left[d(\rho e_T) - e_T d\rho\right] ,\\
du =& d\left(\frac{\rho u}{\rho}\right) = \frac{1}{\rho}\left[d(\rho u) - \rho u d\rho\right] ,\\
dk =& d\left(\frac{u^2}{2}\right) = udu = \frac{u}{\rho} ,\\
de =& de_T - dk = \frac{1}{\rho}\left[d(\rho e_T) - e_T d\rho\right] - \frac{u}{\rho}\left[d(\rho u) - ud\rho\right] = \frac{1}{\rho}\left[d(\rho e_T) + (u^2 - e_T)d\rho - ud(\rho u)\right] ,
\end{aligned} \tag{3.2.19}$$

it is easy to recover the following form of Eq. (3.2.15):

$$\begin{aligned}
dp =& \left[d_1 - \frac{d_2 c_1}{c_2} + \frac{d_2}{c_2\rho}\left(u^2 - e_T\right)\right] d\rho - \frac{d_2 u}{\rho c_2} d(\rho u) + \frac{d_2}{\rho c_2} d(\rho e_T) =\\
=& \Gamma_1 d\rho + \Gamma_2 d(\rho u) + \Gamma_3 d(\rho e_T) .
\end{aligned} \tag{3.2.20}$$

Where:

$$\begin{aligned}
&\left(\frac{\partial p}{\partial \rho}\right)_{T,\mathbf{Y}} = d_1 , \qquad \left(\frac{\partial p}{\partial T}\right)_{\rho,\mathbf{Y}} = d_2\\
&\left(\frac{\partial e}{\partial \rho}\right)_{T,\mathbf{Y}} = c_1 , \qquad \left(\frac{\partial e}{\partial T}\right)_{\rho,\mathbf{Y}} = c_2\\
&\Gamma_1 = d_1 - \frac{d_2 c_1}{c_2} + \frac{d_2}{c_2\rho}\left(u^2 - e_T\right) ,\\
&\Gamma_2 = -\frac{d_2 u}{\rho c_2} ,\\
&\Gamma_3 = \frac{d_2}{\rho c_2} ,
\end{aligned} \tag{3.2.21}$$

have been defined. Next, the total differentials of the conservative variables need to be tied to the spatial and temporal integration. Since in general $\rho = \rho(x,t)$, $\rho u = \rho u(x,t)$ and $\rho e_T = \rho e_T(x,t)$, the total differentials can be easily written with respect to the axial abscissa x and time t:

$$\begin{aligned}
d\rho &= \frac{\partial \rho}{\partial t} dt + \frac{\partial \rho}{\partial x} dx ,\\
d\rho u &= \frac{\partial (\rho u)}{\partial t} dt + \frac{\partial (\rho u)}{\partial x} dx ,\\
d\rho e_T &= \frac{\partial (\rho e_T)}{\partial t} dt + \frac{\partial (\rho e_T)}{\partial x} dx ,
\end{aligned} \tag{3.2.22}$$

which obviously enforce the first principles just like Eq. (3.2.18). In fact, by substituting the time derivatives of Eq. (3.2.18) into Eq. (3.2.22), it is easy to prove that:

$$\begin{aligned} d\rho &= -\rho\frac{\partial u}{\partial x}dt\,, \\ d(\rho u) &= -dt\left[\rho u\frac{\partial u}{\partial x}+\frac{\partial p}{\partial x}\right], \\ d(\rho e_T) &= -dt\left[\rho e_T\frac{\partial u}{\partial x}+\frac{\partial pu}{\partial x}\right]. \end{aligned} \tag{3.2.23}$$

Equation 3.2.23 states that if one addresses the problem of a contact discontinuity where a material jump (density, temperature, energy) exists, however pressure and velocity are maintained the same across the interface, the right-end side is zero identically in time, and $dp = 0$ is recovered identically from Eq. (3.2.20) for any time. However, Eq. (3.2.22) is effectively solved numerically through the solution of Eq. (3.2.18). This means that for the same example of a contact discontinuity traveling at a given velocity and at a given pressure, the right-hand side of Eq. (3.2.23) does not match zero identically because the gradients of u and p are not solved directly but indirectly by integrating the conservative variables. As a result, non zero values of $d(\rho)$, $d(\rho u)$ and $d(\rho e_T)$ are given as inputs to Eq. (3.2.20), which in turn provides a non-zero value of dp, hence a spurious pressure oscillation at a given point and at a given time. The error for the conservative differentials is amplified by the Γ_1, Γ_2 and Γ_3 factors, which are EoS dependent and assume very large (physical) values near contact discontinuities. For this reason, contact discontinuities are the most difficult flow features to capture under strong RG situations without generating pressure oscillations. In fact, as discontinuities, a) they present inherent important numerical challenges because spatial integration in general suffers near discontinuities and b) they provide the most non-linear behavior of the RG EoS. Note that since the problem comes from the spatial integration, one may be tempted to solve the problem by merely switch to a first-order integration scheme, such as the MUSCL scheme discussed in Sec. 3.2.1 where all ξ_i are set to one. This will not help the solution of the problem because with a lower order spatial integration, the spatial derivatives of Eq. (3.2.18) will be represented in an even worse manner, thus making the error larger and not smaller. The solution with the present numerical framework is in fact to increase the grid resolution which is in fact a corresponding alternative to the

increase of the numerical scheme order and not decrease it. On the other hand, higher order derivatives may still suffer near discontinuities so an error will still be produced. As a result, with the present numerical framework is seems that the only way to solve the problem is to increase the grid resolution and maintain the order of the spatial discretization low near contact discontinuities, however the resolution requirements may vary from case to case for the same reasons discussed above.

To illustrate all these concepts, consider the case of a "simple" one-dimensional nitrogen contact discontinuity convection. The contact is generated in a "smoothed top-hat" profile that moves from left to right at constant speed and pressure. A sketch of the setup is given in Fig. 18. The profile extends onto a one-dimensional domain of $L = 0.1$ m. At locations

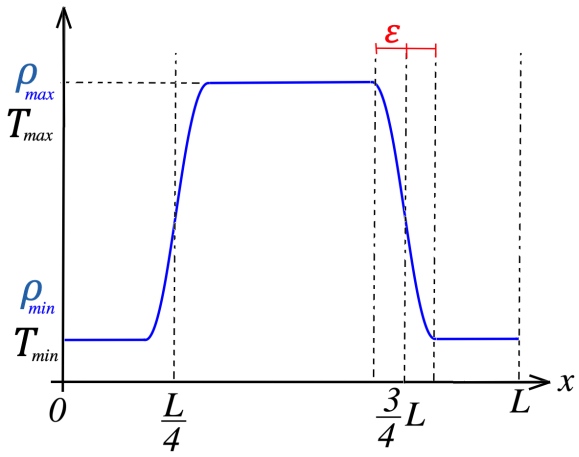

Figure 18: Schematic representation of the one-dimensional N_2 contact discontinuity with a smoothed top-hat profile.

Table 13: Conditions at which the 1D N_2 contact discontinuity is studied.

	$T_{\max}$ (K)	$\rho_{\max}$ (kg/m^3)	$T_{\min}$ (K)	$\rho_{\min}$ (kg/m^3)	p (MPa)	u (m/s)
Case 1	300.0	793.1	100.0	56.9	5.0	100.0
Case 2	298.0	436.6	126.9	45.45	3.97	4.9

$x = L/4$ and $x = 3L/4$, the center of an hyperbolic tangent profile is imposed such that the smoothed profile is achieved. The generic hyperbolic profile for the property Φ is specified as $\Phi(x) = 0.5[(\Phi_{\min} + \Phi_{\max}) + (\Phi_{\max} - \Phi_{\min})\tanh((x - x_0)/\epsilon)]$, where the min/max values

represent the limit conditions at the top-hat extremes given in Tab. 13, depending on the variable that is set. In the formula, x_0 is the center of the hyperbolic profile, whereas $\epsilon = L/50$ is the reference half-width of the profile. In all cases, the left and right boundary conditions are specified as periodic.

The simulation is run for one time step only, using first order time and spatial integration. The first order time integration is achieved by performing only the predictor step of the MacCormack method [111, 5]. Once the integration is complete, all the fields at the time step zero (initial condition) and time step one are used to reconstruct the total pressure variation of Eq. (3.2.20) and compare against the pressure that is obtained after the actual numerical integration. Few important notes are worth:

- the total differentials of the conservative variables of Eq. (3.2.20) are reconstructed using their definition of Eq. (3.2.22), where the derivatives are computed using finite differences. Moreover, the spatial derivative is taken as the minimum of the respective upwinded values. Although minor differences were observed if different spatial gradients reconstruction was performed, the overall conclusion did not change. For example: $(\partial\rho/\partial t)dt \sim \rho_j^{n+1} - \rho_j^n$ and $(\partial\rho/\partial x)dx \sim min[\rho_{j+1}^n - \rho_j^n, \rho_j^n - \rho_{j-1}^n]$ where $j = 1, \cdots, N-1$ is the local cell-center value and N the respective total number of equally-spaced points in the domain;

- the Γ_1, Γ_2 and Γ_3 coefficients of Eq. (3.2.20) are function of time, therefore an averaged value of the quantities involved between the zeroth and the first time step is used to reconstruct those.

Several numerical experiments are carried out by varying the number of (equally-spaced) points in the domain. Specifically $N = [151, 5001, 15001]$ is used, corresponding to an approximate number of points within each smoothed hyperbolic tangent of $N_h = [6, 200, 600]$ points, respectively. Figure 19 shows the Γ coefficients of Eq. (3.2.20) for case 1 as the

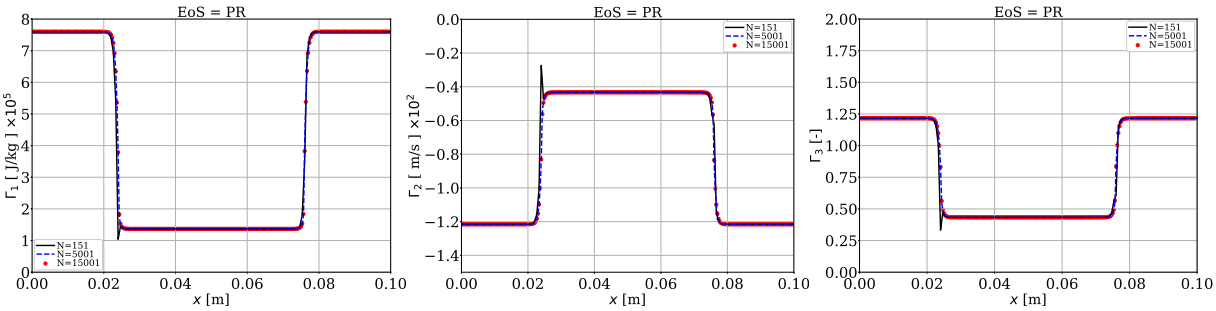

(a) Γ_1 (b) Γ_2 (c) Γ_3

Figure 19: Coefficients of Eq. (3.2.20) for Case 1 using the PR EoS.

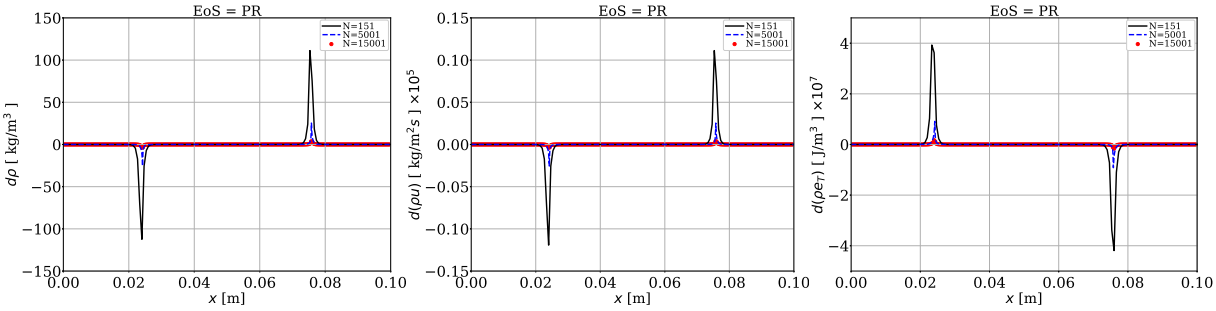

(a) $d\rho$ (b) $d(\rho u)$ (c) $d(\rho e_T)$

Figure 20: Total variation of the conservative variables according to Eq. (3.2.20) for Case 1 using the PR EoS.

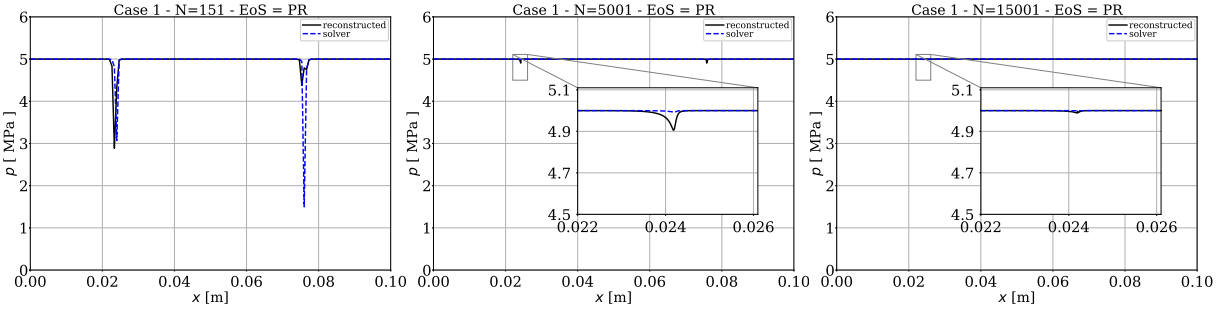

(a) $N = 151$ (b) $N = 5001$ (c) $N = 15001$

Figure 21: Pressure variation after one time step for Case 1 using the PR EoS. The reconstructed method refers to $p_i^{n+1} = p_i^n + dp$ where dp is computed using Eq. (3.2.20), whereas the solver method refers to a pure integration using the first order MacCormack time integration (predictor step only) and the first order MUSCL spatial integration discussed in Sec. 3.2.1.

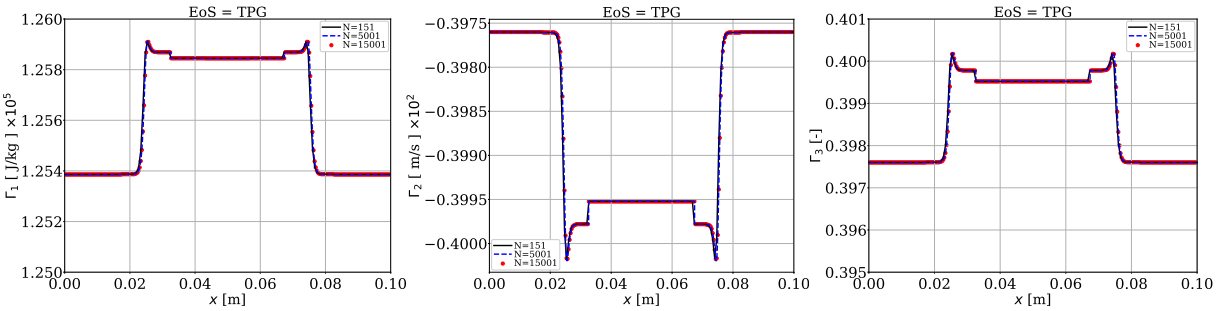

(a) Γ_1 (b) Γ_2 (c) Γ_3

Figure 22: Coefficients of Eq. (3.2.20) for Case 1 using the TPG EoS.

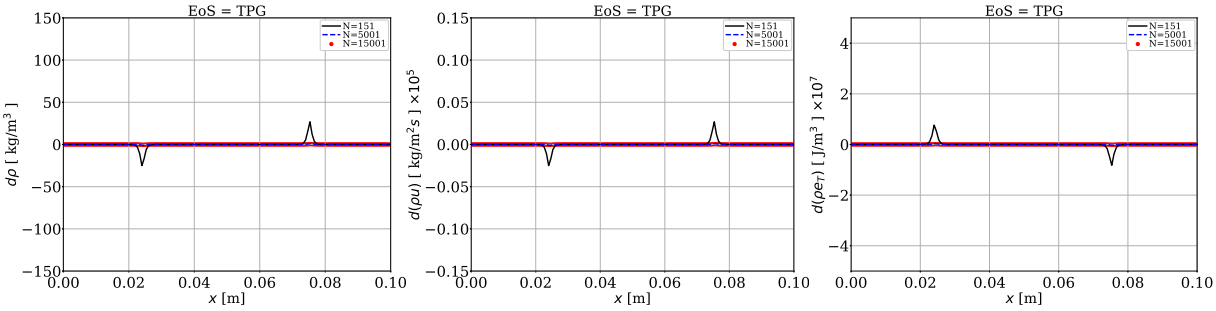

(a) $d\rho$ (b) $d(\rho u)$ (c) $d(\rho e_T)$

Figure 23: Total variation of the conservative variables according to Eq. (3.2.20) for Case 1 using the TPG EoS.

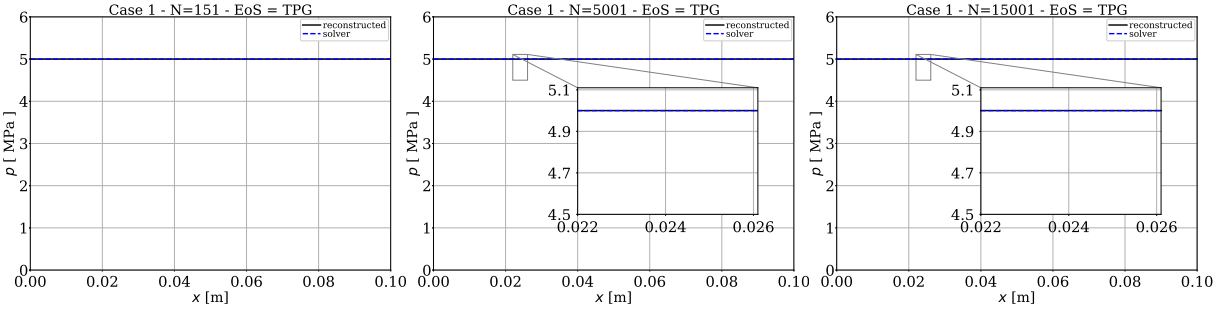

(a) $N = 151$ (b) $N = 5001$ (c) $N = 15001$

Figure 24: Pressure variation after one time step for Case 1 using the TPG EoS. The reconstructed method refers to $p_i^{n+1} = p_i^n + dp$ where dp is computed using Eq. (3.2.20), whereas the solver method refers to a pure integration using the first order MacCormack time integration (predictor step only) and the first order MUSCL spatial integration discussed in Sec. 3.2.1.

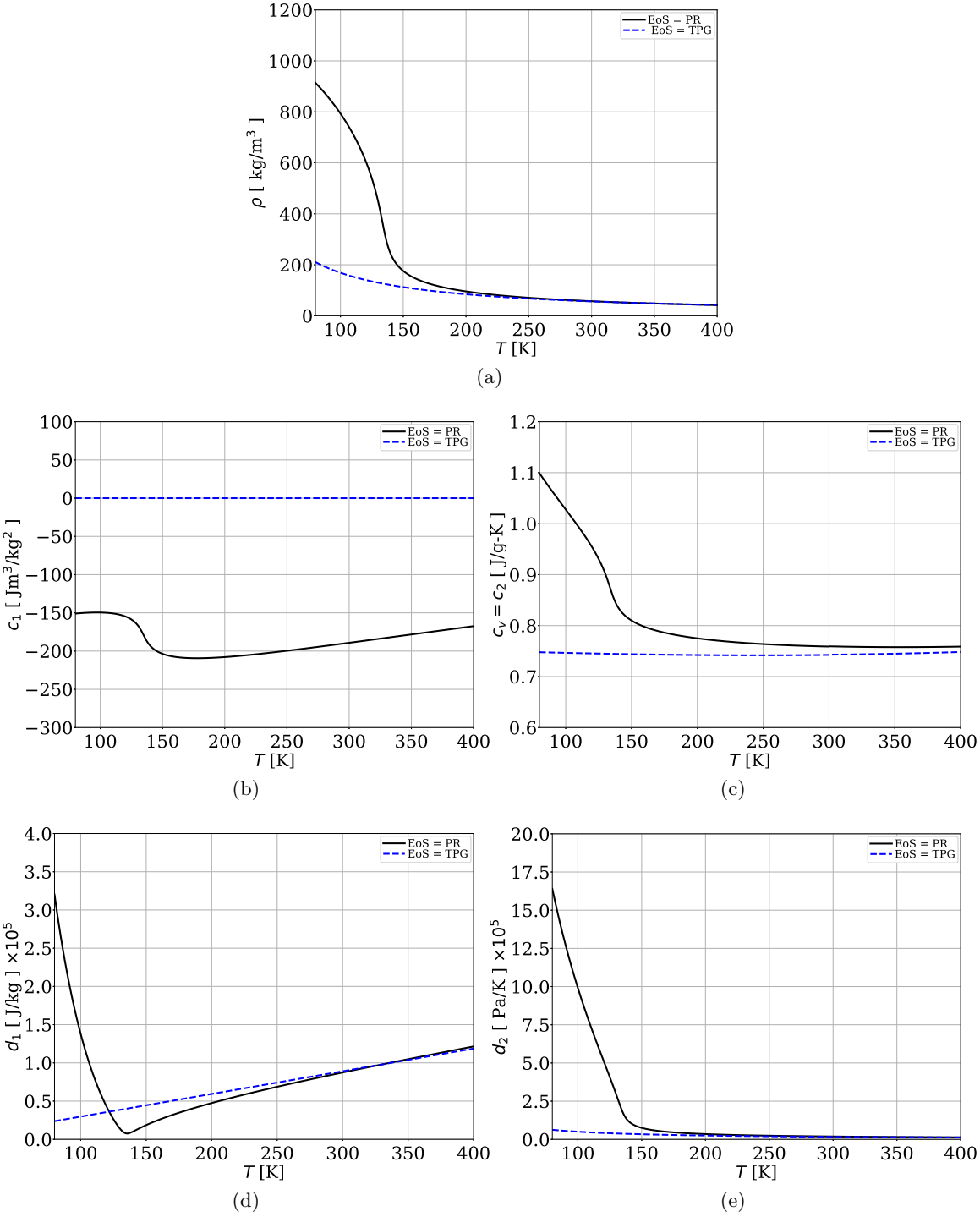

Figure 25: Comparison of a) density, b) c_1, c) c_2, d) d_1 and e) d_2 variables defined in Eq. (3.2.21) that form the Γ coefficients in Eq. (3.2.20) using the PR EoS and TPG EoS for Case 1.

resolution is varied. The PR EoS is used here first. The important thing to highlight here is the fact that the values of the coefficients do not depend on the resolution, as expected, because they are mostly defined by thermodynamic derivatives. However, since some fluid variables appear, such as u, ρ and e_T, spikes are observed for the lowest resolution due to the time-average operation performed which already takes into account the error in these variables produced by the spatial and temporal integration (showed for example in the pressure next). This effect is also responsible for the relatively minor difference between the results directly computed with the numerical method and the results reconstructed with Eq. (3.2.20) which are showed next. Figure 20 shows the total differential of the conservative variables obtained for the three resolutions. It is apparent that the error is localized in correspondence of the neighborhood of the density jump and it decreases as resolution increases as discussed before. Next, the comparison of the actual pressure field obtained after the single iteration and the pressure reconstructed as $p_j^{n+1} = p_j^n + dp$ where dp is given by Eq. (3.2.20) is showed in Fig. 21. As one can easily observe, the pressure oscillations began right where the errors in the conservatives were observed earlier in Fig. 20 and in turn amplified by the Γ coefficients of Fig. 19. The oscillations almost agree identically, except on few points where differences are observed due to the different method used to get to the same result. It is important to understand that in this situation, even the truncation error matters and therefore whether a quantity is computed as x/y or $x * (1/y)$ can make a difference from a numerical point of view. As the resolution increases the error diminishes, as expected.

Next, the same numerical experiment is carried out for case 1, however the EoS is switched to the TPG. In this case, Eq. (3.2.20) still holds identically and the same procedure can be repeated to investigate the results. Figures 22–24 show the same quantities discussed earlier for the PR EoS. Starting from the end, one immediately recognizes the fact that no pressure oscillations are obtained in this case. Looking at Fig. 22 and Fig. 23, the following comments can be made:

- errors in the conservative variables are still obtained in this case, however they are at least one order of magnitude less than the corresponding RG case. The reason is

related to the different densities that for the same pressure and (top-hat) temperature profile are given by the different EoS as showed in Fig. 25a. Since the value of the density in the case of TPG is one order of magnitude smaller than the corresponding RG case, the numerical derivatives carry the same error order, therefore the total differentials provide a much lower error;

- The Γ coefficients reported in Fig. 22 have much less values than the corresponding RG values encountered earlier.

As a result, a smaller error in the conservatives is multiplied by a smaller amplification factor given by the Γ coefficients and as a consequence, an overall near-zero pressure fluctuation is obtained.

Why the Γ coefficients are smaller in the TPG case? Similarly to what discussed for the density in Fig. 25(a), Fig. 25(b)–25(e) provide the coefficients c_1, c_2, d_1 and d_2 defined in Eq. (3.2.21) which compose the Γ coefficients. As one can immediately notice, these coefficients are much different depending on the EoS, especially in the transition zone between the compressed liquid and the super-critical gas, which happens to be exactly the neighborhood of the hyperbolic tangent jump of the top-hat profile. The differences between these coefficients can be roughly estimated to be around one order of magnitude. In conclusion, both the total differentials of the conservative variables and the Γ coefficients show an order of magnitude difference depending on whether the RG EoS is used compared to the TPG EoS. When these two values are multiplied, a huge amplification factor is achieved in the case of the RG EoS, producing non-physical, unacceptable pressure oscillations. Essentially, the reduced error of the TPG EoS is the effect of the fact that the TPG EoS is incapable to correctly reproduce the properties in the compressed liquid regime, which therefore assume values that are much closer to the actual gaseous state, reducing the derivatives. Next, case 2 of Tab. 13 is explored using the same approach. Using the same arguments made before, one immediately recognizes that much smaller pressure oscillations are obtained in this case irrespective of the use of the PR EoS. The reason is related to both changes of

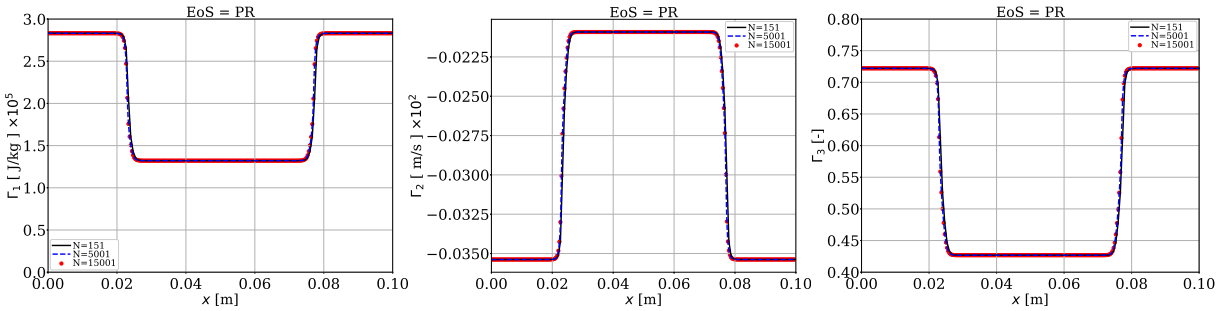

(a) Γ_1 (b) Γ_2 (c) Γ_3

Figure 26: Coefficients of Eq. (3.2.20) for Case 2 using the PR EoS.

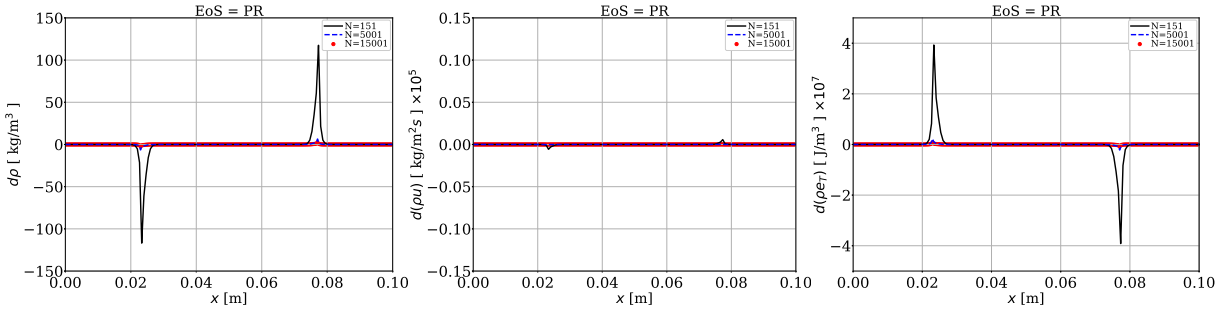

(a) $d\rho$ (b) $d(\rho u)$ (c) $d(\rho e_T)$

Figure 27: Total variation of the conservative variables according to Eq. (3.2.20) for Case 2 using the PR EoS.

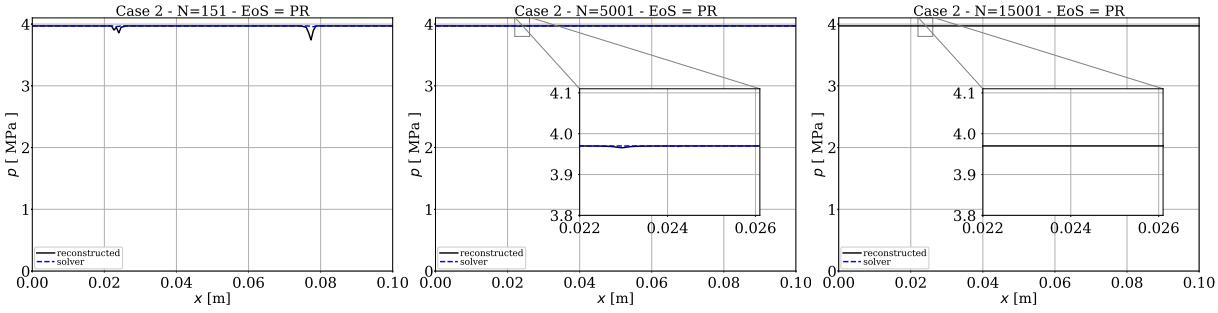

(a) $N = 151$ (b) $N = 5001$ (c) $N = 15001$

Figure 28: Pressure variation after one time step for Case 2 using the PR EoS. The reconstructed method refers to $p_i^{n+1} = p_i^n + dp$ where dp is computed using Eq. (3.2.20), whereas the solver method refers to a pure integration using the first order MacCormack time integration (predictor step only) and the first order MUSCL spatial integration discussed in Sec. 3.2.1.

the operating pressure and (more importantly), the temperature in the compressed liquid regime, that is increased by only 27 K, as well as to the reduction of the operating velocity. First, from Fig. 27 one observes that while the changes in $d\rho$ and $d(\rho e_T)$ are comparable to those obtained for case 1 in Fig. 20, the variation $d(\rho u)$ exhibits a much less value because of the near-zero operating condition which reduces the corresponding error in the spatial discretization. Similarly, the coefficients Γ in Fig. 26, show smaller values compared to the corresponding coefficients of case 1. The reason is because the chosen operating conditions modify the thermodynamic derivatives to a smaller value. This is showed in Fig. 29. Despite the pictures in Fig. 29 look very similar to those of Fig. 25 (the small variation is only achieved because of the change in pressure from 5 to 3.97 MPa), one should not get confused from the fact that now the operating point has changed. This means that the values of c_1–d_2 need to be taken at $T = 128.5$ K and no longer at $T = 100$ K. By doing so, the values of the Γ coefficients get reduced as demonstrated in Fig. 26 and an overall reduction in the pressure oscillation is obtained in the end.

From the analyses showed so far, it is apparent that the problem of pressure fluctuations appearing in the conservative schemes is essentially due to the strong non-linear behavior of the RG EoS. This effect is independent of the inclusion of VLE, which was in fact not considered here and it seems to disappear only when considerable amount of grid points are introduced to accurately represent the mean-flow gradients, depending on the operating condition chosen. For this reason, a different strategy is required to address this issue which has to be numerical in nature due to the cause of the problem. As a result, many approaches might be used in principle to fix the problem and this can be a future research topic by itself (see Tab. 1). For this work, the Double-Flux (DF) method is chosen because its simplicity and effectiveness already demonstrated [108]. The improvement to this method is going to be the inclusion of VLE, which is discussed in Sec. 3.2.3.

3.2.3 The Double-Flux method

Starting from the understanding of the problem of pressure oscillations built in Sec. 3.2.2, it is clear from Eq. (3.2.20) that the problem will never be solved unless:

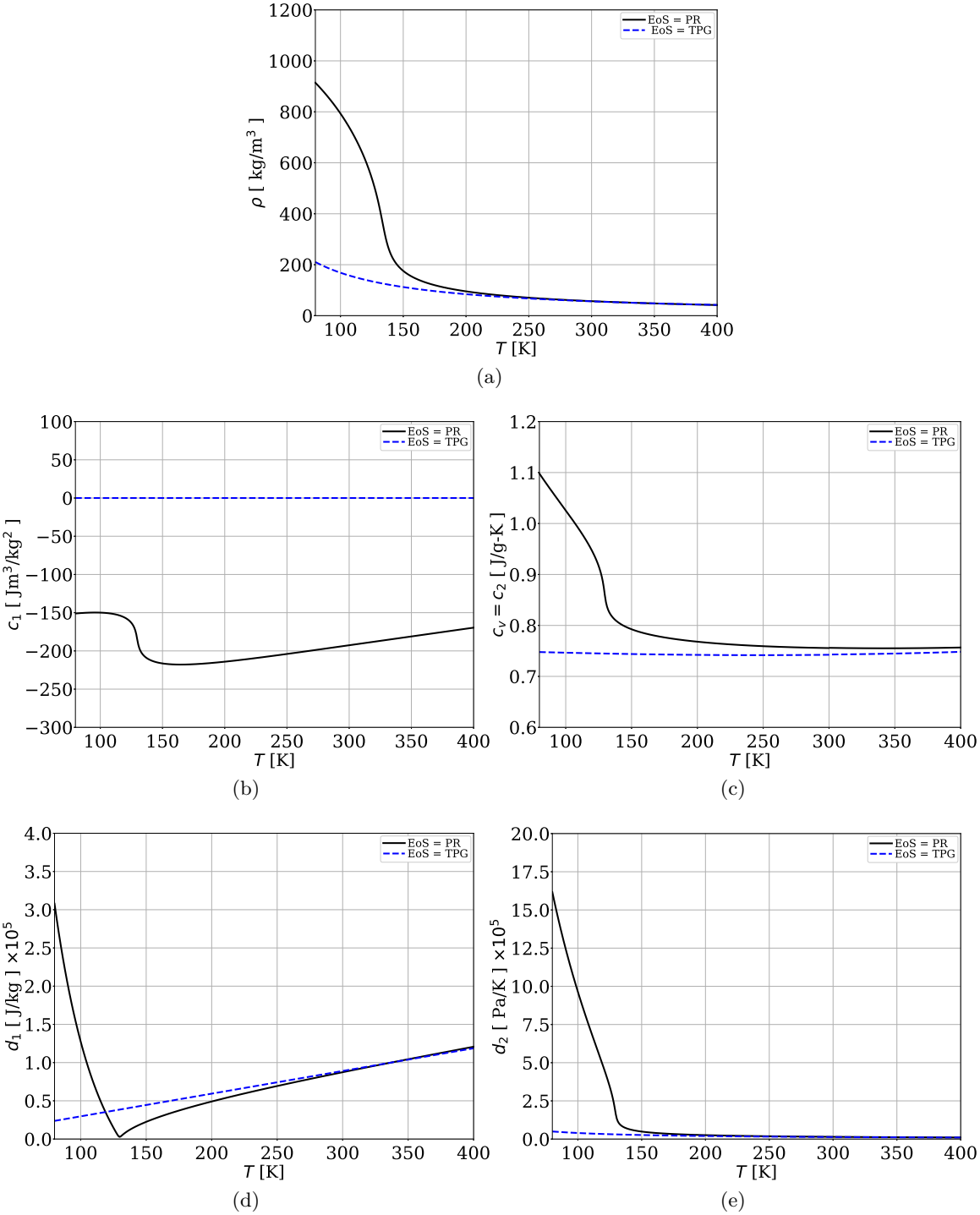

Figure 29: Comparison of a) density, b) c_1, c) c_2, d) d_1 and e) d_2 variables defined in Eq. (3.2.21) that form the Γ coefficients in Eq. (3.2.20) using the PR EoS and TPG EoS for Case 2.

- a very high number of points is used to resolve the discontinuity;
- a non-stiff EoS is chosen, such as the TPG or CPG EoS. This will eliminate the oscillations, but will introduce unacceptable non-physical values of the thermodynamic properties in the non-ideal regime;
- a different functional dependency between pressure, internal energy and density is chosen.

The third approach is the one selected to develop the Double-Flux (DF) model, initially developed by Abgrall and Karni [1] and Billet and Abgrall [15] and later applied by Ma *et al.* [108] for trans-critical flows. In this approach, the pressure dependency between pressure, density and internal energy is selected to be as follows:

$$e = \frac{p}{\rho(\gamma^* - 1)} + e^* \,, \tag{3.2.24}$$

where:

$$\gamma^* = \frac{\rho c^2}{p} \,. \tag{3.2.25}$$

Equation (3.2.24) is not an approximation in general. It can be in fact demonstrated that every functional dependency of $p = p(\rho, e, \mathbf{Y})$ can be reduced to Eq. (3.2.24) by arranging the definitions of γ^* and e^* [108]. For example in a CPG mixture, $e^* = 0$ and $\gamma^* = \gamma = \text{const}$, whereas more in general [108]:

$$\gamma^* = \gamma \left[1 + \frac{\rho}{Z} \left(\frac{\partial Z}{\partial \rho} \right)_{T,\mathbf{Y}} \right] , \tag{3.2.26}$$

where γ is the common specific heats ratio. For this reason, in general γ^* and e^* maintain the same non-linear dependencies on temperature, density and mixture composition. It can be shown [108] that the pressure equilibrium across a contact discontinuity depends on the error carried by both γ^* and e^* with the spatial and temporal integration:

$$p d\left(\frac{1}{\gamma^* - 1} \right) + \frac{1}{\gamma^* - 1} dp + \rho de^* = 0 \,. \tag{3.2.27}$$

As a result, if γ^* and e^* are maintained constant during the spatial and temporal integration, their variation is null and the pressure equilibrium can be recovered if it exists. In this

procedure, the mixture is essentially treated as a local CPG, where its properties are updated at every cell at the beginning of the time integration and maintained constant throughout the rest of the integration step. With this notion, the DF method introduces two fluxes at

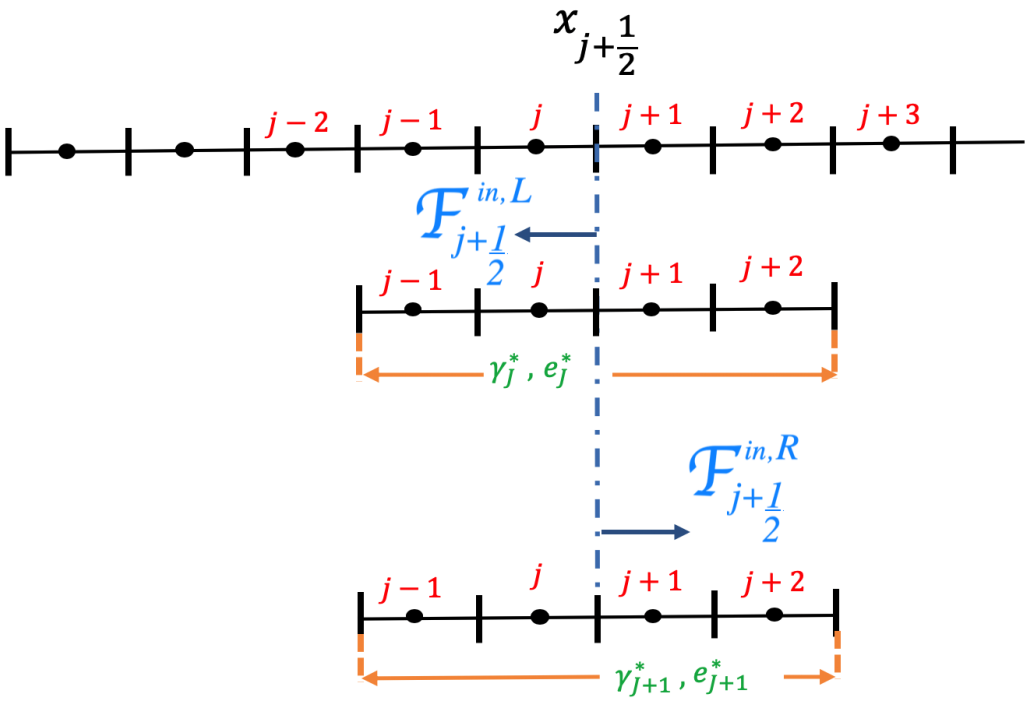

Figure 30: Schematic representation of the spatial integration carried out with the DF method (adapted from [108]).

each cell interface by using the contiguous values of γ^* and e^* between the cells that share the interface. The integration procedure is described as follows:

1. at the beginning of each time step, using the previous information of temperature, pressure, composition and all other thermodynamic properties (as for example internal energy and speed of sound) that have been computed, the values of γ^* is computed with Eq. (3.2.25) and the value of e^* is computed by inversion of Eq. (3.2.24). These are determined for each cell and stored in memory. These values do not change during the whole time step, meaning that if sub-time steps are performed, the same values are still used;

2. with reference to Fig. 30, two fluxes are computed at each cell interface. For the

resolution of the spatial integration, the MUSCL extrapolation described in Sec. 3.2.1 is still used to determine the quantities at the interface, however γ^* and e^* are not extrapolated and their first order extrapolation must be used;

3. with extrapolated density, composition and pressure, temperature is computed at the interface using the EoS;

4. for the solution of the Riemann problem, internal energy at the interface is calculated using Eq. (3.2.24). If the left flux (L) at cell j is being sought, the values of γ_j^* and e_j^* are used for both cells j and $j+1$ as sketched in Fig. 30. Note that the corresponding internal energies at the two sides of the interface computed with Eq. (3.2.24) will still differ because extrapolated densities and pressures will be different. Only the values of γ^* and e^* are copied;

5. interface states of densities, momentum and internal energies are sent to the Riemann solver and the same HLLC approximation can be used. The only difference is that, depending on the flux that is being sought, if the wave speed needs to be approximated, the speed of sound is computed by inversion of Eq. (3.2.25) and not by recomputing it using the extrapolated value of temperature;

6. similar procedure is performed for the right (R) flux;

7. update of the conservatives is performed in the form $\boldsymbol{\mathcal{F}}^{in,L}(j) - \boldsymbol{\mathcal{F}}^{in,R}(j-1)$;

8. after the time integration, density ρ, velocities and species are readily available directly from the vector $\overline{\boldsymbol{\mathcal{U}}}$ using the information of ρu, ρv, ρw and ρY_k;

9. pressure is computed by inversion of Eq. (3.2.24) where $e = (\rho e_T - \rho k)/\rho$ and $k = 0.5(u^2 + v^2 + w^2)$. In this procedure, γ^* and e^* are still maintained the same that were computed at the beginning of the time step;

10. temperature is obtained by solving a PRHO problem using the EoS: $T = T(\rho, p, \mathbf{Y})$;

11. all the thermodynamic and transport properties can be updated. For example internal energy and speed of sound: $e = e(\rho, T, \mathbf{Y})$, $c = c(\rho, T, \mathbf{Y})$;

12. total energy is updated as: $\mathrm{e}_T = e + k$;

13. if this is the end of the last sub-time step, γ^* and e^* are recomputed for each cell using Eq. (3.2.25) and the inversion of Eq. (3.2.24), respectively.

Figure 31 shows the pseudo codes for a sub-time integration step using a) the MUSCL scheme (*i.e.*a fully-conservative (FC) scheme) and b) the DF scheme (*i.e.*a quasi-conservative (QC) scheme). For clarity, at each stage the known quantities are indicated with the $\hat{(\cdot)}$ symbol and the thermodynamic problem to be solved is specified as well. As one can immediately notice, either the PRHO and/or the ERHO problem need to be solved multiple times within the integration stage, depending on the scheme. One intermediate step that is performed in common between the two schemes is the calculation of the cell interface temperature after the Riemann problem is solved. In fact, after the Riemann problem, all the conservatives and the pressure are known [220] and temperature needs to be computed. This temperature is typically used to compute the transport properties at that interface location. The reason is that viscous fluxes are computed using central derivatives, hence the information at the cell interfaces of transport properties is required (this step is lumped in Fig. 31 into the "Update conservatives" step in case a viscous solution is sought).
Next, one can notice that each thermodynamic problem is split in two possible parts, namely the VLE and the non-VLE part, depending on whether the VLE model is activated or not, respectively. This makes a substantial difference in the way the actual thermodynamic problem is solved, as well as the speed required for each single problem (and hence the whole simulation) to be executed. For example the PRHO problem can be solved in the form of $T = T(\hat{\rho}, \hat{p}, \hat{\mathbf{X}})$ for the non-VLE problem or in the form $\rho(T, \hat{p}, \hat{\mathbf{X}}, \beta) = \hat{\rho}$ for the VLE problem. In the first case, an explicit analytical solution may be available, depending on the EoS chosen, whereas in the second case, an iterative solution can be attempted only. In addition, the latter requires to solve a double nested loop where the innermost solves for the VLE problem of Eqs. (2.2.36)–(2.2.37) because β is involved and is unknown, whereas the outer loop tries to match Eq. (2.2.34) or Eq. (2.2.35), depending on whether a PRHO or an ERHO problem are being solved for. More details on this will be given in Sec. 3.4,

which will address the specific solution of each thermodynamic problem with and without VLE. The important thing at this stage is to recognize immediately the difference of the thermodynamic problem that needs to be solved with and without VLE, essentially due to the existence of β (*i.e.*multi-phase) and the different functional dependencies of E and ρ. Another important point to highlight is that the use of VLE now also affects the calculation of the γ^* and e^* properties for the DF method according to Eq. (3.2.24) and Eq. (3.2.25). The reason is that ρ as well as the speed of sound can include the functional dependency on β as discussed in Sec. 2.2.2. As a result, this upgrades the DF model to account for VLE thermodynamics, which is another contribution made in this work.

Finally, it is also important to point out the fact that other works [118, 245] have reported the use of VLE thermodynamics only at the conversion from conservatives to primitives, that is the MUSCL reconstruction (or the alternative spatial integration method) is always treated as if VLE is absent. This makes the spatial integration completely detached from the temporal integration from a thermodynamic point of view because there is an inconsistency between the state assumed for the spatial derivatives that compose the numerical fluxes and the corresponding primitives that result at a later stage after the time integration. As it will be demonstrated in Sec. 3.5.3 and Sec. 3.5.4, ignoring the presence of VLE in the regions where the thermodynamic state falls into the multi-phase regime can produce significant errors in the calculation of all the thermodynamic properties. For this reason, in this work the fully consistent thermodynamic route between the spatial and the temporal integration is chosen at the price to have a significant cost increase for each simulation for the reasons specified above. An alternative way to solve this problem, still maintaining thermodynamic consistency will be described in Sec. 3.3, which will constitute another contribution of this work from a modeling perspective.

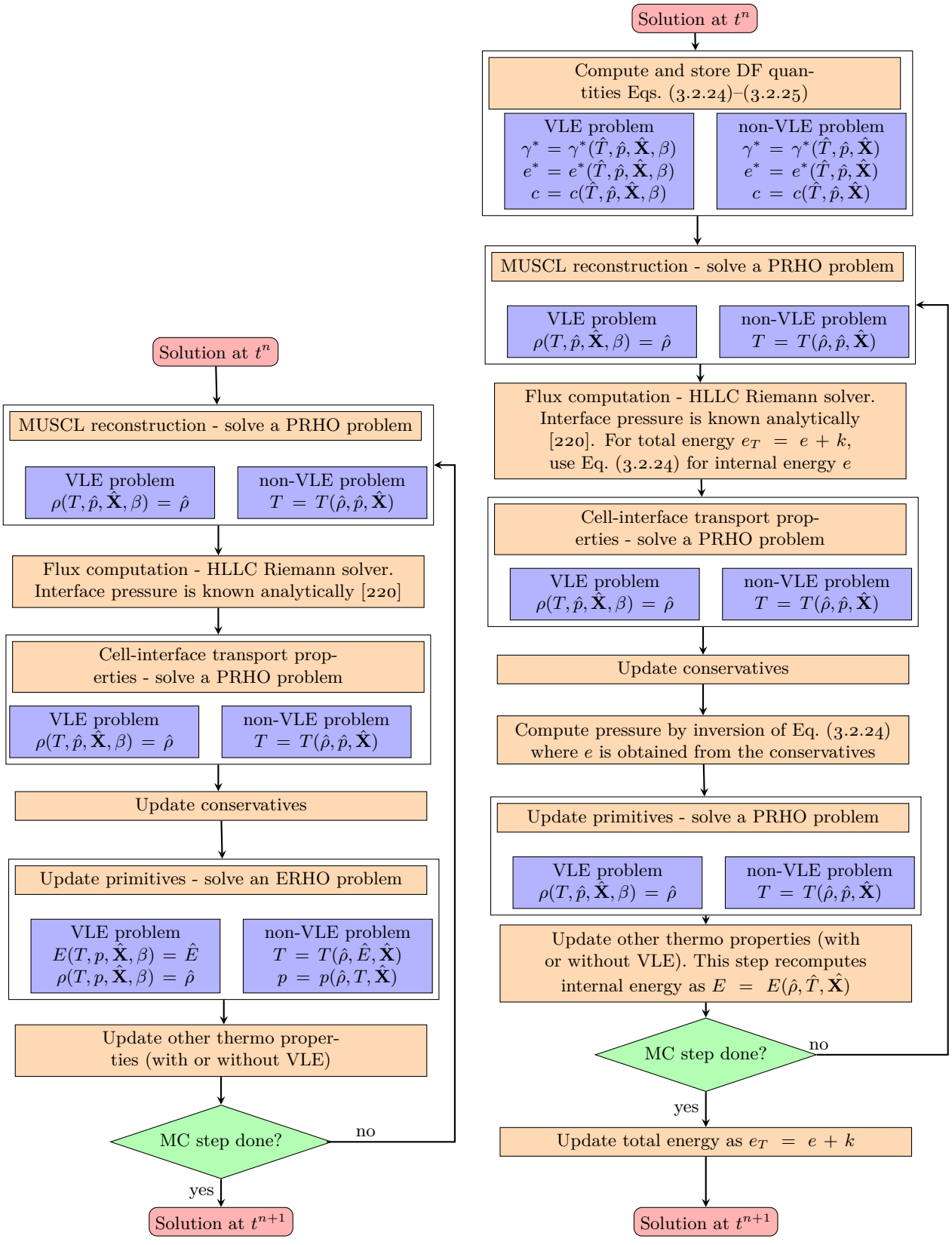

Figure 31: Summary of the time integration steps performed for the hybrid scheme. (a) FC scheme and (b) QC scheme. MC indicates the MacCormack integration step. (adapted from [108]). In this picture, the generic $\hat{(\cdot)}$ quantity indicates a known value, not to be confused with the HLLC interface states in Fig. 17. This helps to clarify in each stage what is given and what is the unknown.

The two schemes of Fig. 31 can be also implemented together to work at the same time within the same simulation. Since the DF method is not only expected to be a more dissipative scheme [108], but also due to the fact that it introduces the conservation error [108, 109], it is convenient to implement both schemes in a way that the DF method would be activated only in those zones that require it in order to avoid the problem of pressure oscillations as discussed in Sec. 3.2.2. Given that this issue occurs near the regions where high density gradients appear, the most intuitive choice to activate the FC or the QC scheme is obviously though a density gradient sensor in the form of $\xi = |\nabla\rho|/\rho$, which is similar to that used by [108]. If ξ is greater than a user-defined threshold, then the DF method is activated, otherwise the FC scheme is retained for the spatial integration. In order to investigate on a proper value of ξ to choose, along with perform the validation of the DF scheme, two relevant cases are selected which are discussed next.

3.2.3.1 One-dimensional (1D) N_2 advection

In the first testcase, the advection of a simple one-dimensional (1D) contact discontinuity is investigated. The contact discontinuity has the form indicated in Fig. 18 whereby only nitrogen is considered. The only difference is the domain length which is chosen to be $L = 1$ m in this case in order to perform some comparison with the results reported by [108]. Moreover, two initial conditions are explored, namely the "smooth" top-hat profile similar to Fig. 18 and the actual top-hat profile that connects the two states with a pure discontinuity. The conditions are those specified for Case 1 in Tab. 13 only, which represents a much more difficult situation to be solved for as discussed earlier in Sec. 3.2.2. Figures 32 to 35 show

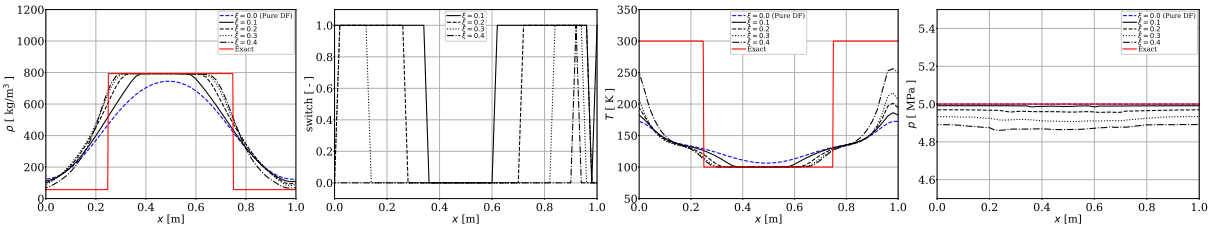

(a) (b) (c) (d)

Figure 32: a) density, b) scheme switch (0 = FC, 1 = QC), c) temperature and d) pressure profiles of the 1D top-hat profile obtained with $N = 51$ grid points.

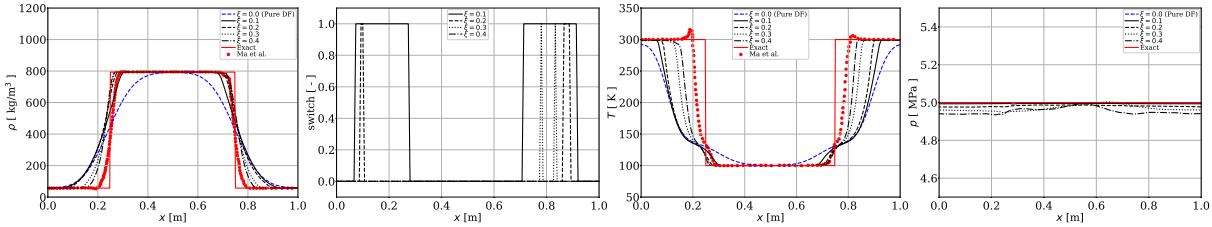

(a) (b) (c) (d)

Figure 33: a) density, b) scheme switch (0 = FC, 1 = QC), c) temperature and d) pressure profiles of the 1D top-hat profile obtained with $N = 151$ grid points

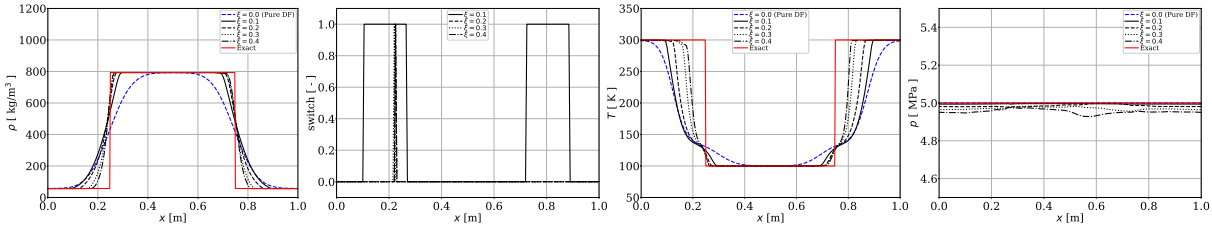

(a) (b) (c) (d)

Figure 34: a) density, b) scheme switch (0 = FC, 1 = QC), c) temperature and d) pressure profiles of the 1D top-hat profile obtained with $N = 201$ grid points.

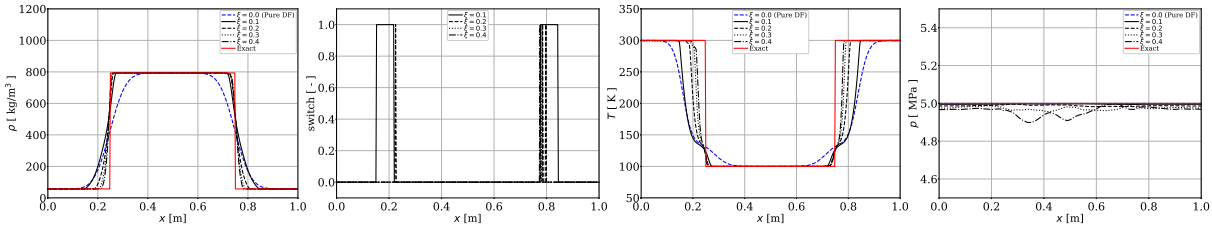

(a) (b) (c) (d)

Figure 35: a) density, b) scheme switch (0 = FC, 1 = QC), c) temperature and d) pressure profiles of the 1D top-hat profile obtained with $N = 401$ grid points.

the evolution of the 1D profile as resolution is varied using $N = 51, 151, 201, 401$ grid points for the top-hat profile. The comparison is taken after one cycle (*i.e.*$t = 0.01$ s) using the pure DF scheme and the hybrid FC/QC scheme with $\xi = 0.1, 0.2, 0.3, 0.4$. Both density and temperature agree well with the results of [108]. Improvements on the solution comparison

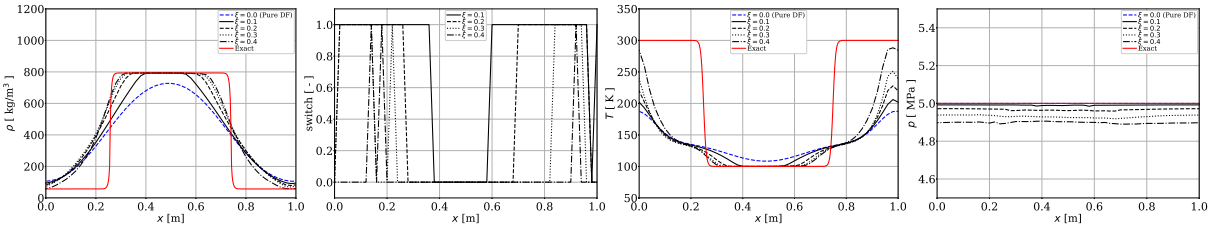

(a) (b) (c) (d)

Figure 36: a) density, b) scheme switch (0 = FC, 1 = QC), c) temperature and d) pressure profiles of the 1D "smoothed" top-hat profile obtained with $N = 51$ grid points.

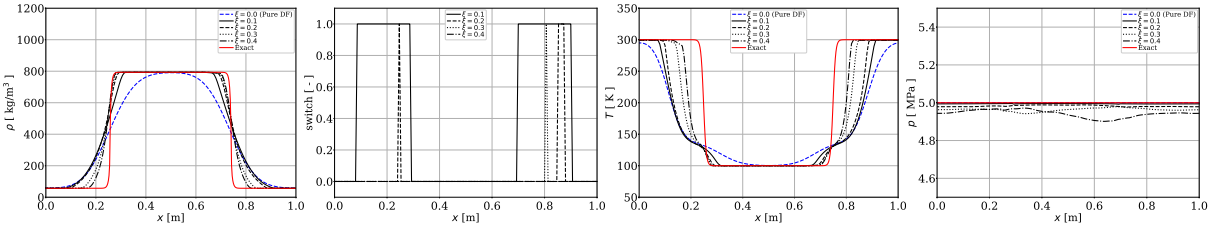

(a) (b) (c) (d)

Figure 37: a) density, b) scheme switch (0 = FC, 1 = QC), c) temperature and d) pressure profiles of the 1D "smoothed" top-hat profile obtained with $N = 151$ grid points.

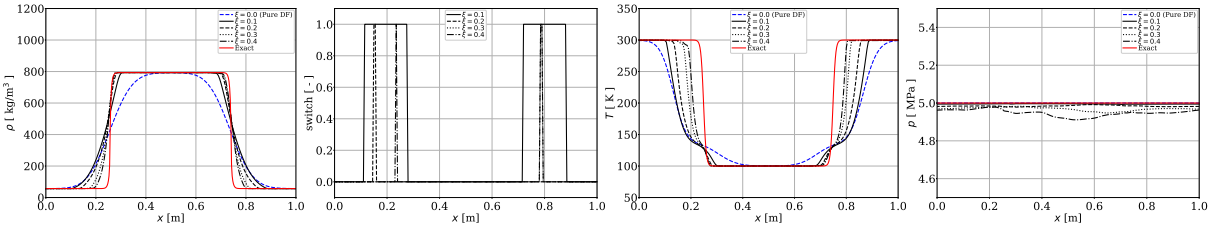

(a) (b) (c) (d)

Figure 38: a) density, b) scheme switch (0 = FC, 1 = QC), c) temperature and d) pressure profiles of the 1D "smoothed" top-hat profile obtained with $N = 201$ grid points.

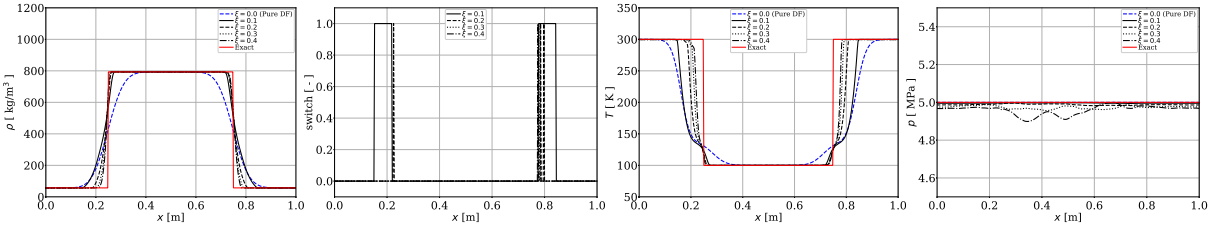

(a) (b) (c) (d)

Figure 39: a) density, b) scheme switch (0 = FC, 1 = QC), c) temperature and d) pressure profiles of the 1D "smoothed" top-hat profile obtained with $N = 401$ grid points.

are observed as the number of grid points is increased, as expected. The DF solution is the most dissipative one compared to the hybrid solutions, however it is the only one that strongly imposes the pressure (and the velocity - not shown) equilibrium across the contact discontinuity. As the FC scheme is activated, even in the regions where the density gradient is lower, an error occurs due to the pressure oscillation error discussed in Sec. 3.2.2. This error increases as the switch threshold increases, obviously, therefore a trade-off between the amount of numerical dissipation and the error in the pressure equilibrium must be accepted. Based on these first calculations, it seems that the threshold of $\xi = 0.3$ represents a good compromise. Analogous conclusions can be inferred from the "smoothed" top-hat profile results showed in Figs. (36)–(39).

3.2.3.2 Two-dimensional (2D) N_2/n-$C_{12}H_{26}$ advection

The second testcase is directly borrowed from [108]. As sketched in Fig. 40 it represents the advection of a 2D n-dodecane blob into a nitrogen environment within a squared domain of side 1 mm. The interface between the two material is considered sharp at $t = 0$. Figure 41

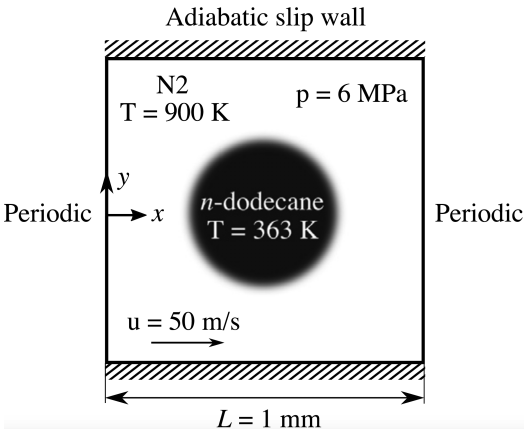

Figure 40: Schematic representation of the 2D N_2/n-$C_{12}H_{26}$ advection testcase (figure borrowed from [108]).

provides the density and fuel profiles along the y direction after one period of simulation ($t = 0.02$ ms). Comparison against the results of [108] provide very good agreement and yet the $\xi = 0.3$ threshold seems to be the best choice for the hybrid scheme. This is further

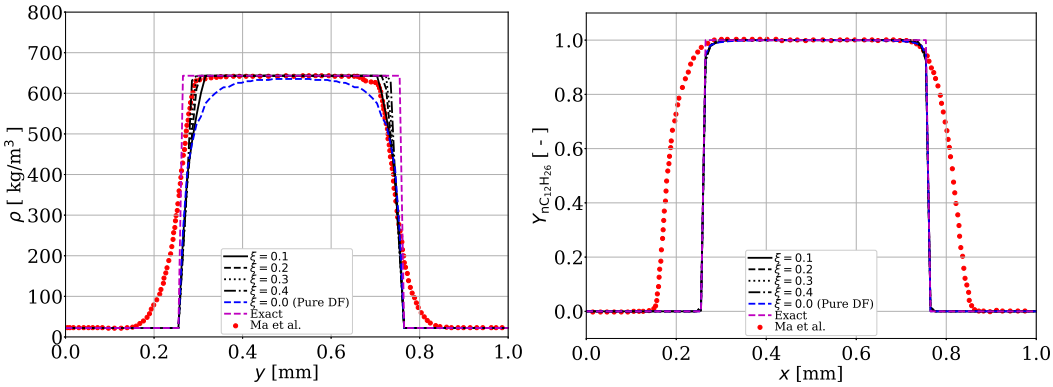

Figure 41: a) Density and b) n-dodecane profiles taken along the y direction after one period of simulation corresponding to $t = 0.02$ ms. The expected exact solution and the results reported by [108] are superimposed for comparison.

emphasized by the pressure results showed in Fig. 42 in which the scheme switch and the corresponding pressure field are illustrated for the different scheme options after one period. Again the pure DF results of Fig. 42(i) are the one that ensure the pressure equilibrium, however considerable amount of dissipation is introduced as shown in Fig. 41(a). Conversely as the parameter ξ is increased, less numerical dissipation is introduced, however larger pressure fluctuations appear due to the same problem discussed before. In conclusion, the $\xi = 0.3$ seems to be the most appropriate choice and therefore it will be used for the rest of the work.

3.3 An alternative way to compute cell-interface temperature

The schematics of Fig. 31 clearly identifies one important limitation of the current numerical framework from the performances point of view. As specifically discussed in Sec. 3.4, solution of thermodynamic problems with VLE involves substantially more amount of calculations, resulting into an overall more expensive simulation. While the ERHO problem is called only at the end of each sub-time iteration for the conversion of conservative to primitive variables, the PRHO problem represents one of the most invoked algorithms in both the FC and QC scheme, especially for the determination of the inviscid fluxes after the MUSCL reconstruction as explained in Sec. 3.2.1 and Sec. 3.2.3.

Improvements on the speed-up of the ERHO solver are made on the algorithm side and

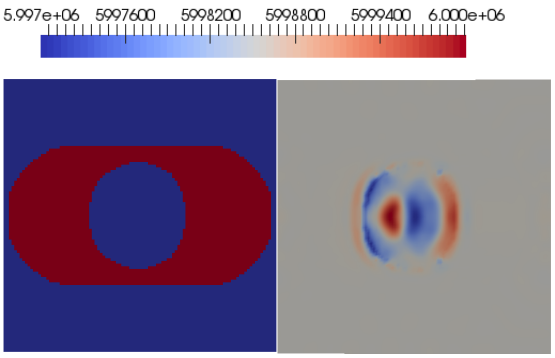

(a) Switch, $\xi = 0.1$

(b) p [Pa], $\xi = 0.1$

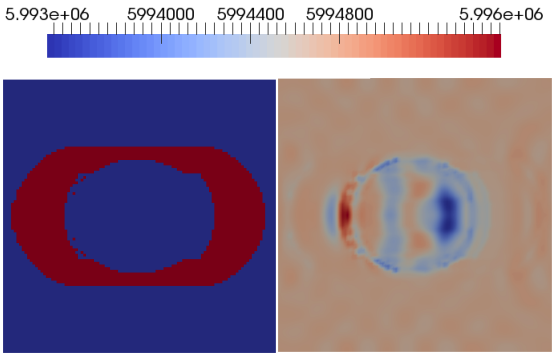

(c) Switch, $\xi = 0.2$

(d) p [Pa], $\xi = 0.2$

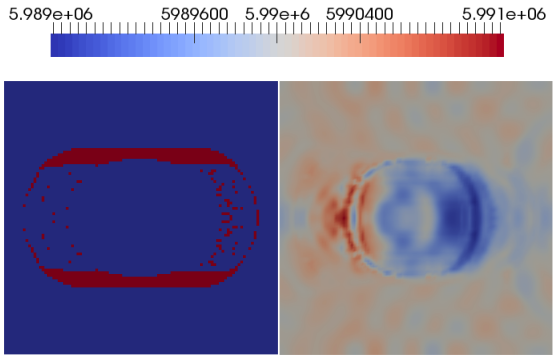

(e) Switch, $\xi = 0.3$

(f) p [Pa], $\xi = 0.3$

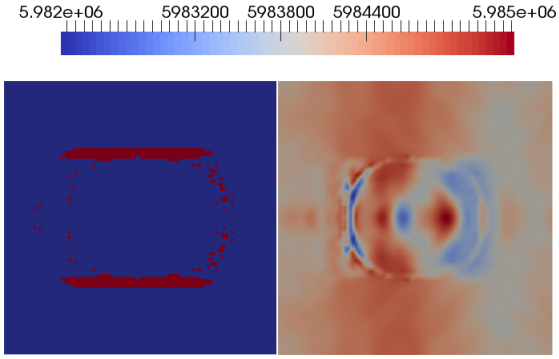

(g) Switch, $\xi = 0.4$

(h) p [Pa], $\xi = 0.4$

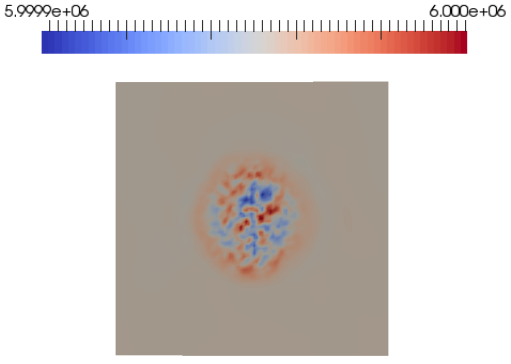

(i) p [Pa], pure DF

Figure 42: Collection of the scheme switch field and the corresponding pressure field obtained for different values of the ξ parameter, as well as the pure DF scheme. In the switch pictures, the red color indicates where the QC scheme is activated only, whereas the blue color indicates the regions where the FC scheme is activated only. The pressure colormap is in [Pa] units.

are explained in Sec. 3.4.3. This section focuses on the improvements of the performances as far as inviscid fluxes computation. The idea is to replace the solution of the PRHO problem after the MUSCL reconstruction with a new, less expensive procedure. Since the most expensive part of the PRHO problem is related to the calculation of the VLE state for given extrapolated values of p, ρ and $\mathbf{X}$, the key argument of the new approach is to exploit the VLE field, already computed from the previous iteration. For this purpose, the phases densities are also required to be computed and stored at each point: $\rho^L = \rho^L(T, p, \mathbf{x})$ and $\rho^V = \rho^V(T, p, \mathbf{y})$. For the present discussion, it is therefore assumed that ρ^L, ρ^V, ρ, p, T, $\mathbf{x}$, $\mathbf{y}$ and $\mathbf{X}$ are available as cell-center values from the previous iteration.

Next, in a similar manner as already done in MUSCL, all the previous variables except temperature are extrapolated at the cell-interface using the same formulas of Eq. (3.2.1) and Eq. (3.2.2). First, with the extrapolated values of $\mathbf{X}$, $\mathbf{x}$ and $\mathbf{y}$, the corresponding thermodynamically-consistent value of β can be computed by solving Eq. (2.2.37) using for example the bisection or Newton method (or combined [129]). This gives the right value of β at the cell interface, consistent with the extrapolated quantities. Next, using the definitions:

$$\rho^L = \frac{pM^L}{Z^L R_u T} \qquad \rho^V = \frac{pM^V}{Z^V R_u T} \qquad \rho = \frac{pM}{Z R_u T} \tag{3.3.1}$$

into Eq. (2.2.34) it is easy to prove the following alternative definition of the blend rule between the phases in terms of the compressibilities:

$$Z = \beta Z^V + (1 - \beta) Z^L \,. \tag{3.3.2}$$

With the known values of ρ^L, ρ^V, ρ, p, $\mathbf{x}$, $\mathbf{y}$ and $\mathbf{X}$ at the cell interface, Eq. (3.3.2) would have only the temperature to iterate on since it is also a non-linear algebraic equation. However, if the coefficient A_m can be written in the form $A_m = c_1 + c_2 T^{c_4} + c_3 T$ as presented in Tab. 6, which happens for all the GCEoS except PR-RK, then following Eq. (2.2.72) it is easy to prove that the compressibility can be written in the following form where the dependency on the temperature is explicit:

$$Z = \frac{M}{M - B_m \rho} - \frac{\rho M}{R_u T} \frac{c_1 + c_2 T^{c_4} + c_3 T}{(M + \delta_1 B_m \rho)(M + \delta_2 B_m \rho)} \,. \tag{3.3.3}$$

The same definition can be applied on the phases separately:

$$
\begin{aligned}
Z^L =& \frac{M^L}{M^L - B_m^L \rho^L} - \frac{\rho^L M^L}{R_u T} \frac{c_1^L + c_2^L T^{c_4^L} + c_3^L T}{(M^L + \delta_1 B_m^L \rho^L)(M^L + \delta_2 B_m^L \rho^L)}\,, \\
Z^V =& \frac{M^V}{M^V - B_m^V \rho^V} - \frac{\rho^V M^V}{R_u T} \frac{c_1^V + c_2^V T^{c_4^V} + c_3^V T}{(M^V + \delta_1 B_m^V \rho^V)(M^V + \delta_2 B_m^V \rho^V)}\,.
\end{aligned} \tag{3.3.4}
$$

In the above, note that the dependency of δ_1 and δ_2 on the phase is dropped since it is assumed that PR-RK is not used here. In a more compact form, Eq. (3.3.4) can be re-written as:

$$
\begin{aligned}
Z^L &= \alpha_0^L + \alpha_1^L \frac{c_1^L + c_2^L T^{c_4^L} + c_3^L T}{T}\,, \\
Z^V &= \alpha_0^V + \alpha_1^V \frac{c_1^V + c_2^V T^{c_4^V} + c_3^V T}{T}\,,
\end{aligned} \tag{3.3.5}
$$

where:

$$
\alpha_0^L = \frac{M^L}{M^L - B_m^L \rho^L}\,, \tag{3.3.6}
$$

$$
\alpha_1^L = -\frac{\rho^L M^L}{R_u (M^L + \delta_1 B_m^L \rho^L)(M^L + \delta_2 B_m^L \rho^L)}\,, \tag{3.3.7}
$$

$$
\alpha_0^V = \frac{M^V}{M^V - B_m^V \rho^V}\,, \tag{3.3.8}
$$

$$
\alpha_1^V = -\frac{\rho^V M^V}{R_u (M^V + \delta_1 B_m^V \rho^V)(M^V + \delta_2 B_m^V \rho^V)}\,, \tag{3.3.9}
$$

have been defined in analogy with Eq. (3.3.4). Equations (3.3.6)–(3.3.9) are supposed to be readily known at the interface because they do not depend on the temperature and can be easily computed by using the extrapolated values of ρ^L, ρ^V, $\mathbf{x}$, $\mathbf{y}$. Next, by substituting Eq. (3.3.5) into Eq. (3.3.2) and using Eq. (2.2.3) to replace Z on the left-hand side, after few manipulations it can be shows that the following result is obtained:

$$
m_1 T^{c_4} + m_2 T + m_3 = 0\,, \tag{3.3.10}
$$

where:

$$
m_1 = \beta \alpha_1^V c_2^V + (1-\beta)\alpha_1^L c_2^L\,, \tag{3.3.11}
$$

$$
m_2 = \beta(\alpha_0^V + \alpha_1^V c_3^V) + (1-\beta)(\alpha_0^L + \alpha_1^L c_3^L)\,, \tag{3.3.12}
$$

$$
m_3 = \alpha_1^V c_1^V \beta + (1-\beta)\alpha_1^L c_1^L - \frac{pM}{\rho R_u}\,. \tag{3.3.13}
$$

To obtain Eq. (3.3.10), the fact that $c_4^V \equiv c_4^L = c_4$ for all GCEoS except PR-RK has been used (*cf.* Tab. 6). The coefficients m_1, m_2 and m_3 can be easily computed with the variables extrapolated at the interface leaving Eq. (3.3.10) to assume in the worst case (PR or SRK) the form of a bi-quadratic algebraic equation, for which the analytic solution is known. This procedure does not involve any iterative component, except the solution of the Rachford-Rice equation Eq. (2.2.37), which is called only once per cell-interface solution. In contrast, the full solution of the PRHO problem would have required, besides other iterative algorithms (see Sec. 3.4.2) to solve for Eq. (2.2.37) many times for each cell-interface because of the double-nested loop involving the solution of the Tp problem.
If in the extrapolation of $\mathbf{x}$ and $\mathbf{y}$ at the beginning of this procedure it turns out that SUM($\mathbf{x}$) $< \epsilon$ or SUM($\mathbf{y}$) $< \epsilon$, then the single phase PRHO problem is followed. It is interesting to note that the above procedure directly falls into the analytical solution of the single-phase PRHO problem discussed later in Eq. (3.4.9), so in a way, the above procedure represents a more generic way to solve the PRHO problem analytically, which can include or exclude VLE. For example, if SUM($\mathbf{y}$) $< \epsilon$, the mixture is taken in the liquid phase, $\beta = 0$ and all the coefficients above with superscript $(\cdot)^V$ are canceled, recovering the form of Eq. (3.4.9). In this work, it was found that a tolerance of $\epsilon = 1\mathrm{e}-7$ was good enough. Given that this new approach represents another important contribution of this work, and overall it does not require any specific new algorithm/knowledge other than those discussed so far, its validation is directly performed with the results in Chap. 5.

3.4 Numerical methods for the thermodynamics

In this section, the focus is on the discussion of thermodynamic problems that are relevant for a general purpose simulation. Depending on the set of governing equations and/or the numerical scheme, different types of thermodynamic problems may be encountered as illustrated in Fig. 31. The scope of each of them is to find a third state property out of two known state properties and mixture composition. First, the solution of the so called Tp problem, which consists of finding density ρ out of temperature, pressure and composition is discussed. This represents the most important piece of the entire thermodynamics

numerical solution as it involves the discussion of the VLE problem solution itself. Next, the single- and dual-variable algorithms, as well as the calculation of all thermodynamic properties are discussed. Finally, zero-dimensional mixing models are given, which are used in Chap. 5. All the proposed numerical recipes are not meant to be the best in terms of performances, however they are absolutely reliable in terms of robustness. That is, even though more algorithms are available in the literature for the solution of the specific thermodynamic problem (cited later accordingly), they still require a backup approach in case of lack of convergence, which is usually the problem of faster numerical recipes due to their requirement of a very close solution to start with. All the algorithms referred in this sections are listed in Appendix D.

3.4.1 Solution of the Tp problem

The Tp problem represents the calculation of mixture density ρ (and compressibility Z) out of temperature T, pressure p and composition $\mathbf{X}$ summarized in Algorithm 2. In case of a multi-phase system, this requires to solve the actual VLE problem, meaning the determination of β, $\mathbf{x}$ and $\mathbf{y}$ as per Eq. (2.2.36) and Eq. (2.2.37). Figure 43 illustrates

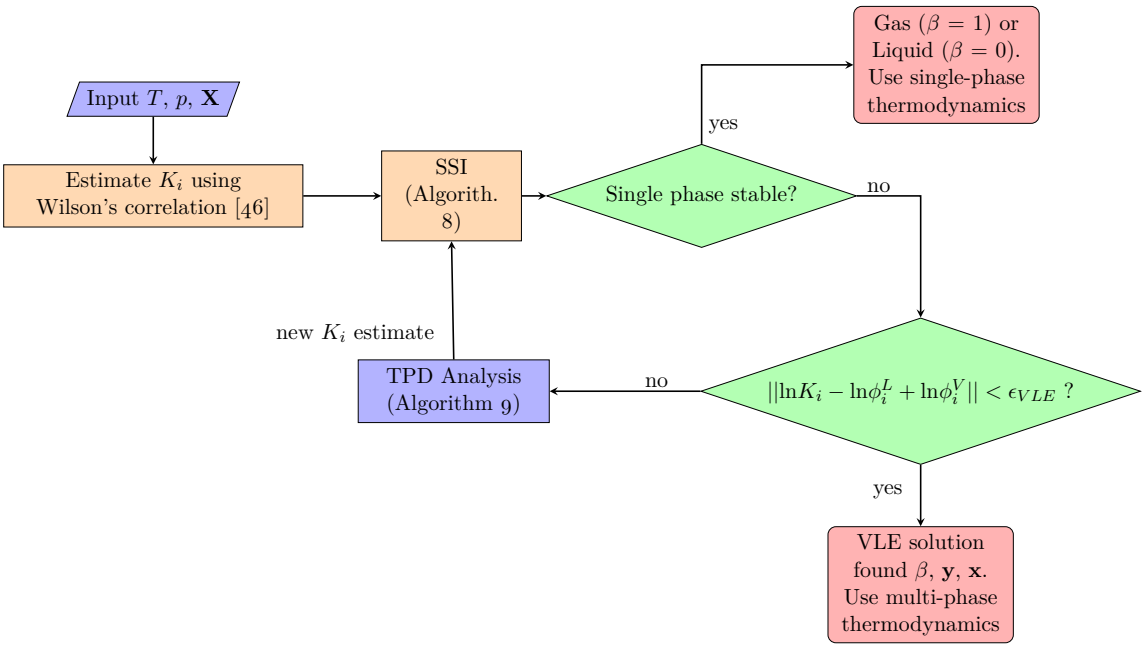

Figure 43: Basic algorithm of the VLE problem solution.

a basic flow diagram for the resolution of the VLE problem. The key numerical tool is the Successive Substitution Iteration (SSI) method. This essentially solves Eqs. (2.2.36)–(2.2.37) and determines whether the present mixture is stable (hence liquid or vapor - single phase thermodynamics applies) or unstable (VLE actually forms and multi-phase thermodynamics must be followed). To start the SSI numerical recipe, an estimation of the K_i coefficients is required. This is usually provided by the Wilson's correlation [46], given in Eq. (3.4.1):

$$K_i = \frac{p_{c,i}}{p} \exp\left[5.37(1+\omega_i)\left(1-\frac{T_{c,i}}{T}\right)\right], \qquad i = 1, \cdots, N_s\,, \tag{3.4.1}$$

where, $p_{c,i}$, $T_{c,i}$ and ω_i are the critical pressure, temperature and acentric factor of each species i in the mixture. With the estimated values of K_i and $\mathbf{X}$, Eq. (2.2.37) can be solved in β. Once β is known, both $\mathbf{x}$ and $\mathbf{y}$ can be computed by using the mass balance equation $\mathbf{X} = \beta\mathbf{y} + (1-\beta)\mathbf{x}$ and the definition of $K_i = y_i/x_i$:

$$x_i = \frac{X_i}{1+\beta(K_i-1)}\,, \qquad i = 1, \cdots, N_s \tag{3.4.2}$$

$$y_i = K_i x_i\,, \qquad i = 1, \cdots, N_s\,. \tag{3.4.3}$$

Next, using the values of $\mathbf{x}$ and $\mathbf{y}$, the fugacity coefficients in both phases can be computed: $\phi_i^V = \phi^V(T,p,\mathbf{y})$, $\phi_i^L = \phi^L(T,p,\mathbf{x})$ using Eq. (M.3.18) and the exit condition of Eq. (2.2.36) can be checked. If a specified tolerance ϵ_{VLE} is not met, a new estimation of K_i can be computed using the same Eq. (2.2.36): $K_i = \phi_i^L/\phi_i^V$, and the procedure repeats until the error tolerance or a maximum number of iterations N_{max} is reached. For the SSI method, the algorithm discussed in [127, 129] is used, which is summarized in Algorithm 8.

In some circumstances, the SSI method can have difficulty to converge or it may converge to the wrong solution. For example it may predict single phase systems in the regions where VLE exists or vice versa. This is due to the initial estimation of K_i coefficients which may be too inaccurate for mixtures at a state very far from ideal. To overcome this issue, the SSI algorithm is usually augmented with the Tangent Plane Distance (TPD) stability analysis introduced by Michelsen [126]. The stability analysis not only provides the information whether the mixture is stable as single phase, but it also provides very good estimations of

the K_i coefficients to start (or continue) the SSI method if the result tells that a two-phase mixture exists.

The stability test represents the distance of the generic *hyper-plane* (i.e. in the N_s-dimensional space) from the mixture Gibbs free energy computed at T, p and $\mathbf{X}$, with "potential" two-phase composition ζ_i which is called *trial* phase. The complete theory of the TPD analysis can be found in [126, 129, 49]. A (modified) TPD function relative to the trial phase η is defined as:

$$\mathrm{TPD}^{\eta}(\mathrm{T,p},\mathbf{X},\boldsymbol{\zeta}) = 1 + \sum_{\mathrm{i}}^{\mathrm{N_s}} \zeta_{\mathrm{i}} \{ \ln\zeta_{\mathrm{i}} + \ln\phi_{\mathrm{i}}^{\eta}(\mathrm{T,P},\boldsymbol{\zeta}) - \underbrace{[\ln X_i + \ln\phi_i(T,p,\mathbf{X})]}_{\mathrm{d_i(T,p,\mathbf{X})=\mathbf{d}}} - 1 \}\,, \quad (3.4.4)$$

where $\phi_i = \phi_i(T,p,\mathbf{X})$ is the i-th component fugacity coefficient in the mixture, evaluated as single-phase. That is for given T, p and $\mathbf{X}$, the mixture compressibility is evaluated using the minimum Gibbs criterion method (discussed in Appendix A). This ensures to start the stability analysis from the (single) phase that has the lowest Gibbs energy. As a result, the vector quantity $d_i(T,p,\mathbf{X}) = \ln X_i + \ln\phi_i(T,p,\mathbf{X})$ is a constant for given T, p and $\mathbf{X}$. Effectively, TPD^{η} represents the minimum (absolute) difference of the Gibbs energy between the actual mixture considered as single phase, and the respective mixture that shows VLE with composition $\boldsymbol{\zeta}$ in the phase η. As a consequence, $\mathrm{TPD}^{\eta} < 0$ is required for VLE to exist, meaning that the mixture that forms phase-split has a lower Gibbs energy than the mixture that is considered as single phase. This modified version introduced by Michelsen [129] is the result of the original TPD function:

$$\mathrm{TPD}^{*,\eta}(\mathrm{T,p},\mathbf{X},\boldsymbol{\zeta}) = \sum_{\mathrm{i}}^{\mathrm{N_s}} \zeta_{\mathrm{i}} \{ \ln\zeta_{\mathrm{i}} + \ln\phi_{\mathrm{i}}^{\eta}(\mathrm{T,P},\boldsymbol{\zeta}) - \underbrace{[\ln X_i + \ln\phi_i(T,p,\mathbf{X})]}_{\mathrm{d_i(T,p,\mathbf{X})=\mathbf{d}}} \}\,, \quad (3.4.5)$$

when an unconstrained optimization problem is sought. It can be proven that Eq. (3.4.4) has the same stationary points of Eq. (3.4.5) and therefore can provide the same information about phase stability with the exception that the problem is more convenient to be solved because it is not formulated as a constrained optimization problem [129]

For the given trial phase $\boldsymbol{\zeta}$, the phase equilibrium condition of Eq. (2.2.31) on the fugacities equality still needs to be enforced. Using the logarithm form, an iterative procedure on the

trial phase $\boldsymbol{\zeta}$ is immediately found:

$$\begin{aligned}
&\ln\zeta_i + \ln\phi_i^{\eta}(T,p,\boldsymbol{\zeta}) - \ln X_i - \ln\phi_i(T,p,\mathbf{X}) = 0\,,\\
&\ln\zeta_i + \ln\phi_i^{\eta}(T,p,\boldsymbol{\zeta}) - d_i(T,p,\mathbf{X}) = 0 \quad \rightarrow \quad \zeta_i^{n+1} = \exp[d_i(T,p,\mathbf{X}) - \ln\phi_i^{\eta}(T,p,\boldsymbol{\zeta}^n)]\,,\\
&i = 1,\cdots,N_s\,. \qquad (3.4.6)
\end{aligned}$$

Equation (3.4.6) is effectively an SSI method for the stability analysis. The last thing to do is how to define the trial phase η. In this work, $\eta = L$ or $\eta = V$ are used directly. This means that with the given K_i already estimated with Eq. (3.4.1) or SSI method at a given iteration, two different trials are computed: the vapor one ($\eta = V$) as $\zeta_i = K_i X_i$ and the liquid one ($\eta = L$) as $\zeta_i = X_i/Ki$. Next, for both of them Eq. (3.4.6) is applied until $||\zeta_i^{n+1} - \zeta_i^n|| < \epsilon_{TPD}$ and the TPD$^{\eta}$ function for both trials is evaluated using Eq. (3.4.4). The phase η that shows the smallest TPD$^{\eta}$ function indicates the direction the current mixture tends to. For example if TPD$^L <$ TPD^V, the current mixture is more "liquid-like" and the new estimation of K_i coefficients is given in the form $K_i = X_i/\zeta_i$. Conversely if TPD$^V <$ TPD^L, the new estimation of K_i coefficients is given in "vapor-like" form: $K_i = \zeta_i/X_i$. This new estimation of K_i coefficients can be given to the SSI method described in Algorithm 8. If both TPD$^{\eta} \sim 0$ it means that the trial phase effectively matches the single phase conditions, i.e. $\boldsymbol{\zeta} \rightarrow \mathbf{X}$, which means that the single phase initially investigated is actually stable and no VLE forms. This condition is called "trivial" solution. More trial phases can be investigated by defining different forms of the K_i coefficients as suggested by [49], in order to start the stability test from different points in the compositional space and ensure that the found composition is the one that provides the smallest value of Eq. (3.4.4), however this requires even more stability tests that can substantially increase the overall computational overhead. In this work it was found that trying both $\eta = L$ or $\eta = V$ was enough for the present purposes as also confirmed in [72]. The stability analysis can be accelerated by using a Newton method or quasi-Newton method discussed in [49, 72]. Algorithm 9 summarizes the steps in order to conduct the stability analysis.

Algorthm 11 for the solution of the VLE problem does not necessarily represent the only

possible choice. In fact, SSI and stability analysis can be run in multiple sequence, by conducting more checks, however this will affect the overall simulation cost. Another possible improvement of the method is to implement the full Newton method to solve Eq. (2.2.31). One possibility is to use the approach of [49] in which β, and $\ln K_i$ are chosen as set of independent variables. Another approach, followed in this work, is that of [129] which uses the molar flows $v_i = \beta y_i$ as independent variables. The theoretical development as well as the algorithm used are summarized in Appendix I. Usually the SSI and the Newton methods are combined together. The SSI method is typically used up to a certain tolerance, larger than the one used for SSI alone, from which the Newton method is started. The Newton method is fast to converge, and it is very suitable for CFD simulations where previous solution can be used as initial guess, however it fails if the mixture is actually single phase or if the initial guess is not close to the final solution and therefore it needs to be switched off and the SSI method has to be recovered in combination with the stability analysis. Usually this happens at the phase boundaries where a computational cell can switch between a single and a double phase condition such that the initial guess is effectively wrong and too far from the final state. As a result, many computational cells can experience fail of the Newton method, for which SSI needs to be used alone, ultimately producing a waste of computational time. Nevertheless, some speedup of about 5% was observed when Newton method was used (see Chap. 5), making its application useful, however the speedup itself may depend on the simulation and the conditions themselves. For example it may depend on how spread out is the VLE region in the first place compared to the overall domain size.

3.4.2 Solution of the single-variable problems

Single-variable problems are identified as those that have only one unknown to iterate on. These are usually obtained when the objective function depends on the unknown only, or if other dependencies are explicitly known. For this work, single-variable problems are identified as the $T\rho$ and $p\rho$ problems, that is when temperature-density and pressure-density (as well as composition $\mathbf{X}$) are known, respectively. Thus, pressure and temperature are sought in the first and second case, respectively. Note that if the single-phase assumption is

invoked at all the times, the $T\rho$ problem reduces to the immediate solution of Eq. (2.2.67), while the $p\rho$ problem requires in general an iterative procedure, still on Eq. (2.2.67) where $F = p(T, \hat{\rho}, \hat{\mathbf{X}}) - \hat{p}$ is used as objective function, whereby $p(T, \hat{\rho}, \hat{\mathbf{X}})$ is the value computed with Eq. (2.2.67), while $\hat{p}$ and $\hat{\rho}$ are the known values. Alternatively the approach with $F = \rho(T, \hat{p}, \hat{\mathbf{X}}) - \hat{\rho}$ is also possible by solving Eq. (2.2.70) in $Z = Z(T, \hat{p}, \hat{\mathbf{X}})$ first and then use Eq. (2.2.3) to find the corresponding $\rho = \rho(T, \hat{p}, \hat{\mathbf{X}})$ and update the objective function. In this case, the value of T is first guessed and then updated by the algorithm.

The update of the unknown itself can be done using any numerical algorithm for non-linear algebraic equations, such as bisection and Newton-Raphson. In the latter case, the derivatives of F with respect to the unknown are either $(\partial p/\partial T)_{\rho,\mathbf{X}}$ or $(\partial \rho/\partial T)_{p,\mathbf{X}}$ readily available for single-phase problems from Eq. (2.2.86) and Eq. (2.2.87) respectively. Additionally, it should be pointed out that the single-phase $p\rho$ problem can be actually solved analytically for all GCEoS except the PR-RK EoS. In fact, as discussed in Sec. 2.2.3.1, with the coefficient A_m expressed as: $A_m = c_1 + c_2 T^{c_4} + c_3 T$, substituting it into Eq. (2.2.67) gives a form of the EoS in which temperature appears explicitly for p, ρ and $\mathbf{X}$ known:

$$p = \frac{\rho R_u T}{M - B_m \rho} - \frac{\rho^2 (c_1 + c_2 T^{c_4} + c_3 T)}{(M + \delta_1 B_m \rho)(M + \delta_2 B_m \rho)} \,. \tag{3.4.7}$$

By defining the (known) coefficients:

$$\begin{aligned} r_1 &= \frac{\rho R_u}{M - B_m \rho} & r_2 &= \frac{\rho^2 c_1}{(M + \delta_1 B_m \rho)(M + \delta_2 B_m \rho)} \\ r_3 &= \frac{\rho^2 c_2}{(M + \delta_1 B_m \rho)(M + \delta_2 B_m \rho)} & r_4 &= \frac{\rho^2 c_3}{(M + \delta_1 B_m \rho)(M + \delta_2 B_m \rho)} \\ r_5 &= r_2 + p \,, \end{aligned} \tag{3.4.8}$$

the following form of the EoS can be obtained:

$$(r_4 - r_1) T + r_3 T^{c_4} + r_5 = 0 \,. \tag{3.4.9}$$

For all GCEoS except PR-RK EoS, the structure of Eq. (3.4.9) is such that it resembles a bi-quadratic algebraic equation at most (when $c_4 = 1/2$), for which an analytical solution is readily available similarly to classical *2nd* order equations, while other cases are even simpler. Regarding PR-RK, there is no such opportunity and a numerical approach similar

to that discussed above has to be followed using any algorithm for the solution of non-linear algebraic equations.

Regarding the multi-phase case, a general Newton-Raphson (NR) method can be employed as discussed next. For convenience, we discuss the $p\rho$ problem only, however the exact approach applies to the $T\rho$ problem as well. The basic NR formula to update the current temperature estimate from step n to step $n+1$ writes as:

$$T^{n+1} = T^n - \frac{F(T^n, \hat{p}, \hat{\rho}, \hat{\mathbf{X}}, \beta^n)}{\left(\frac{\partial F(T^n, \hat{p}, \hat{\rho}, \hat{\mathbf{X}}, \beta^n)}{\partial T}\right)_{p,\mathbf{X}}}, \tag{3.4.10}$$

where $F(T^n, \hat{p}, \hat{\rho}, \hat{\mathbf{X}}, \beta^n) = \rho(T^n, \hat{p}, \hat{\mathbf{X}}, \beta^n) - \hat{\rho}$ and $\left(\partial F(T^n, \hat{p}, \hat{\rho}, \hat{\mathbf{X}}, \beta^n)/\partial T\right)_{p,\mathbf{X}} \equiv$ $\equiv \left(\partial \rho(T^n, \hat{p}, \hat{\mathbf{X}}, \beta^n)/\partial T\right)_{p,\mathbf{X}}$. In the latter, $\rho(T^n, \hat{p}, \hat{\mathbf{X}}, \beta^n)$ is computed with Eq. (2.2.34), while $(\partial \rho(T^n, \hat{p}, \hat{\mathbf{X}}, \beta^n)/\partial T)_{p,\mathbf{X}}$ is now computed through Eq. (2.2.49) in order to take into account multi-phase (VLE) physics. This requires that a Tp problem is solved within the main loop at each step, making the overall calculation much more expensive than the corresponding single-phase method. Equation 3.4.10 is very general because it can be applied to both single and multi-phase thermodynamic calculations. The only difference is the determination of the derivative of F which can be computed with the single- or multi-phase formulas, depending on the value of β at the current iteration. Algorithm 12 summarizes the steps required for the solution of the $p\rho$ problem. Similar steps are required for the solution of the $T\rho$ problem. The initial guess T_0 can come from a previous solution, if known, or from the analytical solution of Eq. (3.4.9) if a single-phase system is initially assumed. However, sometimes the analytical solution may return a complex value of T if a strong VLE solution exists from the known $p, \rho, \mathbf{X}$ state and it is forced to behave as a single-phase by means of Eq. (3.4.9). This part will be further discussed in Sec. 3.5.

3.4.3 Solution of the multi-variable problems

Multi-variable problems are identified as those that have more than one unknown, typically two, to iterate on. In this work, the $E\rho$ and the Ep problems are considered, corresponding to the thermodynamic problems that, beyond composition, have mixture internal energy and density, or mixture internal energy and pressure known respectively. Both problems

can be formulated in a common general fashion described as follows.

Given the presence of two unknowns, namely ϕ and ψ, two objectives functions: $F_1(\phi, \psi, \mathbf{\Omega})$, $F_2(\phi, \psi, \mathbf{\Sigma})$ are required to be satisfied simultaneously. Here $\mathbf{\Omega}$ and $\mathbf{\Sigma}$ represent, in general, known vectors that are auxiliary to the analytic form of each objective function. Application of first order Taylor expansion on both objective functions gives the following compact form:

$$\underbrace{\begin{bmatrix} \left(\frac{\partial F_1^n}{\partial \phi}\right)_\psi & \left(\frac{\partial F_1^n}{\partial \psi}\right)_\phi \\ \left(\frac{\partial F_2^n}{\partial \phi}\right)_\psi & \left(\frac{\partial F_2^n}{\partial \psi}\right)_\phi \end{bmatrix}}_{\text{Jacobian} \quad \mathcal{J}} \underbrace{\begin{pmatrix} \Delta\phi \\ \Delta\psi \end{pmatrix}}_{\mathbf{\Delta}} = -\underbrace{\begin{pmatrix} F_1^n \\ F_2^n \end{pmatrix}}_{\mathbf{R}}, \tag{3.4.11}$$

where superscript n indicates that the quantity is computed at the previous iteration step. The solution update is performed by inverting the Jacobian matrix and by computing Δ such that $\phi^{n+1} = \phi^n + \lambda\Delta\phi$ and $\psi^{n+1} = \psi^n + \lambda\Delta\psi$ can be computed. Here, $\lambda(0, 1]$ identifies a coefficient that applies the so-called *line-search* method. This coefficient de-amplifies (reduces) the change of the variable due to the linearization, usually improving the algorithm robustness. Of course as λ is chosen far from 1, the convergence is slower, however smaller steps are taken in the procedure such that the linearization does not cause a large enough variation to cause numerical instabilities. For this work, this coefficient is chosen as suggested by [25] in the form (see also Algorithm 13):

$$\lambda = \mathrm{MIN}(\lambda_0, \mathrm{ABS}(\Delta \mathrm{T}_{\max}/\Delta \mathrm{T}), \mathrm{ABS}(\Delta \mathrm{p}_{\max}/\Delta \mathrm{p})) \tag{3.4.12}$$

where λ_0 is a minimum value chosen by the user and ΔT_{max}, Δp_{max} represent the maximum increments allowed by the iteration in temperature and pressure, against the current values ΔT and Δp, respectively. These are also chosen by the user and should be usually tuned on the order of magnitude of the pressure and temperature that is being simulated in order to have the best performances. Starting values $\Delta T = \Delta T_0$, $\Delta p = \Delta p_0$ should also be chosen by the user to start the algorithm, following the same rule of thumb.

Table 14 identifies each term of Eq. (3.4.11) for the specific type of problem, while Algorithm 13 provides the corresponding numerical procedure for the $E\rho$ problem. Note that in the Ep problem, the pressure is treated as a variable and density is updated using temperature.

Table 14: Symbols description for the $E\rho$ and Ep multi-variable problems.

problem	ϕ	ψ	$\mathbf{\Omega}$	$\mathbf{\Sigma}$	F_1	F_2	$(\partial F_1/\partial\phi)_\psi$	$(\partial F_1/\partial\psi)_\phi$	$(\partial F_2/\partial\phi)_\psi$	$(\partial F_2/\partial\psi)_\phi$
$E\rho$	T	p	$\mathbf{X}, \hat{E}$	$\mathbf{X}, \hat{\rho}$	$E(T,p,\mathbf{X},\beta)-\hat{E}$	$\rho(T,p,\mathbf{X},\beta)-\hat{\rho}$	$\left(\frac{\partial E}{\partial T}\right)_{p,\mathbf{X}}$	$\left(\frac{\partial E}{\partial p}\right)_{T,\mathbf{X}}$	$\left(\frac{\partial \rho}{\partial T}\right)_{p,\mathbf{X}}$	$\left(\frac{\partial \rho}{\partial p}\right)_{T,\mathbf{X}}$
Ep	T	p	$\mathbf{X}, \hat{E}$	$\mathbf{X}, \hat{p}$	$E(T,p,\mathbf{X},\beta)-\hat{E}$	$p(T,\rho,\mathbf{X})-\hat{p}$	$\left(\frac{\partial E}{\partial T}\right)_{p,\mathbf{X}}$	$\left(\frac{\partial E}{\partial p}\right)_{T,\mathbf{X}}$	$\left(\frac{\partial p}{\partial T}\right)_{\rho,\mathbf{X}}$	$\left(\frac{\partial p}{\partial p}\right)_{\rho,\mathbf{X}}=1$

Additionally, the procedure of Eq. (3.4.11) is valid for both single- and multi-phase system. In the first case, the derivatives of E and ρ are those involving the departure functions of Eqs. (M.2.1)–(M.2.2) and Eqs. (2.2.86)–(2.2.87), whereas in the second case, the derivatives are replaced with Eqs. (K.0.42)–(K.0.43) and Eqs. (2.2.49)–(K.0.32), respectively. The determination of which one needs to be used is once again given by β, for which a Tp problem needs to be solved in the loop as described in Algorithm 13

It should be noted that the single-phase $E\rho$ problem can be also solved in another way by exploiting the functional dependency of E (and its departure function) with ρ directly as in Eq. (2.2.79) and thus its derivative in Eq. (2.2.85). In this way, given that E and ρ are constant, the iteration is made on temperature only similarly to Eq. (3.4.10) and pressure is subsequently obtained by applying Eq. (2.2.67). Obviously this approach will not work in presence of VLE and erroneous results can be obtained if the starting state of E, ρ and $\mathbf{X}$ pertains to a multi-phase state. Additional details can be found in Algorithm 13.

Finally, other methods are worth to be mentioned. For example the solution of the $E\rho$ problem can be attempted by using a full Newton method [128], in which the VLE problem is embedded in the Jacobian matrix, avoiding to solve the Tp problem inside the loop. Other methods (some applicable to other problems too) are based on entropy maximization [77, 205, 25]. Particularly [25] proposed a solution of the $E\rho$ problem by approximating the Jacobian of Eq. (3.4.11). This algorithm is described in Appendix J. The mentioned methods can be used with the proposed methods in this work to achieve good compromise between speed and robustness.

In this work, additional speed up for the solution of the $E\rho$ problem is attempted to be achieved by using the information of the VLE derivatives at the current iteration, such

as $\partial\beta/\partial T$ and $\partial\beta/\partial p$ to predict the next VLE state. Figure 44 illustrates the basic idea

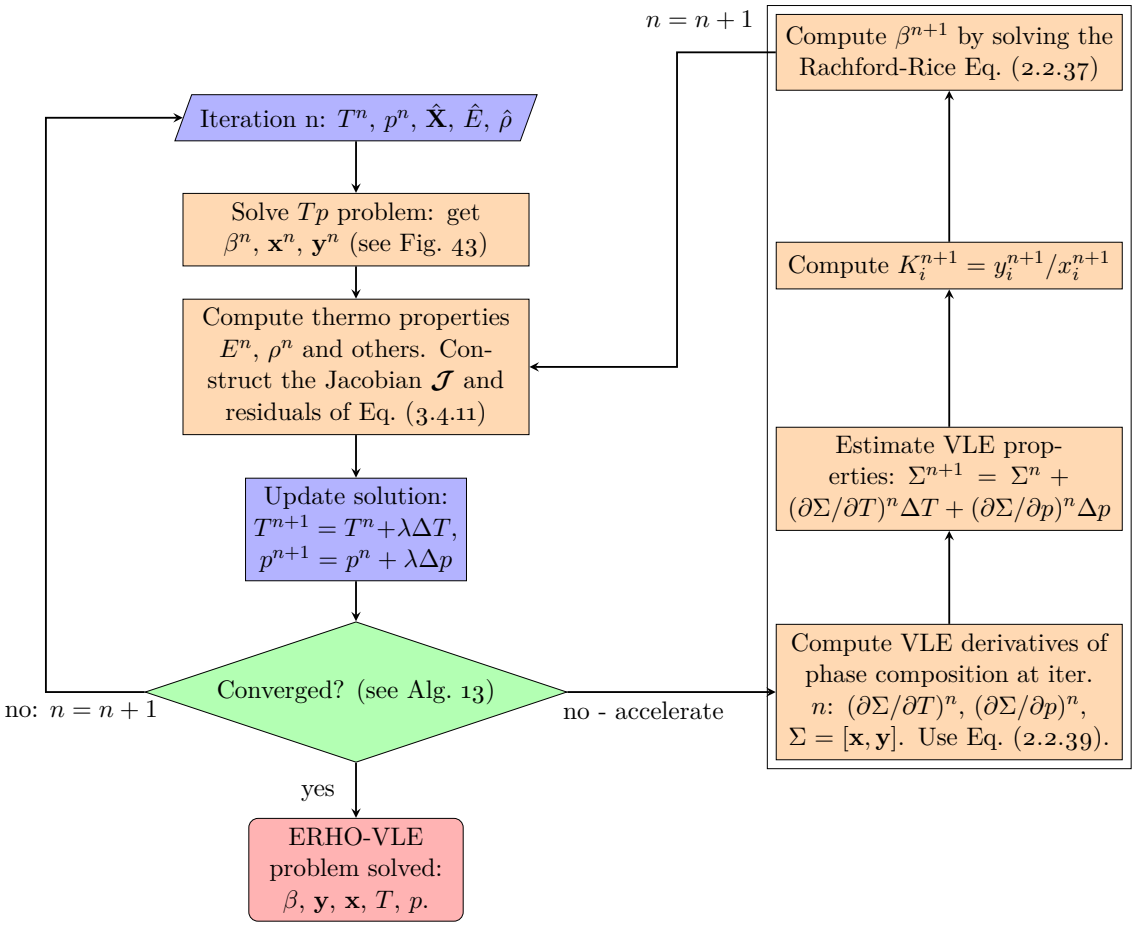

Figure 44: Speed-up mechanism for the ERHO problem.

behind this concept. With the solution at the current iteration n, all the steps to compute the Jacobian and the residuals of Eq. (3.4.11) as well as perform the update are illustrated on the left column. This algorithm is discussed in details in Algorithm 13. In this procedure, the most expensive part is certainly the internal solution of the Tp problem that needs to be performed for each update in temperature and pressure to verify if the current solution is a VLE state or not. This step is that of Fig. 43, hence very expensive because it involves the call to the SSI method and the TPD method at each sub-iteration. In order to mitigate this issue, an acceleration procedure can be embedded into the algorithm. This is illustrated in the right column of Fig. 44. With the knowledge of the solution at time n and the increments ΔT and Δp, the derivatives of the VLE composition can be estimated:

$(\partial \mathbf{y}/\partial T)$, $(\partial \mathbf{y}/\partial p)$, $(\partial \mathbf{x}/\partial T)$, $(\partial \mathbf{x}/\partial p)$ using all the analytical formulation developed for Eq. (2.2.39). Next, if the sum of both estimated vectors is above a certain threshold fixed to $1e-7$ (to ensure that VLE effectively exists), the K_i coefficients can be estimated as $K_i^{n+1} = y_i^{n+1}/x_i^{n+1}$ and therefore β^{n+1} can be obtained by solving the non-linear Rachford-Rice equation of Eq. (2.2.37). In this way, a new estimated VLE information is available, bypassing completely a new full solution of the Tp problem.

Certainly, different many alternatives are possible. For example all the VLE properties can be estimated at once using the derivatives of Eq. (2.2.39). In this way, the solution of Eq. (2.2.37) is also avoided, however an inconsistency between the VLE properties is likely to be introduced, which can make the overall method unstable. The present way was found to be the most stable.

In addition, since the acceleration procedure is essentially a VLE prediction through a linearization of the solution at iteration n, calling too many consecutive times the acceleration step within the algorithm may still result into an unstable route. For this reason, it is suggested to call this acceleration when the overall algorithm error is below a certain threshold ϵ_{acc} and no more than N_{acc} consecutive times within the main loop. If either of the two conditions at the current iteration are not satisfied, the classical, non-accelerated algorithm is suggested to be followed. In this work, these two routes have been used in an hybrid sense, where $\epsilon_{acc} \leq 1e7$ (in the form of ABS(ΔT)+ABS(Δp) - see Algorithm 13) or less and N_{acc} between 5 and 10 were found to be a good compromise. Finally, it is recommended to normalize the VLE compositions before computing K_i^{n+1}, that is $y_i^{n+1} = y_i^{n+1}/\text{SUM}(\mathbf{y}^{\text{n+1}})$ and $x_i^{n+1} = x_i^{n+1}/\text{SUM}(\mathbf{x}^{\text{n+1}})$. Some additional information regarding the performances of this method are given in Sec. 3.5.3.

3.4.4 Adiabatic and isochoric mixing models

Adiabatic and isochoric mixing models have been already used by Ma et *al.* [109] to highlight the effect of the numerical diffusion over the physical diffusion on the real mixing, however these two models were again used always without the VLE model. Although the adiabatic model was adapted to VLE by [168], the present work extends the isochoric model to

incorporate multi-phase effects as well. For a binary mixture, the general definitions of the adiabatic and isochoric mixing models write:

$$H(T_{mix}, p, \mathbf{X}, \beta) = X_1 H_1(T_1, p) + X_2 H_2(T_2, p)\,, \tag{3.4.13}$$

$$V(T_{mix}, p, \mathbf{X}, \beta) = X_1 V_1(T_1, p) + X_2 V_2(T_2, p)\,. \tag{3.4.14}$$

In these models, the inputs are the 2 species and their respective temperatures T_1 and T_2 at which they mix. Pressure is assumed to be fixed for both models. In both cases, the mixture molar enthalpy and molar volume are weighted with the respective species molar enthalpies and volumes at their initial temperatures by using the molar fractions as weights. Thus, the right-hand side of Eqs. (3.4.13)–(3.4.14) are known from the initial conditions and the goal is to find the mixture final temperature T_{mix} that establishes at the end of the mixing process. This temperature, can be found by assuming that VLE forms or not. If VLE is removed from the models, T_{mix} is found by an iterative procedure, similar to the $p\rho$ problem in Algorithm 12 for a single phase mixture, where $V(T_{mix}, p, \mathbf{X}) = M(\mathbf{X})/\rho(T_{mix}, p, \mathbf{X})$ and $H(T_{mix}, p, \mathbf{X}) = H^{ig}(T_{mix}, \mathbf{X}) + \Delta H(T_{mix}, p, \mathbf{X})$ are used as objective functions.
On the other hand, if VLE is also allowed, the objective functions change to $H(T_{mix}, p, \mathbf{X}, \beta) = E + p/\rho$ and $V(T_{mix}, p, \mathbf{X}, \beta) = M/\rho$ where E and ρ are computed from Eqs. (2.2.34)–(2.2.35). This calculation is obviously more expensive since it requires the solution of a Tp problem in the innermost loop.

3.4.5 Numerical computation of multi-phase thermodynamic variables

In Sec. 2.2.2.2–2.2.2.4 the analytical derivation of all thermodynamic properties in presence of VLE was discussed. In this section, the numerical determination of such derivatives is presented with the scope to provide an alternative way of computing some of them and compare later with the analytical method. The basic idea is that properties that involve derivatives in the VLE region must account for the variations of β and all other related quantities (for example in pressure and temperature). Failure to do so would result in an approximate evaluation of such derivative with an associated error. One example is the calculation of $C_p = (\partial H/\partial T)_{p,\mathbf{X}}$: in case H is also a function of β, the only possibility is to perturb the temperature and maintain the pressure constant in order to construct the

perturbed states. These can be later on used to compute the derivative with central or "upwind" differences in the thermodynamic space. For example once the VLE problem is solved at T, p, $\mathbf{X}$ specified and $\beta \in (0,1)$, temperature can be perturbed such that $H^+(T + \Delta T_\epsilon, p, \mathbf{X}, \beta^+)$ and $H^-(T - \Delta T_\epsilon, p, \mathbf{X}, \beta^-)$ are found and similarly for other properties. This means that additional Tp problems need to be solved in series. Sometimes one can use one-sided (i.e. upwind) derivatives, which would reduce the number of Tp problems by half, given that E and H are already known at the end of the time step integration and for example one can compute $C_p = (H^+ - H)/\Delta T_\epsilon$, however this would reduce the accuracy of the results. Regardless, this choice must be selected near phase boundaries, where increment (positive or negative) in temperature or pressure can lead the system outside the two phase region, making the derivative calculation effectively wrong since the dependency of E and H on β is lost. To avoid this, a specific phase sensor can be used in the form:

$$S_\phi = \frac{\left| \dfrac{\phi^+ - \phi}{\Delta^+} - \dfrac{\phi - \phi^-}{|\Delta^-|} \right|}{0.5(\Delta^+ - \Delta^-)}, \tag{3.4.15}$$

Where ϕ is intended to be the generic variable being perturbed (for example H) and $\Delta^{+/-}$ refers to the pressure/temperature algebraic increment. The criterion is that if $\mathrm{MAX}(S_H, S_E) > \epsilon_s$, one sided derivatives are used, otherwise central derivatives are used. In addition, if one sided derivatives are to be used, if the current perturbed value of the phase fraction $\beta^{+/-}$ is greater than the initial value β, one sided derivatives in the form $(\phi - \phi^-)/(|\Delta^-|)$ are used, otherwise the form $(\phi^+ - \phi)/(\Delta^+)$ is used.

Similarly to C_p, derivatives like $(\partial\rho/\partial T)_{p,\mathbf{X}} \approx (\rho^+ - \rho^-)/\Delta T_\epsilon$ and $(\partial p/\partial\rho)_{T,\mathbf{X}} \approx 1/(\rho^+ - \rho^-)/\Delta p_\epsilon$ are obtained in the same way by exploiting the perturbed Tp problems. In this way isobaric expansivity α_p and isothermal compressibility κ_T of Eq. (2.2.21) are calculated. Isentropic compressibility is then readily computed using Eq. (2.2.22). The derivative $(\partial p/\partial T)_{\rho,\mathbf{X}}$ is computed by exploiting the dependency between α_p and $(\partial p/\partial\rho)_{T,\mathbf{X}}$ in Eq. (2.2.21) which are already known. This avoids to solve additional Tp problems in which temperature and pressure are varied at the same time with the constraint to keep the density the same. For the same reason, calculation of C_v is done by using the link between C_p, α_p and κ_T of Eq. (2.2.25). Once C_p and C_v are computed, the two phase mixture

$\gamma = C_p/C_v$ is also computed. For the numerical experiments later showed in this work (or the simulations showed in [226]), the values $\epsilon_s = 0.02$, $\Delta T_\epsilon = 0.001\,\mathrm{K}$ and $\Delta p_\epsilon = 0.5\,\mathrm{Pa}$ were used.

In a similar manner, all the temperature and pressure derivatives in each phase can be computed. Note that mole fraction based numerical derivatives are intrinsically wrong because a perturbation on the i-th species mole fraction: $X_i + \Delta X_\epsilon$ would necessarily result into a perturbation of all other mole fractions to maintain the unity constraint on their sum. As a result, derivatives like $(\partial(\cdot)/\partial X_i)_{\mathbf{X}_i}$ would not be rigorously satisfied. Algorithm 14 reports the procedure to compute the thermodynamic variables using numerical derivatives. A note must be made on the calculation of the speed of sound. Other approximate methods are available, such as that of Lamarre et *al.* [94]:

$$c^2 = \frac{1}{\dfrac{\beta^2\gamma}{c^{2,V}} + \dfrac{(1-\beta)^2}{c^{2,L}} + \beta(1-\beta)\rho^L\left(\dfrac{1}{p} + \kappa_T^L\right)}\,, \tag{3.4.16}$$

where $c^{2,V}$ and $c^{2,L}$ are the speed of sounds of the vapor and liquid phases, respectively, computed using Eq. (2.2.20), ρ^L is the liquid phase density and κ_T^L is the isothermal compressibility of the liquid phase computed using Eq. (2.2.21). The second method is that of Wood et *al.* [242]:

$$c^2 = \frac{1}{\rho\left(\dfrac{1-\beta}{\rho^L c^{2,L}} + \dfrac{\beta}{\rho^V c^{2,V}}\right)}\,. \tag{3.4.17}$$

Sometimes, due to the calculation of numerical derivatives, the approach of c with Eq. (2.2.23) may fail because the value of κ_s is physically very small and therefore is very sensitive to numerical errors. When the approach of Eq. (2.2.23) fails, the second approach of Eq. (3.4.16) can be used and if the latter has also issues, the approach of Eq. (3.4.17) can be used. Although very rarely observed, the latter situation can still happen and therefore the aforementioned methods are implemented in series to improve the overall process robustness [226]. If any of Eq. (2.2.25) or Eq. (3.4.17) are used, isentropic compressibility κ_s is computed by inversion of Eq. (2.2.23) and isothermal compressibility κ_T is computed using Eq. (2.2.25), using the previously computed values of C_p and α_p.

Table 15: Mixture properties for CH_4 and H_2S.

species	$T_c\,(K)$	$p_c\,(bar)$	$\omega\,(-)$	$MW\,(kg/kmol)$	k_{ij}
CH_4	190.6	46	0.011	16	0.0 0.083
H_2S	373.2	89.4	0.097	34	0.083 0.0

3.5 Validation of the VLE framework

In this section, different zero-dimensional (0D) test-cases for the thermodynamics only are used to verify and validate the calculation of the VLE for a generic multi-component mixture. Particularly the attention is given to the TPD method and the solution of the PRHO and ERHO problems. The last two examples are meant to demonstrate the fact that erroneous thermodynamic states are going to be found if an initial state that belongs to a VLE condition is treated as a non-VLE state. Since this issue is completely separate from that introduced by the occurrence of pressure oscillations discussed in Sec. 3.2.2, the conclusions is that the solution of RG mixtures can suffer two errors: one purely numerical and the other purely physical in nature. Both of them can lead to erroneous results and therefore they need to be addressed separately [226]. More results on the 0D VLE testcases, as well as analyses of thermodynamic variables are provided in Chap. 4.

3.5.1 TPD stability analysis method

The Tangent Plane Distance (TPD) analysis is a key tool for the Tp solver. The validation of the TPD is performed against the data published by Qiu et *al.* [170]. First, consider a mixture of CH_4 (methane) and H_2S (hydrogen sulfide). In Tab. 15, the relevant parameters used for the mixture are reported. Note that the interaction parameters k_{ij} have been tuned for PR EoS specifically [170]. The first test is conducted on the TPD function trend for an equi-molar $\mathbf{X} = [0.5, 0.5]$ mixture (called *feed*) at $T = 190.0\,\mathrm{K}$, $p = 4.05\,\mathrm{MPa}$ conditions. The mixing rule of Van der Waals (MR1 in Tab. 3) is used for all the EoS to be consistent with the published data. By varying the methane trial molar composition, (which is ζ_i in Eq. (3.4.4)) the TPD is evaluated using different EoS models. The result is shown in Fig. 45(a).

Table 16: Properties for (A) and (B) mixtures.

species	$T_c\,(K)$	$p_c\,(bar)$	$\omega\,(-)$	$MW\,(kg/kmol)$	$k_{i,CH4}$	k_{i,CO_2}	k_{i,H_2S}
CH_4	190.6	46	0.008	16	0.0	0.0	0.0
H_2S	373.2	89.4	0.1	34	$0.0.0755^B$	0.0999^B	0.0
CO_2	304.2	73.8	0.225	44	0.095^A, 0.1005^B	0.0	0.0
H_2O	647.3	220.5	0.344	18	0.4928	0.0	0.04

First, note that the best agreement is found with PR EoS. This is not surprising as the interaction parameters used are fixed for all the EoS, however they are tuned for PR. Nevertheless the trend is well captured by all the EoS. This TPD is constructed in the following way: first the trial feed is assumed to be liquid: $\boldsymbol{\zeta} = \mathbf{x}$ and $\text{TPD}^{*,L}$ is computed according to Eq. (3.4.5). It can be easily shown that this corresponds to the left branch of Fig. 45(a). Similarly, $\text{TPD}^{*,V}$ is computed with $\boldsymbol{\zeta} = \mathbf{y}$. It can be proven that this corresponds to the right branch of Fig. 45(b). Next, the TPD curve of Fig. 45(a) is essentially constructed as MIN($\text{TPD}^{*,L}$,$\text{TPD}^{*,V}$) which has 5 stationary points: 2 maxima and 3 minima. The largest maxima occurs at TPD= 0.0 and coincides with methane trial mole fraction of 0.5 as the feed, that is $\boldsymbol{\zeta} = \mathbf{X}$. This is the so-called trivial solution, where the trial composition is equal to the feed composition, however it does not represent the solution to the problem because it is not the smallest value in the picture. In fact, the other 3 minima represent the conditions at which the TPD does not provide a trivial solution as it is negative. Those minima correspond to the solution of the phase split, meaning that the mixture tends to form a multi-phase solution at a lower Gibbs free energy. The smallest value is the actual solution. For the present situation the lowest peak corresponds to the liquid branch of around $\zeta_{\text{CH}_4} = x_{\text{CH}_4} \sim 0.95$, from which the corresponding second phase composition y_{CH_4} can be computed from Eqs. (3.4.2)–(3.4.3) and Eq. (2.2.37) iteratively. A second example is provided for the same mixture by computing the (normalized) Gibbs free energy of mixing $\Delta G_{mix}/RuT$. The initial and final states for this calculation are: 1) the 2 species considered separately and 2) the 2 species considered together in the mixture, which is considered *single phase* (i.e. either liquid or gas). This is plotted against the feed (actual)

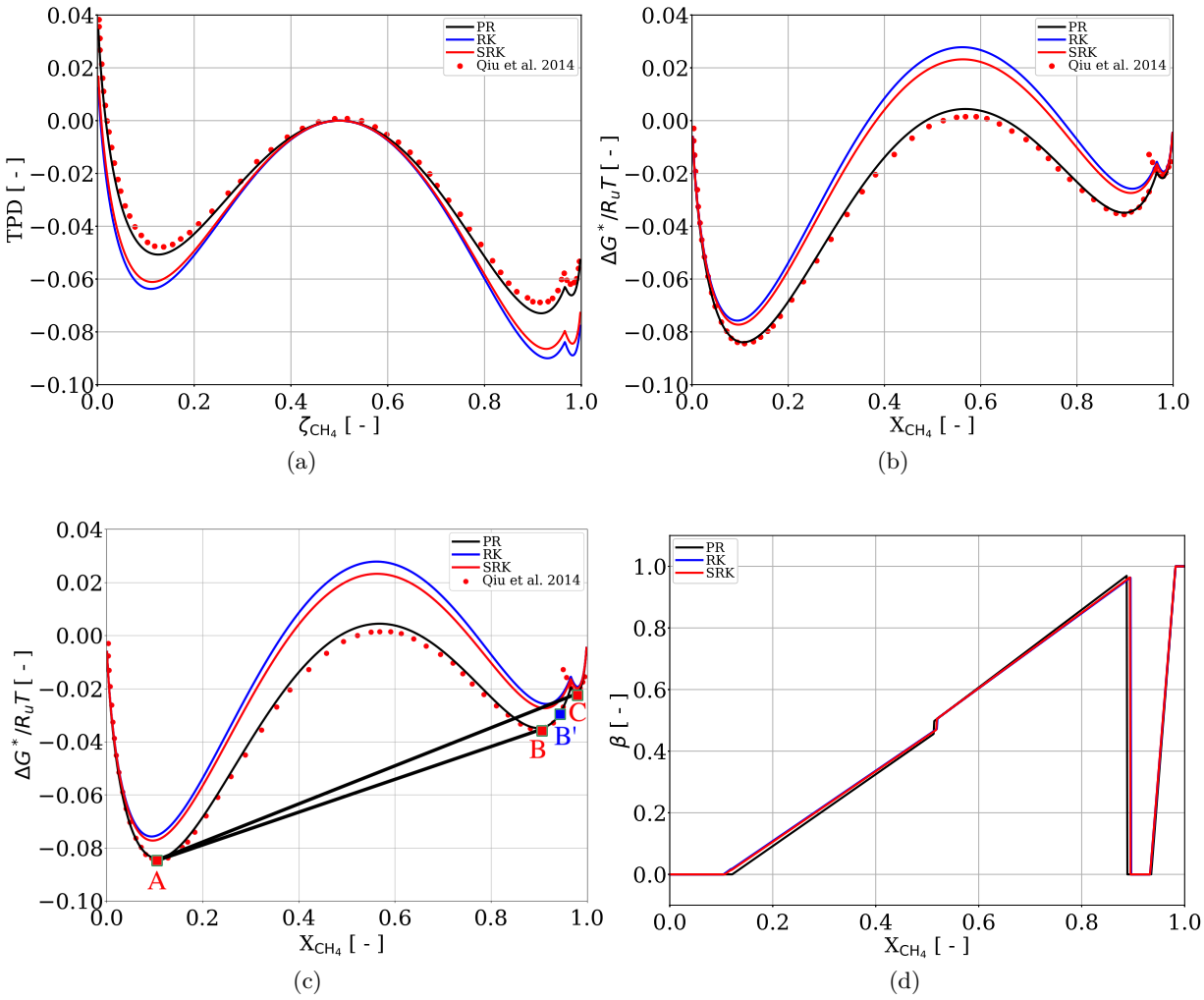

Figure 45: TPD analysis for the CH_4/H_2S mixture. a) TPD function for $\mathbf{X} = [0.5, 0.5]$ composition, b) Normalized Gibbs energy variation as the mixture composition is varied, c) same as b) with some reference lines to help the discussion in the text and d) trend of the phase fraction β.

CH_4 mole fraction in Fig. 45(b) and (c) with some reference lines to help the following discussion. Again the best agreement is obtained for PR EoS for the same reason. This plot represents the Gibbs energy variation from the initial state (two species separated) to the final state (single-phase mixture) as the amount of methane is changed. At each point of this curve, a tangent line can be defined, however a TPD line is the loci that connects the possible minima of this function. There are 2 possible tangent planes connecting all the minimum Gibbs values located at A,B and C. Since the plane connecting A with B along the liquid branch shows a Gibbs energy value which is above it, the mixture is unstable if considered liquid only and therefore it splits in a liquid-liquid way. The previous example of the TPD for $\mathbf{X} = [0.5, 0.5]$ in Fig. 45(a) is contained in this loci. On the other hand, the plane connecting A with C is a fake VLE because there is a region (around B) where the Gibbs energy is below the plane, which would indicate stability. Similar discussion follows for the branch between B and C. Point B cannot connect C without crossing ΔG_{mix}, therefore a specific point B' must exist in between B and C such that by connecting B' with C, the ΔG_{mix} lies completely above the plane, indicating phase instability and therefore split. To summarize: a plot of the ΔG_{mix} of mixing between state 1) species considered separately and 2) species considered in the mixture, where mixture is always assumed single phase indicates that: the region where $X_{\mathrm{CH_4}} \in [0, A]$ will have a stable liquid mixture, the region where $X_{\mathrm{CH_4}} \in [A, B]$ has an unstable liquid mixture, which will split in 2 phases (liquid+liquid, LLE), the region where $X_{\mathrm{CH_4}} \in [B, B']$ will have a stable liquid mixture, the region where $X_{\mathrm{CH_4}} \in [B', C]$ will have both (single) gas and liquid unstable phases, therefore it will split in a gas+liquid (VLE) mixture and the region where $X_{\mathrm{CH_4}} \in [C, 1]$ will have a stable gas phase mixture. This behavior is readily observable in the trend of β provided in Fig. 45(d), where the locations A,B,B' and C are directly translated in a specific behavior of phase stability (β zero or one) or instability (β between zero and one). Note that the central region where $\beta \in (0, 1)$ is actually a liquid-liquid equilibrium for the reasons explained above. Another validation is performed in a point-wise manner for given mixtures and conditions, still reported in [170]. Basically, equilibrium calculations using the Tp and corresponding β are computed. Two types of mixtures are considered: (A) a

Table 17: Results for (A) and (B) mixtures.

mixture	T [K]	p [bar]	composition ($\mathbf{X}$)	stable? (Y/N)	β - PR-MR1	β Qiu et *al.* [170]
(A)	220.0	60.8	$(0.9, 0.1)$	Y (gas)	1.0	1.0
(A)	220.0	60.8	$(0.8, 0.2)$	N	0.9710	0.9701
(A)	220.0	60.8	$(0.7, 0.3)$	N	0.5708	0.5695
(A)	220.0	60.8	$(0.57, 0.43)$	N	0.0505	0.0488
(A)	220.0	60.8	$(0.4, 0.6)$	Y (liquid)	0.0	0.0
(B)	310.95	76.0	$(0.1488, 0.2991,$ $0.0494, 0.5027)$	N	0.4959	0.504
(B)	380.35	129.3	$(0.1496, 0.3009,$ $0.0498, 0.4997)$	N	0.499	0.4936

CH_4-CO_2 mixture and a CH_4-CO_2-H_2S-H_2O mixture. The relevant parameters used for these tests are summarized in Tab. 16. The results of phase-stability and phase-split are shown in Tab. 17. Results are satisfactory and thus provide the conclusion of the correct implementation of the Tp solver with phase stability (TPD) analysis.

3.5.2 Gibbs free energy for a mixture that forms VLE

A second example to provide validation of the VLE framework is given by Fig. 46 already used in Sec. 2.2.2 for model discussion purposes only. Figure 46(a) shows the isotherm VLE diagram for the N_2/C_6H_{14} mixture at $T = 377.9$ K. The VLE curve in black represents the loci of the point where the transition between the single-phase and the multi-phase conditions occur. Inside the VLE curve (dome), two phase condition exists, that is $\beta \in (0, 1)$, whereas outside the VLE dome a single phase condition exists, that is $\beta = 0$ or $\beta = 1$ for liquid and vapor, respectively. A reference isobar is taken at 10 MPa which intersects the VLE curve at two points: the dew point (transition from liquid to VLE) and the bubble point (transition from VLE to vapor). Along this line, the compressibility factor Z and the Gibbs free energy are computed according to the analytic model discussed in Sec. 2.2.2 with and without VLE. Figure 46(b) shows the diagram of the compressibility factor along the reference isobaric line. While the VLE and the non-VLE solutions agree identically outside the VLE dome, they show disagreement within the VLE region due to the effect that β has

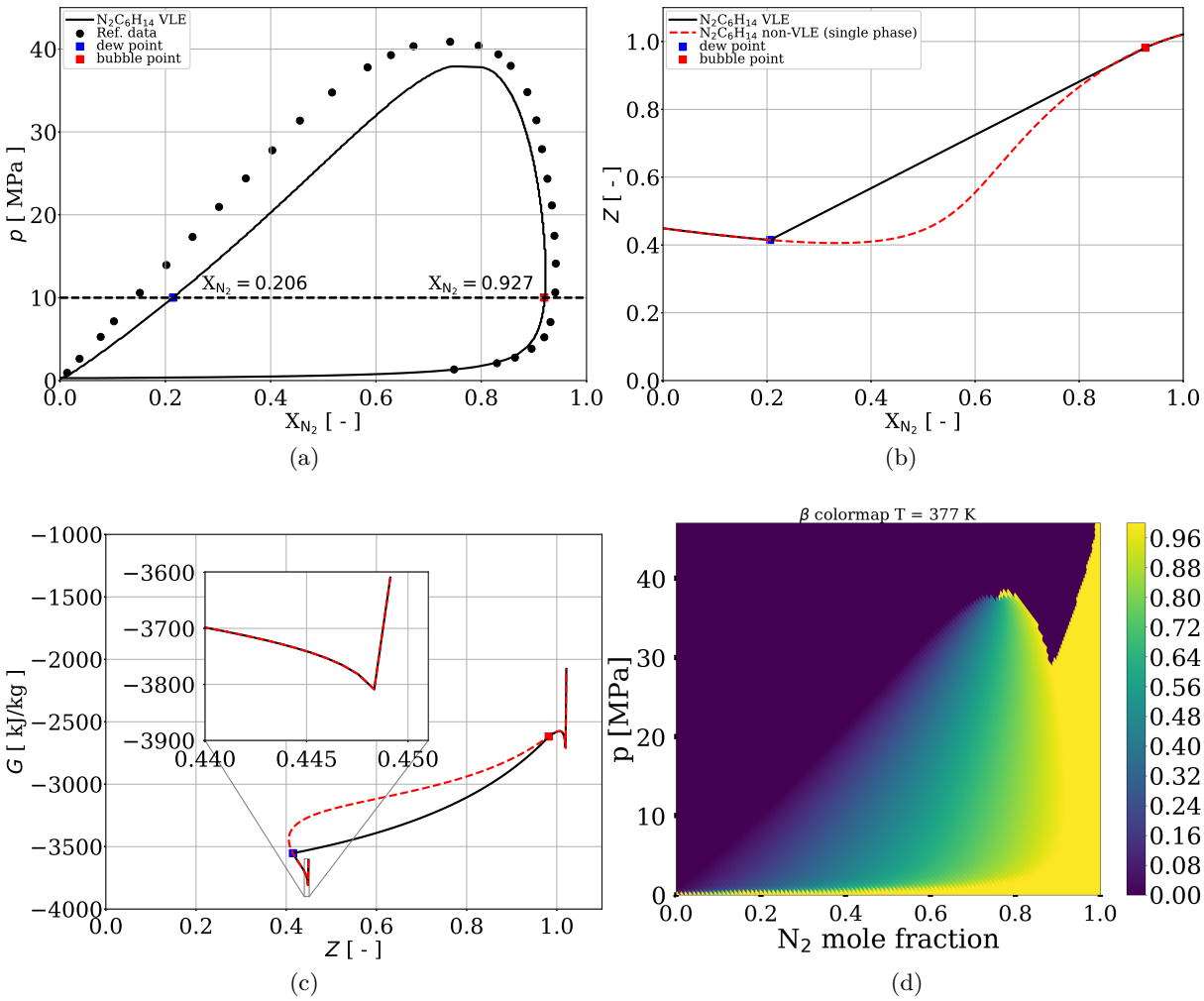

Figure 46: a) VLE diagram of the $N_2C_6H_{14}$ mixture for various iso-therms at different pressures. Reference dotted data is taken from [45]. Horizontal black dashed line indicates the iso-baric reference line at 10 MPa. b) Compressibility factor plotted along the iso-baric line of 10 MPa as a function of the nitrogen mole fraction. The result is showed with and without the VLE model. c) Mixture Gibbs free energy as function of the compressibility factor along the same iso-baric reference line of 10 MPa computed with and without the VLE model. d) Phase fraction (β) colormap diagram of the mixture VLE loci at 377 K.

on the definition of density through Eq. (2.2.34), and therefore Z through Eq. (2.2.3). As one can already guess, this difference within the VLE region will have an impact on all the rest of the thermodynamic properties. This will be the subject of Chap. 4.

Next, if one plots the Gibbs free energy along the curve of Fig. 46(b), the picture of Fig. 46(c) is obtained. As desired and expected, the Gibbs free energies match outside the VLE dome (note the zoomed inset), while inside the VLE dome the one computed with the VLE model always lies below the corresponding value computed with the non-VLE (single-phase) model. This result indicates not only the correctness of the results, but also indicates that the most stable solution, *i.e.*the VLE solution needs to be chosen in this situation. As a consequence, the consistent thermodynamic model for all the thermodynamic properties discussed in Sec. 2.2.2 needs to be followed.

Another interesting point to add is the relevance of the definition of β outside the VLE dome. In analogy with a single-component case, there is no real phase distinction in the super-critical regime. The same happens for mixtures. The liquid $\beta = 0$ and the vapor $\beta = 1$ regions in Fig. 46 must merge at some location above the VLE dome, however there is no real criterion for it. For this work, the criterion of $Z^* = \Omega B_m p / R_u T$ is chosen. If the local compressibility is $Z > Z^*$, the mixture is considered in its vapor-like state and therefore "labeled" with $\beta = 1$, otherwise it is declared in its pseudo-liquid state and $\beta = 0$. Here $\Omega = 2.5$ has been chosen. Figure 46(d) shows the colormap of the β field corresponding to Fig. 46(a). The color yellow indicates the $\beta = 1$ state, while the color purple indicates the $\beta = 0$ state. It should be noted that this distinction would not make any difference in the results, nor the conclusions. However a more rigorous criterion, perhaps based on the Widom line criterion can be added to the list of future work.

3.5.3 Solution of the ERHO problem

In this section, the solution of the ERHO problem is discussed. In this case, the N_2/CH_4 mixture is considered, for which the VLE diagram is reported in Fig. 47. Reference data is taken from [24]. If the reference composition of $\mathbf{X} = [0.5, 0.5]$ is considered, two reference thermodynamic states are identified, namely point A at $T = 150$ K, $p = 3$ MPa and

Table 18: Relevant thermodynamic mixture properties for the N_2/CH_4 VLE diagram of Fig. 47 at the two reference points A and B.

	T [K]	p [MPa]	Z [-]	ρ [kg/m^3]	e [kJ/kg]	β [-]
Point A	150.0	3.0	0.395	134.06	-2070.491	0.538
Point B	150.0	4.5	0.187	424.74	-2130.904	0.0

point B at $T = 150$ K, $p = 4.5$ MPa, respectively. Clearly, point A lies inside the VLE dome, whereas point B lies outside. With the construction of Fig. 47 all the properties are known, specifically density and internal energy are known. These are reported in Tab. 18 along with other relevant properties. Starting from the known values of density and

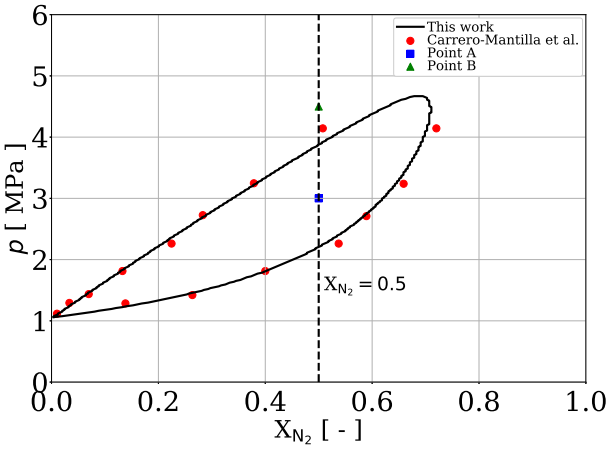

Figure 47: VLE diagram of N_2/CH_4 at fixed temperature of 150 K for a range of pressures and amount of nitrogen in the mixture.

internal energy, the corresponding ERHO problems can be run for both points A and B to recover the initial conditions of T and p. The algorithms are started from $T_0 = 420$ K and $p_0 = 9$ MPa, respectively to mimic the solution of a condition that is very far from the target state. Figure 48 shows the residuals trajectories of a) internal energy and density for point A. In the picture, four trajectories are represented for the ERHO problem: i) the analytical model with VLE, ii) the numerical model with VLE, iii) the analytical model with accelerated strategy with VLE and iv) the non-VLE model treated as single phase

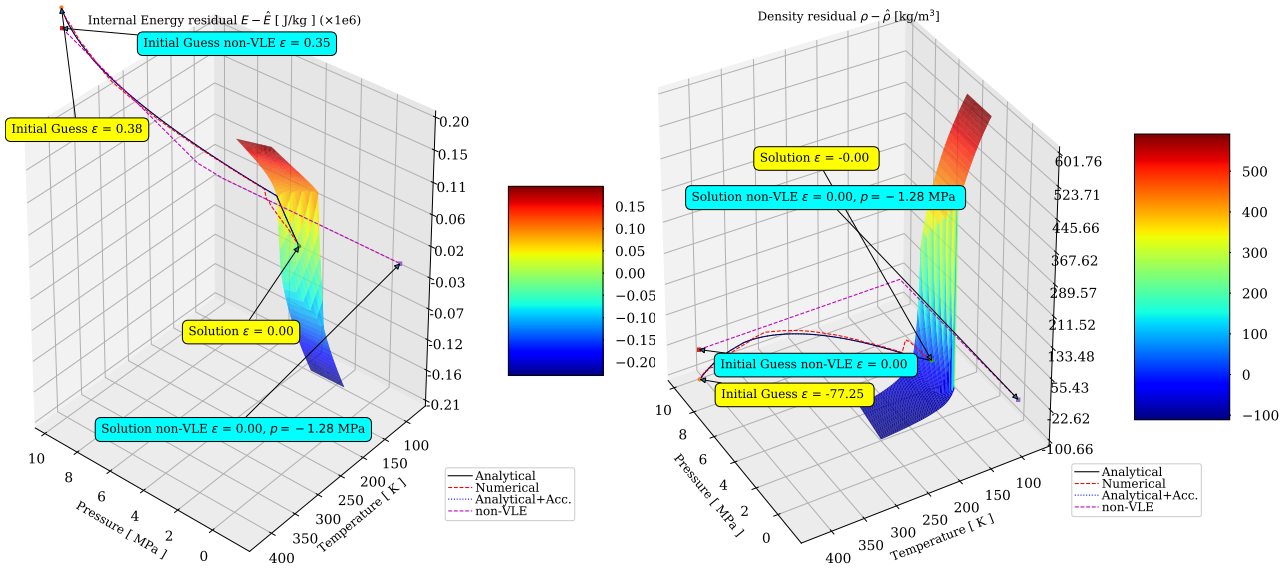

(a) Internal energy residual - Point A

(b) Density residual - Point A

Figure 48: a) Internal energy and b) density residuals 3D trajectories in the thermodynamic space as the ERHO algorithm advances iterations using different models for point A.

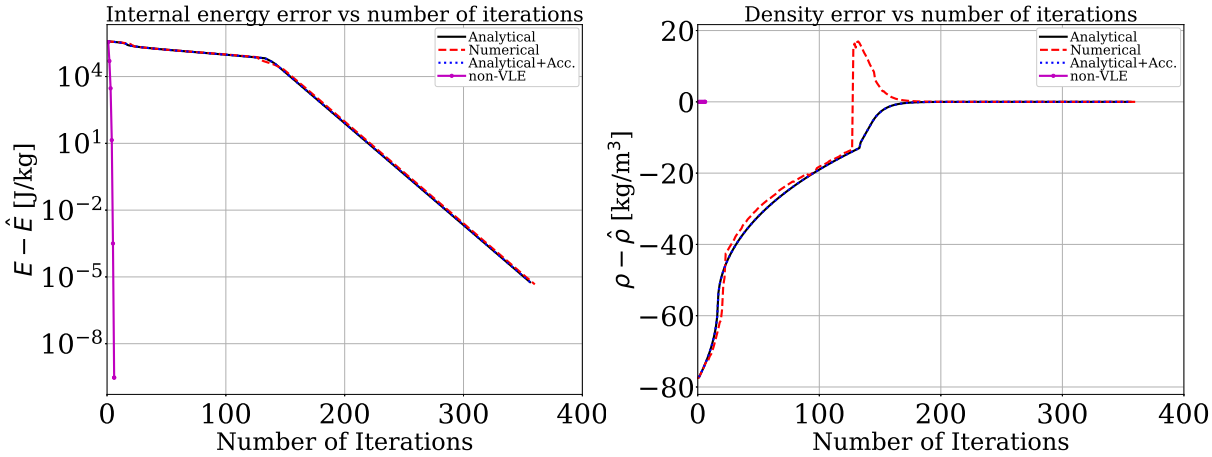

(a)

(b)

Figure 49: a) Internal energy and b) density residuals as a function of the number of iterations for the different models for point A.

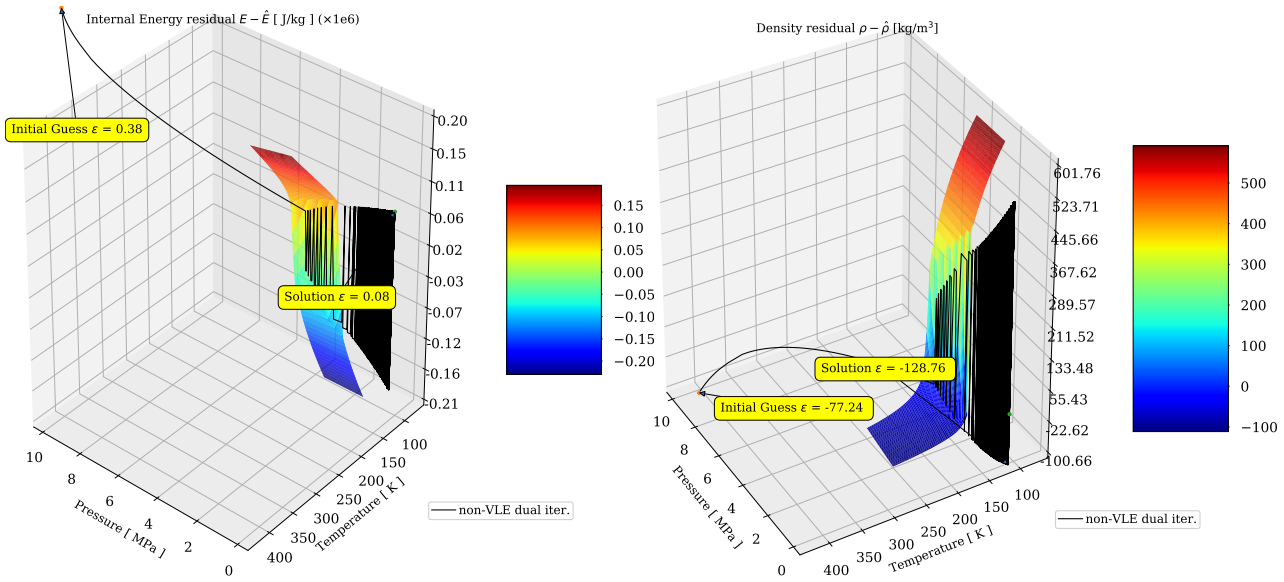

(a) Internal energy residual - point A

(b) Density residual - point B

Figure 50: a) Internal energy and b) density residuals 3D trajectories in the thermodynamic space as the ERHO algorithm advances iterations using the dual-variable algorithm for point A when the non-VLE model is forced to work.

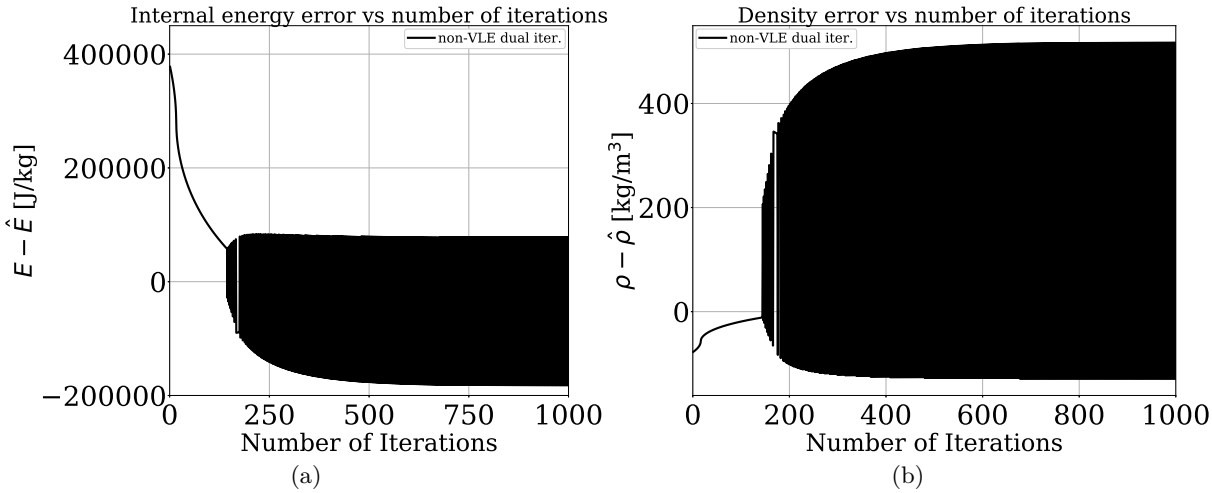

(a)

(b)

Figure 51: a) Internal energy and b) density residuals as a function of the number of iterations using the dual-variable algorithm for point A when the non-VLE model is forced to work.

algorithm. All of the above have been discussed in Sec. 3.4.3. To facilitate the comparison, the solution is placed on the respective residual surface that is drawn in its neighborhood. Based on these pictures, the following conclusions can be drawn:

- there is not much difference in terms of trajectory between the analytical model and the analytical model with acceleration technique, however this does not mean that they converge with the same speed. More insights are given later on this;
- the numerical model shows some differences in the residual trajectories. There are also performance differences which are discussed more next;
- while both the numerical and the analytical models treated with VLE thermodynamics show convergence, substantial difference is observed in the non-VLE model treated as single-variable algorithm. First, the initial residual in internal energy is different because for fixed $\hat{E}$, the corresponding value of E is different and so the residual. This is not observed in the density residual because density is not treated in the single-variable iteration, hence it remains fixed at the known state: $\rho \equiv \hat{\rho}$ at each iteration, because the iteration is conducted on temperature only. For this model, both final states show convergence, however while the temperature convergences to a somewhat physical value ($T \sim 96$ K in Fig. 48(a)), the corresponding pressure computed with Eq. (2.2.67) provides a negative value. This indicates that the non-VLE model as a single-variable iteration finds a solution as per the residual minimization, however that solution is wrong and nonphysical. Note that the pressure for the present case is maintained fixed at the initial value p_0 throughout the algorithm iteration because pressure is not involved. After the internal energy residual is minimized, a sudden jump is observed in the trajectory in Fig. 48(b) due to the application of Eq. (2.2.67).

The above arguments are confirmed by the plots in Fig. 49.

A test about the performances of the non-VLE solution algorithm treated as a double-iteration method is illustrated in Fig. 50 and Fig. 51. In contrast to the single-iteration strategy, this method does not show convergence at all, and instead keeps on oscillating around the minimum residual targets. This strategy would simply recover the last state

obtained when the maximum number of iterations is hit, obviously still providing an erroneous solution. To complete the discussion, Fig. 52 and Fig. 53 show the same test

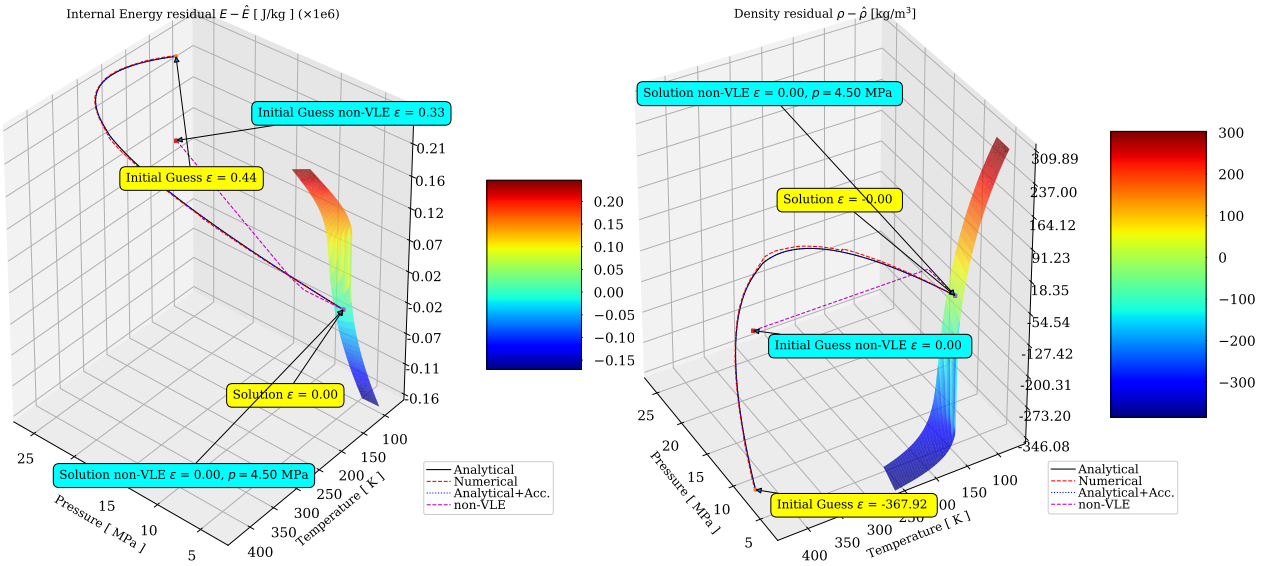

(a) Internal energy residual - point B

(b) Density residual - point B

Figure 52: a) Internal energy and b) density residuals 3D trajectories in the thermodynamic space as the ERHO algorithm advances iterations using different models for point B.

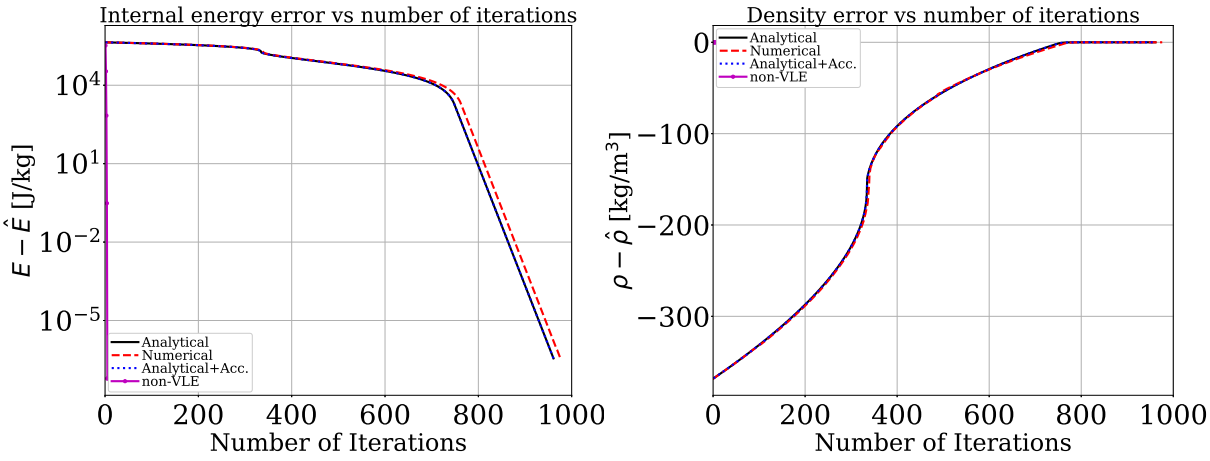

(a)

(b)

Figure 53: a) Internal energy and b) density residuals as a function of the number of iterations for the different models for point B.

conducted on point B starting from the same initial guess as point A. It is interesting to

realize that the two residuals at the first iteration are still different between the single- and dual-variable algorithms, even if the initial point is a non-VLE state. The reason is due to the difference in the functional dependency of the internal energy and density in both methods. While $\rho = \hat{\rho}$ and $E = E(\hat{\rho}, T, \mathbf{X})$ is the functional dependency in the single-variable iteration, $\rho = \rho(T, p, \mathbf{X})$ and $E = E(\rho, T, \mathbf{X})$ is the functional dependency in the dual-variable iteration. For this reason, even at the first iteration, where T and p are the same in both algorithms, ρ is different and hence the internal energy residual is different too. Nevertheless all the methods converge to the same, correct solution. It is important to underline the fact that in this case, the difference in the number of iterations between the single- and the dual- variable iteration methods is huge as shown in Fig. 53(a), making the use of the dual-variable iteration a waste of computational resources. However, one should keep in mind that as the dual-variable iteration method is mandatory in case of VLE occurs, its applicability is strictly tied to whether or not the final state (or even the states that occur in between the initial guess and the final solution) are VLE states or not. In fact, as it has been proven by the previous discussion that the single-variable approach would fail to produce correct results in case VLE appears, it is extremely difficult to know exactly when to use it during a VLE calculation because the discriminant condition is exactly the subject of the algorithm calculation and therefore it is unknown a-priori. For example, one can use the previous knowledge of T and p and β to guess whether the new values of E and ρ pertain to a VLE state or not by setting a threshold in T above which the non-VLE solution is automatically assumed. However, this choice is somewhat arbitrary and can produce errors if it fails to be satisfied during the computation. Another alternative is to exploit the 0D computations as in Fig. 47 to compute and store a-priori the values of E and ρ and compare these to the actual values $\hat{E}$ and $\hat{\rho}$ at the beginning of the ERHO problem to select which algorithm to use. However this approach has also its own limitations. First, pre-computing the values of E and ρ from Fig. 47 is not an easy task as in that figure T is maintained constant as parameter. Varying both p and T within a certain range of interest would still represent a non-trivial task to perform, especially due to the resolution of both variables which can represent another sensible parameter for the simulation.

Another limitation is that this analysis would be relatively simple for two components. If more than two components are of interest, the number of independent variable increases with an associated difficulty to a) produce the pre-computed results within a certain thermodynamic region and b) access these pre-computed data during the simulation. While all these argument can be important hints for future work investigations, in the present work the choice is made upfront once by selecting whether the VLE model is used or not. If the VLE thermodynamics is chosen, the double-iteration algorithm is used everywhere unless a single-component state is detected. If the non-VLE method is chosen instead, the single-variable iteration method is used everywhere. In order to mitigate the effect of slowness of the double iteration method in the regions where it is not really needed, an investigation on the parameters that rule the algorithm is made. Table 19 shows the results obtained for the ERHO problem conducted on point A. The results are shown in terms of number of iterations and run-time execution for the various double-variable iteration methods. The initial condition is still chosen to be 420 K and 9 MPa respectively and an overall tolerance method of 1e-4 is fixed for all cases (see Algorithm 13). Two "macro" cases are investigated. The difference is the parameter λ that regulates the solution update with the line-search method as per Eq. (3.4.12). Case 1 uses a value of 0.1, while Case 2 uses 0.9. Within each case, sub-cases are investigated by also varying the maximum increment in pressure Δp_{max} and temperature ΔT_{max} allowed by the line-search method (*cf.* Eq. (3.4.12)), as well as the initial increments ΔT_0 and Δp_0 used to start the algorithm. Regarding the algorithms, the fully analytical (developed in this work), the fully numerical of [25] and the fully analytical with the acceleration technique discussed in Fig. 44 with specific parameters stated accordingly are used. Results indicate that λ and Δp_{max}, ΔT_{max} play a big role in the convergence acceleration (it is highlighted the fact that Δp_0, ΔT_0 turned out to be not as important as Δp_{max}, ΔT_{max} because they are only used at the first iteration). By varying these parameters a considerable decrease of the number of iterations, as well as the computational time can be achieved. Moreover, application of the acceleration technique offers an additional speed-up, making it attractive to be used in combination with the fully

Table 19: Performances of the solution of the ERHO problem for point A of Fig. 47 using different parameters of the line-search method for the solution update and different dual-variable iteration algorithms. The overall algorithm tolerance is maintained constant at $\epsilon = 0.0001$.

Case 1: $\lambda_0 = \lambda_{01} = 0.1$									
	$\Delta p_0 = 500.0$, $\Delta p_{max} = 5000.0$ $\Delta T_0 = 1.0$, $\Delta T_{max} = 10.0$			$\Delta p_0 = 5000.0$, $\Delta p_{max} = 50000.0$ $\Delta T = 1.0$, $\Delta T_{max} = 100.0$			$\Delta p_0 = 500000.0$, $\Delta p_{max} = 5000000.0$ $\Delta T_0 = 100.0$, $\Delta T_{max} = 1000.0$		
	N_{iter}	[ms]	% sp. up	N_{iter}	[ms]	% sp. up	N_{iter}	[ms]	% sp. up
Numerical	1679	48.7	N/A	363	15.1	N/A	236	12.3	N/A
Analytical	1673	45.8	-5.95	356	14.2	-5.96	236	11.5	-6.50
Analytical+Acc. $\epsilon_{acc} = 1e6$, $N_{acc} = 10$	1673	39.6	-18.68	356	9.1	-39.73	236	5.8	-52.84
Analytical+Acc. $\epsilon_{acc} = 1e7$, $N_{acc} = 10$	1673	31.5	-35.31	355	8.2	-45.69	226	5.1	-58.63
Analytical+Acc. $\epsilon_{acc} = 1e7$, $N_{acc} = 5$	1673	32.1	-34.08	355	9.0	-40.39	226	5.9	-52.03
Case 2: $\lambda = \lambda_{02} = 0.9$									
	$\Delta p_0 = 500.0$, $\Delta p_{max} = 5000.0$ $\Delta T_0 = 1.0$, $\Delta T_{max} = 10.0$			$\Delta p = 5000.0$, $\Delta p_{max} = 50000.0$ $\Delta T = 1.0$, $\Delta T_{max} = 100.0$			$\Delta p_0 = 500000.0$, $\Delta p_{max} = 5000000.0$ $\Delta T_0 = 100.0$, $\Delta T_{max} = 1000.0$		
	N_{iter}	[ms]	% sp. up	N_{iter}	[ms]	% sp. up	N_{iter}	[ms]	% sp. up
Numerical	1506	44.7	N/A	176	9.1	N/A	23	1.9	N/A
Analytical	1500	40.7	-8.94	161	5.7	-37.36	15	1.4	-26.31
Analytical+Acc. $\epsilon_{acc} = 1e6$, $N_{acc} = 10$	1504	36.1	-19.23	166	4.8	-47.25	17	0.97	-48.94
Analytical+Acc. $\epsilon_{acc} = 1e7$, $N_{acc} = 10$	1504	20.3	-54.58	166	3.9	-57.14	19	0.91	-52.10
Analytical+Acc. $\epsilon_{acc} = 1e7$, $N_{acc} = 5$	1500	30.8	-32.70	162	4.1	-54.94	18	1.1	-42.10

analytical method. The present algorithm represents the best compromise made for this work and therefore it will be used for all other simulations unless specified differently.

3.5.4 Solution of the PRHO and TRHO problems

The treatments of the PRHO and TRHO problems are similar to the ERHO problem discussed in the previous section, with the exception that these are intrinsically single-variable iteration algorithms and therefore there is no issue with respect to what algorithm to use. However, some of these have the analytical solution as discussed in Sec. 3.4.2, which is only mathematically possible in the regions that do not have VLE. Similarly to the discussion made for the ERHO problem, there is no generic criterion to be able to choose which route to take (whether the analytical- non VLE or the numerical-VLE) with 100% of certainty. Obviously if the state to be sought is a VLE state there is no choice but the single-variable numerical algorithm, however using the analytical formula in the non-VLE region would definitely be beneficial from a performances point of view, but risky in case a VLE solution is the target state because errors will occur as showed next. For the same reason, starting the single-variable iteration method from the analytical solution is also a dangerous approach. For these reasons, in order to be consistent with the choice made for the ERHO problem, for the present work the single-variable numerical method is always chosen when the VLE option is turned on, unless a single-component state is found during the solution. Improvements of the present method and how to come up with a more efficient but reliable strategy to detect which method to choose in advance will be left to future studies. Nevertheless it should be noted that the single-variable iteration of the PRHO problem is much cheaper than the dual-variable iteration of the ERHO problem, which really represents the bottleneck form a performance point of view and thus it puts considerable amount of limitations on the use of fully conservative (or hybrid) schemes, where this type of method cannot be avoided in the transition form the conservative to the primitive variables.

With the goal to demonstrate the importance to take into account VLE in the solution of a thermodynamic problem that has VLE as target state, the following example is made.

First, the VLE diagram of N_2-C_6H_{14} is represented again in Fig. 54, this time with different isotherms [226]. Next, two different compositions are chosen from Fig. 54(a) namely $\mathbf{X}^* = [X_{N_2}, X_{C_6H_{14}}] = [0.5, 0.5]$ and $\mathbf{X}^{**} = [0.95, 0.05]$ and both $p\rho$ and $T\rho$ problems are explored. For the $T\rho$ problem, the conditions of $\mathbf{X} = \mathbf{X}^*$ and $\mathbf{X} = \mathbf{X}^{**}$ are selected in Fig. 54(a) and both density and pressure for each isotherm are recorded along these lines. Then, using the inputs of temperature and density, pressure re-calculation is attempted using both a VLE and non-VLE based $T\rho$ problem. Similarly for the $p\rho$ problem $\mathbf{X} = \mathbf{X}^*$ and $\mathbf{X} = \mathbf{X}^{**}$ in Fig. 54(a) are selected and pressure and density are recorded for each isotherm along these. Then re-calculation of T out of p and ρ is attempted with an PRHO problem with and without the use of VLE. The results are shown in Fig. 55 and Fig. 56. For $\mathbf{X} = \mathbf{X}^*$ strong departures of the recomputed pressure and temperature from the reference values are observed. These also include negative values of pressures for the smallest value of temperature. As the mixture temperature increases, the error reduces in both cases, as expected, since the VLE effects reduce and thus a calculation with a non-VLE based algorithm becomes close to the actual solution. On the other hand for $\mathbf{X} = \mathbf{X}^{**}$ much smaller errors are observed for both cases. This is because the mixture is mostly made of N_2, which, even at 310 K has gaseous properties, hence minor VLE conditions occur again. It is interesting to note that for the erroneous values of p and T the curve shape is wake-like, with the two extremes that match the real non-VLE conditions. This is not surprising since it is the same behavior observed in case of a single component $T\rho$ problem, shown in Fig. 54(b) for N_2, where wave-like solutions occur within the VLE dome with different levels of errors in the computed pressure, unless an auxiliary method is used to replace the EoS based pressure, as for example the Antoine equation for the saturation pressure as discussed in Appendix E. This occurs because of the impossibility by the EoS in form of Eq. (2.2.67) to predict discontinuities in the derivatives, which is required by the phase boundaries.

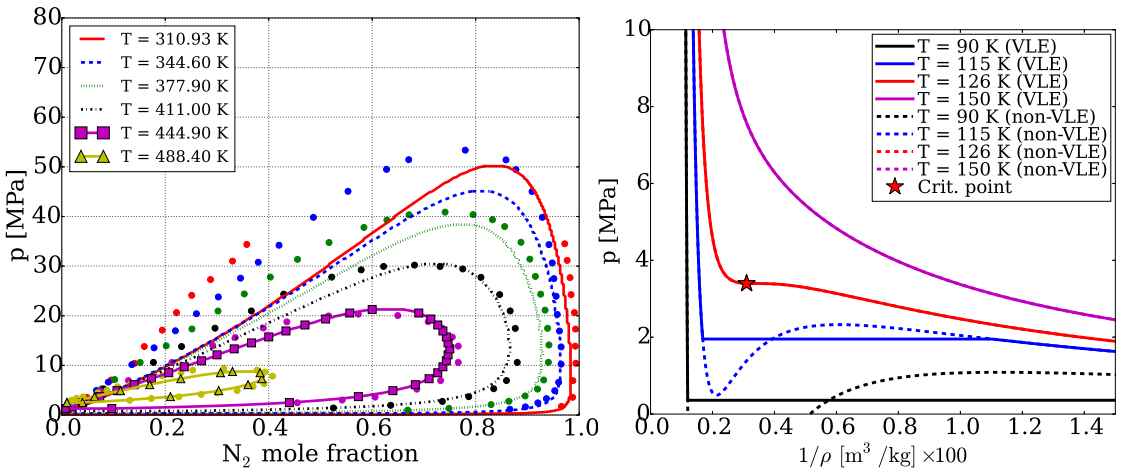

(a) (b)

Figure 54: (a) Solid lines: isothermal VLE diagram for the present mixture for a range of pressures as a function of the N_2 mole fraction. Dots (•): comparison taken from [45, 164]. Colored domes indicate the regions where mixture forms VLE, while outside the domes, single phase is found (either vapor or liquid). (b) $T\rho$ problem for N_2 with and without VLE information, which is provided using Antoine's equation (see Appendix E) [46].

3.6 Summary

In this chapter, extensive evaluation of the numerical methods used for the present thermodynamic model have been discussed and analyzed from both physical and numerical perspectives. The presented material partly addresses the items listed in **Objective 2**. The most important results obtained from this analysis are:

- the origin of the pressure oscillations due to the errors in the spatial and temporal discretization and their relationship with the EoS;
- adaptation of the Double-Flux method to VLE thermodynamics;
- the selection of the hybrid scheme switch parameters between the FC and QC scheme based on the compromise between an acceptable level of pressure fluctuations and numerical dissipation introduced;
- the introduction of a new method to compute temperature out of density, pressure and composition in a consistent manner with VLE thermodynamics;

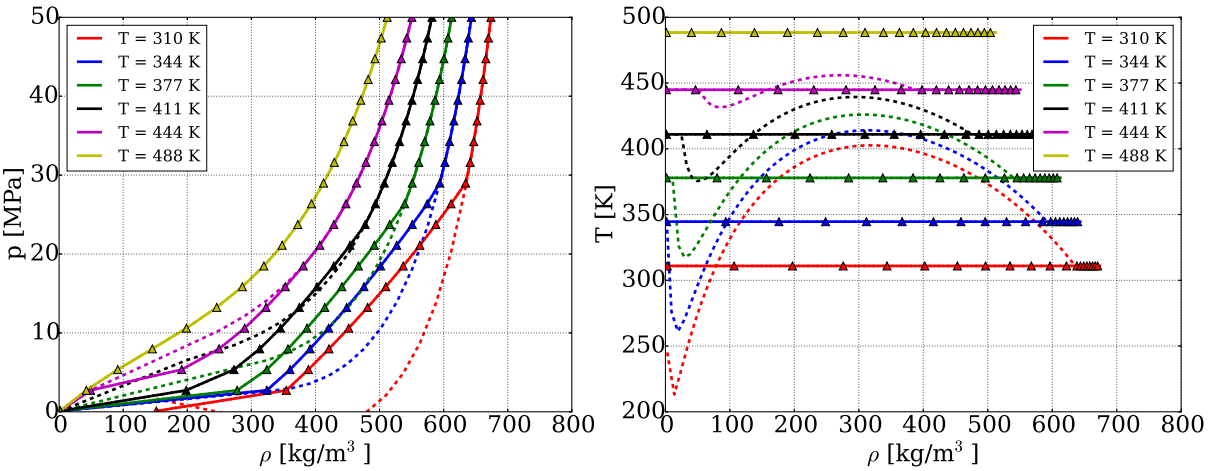

(a) Tρ problem (b) $p\rho$ problem

Figure 55: (a) Constant temperature-density and (b) constant pressure-density diagrams for $\mathbf{X} = \mathbf{X}^* = [0.5, 0.5]$. Solid lines (—) in the legend indicate the reference solution extracted from Fig. 54. Dashed lines (- -) indicate the non-VLE solution, while symbol (▲) indicate the VLE solution.

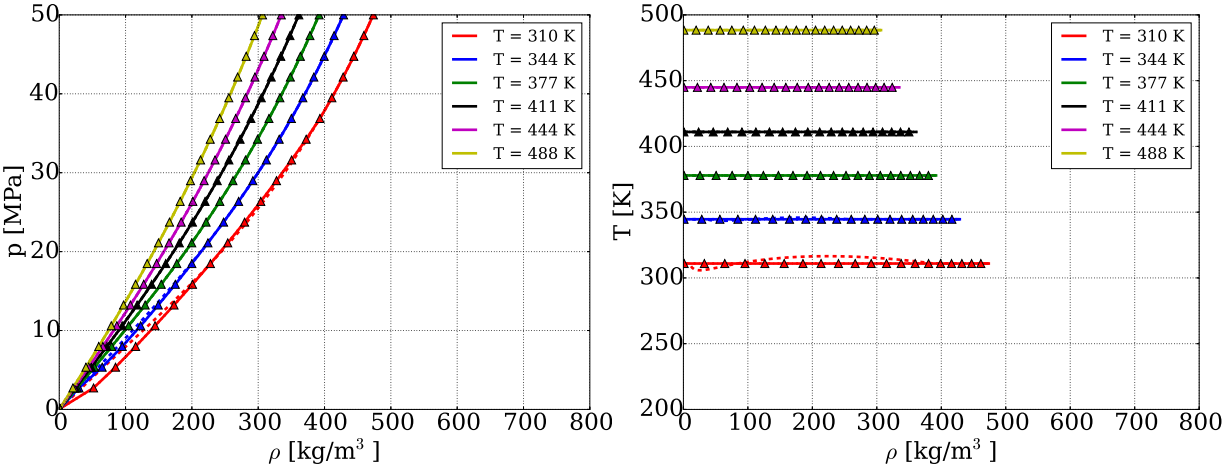

(a) Tρ problem (b) $p\rho$ problem

Figure 56: (a) Constant temperature-density and (b) constant pressure-density diagrams for $\mathbf{X} = \mathbf{X}^{**} = [0.95, 0.05]$. Solid lines (—) in the legend indicate the reference solution extracted from Fig. 54. Dashed lines (- -) indicate the non-VLE solution, while symbol (▲) indicate the VLE solution.

- the characterization of the numerical algorithms used for the resolution of thermodynamic problems involving VLE and their impact on performances;
- the crucial importance to adapt the thermodynamic problem to VLE in case a target

VLE state is sought in order to avoid the occurrence of nonphysical states.

The above points highlight the fact that the simulation of super-critical mixtures can suffer two distinct problems, both leading to the same result of non-physical states. One is related to the numerics only and shows the occurrence of nonphysical pressure and temperature oscillations because the error introduced by the numerical differentiation is fed into the EoS which can amplify it given its stiff nature in regions of high-density gradients. The second can also provide errors in the thermodynamic state, both in temperature and pressure if a VLE state is not treated as such during the resolution of inverse thermodynamic problems. For these reasons, both of these issues must be addressed and as the numerical experiments treated in this chapter show, fixing one does not fix the other. This point has even more insights which will be addressed in Chap. 5.

Chapter IV

RESULTS: ZERO-DIMENSIONAL (0D) THERMODYNAMICS

In this chapter, the results for the zero-dimensional (0D) thermodynamics are provided and discussed. The ultimate goal is to compare different thermodynamic models and prove the existence of different, sometimes substantially, outcomes if multi-phase equilibrium thermodynamics is ignored or accounted in a simplified manner. Different mixtures with increasing complexity are analyzed and discussed by providing the results for all the thermodynamic properties discussed in Sec. 2.2.2 as well as their effect on the mixture transport properties according to the models discussed in Sec. 2.3.

For all the derivatives required by the single- and multi-phase thermodynamics the GCEoS model is used. The EoS models and the MR models are those listed in Tab. 4 and Tab. 3, respectively. Although the baseline EoS-MR model considered throughout the present work is the PR-3 model, some evaluation of the effects of the other combinations is also discussed in this chapter with important conclusions.

For the thermodynamics model, the following results will refer to three models labels as follows:

1. "VLE"to indicate the multi-phase equilibrium model presented in Sec. 2.2.2;

2. "non-VLE"to indicate the single-phase model, that is the one that selects the phase based on the minimum Gibbs free energy criterion of Appendix A;

3. a hybrid, approximate method that is referred to as "frozen VLE". This method is made of two steps: one "exact" step which consists of the calculation of VLE identically to method 1) and a second step which uses the same analytical derivatives of Sec. 2.2.2 in the VLE region, but it assumes that all the VLE derivatives, such as $(\partial\beta/\partial T)_{p,\mathbf{X}}$, $(\partial\beta/\partial p)_{T,\mathbf{X}}$, $(\partial M^V/\partial T)_{p,\mathbf{X}}$, $(\partial\zeta_i/\partial p)_{T,\mathbf{X},\zeta_i}$ are zero. This means that "total" derivatives match with frozen derivatives as for example $(\partial E^\eta/\partial T)_{p,\mathbf{X}} \equiv$

$(\partial E^\eta/\partial T)_{p,\mathbf{X},\boldsymbol{\zeta}}$ related to Eq. (K.0.44). This applies to all the mixture, as well as phase properties discussed in Sec. 2.2.2. This approach leads to the calculation of some thermodynamic properties in the VLE by merely blending phase specific properties as $\Sigma = \beta\Sigma^V + (1-\beta)\Sigma^L$, where Σ, Σ^V and Σ^L represent the generic property in the mixture, vapor phase and liquid phase, respectively. A proof of this statement is given in Appendix C;

A final note is made on the evaluation of partial molar quantities which can be performed with exact (Eq. (2.2.53) and Eq. (2.2.63)) and approximate (Eqs. (3.4.16)–(3.4.17)) formulas. The first approach is associated to the "VLE" model in order to be consistent with the fact that all the properties are consistent with thermodynamic laws, whereas the second approach is associated with the "frozen VLE" method. Note that approximation of Eqs. (3.4.16)–(3.4.17) does not necessarily imply the frozen VLE assumption as these are independent simplifications. Nevertheless they are both lumped together under the "frozen VLE" method in order to avoid unnecessary multiplication of terminology. Concerning the "non-VLE" model, the exact single-phase formulas, such as those listed for GCEoS in Sec. M.4 are employed.

This chapter is organized in the following way: for each chosen mixture, the VLE diagram is first computed and validated against available data published elsewhere. Next, a combination of iso-composition, iso-thermal and/or iso-baric lines are identified in the diagram and specific properties are computed along these using the different thermodynamic models listed above.

4.1 Binary mixture # 1: N_2/CH_4

4.1.1 VLE diagram and main properties

The first binary mixture considered is N_2/CH_4. First, the 3D VLE diagram is provided in Fig. 57(a) along with iso-thermal slices, separately displayed in Fig. 57(b). The red and blue shaded areas in Fig. 57(a) represent the VLE dome boundaries where the mixture pseudo-phase is considered vapor-like or liquid-like, respectively. The pseudo transition here is considered to happen at the condition where $Z^* = 2.5B_m p/R_u T$ as introduced in

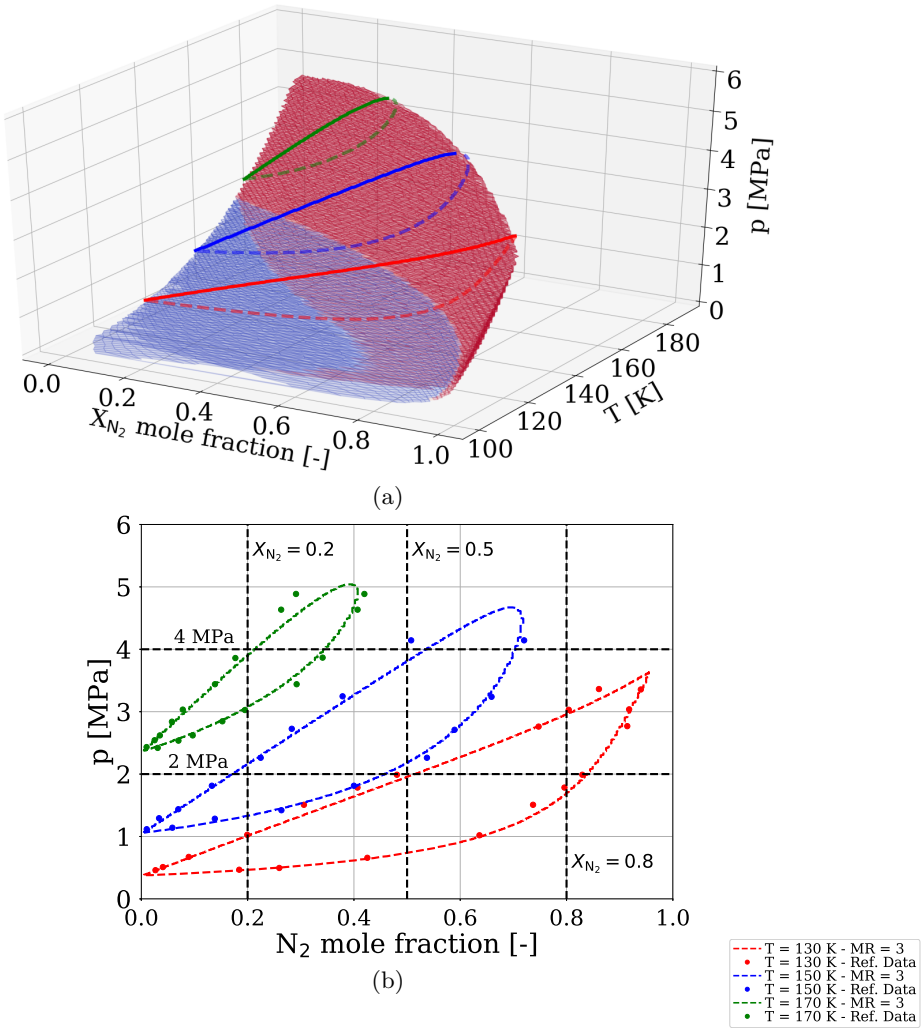

Figure 57: a) 3D VLE diagram for the N_2/CH_4 mixture. The three iso-thermal VLE domes are the same represented also in (b) where dots represent data taken from [24]. Dashed and dotted lines indicate the iso-composition and the iso-baric conditions along with data is analyzed further.

Sec. 3.5.1. The thermodynamic models are evaluated along iso-composition and iso-baric lines sketched in Fig. 57(b).

Figure 58 shows the iso-composition properties of the mixture taken at different amount of N_2 according to Fig. 57(b). Each variable here is able to show different features and therefore the importance of the fully analytical VLE model. For example the β field shows that the variations with respect to the pressure (and indirectly temperature) can be much different as the composition is varied. Particularly, despite the monotonic decreasing trend observed

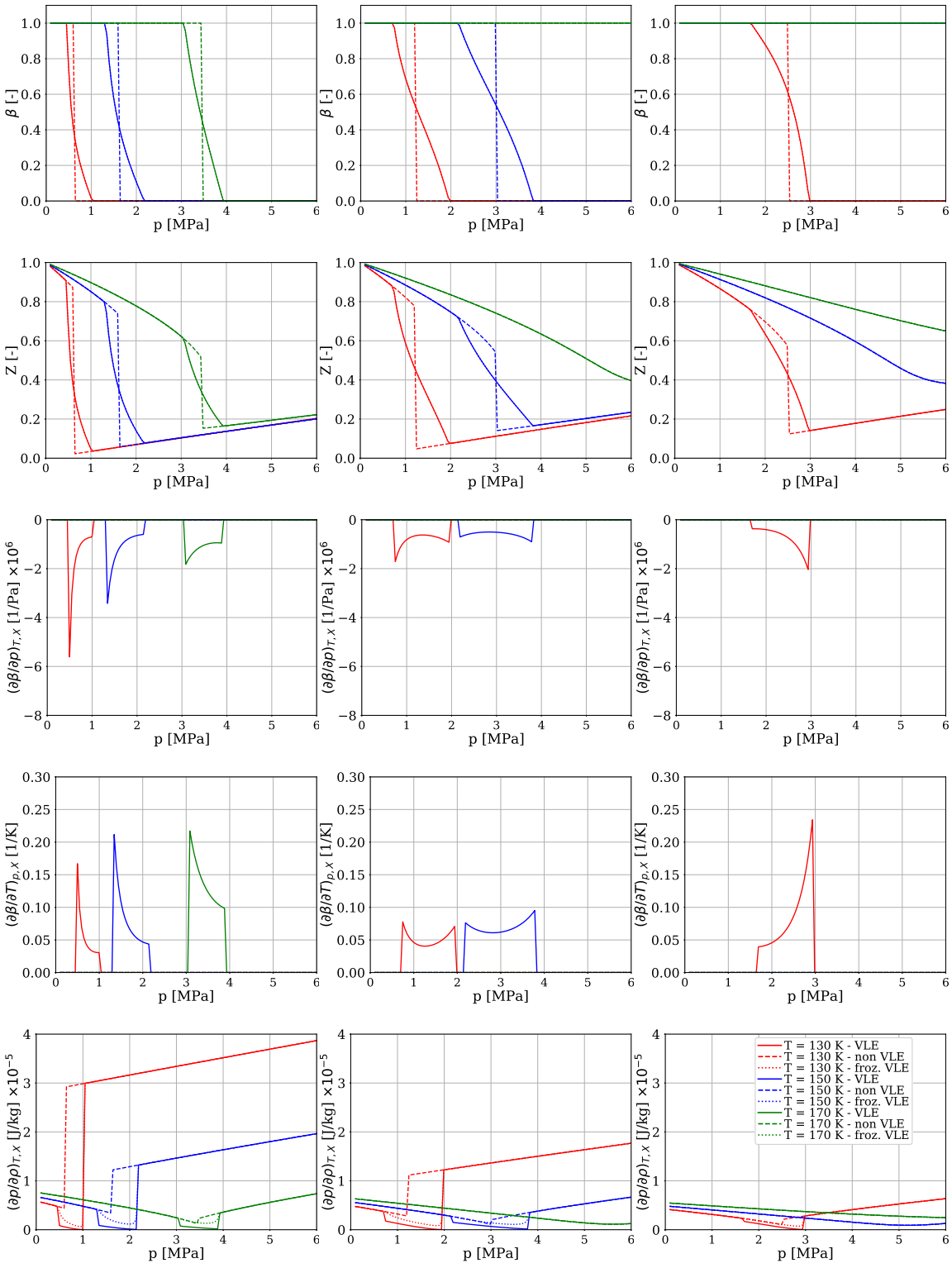
β [-]
Z [-]
$(\partial\beta/\partial p)_{T,x}$ [1/Pa] ×10^6
$(\partial\beta/\partial T)_{p,x}$ [1/K]
$(\partial p/\partial\rho)_{T,x}$ [J/kg] ×10^{-5}
p [MPa]
T = 130 K - VLE
T = 130 K - non VLE
T = 130 K - froz. VLE
T = 150 K - VLE
T = 150 K - non VLE
T = 150 K - froz. VLE
T = 170 K - VLE
T = 170 K - non VLE
T = 170 K - froz. VLE

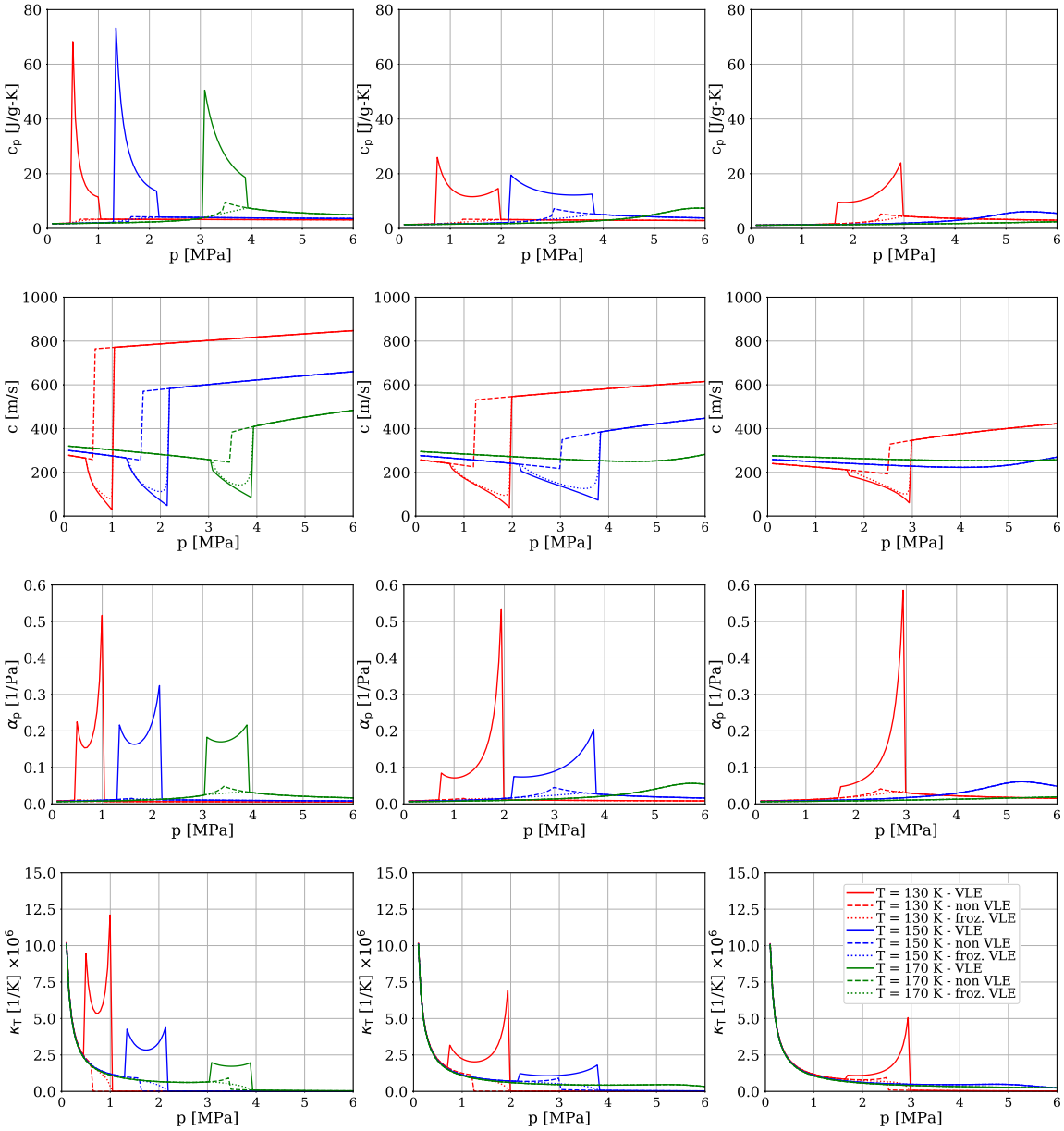

(a) $X_{N_2} = 0.2$ (b) $X_{N_2} = 0.5$ (c) $X_{N_2} = 0.8$

Figure 58: Iso-composition results for the N_2/CH_4 mixture. Variables are organized column-wise with respect to the fixed amount of N_2 mole fraction. Variables labeled as $(\cdot) \times 10^x$ indicate that the represented data is multiplied by the factor 10^x.

in all cases, the first derivative with respect to the pressure can change drastically, up to the point where the second derivative changes sign for the $X_{N_2} = 0.5$ case. This is immediately visible in the $(\partial\beta/\partial p)_{T,\mathbf{X}}$ (and $(\partial\beta/\partial T)_{p,\mathbf{X}}$) pictures. This has a huge consequence on all the thermodynamic variables that use these derivatives, depending on whether the VLE or the frozen VLE model is used. While the disagreement between the VLE and the frozen VLE model in $(\partial p/\partial\rho)_{T,\mathbf{X}}$ and c is somewhat less pronounced with a higher error occurring near the phase boundaries, the error for c_p, α_p and κ_T is huge, with trends that are also drastically different. For example in c_p, the frozen VLE model cannot take into account for sudden jumps near phase boundaries because of the fact that $(\partial\beta/\partial T)_{p,\mathbf{X}}$ is assumed to be zero, however when multiplied by $(E^V - E^L)$ according to Eq. (2.2.38) it introduces a big effect, which is not taken into account in the frozen VLE case. This is also true because the approximation $(\partial\rho/\partial T)_{p,\mathbf{X}} \approx (\partial\rho/\partial T)_{p,\mathbf{X},\boldsymbol{\zeta}}$ and similarly for other involved derivatives is made in the frozen case.

In all cases, the no VLE model performs poorly in the 2-phase region, with the tendency to produce nonphysical discontinuities in the variables and their derivatives. This is due to the fact that the minimum Gibbs criterion suddenly jumps between the phases and selects a completely different compressibility root, as visible in the Z pictures. This choice creates a discontinuity that reflects in all variables and that does not exist in the VLE case where the fields of β and Z are continuous, with discontinuous first derivatives at the phases boundary. Finally, in the single-phase regions all the models agree as expected because all the mathematical assumptions match with the real physics being computed. Figures 59–61 show relevant mixture variables obtained along the iso-baric lines according to Fig. 57(b) where analogous observations can be made. One interesting feature to observe is the trend in the compressibility factor in Fig. 59(e). While the green line at $T = 170$ K for the non-VLE case shows a discontinuity, the curve for the same model at 150 K is not discontinuous but smooth. Nevertheless a difference still persists between the non-VLE model and the VLE

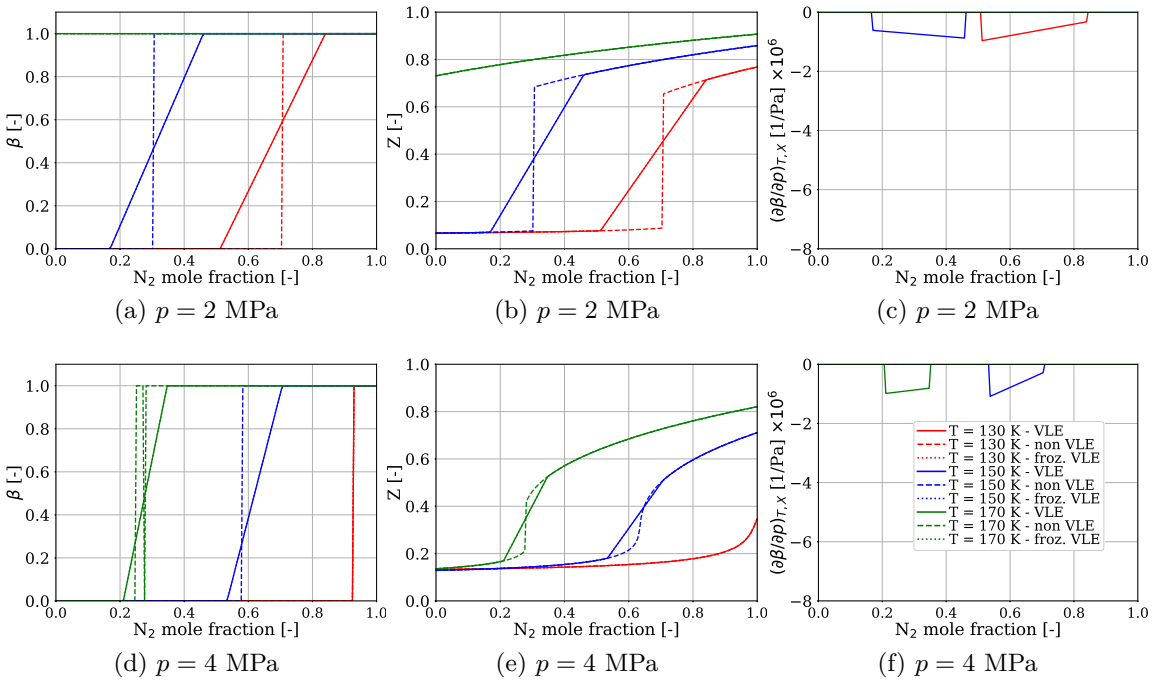

(a) $p = 2$ MPa (b) $p = 2$ MPa (c) $p = 2$ MPa

(d) $p = 4$ MPa (e) $p = 4$ MPa (f) $p = 4$ MPa

Figure 59: Iso-baric results for the N_2/CH_4 mixture. Variables: β, Z and $d\beta/dp$.

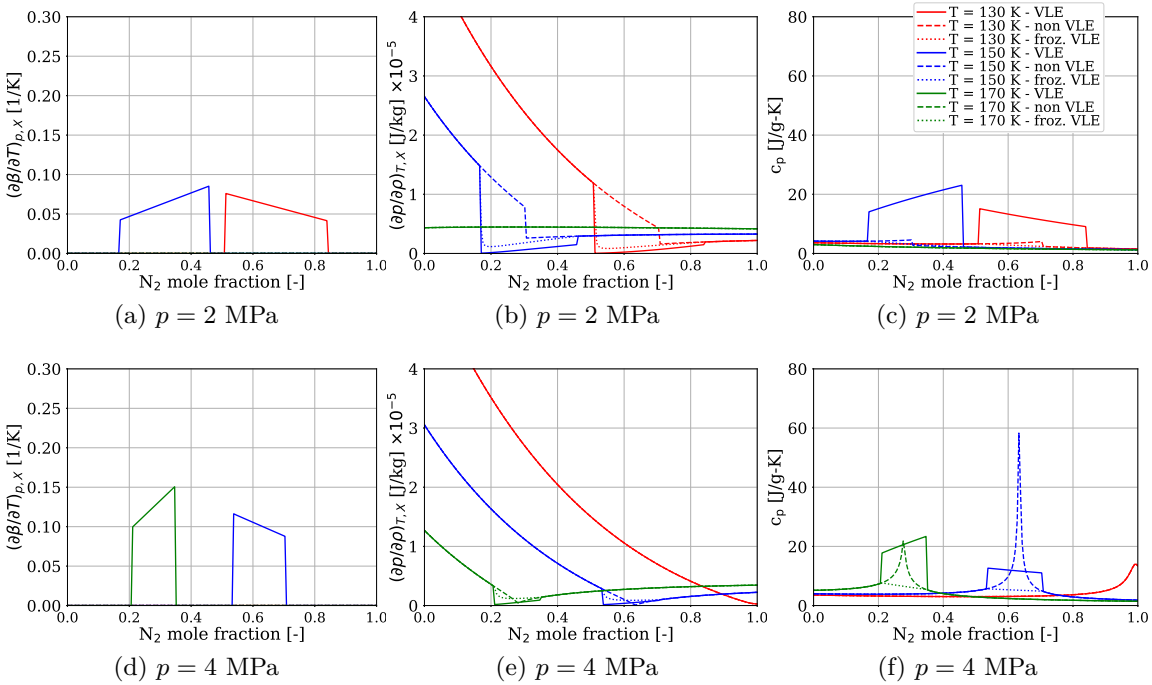

(a) $p = 2$ MPa (b) $p = 2$ MPa (c) $p = 2$ MPa

(d) $p = 4$ MPa (e) $p = 4$ MPa (f) $p = 4$ MPa

Figure 60: Iso-baric results for the N_2/CH_4 mixture. Variables: $d\beta/dT$, $dp/d\rho$ and c_p.

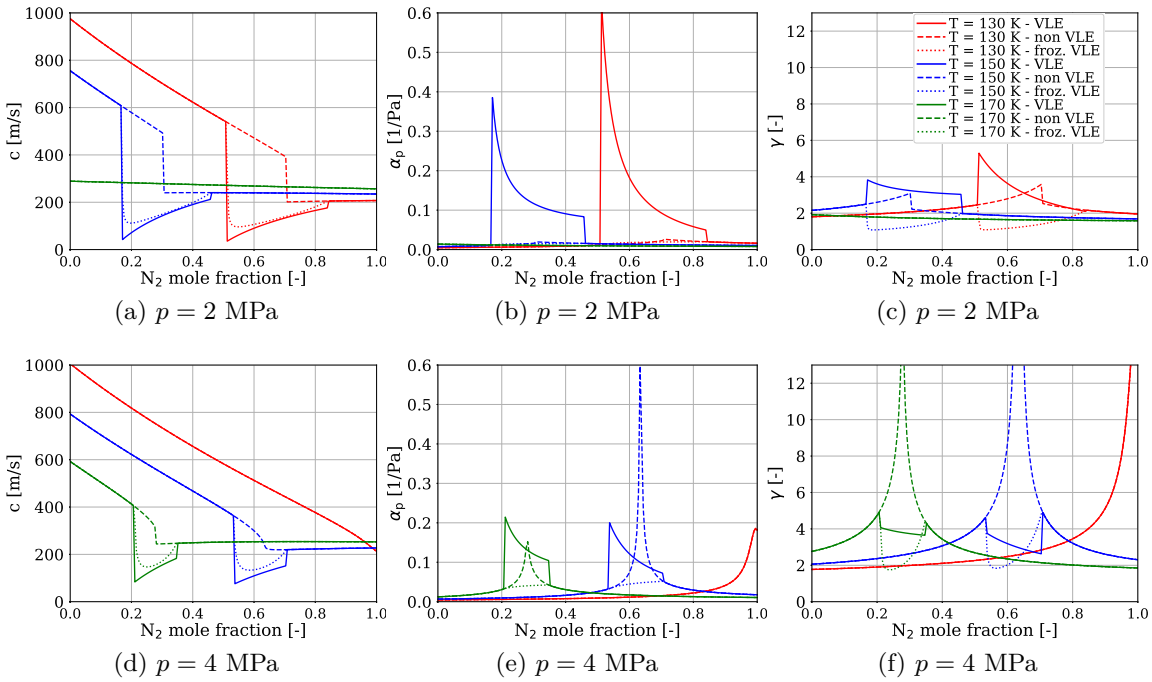

(a) $p = 2$ MPa (b) $p = 2$ MPa (c) $p = 2$ MPa

(d) $p = 4$ MPa (e) $p = 4$ MPa (f) $p = 4$ MPa

Figure 61: Iso-baric results for the N_2/CH_4 mixture. Variables: c, α_p and γ.

model. For the non-VLE model, the first trend occurs when two distinct real roots appear in Eq. (2.2.70) and one of them is selected according to the minimum Gibbs energy criterion of Appendix A. The model switches between the two roots when the energy criterion is met, creating a physical discontinuity in the thermodynamic space. On the other hand the second type of trend is not associated with the existence of two distinct real roots, but only one is present. Hence, the minimum Gibbs criterion is not even invoked since there is no choice to be made. However in both cases the VLE solution shows a different trend. This demonstrates the fact that the presence of VLE is not associated with the case that multiple real roots appear in the compressibility since even in the case of a single root, the VLE algorithm may reveal the existence of a lower Gibbs energy solution associated with a multi-phase state.

This point is important because it suggests that the VLE (or the TPD stability analysis) should be attempted virtually always because there is no real a-priori information (not even the fact that a single real compressiblity root exists) that can be used to bypass the Tp problem solution of Fig. 43 and establish with 100% accuracy that VLE will not

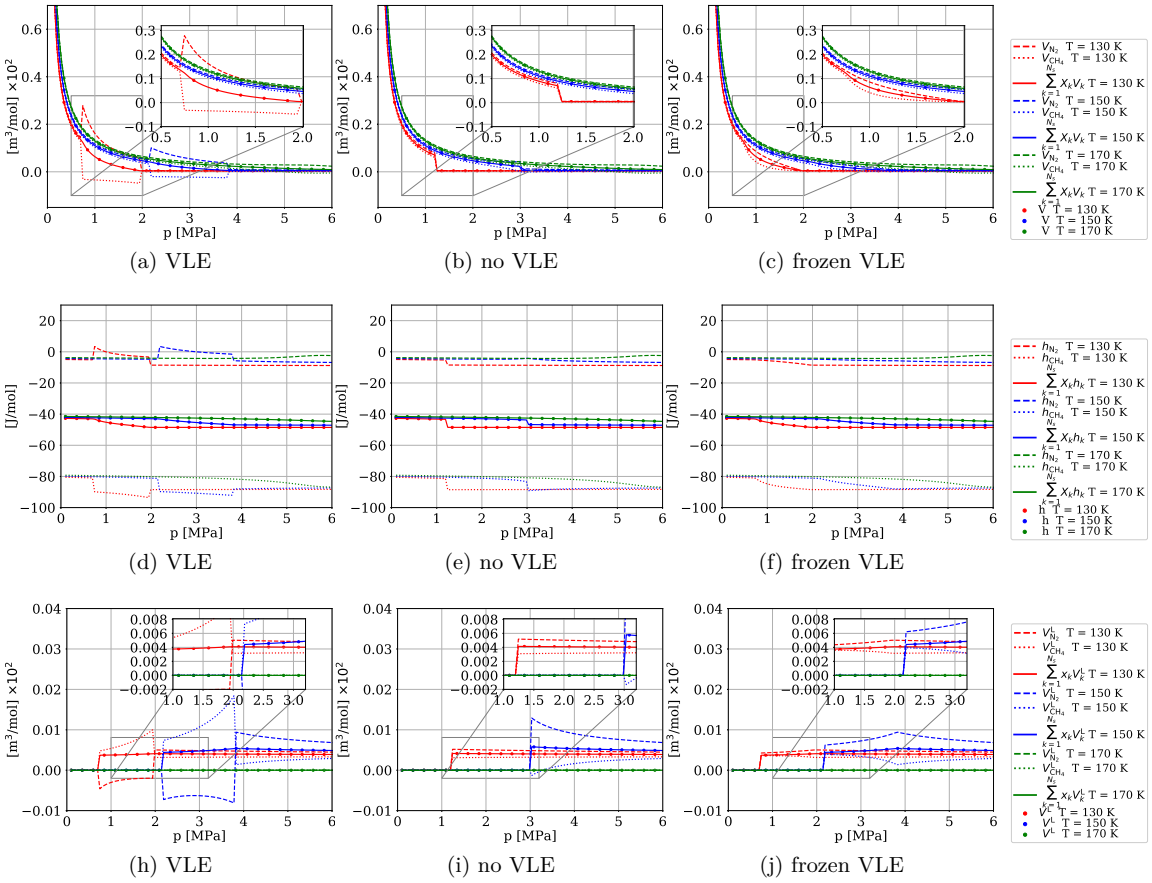

(a) VLE (b) no VLE (c) frozen VLE

(d) VLE (e) no VLE (f) frozen VLE

(h) VLE (i) no VLE (j) frozen VLE

Figure 62: Partial molar volume (top row), enthalpy (mid row) and liquid-phase partial molar volume (bottom row) computed along iso-composition line $X_{N_2} = 0.5$ using the three different thermodynamic models.

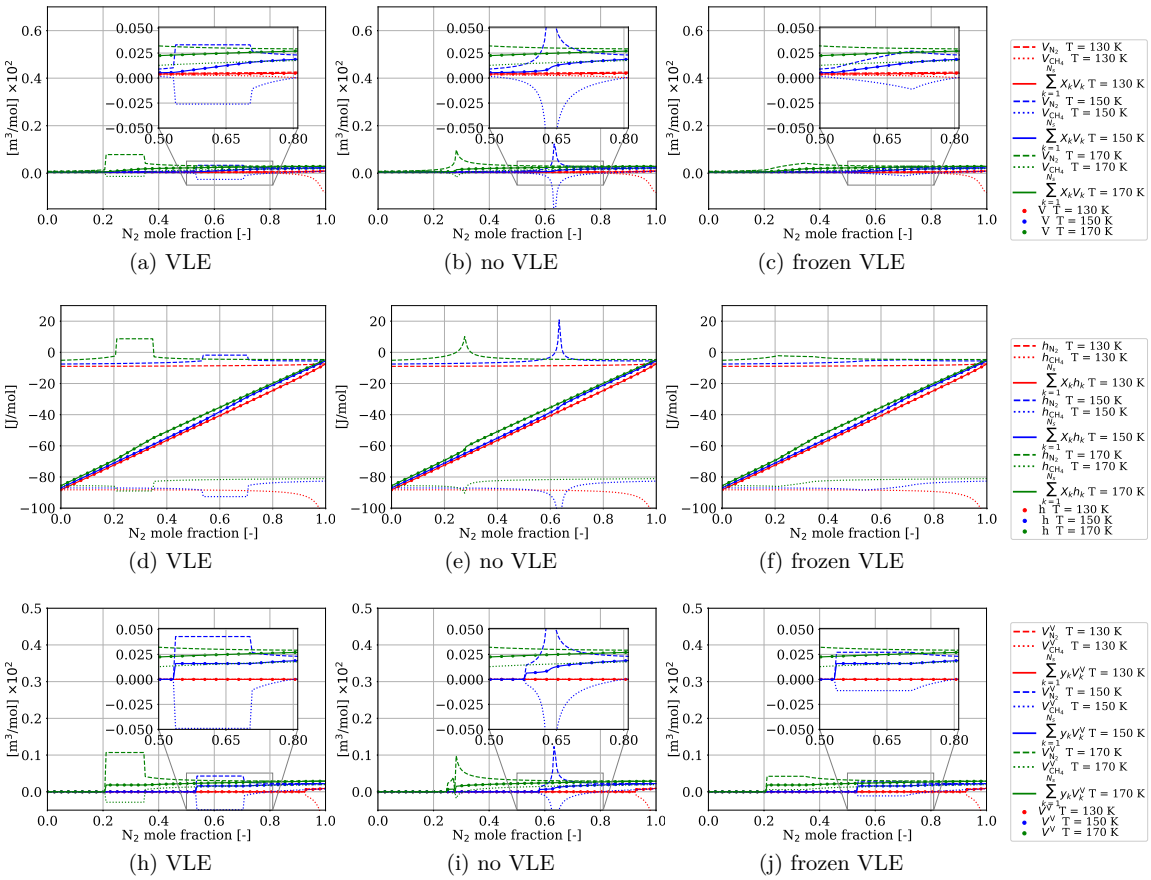

(a) VLE (b) no VLE (c) frozen VLE

(d) VLE (e) no VLE (f) frozen VLE

(h) VLE (i) no VLE (j) frozen VLE

Figure 63: Partial molar volume (top row), enthalpy (bottom row) and vapor-phase partial molar volume (bottom row) computed along the iso-baric line $p = 4$ MPa using the three different thermodynamic models.

form. This aspect is another consequence of the higher cost associated with this equilibrium thermodynamics with RG EoS. Of course, one can use the assumption that for temperatures and pressures above certain T^* and p^* threshold values, VLE does not form, however these values are problematic to be found. For simple mixtures (2 or 3 species at most), these could be identified with some 0D studies like those presented in this chapter, however if the mixture gets too complex, this option is difficult to apply. Furthermore, in procedures like the ERHO or PRHO problems, the values of T and/or p are unknown a-priori and therefore cannot be compared with any threshold value, hence assumption of VLE or non-VLE must be done a-priori and then verified with the algorithm itself, increasing the overall computational cost.

Figure 62 and 63 illustrate the partial molar volume and partial molar enthalpy for the mixture as well as a selected phase obtained for the iso-composition (only $X_{\mathrm{N}_2} = 0.5$ shown) and iso-baric (only $p = 4$ MPa shown) case, respectively. The pictures are differentiated according to the thermodynamic model indicated in the label. Each picture shows the partial molar property for each species (such as V_{N_2}), the overall mixture property (such as $V = M/\rho$ or $V^L = M^L/\rho^L$) and the thermodynamic constraint that has to be satisfied by definition (such as $\sum_{k=1}^{N_s} X_k V_k = V$ or $\sum_{k=1}^{N_s} x_k V_k^L = V^L$) at each examined temperature according to Fig. 57(b). The goal of this is to conclude the following information: while the thermodynamic constraint is satisfied in all conditions, the individual partial molar properties can exhibit significant departures depending on the thermodynamic model. This leads to the conclusion that although the model provided by Eqs. (3.4.16)–(3.4.17) can give a reasonable estimation of the actual property, errors can be made with the computation of energy diffusion terms as per Eq. (2.1.14). As a result, this can play an important role in problems where such terms are dominant as for example in heat and mass transfer studies. This conclusions is valid for the mixture, as well as specific phase properties.

4.1.2 Effect of VLE on transport properties

Figures 64 and 65 illustrate the transport properties of the N_2/CH_4 mixture computed along the same iso-composition and iso-baric lines of Fig. 57(b), respectively. In the pictures, the

dynamic viscosity, the thermal conductivity and the binary mass-diffusion coefficients $\mathcal{D}_{A,B}$ used in Eq. (2.1.16) are provided. It is emphasized that all these properties are already computed with all the high-density corrections since the importance of accounting it has been already discussed in Sec. 2.3. The first thing to notice is that the frozen VLE

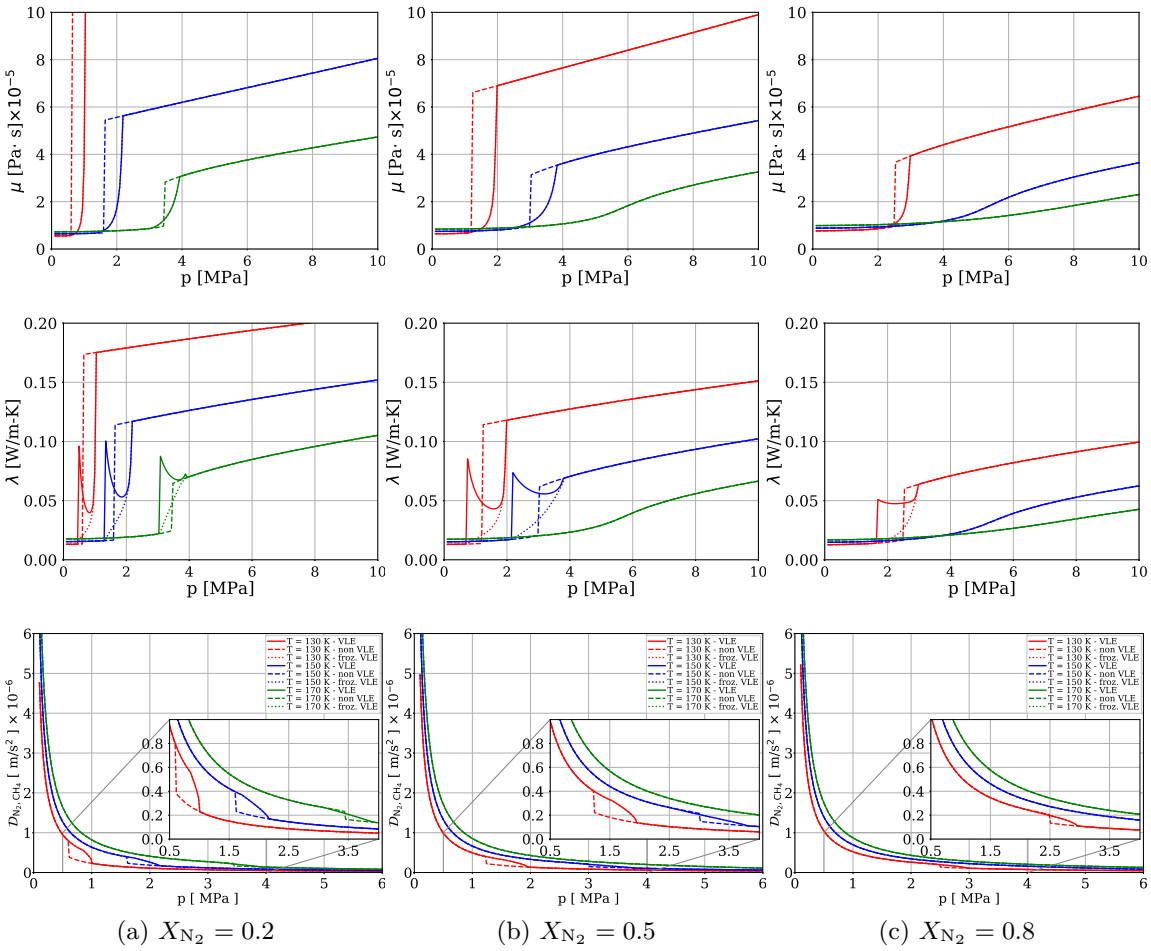

(a) $X_{N_2} = 0.2$ (b) $X_{N_2} = 0.5$ (c) $X_{N_2} = 0.8$

Figure 64: Dynamic viscosity μ, thermal conductivity λ and binary mass diffusion coefficient $\mathcal{D}_{N_2,CH_4}$ computed along the three iso-composition lines of Fig. 57(b) using the three different thermodynamic models. Data is organized column-wise with the labels (a), (b) and (c) indicating the column of the relative composition.

model matches with the VLE model for the viscosity and the mass diffusion coefficients, whereas differences are observable for the thermal conductivity in both pictures. This is related to the fact that the model of Chung [31] for the viscosity and the model of Fuller [52] with the Riazi correction [178] are only function of basic thermodynamic properties,

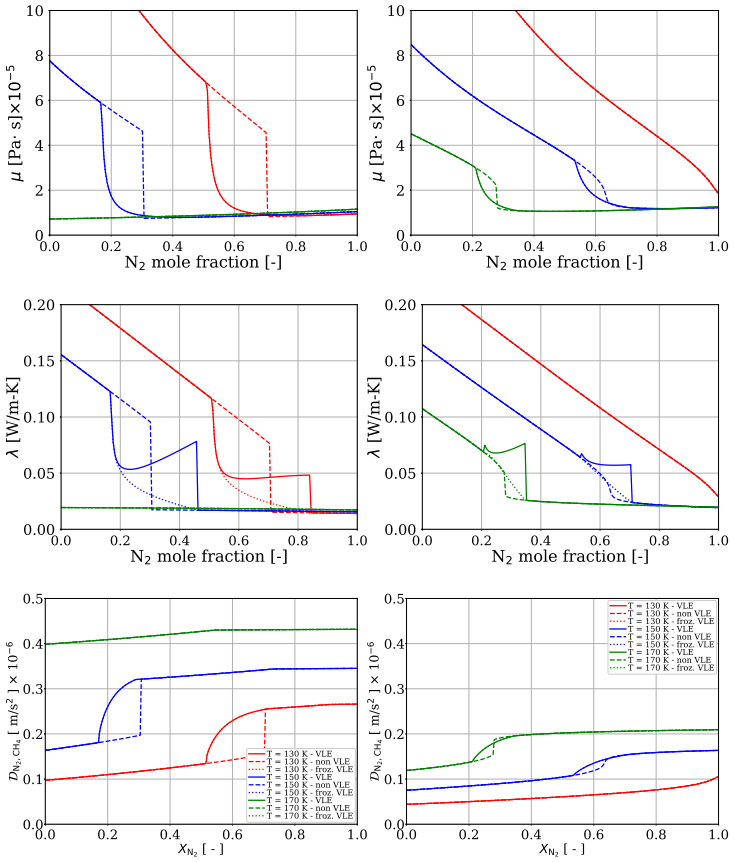

(a) $p = 2$ MPa (b) $p = 4$ MPa

Figure 65: Dynamic viscosity μ, thermal conductivity λ and binary mass diffusion coefficient $\mathcal{D}_{\mathrm{N_2,CH_4}}$ computed along the three iso-baric lines of Fig. 57(b) using the three different thermodynamic models. Data is organized column-wise with the labels (a) and (b) indicating the column of the relative pressure.

such as pressure, temperature and density. These, as already demonstrated in Fig. 59 are transparent to the frozen VLE model which is only effective after these are computed. In fact, since the thermal conductivity is a function of the mixture C_v (*cf.* Eq. (2.3.21)), a difference exists because the VLE and non-VLE assumptions have different ways to compute this quantity as discussed above. In all cases, the non-VLE model provides a drastically different answer that can play a significant role if any of these parameters have a dominant effect in a simulation.

4.1.3 Effect of other GCEoS/MR combinations

Figures 66–69 show the study performed on the different type of combinations of GCEoS-MR presented in Sec. 2.2.3 along the iso-composition line $X_{N_2} = 0.2$. The results are showed with the VLE model only in order to reduce the amount of variables and improve the pictures readability. The first thing to highlight is that no EoS combination with MR-2 is able to provide any VLE diagram. The algorithm fails to converge so the phase boundaries are not detected. This clearly identifies the MR-2 model are not suitable for VLE calculations. The reason is hidden in the fact that this formula forces the mixing to behave in a linear manner, whereas a non-linear representation of the non-ideal mixing is necessary to capture the phase boundaries. For this reason, this mixing rule is discarded.
Next, another combination that does not work properly is the PR-RK with MR-4. As illustrated in Fig. 69, the phase boundaries for this combination produces wrong results, hence this combination is also discarded and anything else showed on the PR-RK EoS will not contain this MR.
Overall, all the other combinations of EoS and MR worked fairly well. The major effect on the results is certainly provided by the EoS choice itself rather than the MR. For example the VDW EoS in Fig. 66 produces poor agreement with the reference data. This reflects in all other properties, such as density and speed of sound in Fig. 66(b) and (c). The latter can be easily compared with the baseline PR MR-3 combination showed in Fig. 58(a).
The RK and SRK EoS performed similarly, with good agreement of the VLE diagram and properties compared to the baseline PR MR-3. On the MR side, very minor difference is

observed. The MR-4 is found to be essentially overlapped to MR-1, while some very minor differences are visible for the MR-3 model. Overall, this makes MR-4 not that attractive because a) it cannot be applied to all the present GCEoS models and b) it comes with a slight additional cost between 5% and 10% due to the additional number of floating point operations involved in the calculations that are clearly visible by looking at the analytic formulas in Sec. 2.2.3. This additional cost is not really justified since identical results can be obtained with the other MR. Specifically, MR-1 and MR-3 perform very similar, even from a computational point of view, where no significant difference has been observed between the two.

The PR-RK EoS has also some controversial behavior and certainly it cannot be preferred from a computational point of view since the substantially more floating point operations that come with it result into a cost increase which has a baseline of 150% up to peaks of 300% compared to PR and SRK depending on the problem. Figure 69(a) shows that the VLE diagram is more accurately represented for the 170 K, however not so well represented for the 150 K and 170 K, especially for the lower branch of the dome.

This first analysis on the EoS seems to suggest that PR, SRK and RK with MR-1 or MR-3 are valid combinations that provide the best compromise between cost and accuracy. This point will be also analyzed for the next binary mixture.

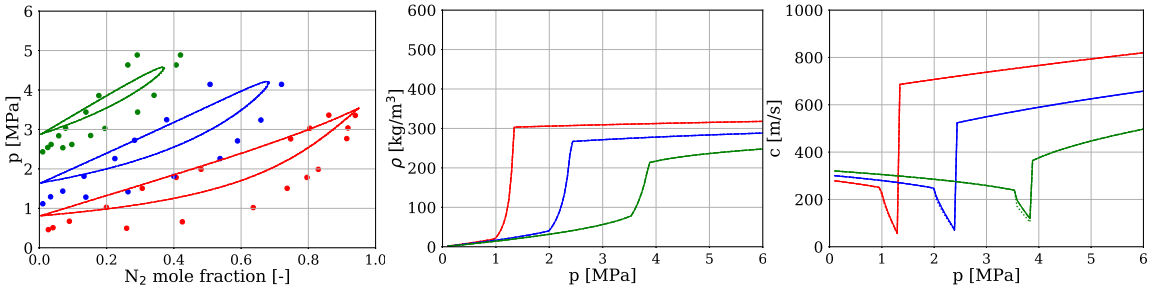

(a) (b) (c)

Figure 66: (a) VLE diagram, (b) density profiles and (c) speed of sound profiles obtained with the VDW EoS for the iso-composition $X_{N_2} = 0.2$ case. Dotted data is taken from [24].

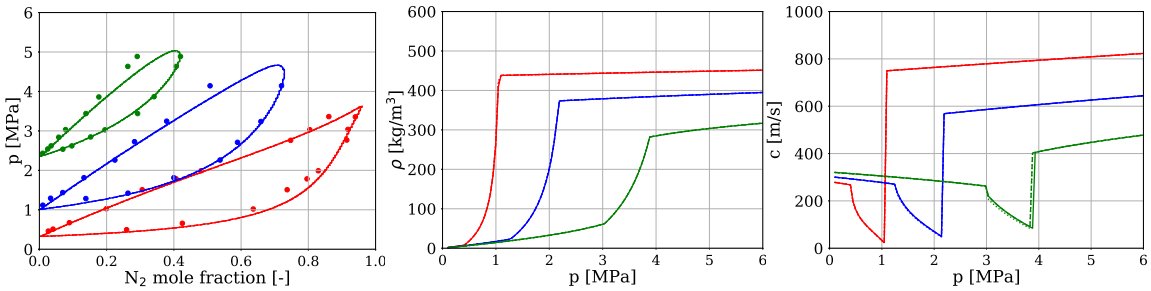

(a) (b) (c)

Figure 67: (a) VLE diagram, (b) density profiles and (c) speed of sound profiles obtained with the RK EoS for the iso-composition $X_{N_2} = 0.2$ case. Dotted data is taken from [24].

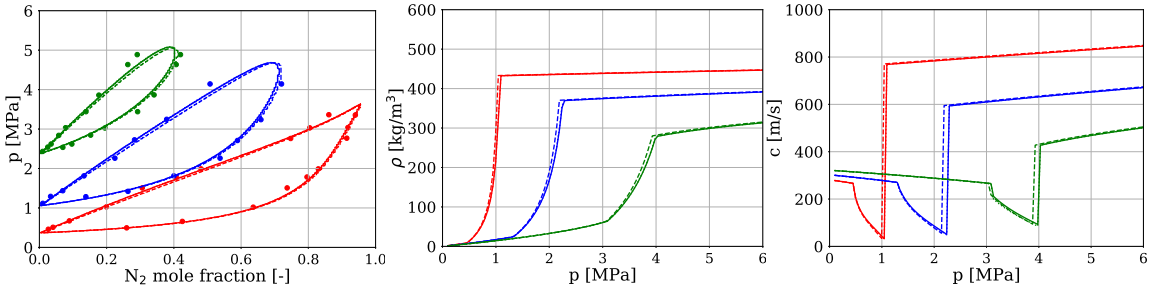

(a) (b) (c)

Figure 68: (a) VLE diagram, (b) density profiles and (c) speed of sound profiles obtained with the SRK EoS for the iso-composition $X_{N_2} = 0.2$ case. Dotted data is taken from [24].

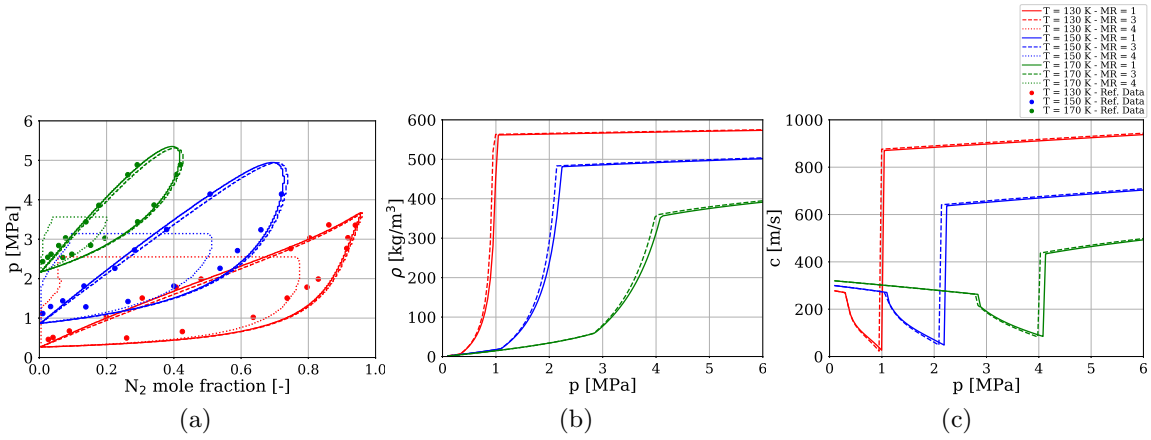

(a) (b) (c)

Figure 69: (a) VLE diagram, (b) density profiles and (c) speed of sound profiles obtained with the PR-RK EoS for the iso-composition $X_{N_2} = 0.2$ case. Dotted data is taken from [24].

4.2 *Binary mixture # 2: CH_4/CO_2*

4.2.1 VLE diagram and main properties

The second mixture under consideration is another binary mixture with CH_4/CO_2. For this mixture, interaction parameters of $k_{ij} = 0.048,\ i \neq j$ are used with the PR MR-3 (baseline) combination. Figure 70(a) shows the iso-thermal VLE diagram with reference data. In order to avoid repetition with the previous results, for this case the analyses conducted at iso-baric conditions are carried out, for which the respective VLE diagram is illustrated in Fig. 70(b). Furthermore in Fig. 71 and Fig. 72 the relevant mixture properties for the iso-composition taken at $X_{CH_4} = 0.1$ (left column) and iso-thermal taken at $T = 220$ K (right column) conditions are showed only, for brevity (analyses conducted onto other lines lead to the exact conclusions). Similarly to what discussed earlier, the first derivatives of the main VLE

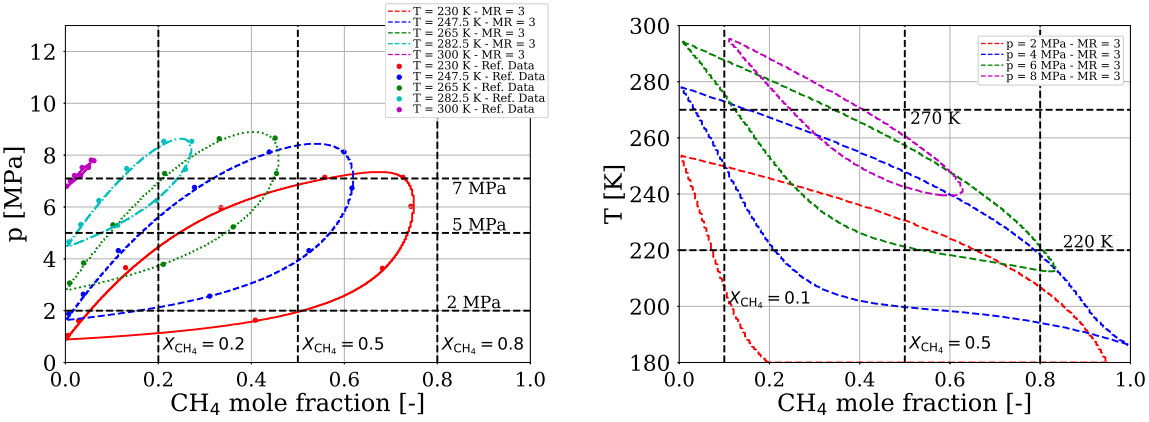

(a) iso-thermal VLE (Dotted data from [240])

(b) iso-baric VLE

Figure 70: a) Iso-thermal and b) iso-baric VLE diagrams for CH_4/CO_2 mixture.

properties play a crucial role for the mixture thermodynamic derivatives. The departures among the thermodynamic models observed for c_p and γ are simply unacceptable and even the error in the speed of sound between the VLE and the frozen VLE model appears larger than the previous case and it increases as pressure increases. Other observations regarding the no VLE model and the behavior in the single-phase regions remain the same, leading to the same conclusions as before. The same discussion holds for the partial molar quantities

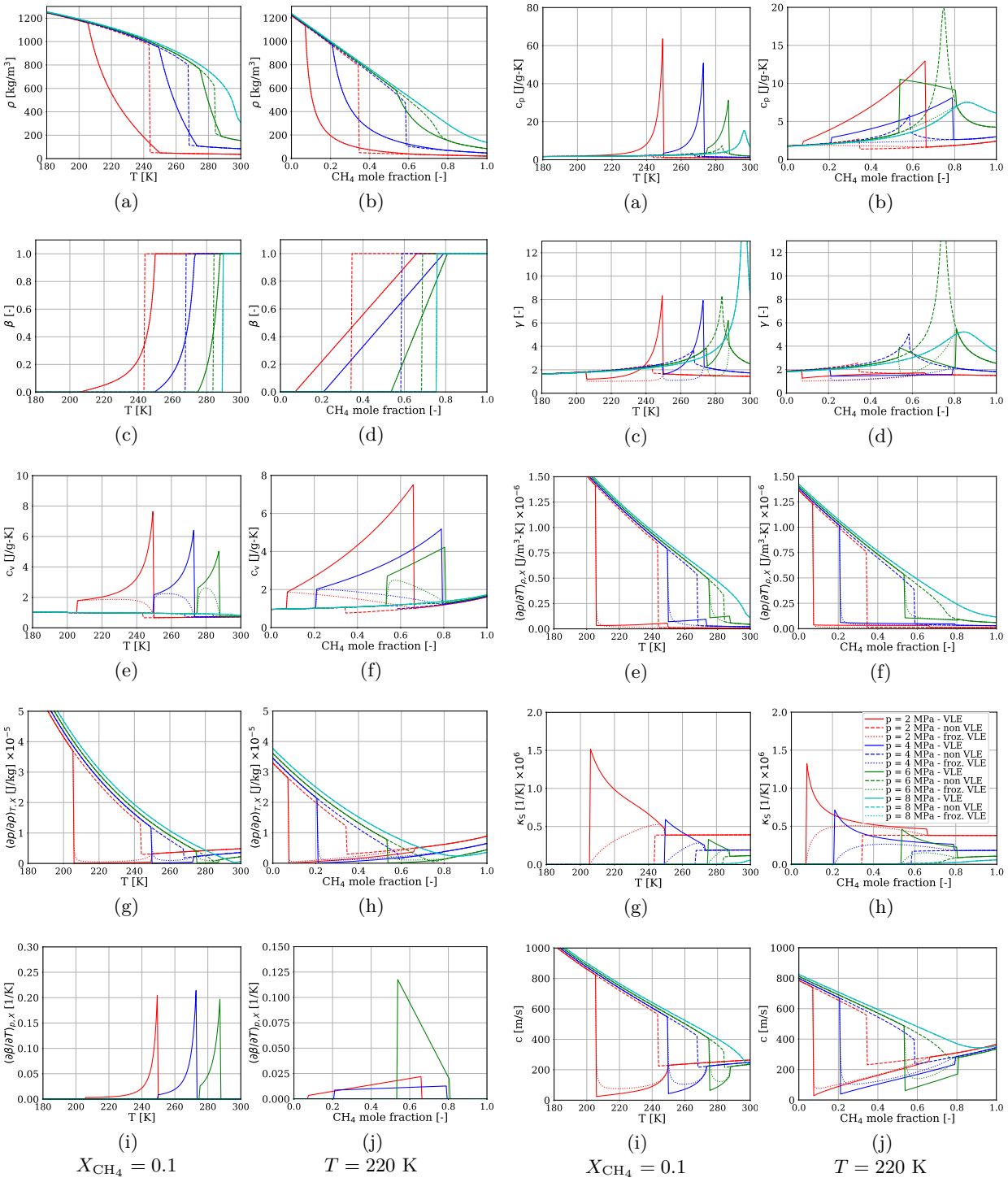

Figure 71: Iso-composition (left column) and iso-thermal (right column) results set # 1 (ρ, β, c_v. $\partial p/\partial \rho$ and $\partial \beta/\partial T$) for the CH_4/CO_2 mixture.

Figure 72: Iso-composition (left column) and iso-thermal (right column) results set # 2 (c_p, γ, $\partial p/\partial T$, κ_S and c) for the CH_4/CO_2 mixture.

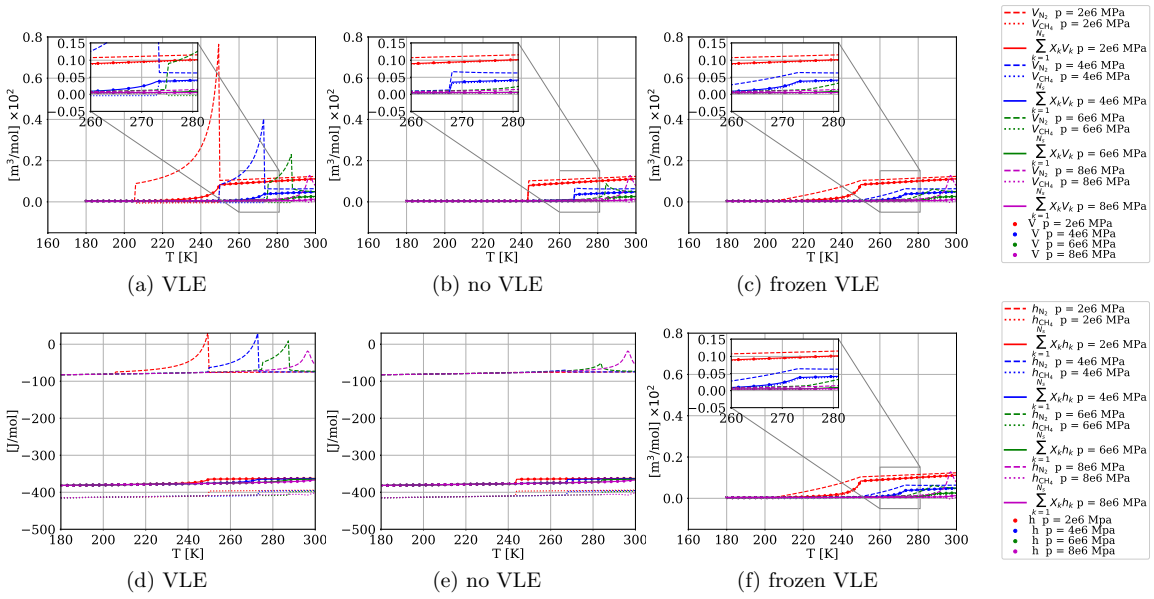

(a) VLE (b) no VLE (c) frozen VLE

(d) VLE (e) no VLE (f) frozen VLE

Figure 73: Partial molar volume (top row) and enthalpy (bottom row) computed along iso-composition line $X_{CH_4} = 0.1$ using the three different thermodynamic models.

as well, here displayed in Fig. 73 for the iso-composition case of $X_{CH_4} = 0.1$ only, for brevity. Analogously to the N_2/CH_4 mixture, some partial molar quantities are analyzed here. The goal is to first validate the overall approach by ensuring that the thermodynamic consistency is achieved in the VLE region and then explore the sensitivity of the various thermodynamic models on these properties. Figure 73 shows the mixture overall partial molar volume and enthalpy with the various models along the $X_{CH_4} = 0.1$ iso-composition line. Again the criterion used here is to plot each species partial molar quantities, their thermodynamic constraint and the whole mixture property, separately computed with its own formula. Again substantial differences are observed between the VLE and the frozen VLE models, which can be quantified to be on the order of 500% or more, whereas even larger discrepancy is observed with the no VLE model. Note that for the $p = 8$ MPa case, all the three models agree because no VLE dome is intersected (*cf.* Fig. 70(b))

Figure 74 shows both the partial molar volumes in the liquid (top row) and the vapor (bottom row) phases. For the full VLE model, these are given by Eqs. (2.2.57)–(2.2.58), whereas for the frozen VLE model these are given by Eq. (2.2.64), respectively. By looking at these results, it is easy to recognize that the same arguments made so far still apply on

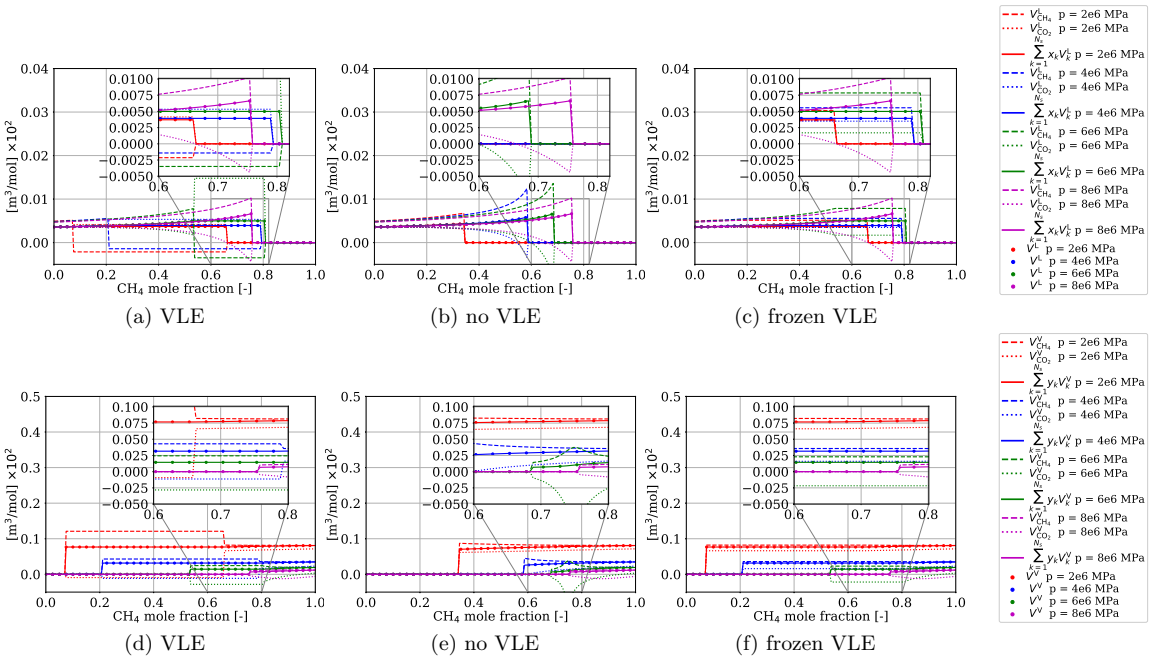

(a) VLE (b) no VLE (c) frozen VLE

(d) VLE (e) no VLE (f) frozen VLE

Figure 74: Liquid phase partial molar volume (top row) and vapor phase partial molar volume (bottom row) computed along iso-composition line $X_{\mathrm{CH_4}} = 0.1$ using the three different thermodynamic models.

the phases taken separately.

4.2.2 Effect of VLE on transport properties

For this case, the transport properties are analyzed along the iso-composition ($X_{\mathrm{CH_4}} = 0.1$) and iso-thermal ($T = 220$ K) case identified in Fig. 70(b). These are given in Fig. 75 and Fig. 76, respectively. Similarly to the conclusions drawn in the previous case, one can easily notice that the viscosity and mass diffusion binary coefficients are not affected by the choice of the VLE, versus the frozen VLE model, while the thermal conductivity does. In all cases, disagreement within the VLE region can span between 50% and 500%, depending on the model and the conditions that are considered.

4.2.3 Effect of other GCEoS/MR combinations

Effect of different EoS and MR is also investigated in this case. The numerical tests are reported in Figs. (77)–(80), where the isothermal case of $T = 220$ K highlighted in Fig. 70(b) is discussed only here for brevity. Other tests led to the same conclusions. For these cases,

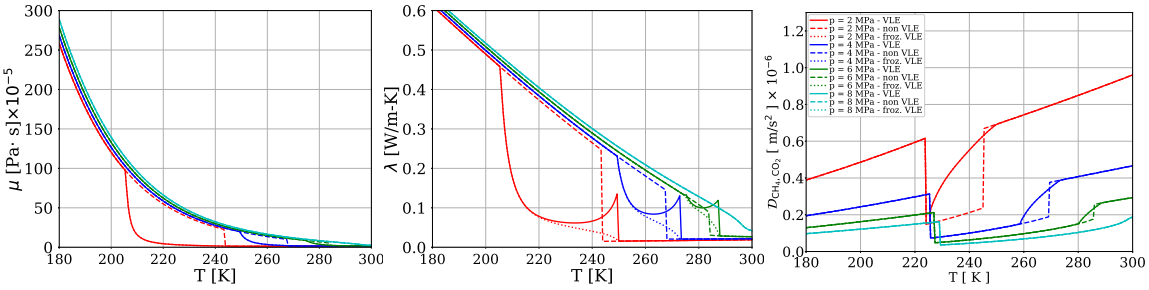

Figure 75: a) dynamic viscosity b) thermal conductivity and c) binary mass diffusivity for the CH_4/CO_2 mixture at $X_{CH_4} = 0.1$ using the three different thermodynamic models.

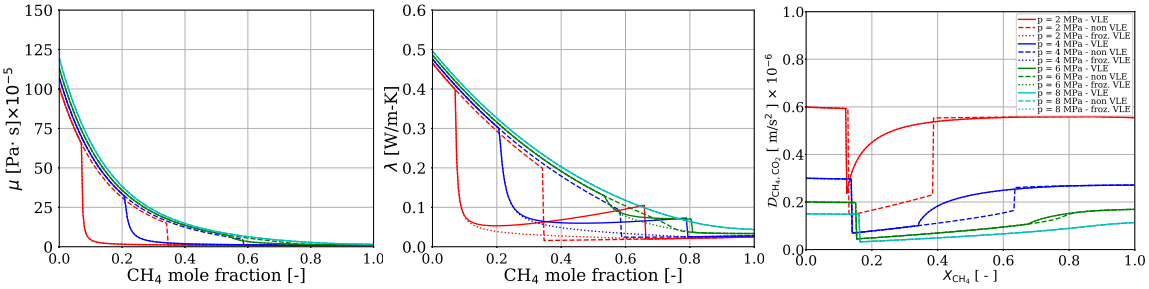

Figure 76: a) dynamic viscosity b) thermal conductivity and c) binary mass diffusivity for the CH_4/CO_2 mixture at $T = 220$ K using the three different thermodynamic models.

the binary interaction parameters have been tuned to match the experimental data at the best (just like the PR MR-3 case discussed previously). These are provided in the figures caption.

First, similarly to the observations made for the N_2/CH_4 case, the VDW EoS performs poorly. Although it may be useful for other applications, this EoS is discarded for the rest of the work. Similarly, the accuracy of the PR-RK EoS is not as high as expected (other tested binary interaction parameters did not improve the results thoroughly), and its higher computational cost makes it not suited for the present work. Therefore, although it may be useful for other applications, this EoS is discarded for the rest of the present work.

The RK EoS in Fig. 78 also shows some limitations in this case. It is well known [114] that this EoS has a lower accuracy compared to SRK or PR, mainly because of the dependency on the acentric factor ω_i, which is dropped for the RK case as visible in Tab. 4. In the previous N_2/CH_4 case, this effect was not that visible because both N_2 and CH_4 have ω on the order of 10^{-2}. Since CO_2 has ω_i on the order of 10^{-1} (see Tab. 35), this effect is much

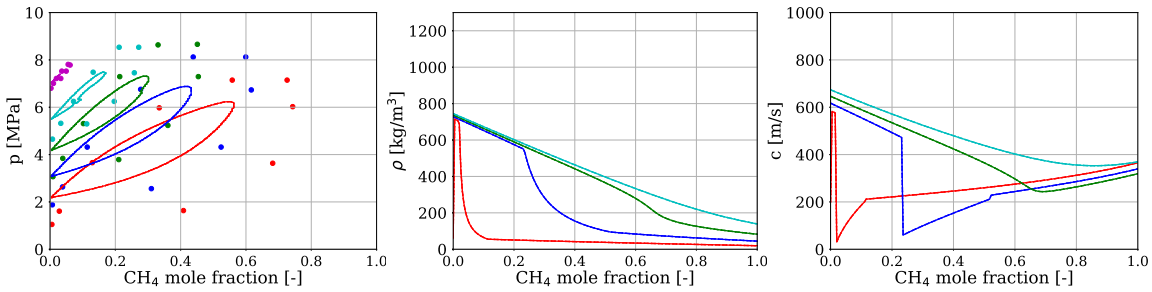

(a) (b) (c)

Figure 77: (a) VLE diagram, (b) density profiles and (c) speed of sound profiles obtained with the VDW EoS for the iso-thermal $T = 220$ K case. Dotted data is taken from [240]. The binary interaction parameters used in this case are $k_{ij} = [0.0, 0.135, 0.135, 0.0]$.

more visible for the present mixture and therefore the limitation of the RK EoS is more highlighted. For this reason, the RK EoS is dropped for the rest of the work.

Finally, SRK has performances that are very close to PR. Ultimately there is no real factor that makes one EoS to be more preferred to the other, in fact these two are the most widely used in the propulsion/combustion community. There is also no particular difference in terms of computational cost since they share some sub-models (*cf.* Tab. 4) and therefore code routines. In addition, the superior performance of MR-3 over MR-1 is also highlighted through the SRK case by looking at the VLE plot of Fig. 79(a). With these arguments, it can be concluded that either SRK or PR with MR-3 or MR-1 can be used with almost identical outcome in terms of both accuracy and performances.

For this reason the PR MR-3 model is going to be chosen as a preferred model (mostly because of lab history) over SRK, which again can be chosen just like PR with no much differences in the outcome (and in fact it is now available in the CFD solver).

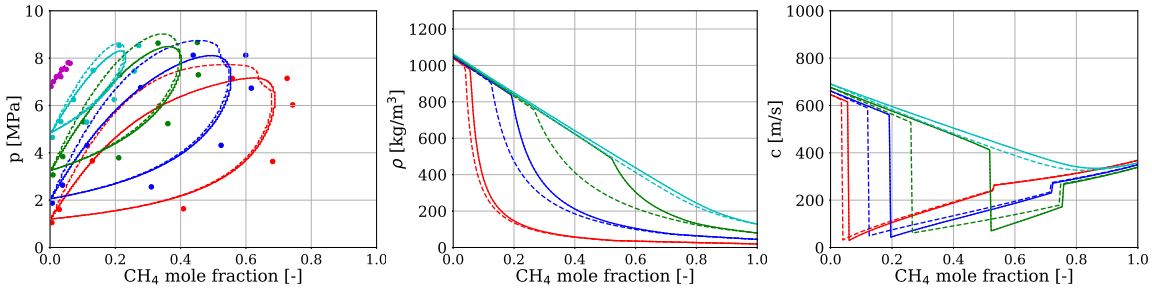

(a) (b) (c)

Figure 78: (a) VLE diagram, (b) density profiles and (c) speed of sound profiles obtained with the RK EoS for the iso-thermal $T = 220$ K case. Dotted data is taken from [240]. The binary interaction parameters used in this case are $k_{ij} = [0.0, 0.125, 0.125, 0.0]$.

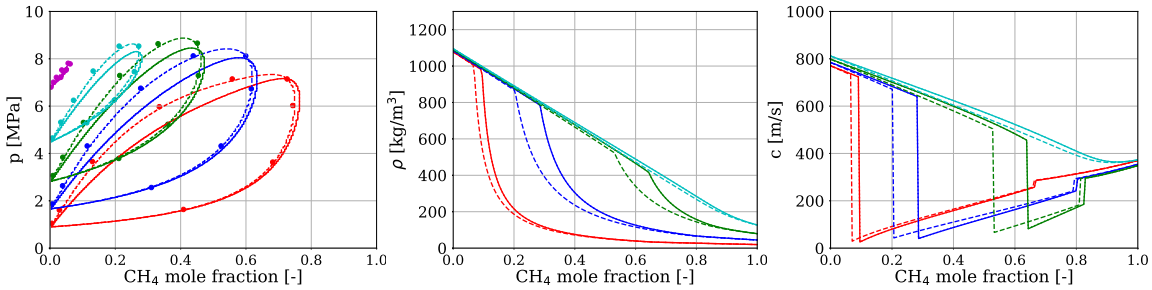

(a) (b) (c)

Figure 79: (a) VLE diagram, (b) density profiles and (c) speed of sound profiles obtained with the SRK EoS for the iso-thermal $T = 220$ K case. Dotted data is taken from [240]. The binary interaction parameters used in this case are $k_{ij} = [0.0, 0.048, 0.048, 0.0]$.

4.3 Ternary mixture: $CH_4/N_2/C_2H_6$

4.3.1 VLE diagram and main properties

The third case discussed is that of a ternary mixture involving species $CH_4/N_2/C_2H_6$. The ternary VLE diagram for various iso-baric and iso-thermal conditions is shown in Fig. 81 along with reference data, for validation. Data is analyzed for all cases along different "test lines" which consider only mixture composition variations. These lines are shown in Fig. 81 for reference and are obtained as follows:

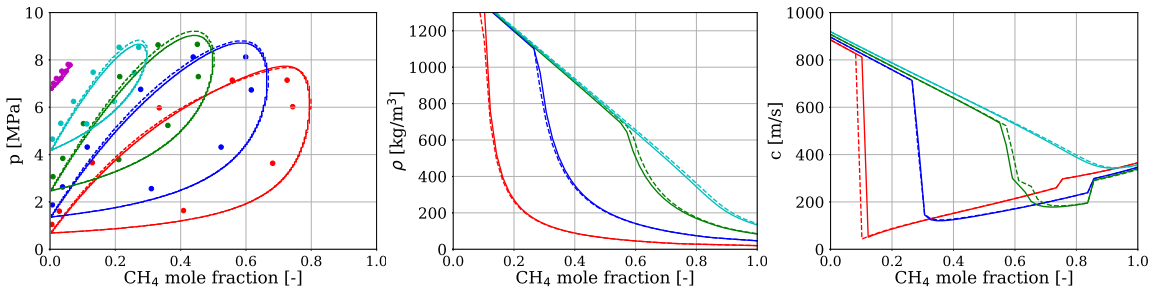

Figure 80: (a) VLE diagram, (b) density profiles and (c) speed of sound profiles obtained with the PR-RK EoS for the iso-thermal $T = 220$ K case. Dotted data is taken from [240]. The binary interaction parameters used in this case are $k_{ij} = [0.0, 0.015, 0.015, 0.0]$.

- test line 1: $X_{N_2} = 0.2$, $X_{CH_4} \in [0.0, 1.0 - X_{N_2}]$, $X_{C_2H_6} = 1.0 - X_{N_2} - X_{CH_4}$;
- test line 2: $X_{N_2} \in [0.0, 1.0 - X_{CH_4}]$, $X_{CH_4} = 0.2$, $X_{C_2H_6} = 1.0 - X_{N_2} - X_{CH_4}$;
- test line 3: $X_{N_2} = 1.0 - X_{CH_4} - X_{C_2H_6}$, $X_{CH_4} \in [0.0, 1.0 - X_{C_2H_6}]$, $X_{C_2H_6} = 0.2$.

Since the conclusions are the same for every test line analyzed, only the results pertaining to test line 3 are showed in Fig. 82 and Fig. 83. These correspond to the conditions of Fig. 81(d) and Fig. 81(f), respectively. The conclusions for the present case are identical to those discussed earlier for both binary mixtures. The scope of the present test case is simply to demonstrate that the discrepancies between the models are not limited to the cases of binary mixtures, but as expected, they extend to any arbitrary complex mixture that shows VLE. One interesting difference between the results of $T = 140$ K and those of $T = 200$ K is that in the first case, the test line 3 is initially in the liquid regime and enters the VLE dome for larger amount of N_2, while in the second case test line 3 is completely in the VLE dome and in fact it starts with a $\beta > 0$ value for N_2 close to zero (see Fig. 82, column b)). This reflects on all the thermodynamic properties, including partial molar quantities, which are discussed next.

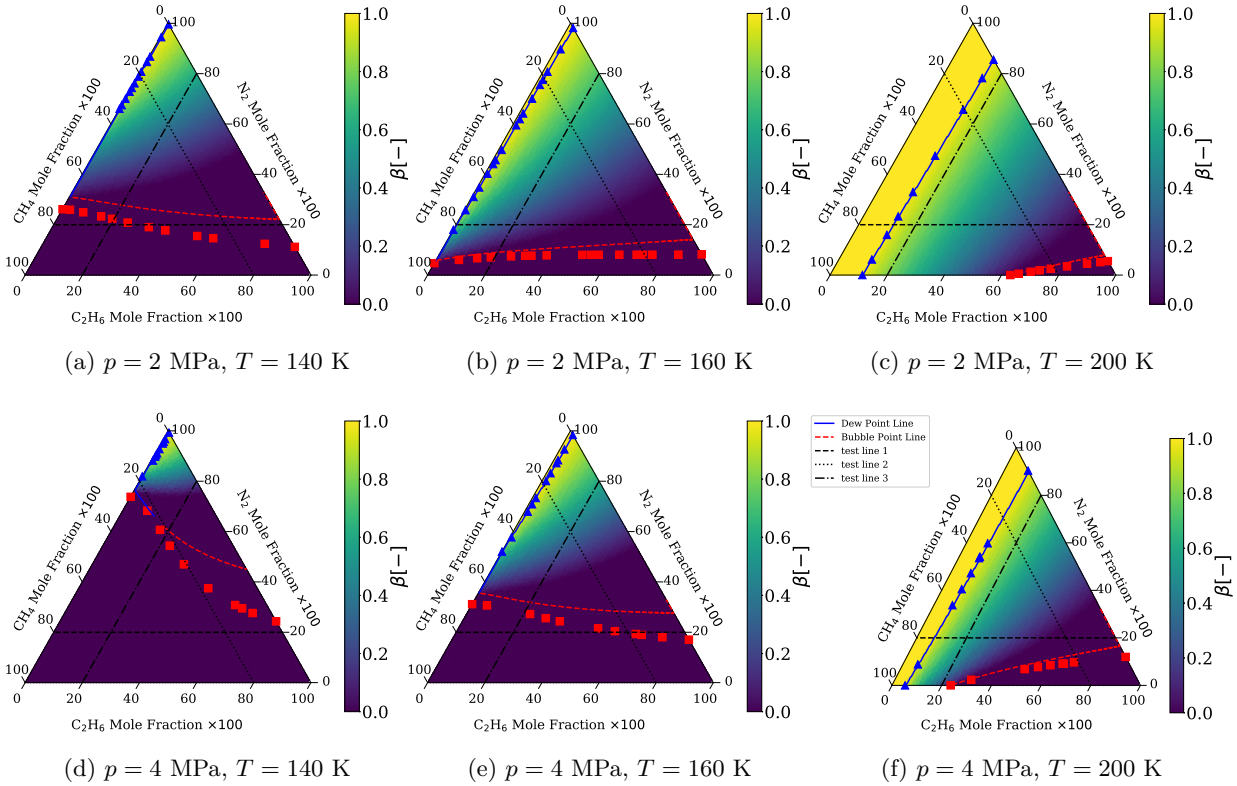

(a) $p = 2$ MPa, $T = 140$ K (b) $p = 2$ MPa, $T = 160$ K (c) $p = 2$ MPa, $T = 200$ K

(d) $p = 4$ MPa, $T = 140$ K (e) $p = 4$ MPa, $T = 160$ K (f) $p = 4$ MPa, $T = 200$ K

Figure 81: Ternary VLE diagrams for $CH_4/N_2/C_2H_6$ mixture at different pressures and temperatures. Solid blue and dashed red lines indicate the dew and bubble point contours. Symbols are taken from [222].

For completeness, the partial molar volume and enthalpy along the test line 3 of Fig. 81(d) and (f) are reported in Fig. 84. This time, an even complex representation appears because of the existence of three different partial molar quantities, one for each species in addition to the thermodynamic constraint and the mixture property. Once again, as the thermodynamic model is changed, substantial differences are observed in the outcome. It is also interesting to note how for test line 3 of the $T = 200$ K case, some thermodynamic and transport properties (discussed later) show a good agreement between the VLE and the non VLE case for $X_{N_2} > 0.2$. This is already visible in the density plot of Fig. 82 (b) (top), where the differences between the VLE and the non VLE model for $X_{N_2} > 0.2$

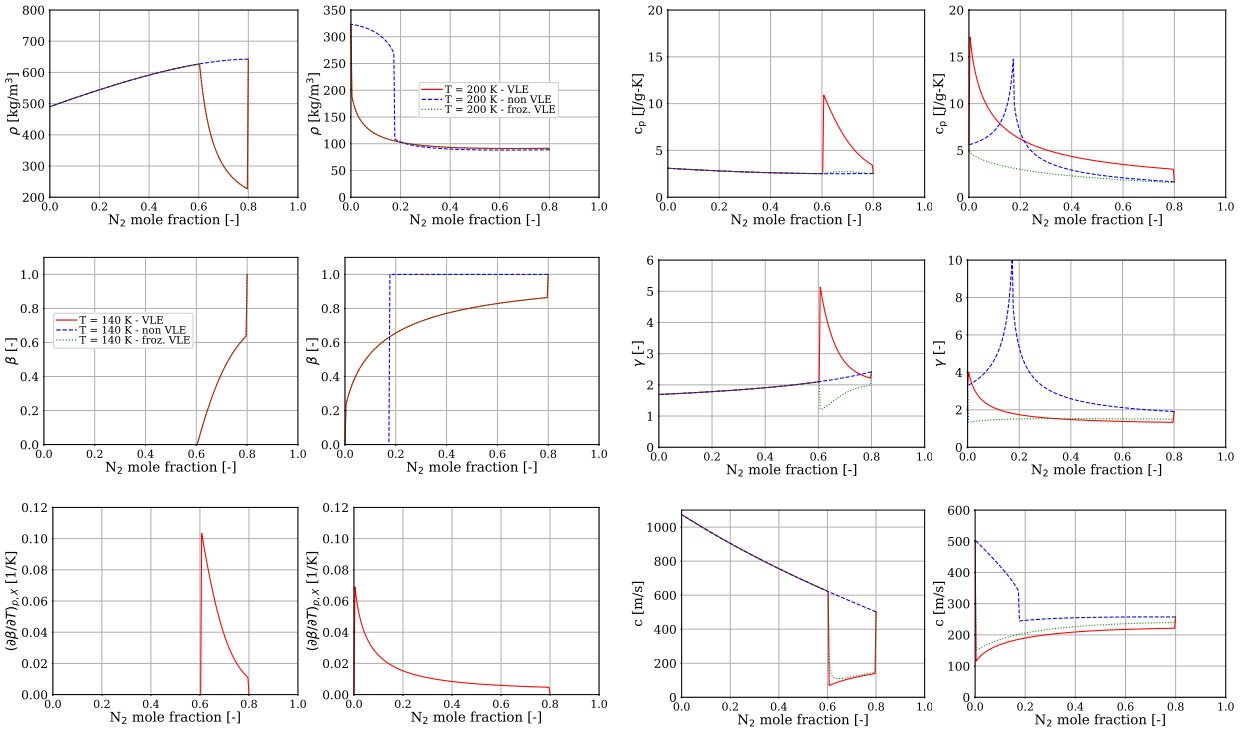

(a) $T = 140$ K (b) $T = 200$ K

Figure 82: Ternary mixture relevant properties set # 1 (ρ, β and $\partial\beta/\partial T$) analyzed along the test line # 3 of Fig. 81 for $p = 4$ MPa and varying the temperature: $T = 140$ K (left column) and $T = 200$ K (right column). These correspond to the test line # 3 of Fig. 81(d) and Fig. 81(f) respectively.

(a) $T = 140$ K (b) $T = 200$ K

Figure 83: Ternary mixture relevant properties set # 2 (c_p, γ and c) analyzed along the test line # 3 of Fig. 81 for $p = 4$ MPa and varying the temperature: $T = 140$ K (left column) and $T = 200$ K (right column). These correspond to the test line # 3 of Fig. 81(d) and Fig. 81(f) respectively.

are less than 5%. The same difference is transferred to the transport properties μ and the mass diffusivities showed next. The reason of this behavior is explained in Fig. 85 where the phase densities are plotted separately for all the models. This figure shows that the vapor contribution in density ρ^V is very close between the VLE and the non VLE models as $X_{N_2} > 0.2$. This means that $\mathbf{y} \sim \mathbf{X}$ for this particular condition. Therefore, as β also increases with X_{N_2} (*cf.* Fig. 82 column (b)), the importance of the liquid density contribution ρ^L decreases in the overall mixture density balance and both models agree quite well.

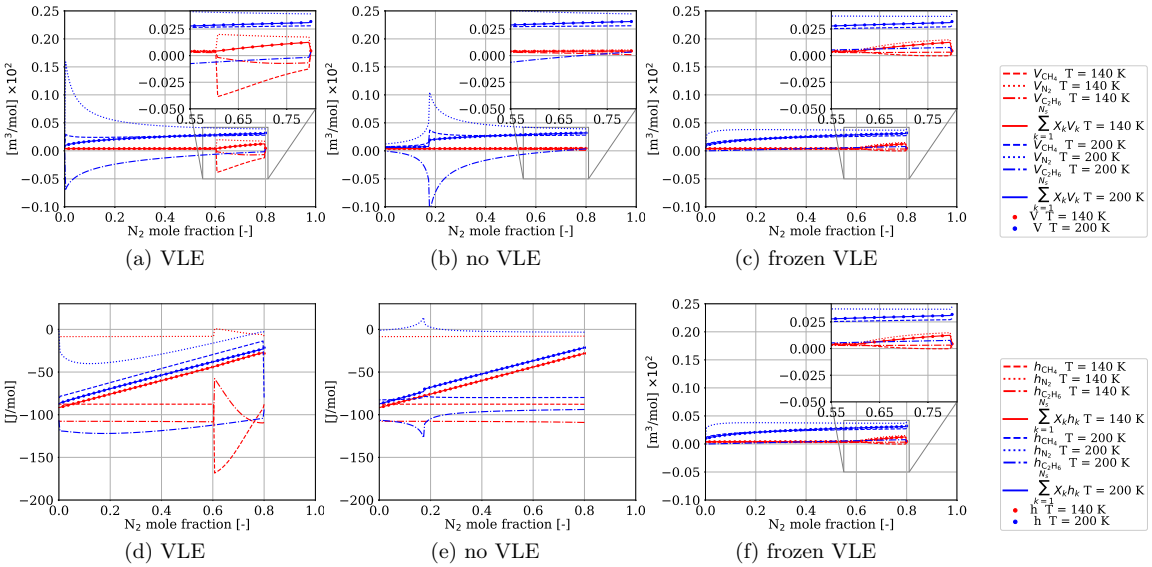

(a) VLE (b) no VLE (c) frozen VLE

(d) VLE (e) no VLE (f) frozen VLE

Figure 84: Partial molar volume (top row) and enthalpy (bottom row) computed along test line # 3 of Fig. 81(d) ($T = 140$ K, $p = 4$ MPa) and Fig. 81(f) ($T = 200$ K, $p = 4$ MPa).

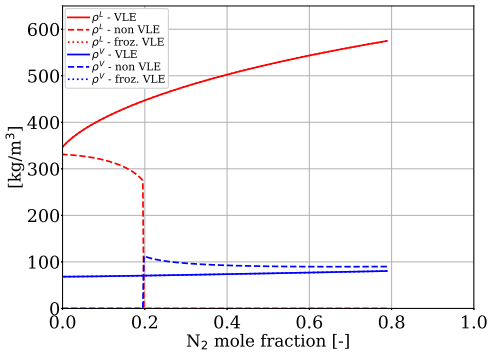

Figure 85: Investigation about the behavior of the phases densities for the $T = 200$ K, $p = 4$ MPa case of Fig. 82f.

4.3.2 Effect of VLE on transport properties

Transport properties are illustrated in Fig. 86 and Fig. 87 for this ternary mixture. The conditions refer again to the test line # 3 of Fig. 81(d) and Fig. 81(f). For simplicity, mass diffusion properties in this case are reported directly in the Hirschfelder-Curtiss approximation [70] of Eq. (2.1.16). Similar considerations made previously apply here too. Note that the error in the transport properties that would occur between the VLE and the non VLE method within the multi-phase region would be very high for the Fig. 81(d) case. Conversely, for the Fig. 81(f) case, is possible to notice the agreement between the non VLE and the VLE models for $X_{N_2} > 0.2$ for the viscosity and the mass diffusion coefficients because of the reasons explained before. On the other hand, thermal conductivity also shows differences in case Fig. 81(f) as illustrated in Fig. 87(b). Again this behavior is explained by the dependency of λ on c_v according to Eq. (2.3.21). Since c_v shows discrepancies between the VLE and the non VLE model (*cf.* Fig. 83 (b)), this is transferred to λ.

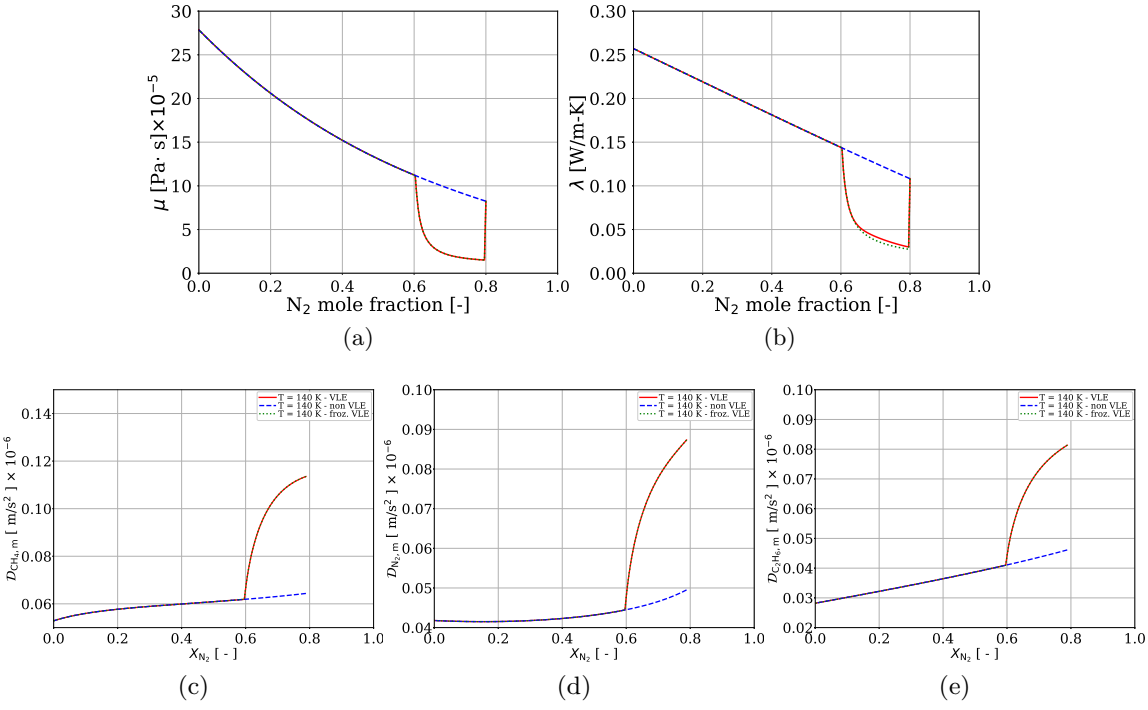

Figure 86: a) dynamic viscosity b) thermal conductivity and c)-d)-e) mass diffusivity coefficients (in Hirschfelder-Curtiss form) for the $T = 140$ K, $p = 4$ MPa case, corresponding to Fig. 81(d)

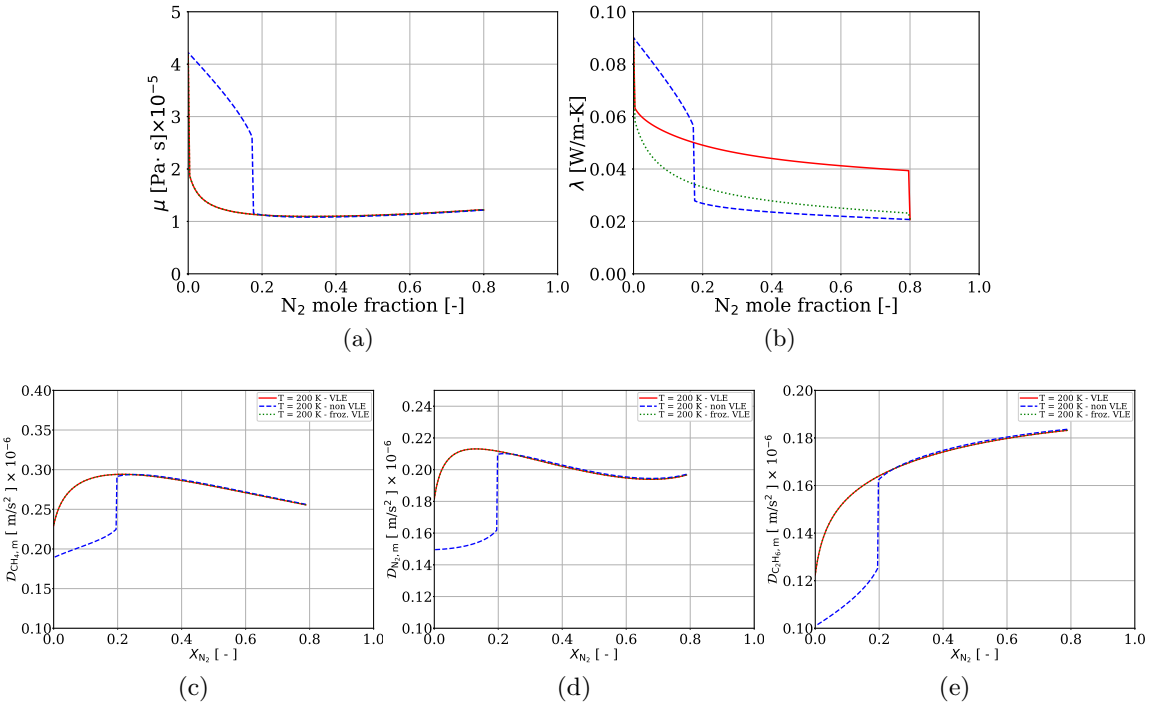

Figure 87: a) dynamic viscosity b) thermal conductivity and c)-d)-e) mass diffusivity coefficients (in Hirschfelder-Curtiss form) for the $T = 200$ K, $p = 4$ MPa case, corresponding to Fig. 81(f)

4.4 Prudhoe bay mixture

4.4.1 VLE diagram and main properties

The final mixture considered for this study is the Prudhoe bay gas [159], which consists of 14 species involving different hydrocarbons, including CH_4, as well as O_2, N_2 and CO_2. The VLE diagram of this mixture is provided in [159] for a constant composition reported in Tab. 20 and by varying temperature and pressure. This VLE data is first used to

Table 20: Mixture composition in mole fractions for the Prudhoe bay gas [159].

species	CH_4	C_2H_6	C_3H_8	i-C_4H_{10}	n-C_4H_{10}	i-C_5H_{12}	n-C_5H_{12}
X_i	0.83331	0.096155	0.035998	0.003417	0.004585	0.0403E-2	0.0342E-2
species	C_6H_{14}	C_7H_{16}	C_8H_{18}	C_7H_8	N_2	O_2	CO_2
X_i	0.0046E-2	0.0003E-2	0.0001E-2	0.0002E-2	1.4992E-2	0.0008E-2	1.0738E-2

further validate the present multi-phase equilibrium model in Fig. 88(a). Next, iso-baric lines indicated in the same picture are analyzed and compared with available data in the

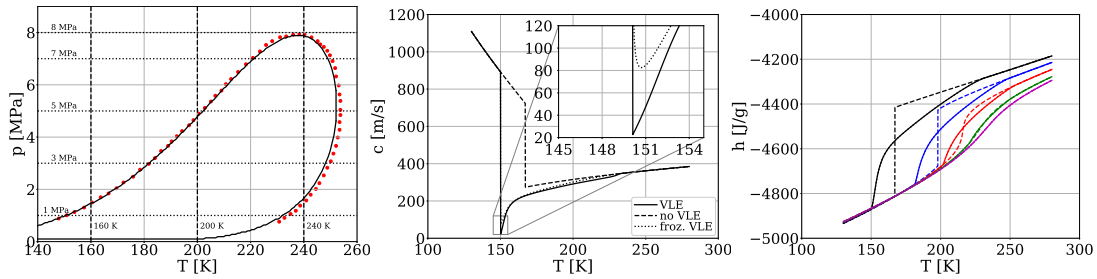

(a) VLE diag. at const. comp. (b) speed of sound (comparison # 1) (c) enthalpy

(d) speed of sound (comparison # 2) (e) isentropic compressibility (f) spec. heat const. p

Figure 88: a) VLE diagram of the Prudhoe gas at fixed composition (dotted data taken from [159]), b) speed of sound comparison along $p = 1$ MPa with different models: (—) VLE, (– –) no VLE, (...) frozen VLE, c) Iso-baric enthalpy (cfr. Fig. 88(a)), d) speed of sound along iso-baric lines (Fig. 88(a), dotted data taken from [159]), e) isentropic compressibility along iso-baric lines (Fig. 88(a), dotted data taken from [139]), f) specific heat and constant pressure (cfr. Fig. 88(a)). In b) and d) solutions are as follows: (—) VLE, (...) frozen VLE, (– –) Wood's equation [242]. In c) and f) solutions are as follows: (—) VLE, (...) frozen VLE, no VLE (– –).

literature. Figure 88(b) shows the comparison of the calculated speed of sound at fixed pressure of 1 MPa using all three thermodynamic models (indicated in the picture legend). While the single-phase (no VLE) model again shows very low performances for the same reasons discussed earlier, the frozen VLE model shows acceptable results, with reasonably good capability to capture the mixture phase boundaries. Still, an error of about 300% is achieved for the lowest peak, which can be unacceptable, depending on the application. Next, Fig. 88(d) displays more iso-baric curves for the speed of sound, now including reference data, the frozen VLE model and the Wood's equation [242]. The purpose of this picture is to essentially compare the frozen VLE assumption and the Wood's equation. It is apparent that the difference between the two approaches is significant and leads to the following conclusions: a) the frozen VLE model performs much better than the simple Wood's correlation; given that both require the knowledge of the VLE data (*i.e.*β, x_i and y_i), the computational cost of both models is about the same because no VLE derivatives are required, however significant improvement can be achieved, b) the reason why the frozen VLE model performs better compared to the Wood's equation is related to some non-linear terms between the phase properties that are neglected in the Wood's correlation. These appear to be crucial to capture the phase boundaries reasonably well, although the full VLE model contains all the necessary information to get the correct result. More insights between the frozen VLE assumption and the Wood's equation are given in Appendix C. In the same appendix, some additional explanations regarding the reason why the frozen VLE assumption performs better on the speed of sound and not as good in the specific heats calculation (see Fig. 88(f)) are also given. Figure 88(e) shows the comparison of the isentropic compressibility κ_S with reference data computed with the different models. Analogous discussion made for the speed of sound holds. Finally, Fig. 88(c) and (d) show the mixture enthalpy and specific heat at constant pressure for the same iso-baric lines. It is possible to formulate the following conclusions:

- the single-phase (no VLE) model shows the same features discussed earlier. This model is incorrect to predict properties within the multi-phase region, as expected;

- the frozen VLE model predicts the same value of enthalpy as the full VLE model (lines are overlapped). This is not surprising since the multi-phase enthalpy is only a function of the VLE variables and not their derivatives;

- on the other hand, the value of c_p shows huge departures between the VLE and the frozen VLE model, again due to the lack of representation of correct phase-boundaries trends introduced by the VLE derivatives which are not taken into account by the frozen VLE method. Once again this underlines the fact that with the frozen VLE model, errors and inconsistencies can be introduced and, depending on the type of analysis being performed, this can play a crucial role in the outcome. This will have a consequence on the thermal conductivity (see next);

- in the real single-phase zone represented by the 8 MPa curves, all the models collapse to a unique (correct) solution.

4.4.2 Effect of VLE on transport properties

Two examples are chosen to analyze the transport properties on this mixture, namely the iso-thermal condition at $T = 200$ K and the iso-baric condition at $p = 5$ MPa. The results of dynamic viscosity and thermal conductivity for these cases are showed in Fig. 89 and Fig. 90, respectively. Identical conclusions discussed for the previous cases apply.

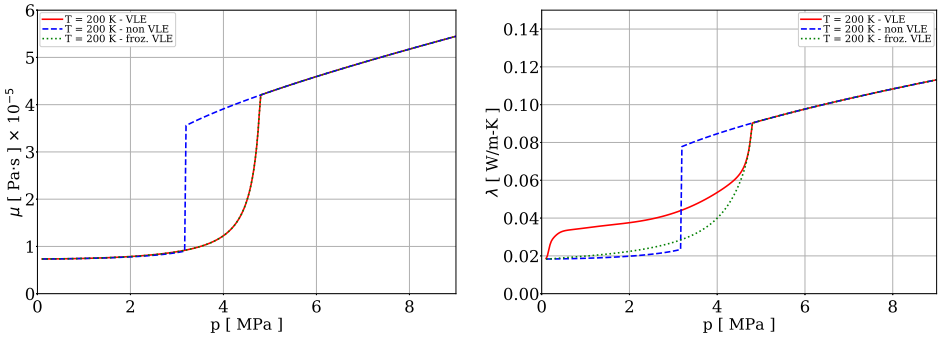

Figure 89: a) Dynamic viscosity and b) thermal conductivity for the iso-thermal condition at $T = 200$.

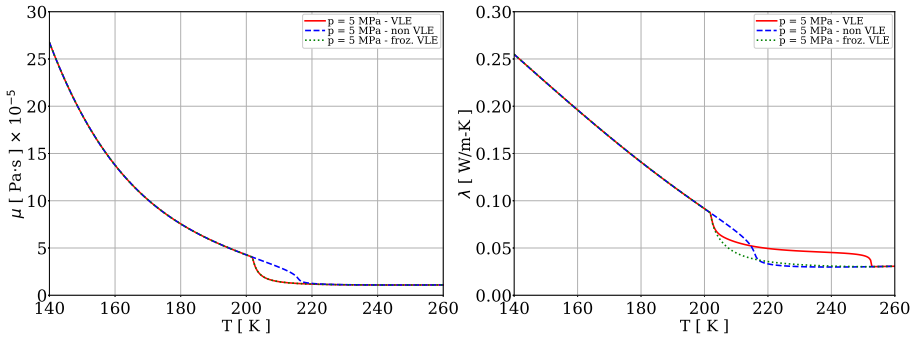

(a) (b)

Figure 90: a) Dynamic viscosity and b) thermal conductivity for the iso-baric condition at $p = 5$ MPa.

4.5 Considerations on numerical vs analytical derivatives for the calculation of VLE properties

The present VLE model discussed so far for two-phase equilibrium systems represents the analytical version of a numerical approach initially proposed by [139] and later used by [223] and [226]. This is the one discussed in Sec. 3.4.5. One can compute all the thermodynamic properties in a VLE system by constructing finite differences in the thermodynamic space of all the derivatives discussed in this work. Although consistency and correctness is achieved [139, 223, 226], particular attention has to be given near the phase boundaries, where the perturbation of the current VLE state to construct the numerical derivative can fall outside the actual VLE dome, affecting the overall result of the derivative itself in an erroneous manner. This issue is briefly pointed out in [139], and only in [226], a specific phase sensor was proposed. Nevertheless, the sensor itself can be problem-dependent and case-specific tuning procedure might be required upfront. On the other hand, the present analytical model completely eliminates the issue because once the VLE is found, ($\beta \in (0, 1)$), the derivatives are computed in an analytical manner, without any perturbation of the current state.

Another advantage of the present model is related to the gain in the calculation speed to compute all the properties. Although the present model requires substantial amount of floating point operations, including linear system solutions with associated matrix inversions

(see Appendix D), it is still computationally more efficient than solving for the numerical derivatives as in [139, 223, 226] because the latter requires to solve additional VLE problems of Eqs. (2.2.36)–(2.2.37) in the perturbed temperature or pressure states to construct the derivatives with finite differences. To illustrate this point, Tab. 21 reports the computational cost, in terms of time to compute all the thermodynamic properties *after* the solution of the VLE problem with both the numerical [139, 223, 226] and the analytical (present) VLE models. It is immediately clear that at least a speed up of 30% is achieved with the present analytical model, even in the Prudhoe gas case which contains 14 species, confirming the advantage of the present model over the numerical model. Note that both models have the same computational time when no VLE calculations are involved. Additional information regarding the speed-up will be addressed in Sec. 5.1.2 and Sec. 5.2.2 where the present thermodynamic model is attached to the CFD solver.

Table 21: Comparison of computational times to calculate all the thermodynamic properties between the numerical model [139] and the analytical model (present work). Data is collected based on the mixtures considered above.

Mixture	Case	Details	Num. points computed	Numer. model [ms]	Analyt. model [ms]	Time reduction (%)
N_2/CH_4	iso-X 0.2	$T = 130\,\mathrm{K}\,, \mathrm{p} \in [0.1, 6]\,\mathrm{MPa}$	2000	43.19	27.54	-36.23
N_2/CH_4	iso-X 0.2	$T = 150\,\mathrm{K}\,, \mathrm{p} \in [0.1, 6]\,\mathrm{MPa}$	2000	55.23	30.19	-45.33
N_2/CH_4	iso-X 0.2	$T = 170\,\mathrm{K}\,, \mathrm{p} \in [0.1, 6]\,\mathrm{MPa}$	2000	58.53	30.79	-47.39
N_2/CH_4	iso-X 0.5	$T = 130\,\mathrm{K}\,, \mathrm{p} \in [0.1, 6]\,\mathrm{MPa}$	2000	72.88	33.83	-53.58
N_2/CH_4	iso-X 0.5	$T = 150\,\mathrm{K}\,, \mathrm{p} \in [0.1, 6]\,\mathrm{MPa}$	2000	91.71	36.68	-60.00
N_2/CH_4	iso-X 0.5	$T = 170\,\mathrm{K}\,, \mathrm{p} \in [0.1, 6]\,\mathrm{MPa}$	2000	23.46	23.46	-00.00
N_2/CH_4	iso-p 2 MPa	$T = 130\,\mathrm{K}\,, \mathrm{X}_{\mathrm{N}_2} \in [0, 1]$	2000	92.14	35.13	-61.87
N_2/CH_4	iso-p 2 MPa	$T = 150\,\mathrm{K}\,, \mathrm{X}_{\mathrm{N}_2} \in [0, 1]$	2000	75.41	32.22	-57.27
N_2/CH_4	iso-p 2 MPa	$T = 170\,\mathrm{K}\,, \mathrm{X}_{\mathrm{N}_2} \in [0, 1]$	2000	23.24	23.24	-00.00
N_2/CH_4	iso-p 4 MPa	$T = 130\,\mathrm{K}\,, \mathrm{X}_{\mathrm{N}_2} \in [0, 1]$	2000	27.39	27.39	-00.00
N_2/CH_4	iso-p 4 MPa	$T = 150\,\mathrm{K}\,, \mathrm{X}_{\mathrm{N}_2} \in [0, 1]$	2000	70.25	36.69	-47.77
N_2/CH_4	iso-p 4 MPa	$T = 170\,\mathrm{K}\,, \mathrm{X}_{\mathrm{N}_2} \in [0, 1]$	2000	52.66	28.93	-45.06
Ternary	test line # 3	$T = 140\,\mathrm{K}\,, \mathrm{p} = 4\,\mathrm{MPa}$	2000	180.61	76.94	-57.39
Ternary	test line # 3	$T = 200\,\mathrm{K}\,, \mathrm{p} = 4\,\mathrm{MPa}$	2000	253.13	60.62	-76.05
Prudhoe gas	iso-T 160 K	$p \in [0.1, 8]\,\mathrm{MPa}$	2000	460.36	335.54	-27.11
Prudhoe gas	iso-T 200 K	$p \in [0.1, 8]\,\mathrm{MPa}$	2000	1209.98	675.03	-44.21
Prudhoe gas	iso-T 240 K	$p \in [0.1, 8]\,\mathrm{MPa}$	2000	1545.95	730.33	-52.76
Prudhoe gas	iso-T 260 K	$p \in [0.1, 8]\,\mathrm{MPa}$	2000	253.18	253.18	-00.00
Prudhoe gas	iso-p 1 MPa	$T \in [140, 260]\,\mathrm{K}$	2000	993.88	580.04	-41.63
Prudhoe gas	iso-p 3 MPa	$T \in [140, 260]\,\mathrm{K}$	2000	1013.89	563.43	-44.42
Prudhoe gas	iso-p 5 MPa	$T \in [140, 260]\,\mathrm{K}$	2000	1017.69	548.64	-46.08
Prudhoe gas	iso-p 7 MPa	$T \in [140, 260]\,\mathrm{K}$	2000	1231.07	596.13	-51.57
Prudhoe gas	iso-p 8 MPa	$T \in [140, 260]\,\mathrm{K}$	2000	511.55	511.55	-00.00

4.6 Summary

In this chapter, important physical and computational details about the complete multi-phase thermodynamic model introduced in Sec. 2.2.2 are presented. The validation is made against several mixtures with increasing complexity using different thermodynamic models: the fully analytical VLE model, the single-phase (no VLE) model and the frozen VLE model which does not take into account the VLE variables derivatives in the calculation of thermodynamic properties. Separate studies on the difference EoS and MR are performed as well. The material presented in this chapter completes the fulfillment of the requisites listed in **Objective 1**.

The results show that the single-phase model does not perform well in the two-phase regions as expected, therefore it should be avoided for such conditions. On the other hand, the frozen VLE method performs much better, with primary thermodynamic properties that match with the VLE model, however secondary thermodynamic properties, such as specific heats and speed of sounds can show discrepancies ranging from few percent to some orders of magnitudes, depending on the variable and the chosen conditions. These differences can be also transferred to the transport properties, particularly the thermal conductivity.

Studies on different EoS-MR combinations reveal that the EoS model plays the biggest role in the results compared the MR model. Particularly MR-2 (arithmetic) is found to be useless for VLE calculations because it does not retain the intrinsic non-linear mixing that is peculiar of the other models. The preferred EoS remain PR and SRK, which best compromise cost and accuracy. There is no specific criterion that would prefer one to the other because they perform very similar. The MR-4 is more expensive than 1 and 3 due to the larger amount of floating point operation involved and it does not perform well with PR-RK therefore it is discarded. In the end, MR-1 and MR-3 are those that seem to be quite equivalent for practical computational purposes.

Finally, investigations on performances of the fully analytical VLE model and the corresponding fully numerical model reveal a superior outcome of the present analytical model. Speed-up of a 30% baseline is observed with all the considered mixtures, mainly because

multiple calculations in series of VLE problems to construct finite differences in the thermodynamic space is avoided.

Chapter V

RESULTS: SIMULATION OF NON-REACTING AND REACTING FLOWS

In this chapter, the results on the simulations of non-reacting and reacting flows are discussed. The overall goal is to investigate on the effect of VLE thermodynamics on fluid-mechanics according to **Objective 3**. In addition, **Objective2** is completed. To do so, complex setups from a geometrical point of view are disregarded in this analysis for mainly two reasons. One: the use of multi-component VLE requires very expensive calculations at a given point in space and time; as it will be demonstrated this becomes quickly very impractical to be translated to large scales computations as they would require, with the present implementation, an enormous amount of computational resources and time. Two: nevertheless, for the scope of demonstrating the effects of VLE thermodynamics on the flow field, relatively simple configurations are enough, and in fact they would provide more insights than complex configurations as a number of unnecessary complexities, such as turbulence closure, would carry their own model uncertainty. On the other hand, simple configurations are more manageable as parametric studies can be performed more quickly and can provide important understanding on the resolution, numerics, thermodynamics and their non-linear coupling.

5.1 One-dimensional (1D) advection of a multi-species contact discontinuity

The first case investigated is on the advection of a simple one-dimensional (1D) contact discontinuity made of two components. The selected mixture is N_2/C_6H_{14}, already validated for VLE in Sec. 3.5.2. The goal of this simulation is to demonstrate the independence between the error generated by the conservative scheme, addressed by the Double-Flux method as discussed in Sec. 3.5.2, and the error in the thermodynamic state committed if single-phase thermodynamics is used when multi-phase conditions are expected to occur.

The latter was already proved for 0D thermodynamics in Chap. 4, however in this chapter, the same argument is proven when the governing equations are solved in a region where multi-phase conditions occur.

The viscous fluxes are turned off here with the following two goals: a) validate the effect of a pure QC scheme over the FC scheme as done by [109] and b) demonstrate that even in a very simple test a difference between VLE and non-VLE thermodynamics can occur irrespective of the resolution and the numerical scheme. It is very important to underline that the goal is not to explore the conditions under which VLE and non-VLE thermodynamics provide the biggest difference, which in fact can be a non-trivial task to perform by itself due to the number of variables (the space is at least three dimensional in p, T and one mole fraction) to vary even in a binary mixture, rather to prove the existence of a difference, which is relatively unexplored. This is in fact very important to isolate from the resolution and scheme effects [226].

5.1.1 Case setup and results discussion

The one-dimensional domain is chosen of length $L = 0.2$ mm and the initial interface between the two species is positioned at $x_0 = 0.05$ mm. The contact moves from left to right and it is initialized with uniform pressure and velocity of $p = 5$ MPa and $u = 50$ m/s respectively. Finally, the species and temperature profiles are imposed along the x axis using an hyperbolic tangent profile of the following form: $T(x) = 0.5(T_{\mathrm{N_2}} + T_{\mathrm{C_6H_{14}}}) + 0.5(T_{\mathrm{N_2}} - T_{\mathrm{C_6H_{14}}})\tanh[(\mathrm{x} - \mathrm{x_0})/\mathrm{w}]$, $X_{\mathrm{N_2}} = 0.5 - 0.5\tanh[(\mathrm{x} - \mathrm{x_0})/\mathrm{w}]$, $X_{\mathrm{C_6H_{14}}} = 1 - X_{\mathrm{N_2}}$, where $w = 0.005$ mm is the initial interface thickness. Two different cases are studied, whereby the difference is on the species temperatures. Specifically for Case 1, $T_{\mathrm{N_2}} = 350$ K and $T_{\mathrm{C_6H_{14}}} = 595$ K is used, while for Case 2 $T_{\mathrm{N_2}} = 293$ K and $T_{\mathrm{C_6H_{14}}} = 479$ K is used. Inflow and outflow conditions are imposed on the left and right side, respectively.

Preliminary analysis of adiabatic (H) and isochoric (V) zero-dimensional mixing models (*cf.* Sec. 3.4.4) conducted with and without VLE show the occurrence of two distinct mixing behaviors as shown in Fig. 91. The VLE dome corresponding to 5 MPa is also superimposed. Observations indicate strong differences between H and V mixing models. In addition, im-

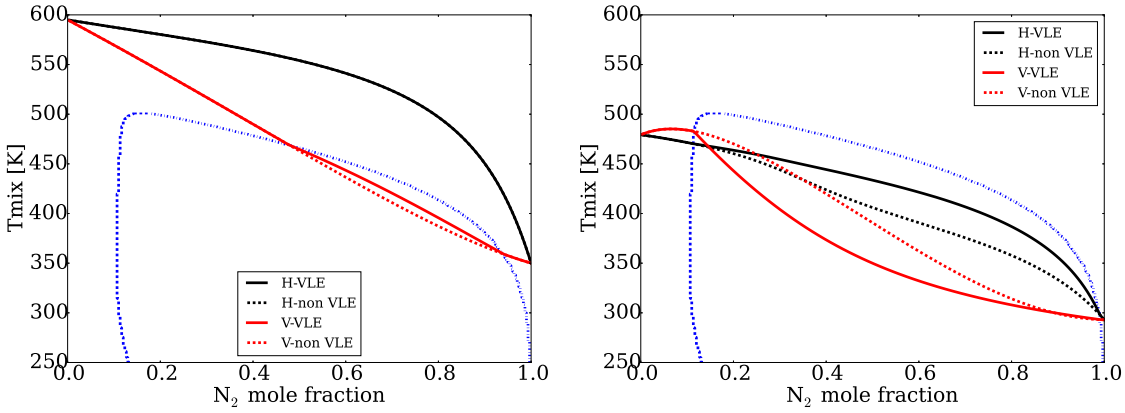

(a) Case 1 (b) Case 2

Figure 91: Adiabatic (H) and isochoric (V) mixing lines with and without VLE thermodynamics at $p = 5$ MPa conducted for (a) case 1 and (b) case 2. VLE dome is also superimposed with blue, dotted/dashed lines to indicate the bubble and dew curves, respectively.

portant differences are observed between the VLE and the non-VLE solutions, especially for Case 2, where the mixing occurs almost completely in the VLE dome and thus accounting for these effects becomes more important than Case 1, where only marginally differences are observed for the V curves only since the H curves do not intersect the VLE dome at all. Moreover, it is clear that both VLE and non-VLE models completely agree outside the dome, as expected.

Next, simulations are conducted for the two test cases over a total physical time of $2\,\mu s$, corresponding to the time needed by the interface to reach the final abscissa $x_f = 0.15$ mm. To have a direct interpretation of the 0D mixing models, both FC and QC schemes are employed separately with and without VLE. In addition, increase the resolution using $N = 128$, 1024 and 8192 grid points is systematically done. The results are shown in Fig. 92 and Fig. 93 for Case 1 and 2 respectively. Several observations and conclusions can be drawn. Pressure deviations/fluctuations are first obtained for the FC scheme as the resolution is coarsened. Due to the relatively small density gradient imposed across the interface for Case 1 ($\Delta\rho = \rho_{C_6H_{14}}/\rho_{N_2} = 2.85$), initial small pressure fluctuations are convected out of the domain and the final pressure field reaches a drifted value with respect to the true solution.

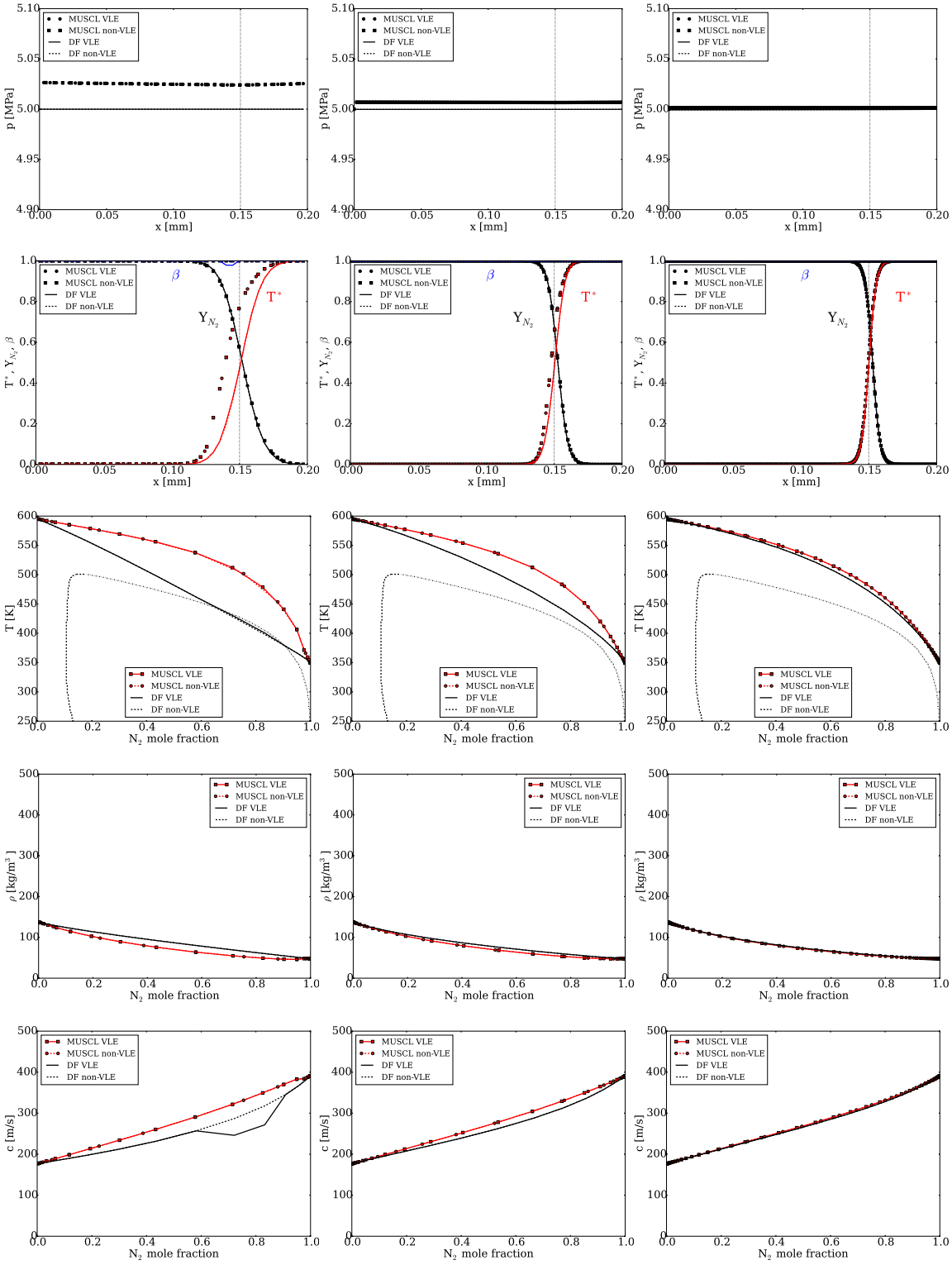
MUSCL VLE
MUSCL non-VLE
DF VLE
DF non-VLE
p [MPa]
x [mm]
β
T*
Y_{N_2}
T*, Y_{N_2}, β
T [K]
N_2 mole fraction
ρ [kg/m³]
c [m/s]

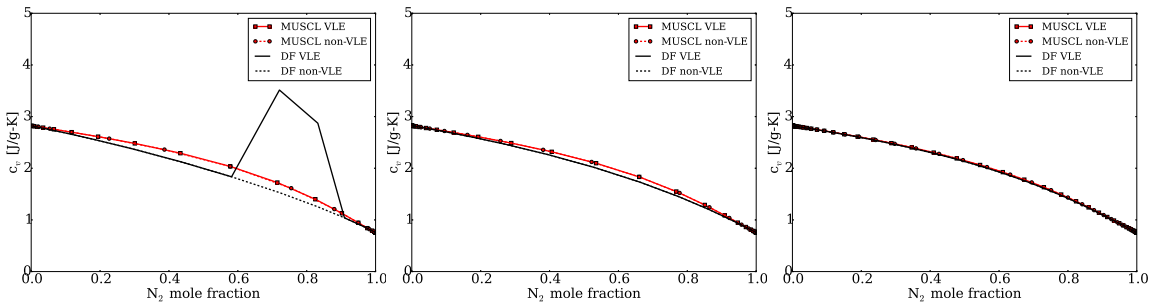

(a) $N = 128$ (b) $N = 1024$ (c) $N = 8192$

Figure 92: Sequence of pressure p, phase fraction β, reduced temperature T^*, nitrogen mass fraction Y_{N_2}, mixing temperature T, density ρ, speed of sound c and specific heat at constant volume c_v for case 1. Sensitivity analysis on numerical scheme, thermodynamics and resolution is shown.

Conversely in Case 2, the density ratio is more than doubled ($\Delta\rho = \rho_{C_6H_{14}}/\rho_{N_2} = 7.59$), corresponding to an initial density gradient that is larger over the chosen interface width. As a result, in accordance with the observation of [109] and the discussion of Sec. 3.2.2, pressure fluctuations are observed. These reduce as the resolution increases, eventually leading to a complete overlap between the FC and the QC solutions. This is irrespective of the use of VLE thermodynamics. Moreover QC solutions do not show any pressure drift, as expected.

Next, the trends of the phase fraction β, reduced temperature $T^* = (T - T_{N_2})/(T_{C_6H_{14}} - T_{N_2})$, nitrogen mass fraction Y_{N_2} and additional mixing variables are analyzed across the interface. The major conclusion obtained from this data is the presence of a fake VLE region for the QC scheme at low resolution for Case 1, also in agreement with [109]. The reason is the tendency of the QC scheme to behave as a perfectly iso-choric mixing model at low resolutions. As a result, the mixing line enters the VLE dome for a range of N_2 mole fraction approximately between 0.65 and 0.85. As the resolution increases, the two mixing lines and the other profiles tend to overlap completely. This is true for all the variables analyzed across the interface (discrepancies can be clearly observed in all the properties at low resolution where the fake VLE region occurs).

On the other hand, the story for Case 2 is different as in this case the solution pertains to a real VLE condition. From a physical point of view, the profile of β provides insights

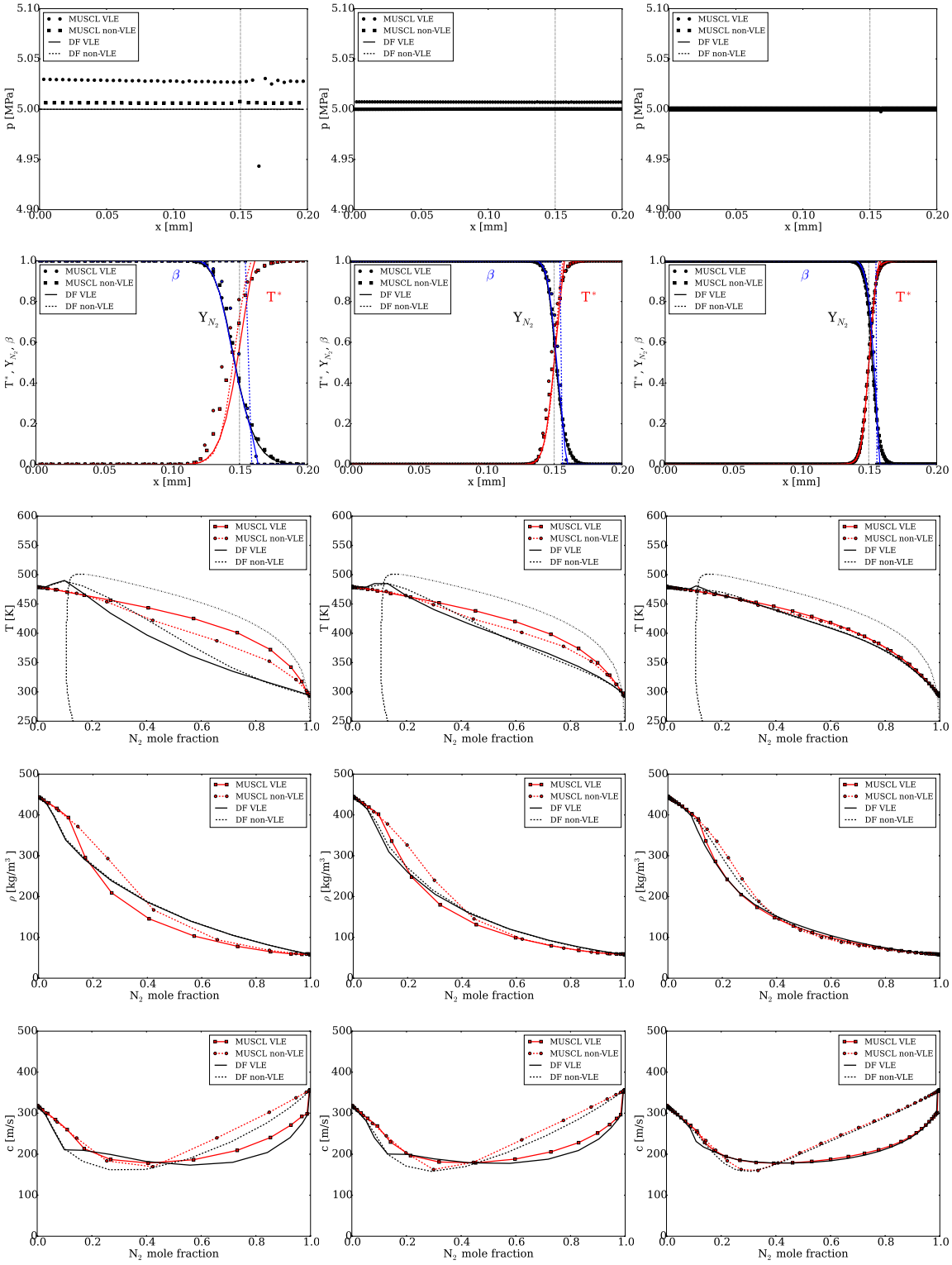
MUSCL VLE
MUSCL non-VLE
DF VLE
DF non-VLE
p [MPa]
x [mm]
β
T*
Y_{N_2}
T*, Y_{N_2}, β
T [K]
N_2 mole fraction
ρ [kg/m³]
c [m/s]

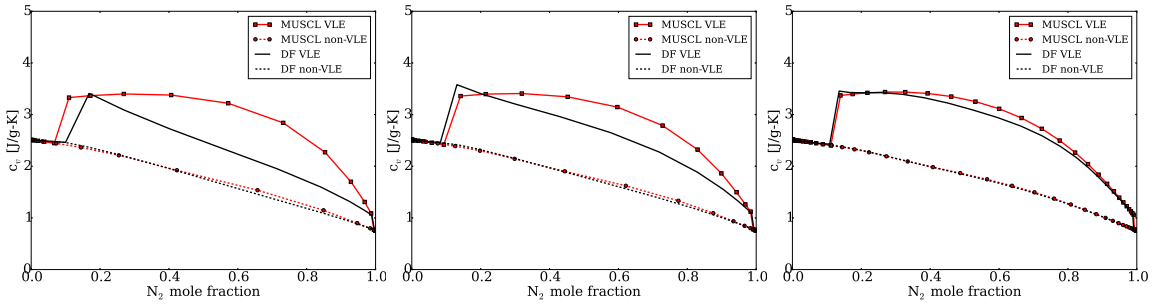

(a) $N = 128$ (b) $N = 1024$ (c) $N = 8192$

Figure 93: Sequence of pressure p, phase fraction β, reduced temperature T^*, nitrogen mass fraction Y_{N_2}, mixing temperature T, density ρ, speed of sound c and specific heat at constant volume c_v for case 2. Sensitivity analysis on numerical scheme, thermodynamics and resolution is shown.

on the VLE thickness, which almost matches the whole interface thickness due to the fact that all binary composition lie inside the VLE dome as observable from the mixing temperature curves of Fig. 91(b). Conversely, the non-VLE solution, as expected provides a sudden change in β from zero to one, indicating the transition from pure liquid to pure gas at another physical location. Despite the resolution increase, this difference does not vanish and is still observed at the highest resolution of $N = 8192$.

Regarding the thermodynamic variables analyzed across the interface, the situation is even more interesting. First of all the mixing temperature at low resolution almost matches the profiles of Fig. 91. As the resolution increases all the models tend to overlap until the mixing temperature differences are not very appreciable ($\sim$ 10 K at most). This is actually not very surprising because the problem under study concerns a simple interface convection, with a temperature profile that is imposed as initial condition in all cases and it is supposed to be transported downstream without alterations, given the fact that also diffusive fluxes are not taken into account. Conversely, derived thermodynamic properties, i.e. properties that are computed from the imposed temperature and pressure profiles, now show large departures as VLE and non-VLE thermodynamics is employed. These differences can be easily observed in density, speed of sound, specific heat at constant volume and all other properties that use these (not shown). These differences can have a range of error up to 70%-80% and do not disappear with resolution increase, rather become more clear and

"converged". It is very difficult to establish a-priori the error magnitude on each variables. For example, while the error in density is more visible for low amounts of N_2 and seems to reduce at higher concentrations of N_2, this is not true for speed of sound, where the error trend is in fact reversed. This provides a further emphasis on the non-linearity of the problem.

This simple simulation proves that the effects of the use of Double-Flux, versus VLE thermodynamics are different in the simulations of super-critical mixtures and given the obvious coupling of the two effects through the governing equations, one can influence the other in a deceptive manner. For this reason, it is absolutely important to use the QC scheme only in the regions where numerical artifacts would otherwise occur.

5.1.2 Performance evaluation

The previous 1D case is tested with various combination of models in order to assess the performances. Since the previous simulations used the fully numerical PRHO problem to reconstruct the interface states as illustrated in Fig. 31, the first test is to evaluate the performances between the use of numerical derivatives and analytical derivatives to compute the thermodynamic properties in the VLE region, as well as to solve all the thermodynamic problems (ERHO and PRHO). Before doing so, a clarification is made:

1. by "numerical" model is meant all the numerical framework that does not use any formulas derived in Sec. 2.2.2. Specifically:
    - the ERHO problem is solved with the numerical Jacobian as suggested by Castier [25]. This algorithm is given in Appendix J. Note that generally speaking this can be used for both single- and multi-phase conditions with the relatives drawbacks discussed in Sec. 3.4.3 and Sec. 3.5.3;
    - all the thermodynamic properties in the VLE regions are computed using second-order differentiation of the actual state as described in Sec. 3.4.5 with the relative numerical recipe given in Algorithm 14;
    - the PRHO problem is solved using the Newton method as per Eq. (3.4.10) where the $(\partial\rho/\partial T)_{p,\mathbf{X}}$ is the one computed with finite differences at the step above;

- this method (where applicable *i.e.*in case viscous fluxes are also taken into account), computes the partial molar properties in the approximate way given by Eqs. (3.4.16)–(3.4.17).

2. by "analytical" model is meant all the numerical framework that does use all the formulas derived in Sec. 2.2.2. Specifically:

   - the ERHO problem is solved with the method described in Sec. 3.4.3 using the analytical Jacobian computed using the VLE derivatives listed in Tab. 14 with the corresponding analytical formulas provided in Sec. 2.2.2;
   - the thermodynamic properties in the VLE region are computed using the analytical framework discussed in Sec. 2.2.2;
   - the PRHO problem is again solved using the Newton method as per Eq. (3.4.10), however this time the derivative $(\partial\rho/\partial T)_{p,\mathbf{X}}$ is computed analytically at the step above;
   - where applicable, this framework computes the partial molar properties in the VLE region with the exact formulas of Sec. 2.2.2.4.

Note that a first performance evaluation between the "numerical" and and the "analytical" model was already made in Sec. 4.5 for the calculation of thermodynamic properties, leading to the conclusion that the analytical model was significantly faster for 0D calculations.

For the present purpose, the reference case is selected to be Case 2 with resolution $N = 1024$ points. The results are listed in Tab. 22: Table 22 shows the simulation times, in seconds, using the various models. The top part of the table refers to the use of the SSI method for VLE only, described in Fig. 43, whereas the bottom part of the table refers to the same cases, where now the VLE (Tp) problem, whenever encountered, is solved with blended SSI and full Newton method (reported in Appendix I). The switch factor is selected to be $\epsilon_s = 1e-6$ over an overall algorithm tolerance of $1e-8$. A larger switching tolerance was

Table 22: Comparison of computational times to solve Case 2 on the $N = 1024$ grid with the two different numerical schemes and by using the fully numerical and fully analytical framework for the VLE thermodynamics (top). Investigation on the use of the full Newton method (see Algorithm I) is also done for the same cases (bottom). The switch between the SSI and full Newton for VLE is chosen to $\epsilon_s = 1e-6$, while the overall algorithm tolerance is set to $\epsilon = 1e-8$. For this latter case, the additional speed up due to the use of the Newton method is also provided in parentheses with respect to the cases conducted with the SSI method only.

Without full Newton for VLE			
Scheme	**Numerical model [s]**	**Analytical model [s]**	**speed up [%]**
Pure MUSCL	3.65E+03	7.12E+02	+80.49
Pure DF	3.11E+03	7.74E+02	+75.11
With full Newton for VLE ($\epsilon_s = 1e-6$)			
Scheme	**Numerical model [s]**	**Analytical model [s]**	**speed up [%]**
Pure MUSCL	3.10E+03	6.91E+02	+77.70 (+2.9)
Pure DF	2.76E+03	7.32E+02	+73.47 (+5.4)

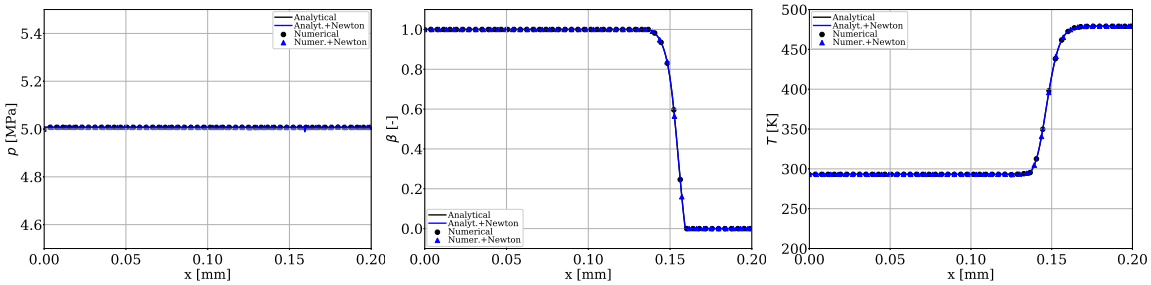

Figure 94: Solution comparison of the 1D advection for Case 2 of Tab. 22. Results are carried out using the FC (MUSCL) scheme only with VLE thermodynamics. The different lines pertain to the different algorithms used to solve for VLE thermodynamics: (−) Fully analytical VLE model, (−) fully analytical VLE model with the use of the Newton method, (•) fully numerical VLE model, (▲) fully numerical VLE model with Newton method. Results show (a) the pressure field, (b) the phase fraction field and (c) the temperature field.

in fact observed to lead to an increase of computational cost due to the larger number of times where the Newton method would fail, hence SSI method would be called from scratch, causing an overall cost increase.

It is apparent that the use of the analytical approach has superior performances over the numerical approach with a cost saving (speed up) up to 80%. The additional use of the Newton method for the VLE problem adds a small additional improvement around 5%.

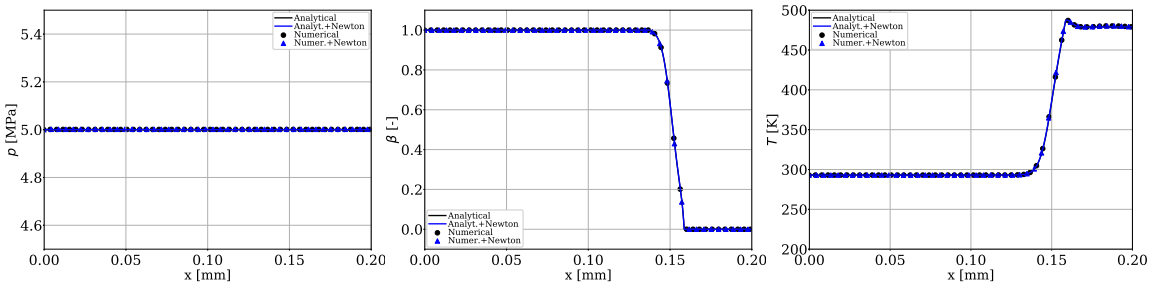

Figure 95: Solution comparison of the 1D advection for Case 2 of Tab. 22. Results are carried out using the QC (DF) scheme only with VLE thermodynamics. The different lines pertain to the different algorithms used to solve for VLE thermodynamics: (−) Fully analytical VLE model, (−) fully analytical VLE model with the use of the Newton method, (•) fully numerical VLE model, (▲) fully numerical VLE model with Newton method. Results show (a) the pressure field, (b) the phase fraction field and (c) the temperature field. Both PRHO and ERHO problems have fixed tolerances of $1e-5$ with $\lambda_0 = 0.9$, $\Delta T_{max} = 100$ K and $\Delta p_{max} = 0.5$ MPa.

This is due to the fact that the use of the Newton method still requires significant amount of floating point operations, such as the matrix of the fugacity derivatives with respect to the phase molar composition and the Jacobian matrix inversion itself (*cf.* Appendix I). Comparison between all the methods is displayed in Fig. 94 and Fig. 95. Final pressure, density and phase fraction fields are represented with 100% agreement between all the approaches. All the other variables show the same agreement.

A second study is done on the performances evaluation between the use of the fully numerical PRHO problem for the reconstruction of cell-interfaces thermodynamic problems as in Fig. 31 (solved through Eq. (3.4.10)) and the use of its analytical version described in Sec. 3.3. For this test, the thermodynamic analytical model for VLE is used only (when applicable - *i.e.*when VLE thermodynamics is used). Tables 23–26 show the performances obtained for the simulations of Case 1 and 2, by varying the interface reconstruction model in presence of VLE only. This analysis is conducted on the different grids used earlier (the number of processors for each grid is showed in parentheses). Data is then plotted in

Table 23: Comparison of computational times to solve Case 1 on different grids using different thermodynamic models (VLE and non VLE). This data refers to the PRHO problem solved numerically as in Sec. 3.4.2. For each grid resolution, the number of processors used to run the case is given in parentheses. Simulation time is given in seconds.

Case 1 - Fully numerical PRHO - Eq. (3.4.10)			
Scheme	$N = 128$ **(1)**	$N = 1024$ **(64)**	$N = 8192$ **(128)**
Pure DF - VLE	2.31E+01	8.59E+01	2.37E+03
Pure DF - non VLE	2.66E+00	2.46E+01	3.24E+02
Pure MUSCL - VLE	4.94E+01	2.78E+02	7.00E+03
Pure MUSCL - non VLE	3.44E+00	2.18E+01	3.42E+02

Table 24: Comparison of computational times to solve Case 1 on different grids using different thermodynamic models (VLE and non VLE). This data refers to the PRHO problem solved analytically using the framework discussed in Sec. 3.3. For each grid resolution, the number of processors used to run the case is given in parentheses. Simulation time is given in seconds.

Case 1 - Fully analytical PRHO - Eq. (3.3.10)			
Scheme	$N = 128$ **(1)**	$N = 1024$ **(64)**	$N = 8192$ **(128)**
Pure DF - VLE	1.24E+01	6.36E+01	1.20E+03
Pure DF - non VLE	2.90E+00	2.52E+01	3.14E+02
Pure MUSCL - VLE	4.07E+01	2.37E+02	3.45E+03
Pure MUSCL - non VLE	3.24E+00	2.01E+01	3.21E+02

Table 25: Comparison of computational times to solve Case 2 on different grids using different thermodynamic models (VLE and non VLE). This data refers to the PRHO problem solved numerically as in Sec. 3.4.2. For each grid resolution, the number of processors used to run the case is given in parentheses. Simulation time is given in seconds.

Case 2 - Fully numerical PRHO - Eq. (3.4.10)			
Scheme	$N = 128$ **(1)**	$N = 1024$ **(64)**	$N = 8192$ **(128)**
Pure DF - VLE	5.89E+01	7.12E+02	2.21E+04
Pure DF - non VLE	2.40E+00	2.28E+01	2.51E+02
Pure MUSCL - VLE	9.29E+01	7.74E+02	2.33E+04
Pure MUSCL - non VLE	3.16E+00	2.03E+01	2.95E+02

Table 26: Comparison of computational times to solve Case 2 on different grids using different thermodynamic models (VLE and non VLE). This data refers to the PRHO problem solved analytically using the framework discussed in Sec. 3.3. For each grid resolution, the number of processors used to run the case is given in parentheses. Simulation time is given in seconds.

Case 2 - Fully analytical PRHO - Eq. (3.3.10)			
Scheme	$N = 128$ **(1)**	$N = 1024$ **(64)**	$N = 8192$ **(128)**
Pure DF - VLE	2.02E+01	2.31E+02	7.39E+03
Pure DF - non VLE	2.65E+00	2.48E+01	2.55E+02
Pure MUSCL - VLE	4.42E+01	2.71E+02	7.56E+03
Pure MUSCL - non VLE	2.70E+00	2.35E+01	2.96E+02

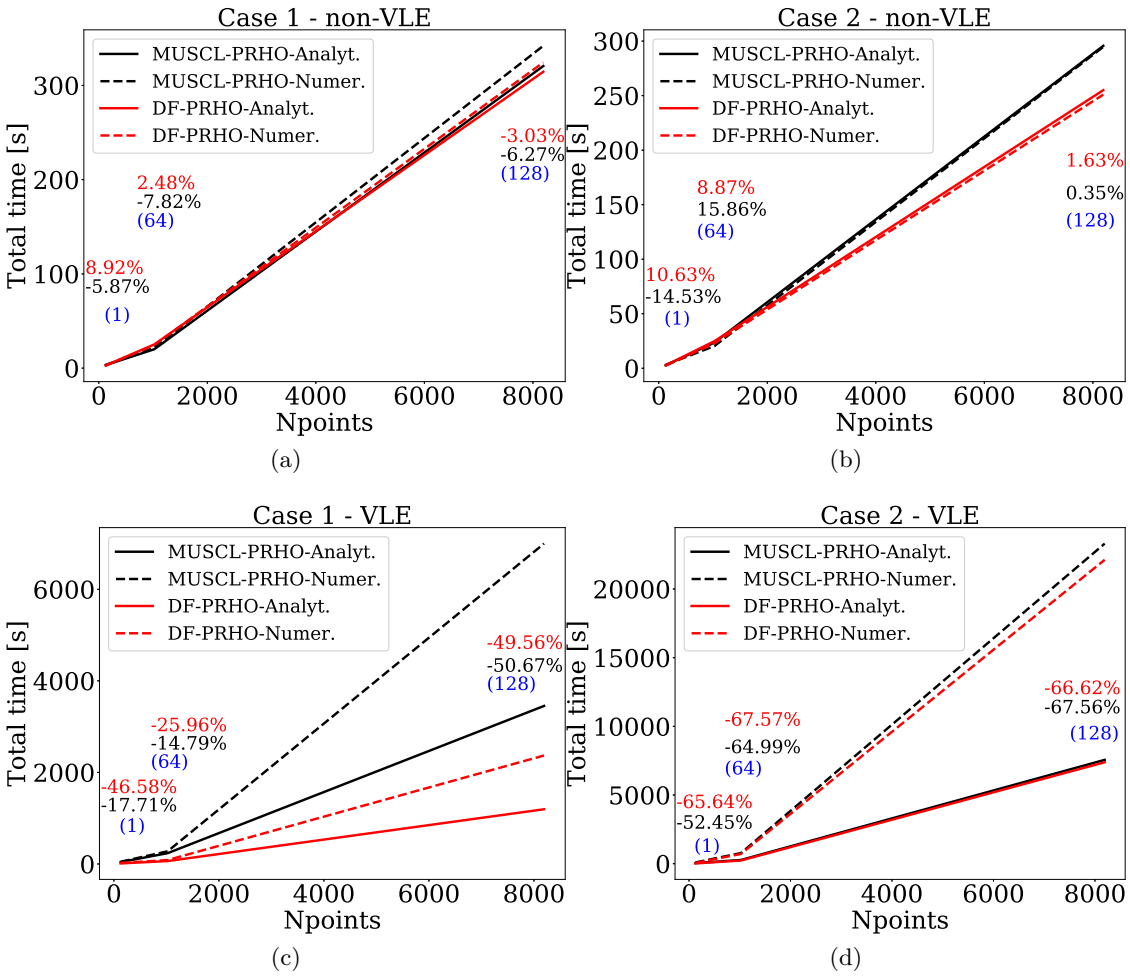

Figure 96: Performances comparison on the simulations of Case 1 and Case 2 with all schemes, thermodynamic model and PRHO solution combinations. Pictures refer to the data reported in Tab. 23–Tab. 26.

Fig. 96 for better comparison. For each run, the number of processors is displayed in blue parentheses, while the speedup between the two PRHO interface models is showed for the FC and QC scheme separately. The comparison is made on the analytical model over the numerical model, hence a negative number actually indicates performances improvement. When VLE is turned off, good performance improvement is observed for nearly all the FC and QC cases. Some positive small numbers are observed as well, which may be the effect of the additional variables communication (such as ρ^L and ρ^V) which is still done even if there is a single phase field everywhere. Overall, without the use of VLE, it seems that both models are nearly equivalent from a performance point of view.

On the other hand, when VLE is used, the results show a difference. In particular all runs show negative numbers indicating a net improvement of the analytical PRHO model over the numerical one. This difference is even more emphasized for Case 2, where the VLE region is more spread out and requires substantial use of the VLE-based cell-interface temperature determination. Note that for Case 1, in the high resolution regime the case does not exhibit VLE as known from Fig. 92, yet a considerable increase of the cost is observed compared to the case where VLE is a-priori turned off. This is the issue discussed in Sec. 3.4.3 and Sec. 3.5.3. When the existence of VLE is a-priori unknown, attempt to solve the Tp problem with the SSI method (or call of the stability analysis) is mandatory, however if the state turns out to be a single-phase one, an overall computational waste is effectively made. Methods to know VLE existence a-priori and thus select before-hand which method to use, can be only confined to binary mixtures for which VLE diagrams are readily available to span a 3D thermodynamic space, however for all other cases the complete SSI approach needs to be run. As mentioned before, in this work the full approach is considered always, assuming that no VLE information is available a-priori. Additional methods to avoid unnecessary computations, such as feeding pre-computed VLE diagrams to the CFD solver (for example using tabulation), can be explored in future works. For completeness, the validation of the fully analytical PRHO model over the fully numerical PRHO model for cell-interface temperature reconstruction are given in Sec. Q.1. It is immediate to recognize that Figs. (155)–(156) match identically with Figs. (92)–(93).

5.2 Two-dimensional (2D) shock/bubble interaction

A second test case is conducted on a two-dimensional domain and simulates the interaction of a shock with a super-critical droplet. The case is schematized in Fig. 97(a). The scope of this test case is to study the transition of the droplet interface from a VLE to a non-VLE condition, as the thermodynamic state is suddenly changed by the shock.

5.2.1 Case setup and results discussion

For this test case diffusive fluxes are once again turned off, however the hybrid scheme employing both the QC and FC scheme with a switch threshold of $\epsilon_\rho = 0.3$ is directly used. The 2D domain is of squared shape with side $L = 1$ m and the uniform grid is discretized using 256×256 grid points. The initial droplet is placed at the center of the square with a diameter $d = L/4$. The droplet is composed of C_6H_{14}, whereas the surrounding environment is assumed to be N_2. A mixing buffer thickness $t_M = L/15$ is adopted to initialize a mixing region between the two species using again a hyperbolic tangent profile, similar to that used for the 1D convection case, with a width parameter $w = 0.01$ for the tanh function. The initial shock position corresponds to $L/10$ from the left side.

The initial state of the unperturbed ($u = v = 0$) region is set to $p = 20$ MPa and $T = 311$ K: a condition that is expected to form VLE for this mixture according to Fig. 54(a). On the other hand, post shock conditions are computed according to [85] and correspond to $p = 56.98$ MPa, $u = 266.75$ m/s and $T = 425.70$ K with nitrogen only: this condition is expected to instead push the mixture away from the VLE dome. Analysis is conducted by taking four instantaneous snapshots corresponding to four different time instants: $t_1 = 29.47\,\mu s$, $t_2 = 48.92\,\mu s$, $t_3 = 65.88\,\mu s$ and $t_4 = 92.81\,\mu s$, roughly corresponding to an interaction of the shock with 0, 25, 75 and 100 percent of the bubble (initial) surface, qualitatively illustrated in Fig. 97(b). With these snapshots, first data is extracted in the region confined by a nitrogen mass fraction concentration between 0.1 and 0.9. Next, a conditional average based on the nitrogen mole fraction is performed on all the data using 20 bins. With this operation, mean and standard deviation of every property is computed

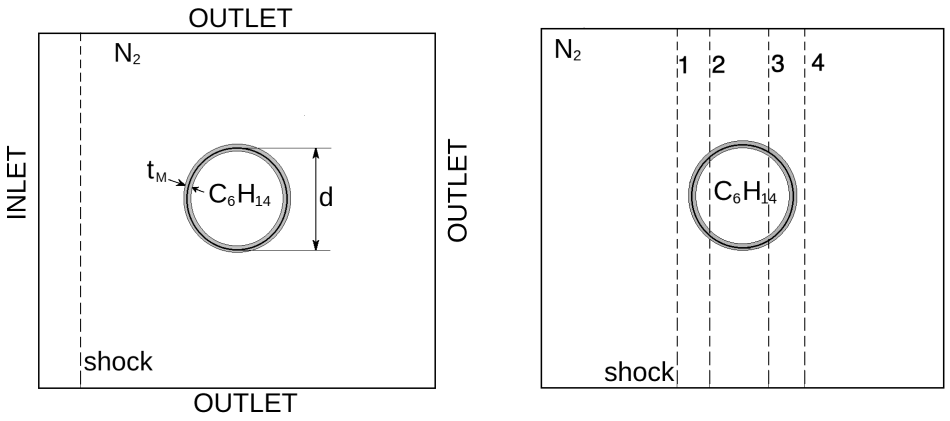

Figure 97: Schematic of the 2D shock-droplet interaction with (a) relevant dimensions and (b) shock qualitative position at which data is analyzed. Top and bottom outlets, as well as the inflow are treated as subsonic conditions, whereas the right outlet is treated with the supersonic condition.

inside each bin. Results are shown in the following.

First, the data collected over the four time instants is plotted such that pressure appears as function of N_2 mole fraction and data is also colored with the phase fraction β. This is showed in Fig. 98 along with a representation of the time sequence contour plots of the phase fraction, pressure and temperature in Fig. 99. This first data set has been obtained with the fully numerical PRHO problem approach described in Fig. 31. By looking at the plots, one may observe that the points within the interface experience an abrupt change in their thermodynamic state dictated by the post-shock conditions and its reflection with the bubble itself due to the different impedance of the fluid states through which the shock propagates. At the initial condition, most of the points lie inside the VLE dome, as expected and confirmed by the envelope of the $T = 310.93$ K isotherm directly taken from Fig. 54. Next, as pressure and temperature increase the interface points exit the dome, which in turn also changes its shape, particularly reduces, as confirmed by the $T = 488.40$ K isotherm also taken from Fig. 54 for reference. Next, the conditional averaged data is analyzed. Figure 100 shows density, speed of sound, temperature and specific heat at constant pressure mean and (shaded) standard deviation within the interface at the same time instants. This time, the plots show concurrently the results obtained with all the models: VLE, non-VLE

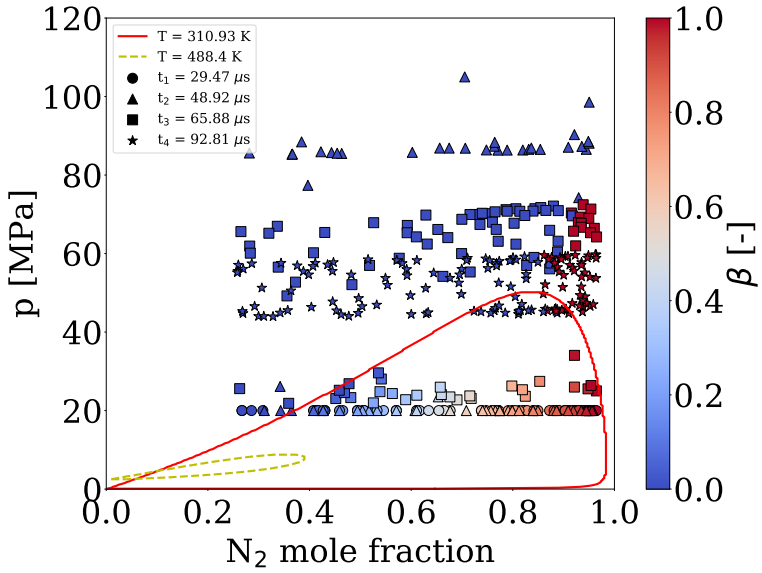

Figure 98: Representation of the bubble interface thermodynamic state during the four time instants analyzed. Symbols correspond to the different times and they are colored based on the local value of the phase fraction β. VLE domes at $T = 310.93$ K and $T = 488.4$ K are directly taken from Fig. 54. Symbols are scattered from the initial raw data with an interval of 7 to improve picture readability. This data is obtained by using the fully numerical PRHO problem solution for the temperature interface reconstruction for the VLE problem.

and frozen VLE. The results are very clear: the thermodynamic states computed with and without VLE show large differences (up to $\sim 80\%$) at $t = t_1$ where the interaction has not occurred yet. This further confirms the fact that using VLE and non-VLE thermodynamics may have a strong impact on all the properties. As the shock-bubble interaction continues, the differences tend to reduce because there is more and more region of the bubble contour that now belongs to a non-VLE state (confirmed by Fig. 98). However, residual discrepancies are still present, even in the final time instant where both solutions are expected to completely lie in the non-VLE state. This residual error is generated by the history of the local solution and its interaction with the fluid-mechanics. On the other hand, more agreement is observed between the VLE and the frozen VLE results. Note that given the fact that Euler equations are solved only, for the FC scheme, the difference between the VLE and the frozen VLE models come through the speed of sound, for which its definition through the $(\partial p/\partial \rho)_S$ derivative of Eq. (2.2.23) has a different outcome because of the effects of VLE derivatives. This difference is however small at the beginning as pointed

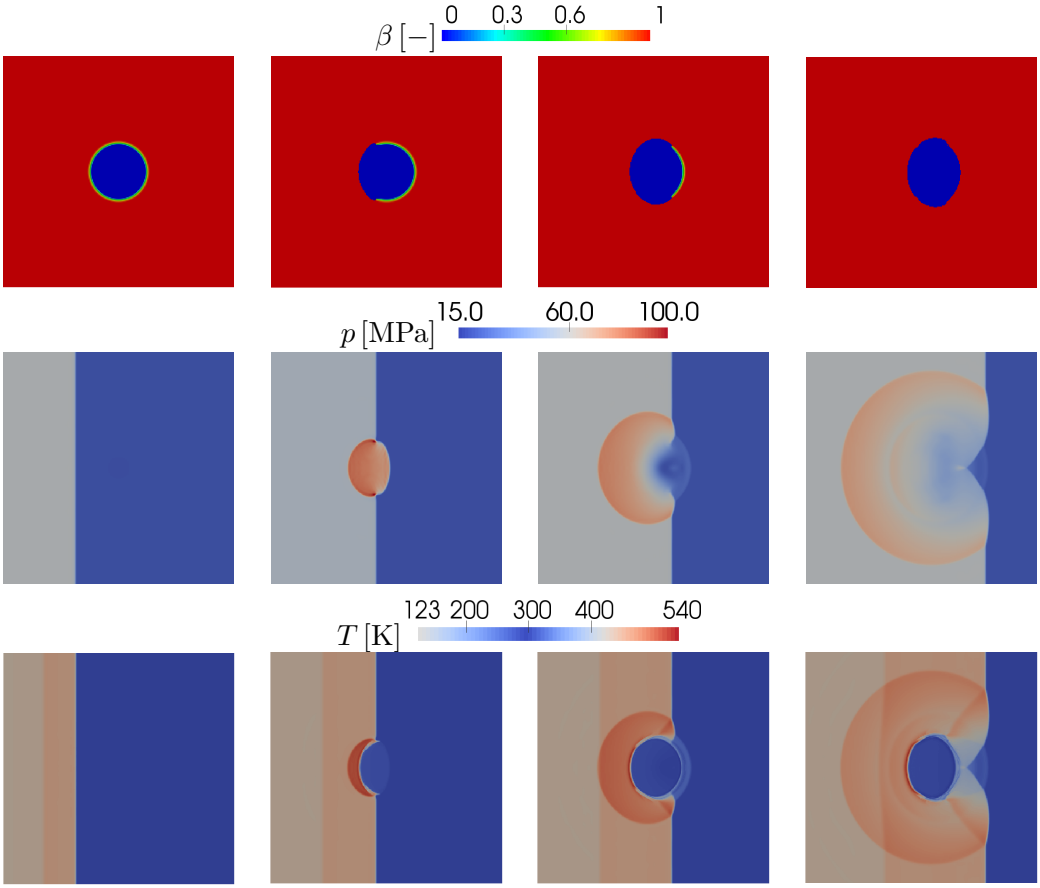

(a) $t = t_1$ (b) $t = t_2$ (c) $t = t_3$ (d) $t = t_4$

Figure 99: Time sequence contour snapshots of phase fraction β, pressure p and temperature T. This data is obtained by using the fully numerical PRHO problem solution for the temperature interface reconstruction for VLE.

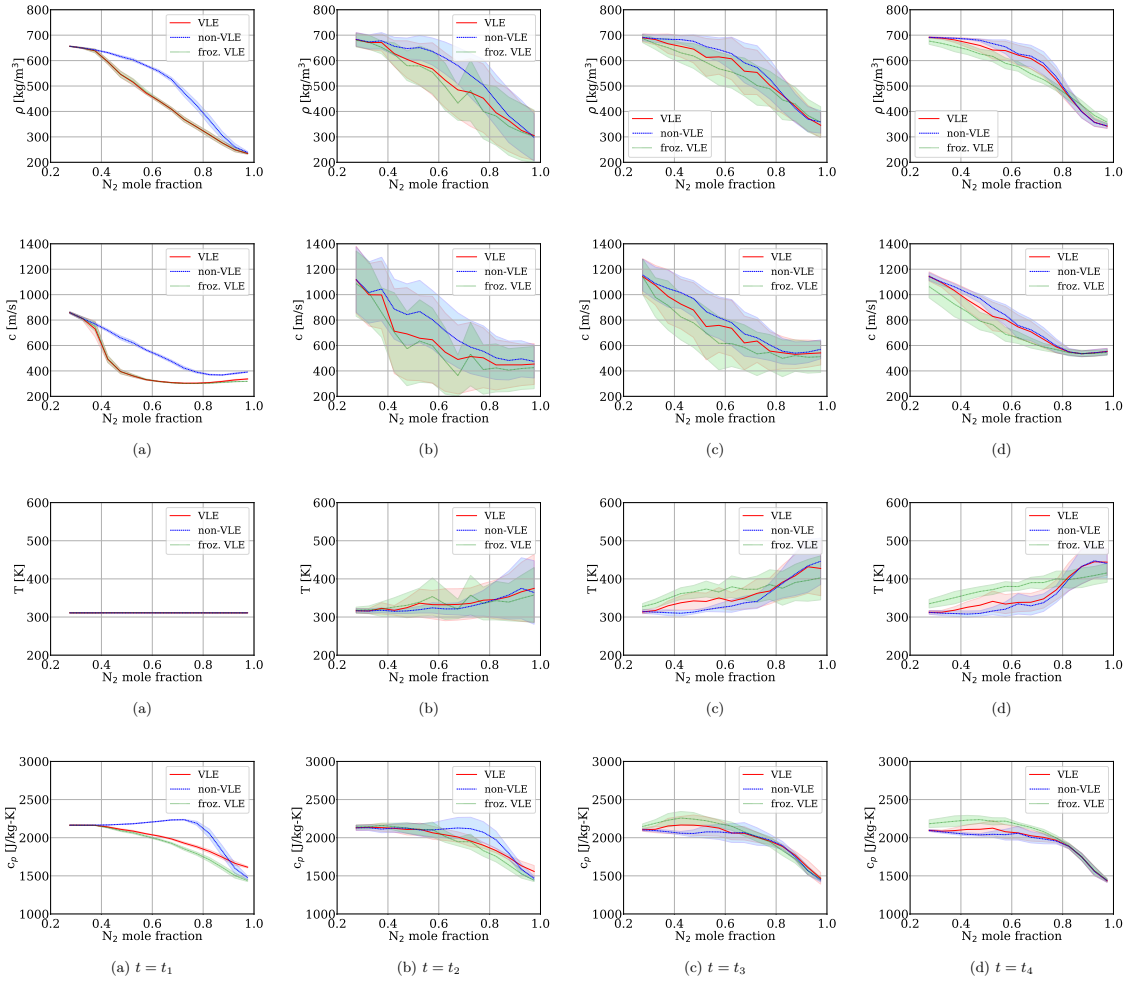

Figure 100: From top to bottom: density, speed of sound, temperature and specific heat at constant pressure sequence conditional averages (with shaded) standard deviations for the four time instants. The results are for the VLE, non-VLE and frozen VLE models.

out by Fig. 100 Regarding the QC scheme, the difference between the VLE and non-VLE models is coupled through c_p because of the calculation of γ^* in Eq. (3.2.25), later used to compute the internal energy in Eq. (3.2.24) and therefore everything else. Overall, the frozen VLE model performs better compared to the single-phase (no VLE) model, confirming the observations and the conclusions already drawn in Chap. 4.

When the same problem is run with the fully-numerical PRHO problem for the temperature cell-interface reconstruction of Sec. 3.3, similar results with identical conclusions are obtained. These results are summarized in Sec. Q.2, providing further confirmation regarding the validity of both approaches to reconstruct the cell-interface temperature during the solution of the inviscid fluxes. Analogously, identical conclusions were obtained when a 512×512 grid points domain was used (not shown), confirming the separation between the error committed when non-VLE thermodynamics is used from the error related to the scheme and resolution are already pointed out in Sec. 5.1.

5.2.2 Performance evaluation

The 256x256 case was simulated on 256 processors with uniform work load distribution (same number of cells/processor). The simulation is composed of 960 iterations. The study is performed by varying the numerical method to compute the reconstructed temperature at the cell interface using the fully numerical or the fully analytical PRHO model and the thermodynamic model. All the cases are run with the "analytical" model as per the definition given in Sec. 5.1.2. The numbers in parentheses refer to the relative cost increase with respect to the non-VLE model. For convenience, this is expressed in "number of times" the cost of the associated non-VLE simulation. For the accelerated simulation, the $\epsilon_{acc} = 1e5$ with $N_{acc} = 5$ was used. First, one can notice that the simulations conducted with the VLE model are roughly one order of magnitude more expensive than the corresponding ones where the single-phase thermodynamics is used. Surprisingly, the frozen VLE case happened to be slightly more expensive than the corresponding VLE case or roughly close. This is a bit counter-intuitive because the frozen VLE model does not perform the same amount of floating point operations in the calculation of thermodynamic derivatives however

Table 27: Comparison of computational times to solve the 2D shock/bubble interaction using different numerical/thermodynamic models. The main comparison (row) is made on the method to reconstruct the temperature at cell interface using the fully numerical approach PRHO approach of Fig. 31 or the fully analytical PRHO approach of Sec. 3.3. The second criterion (column) is the thermodynamic model ranging from the non-VLE to the frozen VLE, to the full VLE models. Investigation is also made on the use of the ERHO problem acceleration technique discussed in Sec. 3.5.3 when it is coupled with the full VLE model. Additional results for the present analyses are given in Sec. Q.2.

Simulation runtime [s]				
	non-VLE	frozen VLE	VLE	VLE+ERHO acceleration
fully numerical PRHO	106	1223 (11.5×)	1145 (10.8×)	1021 (9.6×)
fully analytical PRHO	65	521 (8.0×)	531 (8.1×)	489 (7.5×)

a more detailed analysis revealed that some cells required more iterations, sometimes hitting the maximum number specified because of the following reason. When for example the ERHO problem is solved in the VLE region with Eq. (3.4.11), the objective functions contain the correct information of the VLE. This is because the functional dependency of internal energy and density as per Eq. (2.2.34) and Eq. (2.2.35) does not require any approximation: β is computed through the consistent Tp method of Fig. 43. However, when the Jacobian is computed, it contains derivatives of E and ρ. These, according to the frozen VLE model are approximated. If one thinks in a one-dimensional sense, the Newton method solution update becomes $x^{n+1} = x^n - \lambda F/F'$ where F is computed correctly, however F' is approximated. As a result, this can lead to more iterations or oscillations near the solution itself that, despite the fact to be close to the actual value it does not meet the tolerance criteria, hence producing an overall cost increase. A workaround to this issue was found by decreasing the value of λ, say from 0.9 to 0.6. This reduces the Newton step size and avoids the issue of jumping on either side of the solution because of a large increment. Though this solved the problem, it also affected the iterations where this does not naturally occur and the initial value of λ would have been enough to converge, causing again an overall cost increase.

On the other hand, the use of the ERHO problem acceleration produced some cost saving on the order of 10 and 8 percent compared to the corresponding full VLE model. However, this was found to be very sensitive to the parameters ϵ_{acc} and N_{acc}. This is not surprising since these provide a linearization of the VLE problem and especially at cells that define

the phase boundary, this can lead to a lack of convergence. As a general rule of thumb, it is recommended to keep these values low and not to force the problem to use the linearized solution too much, otherwise lack of convergence, resulting into an increase of cost (because the non accelerated method is then recovered from scratch).

One key result of Tab. 27 is given by the use of the fully analytical PRHO method over the fully numerical one. In general, the cost reduces by one order of magnitude in all cases, including the non-VLE case. This is not surprising because even in the non-VLE case the numerical PRHO model requires (in general) iterations as per Eq. (3.4.10). However, if the analytical formula can be used, Eq. (3.3.10) effectively becomes Eq. (3.4.9), with an analytical solution.

The results of some of these combinations are given in Sec. Q.2, for completeness. It is therefore proven that the numerical and analytical approaches to resolve the PRHO problem at cell-interface is equivalent, with the major exception that the second approach is much faster than the first.

5.3 Three-dimensional (3D) non-reacting temporal mixing layer (TML)

A 3D laminar temporal mixing layer (TML) is studied next. The scope of this example is to further establish the relationship between numerical scheme, resolution and thermodynamic model, now with inclusion of viscous fluxes [226]. These effects have not been extensively studied in the literature, thus their mutual effects need to be isolated on relatively simple configurations.

5.3.1 Case setup and results discussion

The TML configuration (shown in Fig. 101 along with the relevant dimensions) is a well known setup. Periodic boundary conditions along the x (streamwise) and z (spanwise) directions are used, while non-reflective outflow is used along the y (crosswise) direction. This configuration has been used in many DNS studies of super-critical mixing but this is the first study of two-phase mixing using VLE, with or without DF. The initialization is designed to create a perturbed mixing layer that results in a vortex roll-up due to amplification of the perturbing mode.

The domain is rectangular of sizes $L_x \times L_z \times L_y$, and the focus is on TML evolution in a cubic sub-domain of $L_x \times L_z \times H_{TML}$ where $H_{TML} = L_y/3$. Two additional cubic sub-domains are added on the top and the bottom of the center one, each of them of length $L_{buff} = L_y/3$ as well. While the center domain is discretized using an uniform mesh in all directions, the top and bottom sub-domains have stretched grid along the cross direction using an hyperbolic tangent function (see Fig. 101). The domain sizes are computed using the method discussed by [134] and summarized in Appendix P. The value of the Reynolds number is fixed to 600, the nominal convective Mach number to 0.4 and the pressure to 5 MPa for all cases. Top stream is filled with n-hexane (C_6H_{14}) with three different temperatures, while the bottom stream is filled with nitrogen at fixed temperature for a total of three cases summarized in Tab. 28. Initial vorticity thickness, stream velocities and domain sizes are given in Tab. 28. The focus is on the study of a single vortex, excited with a 2D perturbation. The initialization approach follows the work of Miller et *al.* [134]. Mean streamwise velocity, temperature and species profiles are based on the error function as indicated in Eq. (5.3.1) ($\bar{\boldsymbol{\zeta}} = (\bar{u}, \bar{T}, \bar{Y}_{N_2})$, $\boldsymbol{\zeta}_B = (u_B, T_B, Y_{N_2,B})$, $\boldsymbol{\zeta}_T = (u_T, T_T, Y_{N_2,T})$), however the initial perturbation is imposed in a 2D fashion with the distribution indicated by Eq. (5.3.2) for the cross-wise velocity component only.

$$\bar{\boldsymbol{\zeta}}(y) = \boldsymbol{\zeta}_B + \frac{1}{2}(\boldsymbol{\zeta}_B + \boldsymbol{\zeta}_T)\left[1 - erf\left(\frac{\sqrt{\pi}y}{\delta_{\omega,0}}\right)\right], \tag{5.3.1}$$

$$v'(x,y) = F_{2D}\sin\left(\frac{2\pi x}{L_x}\right)e^{-\pi(y/L_x)^2}. \tag{5.3.2}$$

In this way $u(x,y,z) = u(y)$, $v(x,y,z) = v'(x,y)$, $w(x,y,z) = 0$, $T(x,y,z) = T(y)$, $Y_{N_2}(x,y,z) = Y_{N_2}(y)$ and $Y_{C_6H_{14}}(x,y,z) = 1 - Y_{N_2}(y)$ are obtained. For all the simulations $F_{2D} = 30$. In the following, the case of 64^3 grid (in the TML box) is considered as the reference resolution, however effects of grid resolutions on the results is also addressed. First, different grids are analyzed to establish the solver capability to predict typical TML characteristics. Figure 102 shows the time history of the normalized momentum thickness as a function of the normalized time $\tau = t\Delta u/\delta_{\omega,0}$ where t is the physical time and $\Delta u = |u_T - u_B|$ (defined in Tab. 28), for all three cases using three different resolutions. The

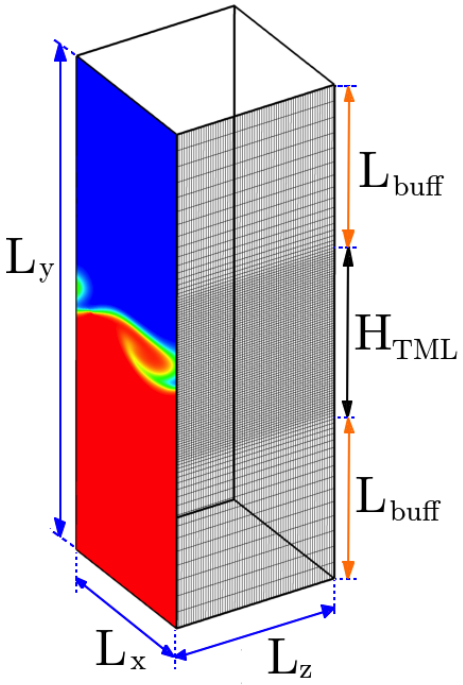

Figure 101: Illustration of the grid setup used for TML with relevant dimensions. Top stream is filled with C_6H_{14}, while bottom stream is filled with N_2.

Table 28: Conditions for Case 1 to Case 3 for the TML. Lengths values are in $\times 10^{-6}$, while vorticity thickness values are in $\times 10^{-7}$ units. Subscripts T and B refer to "TOP"and "BOTTOM", respectively. For all cases: $p = 5\,\text{MPa}$, $Re_0 = 600$, $M_0 = 0.4, T_\text{B} = 293.0\,\text{K}$, $\rho_\text{B} = 58.44\,\text{kg/m}^3$, $Z_\text{B} = 0.984$, $T_B/T_c = 2.32$, $p_B/p_c = 1.47$.

Case 1: $T_\text{T} = 595\,\text{K}$, $\rho_\text{T} = 136.88\,\text{kg/m}^3$, $Z_\text{T} = 0.636$ $T_T/T_c = 1.17$, $p/p_c = 1.65$					
L_x [m]	L_y [m]	L_z [m]	u_B [m/s]	u_T [m/s]	$\delta_{\omega,0}$ [m]
4.3024	12.907	4.3024	-88.322	106.914	5.901
Case 2: $T_\text{T} = 555\,\text{K}$, $\rho_\text{T} = 202.09\,\text{kg/m}^3$, $Z_\text{T} = 0.462$ $T_T/T_c = 1.09$, $p/p_c = 1.65$					
L_x [m]	L_y [m]	L_z [m]	u_B [m/s]	u_T [m/s]	$\delta_{\omega,0}$ [m]
3.9676	11.902	3.9676	-79.122	99.1887	5.442
Case 3: $T_\text{T} = 479\,\text{K}$, $\rho_\text{T} = 443.14\,\text{kg/m}^3$, $Z_\text{T} = 0.244$ $T_T/T_c = 0.94$, $p/p_c = 1.65$					
L_x [m]	L_y [m]	L_z [m]	u_B [m/s]	u_T [m/s]	$\delta_{\omega,0}$ [m]
2.9612	8.8837	2.9612	-115.27	155.477	4.062

momentum thickness is computed as in [133] with formulas described in Appendix P. All these simulations are run with the hybrid FC/QC scheme and VLE thermodynamics. In all cases one may observe that the 32^3 resolution tends to slightly overestimate the momentum thickness, while the 64^3 and the 128^3 cases agree reasonably well. As a result, based on the conclusions of the test cases of Sec. 5.1 and Sec. 5.2, the 64^3 cases is considered as a reference for further exploration here.

It is further observed that the trend and the magnitudes of Cases 1 and 2 are very close (for different grids), while Case 3 shows both a smaller momentum thickness magnitude and a plateau value that is reached approximately after $\tau = 15$ for all grids. This behavior can

be attributed to the fact that Case 3 has a much larger inertia within the n-hexane stream because of its larger density value. One can see from Fig. 3(c) and Fig. 4(c) how n-hexane for both Case 1 and Case 2 lies more towards the pseudo-gas phase (corresponding to a lower density), while it lies in the liquid-like side for Case 3. As a result, the higher density in the top stream for Case 3, produces a higher inertia effect, which tends to slow down the formation of stream-wise momentum gradients along the crosswise direction and thus the vortex formation. This was also reported by [134] who discussed the reduction of kinetic energy production within the roll-up as density was increased. Figure 103 shows the com-

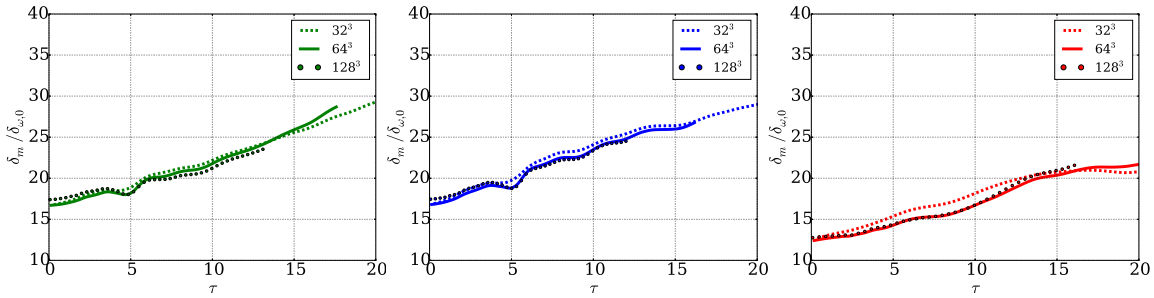

(a) Case 1 (b) Case 2 (c) Case 3

Figure 102: Comparison of the normalized momentum thickness for all cases for different resolutions of the TML box: 32^3, 64^3 and 128^3. For these simulations VLE thermodynamics is always used.

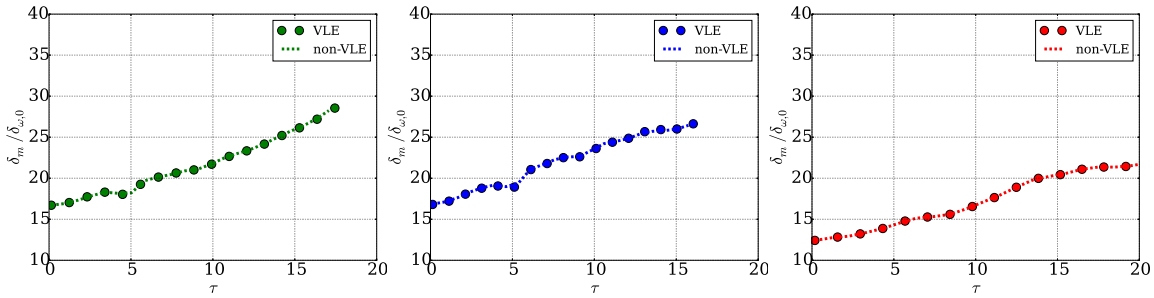

(a) Case 1 (b) Case 2 (c) Case 3

Figure 103: Comparison of the normalized momentum thickness for the 64^3 cases with and without VLE.

parison of the momentum thickness for the hybrid scheme with and without VLE at the fixed resolution of 64^3. No difference is apparent between the two thermodynamic models

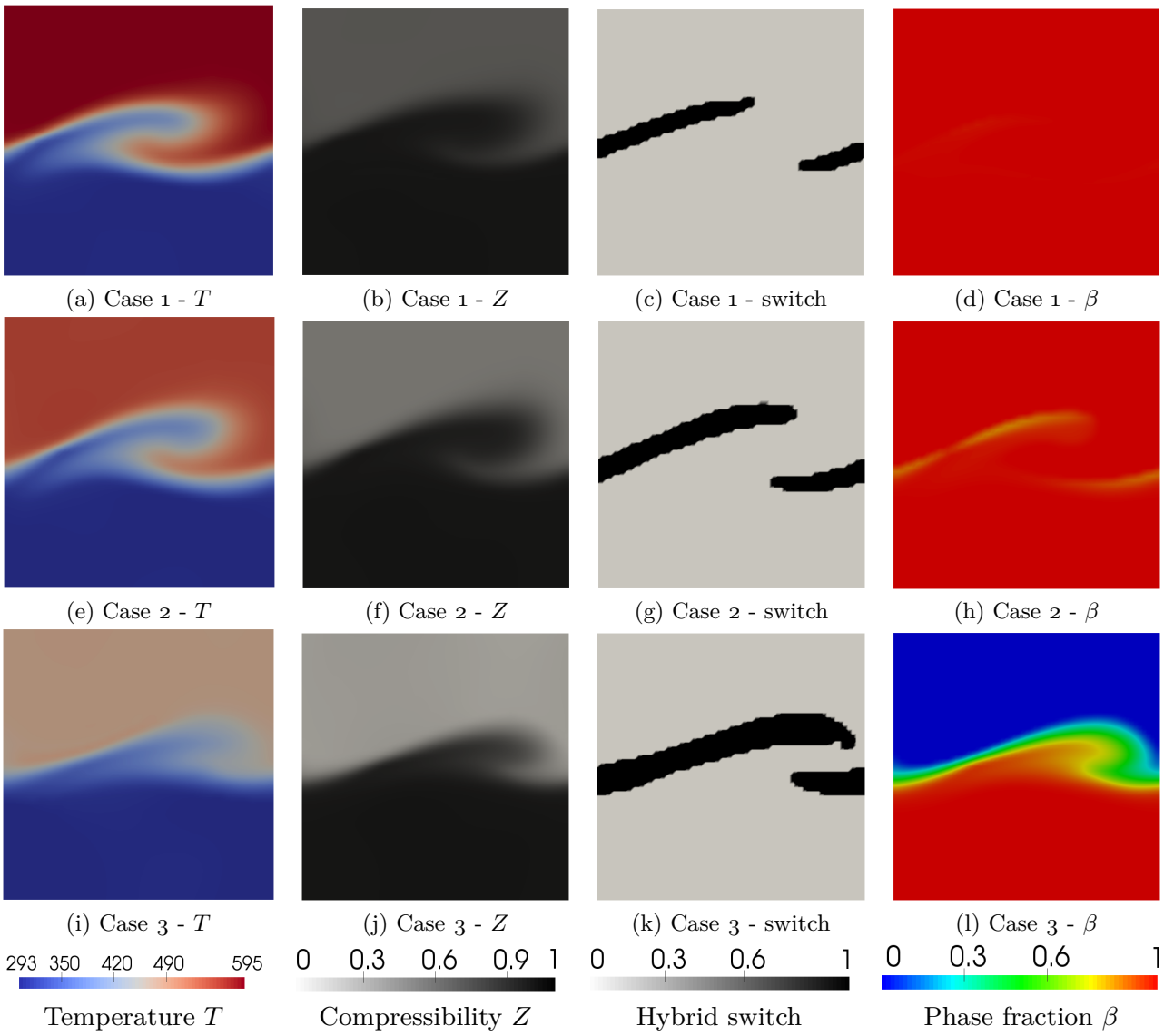

Figure 104: Instantaneous contour plots of relevant quantities at $\tau = 10$ for (a)-(b) Case 1, (c)-(d) Case 2 and (e)-(f) Case 3. Figures refer to the hybrid, VLE simulations at 64^3 resolution for all cases. For the hybrid switch, only discrete values must be considered: white (zero) FC scheme activated, black (one) QC scheme activated.

at least within the time window under study, during the initial growth. Figure 104 shows instantaneous snapshots for some of the relevant variables of all three cases at $\tau = 10$. First, notice that temperature and compressibility extremes reflect the nominal values reported in Tab. 28. Additionally a phase split is visible on the phase fraction plots. While for Case 1, phase split is completely absent (i.e., gas phase always occurs as $\beta = 1$), moderate phase split is observed for Case 2, where β ranges between 0.7 and 1. Finally, strong phase split is

observed for Case 3, where β spans all the available range in a continuous manner. Analysis also shows that the QC algorithm is activated automatically in the interface region that contains higher density gradients (see Fig. 104(c), (g) and (k)).

A conditional average of the mixing temperature versus the N_2 mole fraction is performed using 30 bins and all the available simulations time history. For the hybrid cases, the results are shown in Fig. 105 along with adiabatic (H) and isochoric (V) zero-dimensional mixing models used with and without VLE. The mixing line lies between the two extremes identified by the H and V curves. While for Case 1 and Case 2 very small differences are observed between the VLE and non-VLE simulations, more differences are observed for Case 3, where discrepancies up to 20 K are clearly visible, especially within the center region, where the VLE is important because the combination of temperature, pressure and composition places the mixture at the center of the VLE dome. These error magnitudes are in agreement with Fig. 55(b) and Fig. 56(b), suggesting that an a-priori run of the $p\rho$ problem for the mixture at given operating conditions with and without VLE can provide a reasonably reliable estimate of the error expected during the simulation, and thus one can determine whether VLE is needed or not. In addition, a larger discrepancy of the mixing temperature lines are visible in this case compared to the simple one-dimensional test case discussed in Sec. 5.1. This is related to the dual effect of the diffusive fluxes that contribute to spread out the initial profiles, producing different states that generate a corresponding difference in the thermodynamics, and the multi-dimensionality of the problem. While the test case of Sec. 5.1 is a pure convection problem, this is not and the effects of mass, momentum and energy transfer in the other directions (mainly the cross-wise), produce an additional variation of the thermodynamic states which reflect into different properties depending on whether VLE is activated or not. Also note for Case 3 that differences between H-VLE and H-non VLE curves are in agreement with the results of [169, 118], who attribute the higher temperature in the H-VLE lines to the heat released by the phase change. Finally, the similar wave-like structure of the non-VLE mixing line is observed. The same trend is observed for the zero-dimensional models that do not employ VLE, however the differences are more significant for the V curves. This wave-like shape, once again in agreement with

the 0D results of Fig. 55(b) and Fig. 56(b) confirms the fact that within the VLE region, the single-phase EoS tends to form this shape to accommodate the mathematical model, but producing erroneous results.

To provide more emphasis on the real mixing, the same simulations are run without the use of the hybrid scheme, i.e., by using the pure FC and the QC schemes separately, with and without VLE and by varying the resolution as well for a total of additional 36 different realizations. Looking at Fig. 106 and Fig. 107, the following observations can be made

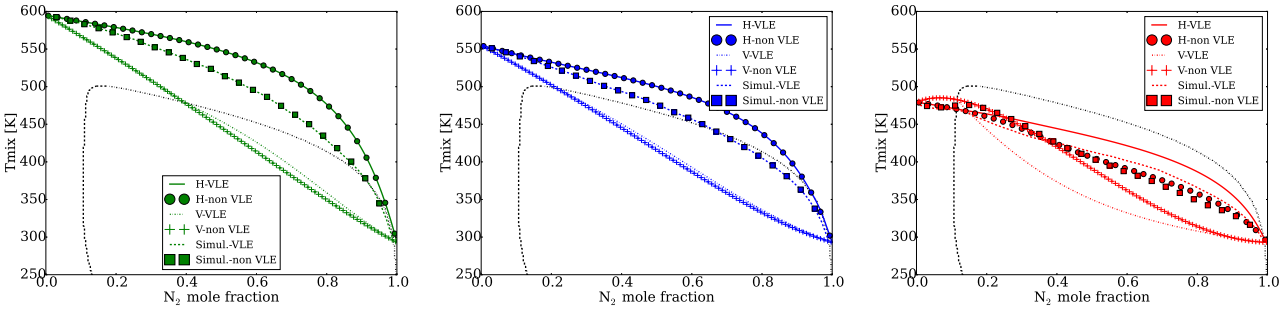

(a) Case 1 (b) Case 2 (c) Case 3

Figure 105: Hybrid 64^3 real mixing curves for all three cases with and without VLE.

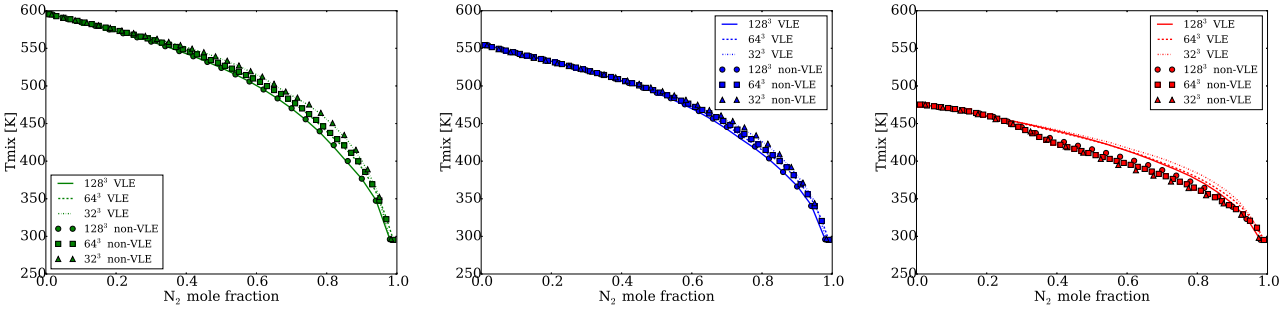

(a) Case 1 (b) Case 2 (c) Case 3

Figure 106: Effect of the resolution and VLE thermodynamics with pure FC scheme.

(H and V curves are removed to improve figures readability):

- In Cases 1 and 2 an increase in the resolution makes FC and QC lines closer. The FC curves tend to match with the H curves, while QC curves tend to match the V

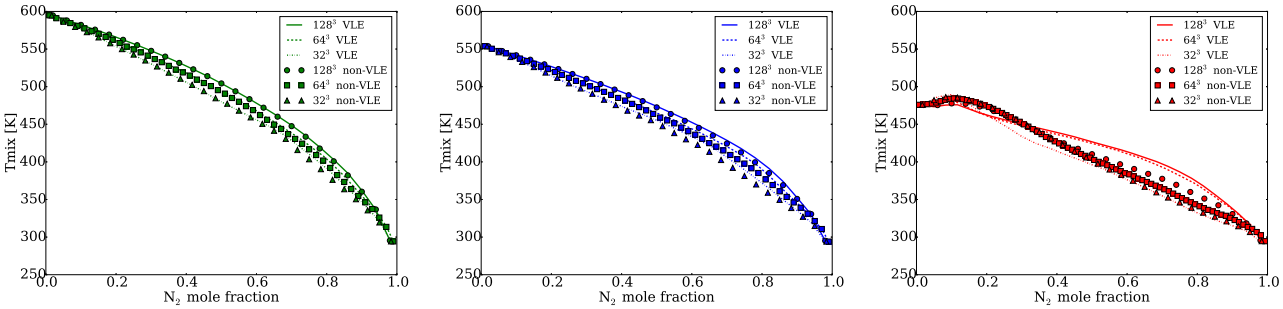

(a) Case 1 (b) Case 2 (c) Case 3

Figure 107: Effect of the resolution and VLE thermodynamics with pure QC scheme.

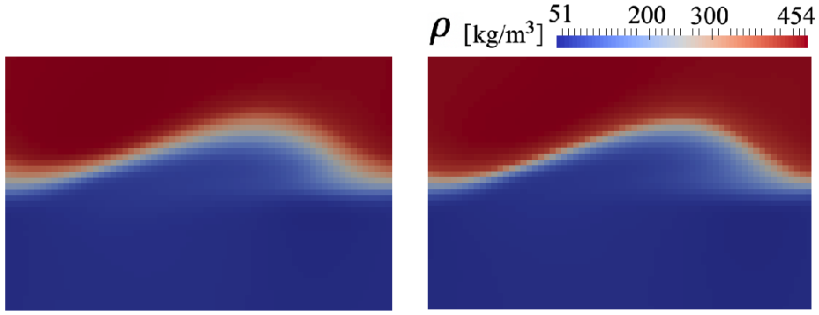

(a) Pure DF (QC) (b) Pure MUSCL (FC)

Figure 108: Density contours for the (a) QC and (b) FC scheme at $\tau = 5$.

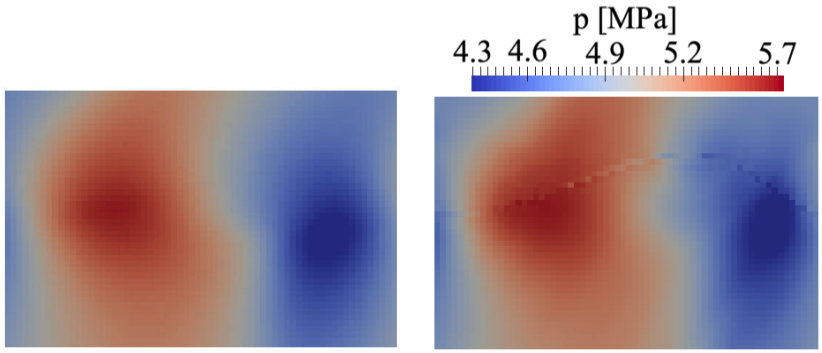

(a) Pure DF (QC) (b) Pure MUSCL (FC)

Figure 109: Pressure contours for the (a) QC and (b) FC scheme at $\tau = 5$.

curves as resolution decreases (refer to Fig. 105 for H and V curves). This is in agreement with other observations [109][118], as well as the 1D case discussed in Sec. 5.1. Furthermore the effect of VLE is minor, as expected, and it always points towards a larger temperatures in the regions where the curves enter the dome (especially true for Case 2);

- In Case 3, the situation is much more different. It is still true that increasing the resolution reduces the differences between FC and QC, and that each curve tends to the H and V extremes; however, the extremes itself are different, depending on whether VLE is used or not. As a result, similarly to the conclusions drawn in Sec. 5.1, substantial discrepancies are observed in both the trend and the magnitude of the mixing curves. Also note that the non-VLE curves again exhibit a "wave-like" behavior. Another important observation is that increasing the resolution for the non-VLE simulations does not compensate the VLE effect. In other words, similarly to the observations for the test cases in Sec. 5.1, VLE is a physical phenomenon that cannot be compensated for by an increase in the resolution and its role as a sub-grid closure model becomes hence questionable [118]. VLE does not represent a phenomenon that is not resolved. VLE is a thermodynamic model that for a set of $(T, p, \mathbf{X})$ provides an answer on whether phase-split occurs or not. It does not matter whether that set of values is obtained on a DNS-type grid or a coarse grid. In a different perspective, if VLE occurs at a location with some non-zero and non-unity value of β, it is not true that if resolution is increased, the stage of $\beta = 0$ and $\beta = 1$ is reached. This is proven by these results, although the same conclusion could have been formulated based on the 0D results of Chap. 4. On the other hand, this does not mean that effects of turbulence and its resolution (or modeling) will not play a role. In fact if turbulence effects are included, the mixing will be affected by it and so the thermodynamic state at a given point, which can ultimately change the VLE. These observations emphasize the fact that while DF model is a numerical method that serves to stabilize the resolution of sharp density gradients interfaces, its utility reduces as the resolution increases [108, 226]. On the other hand, VLE is independent of grid resolution and is needed to get the correct thermodynamic state that otherwise would exhibit errors.

In addition, the same conclusion that H and V curves are related to the use of the pure FC and QC schemes in accordance with the analysis performed by [109] and the observations of [118] are made. In other words, the mixing mechanism established by a pure QC scheme

can be very different from that generated by the FC scheme, with a trend that resembles that of the V curve. This is related to the non-conservative nature of the QC scheme [118], and confirms that the use of an hybrid scheme between a FC and QC method becomes a must in order to mitigate this effect and confine the use of a QC scheme only to the regions where it is absolutely necessary. Note, this extends to any QC scheme, including those based on the pressure transport equation as pointed out by [118]. For completeness, the

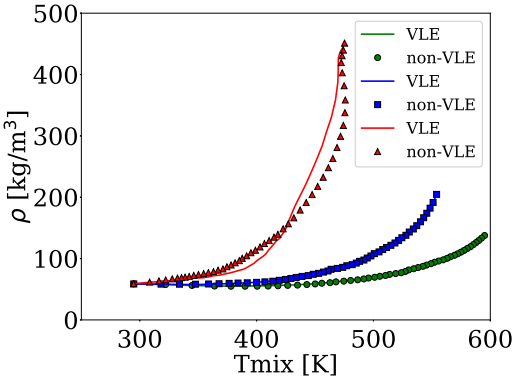

(a) Density

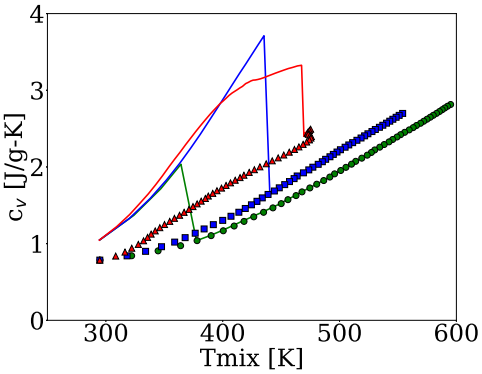

(b) Spec. heat at constant volume

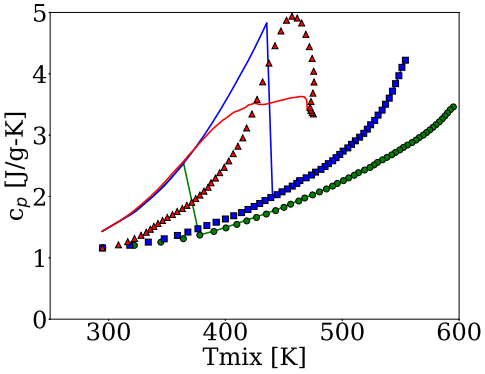

(c) Spec. heat at constant pressure

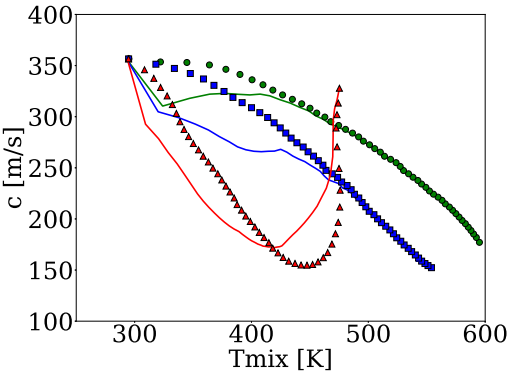

(d) Speed of sound

effect of the use of the FC or the QC scheme alone is showed in Fig. 108 and Fig. 109 for Case 3. In particular Fig. 108 shows the density field extracted at $\tau = 5$ for the (a) pure Double-Flux (QC) and (b) pure MUSCL (FC) scheme, respectively. Similarly, Fig. 109 shows the pressure field for the identical snapshots in both cases. One can immediately observe that while the QC scheme does not show any pressure artifact , the FC scheme clearly displays localized pressure oscillations in correspondence of the density gradient. Though not exagerated because of the accurate resolution of the density gradient itself,

these oscillations perturb the field and can get worse in case the density gradient increases for fixed grid, or the resolution reduces for fixed density gradient as discussed in Sec. 3.2.2. These results once again prove the issue of pressure oscillations related to the use of FC scheme and the benefit that comes from the use of any associated QC scheme.

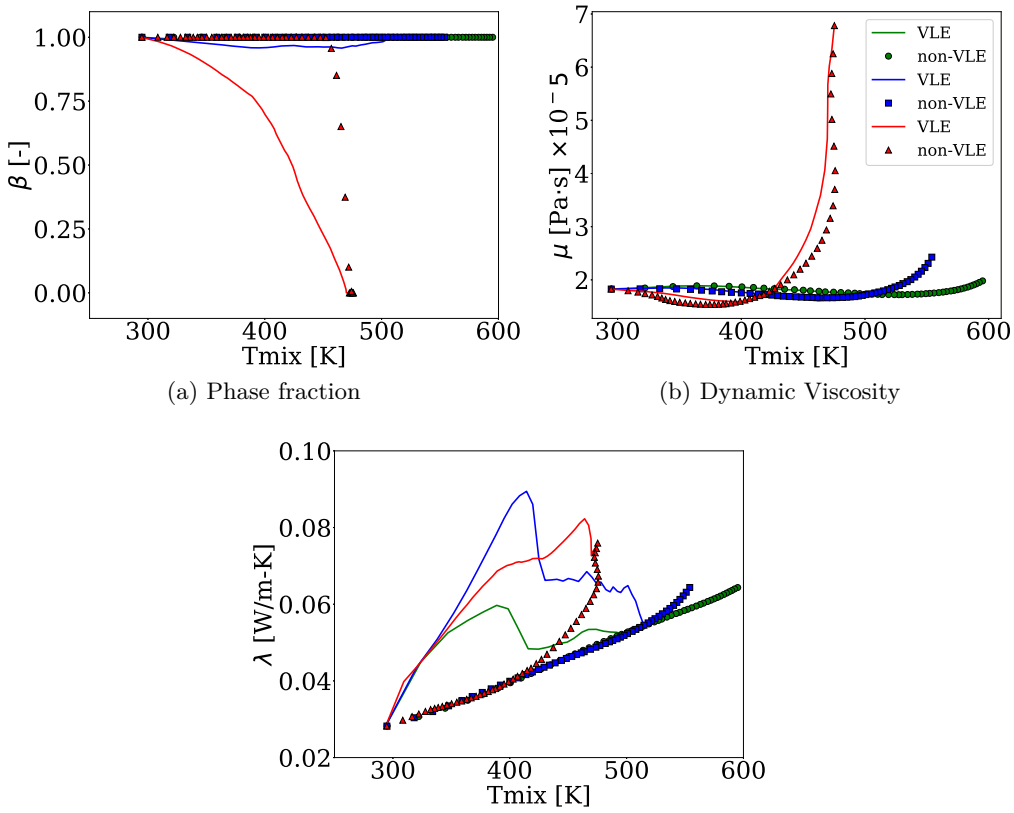

(a) Phase fraction

(b) Dynamic Viscosity

(c) Thermal conductivity

Figure 110: Relevant properties computed along the mixing lines for the hybrid 64^3 case of Fig. 105 with and without VLE. (a) Density, (b) specific heat at constant volume, (c) specific heat at constant pressure, (d) speed of sound, (e) phase fraction, (f) dynamic viscosity, (g) thermal conductivity. Note that the triangles symbols for $\beta \in (0, 1)$ obtained for the non-VLE case are artificially obtained through the conditional average operation and indicates the fact that some points switch between pure liquid ($\beta = 0$) or pure gas ($\beta = 0$), such that their time- and conditional-averaged value is $0 < \beta < 1$.

Figure 110 presents the results of some thermodynamic mixture properties computed along the mixing lines of the hybrid 64^3 case of Fig. 105 with and without VLE to further emphasize the role of phase equilibrium on other properties. The following conclusions can be drawn:

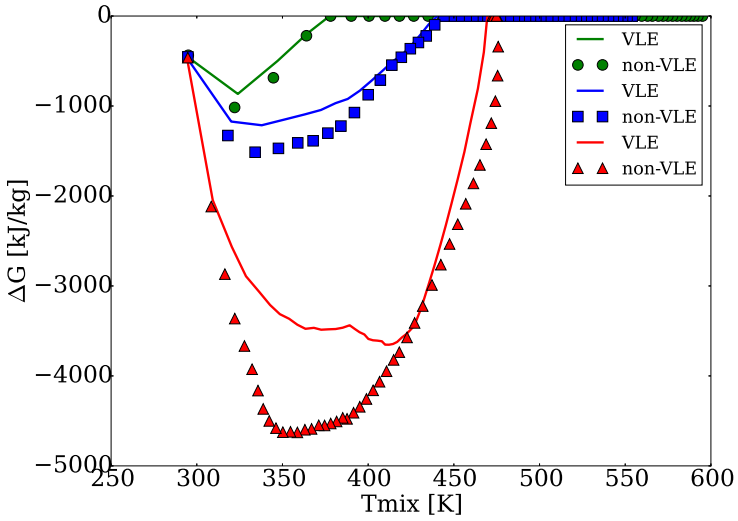

Figure 111: Gibbs energy variation computed along the mixing lines for the hybrid 64^3 case of Fig. 105 with and without VLE.

- overall, large discrepancies in the properties can be observed when VLE is not used. Observations indicate errors as large as 80%, depending on the variable. Also inconsistencies in the trends are observed.

- specific heat at constant volume exhibits enormous departures. This would correspond to an non-physical value of $\gamma = c_p/c_v$. On the other hand, use of VLE is able to re-establish the correct trend and maintain $\gamma \sim O(1)$.

- the big differences observed in the speed of sound may have a significant impact in a problem acoustically dominated. This is especially true for an injector-chamber acoustic interaction where the mixing zone, not yet reacted, can produce these drifts in the acoustic frequencies, having a strong impact on the results.

- the field of β is continuous, with first derivative discontinuities at the phase boundaries. This occurs for all other properties. The field of β also reflects the colored plots of Fig. 104.

- the trend of λ reflects the trend of c_p, used to compute it according to the model of Chung [31]. The big differences observed in the λ field suggest also the importance that VLE effects may have in heat transfer problems.

Finally, Fig. 111 shows the Gibbs free energy variation ΔG computed along the mixing line for the same cases. This variation is defined as $\Delta G = G^{VLE}(T, p, \mathbf{X}) - G^{nVLE}(T, p, \mathbf{X})$ and is computed in the following way: for each of the three cases computed with and without VLE the fields of pressure, temperature and mass fractions are given as input to perform a Tp problem returning all the variables, including the Gibbs energy. This operation is performed with and without VLE with the scope to analyze the solution that would be returned independently of the simulations options. The reason is the fact that VLE thermodynamics returns, by definition [126, 127], a lower Gibbs energy compared to the corresponding single phase assumption, when the initial state is the same. Since between the VLE and the non-VLE simulations, there is a difference (even small), between the mixing lines, the two solutions cannot be compared directly for the Gibbs energy. Thus, for each simulation result, a corresponding VLE and non-VLE solution is computed offline with the goal to get both G^{VLE} and G^{nVLE}, through which ΔG is computed and compared. First, one may observe that all the curves have data which is less or equal to zero. Clearly, the zones where $\Delta G = 0$ correspond to the single phase regions. Conversely, the regions with $\Delta G < 0$ indicate that the most stable solution is the one computed with VLE because its Gibbs energy is lower compared to the one computed without VLE. However, the major point to highlight is that while this is quite logical for the solutions computed directly with VLE (solid curves in Fig. 111) because they indicate the correctness of the computed solution with respect to the corresponding non-VLE solution, this is also observed for the data computed without VLE (symbols in Fig. 111). This confirms that for the simulations run without VLE, the answer corresponds to a thermodynamic state, for which a more stable solution exists and it is not reached during the simulation, because of the single-phase assumption invoked.

The relevance of these observations is that in practical problems of super-critical mixing in complex configurations, regimes where VLE is needed may co-exist with non-VLE regimes both locally in space and in time. Thus, for robustness algorithms must deal with both such regimes without encountering instability that will be unacceptable when large scale simulations are being performed. Forcing the problem to meet the non-VLE single phase

solution may not be an optimal solution to this problem.

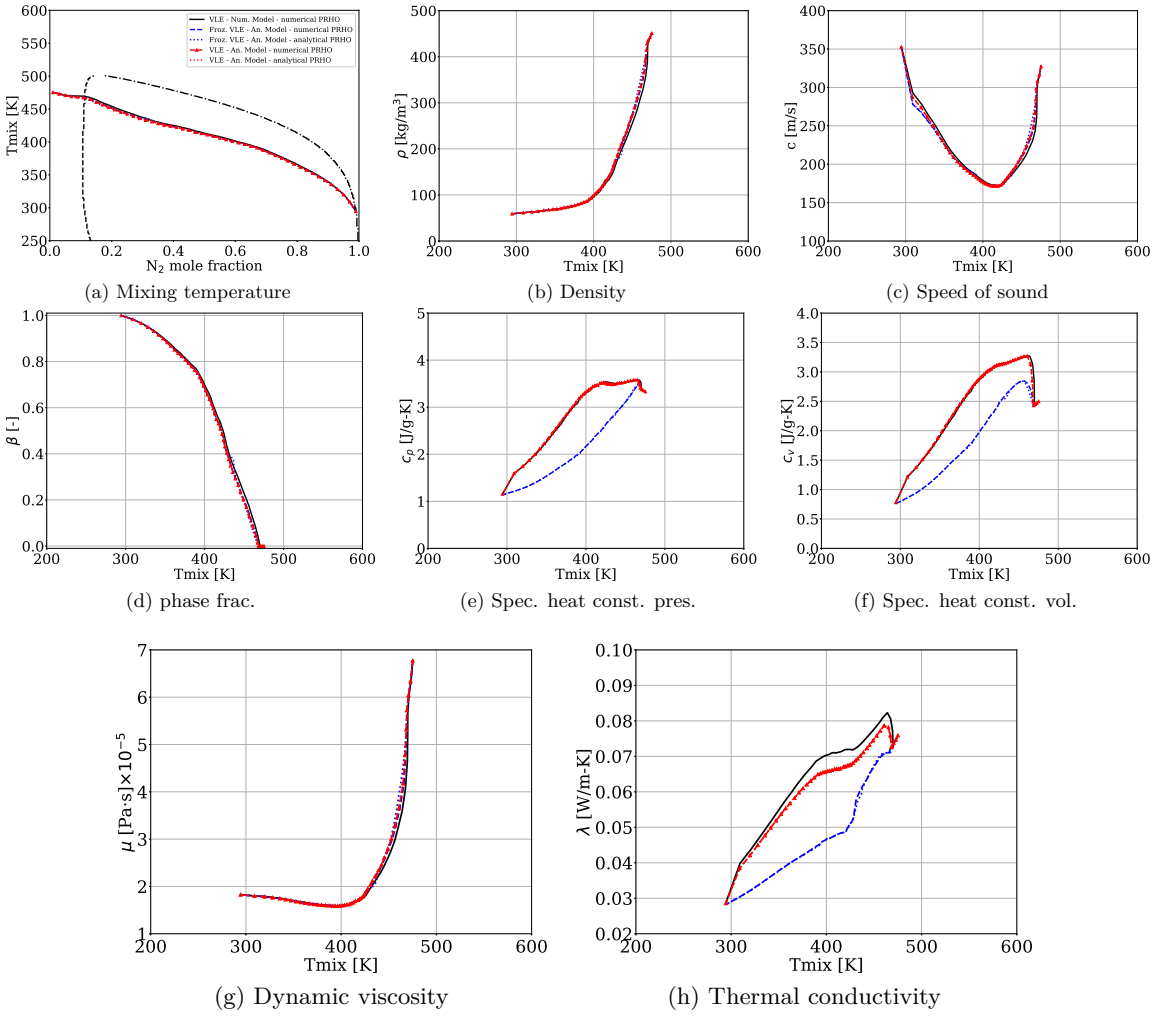

(a) Mixing temperature (b) Density (c) Speed of sound

(d) phase frac. (e) Spec. heat const. pres. (f) Spec. heat const. vol.

(g) Dynamic viscosity (h) Thermal conductivity

Figure 112: Relevant properties computed along the mixing lines for the hybrid 64^3 case 3 of Fig. 105 with different combinations of VLE model, VLE derivatives model and PRHO model for temperature reconstruction. Mixture properties are showed along the mixing line.

5.3.2 Effect of the frozen VLE model and performance evaluation

The effect of different VLE models is isolated and studied separately. Since Case 3 is the one that shows more significantly the effect of phase-split, simulations are run again for this case only by varying few options. This is done because all the results showed before for VLE were run with the fully numerical model for VLE thermodynamics (described in Sec. 3.4.5) and the fully numerical model for the PRHO model for interface temperature

reconstruction [226]. In the following, the VLE model itself is tested and verified again by using the fully analytical model for the thermodynamics described in Sec. 2.2.2, as well as the different methods to reconstruct the interface temperature in the PRHO problem. The simulations are organized as follows:

- the full VLE model is run with the fully analytical thermodynamics according to the definition given in Sec. 5.1.2 by varying the PRHO problem solution: the numerical one (as per Eq. (3.4.10)) and the analytical one (as per Eq. (3.3.10));
- identical simulations are run with the options specified above, but setting the thermodynamic model to the frozen VLE;
- reference solution conducted with the numerical VLE derivatives and numerical PRHO problem is also provided, for reference.

Figure 112 shows the similar results discussed in the previous section. Overall, all the VLE simulations agree very well with past simulations confirming once again that a) both the numerical and the analytical model to compute thermodynamic quantities within the VLE region are equivalent and b) both the methods to resolve the PRHO problem at cell-interface are equivalent.

The interesting thing to notice is the effect of the use of the frozen VLE model over the full VLE model. While minor differences are observable in the mixing temperature, density, dynamic viscosity and phase fraction, some clear deviations are noticeable in the speed of sound, however considerable differences are observable in the specific heats, which in turn affect the thermal conductivity. This is in perfect agreement with the conclusions drawn for the 0D thermodynamics in Chap. 4: setting to zero some important VLE derivatives has a direct effect on the thermodynamic derivatives. Particularly in this case this effect is more evident in the values of the specific heats and the thermal conductivity.

Some additional information regarding the simulation speed are provided in Tab. 29 in terms of time per step. These data refers to the simulations run on 256 processors with uniform load balancing. For these cases, no acceleration techniques are used for VLE and the hybrid

Table 29: Time-per-step comparison of the Case 3 simulation using different thermodynamic and reconstruction models for the PRHO problem. All the simulations refer to the hybrid FC/QC scheme with switch threshold of 0.3. Numbers in parentheses report the cost increase (ratio) with respect to the non-VLE simulation.

Time per step [s] on 256 processors with uniform load distribution				
	non-VLE	VLE (num. model)	frozen VLE (an. model)	VLE (an. model)
fully numerical PRHO	0.38	74 (195×)	33 (86×)	21 (55×)
fully analytical PRHO	0.40	—	21 (55×)	9 (22×)

FC/QC scheme is always used with switch threshold of 0.3. The results show what was already highlighted for the 1D and 2D cases discussed before. The simulation employing VLE is at least one order of magnitude more expensive than the corresponding simulation employing single-phase RG thermodynamics. In addition, by varying the strategy of the PRHO problem solution, significant improvements can be achieved. The worst case is that employing numerical derivatives with the fully numerical PRHO problem, which can take up to 74 seconds per iteration for the present setup. On the other hand, the combination of analytical VLE thermodynamics with fully analytical PRHO problem provides the best performance. Note that for the VLE case with analytical model, use of the analytical instead of the numerical approach for the PRHO problem at cell-interface provides a cost reduction of about 2.3×, which is quite significant. On the other hand, the cost for the frozen VLE model shows larger values with respect to the VLE model in both cases due to the lack of convergence of some points during the simulation as discussed in Sec. 5.2.2 (in this case the factor λ was kept constant across all the simulations). For this reason, and given the fact that the frozen VLE does not give fully correct results in the thermodynamic/transport space, this model is no longer investigated for the rest of this work.

Finally, notice the small cost increase (about 5%) of the fully analytical PRHO problem in case the non-VLE model is used. This is consistent with what already reported for the 1D case in Sec. 5.1.2. This cost increase is associated with the additional variable communication that needs to be done. The results obtained for the non-VLE simulations are also compared in Sec. Q.3 for the purpose to further validate the approach of the two PRHO methods for the single-phase calculations. These results along with those presented in the

previous test cases are satisfactory for validation purposes, therefore no more validations are required.

5.4 Two-dimensional (2D) non-reacting spatial mixing layer (SML)

The next problem represents an extension of the previous TML. The scope is to investigate if any of the differences occurring locally in the thermodynamic properties have any macroscopic effect on the evolution of the fluid-mechanic structures, ultimately affecting mixing. If any difference shows, then it is possible to clearly state that VLE has an impact on the mixing.

5.4.1 Case setup and results discussion

The best configuration to employ for the present purposes is a spatial mixing layer (SML), schematically represented in Fig. 113. Given the considerable computational expense that VLE requires, identified in the previous sections, the problem is simplified to a two-dimensional (2D) configuration. Despite the obvious consequences that this simplification produces (absence of three-dimensional flow structures and mixing, vortex stretching in the vorticity production) in the results, the goal here is to compare one-to-one the VLE to the non-VLE model to identify if any modification in the flow-field occurs by running a longer simulation in comparison to the previous TML setup.

For this reason, the numerical setup is chosen to employ the analytical model for the VLE thermodynamics as well as the full analytical PRHO model for both VLE and non-VLE case to reconstruct the cell-interface temperature. As demonstrated in Tab. 29, this combination provides the best performances in terms of computational speed for the VLE simulations and although the numerical PRHO problem can be used almost transparently for the non-VLE case from a computational point of view, even minor differences are avoided here by choosing the exact numerical setup between the two analyses. In this way, the only difference between the two will be retained in the thermodynamic model.

As a consequence, despite the 2D simplification, in case any difference in the flow-field occurs, a similar conclusions is expected to be found in a 3D setup because the only difference

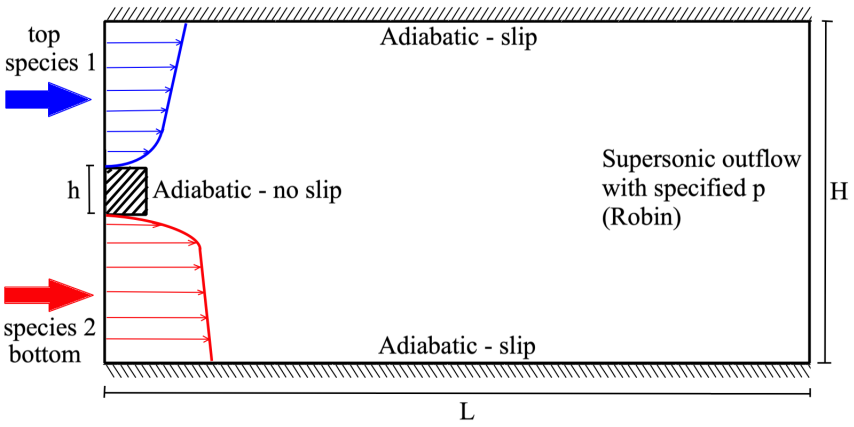

Figure 113: Sketch of the generic spatial mixing layer (SML) setup. Main dimensions are indicated along with the boundary conditions.

is in the thermodynamics. Figure 113 shows the schematic representation of a SML. A similar configuration was already used in many past works involving super-critical studies [188, 92, 108], however this is the first time that it is employed with VLE and particularly used to identify the differences between the single- and multi-phase equilibrium model in RG mixtures. Two different streams (top and bottom) with different species are initially flowing from left to right at their own speed and thermodynamic condition. The two fluids are separated by a solid wall flat plate of square shape with side h. The other relevant dimensions are chosen as $L = 21h$ and $H = 10h$ [188, 92, 108] with chosen size for the splitter plate is $h = 0.24mm$. The reason for this choice is related to the injector dimensions of a sub-scale rocket combustor [76]. Although the present configuration does not employ the same injection conditions, the scale is chosen similar to that in order to establish whether the flow structures generated by a splitter plate of this size can trigger the formation of VLE if the thermodynamic states of the incoming species are also chosen to trigger it. Nevertheless the same geometry configuration will be used later to study the reacting flow in Sec. 5.6. The reference frame is placed at the middle-right side of the square plate. Top and bottom boundaries are treated as slip, adiabatic walls, whereas the splitter plate is treated with no-slip adiabatic condition. Subsonic, characteristic-based inflow boundaries are specified for the top and bottom streams, while the supersonic outflow with specified pressure is selected as outflow boundary [39].

Mean axial velocity profiles are specified for both streams to mimic the formation of the boundary layer [188, 92, 108]. These are specified in the form $u(y)/U_b = [(y - y_{ref})/w]^{1/7}$, where U_b represents the bulk velocity of each stream, y_{ref} the reference coordinate where the no-slip condition must be enforced and w is a width that indicates how fast the free stream velocity has to be recovered [188, 92, 108]. For the present case, Tab. 30 summarizes all the necessary information. The chosen operating pressure is 5 MPa. In this way the

Table 30: Relevant properties used to initialize the 2D SML non-reacting setup.

2D SML non-reacting setup						
	species	U_b [m/s]	T [K]	y_{ref} [mm]	w [mm]	p [MPa]
top stream	C_6H_{14}	30	479	$h/2$	$4.5h$	5
bottom stream	N_2	50	293	$-h/2$	$-4.5h$	5

same conditions as Case 3 of Tab. 28 are reproduced, however this time in a different configuration, which is of particular interest for any injector-type problem with species streams initially separated.

The computational domain is discretized using 750 cells along the x (length) direction and 250 cells along the y (height) direction. Out of these, 50 are used to discretize the square splitter plate in both directions. Next, a stretching factor of 3% is applied in both directions after L/2 and ±H/4 to fit the number of cells into the domain sizes. This also helped to save some computational time avoiding to over-fit the grid in the regions away from the splitter plate and at the same time help to dissipate vortical structures along the x direction, close to the outlet to avoid formation of back-flow effects that are known to cause numerical instabilities. Grid is showed in Fig. 114. The simulation is initially run for 0.945 ms to eliminate any effect of the initial condition. This physical time corresponds to roughly 7.5 flow-through time (FTT) where FTT is computed as $L/\overline{U} = 126\mu s$ where $\overline{U} = 40.0$ m/s is a good representative value of the flow average velocity along the axial direction. Given the fact that this initial simulation time is meant to simply eliminate any effect of the initial condition, there is no need use VLE here, hence the non-VLE model is used only. Next, from $t_1 = 0.945$ ms, now renamed as $t_1 = 0.0$ s to indicate a new (current) value of the

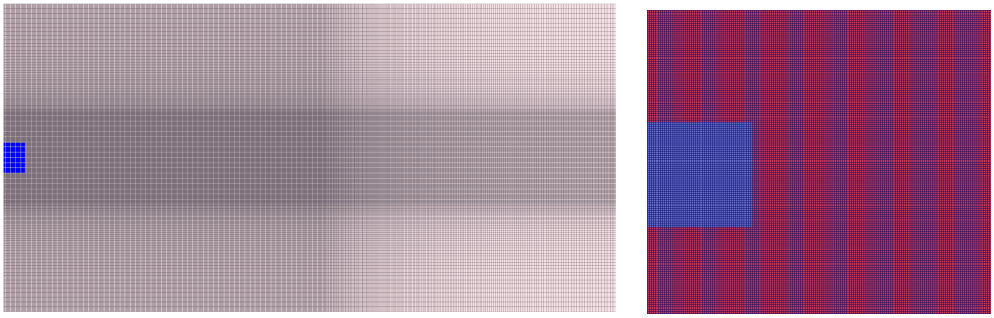

(a) (b)

Figure 114: Computational domain discretization: (a) broad view and (b) near splitter-plate zoomed view.

initial condition, both the VLE and the non-VLE simulations are run again for 1 ms more, during which statistics are collected.

To emphasize once again the computational expense required by VLE to run, two significant values are reported. The time-per-step required by the non-VLE simulation on 512 processors was 0.12 seconds, while the time-per-step required by the VLE simulation on 1024 processors was 1.7 seconds. Thus assuming perfect scaling between the two simulations, this puts once again the VLE model to be roughly 28 times more expensive than the corresponding single-phase model. This is in agreement with the analysis showed earlier for the TML and reported in Tab. 29. Note that according to the same previous analysis, other choices regarding the numerics would have significantly impacted the cost, making even the simulation of a 2D setup very challenging from a computational time point of view.

In addition to time-averaged data, instantaneous data is saved at time intervals of $\Delta t = 2.5\mu s$ for the purpose to investigate about local mixing differences in both space and time.

Figures 115 and 116 show the time sequence of density, phase fraction and speed of sound for the VLE and non-VLE simulation, respectively. The five snapshots are taken at time intervals of 30 μs starting from the initial condition (identical in both) to the physical time $120\mu s$, almost corresponding to one FTT.

One first observation is that the field of β spans again all the range between zero and one for the VLE case, whereas the non-VLE case contains only zero or one values, as expected.

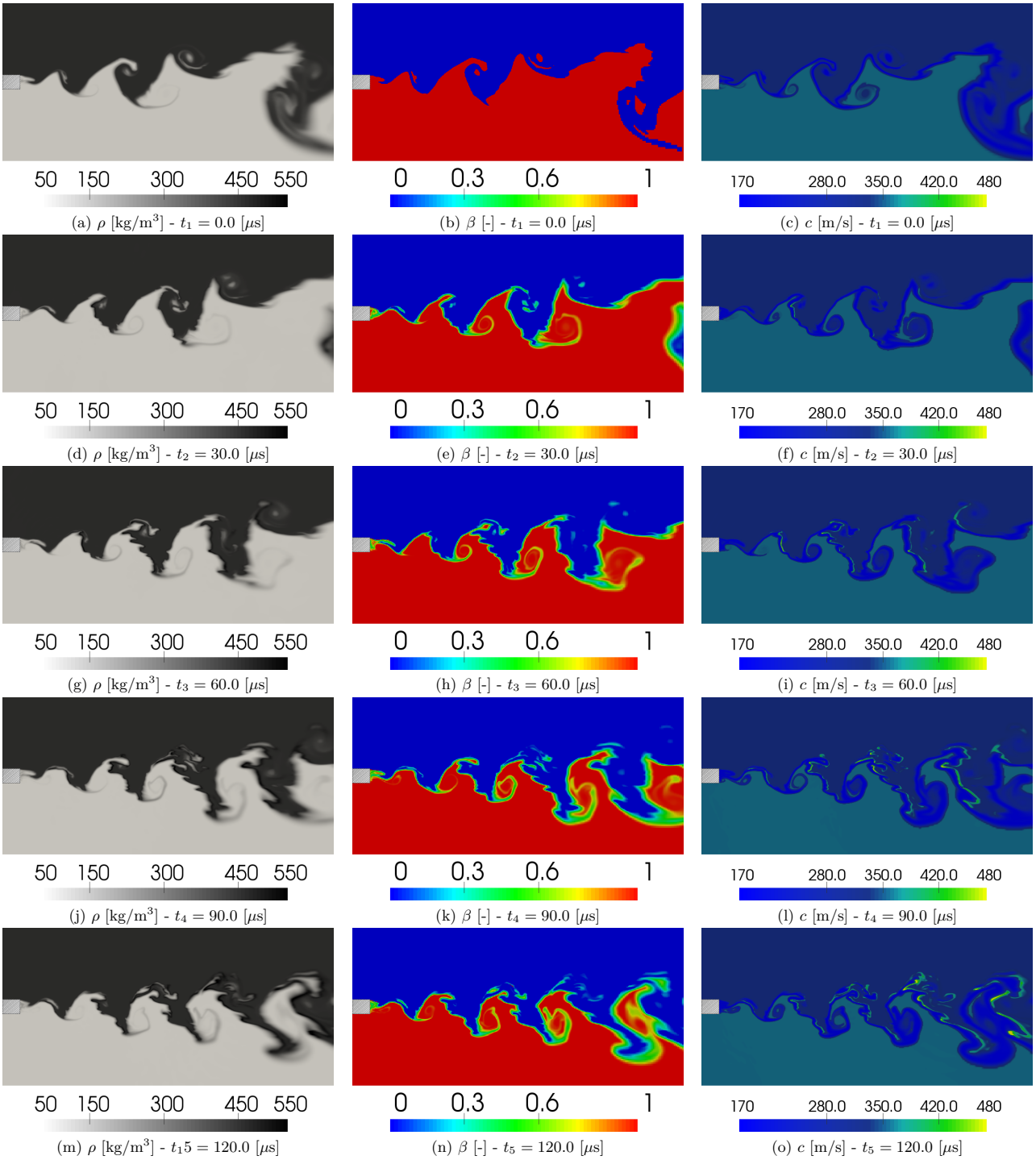

(a) ρ [kg/m^3] - $t_1 = 0.0$ [μs] (b) β [-] - $t_1 = 0.0$ [μs] (c) c [m/s] - $t_1 = 0.0$ [μs]

(d) ρ [kg/m^3] - $t_2 = 30.0$ [μs] (e) β [-] - $t_2 = 30.0$ [μs] (f) c [m/s] - $t_2 = 30.0$ [μs]

(g) ρ [kg/m^3] - $t_3 = 60.0$ [μs] (h) β [-] - $t_3 = 60.0$ [μs] (i) c [m/s] - $t_3 = 60.0$ [μs]

(j) ρ [kg/m^3] - $t_4 = 90.0$ [μs] (k) β [-] - $t_4 = 90.0$ [μs] (l) c [m/s] - $t_4 = 90.0$ [μs]

(m) ρ [kg/m^3] - $t_15 = 120.0$ [μs] (n) β [-] - $t_5 = 120.0$ [μs] (o) c [m/s] - $t_5 = 120.0$ [μs]

Figure 115: Time sequence for the VLE 2D SML. Snapshots show the density, phase fraction and speed of sound at the five time instants starting from the initial condition (top row).

For correctness, the phase fraction field in both cases is reported as “cell-centers” values

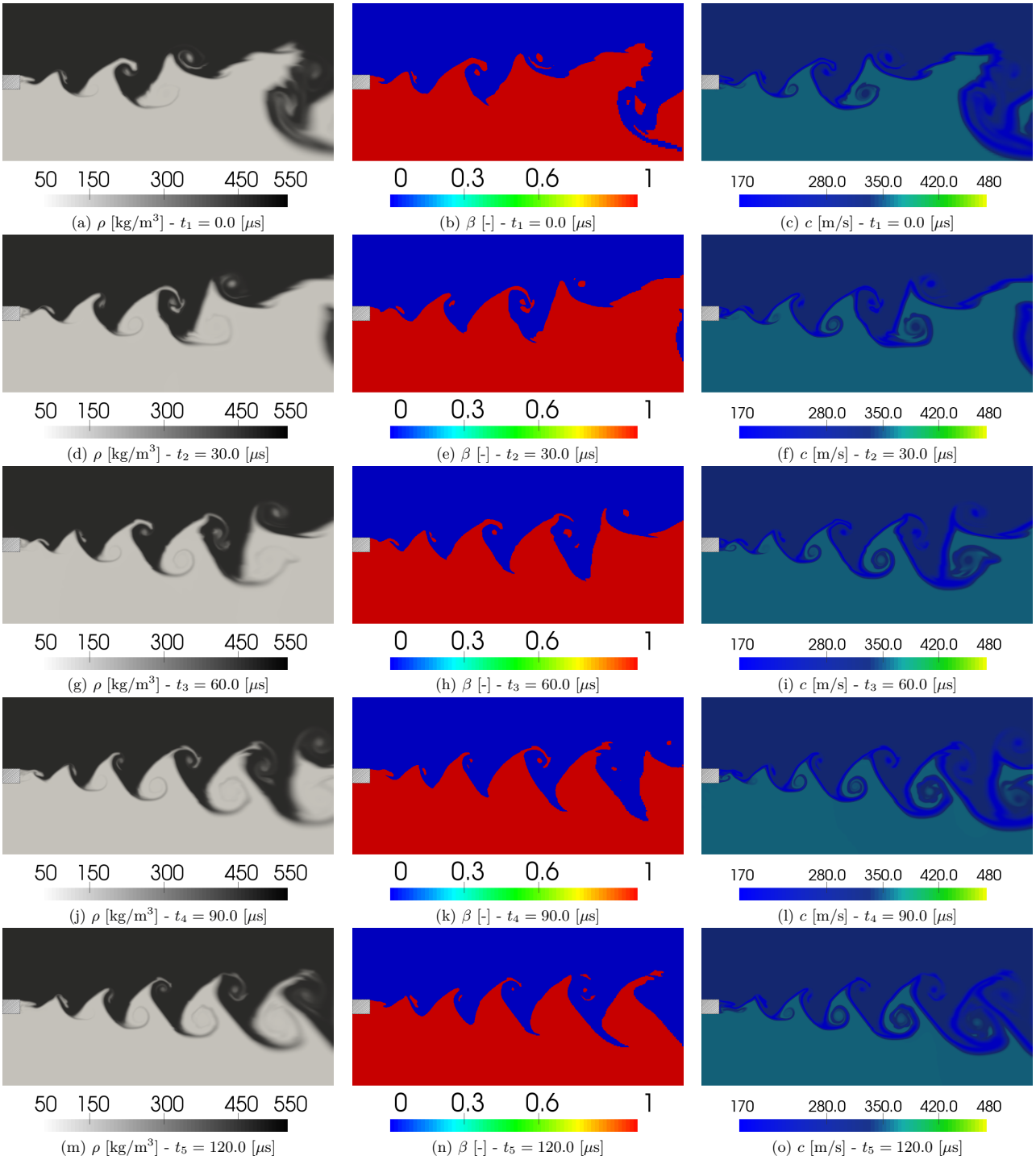

(a) ρ [kg/m^3] - $t_1 = 0.0$ [μs] (b) β [-] - $t_1 = 0.0$ [μs] (c) c [m/s] - $t_1 = 0.0$ [μs]

(d) ρ [kg/m^3] - $t_2 = 30.0$ [μs] (e) β [-] - $t_2 = 30.0$ [μs] (f) c [m/s] - $t_2 = 30.0$ [μs]

(g) ρ [kg/m^3] - $t_3 = 60.0$ [μs] (h) β [-] - $t_3 = 60.0$ [μs] (i) c [m/s] - $t_3 = 60.0$ [μs]

(j) ρ [kg/m^3] - $t_4 = 90.0$ [μs] (k) β [-] - $t_4 = 90.0$ [μs] (l) c [m/s] - $t_4 = 90.0$ [μs]

(m) ρ [kg/m^3] - $t_5 = 120.0$ [μs] (n) β [-] - $t_5 = 120.0$ [μs] (o) c [m/s] - $t_5 = 120.0$ [μs]

Figure 116: Time sequence for the non-VLE 2D SML. Snapshots show the density, phase fraction and speed of sound at the five time instants starting from the initial condition (top row). Note that the phase fraction field has been intentionally left in the cell-center based solution in order to not artificially produce $\beta \in [0, 1]$ during the post-processing.

as directly obtained form the numerical integration. This is because visualization post-processing may interpolate data from cell-centers to cell-nodes, creating artificial $\beta \in [0, 1]$ values that could be deceptive. Note that VLE is constantly appearing right at the splitter plate front, where vortices are formed due to the high strain rate.

Next, one may observe that although the main vortex propagation between the two cases is similar and no difference in the number of vortices is observed at a given time, substantial differences in the local vortex features, predominantly forming at the leading edges can be noticed in the VLE case in comparison with the non-VLE case. Once formed locally, these flow features propagate upward along the vortex edge, creating smaller structures that modify the local vorticity value as showed in Fig. 117, ultimately modifying the macroscopic vortex shape, which appears more fragmented.

Because these features are generated locally after each vortex is shed from the splitter plate, it is possible to introduce the definition of a "micro-mixing" characteristic that shows only when VLE is turned on. As a result, a big difference between the two sequences appear: while the non-VLE case clearly shows spatial hydrodynamic instability that is mostly linear, the VLE case displays these micro-mixing features that are clearly generated by a non-linear effect, thus although the main vortex linear growth is observable, local disruption of these is superimposed on it. One hint that can drive the explanation of such behavior is the density and speed of sound fields displayed in Fig. 115. Vortex leading fronts show local peaks in both density and speed of sound that are not visible in the non-VLE case. Particularly the increase in the speed of sound causes a reduction in the simulation CFL determination up to 50% with respect to the non-VLE case, adding additional simulation overhead.

In order to analyze the possible reason of such behavior, a study is conducted on the vortex leading edge interface for both simulations. Data is extracted across the vortex front using a segment that moves with the vortex itself. Figure 161 shows the evolution of this line and its exact location for both cases. Due to the physics complexity and the strong non-linear behavior among all the variables, an ensemble of these is necessary to look concurrently.

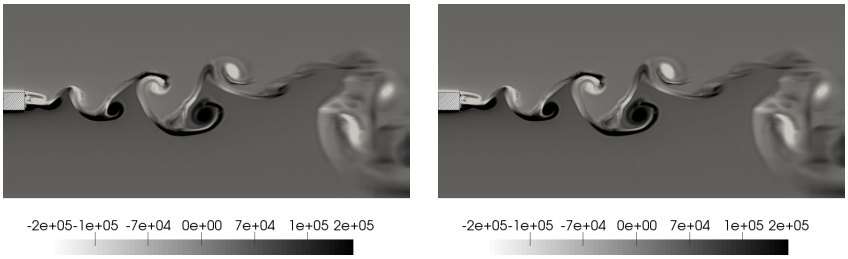

(a) ω_z [1/s] - $t_1 = 0.0$ [μs] - VLE

(b) ω_z [1/s] - $t_1 = 0.0$ [μs] - non-VLE

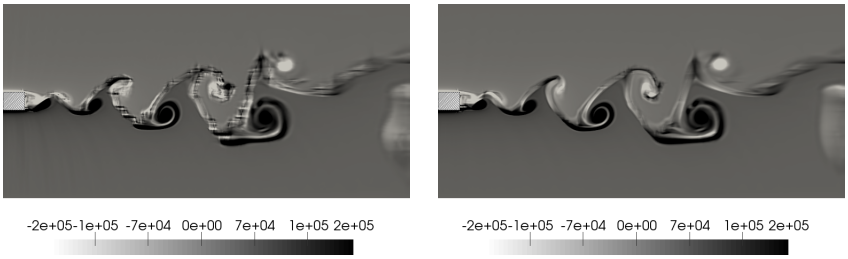

(c) ω_z [1/s] - $t_2 = 30.0$ [μs] - VLE

(d) ω_z [1/s] - $t_2 = 30.0$ [μs] - non-VLE

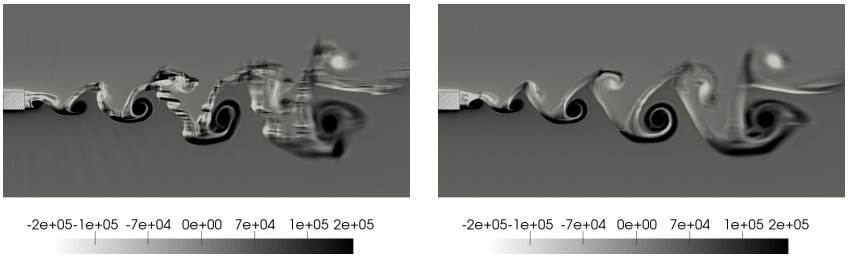

(e) ω_z [1/s] - $t_3 = 60.0$ [μs] - VLE

(f) ω_z [1/s] - $t_3 = 60.0$ [μs] - non-VLE

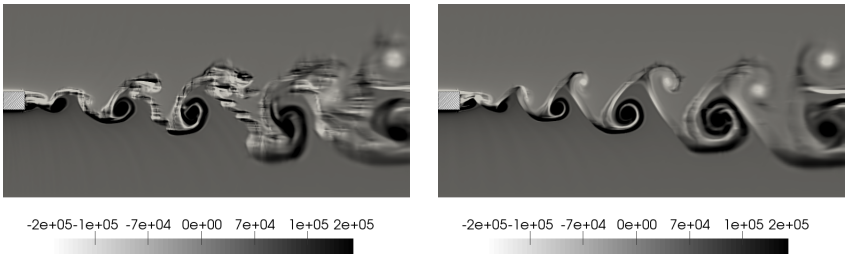

(g) ω_z [1/s] - $t_4 = 90.0$ [μs] - VLE

(h) ω_z [1/s] - $t_4 = 90.0$ [μs] - non-VLE

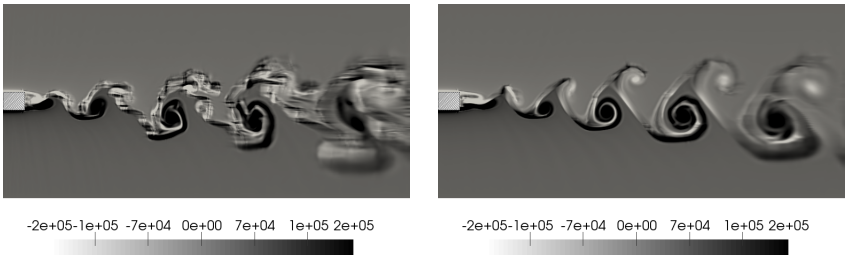

(i) ω_z [1/s] - $t_5 = 120.0$ [μs] - VLE

(j) ω_z [1/s] - $t_5 = 120.0$ [μs] - non-VLE

Figure 117: Time sequence of the five snapshots of the vorticity z component for the VLE (left column) and non-VLE (right column). Micro-mixing generated by the non-linear coupling between VLE thermodynamics and fluid-mechanics enhances vortex breakdown. This is accompanied by a vorticity field that is both positive and negative along the vortex edge.

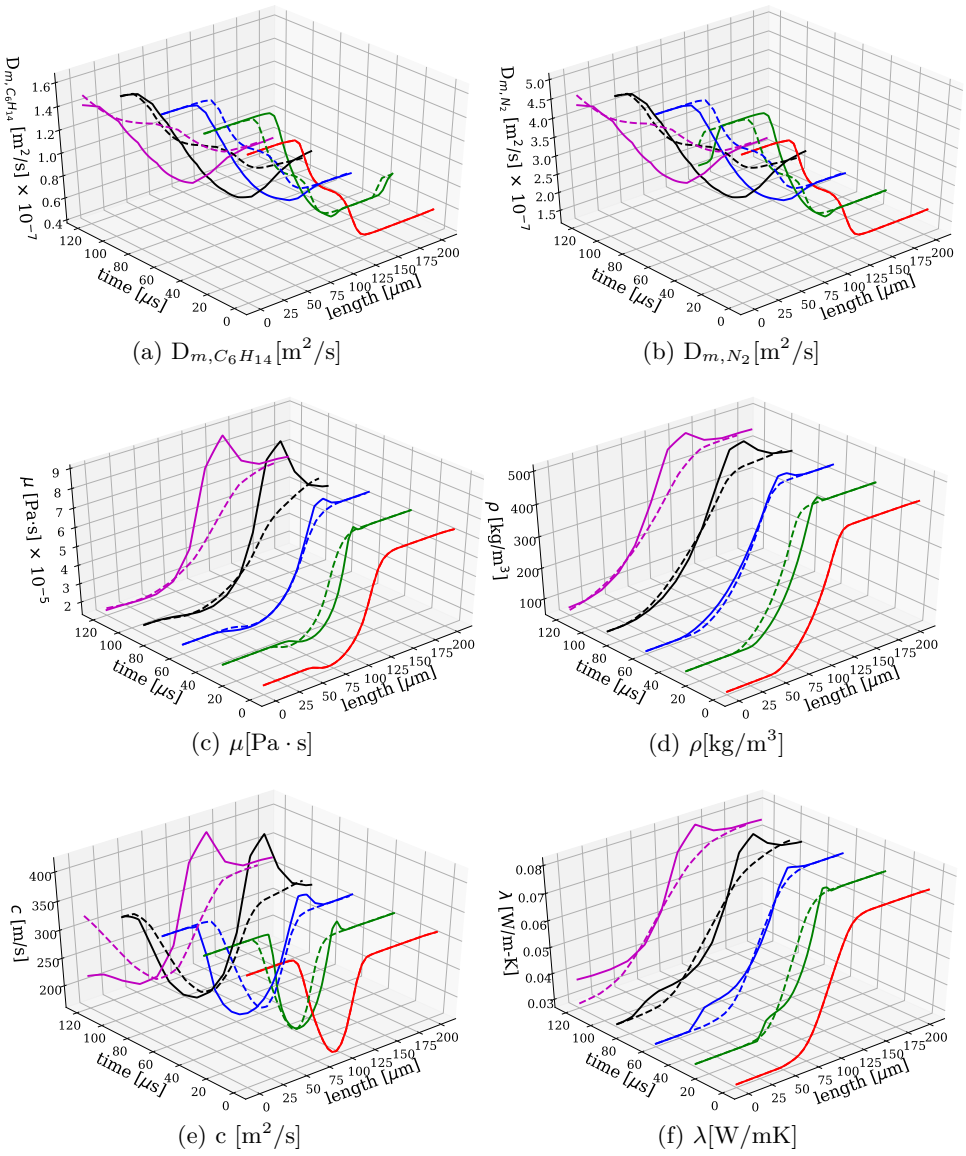

(a) $D_{m,C_6H_{14}}$[m^2/s] (b) D_{m,N_2}[m^2/s]

(c) μ[Pa · s] (d) ρ[kg/m^3]

(e) c [m^2/s] (f) λ[W/mK]

Figure 118: First set of properties collected across the reference abscissa s at the vortex leading edge (*cf.* Fig. 161) for both simulations: (a) C_6H_{14} mass diffusion coefficient, (b) N_2 mass diffusion coefficient, (c) dynamic viscosity, (d) density, (c) speed of sound and (d) thermal conductivity. Colors refer to the time instant (indicated on the axis). Solid lines indicate the VLE solution, while dashed lines indicate the non-VLE solution.

Figures 118 and 119 show relevant variables collected across the reference abscissa s at the vortex leading edge.

First, it is possible to observe the peaks reached in density (Fig. 118(d)) and speed of sound (Fig. 118(e)) indicated earlier. These occupy the final portion of the VLE region, where the

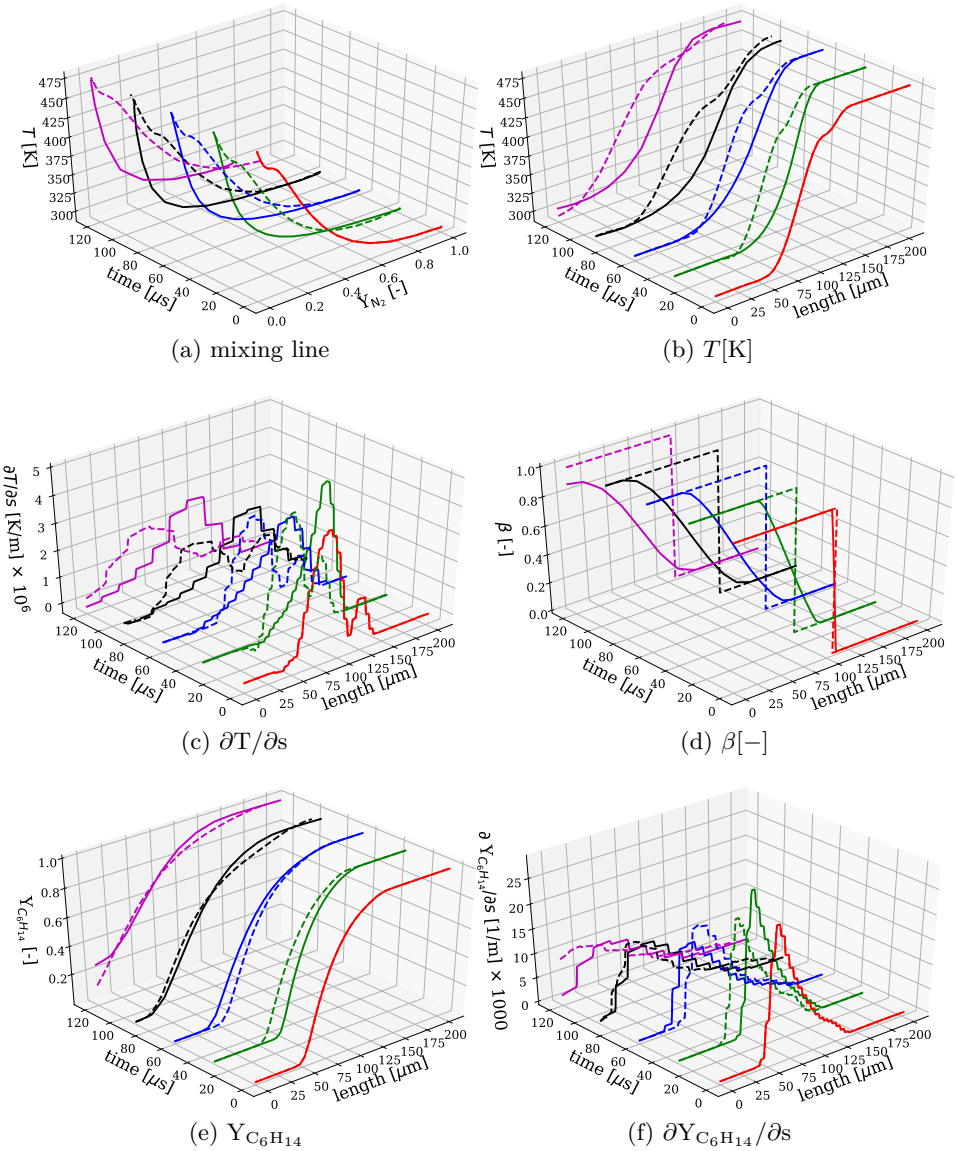

(a) mixing line (b) T[K]

(c) ∂T/∂s (d) β[$-$]

(e) $Y_{C_6H_{14}}$ (f) $\partial Y_{C_6H_{14}}/\partial$s

Figure 119: Second set of properties collected across the reference abscissa s at the vortex leading edge (*cf.* Fig. 161) for both simulations: (a) temperature vs N_2 mass fraction (mixing line), (b) temperature, (c) temperature gradient, (d) phase fraction, (c) C_6H_{14} distribution (d) C_6H_{14} gradient. Colors refer to the time instant (indicated on the axis). Solid lines indicate the VLE solution, while dashed lines indicate the non-VLE solution.

two-phase zone merges with the single-phase zone predominantly made of C_6H_{14} at approximately $s = 150\mu m$ (see Fig. 119(d) and (e)). These are formed by low-probability events that are characterized by pockets of fluid largely composed of C_6H_{14} at a lower temperature than the injection temperature (479 K). This is confirmed by the joint PDFs reported in

Fig. 120 between C_6H_{14} mass fraction and temperature and speed of sound and C_6H_{14} mass fraction. This speed of sound joint PDF (Fig. 120(b)) shows a peak value corresponding

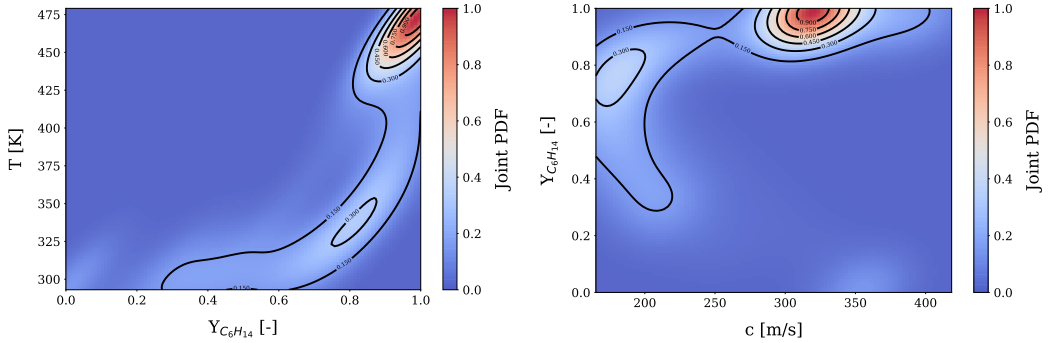

Figure 120: Joint PDF between (a) n-hexane mass fraction and temperature and (b) speed of sound and temperature. Data refers to the line segment extracted for the VLE simulation at vortex leading edge.

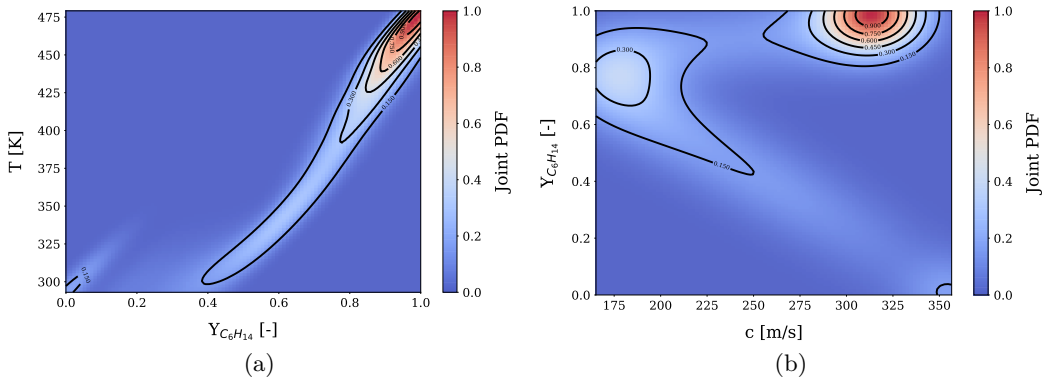

Figure 121: Joint PDF between (a) n-hexane mass fraction and temperature and (b) speed of sound and temperature. Data refers to the line segment extracted for the non-VLE simulation at vortex trailing edge.

to the most probable event across the vortex front. This is characterized by pure/almost pure n-hexane ($> 99\%$ by mass) at a temperature very close to the injection one with a corresponding speed of sound around 320 m/s. Other small peaks are:

- medium to high mass fraction of n-hexane with corresponding low speed of sound ($\sim$ 155 m/s). This region represents the low-diluted VLE state;

- low mass fraction of n-hexane corresponding to values of speed of sound close to the pure hexane ($\sim$ 320 m/s). This is the high-diluted VLE state;
- high mass fraction of n-hexane with corresponding high speed of sound around 400-450 m/s. This is the region where almost pure n-hexane gets colder and it is responsible for the low-probability regions of high speed of sound (*cf.* Fig. 120(a)). Note that this region does not necessarily fall into VLE as illustrated in Fig. 122(a), however it is a region that evolves right next to it.
- the same observations cannot be made for the non-VLE solution in Fig. 121, where it is immediately clear that mixture states with high amount of n-hexane never reach temperatures lower than the injection value. In fact, whenever n-hexane portions gets colder, there is also sufficient amount of N_2 in the mixture such that a diluted solution is formed.

All the above observations are confirmed by looking at Fig. 122(a), which shows the speed of sound trend with respect to temperature as the amount of n-hexane is changed in the mixture. This data is computed off-line to emphasize the one-to-one comparison between the data obtained with the simulations and the stand-alone RG-VLE thermodynamics. Symbols are also colored by the phase fraction in order to increase picture quality. This

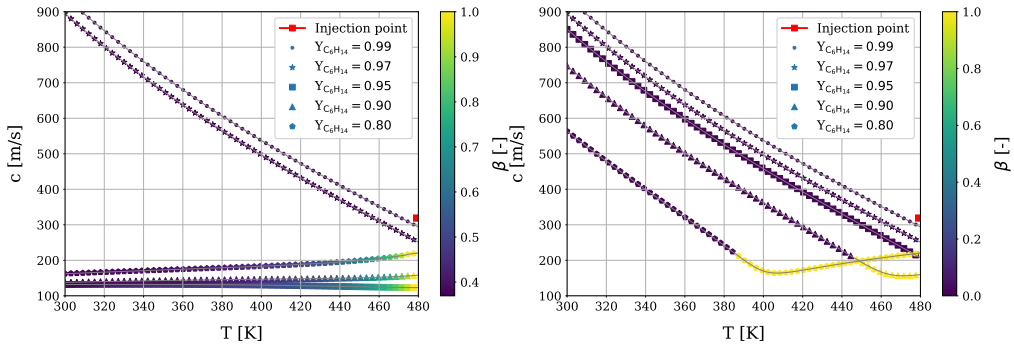

(a) VLE (b) non-VLE

Figure 122: Speed of sound versus temperature for different amounts of hexane in the mixture. Symbols are also colored by the phase fraction to indicate the presence or absence of VLE. For clarity, the injection point for C_6H_{14} is also indicated.

picture shows that as the mixture is diluted with N_2, it falls into the VLE region with a corresponding decrease in the speed of sound. This value can get very close to that of pure n-hexane at larger temperatures. This explains why high-diluted VLE regions have comparable speed of sound as pure C_6H_{14} at its injection point. On the other hand, for almost pure n-hexane composition, if temperature is reduced from the injection condition, speed of sound can increase dramatically because of the large gradients that characterize the n-hexane in its initial state (this is valid for all other properties).

The question that remains to answer is why n-hexane gets so cold at the vortex front edge and why this does not happen for the non-VLE simulation, especially because as showed in Fig. 122(a) these peaks are more likely to happen where VLE does not form directly. The answer is hidden into the transport properties and their non-linear coupling with all other variables.

As illustrated in Fig. 118, the thermal conductivity λ contains a peak within the VLE region and similarly occurs for viscosity. This does not occur for the non-VLE case. At the same time, mass diffusion coefficients exhibit lower values in the VLE region compared to the corresponding non-VLE case. Since (almost pure) n-hexane is located on the same side of the peaks, it is clear now that the VLE thickness acts as a barrier for the mass diffusion of N_2 into C_6H_{14}, while promoting temperature diffusion with respect to the non-VLE simulation. As a result, the (almost pure) n-hexane that lies right next to the VLE front experiences less dilution effects and larger temperature diffusion, hence zones of very high n-hexane concentration with lower injection temperature are created locally, producing the effect explained in Fig. 122(a) where n-hexane tends to become more liquid-like with increased density and speed of sound.

This effect does not happen in the non-VLE situation because transport properties, especially the thermal conductivities do not show any peaks. As a consequence, there is no dominant effect between mass and thermal diffusion. The n-hexane in the neighborhood of VLE experiences both N_2 entrainment and temperature reduction at the same rate so the mixture becomes both colder and diluted, with the result to behave more as a gas-like state, exhibiting lower speed of sound and density values. This is shown in Fig. 122(b) for

completeness. Note that in this case, as the mixture gets diluted the speed of sound tends to decrease at lower temperature in contrast to the VLE case. One way to lump this effect

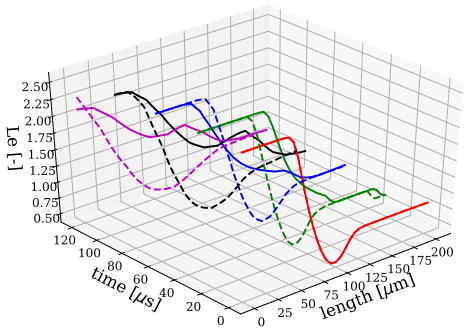

Figure 123: Lewis number calculated across the reference abscissa s at the vortex leading edge (*cf.* Fig. 161).

into a single parameter is to look at the Lewis number defined as the ratio between the thermal α and mass diffusivity. If $Le = \alpha / D_{m,\mathrm{C_6H_{14}}}$ is defined with respect to the n-hexane diffusivity and plotted along the same abscissa across the vortex leading edge, Fig. 123 is obtained. As one can immediately see, all profiles are characterized by a larger Le for the VLE simulation over the non-VLE simulation, confirming the fact that the VLE thickness enhances thermal diffusion over mass diffusion, promoting the transition of the near $\mathrm{C_6H_{14}}$ pockets toward a more pseudo-liquid state.

Next, another interesting question to answer is why the same effect does not happen or is significantly reduced at the vortex trailing edge. To do so, the same identical analysis is conducted on a line segment intersecting the vortex trailing edge (representation is given in Fig. 162), however the pictures are provided in Sec. Q.4 through Figs. (163)–(167) in order to reduce the present section length. Key observations are now focused at $s = 50\,\mu m$ where the vortex trailing edge approximately begins and are given in the following discussion:

- at $s \sim 50\,\mu m$ mass diffusion coefficients of both species in the VLE simulation are less or equal than the corresponding non-VLE solution. Overall, their magnitude is similar to the leading edge case so this information is not enough to establish what is happening;

- peaks in viscosity, density, speed of sound and thermal conductivity are absent or drastically reduced. This is an observation that can be directly made in Fig. 116. In addition, the magnitudes of μ and λ are smaller than the leading edge case of about 15%;

- the VLE thickness is considerably reduced in this case as observable from the phase fraction plot in Fig. 164(d). This forces species and temperature gradients to be higher than the leading edge case. This is directly observable by comparing Fig. 119(c) and (f), with Fig. 164(c) and (f). Particularly the C_6H_{14} gradient almost doubles, whereas the temperature gradient has moderately higher values (about 35% at the largest peak);

- with the above considerations, and by also looking at the Lewis number plot in Fig. 167, the vortex trailing edge is characterized by roughly equal rates of thermal and mass diffusion in the VLE case. In addition, both temperature and species gradients are higher than the corresponding leading edge because the VLE thickness is reduced, therefore both energy and mass transfer find highly favorable conditions. As a result, the moment C_6H_{14} gets colder, it also gets diluted enough by N_2 so that properties do not have time to shift toward the liquid-like state[1]. This is further proven in the joint PDFs of Figs. (165)–(165) where absence of the high n-hexane with low temperature regions is noticed.

Finally, time-averaged density and temperature contour fields are showed in Fig. 124 and Fig. 125, respectively. By looking at both fields, one recognizes that the SML thickness is smaller in the VLE case compared to the non-VLE case. This is more quantitatively showed in Fig. 126 where reference minimum and maximum contour values of density and temperature are extracted from the same pictures along with a reference line of 0.5 N_2 mass fraction. In the non-VLE case, the shear layer appears thicker along the y axis because of

[1]Again here the concept of time is used in analogy to the fluid-mechanics only. The assumption of phase equilibrium does not capture any time-dependent thermodynamic transition.

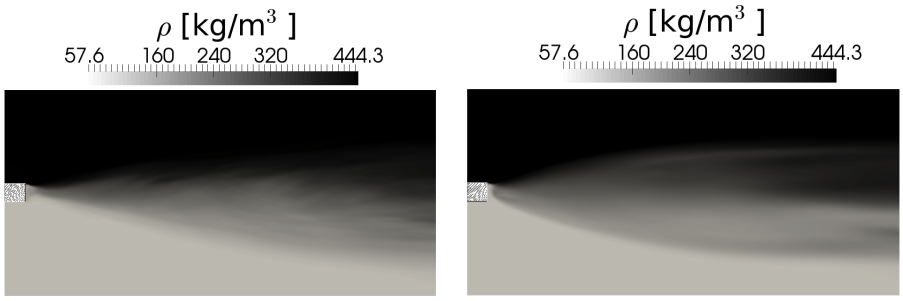

(a) ρ - VLE (b) ρ - non-VLE

Figure 124: Time-averaged density fields for the (a) VLE and (b) non-VLE case.

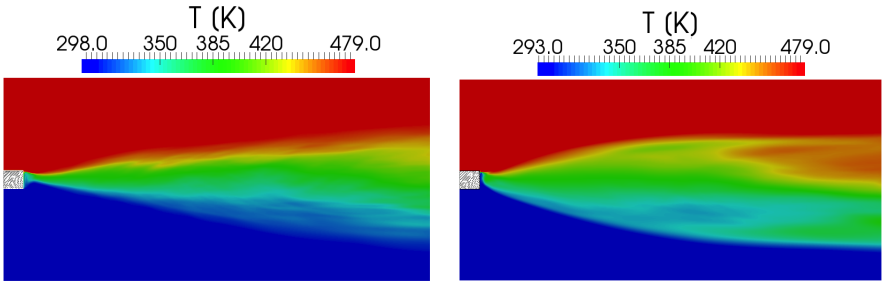

(a) T - VLE (b) T - non-VLE

Figure 125: Time-averaged temperature fields for the (a) VLE and (b) non-VLE case.

the vortex spatial instability that propagates in space and time without any superimposed effect. On the contrary in the VLE case, the same effect is limited by the local instability caused by the Le number effect discussed earlier, with the overall effect to produce a thinner layer.

It is also interesting to point out the different shear layer attaching mechanism visible from all the pictures. This is particularly evident from Fig. 126(c) which shows the reference $Y_{N_2} = 0.5$ line in opposite direction near the splitter plate. This is further confirmed by the additional quantities that are plotted at different axial locations in Figs. (168)–(172) in Appendix Q.4.

Another observation that follows from the above ones is that as the VLE shear layer is thinner, the local unsteady phenomena dictated by the Le effect can be also interpreted as a potential source of mixing improvement, ultimately affecting mixing efficiency, that is not observed in the non-VLE case.

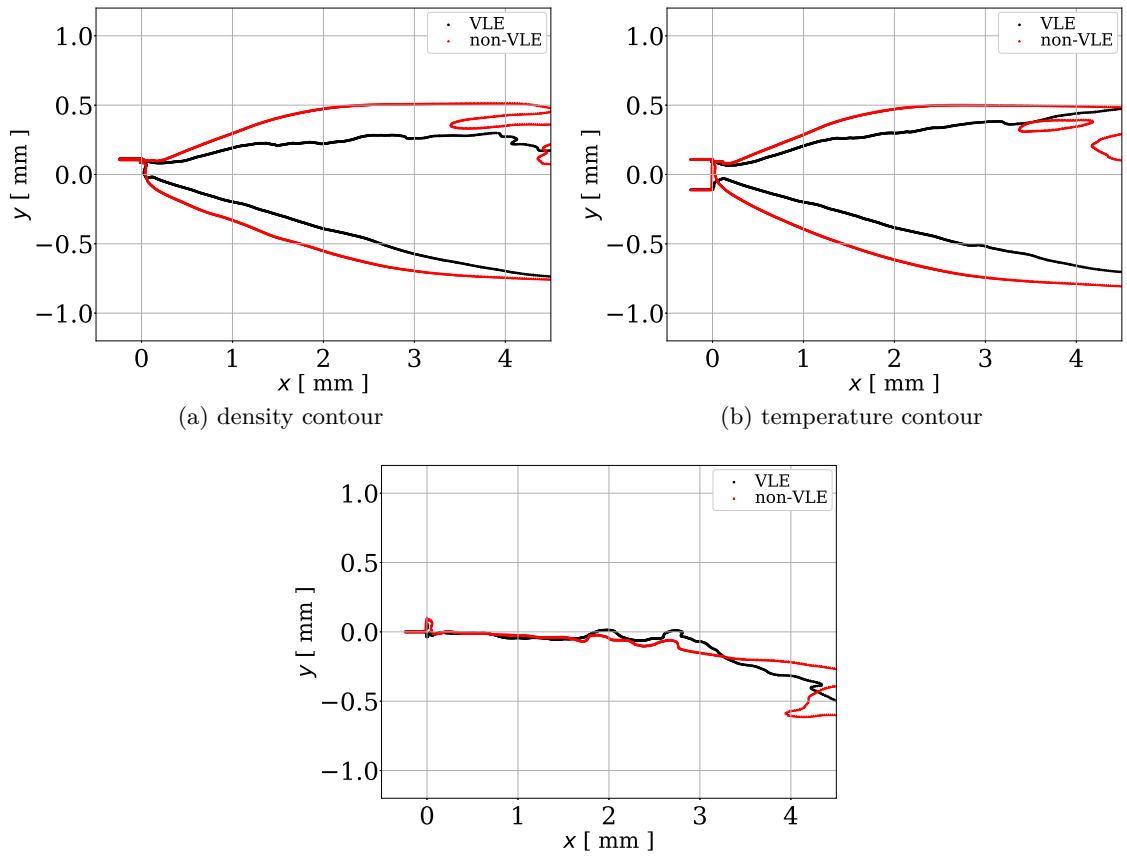

(a) density contour

(b) temperature contour

(c) N_2 mass fraction contour

Figure 126: (a) Density contour lines extracted from the time-averaged field at the values of $\rho_{\min} = 120\,kg/m^3$ (N_2 side - bottom) and $\rho_{\max} = 380\,kg/m^3$ (C_6H_{14} side - top), (a) temperature contour lines extracted from the time-averaged field at the values of $T_{\min} = 320\,K$ (N_2 side - bottom) and $T_{\max} = 450\,kg/m^3$ (C_6H_{14} side - top), (c) N_2 mass fraction contour lines extracted from the time-averaged field at the value of 0.5.

The key conclusion of this first part of the results section is that VLE definitely can affect mixing. Local thermodynamic and transport properties are strongly coupled with the whole system of equations, thus local change in their values dictated by the phase-split has an impact over the fluid mechanics and ultimately mixing.

5.5 Three-dimensional (3D) reacting temporal mixing layer (TML)

In this section, the first reacting case is presented. The scope of this simulation is to analyze first whether or not VLE would occur in a pure reacting flow, that is the condition established by the mixing between the combustion products and one or both the reactants as described in the **Objective 3** in Sec. 1.4 and not by the reactants independently (which

would fall back into the non-reacting cases discussed earlier in Sec. 5.3 and Sec. 5.4). Secondly, the objective is to study its effect on the main flow properties compared to the non-VLE simulations as done for the non-reacting simulations.

The first step to complete before the actual simulation is the choice of the reactants and their chemical mechanism for the finite-rate model discussed in Sec. 2.4. This part is discussed in the next section.

5.5.1 Choice of the finite-rate kinetics

Due to the significant interest of methane in the aerospace community as a potential fuel for high-pressure devices, such as the private-sector programs developed at SpaceX with the Raptor engine and BlueOrigin with the BE-4 engine, as well as the increasing interest in the Rotating-Detonation-Engine (RDE) technology [209, 166] as a potential alternative architecture for future engines, the methane/oxygen combination is primarily investigated in this work as a reacting mixture.

The interest of methane over hydrogen and kerosene (RP-1) combinations to drive a flying vehicle can be summarized in the following points [213, 69]:

- methane produces lower specific impulse than hydrogen, however the complications in the architecture that the H_2-based engine requires are significantly larger. This includes for example the design and manufacturing of the turbo-pumps for pump-fed systems. Due to the big difference between H_2 and O_2 in terms of critical properties and boiling point, fuel and oxidizer manifolds and rotating parts undergo to a significantly different design and realization process. On the other hand, CH_4 and O_2 are more similar from this point of view, thus providing a more similar approach to the design of the engine components;

- methane is heavier than hydrogen but lighter than RP-1. However methane contains a larger chemical energy per unit mass than RP-1. This means that methane produces a hotter flame for a given pressure and initial propellants temperature than RP-1. This has an overall benefit on the characteristic speed and the specific impulse, which can be found to be 5% higher for the same operating pressure;

- due to the larger density than H_2, methane requires smaller tanks, with an overall weight reduction of the whole vehicle. In addition, methane does not exhibit the phenomenon of material embrittlement, caused by the diffusion of hydrogen molecules into the material which can cause severe structure failure under high-pressure regimes;

- methane does not form coke in its combustion products as RP-1. This is particularly undesirable for the re-usability philosophy as it makes very difficult to use the same engine again because of these particles deposit inside the engine circuits;

- in contrast to hydrogen and RP-1, methane also pressurizes itself in its tanks by a process called autogenous pressurization, which means that complex pressurization systems (such as involving different gases separated by bulkheads) can be avoided, increasing the overall vehicle simplicity and reliability;

- methane works better as a coolant compared to RP-1 and also because of the absence of the coking phenomenon. This makes it also attractive for its use not only for primary stages, but also upper stages that may involve the use of expander cycles [99];

- Even more interestingly, methane has the potential to be produced on Mars, in which case, both mission duration and vehicle architecture would benefit considerably.

Overall, the choice of methane as fuel is driven by the impact that the consequent engine and launch vehicle architecture would make on the program cost and maintenance, promoting the development of safer, cheaper and more affordable space missions.

Generally speaking, the choice of the chemical mechanism for high-pressure combustion represents by itself an open area of active research for which a complete agreement has not been reached yet. One important choice that needs to be made first is the selection of the mechanism complexity, for which the two main categories: i) the detailed/skeletal or ii) the quasi-global/global. The detailed/skeletal mechanism class typically achieves high accuracy in the prediction of flame properties such as flame speed, ignition delay, flame structure and adiabatic flame temperature for a broad range of temperatures and pressures. Typically

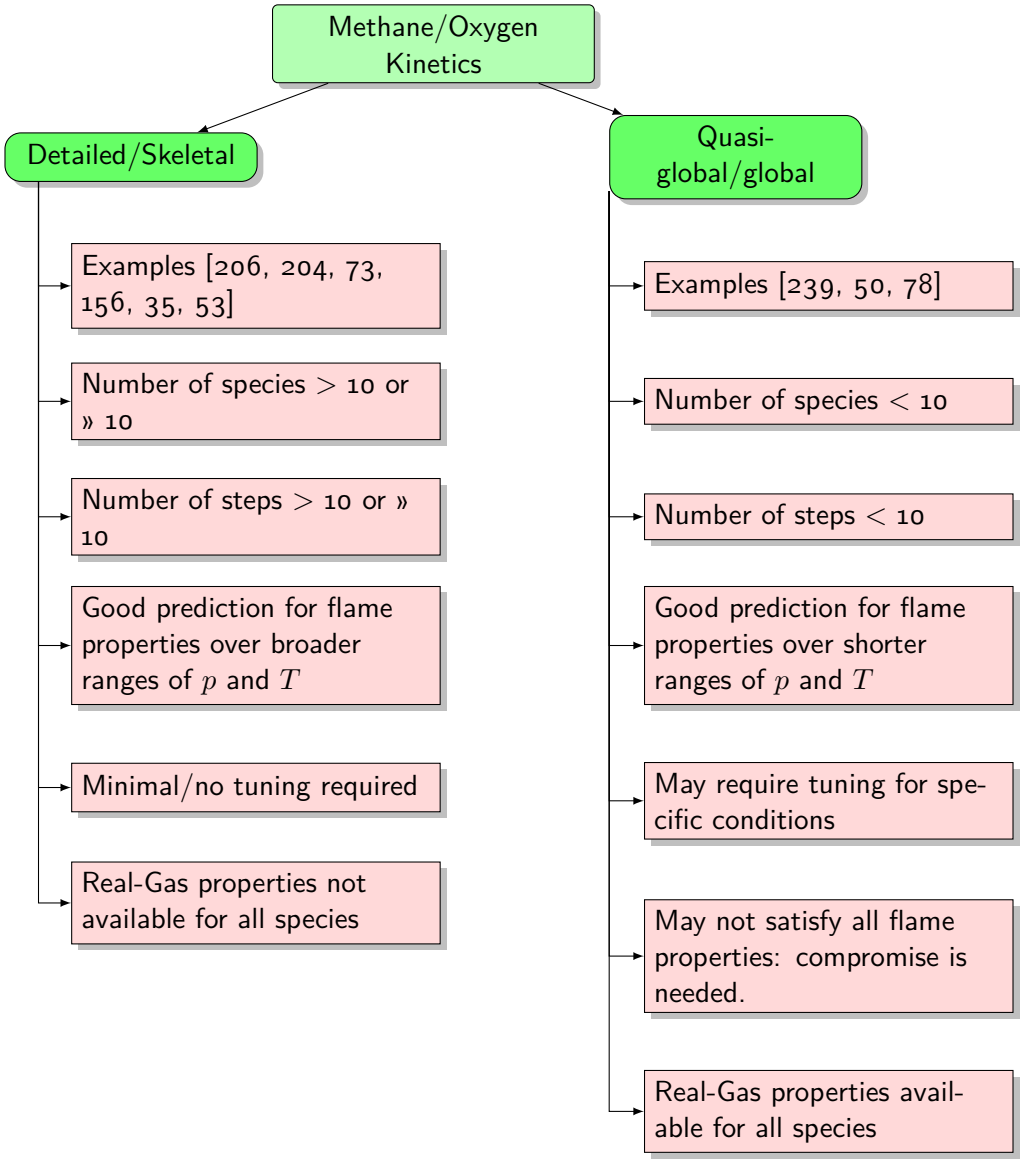

Figure 127: Tree diagram of the main differences between the class of detailed/skeletal mechanism and the quasi-global/global.

these mechanisms are designed to obtain very high accuracy in the breakdown pathway followed by the fuel and oxidizer as they shift from their pure reactants state to the stable products at equilibrium conditions. For this reason, these mechanism are characterized by intermediate species (radicals), which may appear only during a transient phase and then disappear again. For these species, real-gas constants, such as those listed in Tab. 35 are still unknown or limited to some arbitrary values [163], making the overall application of RG thermodynamics difficult, or at least affected by another level of uncertainty.

On the other hand, quasi-global or global models do not show this issue because they are mostly limited to the use of major species, *i.e.*radicals are absent, for which RG thermodynamics constants are well-known. Of course, due to the model reduction, flame properties cannot be predicted all with the same accuracy for a broad range of temperatures and pressures and specific tuning procedures can be instead adopted to match some properties that are more relevant for the case under study. One example is the work of Frassoldati *et al.* [51] who modified the mechanisms of Westbrook-Dryer [239] (WD) and John-Lindstedt [78] (JL) to match the one-dimensional diffusion flame species distribution and the NOx formation at ambient pressure. Another example is the work of Andersen *et al.* [4] who tuned the same mechanisms rate constants to improve the prediction of CO and CO_2 using plug-flow reactor simulations again at 1 atm.

Another important consideration that applies for this work is the fact that an increase in the number of species dictated by the detailed model does require a significant cost increase in the simulation, particularly for the VLE routines that are already expensive. Some operations, such as the calculation of the $\mathcal{A}_{ij}$ or $\mathcal{C}_{ij}$ matrices of Eq. (K.0.23) and Eq. (L.0.23) respectively (along with their inversion to compute the unknowns) would scale as N_s^2. Since the present work aims to investigate the use of finite-rate kinetics with VLE for the first time in oxy-methane conditions, and given that the formation of minor species are expected to have a small impact on that because of i) their low amount within the flame and ii) very high temperature at which they form, the simplified global mechanism of WD [239] is employed for this exercise.

Next, once the mechanism is chosen, the operating conditions need to be chosen as well

before tuning. For the present work, the attention is on the CH_4-LOX conditions at which a sub-scale rocket engine was investigated experimentally and for which extensive amount of data is available [76]. These conditions are reported in Tab. 31. With these conditions,

Table 31: Operating conditions of the sub-scale rocket engine described in the work of [76].

Sub-scale rocket engine operating conditions				
	species	u [m/s]	T [K]	p [MPa]
fuel stream	CH_4	153.0	263.7	13.3
oxidizer stream	O_2	20.0	115.3	13.3

the WD mechanism is tuned against GRI [206] for the prediction of the ignition delay in a constant-pressure environment, as well as one-dimensional diffusion flame for the prediction of major species concentration. These two criteria are considered adequate for the present case due to the non-premixed nature of the flame. The details are discussed next.

The WD mechanism is composed of 5 species: CH_4, O_2, CO, CO_2 and H_2O. For all these, the RG constants are well-known and are provided in Tab. 35. The WD model is composed of two steps, one of which is reversible, making effectively a 3-steps mechanism. These are given in Eq. (5.5.1):

$$\begin{aligned} &\textbf{(1)} \qquad CH_4 + 1.5O_2 \rightarrow CO + 2H_2O \\ &\textbf{(2)} \qquad CO + 0.5O_2 \rightarrow CO_2 \\ &\textbf{(3)} \qquad CO_2 \rightarrow CO + 0.5O_2\,. \end{aligned} \tag{5.5.1}$$

For each step, the forward rates are expressed using the Arrhenius form similar to Eq. (2.4.7), where species reaction orders are additionally added to capture more non-linear effects [239]. Table 32 reports the values of these constants after the tuning procedure. First the adiabatic flame temperature is compared against the detailed mechanisms for different equivalence ratios. Note that this analysis does not involve the use of the finite-rate constants showed in Tab. 32 as it is performed at the chemical equilibrium conditions where only the number of species involved (with respect to their heat of formation) matters. Figure 128 shows relevant results obtained for the tuned WD mechanism against the GRI. All the results are

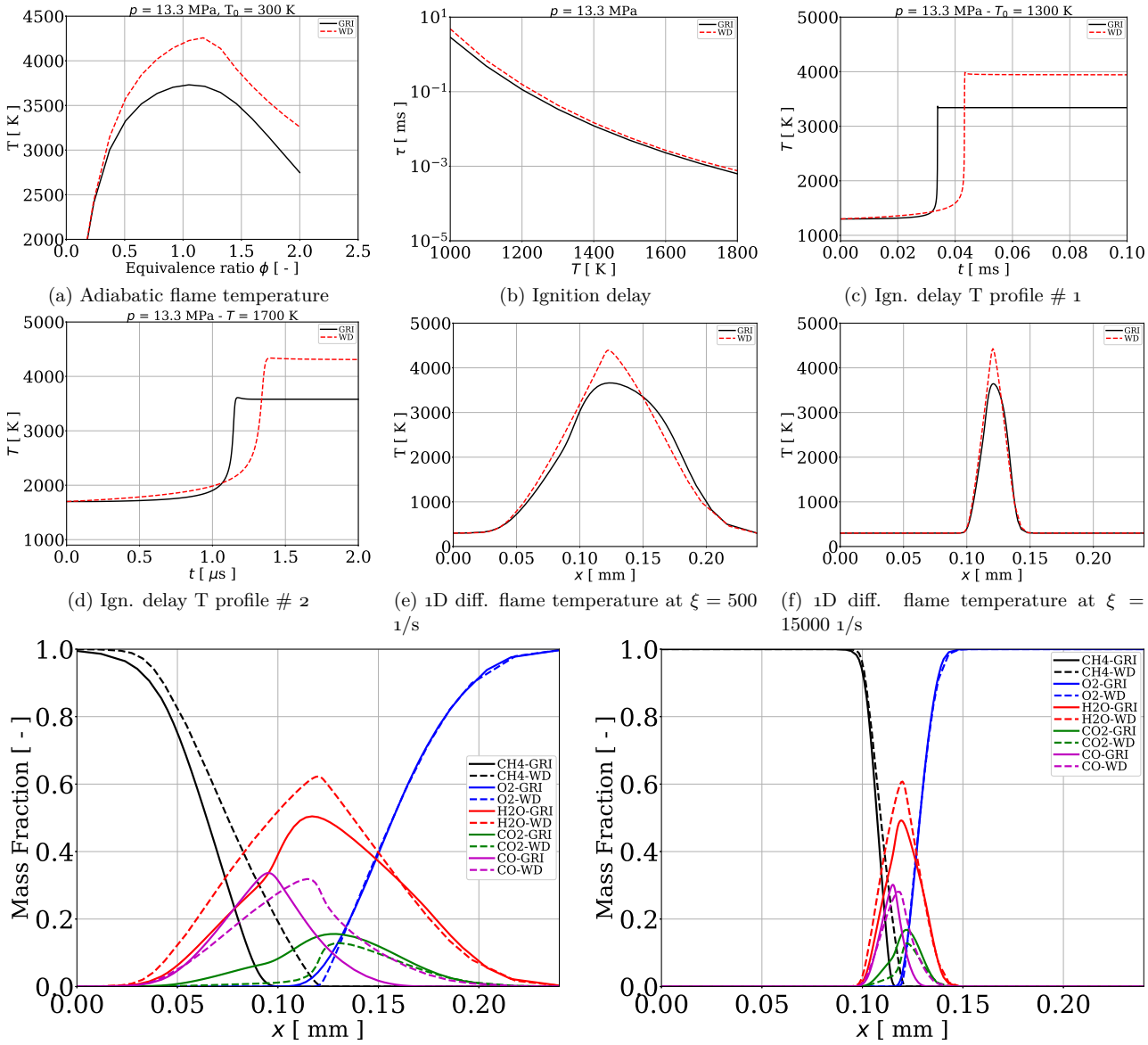

(a) Adiabatic flame temperature

(b) Ignition delay

(c) Ign. delay T profile # 1

(d) Ign. delay T profile # 2

(e) 1D diff. flame temperature at $\xi = 500$ 1/s

(f) 1D diff. flame temperature at $\xi = 15000$ 1/s

(g) 1D diff. flame species at $\xi = 500$ 1/s

(h) 1D diff. flame species at $\xi = 15000$ 1/s

Figure 128: Relevant results collected for the comparison between the WD [239] global mechanism and the GRI [206] detailed mechanism at 13.3 MPa. Results include: (a) adiabatic flame temperature, (b) ignition delay versus mixture initial temperature for $\phi = 1$, (c) temperature history for ignition delay at $T_0 = 1300$ K, (d) temperature history for ignition delay at $T_0 = 1700$ K, (e) temperature distribution within the 1D diffusion flame for strain rate of 500 s^{-1}, (f) temperature distribution within the 1D diffusion flame for strain rate of 15000 s^{-1}, (g) species distribution within the 1D diffusion flame for strain rate of 500 s^{-1}, (h) species distribution within the 1D diffusion flame for strain rate of 15000 s^{-1}.

Table 32: Forward rates used for each reaction of Eq. (5.5.1). Tuning procedure has been performed against GRI [206]. Units are in *cm*, *s*, *mol* and *cal*.

Arrhenius model for the WD mechanism at 13.3 MPa	
reaction	forward reaction rate
(1)	$k_{f,1} = 1.59 \cdot 10^{12} exp(-47.8e3/R_u T)[\mathrm{CH_4}]^{0.7}[\mathrm{O_2}]^{0.8}$
(2)	$k_{f,2} = 3.38 \cdot 10^{13} exp(-40.7e3/R_u T)[\mathrm{CO}][\mathrm{O_2}]^{0.25}$
(3)	$k_{f,3} = 5.0 \cdot 10^{12} exp(-40.7e3/R_u T)[\mathrm{CO_2}]$

obtained at a pressure of 13.3 MPa. First, Fig. 128(a) shows the adiabatic flame temperature for different equivalence ratios. As expected, due to the absence of minor species, the adiabatic flame temperature shows higher values. This cannot be corrected and must be retained as model limitation, however additional considerations are going to be made in the results discussion in Sec. 5.5.3 to put this point in perspective.

Figures 128(b), (c) and (d) show the ignition time delay as a function of the initial mixture temperature (at stoichiometric conditions) and two temperature histories for these cases, respectively. In this case, the agreement is found quite satisfactory. Finally, Fig. 128(e), (f) show the temperature profiles of the one-dimensional opposed diffusion flame for two different strain rates ξ, while Fig. 128(g), (h) show the corresponding major species profiles. The 1D diffusion flame has been run using the Cantera package. Due to the absence of an extensive RG capability, these simulations are run using the TPG thermodynamics and for this reason, both reactants are initially set to the temperature of 300 K. Despite this assumption, this approximation is not too far from what is effectively expected to happen since at temperatures of 300 K or lower, the mixture does not react as known (and proven with the constant-pressure ignition delay studies). On the other hand, at sufficiently high temperatures, the mixture is expected to behave as a perfect gas, therefore the present approach to justify the kinetics is considered adequate. Opposed-flame studies are run for different values of mass-flux rates by varying the strain-rate factor ξ according to the

following formulas [162]:

$$\dot{m}''_{O_2} = \frac{\xi \Delta x}{1 + \sqrt{\frac{\rho_{O_2}}{\rho_{CH_4}}}} \rho_{O_2} \tag{5.5.2}$$

$$\dot{m}''_{CH_4} = \frac{\xi \Delta x}{1 + \sqrt{\frac{\rho_{CH_4}}{\rho_{O_2}}}} \rho_{CH_4} \tag{5.5.3}$$

where the reactants densities are associated to the single streams conditions of temperature and pressure. In the above, ξ represents the strain rate in s^{-1} and Δx corresponds to the flame width. In this case, the selected value is 0.24 mm, which is representative of the injector post-tip width relative to the case under study [76]. By varying ξ, different flow rates are obtained. For this study, and interval of $\xi \in [50, 15000]$ has been investigated. For $\xi < 500\, s^{-1}$ both mechanisms started to exhibit low temperature flames, with high width beyond the chosen value of Δx (see also Fig. 173). On the other hand, for $\xi > 15000$, no convergence of the steady-state algorithm was achieved, indicating that both mechanisms at the current condition also show a similar extinction strain rate. By looking at temperature and species distribution within the flame, as well as the ignition time delay, the present approximate kinetics model offers a reasonably good representation of the flame properties, hence it can be used for the following analyses.

5.5.2 VLE diagram for CH_4/O_2

Before running the actual simulation, the VLE diagram for the reactants is investigated first. The reason is to verify that the conditions at which the simulation will run (further verified a-posteriori) do not form VLE between the reactants. For this reason, the CH_4/O_2 mixture is studied similarly to what showed earlier in Fig. 46(a) with N_2/C_6H_{14} combination and the presence of multi-phase conditions is analyzed by varying the pressure and composition for different isotherms. The result is showed in Fig. 129. As immediately apparent, for the present mixture VLE forms only for pressures that are approximately equal or less than 5 MPa. This means that the current operating condition of 13.3 MPa will not show multi-phase conditions, as desired (the goal here is to explore whether or not the combustion products can form VLE). Furthermore, one important thing to notice is that the 5 MPa

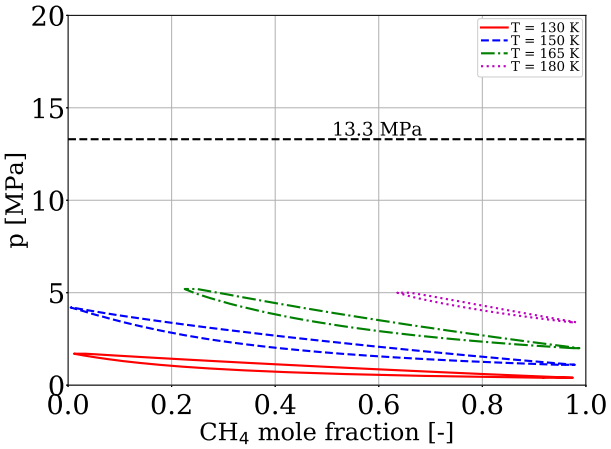

Figure 129: VLE diagram for the CH_4/O_2 combination. Dashed black line indicates the operating condition for the present TML case.

threshold approximately represents a limit between the sub-critical and the super-critical state for the present mixture. In fact, given the values of the critical pressure of methane and oxygen that are very close to 5 MPa (see Tab. 35), running the present mixture at pressure below this value to investigate VLE effects, would be erroneous because of the sub-critical condition that would be reached by the two species in their respective stream. As a result, the present thermodynamic and numerical framework would not be consistent with the physics as far as the single-component behavior.

5.5.3 Case setup and verification of the non-reacting solution

The TML geometry for the present case is set up in the same way as done for the N_2/C_6H_{14} case discussed in Sec. 5.3.1. With reference to Fig. 101, sizes are chosen as follows: $H_{TML} = L_x = L_z = L_{buff} = 0.8\,mm$. This size is roughly three times the injector post-tip width reported in the experiment [76], thus the present application is qualitatively representative of the thermodynamic conditions and length-scales occurring in that application in the near-injector region. It is emphasized that the goal is not to study the true experimental condition and geometry through a simplified exercise, which would be in fact too pretentious. Instead, the goal is to investigate its operating condition from a thermodynamic and VLE perspective only by choosing a simplified model (a 3D box) that despite the number of assumptions employed, contains some similarities with that experiment, particularly the

conditions in the vicinity of the injector where the reactants mix and start to burn.

The domain is uniformly discretized using 96^3 points in the central H_{TML} box, while hyperbolic stretching along the y direction is applied along the two adjacent boxes using 33 points. Non-reflecting, subsonic outflow is applied at the top and bottom boundaries. Slip, adiabatic conditions are imposed along the span-wise direction, while periodic conditions are applied along the stream-wise direction.

The mean flow initial conditions are prescribed using a tanh function for the stream-wise velocity component, temperature and composition in the form of $\overline{\zeta}(y) = 0.5[(\zeta_T + \zeta_B) + (\zeta_T - \zeta_B)\tanh(y/w_0)]$, where $w_0 = 5 \cdot 10^{-5}$ and the T and B subscripts correspond to the "TOP" (O_2 stream) and "BOTTOM" (CH_4 stream) conditions given in Tab. 31. Pressure is uniformly specified.

Regarding the perturbation, pre-computed turbulence is preferred in this case in contrast to a prescribed perturbation field. The reason is to explore another way to excite the formation of random vortices and their impact on VLE (if any). Incompressible, isotropic turbulence is pre-computed and summed to the main flow in the form of pressure and velocity. The incompressible turbulent field is calculated using the model of Kraichnan [86] for the energy spectrum. The u_{RMS} for each stream is specified to be 5% of the O_2 stream-wise velocity component. It was in fact observed that higher perturbation would cause loss in numerical stability due to the fact that strong vortices in the LOX side would produce big pressure fluctuations. On the other hand, imposition of two different perturbation fields would have required to impose artificial smoothing at the interface. The present choice was verified to be the most robust solution that offers a good compromise between the physical meaning and the numerical robustness of the initial condition.

Regarding the reacting simulation, none of the laminar diffusion flame profiles could be used as an initial profile because i) they did not have the correct boundary values of temperature for the reactants and ii) they were computed by iterating on the strain-rate in the direction perpendicular to the flame brush, which is not known for this specific initial condition. As a consequence, the top 1/4 of H_{TML} is initialized by specifying tanh profiles of temperature and H_2O/CO_2 products at $\sim$ 2000 K using a similar function as given above. The profiles

are imposed such that the temperature smoothly matches that of the O_2 free stream, while water and carbon dioxide start from 85% and 5% by mass to zero. The remaining part is specified as methane. Regarding the bottom 1/4 of H_{TML}, the same criterion is applied, however the oxygen is now imposed as left-over. This is done in order to mimic reactants diffusion, trigger combustion and at the same time initialize a burnt solution. For the profiles of H_2O and CO_2, the decaying factor in the hyperbolic tangent profile has been chosen as $w_0/2$ and $w_0/3$, respectively. Figure 130 and 131 show the relevant fields at the initial condition.

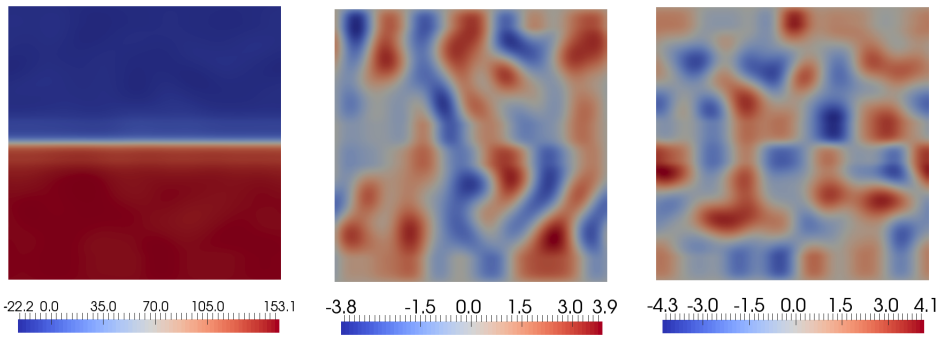

(a) x-velocity [m/s] (b) y-velocity [m/s] (c) z-velocity [m/s]

Figure 130: Initial conditions used for the 3D TML: velocity component fields.

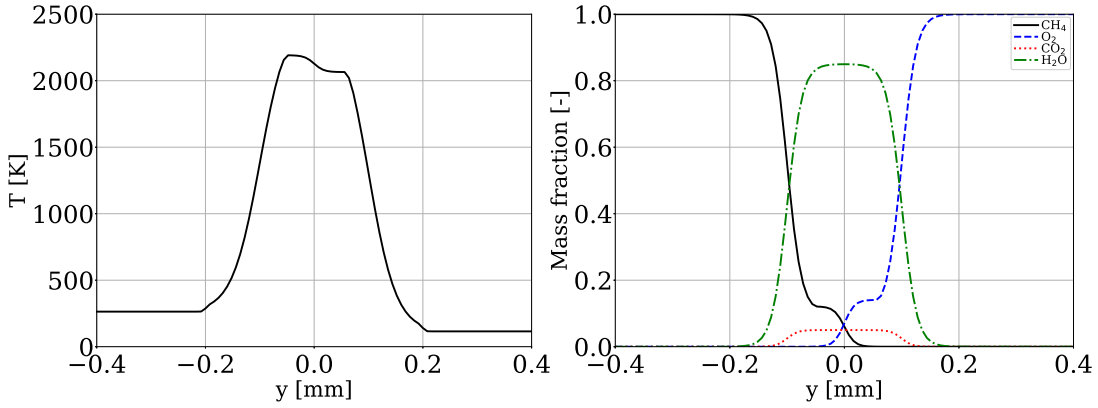

(a) T [K] profile across H_{TML} (b) Species profiles across H_{TML}

Figure 131: Initial conditions used for the 3D TML: burnt solution.

Before running the reacting solution, the non-reacting solution is first performed (without

the burnt initial condition) to verify the absence of VLE between methane and oxygen at the present conditions according to the diagram of Fig. 129. Figure 132 and 133 show the

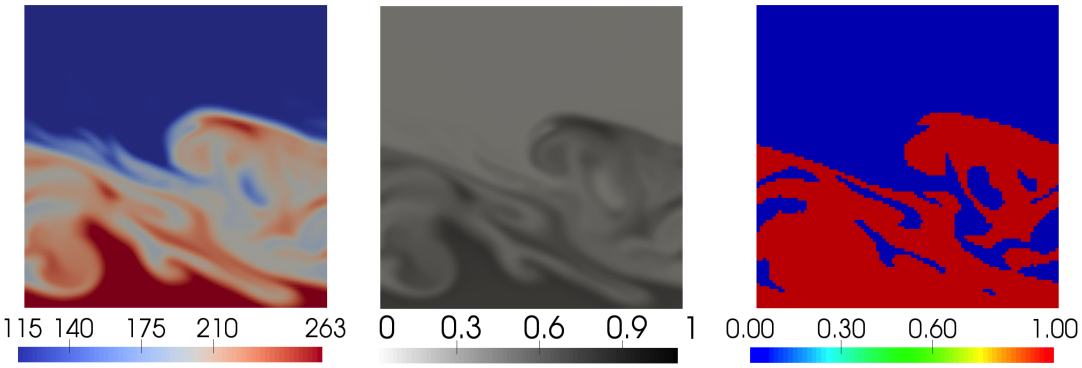

(a) T [K] (b) Z [-] (c) β [-]

Figure 132: Non-reacting fields: XY plane. (a) Temeprature, (b) compressibility factor and (c) phase-fraction.

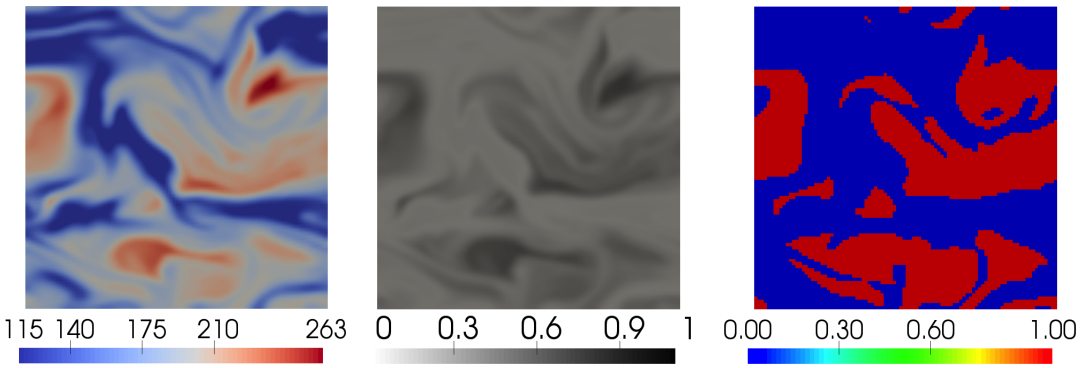

(a) T [K] (b) Z [-] (c) β [-]

Figure 133: Non-reacting fields: XZ plane. (a) Temeprature, (b) compressibility factor and (c) phase-fraction.

temperature, compressibility factor and phase fraction fields along the XY and XZ planes, respectively. It is recognized that, despite the whole range of continuous temperature values achieved by the mixing between the two species, no VLE formation is recovered. That is, the mixture is its pure super-critical state and no multi-phase conditions are obtained. The mixture moves from the compressible liquid ($\beta = 0$) to the super-critical fluid ($\beta = 1$) conditions without any intermediate state. This pseudo-phase transition condition is detected

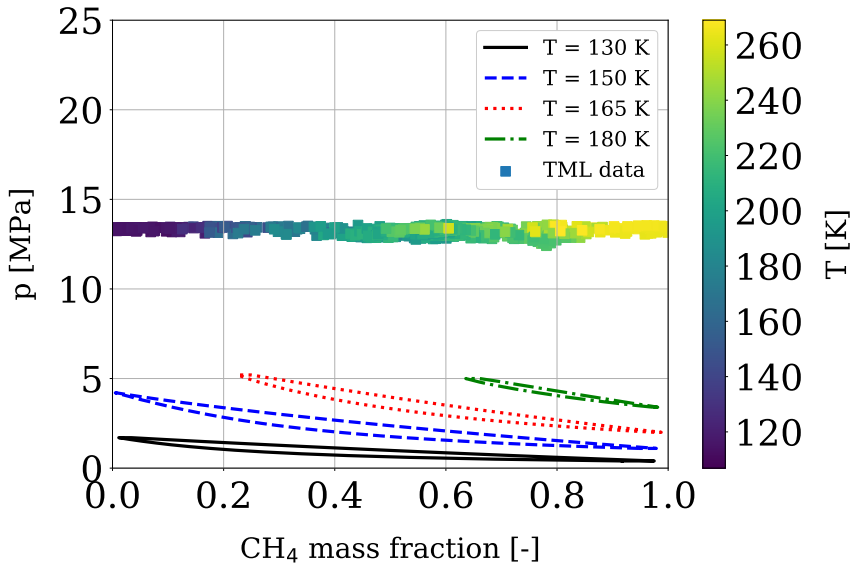

Figure 134: Non-reacting field: scatter plot of the temperature data.

using the Z^* criterion given in Sec. 4.1.1. This is further showed in Fig. 134 where a scatter plot of the temperature field is superimposed to the original VLE diagram illustrated earlier in Fig. 129. This is another proof of the predictive capability of the 0D thermodynamics with respect to the actual simulation regarding the formation of VLE.

5.5.4 Justification of the implicit integrator use for chemistry

One issue that has been observed during the simulation of the reacting case was the occurrence of non-physical values of the reaction rates, as well as product species. Further investigations revealed that the time-step used for the integration of the governing equations was not sufficient to capture the chemical time scales of the reaction mechanism employed, particularly the CO-CO_2 dissociation/recombination (reactions 2 and 3 in Eq. (5.5.1)). To solve this issue, use of an implicit integrator by means of the package DVODE [20] was required instead of using explicit time integration of the chemical kinetics.

To illustrate this need, an intermediate (evolved) solution computed with DVODE is restarted using a direct explicit integration of the chemical reaction rates with the time step computed in the conventional way [111, 5]. After few time steps, the reaction rates are compared with the corresponding DVODE solution. The results are showed in Fig. 135 and Fig. 136,

respectively. One can immediately notice the erroneous values of the reaction rates both in

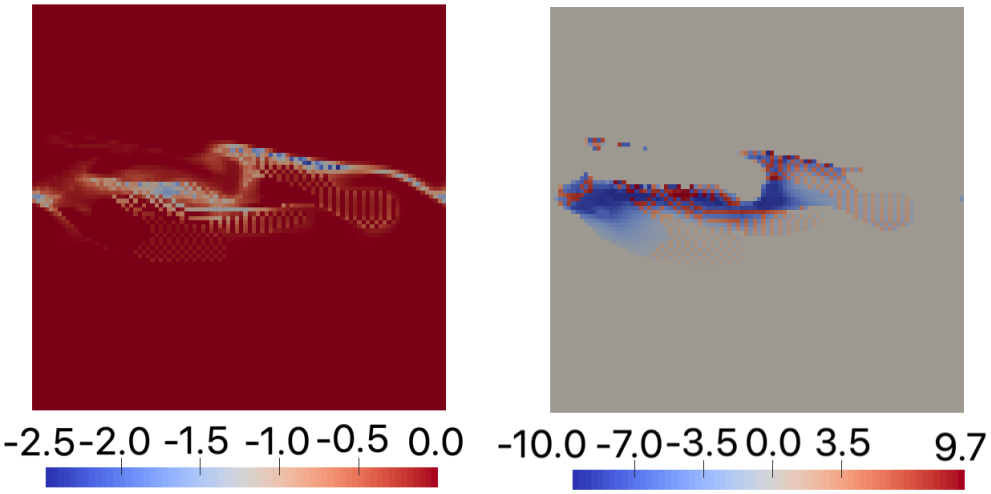

(a) $\dot{\omega}_{CH_4}[kg/m^3s] \times 10^5$ (b) $\dot{\omega}_{CO_2}[kg/m^3s] \times 10^8$

Figure 135: Methane (a) and carbon dioxide (b) reaction rates computed with explicit time integration.

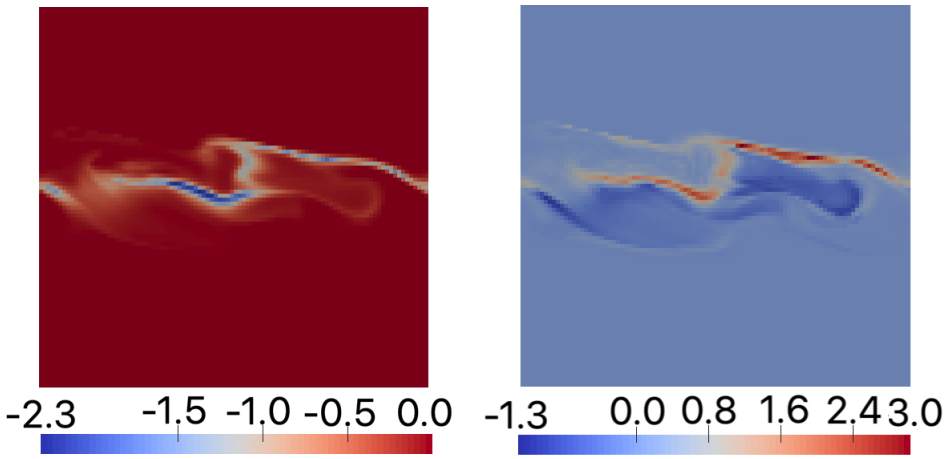

(a) $\dot{\omega}_{CH_4}[kg/m^3s] \times 10^5$ (b) $\dot{\omega}_{CO_2}[kg/m^3s] \times 10^5$

Figure 136: Methane (a) and carbon dioxide (b) reaction rates computed with implicit time integration using DVODE [20].

terms of spatial distribution and magnitude in case the explicit solved is used. On the other hand with the implicit solver these artifacts go away and the field smoothness is recovered. Similar fields related to other species showed the same effects.

Further analysis was conducted to prove the initial hypothesis. Characteristic chemical

time-scales for each reaction step were estimated following the method suggested by Turns [228], for uni-molecular and bi-molecular reactions. Application of these criteria resulted in the equations Eqs. (5.5.4)–(5.5.6) where $e = 2.7182$ and $k_{f,1}$, $k_{f,2}$ and $k_{f,3}$ were calculated directly using those listed in Tab. 32 and all the species concentrations were calculated using the reference solution.

$$\tau_{c,1} = \frac{\ln\left[e + (1-e)\dfrac{[\mathrm{CH_4}]}{[\mathrm{O_2}]}\right]}{([\mathrm{O_2}] - [\mathrm{CH4_4}])\mathrm{k_{f,1}}} \tag{5.5.4}$$

$$\tau_{c,2} = \frac{\ln\left[e + (1-e)\dfrac{[\mathrm{CO}]}{[\mathrm{O_2}]}\right]}{([\mathrm{O_2}] - [\mathrm{CO}])\mathrm{k_{f,2}}} \tag{5.5.5}$$

$$\tau_{c,3} = \frac{1}{k_{f,3}}\,. \tag{5.5.6}$$

Figure 137 shows all three chemical time scales. Given that the CFL time-step observed

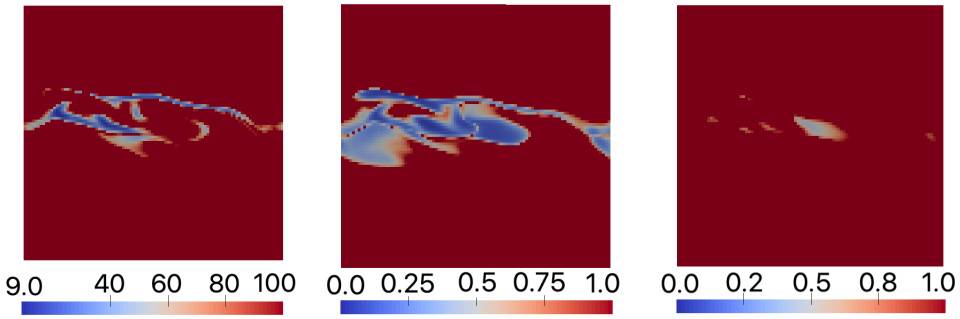

(a) $\tau_{c,1}$ [ns] (b) $\tau_{c,2}$ [ns] (c) $\tau_{c,3}$ [ns]

Figure 137: Characteristic chemical time scales associated with each reaction step listed in Eq. (5.5.1).

during the simulations was oscillating between 1.5 and 1.7 nanoseconds, it is immediate to recognize the fact that both reactions 2 and 3 would have an under-resolved progression rate in time, which would result in wrong/non-physical production rates and ultimately species. Note that even though the first reaction would not exhibit such restriction, its non-linear coupling with the O_2 recombination makes it also affected by the same issue. The present analysis justifies the use of the implicit integration method for chemistry. Unfortunately this has observed to add an additional 2-3$\times$ in the computational overhead with respect to the explicit integration. An alternative to DVODE can be the use of multiple explicit

sub-iterations that can reduce the integration step and follow a smoother integration path. However, based on Fig. 137 it is apparent that at least 10 sub-iterations would have been required. Since each sub-iteration requires the update of density, hence the solution of a Tp problem, this approach has been found to be even more expensive than the DVODE one, therefore it was discarded as option. The simulation was carried out for roughly 37 μs, approximately corresponding to 6 FTT (based on the averaged TML velocity).

5.5.5 Results and discussion

A first analysis is conducted on the fields snapshots taken on the YZ and XZ center planes. These are given in Figs. (138)–(142) and Figs. (174)–(178), respectively. The snapshots are taken at 5 equally-spaced time intervals between the VLE and the non-VLE solutions. By looking at the β field of these images it is possible to recognize that effectively VLE forms within two different narrow regions at the top and the bottom of the flame next to the colder reactants streams. The two regions of VLE present different features: the one at the top (VLE-OX) spans all the TML width and comprises values of β that are larger or equal than 0.95. That is, the phase separation is mostly formed by vapor phase. This region forms almost immediately, as soon as hot reactants start to diffuse into the oxygen stream. On the other hand the bottom VLE region (VLE-F) is characterized by a delayed appearance in time, as well as larger values of the phase fraction ($\beta \geq 0.98$) and a more irregular spatial distribution. This is visible in both X and Y planes (*cf.* Sec. Q.6). The occurrence of VLE in both regions next to the flame do not seem to produce significant differences in the other field variables. Some differences can be qualitatively observed in the speed of sound magnitude, which happens to be lower within the VLE zones, as learned from all the previous analyses. Other than that, wrinkling features and even the spatial distribution of the heat release do not appear significantly different between the two simulations.

To investigate more, the centerline data is plotted during the same time snapshots in

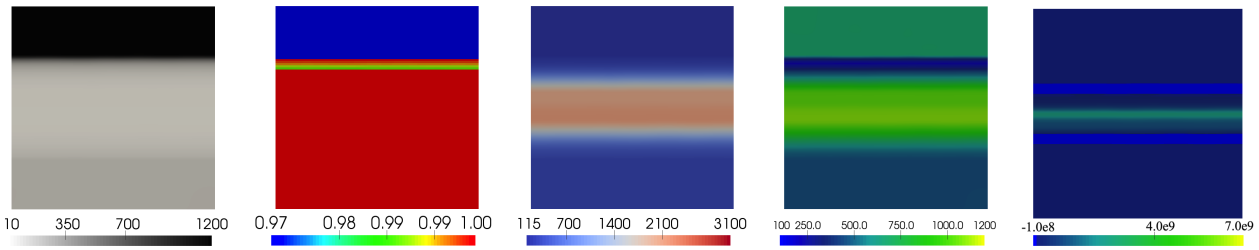

(a) ρ [kg/m^3] (b) β [-] (c) T [K] (d) c [m/s] (e) HRR [W/m^3]

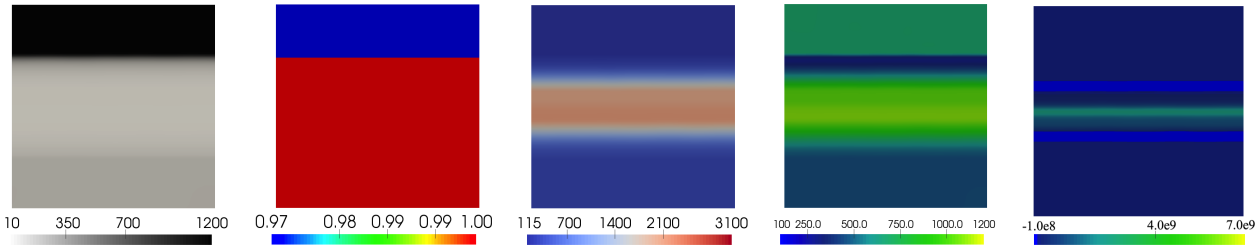

(f) ρ [kg/m^3] (g) β [-] (h) T [K] (i) c [m/s] (j) HRR [W/m^3]

Figure 138: Relevant field variables obtained for the VLE (top) and non-VLE (bottom) solutions on plane YZ at time $t_1 = 0.21\,\mu$s .

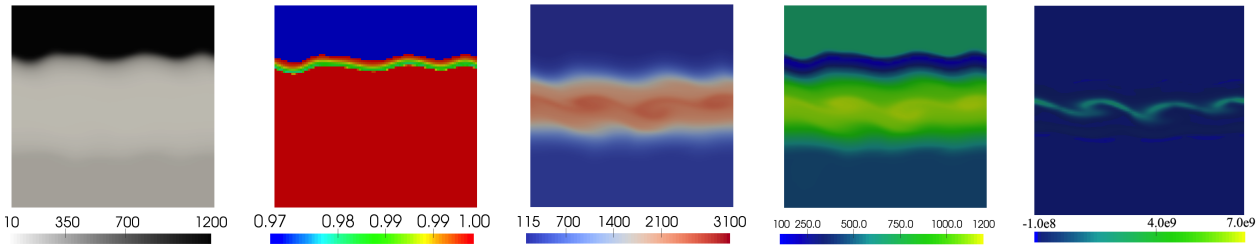

(a) ρ [kg/m^3] (b) β [-] (c) T [K] (d) c [m/s] (e) HRR [W/m^3]

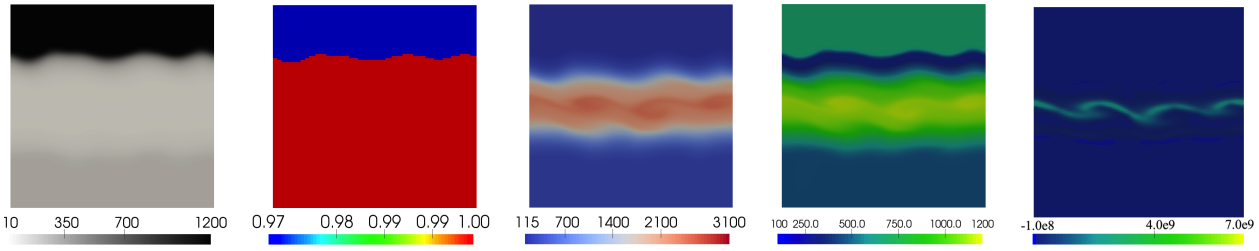

(f) ρ [kg/m^3] (g) β [-] (h) T [K] (i) c [m/s] (j) HRR [W/m^3]

Figure 139: Relevant field variables obtained for the VLE (top) and non-VLE (bottom) solutions on plane YZ at time $t_2 = 10.18\,\mu$s .

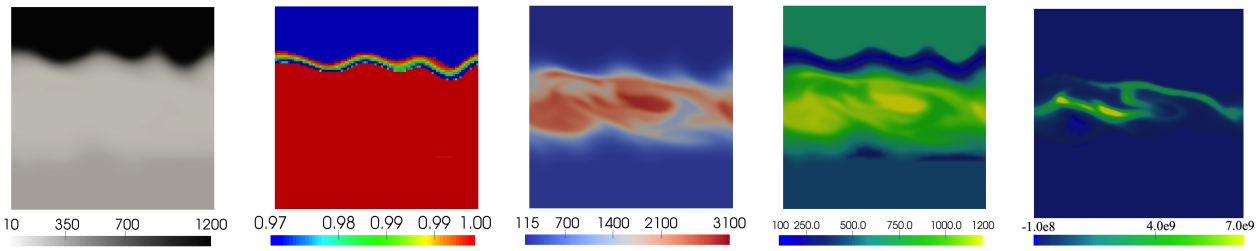

(a) ρ [kg/m^3] (b) β [-] (c) T [K] (d) c [m/s] (e) HRR [W/m^3]

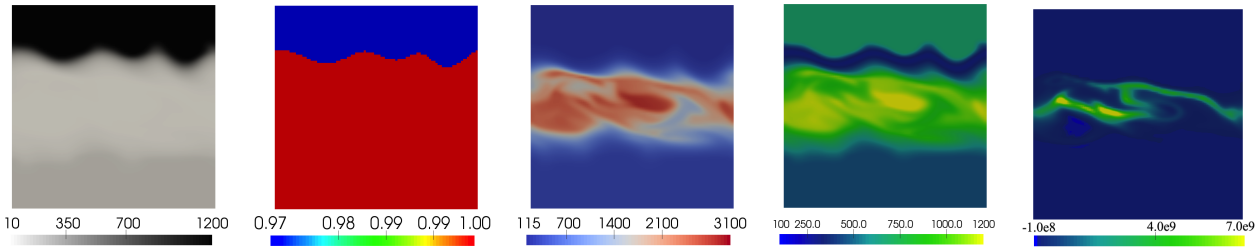

(f) ρ [kg/m^3] (g) β [-] (h) T [K] (i) c [m/s] (j) HRR [W/m^3]

Figure 140: Relevant field variables obtained for the VLE (top) and non-VLE (bottom) solutions on plane YZ at time $t_3 = 19.30\,\mu$s .

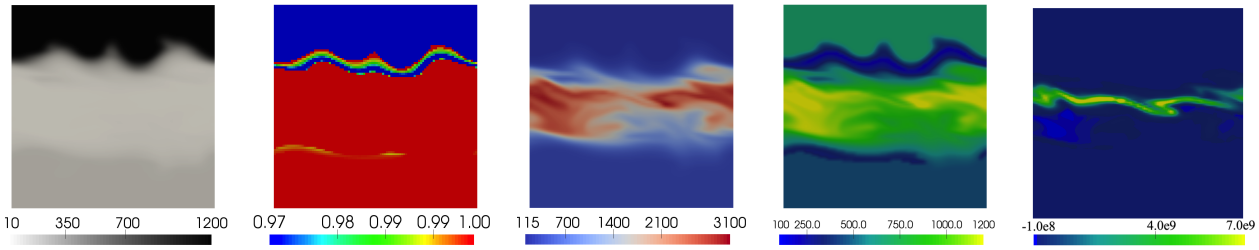

(a) ρ [kg/m^3] (b) β [-] (c) T [K] (d) c [m/s] (e) HRR [W/m^3]

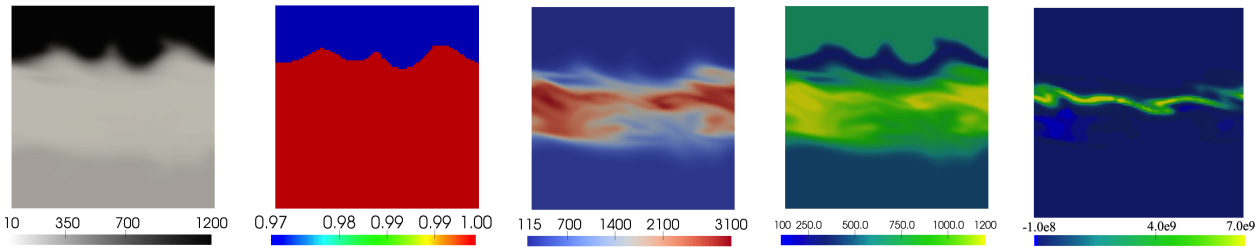

(f) ρ [kg/m^3] (g) β [-] (h) T [K] (i) c [m/s] (j) HRR [W/m^3]

Figure 141: Relevant field variables obtained for the VLE (top) and non-VLE (bottom) solutions on plane YZ at time $t_4 = 28.22\,\mu$s .

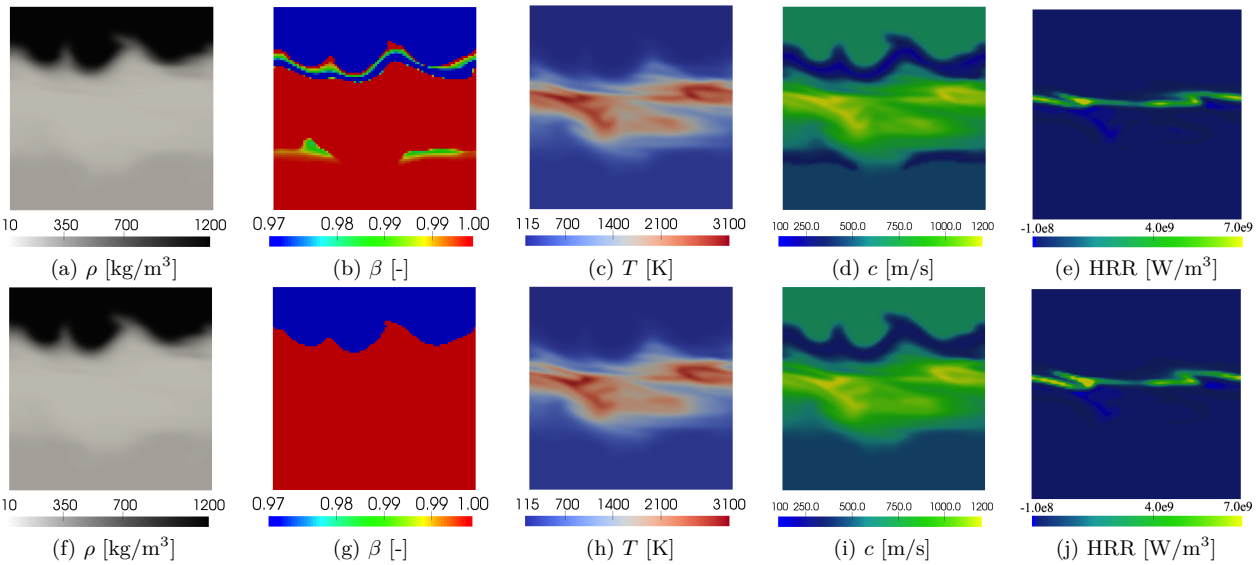

(a) ρ [kg/m^3] (b) β [-] (c) T [K] (d) c [m/s] (e) HRR [W/m^3]

(f) ρ [kg/m^3] (g) β [-] (h) T [K] (i) c [m/s] (j) HRR [W/m^3]

Figure 142: Relevant field variables obtained for the VLE (top) and non-VLE (bottom) solutions on plane YZ at time $t_5 = 37.09\,\mu$s .

Fig. 143 for both the simulations. The difference in the values of the speed of sound is now quantitatively visible in Fig. 143(c), where discrepancies in the values up to 35% appear right where VLE forms predominantly ($y \sim -0.2$ and $y \sim 0.2$ mm) as it can be seen from the β field in Fig. 143(e). In the other regions, these differences are not that high, although the solution lines between the VLE and the non-VLE regions do not match exactly. Since the VLE solution shows nearly complete vapor contribution, while the non-VLE is completely vapor in the same regions, the differences are not expected to be significant. Additional post-processing is conducted by performing a subdivision in 10 sectors along the y axis. This division is schematically represented in Fig. 144 for clarity. Volume-averaged properties are computed in each sector at each time and relevant results are showed in Fig. 145 for sectors 3, 8 and 9 (others did not show anything different). As a confirmation of the previous observations, the properties, except the speed of sound do not show a significant departure between the two thermodynamic models. One last important analysis to perform is the understanding of the VLE formation and whether it can be predicted by off-line calculations. For the present discussion, the $t = t_5 = 37.09\,\mu s$ instant is considered. Analyses on other

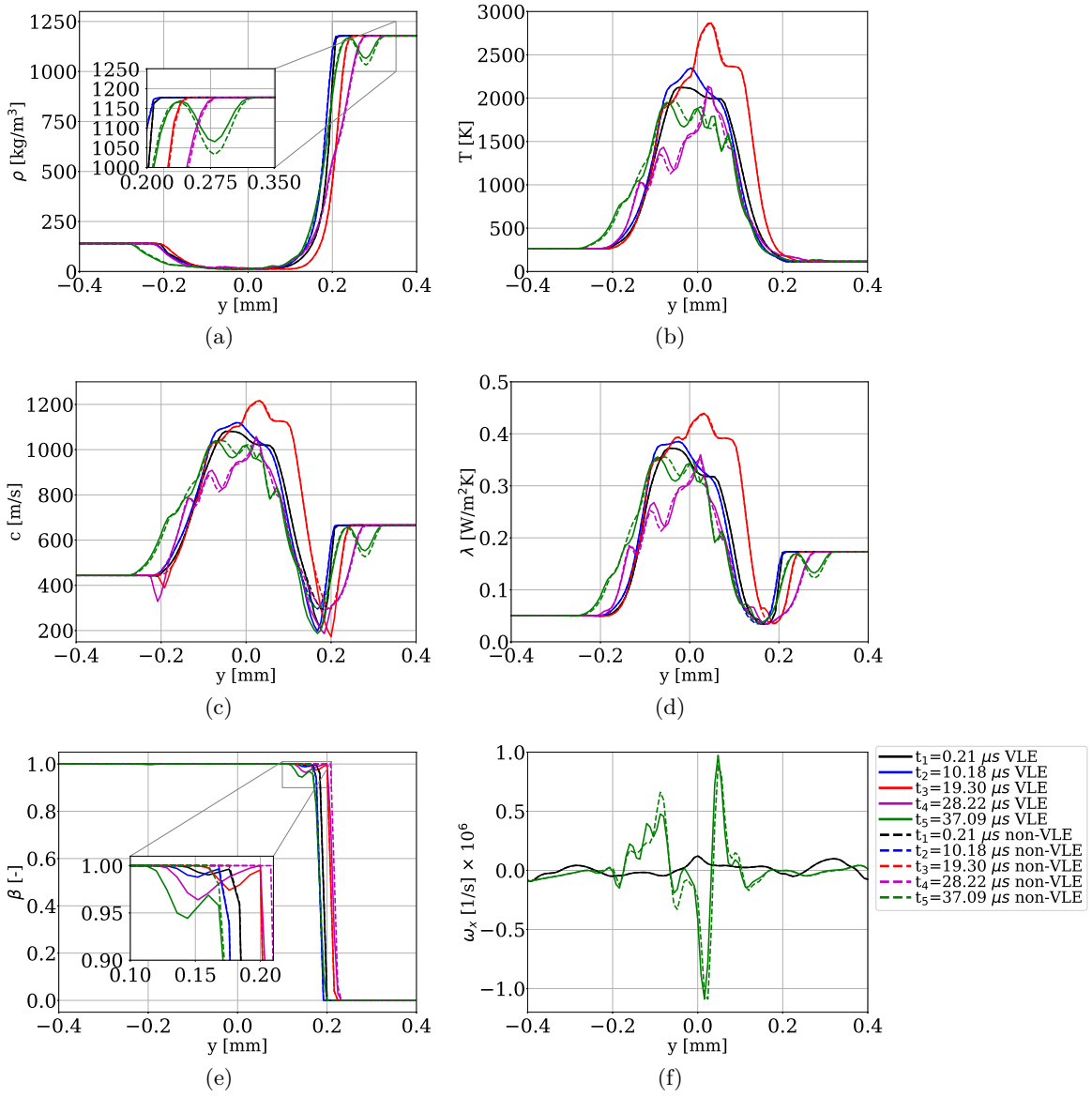

Figure 143: Relevant field variables plotted along the TML centerline for the same time instants indicated in Figs. (138)–(142). Vorticity plot in Fig. (f) is limited to the first and last time instants in order to achieve a better picture quality. Variables are: (a) density, (b) temperature, (c) speed of sound, (d) thermal conductivity, (e) phase fraction, (f) vorticity x component.

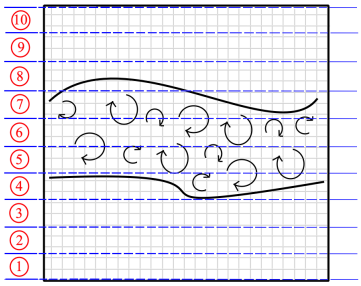

Figure 144: 3D TML domain subdivision in sectors.

time instants revealed the identical conclusions.

First, the VLE data is split in two parts. Given that the VLE distribution clearly shows differences in the way it is distributed in space and time, the VLE-OX data and the VLE-F data are first separately collected (that is all the variables are stored only when $0 < \beta < 1$ in both regions) and then average μ and standard deviation σ are computed to understand what is the state that forms VLE. Table 33 shows the results for both the regions: By

Table 33: Mean and standard deviation values computed within the VLE-OX and VLE-F regions at $t = t_5$.

VLE-OX, $t = t_5$							
	T **[K]**	p **[MPa]**	Y_{CH_4}	Y_{O_2}	Y_{H_2O}	Y_{CO_2}	Y_{CO}
μ	292.16	13.353	1.18e-4	0.965	0.0325	1.27e-3	5.86e-4
σ	81.82	0.0051	6.71e-5	0.027	0.0252	1.26e-3	6.70e-4
VLE-F, $t = t_5$							
	T **[K]**	p **[MPa]**	Y_{CH_4}	Y_{O_2}	Y_{H_2O}	Y_{CO_2}	Y_{CO}
μ	311.11	13.355	0.988	1.24e-4	0.0113	1.98e-4	4.58e-4
σ	35.56	0.01108	0.0111	1.72e-5	0.0104	1.95e-4	5.48e-4

reading the data in the table, the following conclusions can be drawn:

- the pressure is essentially constant at 13.3 MPa. This value can be maintained constant for the subsequent analysis;
- in the VLE-OX region, the major species are oxygen and water. Carbon monoxide and methane have very small concentration, therefore they can be neglected in the following. It is not clear what is the role of carbon dioxide in the VLE (which also shows largely scattered distribution), therefore it is considered for the next analysis;

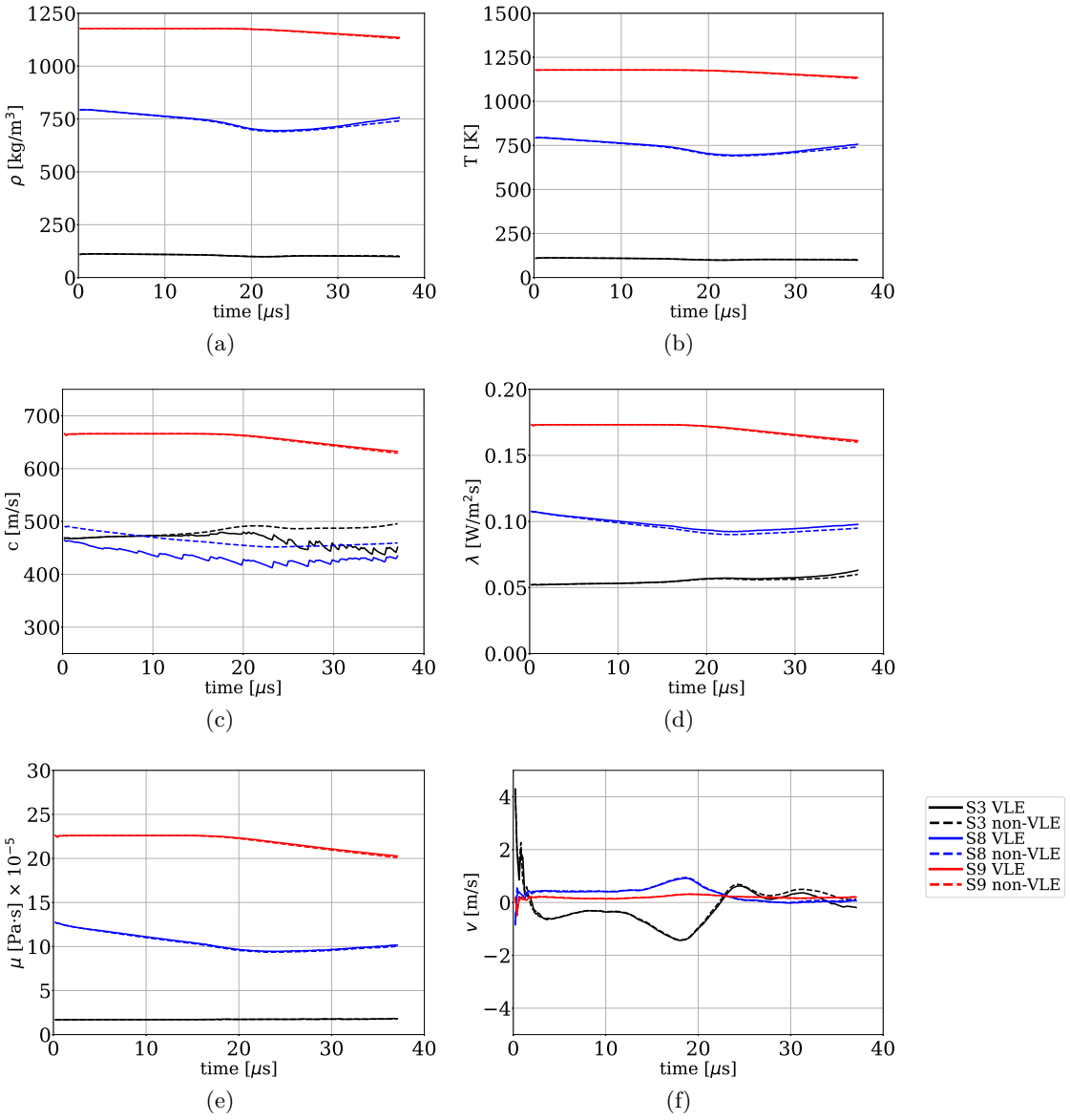

Figure 145: Sector-averaged variables as function of time. Only sectors number 3, 8 and 9 are showed in order to improve the picture clarity. Other sector-averages showed similar behavior. Variables are: (a) density, (b) temperature, (c) speed of sound, (d) thermal conductivity, (e) dynamic viscosity, (f) velocity y component.

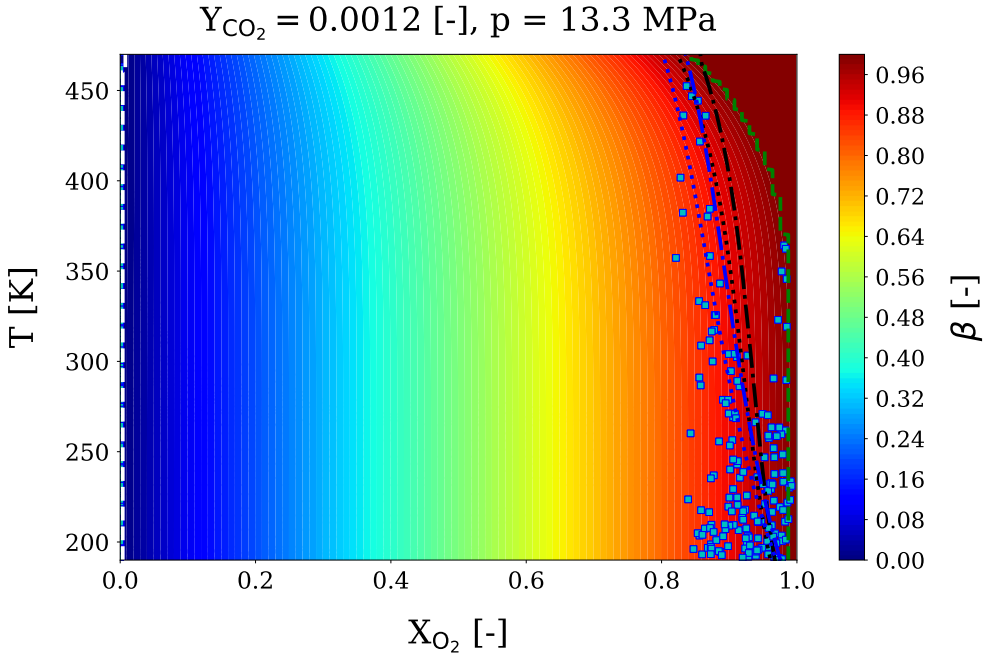

Figure 146: Temperature-Oxygen mole fraction diagram for the top side of the TML for $Y_{CO_2} = 0.0012$. The color map refers to the phase fraction field as the amount of oxygen and temperature are varied. Dew line is represented with a white dashed line at approximately constant $X_{O_2} = 0.00379$. Bubble line is represented with a green dashed curve on the right side of the picture (*cf.* the value of the β field). Blue and black lines indicate the isochoric and adiabatic mixing models. Specifically: blue line (. . .) indicates the isochoric mixing with $T_{H_2O} = T_{CO_2} = 2000$ K, black line (. . .) indicates the adiabatic mixing with $T_{H_2O} = T_{CO_2} = 2000$ K, blue line (.-) indicates the isochoric mixing with $T_{H_2O} = T_{CO_2} = 2500$ K, black line (.-) indicates the adiabatic mixing with $T_{H_2O} = T_{CO_2} = 2500$ K. In all cases the initial oxygen temperature is set to 115 K. Squared blue symbols refer to the data directly extracted from the TML.

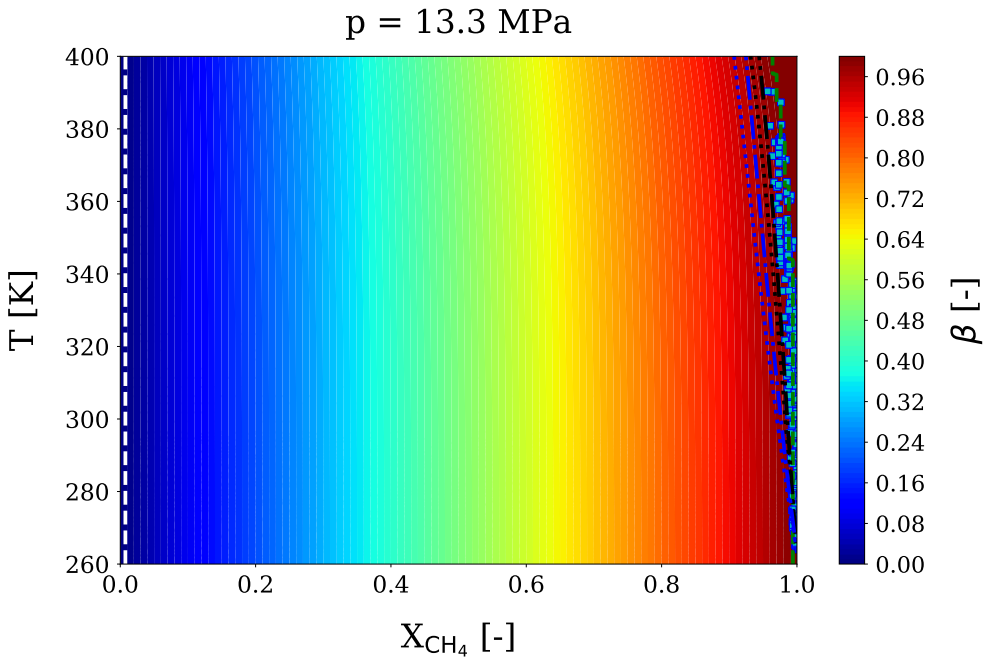

Figure 147: Temperature-methane mole fraction diagram for the bottom side of the TML. The mixture is considered binary with water only. The color map refers to the phase fraction field as the amount of methane and temperature are varied. Dew line is represented with a white dashed line at approximately constant $X_{\mathrm{CH_4}} = 0.00753$. Bubble line is represented with a green dashed curve on the right side of the picture (*cf.* the value of the β field). Blue and black lines indicate the isochoric and adiabatic mixing models. Specifically: blue line (. . .) indicates the isochoric mixing with $T_{\mathrm{H_2O}} = 2000$ K, black line (. . .) indicates the adiabatic mixing with $T_{\mathrm{H_2O}} = 2000$ K, blue line (.-) indicates the isochoric mixing with $T_{\mathrm{H_2O}} = 2500$ K, black line (.-) indicates the adiabatic mixing with $T_{\mathrm{H_2O}} = 2500$ K. In all cases the initial methane temperature is set to 263 K. Squared blue symbols refer to the data directly extracted from the TML.

- in the VLE-F region, all species except methane and water have very small amount, hence these will be neglected.

With the above observations, the following 0D analysis is separately conducted on both VLE regions by performing constant pressure Tp problems at 13.3 MPa and assuming that the top VLE region is composed only by O_2-H_2O-CO_2, whereas the bottom region is composed only by CH_4 and H_2O. Using the data in Tab. 33, the thermodynamic states are varied between 190 K and 460 K for the VLE-OX part, while 260 K - 400 K are used as extremes for the VLE-F counterpart. Additionally, for the VLE-OX region, the amount of CO_2 is varied as a fixed parameter as 0.0001, 0.0012, 0.0024 and 0.0036 for a total of 4 zero-dimensional simulations. These four values are considered representative of its scattered distribution obtained in Tab. 33.

The results for VLE-OX in the case of $Y_{CO_2} = 0.0012$ and VLE-F are given in Fig. 146 and Fig. 147, respectively. Other results for VLE-OX are provided in Sec. Q.6 for completeness, however they do not add significant flavor to the following analysis. The pictures represent the VLE diagrams of temperature as a function of oxygen and methane mole fractions, respectively. Note that in Fig. 146 the amount of O_2 does not reach exactly one because of the fixed amount of CO_2 in the mixture. First, by looking at Fig. 146 compared to the other pictures in Sec. Q.6, the amount of CO_2 does not play a crucial role, therefore it can be concluded that the VLE-OX is predominantly formed by O_2 and H_2O. In both cases, the field of β is imposed as color map. One may observe that the VLE zone spans almost all the boundaries, with exception of the zones of high-concentration, high-temperature of O_2 and CH_4 that fall in the pure super-critical state with respect to the single component. This is confirmed by the Dew (dashed white on the left) and Bubble (dashed-dot green) lines plotted at the left and right of each picture, indicating the limits of the multi-phase regions.

The TML data referring to the specific VLE region is scattered and super-imposed to the β fields. It is evident that this data falls on the high-range of β, and it is enclosed in the region of high species concentration as expected. To add more emphasis on the discussion, adiabatic (black) and isochoric (blue) mixing lines are super-imposed on the picture. These

lines are computed with the following criteria: a) for the VLE-OX region (Fig. 146), oxygen, water and carbon dioxide are mixed by assuming 115 K for O_2 and two different (common) temperatures of the other two species: 2000 K and 2500 K, plotted using the dotted and the dashed-dotted lines, respectively; b) for the VLE-F region (Fig. 147), methane and water are mixed by assuming 263 K for CH_4 and the same two different temperatures for water: 2000 K and 2500 K, plotted using the dotted and the dashed-dotted lines, respectively.

These results reveal that 0D mixing models can reasonably well capture the VLE trends in both cases therefore they can be used as a predictive tool to investigate whether VLE will form or not even in the reacting case. Note that scattered data are in β regions that are smaller than those observed in Fig. 142. For example in Fig. 146, dots fall in the regions for $\beta \geq 0.8$ rather than 0.95. This is due to the fact that TML data do not exactly correspond to the offline VLE calculations, nor mixing calculations. In fact, scattered dots may refer to pressure values that are not exactly 13.3 MPa and additionally contain traces of other species that slightly modify the VLE state, even if by a small amount. Despite these differences zero dimensional analyses reveal quite good prediction of the VLE states.

One last observation is related to the mixing models. VLE diagrams clearly suggest that there could potentially be regions where β spans all the values between zero and one. This does not happen in the present case because of the mixing process between (hot) water and the other two cold reactants. For example in Fig. 146 a $\beta \sim 0.1$ would be obtained (regardless of the amount of CO_2) if the composition would be 90% water and 10% O_2. Potentially, this can show more significant discrepancies in the flow field as showed in the non-reacting SML application of Sec. 5.4. However, this cannot happen in the present case because water can be only formed by the flame, therefore as soon as it is produced it comes with a high temperature. As a result, oxygen and water can never mix in a way such that 90% H_2O would fall in the $200\,K < T < 460\,K$ region, which is confirmed by the 0D mixing models. On the other hand, another application (such as cooling) involving liquid water and at the same time mixing with (even warm) oxygen, can now fall in the $\beta \sim 0.1$ region, producing completely different effects.

The latter analysis is to emphasize the fact that thermodynamic states, especially involving

phase equilibrium represent delicate conditions that once perturbed, may show drastically different results.

5.6 Unsteady VLE formation in a 2D reacting spatial mixing layer (SML)

The last testcase explored is a spatial mixing layer (SML) in reacting conditions. The geometry, grid and setup is identical to that indicated in Fig. 113, however the conditions are taken again from Tab. 31 with the goal to investigate if a different geometry can produce substantially different results between the two thermodynamic models compared to the 3D TML case (in accordance with **Objective 3**). The chemical kinetics is the same discussed in Sec. 5.5.1, therefore once again the DVODE routines are used for the chemical kinetics integration. The top stream is composed of methane, while the bottom stream is composed of oxygen. The non-reacting simulation is first run for roughly 2 ms corresponding to approximately 30 FTT to eliminate the effect of the initial transient. As illustrated in Fig. 148,

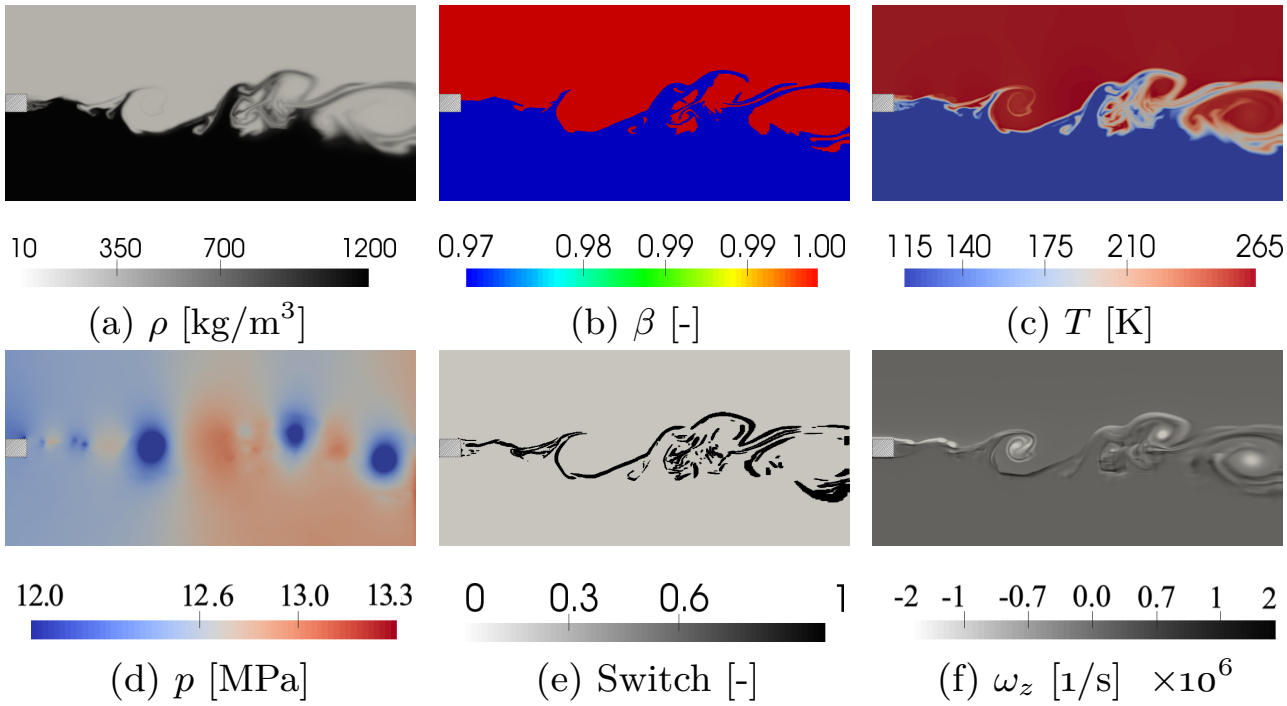

Figure 148: Relevant flow field properties computed at the evolved non-reacting solution, before the ignition. The phase fraction field (a) shows no VLE formation, in agreement with both 0D thermodynamics of Fig. 129 and the TML results of Figs. (132)–(134).

the evolved solution of the non-reacting field does not show VLE formation between the two reactants at the present conditions. This is not surprising given the analysis performed before hand with the 0D thermodynamics of Fig. 129 and the TML results of Fig. 132. The dynamic switch between the FC and the QC scheme is also illustrated in Fig. 148(e) for completeness along with the pressure field in Fig. 148(d). It is stressed that without the use of the QC scheme, the simulation was showing strong pressure oscillations due to the large density gradients (*cf.* Fig. 148(a)), eventually failing after few tens of iterations. This is once again not surprising given the strong difference in densities of the two streams as discussed in Sec. 3.2.2.

The solution of Fig. 148 is ignited by using the following criterion: computational cells that show an equivalence ratio $0.95 < \phi < 1.05$ are provided with products (80% H_2O, 20% CO_2 by mass) at the temperature of 2500 K; on the other hand regions outside this range of equivalence ratio are provided with a temperature that smoothly merges between a nominally burning solution of 2500 K and the temperature in the reactants' free stream using a linear profile, depending on the amount of the fuel or oxidizer amount in the computational cell. Many different initialization procedures have been tested, however no significant differences were observed in the outcome as far as VLE production and its correlation with the field variables. The initialized burnt solution is further simulated for a physical time of 51 μs, half of it corresponding to the time during which the flame was observed to extinguish, possibly due to the approximations introduced with the chemical kinetics and the overall case setup, such as the geometry. Nevertheless, this computational time was enough to obtain a comparison of the reacting solution between the VLE and the non-VLE model during the unsteady flow field evolution, which is once again the only objective of the present computational exercise. Insights from this relatively simple, yet complex simulations (from a numerical, theoretical, physical and computational overhead point of view) are intended to determine the effect (if any) of a multi-phase RG solution on the major field variables as done with the other cases discussed so far.

The use of DVODE resulted into the computational expense of roughly 5.6 seconds per iteration on 1024 processors for the VLE case, compared to the 0.23 seconds per iteration

for the non-VLE setup using the same number of processors. This places again the non-VLE option around 20 times faster than the VLE counterpart, in agreement with all the cases discussed before.

Figure 149 and Fig. 150 show some field variables collected from the VLE and the non-VLE simulations, respectively. The pictures show time instants starting from $t = 0$ corresponding to the ignition time to $t = 25\,\mu s$, roughly corresponding to the time after which the flame was extinguished because a lower temperature was reached in the flammable mixture, preventing reactions to self-sustain. This was observed in both simulations.

The VLE solution clearly displays regions in which multi-phase conditions occur, however they are mostly restricted to values of $\beta \geq 0.98$ as observable in Fig. 149(a)–(c). This has an obvious consequence on the flow field that is, the VLE solution is expected to behave very close to the non-VLE solution. In addition, VLE regions do not appear directly inside the flame (*cf.* Fig. 149(m)–(o)) as obviously expected, because of the high temperature condition, and rather they appear in its neighbor, where the temperature and composition reach the possible value for its formation. This is discussed later. One major observed difference is reported in the value of the speed of sound that drastically reduces within the VLE region. This was continuously observed in the 0D cases studied in Chap. 4 as well. In the VLE simulation in fact, the lowest value of speed of sound is about 165 m/s, which is the lowest peak throughout the simulation. On the contrary, the same regions in the non-VLE simulation display a lower peak of approximately 300 K. This difference, although important, does not seem to produce macroscopic differences in the flow field major variables, at least qualitatively within the time window simulated.

However using the concepts learned from the non-reacting cases simulated before, the simulations are run further up to 51 μs to explore the possibility of macroscopic differences as the VLE regions, once formed, continue to evolve in space and time.

Figure 151 shows the phase fraction, density and mixture fraction fields computed at $t = 51\,\mu s$ for the VLE (top row) and non-VLE (bottom row) simulation, respectively.

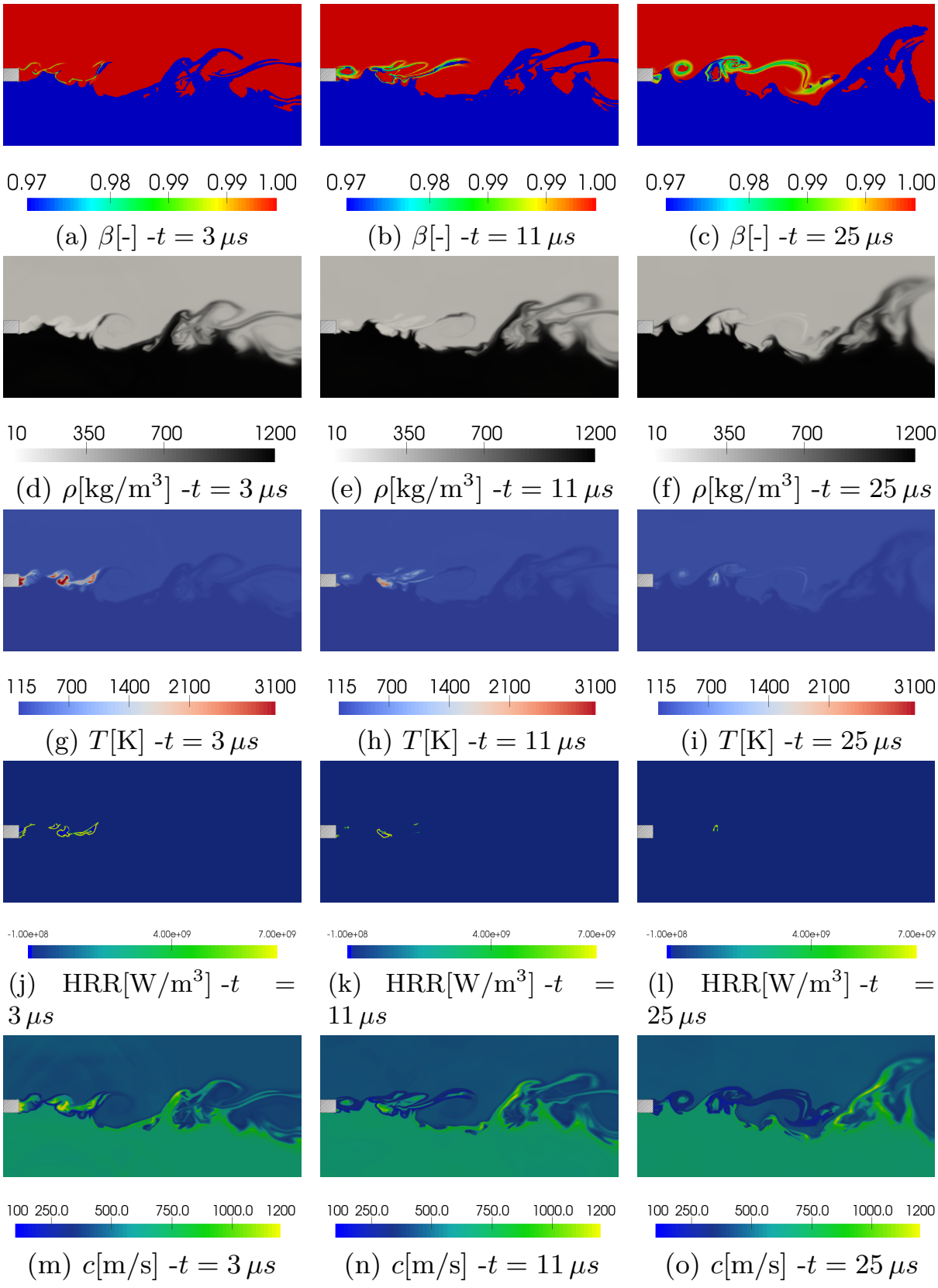

(a) β[-] -$t = 3\,\mu s$ (b) β[-] -$t = 11\,\mu s$ (c) β[-] -$t = 25\,\mu s$

(d) ρ[kg/m^3] -$t = 3\,\mu s$ (e) ρ[kg/m^3] -$t = 11\,\mu s$ (f) ρ[kg/m^3] -$t = 25\,\mu s$

(g) T[K] -$t = 3\,\mu s$ (h) T[K] -$t = 11\,\mu s$ (i) T[K] -$t = 25\,\mu s$

(j) HRR[W/m^3] -$t = 3\,\mu s$ (k) HRR[W/m^3] -$t = 11\,\mu s$ (l) HRR[W/m^3] -$t = 25\,\mu s$

(m) c[m/s] -$t = 3\,\mu s$ (n) c[m/s] -$t = 11\,\mu s$ (o) c[m/s] -$t = 25\,\mu s$

Figure 149: Field variables extracted from the VLE simulation at three different time instants after which the flame was extinguished.

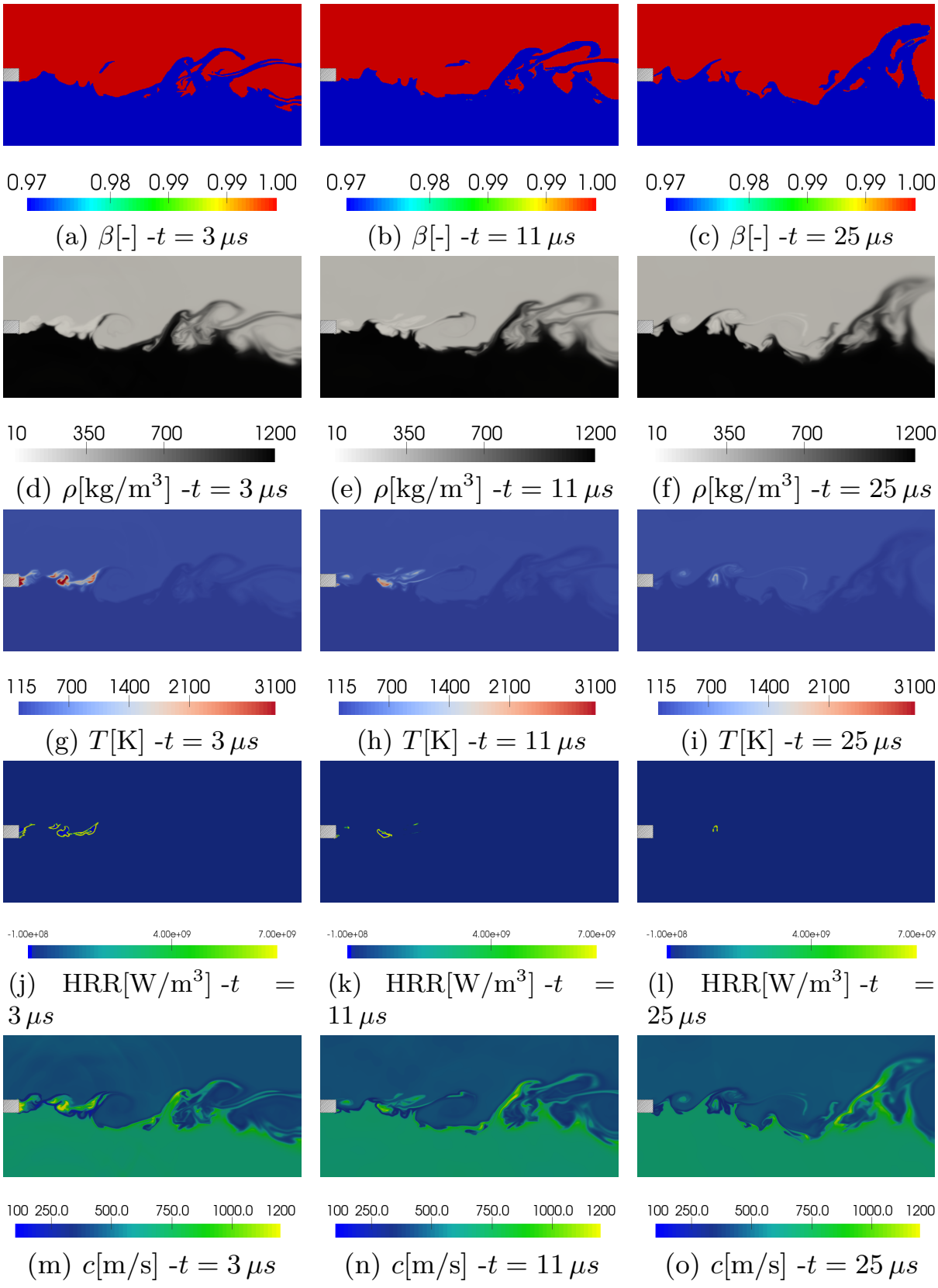

(a) β[-] -$t = 3\,\mu s$ (b) β[-] -$t = 11\,\mu s$ (c) β[-] -$t = 25\,\mu s$

(d) ρ[kg/m^3] -$t = 3\,\mu s$ (e) ρ[kg/m^3] -$t = 11\,\mu s$ (f) ρ[kg/m^3] -$t = 25\,\mu s$

(g) T[K] -$t = 3\,\mu s$ (h) T[K] -$t = 11\,\mu s$ (i) T[K] -$t = 25\,\mu s$

(j) HRR[W/m^3] -$t = 3\,\mu s$ (k) HRR[W/m^3] -$t = 11\,\mu s$ (l) HRR[W/m^3] -$t = 25\,\mu s$

(m) c[m/s] -$t = 3\,\mu s$ (n) c[m/s] -$t = 11\,\mu s$ (o) c[m/s] -$t = 25\,\mu s$

Figure 150: Field variables extracted from the non-VLE simulation at three different time instants after which the flame was extinguished.

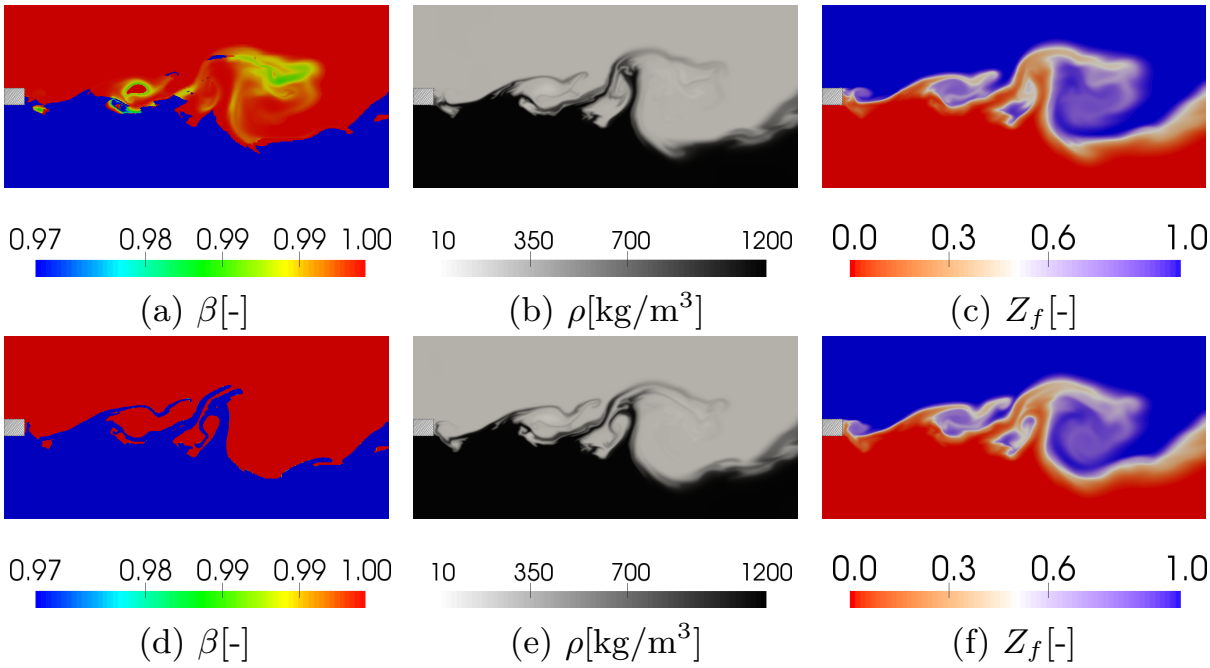

Figure 151: Phase fraction, density and mixture fraction fields at $t = 51\,\mu s$ for the VLE (top) and non-VLE (bottom) models.

The mixture fraction was defined as [155]:

$$Z_f = \frac{\nu Y_{CH_4} - Y_{O_2} + Y^0_{O_2}}{\nu Y^0_{CH_4} + Y^0_{O_2}}\,, \qquad \nu = \frac{\nu_{O_2} MW_{O_2}}{\nu_{CH_4} MW_{CH_4}}\,, \tag{5.6.1}$$

where $\nu = 4$ is computed for the stoichiometric reaction and $Y^0_{CH_4}$, $Y^0_{O_2}$ represent the amount of methane and oxygen in the fuel and oxidizer streams, respectively (both equal to one). From these pictures, one may observe that once again the differences between the two simulations are very minor. A more quantitative comparison is provided in Fig. 152, where iso-lines of density and mixture fraction are compared between the two models at two different time instants. As one can immediately observe, the differences between the two models are very small, although the two curves are not exactly overlapped either. Local differences can be appreciated, however global flow features are retained in contrast to what was observed with the non-reacting SML. The same is observed in Fig. 180 which shows a different iso-density contour. This confirms the initial observation that the occurrence of VLE states with near-one phase fraction values can perturb the flow field only a little, causing very small effects on the overall flow field in agreement with the observations made

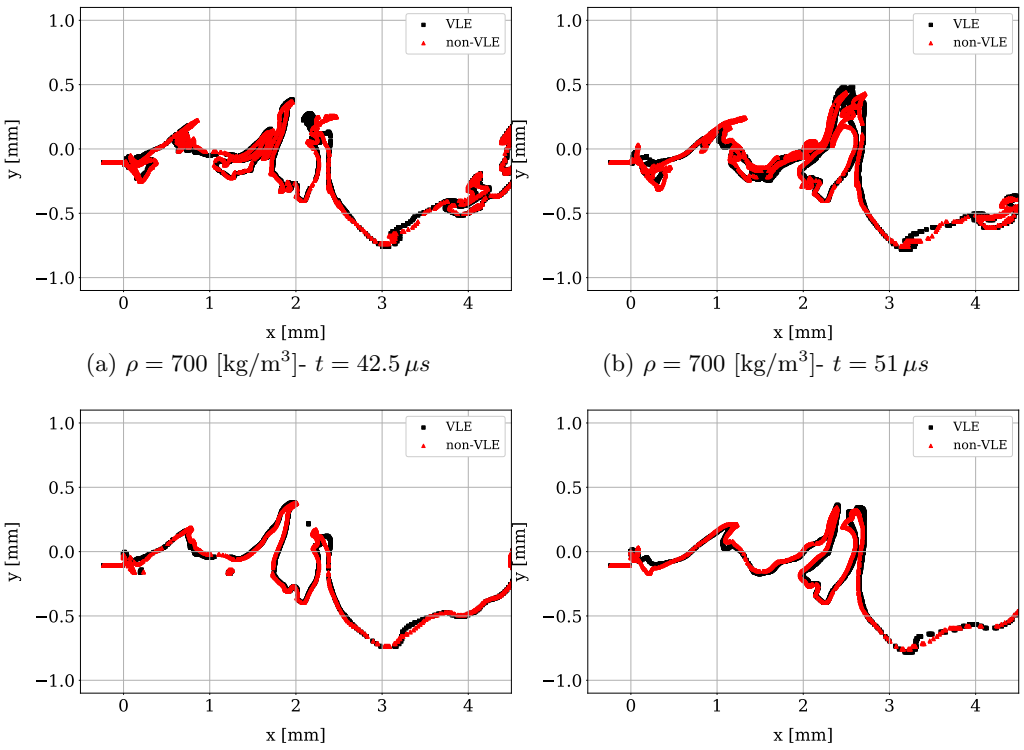

(a) $\rho = 700$ [kg/m^3]- $t = 42.5\,\mu s$ (b) $\rho = 700$ [kg/m^3]- $t = 51\,\mu s$

(c) $Z_f = 0.2$ [-]- $t = 42.5\,\mu s$ (d) $Z_f = 0.2$ [-]- $t = 51\,\mu s$

Figure 152: Iso-density (top) at 700 kg/m^2 and iso-mixture fraction (bottom) at stoichiometric value of 0.2 comparison between the two thermodynamic models at two different time instants.

for the 3D TML discussed in Sec. 5.5.5.

Following the similar approach adopted for the 3D TML, offline investigations about the states at which VLE forms are separately made in order to confirm the fact that all the visualized VLE states can be predicted before-hand using the 0D tools. Table 34 shows

Table 34: Mean and standard deviation values computed within the VLE region at $t = 42.5\,\mu s$.

VLE data, $t = 42.5\,\mu s$							
	T **[K]**	p **[MPa]**	Y_{CH_4}	Y_{O_2}	Y_{H_2O}	Y_{CO_2}	Y_{CO}
μ	268.26	12.98	0.701	0.288	0.0058	0.0017	0.0003
σ	34.12	0.28	0.158	0.164	0.0052	0.0015	0.0002

the mean and the standard deviations of the mixture properties obtained with the VLE ensemble at $t = 42.5\,\mu s$. In this case, it is interesting to notice that there is no clear distinction between how much methane or oxygen contributes most to the VLE formation and it rather seems that both of them contribute. However, since it has been already confirmed many times that VLE does not occur between methane and oxygen only at these pressures, a third species has to inevitably be taken into account. In this case, while CO is the least amount in the mixture, it is assumed that it does not contribute at all, similarly to what has been done earlier. On the other hand, H_2O and CO_2 show a similar order of magnitude both in the average and the standard deviation. For this reason, a ternary VLE diagram is employed in this case. The main species are chosen to be methane, oxygen and water, while carbon dioxide is varied as a fixed parameter for each run. The results are showed in Fig. 153 for fixed $Y_{CO_2} = 0.002$. Other combinations of this value ranging from 0.0001 to 0.004 did not provide any substantial difference in the outcome. The VLE diagrams are explored for fixed pressure at $p = 13.0$ MPa (small variations of this value also did not produce any appreciable difference in the outcome). Data from the simulation at $t = 42.5\,\mu s$ is extracted with the following criteria: $\beta \in (0, 1)$ and $T \in [T_i - 1, T_i + 1]\,K$, where $T_i = 240\,, 265\,, 300\,K$ and superimposed to the respective ternary diagram with blue triangles. The results are clear: simulation data lies in the region of $\beta \geq 0.97$, very close

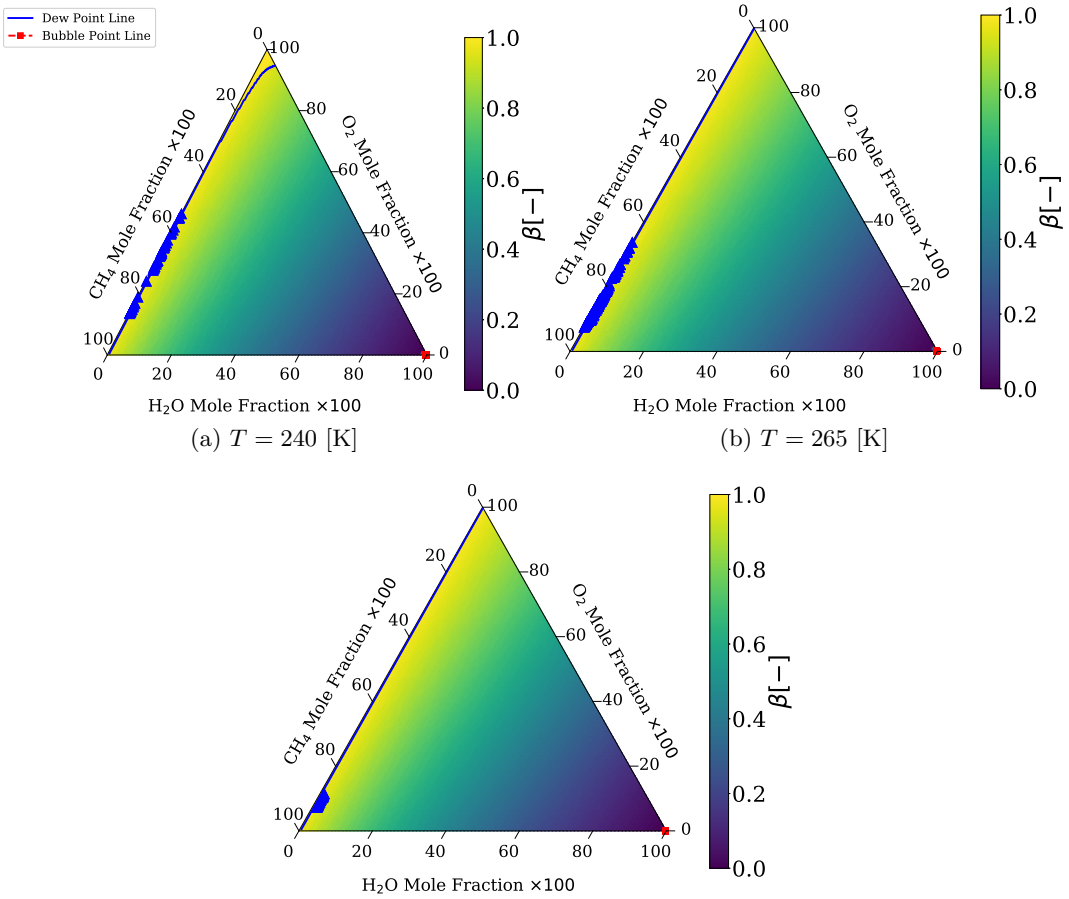

(a) $T = 240$ [K]

(b) $T = 265$ [K]

(c) $T = 300$ [K]

Figure 153: Ternary VLE diagrams between $CH_4/O_2/H_2O$ at $p = 13.0$ MPa for $Y_{CO_2} = 0.002$. Simulation data is superimposed with blue triangles.

to the dew point line. It is very interesting to notice that VLE would exists for the whole range of H_2O amount, spanning all the possible values of phase fraction (note the bubble point lines confined to the almost 100% amount of water), however, this is very unlikely to be obtained in a pure reacting system, where the only way to produce water and carbon dioxide is by means of a flame.

5.7 Summary

In this chapter, various applications of the VLE thermodynamics coupled with CFD have been investigated with the ultimate goal to quantify the differences (where applicable) of the VLE versus the non-VLE model. Canonical configurations ranging from 1D to 3D setups have been employed and systematic investigations have been targeted for each test case by varying the geometry, the conditions, the thermodynamics and the resolution, depending on the case. These test cases complete the fulfillment of **Objective 2** and address the **Objective 3**. The major points found can be summarized as follows:

- resolution itself does not impact the VLE formation in the sense that VLE does not represent an "unresolved" phenomenon that disappears as the grid is refined. The multi-phase thermodynamic model is a point-wise calculation that requires 2 independent thermodynamic variables, plus composition to be checked at every point in space and time. It does not matter whether this set of variables is produced by a turbulent, laminar, non-reacting or reacting flow with any type of resolution. If the type of flow being solved produces the same set through the coupling with fluid mechanics, the same VLE result will be obtained. In that sense, if the flow inputs contains approximations and/or errors due to an unresolved field, the same errors may translate into the presence of VLE. On this regard, the approximations introduced by the global chemical mechanism need to be put in perspective. Even if the thermodynamic conditions that followed in the CFD calculations are slightly off due to the kinetics approximations, a systematic one-to-one comparison has been carried out between the two thermodynamic models. Hence, even with a detailed

model, if the same conditions occur, the same VLE formation (along with all the outlined effects) is expected as well;

- following the previous statement, use of the QC scheme by means of the Double-Flux model should be limited only to the regions of high density gradients. In fact, due to the numerical approximations of the thermodynamic states introduced with its algorithm, fake VLE states can occur, unless the resolution is increased;

- when the non-VLE model is used, a higher Gibbs free energy solution is effectively reached if the conditions fall in a multi-phase state;

- in non-reacting solutions, the VLE model can produce drastically different results in the flow-field variables compared to the non-VLE solution. This is mainly due to the fact that the β field spans all the possible values between zero and one and therefore, in contrast to the non-VLE case where either the vapor or the liquid solution are chosen, non-linearly blended values of the vapor and the liquid solutions are instead chosen. As a result, not only the VLE region can express considerably different values of the flow properties, but it has been found that their non-linear coupling with the transport properties (in turn affected by the VLE solution in a non-linear fashion), can exhibit a critical role in the flow structure development. On this regard, a competing effect between mass and heat diffusion has been isolated as a possible explanation of this effect through the Lewis number;

- on the other hand, in pure reacting solutions, the differences between the VLE and the non-VLE models do not appear as big, but rather confined in minor flow properties differences that are localized in space and time. The main reason for this is the fact that the only way VLE can form is through the introduction of small amount of hot products in large amount of colder reactants, such that the mixture falls in temperature values between 190 K and 300 K with values of β that always exceeded 0.95;

- in all cases, 0D thermodynamic tools have been demonstrated to be a valid approach

to estimate, with good accuracy, the occurrence of VLE. These, can be therefore used as an a-priori model to understand if, and how important, the VLE effect can be in a simulation, depending on the conditions.

Chapter VI

CONCLUDING REMARKS

6.1 Summary

A primary focus of this work has been the understanding, followed by the determination of a correct analytical thermodynamic framework of RG mixtures in presence of vapor-liquid equilibrium (VLE), which was found particularly missing in past works. While the solution of the multi-phase, multi-component equilibrium problem that minimizes the mixture Gibbs free energy at fixed temperature, pressure and composition to find the amount of liquid and vapor in the mixture is a well-established tool, the overall set of thermodynamic VLE quantities necessary for a CFD calculation were not extensively treated so far. This point was considered as a major objective because it establishes the role of VLE compared to the single-fluid (non-VLE) approach in a flow simulation. Reduced-order models or simplified models might in fact return a biased solution to the extent that a direct comparison between the two models could not rigorously carried out.

These VLE thermodynamic properties use a different set of independent variables than those attempted in other works (which did not provide the whole ensemble of quantities necessary for a CFD calculation), whereby the product between the phase-fraction and the vapor molar fractions was used, providing extreme flexibility in all the subsequent derivations. In this process, emphasis was given to the role of the frozen part of the derivative, compared to the actual VLE contribution: the first assumes that no variation of the VLE properties occurs as temperature and/or pressure are varied, while the second part takes this effect into account. The latter contribution was the most challenging term to determine, which resulted in approximated formulas or numerical differentiation in past works. Thanks to the adopted change in variables, this term was easily computed and it helped to identify the main differences when this framework was subsequently compared to the non-VLE counterpart.

This model was applied on different mixtures with different levels of complexity in comparison to other two simplified models: the single-fluid (non-VLE) and the frozen VLE model, the latter obtained by neglecting all the VLE derivatives discussed earlier. This was found to resemble some approximated models reported in the literature. The three models showed different results, highlighting the fact that the VLE derivatives play a crucial role in terms of trend and magnitudes on all properties. In particular, the VLE model displays continuous trends that connect the liquid/vapor limiting states, however with discontinuous first derivatives. This near-phase-boundary trend cannot be captured by the single-phase model because of the sudden switch it uses between the liquid or the vapor phase based on the local value of the Gibbs free energy. On the other hand the frozen VLE model matches the primary thermodynamic functions trends but it fails to correctly predict their derivatives because of the employed assumption.

While this study was conducted on the selected mixtures by maintaining fixed pressure, temperature or composition, the thermodynamic results were directly fed into the transport coefficients models. Therefore the present work also provides a first study on the effect of VLE on transport properties from a modeling perspective. It was shown that as the thermodynamic properties vary inside the VLE region, an associated departure corresponded in the transport properties, particularly thermal conductivity and mass diffusion coefficients, which displayed sensible differences when computed with the other thermodynamic models. In addition, the investigation of RG mixtures with VLE was extended to the evaluation of different EoS models of the cubic family (GCEoS) combined with different mixing rules, all relevant for CFD applications. The analysis helped to restrict the attention to the use of the PR EoS or SRK EoS combined with the mixing rule of either Van der Waals or Harstadt for the best outcome in terms of computational speed and accuracy. Nevertheless it is emphasized that the provided VLE analytical model is EoS-independent and potentially any EoS can be used in place of the GCEoS. The present analytical model was found to outperform the corresponding numerical framework by at least 30% in gain of computational speed when applied to the selected mixtures.

In parallel to the development of a correct VLE thermodynamic model, a robust numerical

algorithm to compute the inviscid fluxes in presence of high-density gradients was implemented to work with and without VLE in a consistent manner. First, a detailed explanation of the problem of pressure oscillation was provided in an analytical fashion and compared to the numerical simulations. This was the first time such explanation was given in this form. Moreover, this approach was applied to both RG and TPG cases using the same case setup and resolution, proving that i) the EoS non-linear response is the major factor that is responsible for the error magnification that comes from the spatial and temporal integration and ii) the input error that comes from the integration cannot be mitigated by simply reducing the order of accuracy of the numerical scheme, which would in fact increase it.

Based on the literature survey, it was found that currently there is no unique choice in the CFD community to handle this problem and that the solution offered by the Double-Flux (DF) method is an easy and robust way to circumvent the issue of spurious numerical oscillations in purely conservative schemes. This scheme, was implemented to work with a fully conservative scheme based on the MUSCL extrapolation at cell-interfaces so that a novel hybrid scheme was obtained. An additional improvement was the derivation of an analytical solution to the PRHO problem for the determination of the reconstructed temperature at the cell interfaces with given density, pressure and composition in presence of VLE (required by the DF method). This analytical formula was already available for single-phase conditions only, whereas in this work, its extension to VLE was found applicable to a class of cubic EoS and later proven to be particularly useful to improve the computational cost of VLE simulations because it avoided the more expensive iterative PRHO alternative algorithm.

The VLE algorithms were extensively validated and the importance of the solution of a VLE state with a VLE physical model was highlighted: if a thermodynamic state corresponds to a VLE condition and a reversed thermodynamic problem is attempted, failure to treat it with the correct VLE thermodynamics may result in errors which are completely independent of the errors caused by the numerical integration. This aspect already provided the

important conclusion that pressure oscillations caused by the numerical integration (corrected by the DF method) and erroneous thermodynamic states found by using the wrong thermodynamic model for a given state are independent, therefore both solutions are required in a RG simulation whose condition falls in the mixture VLE state.

The present numerical and physical model was then applied to canonical configurations to study its effect on non-reacting and reacting flows. The results provided the following conclusions. 1) The use of DF must be limited to only the regions of high-density gradients as its use can generate erroneous thermodynamic states (including VLE) due to the non-conservative error in temperature. This confirmed the same conclusions reported in earlier works [109]. 2) The VLE states are independent of resolution, that is if the grid is refined it does not disappear, thus it represents a physical model that captures a different physics: the same physics cannot be captured by not using it and by refining the grid. 3) Flow properties differ between VLE and non-VLE simulations. Particularly while these were not found to have macroscopic effects on a single vortex evolution in a 3D TML, they showed an important effect on a 2D SML where clear differences were observed in both the instantaneous and time-averaged flow field. It was particularly interesting to investigate the reasons of this difference. It was in fact found that the non-linear coupling between the VLE states and the transport properties caused a strong imbalance between the thermal conductivity and mass diffusivity at the vortex leading edges as they were formed downstream the splitter plate. This had the effect to promote the quicker transition of the VLE front edge to a non-VLE state due to heat transfer, with the ultimate effect to change the vortex dynamics by reducing its width along the cross-wise direction. This was directly observable in the time-averaged field that showed a thinner SML width compared to the non-VLE counterpart. This study proved that the VLE can have a big impact to the flow field evolution and that its non-linear coupling with the transport properties can actually unveil different flow dynamics: a point that was never showed before.

Regarding the reacting cases, the focus has been on the investigation of VLE states produced by purely reacting conditions, that is the reactants do not form VLE by themselves (as it would have fallen in the previously treated case). For this scope, methane/oxygen

was selected as combination. Before running the simulations in fact, off-line thermodynamic investigations revealed the absence of VLE for pressures above 5 MPa. This pressure is also very close to the critical pressures of both species, therefore pressures below this threshold would have resulted in falling directly in the sub-critical regime for the components themselves, not directly accounted by the present numerical and physical framework. A preparatory study was then conducted on the chemical mechanism to be used to represent the finite-rate kinetics. A 3-steps global mechanism was chosen with respect to a detailed one, mainly because of two reasons: i) further increase in the computational simulation cost as the number of species was increased and ii) lack of RG parameters for the minor species that would have been taken into account. The chemical mechanism was tuned against a detailed model to take into account the different operating conditions, especially in pressure (13.3 MPa). Unfortunately, the tuning of this mechanism was observed to require a chemical time-scale resolution that was below that of the explicit time step based on the CFL condition. Therefore to avoid erroneous calculations of the species reactions rates, an implicit ODE solved was required. This further increased the simulation cost between 2 and 3 times that significantly impacted the (already high) overhead of the VLE cases.

The simulations were carried out in both a 3D TML and a 2D SML. In both cases, VLE was observed to be formed between hot products and cold reactants as postulated in the thesis objectives, however its effect was found particularly minor, mainly because of the value of the phase fraction that were equal or above 0.95, thus very close to a pure gaseous solution.

Though the post-processing carried out from the reacting cases did not show significant differences between the VLE and the non-VLE solution, it was interesting to observe that VLE can form in the vicinity of a flame. Use of VLE thermodynamics combined with finite-rate kinetics was also done in this work for the first time.

Nevertheless it should be pointed out that unsteady VLE formation in reacting systems may become important in other combustion applications that for example operate at marginal conditions. These include ignition, blow off or lifted flames, where the role of the reacting

mixture before the actual reaction can form VLE, ultimately producing a change in the evolution of the subsequent combustion. This is also suggested by the fact that VLE pockets formed by the vortex breakdown in the non-reacting SML case were following a different spatial and temporal evolution downstream the splitter plate compared to the non-VLE case.

In all the simulations, the role of zero-dimensional thermodynamics has been demonstrated to be particularly useful in both pre- and post-processing. Off-line solution of Tp problems to extract the VLE diagrams combined with the mixing models (adiabatic and isochoric) has been extensively used to either predict or confirm the VLE formation. These tools can be used to investigate the formation of VLE states regardless of the number of components (although the analysis would considerably complicate with many species of the same amount), and can therefore help to establish a-priori if VLE forms or not.

Some major limitations of the present work are also highlighted as these help to open the future research. The assumption of phase equilibrium throughout the calculations may not be sufficient to physically represent the inter-facial behavior of multi-component mixtures, however it is not clear to what extent can be considered correct. Formulation of a consistent phase non-equilibrium model and its comparison against the VLE counterpart is definitely an objective to pursue. In addition, the VLE thermodynamic properties have not been extensively validated in this work, mainly because of lack of data. The only validation that has been performed in this work against experimental data is that of the speed of sound for the Prudhoe gas which, although being a quite complex mixture, it does not provide an ultimate validate of the whole formulation. Despite the correctness of their mathematical formulation in fact, it is known that EoS models can predict properties with poor accuracy. These would affect the VLE properties as well. As a result, experimental apparatus that can measure VLE properties of various multi-component mixtures and/or accurate molecular dynamics simulations can help on this regard. Typically, these should not be limited to the characterization of VLE diagram but possibly extended to more complex variables such as fluid compressibilities, speed of sound and even transport properties.

6.2 Achievements/contributions

The following contributions are identified for this work [226, 227].

Contributions on the modeling side:

- developed a fully consistent, analytical, EoS-independent model for RG multi-component mixtures with phase-equilibrium thermodynamics;
- extended 0D mixing models to incorporate VLE;
- provided a detailed, analytical explanation for the occurrence of pressure oscillations in conservatives schemes when RG thermodynamics is employed;
- extended the Double-Flux model to work consistently with VLE;
- found an analytical formula to compute the interface temperature in presence of VLE, when density, pressure and composition are known;
- developed a fully consistent numerical hybrid scheme that can account for VLE thermodynamics: from the spatial integration, to the calculation of transport properties;
- demonstrated the effects that VLE thermodynamics has on reversed thermodynamic problems;
- demonstrated the independence of the error generated by the numerical scheme over the error generate by the thermodynamic model;
- run a first VLE-finite rate kinetics coupled simulation;
- provided a generic formulation to compute the Widom line in case the GCEoS is used.

Contributions on the physics side:

- demonstrated the effect of VLE on the transport properties;
- demonstrated the difference in the states predicted by VLE thermodynamics over the single-fluid approach, as well as the frozen VLE model;
- demonstrated the independence of the VLE model over the grid resolution;

- found a novel, Lewis number-driven effect that is caused by the non-linear coupling between the VLE states and their effect on the transport properties;
- proved the formation of VLE states in reacting systems in the flame vicinity,

6.3 Future work

As extensively discussed so far, employment of RG thermodynamics with VLE required to touch several aspects of the simulation framework on either the numerics and the physics sides. This means that each of these aspects can be further studied and improved.
In general, this work has provided new insights about the physics of RG mixtures in presence of phase-equilibrium. In particular the role of the compressibility effects dictated by the RG model, coupled with the VLE thermodynamics and transport has shown a new type of vortex breakdown that could not be captured by the non-VLE case. From a modeling perspective, this also suggests that a consistent and robust RG-VLE numerical framework is indispensable to be used and failure to adjust even one aspect in the simulation pipeline (thermodynamic algorithms, spatial integration and VLE properties) may produce differences in the results.
In the following some suggestions on the future outlooks are given:

- research about how to mitigate the non-conservative error carried by the DF model. This would benefit both the VLE and the non-VLE simulations;
- the present analytical model can be further expanded by relaxing the pressure equilibrium condition between the two phases and account for capillarity effects;
- one of the most limiting conditions found in the present work has been the enormous cost associated with the VLE calculations. To mitigate this issue and make the VLE model fully applicable to large scale geometries, one idea can be to exploit the conclusions obtained through the reacting cases. Although restricted to methane/oxygen combinations, these simulations essentially proved that in a pure reacting system, VLE formation is a minor effect and therefore it can be neglected, especially if the purpose of the simulations is not purely scientific, as done in this work. As a consequence, by

using the zero-D thermodynamics and mixing models, one may first understand if the reactants produce VLE by themselves. If yes, then one may explore the possibility to tabulate the VLE properties upfront for the binary reactants only and for a range of temperatures and pressures that is reasonably representing the desired operating conditions. Then, one may consider only the VLE formed by the reactants and use the single-fluid assumptions alone where the temperature is sufficiently high, or where the composition is no longer binary (hence hot products are found). However one should keep in mind that if the VLE conditions already occur for a non-reacting mixture that is already non-binary (e.g. ternary or more), this tabulation approach can be quickly become difficult to apply as well;

- more in general, use of tabulation or any sort of acceleration techniques (e.g. GPU) or neural networks to increase the computational efficiency of VLE calculations can be definitely explored;

- from an application point of view, there can be multiple options, ranging from jet in cross flows, to other types of injectors that use different species. Again the fact that VLE may not be important in a purely reacting system (*i.e.*next to the flame), does not mean that if the system is reacting it can be ignored upfront. In fact, if the reactants form VLE by themselves before reacting, the whole range of phase fraction can be reached with all the same potential consequences that have been discussed in this work for the non-reacting results;

- obviously, the role of LES closures has not been addressed in this work and therefore it represents another area of study where combined effects between VLE and turbulence are worth to be investigated further. This would effectively mean to find a model for the unresolved, filtered component of all the thermodynamic equations given in this work;

- extensive validation of VLE thermodynamic properties in multi-component mixtures using either experimental apparatus and/or molecular dynamics simulations;

- implement the method of [67] to calculate the mixture critical loci as a function of two thermodynamic variables and composition. Explore the possibility on how to use this tool to establish an a-priori knowledge of the VLE diagram that can be exploited during the calculation to avoid unnecessary calculation. These include for example the solution of the ERHO problem using VLE only in the regions that are potentially showing it, while using the single-phase approach in the regions above the mixture critical point;

- exploration of the role of phase non-equilibrium to establish the role of temperature and pressure gradients across the VLE interface. This aspect can be potentially carried out by introducing a transport equation for the phase fraction β, hence it would be no longer linked to Eq. (2.2.36). The challenge for this task it to find a proper model for the rate of change of β itself, which would go as a source term in the above transport equation, similarly to what is commonly done for finite-rate chemical reactions. Nevertheless it is important to underline the fact that even in the case phase non-equilibrium is considered, the thermodynamic relations derived in the present work will still hold in the hypothesis of local thermodynamic equilibrium, unless the additional assumption of local thermodynamic non-equilibrium is superimposed on it (in which case the EoS will take the form of an ODE, *i.e.*, no longer in an algebraic form).

In addition, few ideas about where the present work may produce some spin-offs in similar areas of study are given:

- in sub-critical regimes, Eulerian-Lagrangian numerical framework require the VLE model to match the droplet-environment jump conditions. These are usually restricted to simplified models (e.g. Clausius-Clapeyron) based on single-component thermodynamics. If one wants to extend this approach to a multi-component strategy, the analytical framework presented in this work is the one to use (especially when accounting for capillarity effects). In that case, since either mass and energy transfer are imposed at the droplet interface, all the properties derived in this work are

necessary;

- the present framework can be used "as is" for every problem that required the modeling of no more than 2 phases in equilibrium. For example if one is interested to evaluate solid-liquid or solid-vapor states, this framework is already good enough, provided that proper EoS are supplied to the solid phase.

Appendix A

MINIMUM GIBBS CRITERION FOR COMPRESSIBILITY ROOT SELECTION

For a cubic EoS, substitution of Eq. (2.2.3) into Eq. (2.2.2) leads to a unique cubic equation in the compressibility factor in the form $a_1 Z^3 + a_2 Z^2 + a_3 Z + a_4 = 0$, which can be solved in an analytical manner. First the two quantities are computed:

$$Q = \frac{A^2 - 3B}{9}, \qquad R = \frac{2A^3 - 9AB + 27C}{54}. \tag{A.0.1}$$

Where $A = a_2/a_1$, $B = a_3/a_1$ and $C = a_4/a_1$. Then a decision is made out of the sign of the quantity $Q^3 - R^2$:

- if $Q^3 - R^2 < 0$, the cubic equation has only one real root:

$$Z = -sign(R)\left\{\left[(R^2 - Q^3)^{1/2} + |R|\right]^{1/3} + \frac{Q}{\left[(R^2 - Q^3)^{1/2} + |R|\right]^{1/3}}\right\} - \frac{A}{3}, \tag{A.0.2}$$

- if $Q^3 - R^2 \geq 0$, three distinct real roots occur:

$$Z_1 = -2\sqrt{Q}\cos\left(\frac{\theta}{3}\right) - \frac{A}{3}, \tag{A.0.3}$$

$$Z_2 = -2\sqrt{Q}\cos\left(\frac{\theta + 2\pi}{3}\right) - \frac{A}{3}, \tag{A.0.4}$$

$$Z_3 = -2\sqrt{Q}\cos\left(\frac{\theta + 4\pi}{3}\right) - \frac{A}{3}, \tag{A.0.5}$$

$$\theta = \arccos\left(\frac{R}{Q^{3/2}}\right). \tag{A.0.6}$$

Given the fact that the middle root Z_2 corresponds to an unstable state [46] we re-define: $Z_1 = \text{MAX}(Z_1, Z_3)$ and $Z_2 = \text{MIN}(Z_1, Z_3)$. At this point, the following distinctions must be made:

- if this is a phase structure calculation, such as that required for Algorithm 1 in Appendix D, the choice of the correct value of Z is made based on the known phase that is being solved for. If this is a liquid ($\eta = L$) calculation, then $Z = Z_2$, while if this is a vapor ($\eta = V$) calculation, then $Z = Z_1$. Note that all coefficients a_1-a_4 need to be computed in the specific phase η;

- if this is a direct calculation of the mixture compressibility using the single-fluid assumption, the choice is made based on the mixing Gibbs free energy [49]. By defining the quantity:

$$\frac{\Delta G_{mix}}{R_u T} = \sum_{i=1}^{N_s} X_i \left(\ln f_i(T, p, \mathbf{X})|_{Z=Z_2} - \ln f_i(T, p, \mathbf{X})|_{Z=Z_1} \right) . \tag{A.0.7}$$

  Where f_i are the species fugacities calculated using their respective fugacity coefficient in Eq. (2.2.30), using either the liquid or the vapor compressibility, wherever it is required in the formulas. If $\Delta G_{mix}/R_u T \geq 0$, the vapor solution is chosen: $Z = Z_1$ and the mixture is considered in the vapor state, otherwise, the liquid solution is chosen: $Z = Z_2$ and the mixture is considered in the liquid state. This means that the mixture is always going to be made of a single phase and no VLE is possible to predict with this approach.

Appendix B

MOLE NUMBER TO MOLE FRACTION DERIVATIVE CONVERSION

Let $M = M(T, p, \mathbf{X})$ a generic thermodynamic variable that depends on $N_s + 2$ state variables, say temperature, pressure and species mole fractions. The same dependency can be expressed in terms of number of moles: $M = M(T, p, \mathbf{N})$. Here $\mathbf{X} = \{X_i \,|\, i = 1, \cdots, N_s\}$ and $\mathbf{N} = \{N_i \,|\, i = 1, \cdots, N_s\}$. Since by definition $X_i = N_i/N$ where $N = \sum_{j=1}^{N_s} N_j$, every mole number is independent of each other, whereas every mole fraction is not. This leads to the trivial conclusion that $X_j = X_j(\mathbf{N})$ for each j. As a result, variation of a single mole number has the consequence to modify all species mole fractions. That is, after writing the total differential of $M = M(T, p, \mathbf{X}(\mathbf{N}))$ and setting both T and p constant, one gets:

$$\left(\frac{\partial M}{\partial N_i}\right)_{T,p,\mathbf{N}_i} = \sum_{j=1}^{N_s} \left(\frac{\partial M}{\partial X_j}\right)_{T,p,\mathbf{X}_j} \left(\frac{\partial X_j}{\partial N_i}\right)_{\mathbf{N}_i} . \tag{B.0.1}$$

The second term in parenthesis can be further manipulated as follows:

$$\left(\frac{\partial X_j}{\partial N_i}\right)_{\mathbf{N}_i} = \left(\frac{\partial N_j/N}{\partial N_i}\right)_{\mathbf{N}_i} = \frac{\frac{\partial N_j}{\partial N_i} N - N_j \frac{\partial \left(\sum_{k=1}^{N_s} N_k\right)}{\partial N_i}}{N^2} = \cancel{1}$$
$$= \frac{\delta_{ji} N - N_j}{N^2} = \frac{\delta_{ji} - X_j}{N} . \tag{B.0.2}$$

As a result, Eq. (B.0.1) writes:

$$\left(\frac{\partial M}{\partial N_i}\right)_{T,p,\mathbf{N}_i} = \sum_{j=1}^{N_s} \left(\frac{\partial M}{\partial X_j}\right)_{T,p,\mathbf{X}_j} \frac{\delta_{ji} - X_j}{N} . \tag{B.0.3}$$

Appendix C

PHYSICAL MEANING OF THE "FROZEN" VLE ASSUMPTION

In this appendix, we provide some details regarding the meaning of the "frozen" VLE assumption. First we begin with the derivative of the mixture density with respect to the temperature. Starting from Eq. (2.2.49) and using the fact that by assumption $(\partial\beta/\partial T)_{p,\mathbf{X}} = (\partial M^V/\partial T)_{p,\mathbf{X}} = (\partial M^L/\partial T)_{p,\mathbf{X}} = 0$ one obtains the following:

$$\left(\frac{\partial\rho}{\partial T}\right)_{p,\mathbf{X}} = \frac{\rho^2}{M}\left[\frac{\beta}{\rho^{V^2}}M^V\left(\frac{\partial\rho^V}{\partial T}\right)_{p,\mathbf{X}} + \frac{1-\beta}{\rho^{L^2}}M^L\left(\frac{\partial\rho^L}{\partial T}\right)_{p,\mathbf{X}}\right]. \tag{C.0.1}$$

Note that it is not possible to completely separate the liquid portion from the vapor portion (thus writing the derivative in the form $\Sigma = \beta\Sigma^V + (1-\beta)\Sigma^L$) because of ρ as in Eq. (2.2.34). As a result, an intrinsic non-linearity remains between the two phases for this specific term. Next, we consider the specific heat at constant pressure. Starting from Eq. (2.2.38) and applying the frozen VLE conditions gives:

$$C_p = \beta\left(\frac{\partial E^V}{\partial T}\right)_{p,\mathbf{X}} + (1-\beta)\left(\frac{\partial E^L}{\partial T}\right)_{p,\mathbf{X}} - \frac{pM}{\rho^2}\left(\frac{\partial\rho}{\partial T}\right)_{p,\mathbf{X}}. \tag{C.0.2}$$

Using the result of Eq. (F.0.1) and rearranging, one can easily verify the following steps:

$$\begin{aligned}
C_p =& \beta\left[\left(\frac{\partial E^V}{\partial T}\right)_{p,\mathbf{X}} + pM^V\frac{\partial}{\partial T}\left(\frac{1}{\rho^V}\right)_{p,\mathbf{X}}\right] + (1-\beta)\left[\left(\frac{\partial E^L}{\partial T}\right)_{p,\mathbf{X}} + pM^L\frac{\partial}{\partial T}\left(\frac{1}{\rho^L}\right)_{p,\mathbf{X}}\right] = \\
=& \beta\frac{\partial}{\partial T}\left(E^V + \frac{pM^V}{\rho^V}\right)_{p,\mathbf{X}} + (1-\beta)\frac{\partial}{\partial T}\left[E^L + \frac{pM^L}{\rho^L}\right]_{p,\mathbf{X}} = \\
=& \beta\left(\frac{\partial H^V}{\partial T}\right)_{p,\mathbf{X}} + (1-\beta)\left(\frac{\partial H^L}{\partial T}\right)_{p,\mathbf{X}} = \\
=& \beta C_p^V + (1-\beta)C_p^L,
\end{aligned} \tag{C.0.3}$$

which is exactly the approach used in [169].

Using analogous concepts, the isothermal compressibility and the isobaric expansivity are obtained in the frozen VLE regime:

$$\alpha_p = -\frac{\rho}{M}\left[\frac{\beta}{\rho^{V^2}}M^V\left(\frac{\partial\rho^V}{\partial T}\right)_{p,\mathbf{X}} + \frac{1-\beta}{\rho^{L^2}}M^L\left(\frac{\partial\rho^L}{\partial T}\right)_{p,\mathbf{X}}\right]. \tag{C.0.4}$$

$$\kappa_T = \frac{\rho}{M}\left[\frac{\beta}{\rho^{V^2}}M^V\left(\frac{\partial\rho^V}{\partial p}\right)_{T,\mathbf{X}} + \frac{1-\beta}{\rho^{L^2}}M^L\left(\frac{\partial\rho^L}{\partial p}\right)_{T,\mathbf{X}}\right]. \tag{C.0.5}$$

Next, the isentropic compressibility is still computed with Eq. (2.2.22) and the speed of sound with Eq. (2.2.23). Note that a lot of non-linearities are retained even with the frozen assumption. This is mainly due to the density factor that pre-multiplies the terms representing each phase separately.

In is finally interesting to determine further insights on the speed of sound, and particularly on the way it is approximated with the classical Wood's equation [242]. First, Eq. (C.0.4) and Eq. (C.0.5) need to be further simplified and forced to be represented by a pure linear composition between the terms in each phase. To do so, we have to imagine to decompose the density factor and eliminate the non-linear terms. Note this is not possible explicitly (easy to verify) and therefore this represents a strong assumption. In such a case, the above quantities become:

$$\alpha_p \approx -\left[\frac{\beta}{\rho^V}\frac{M^V}{M}\left(\frac{\partial\rho^V}{\partial T}\right)_{p,\mathbf{X}} + \frac{1-\beta}{\rho^L}\frac{M^L}{M}\left(\frac{\partial\rho^L}{\partial T}\right)_{p,\mathbf{X}}\right] = \beta\alpha_p^V + (1-\beta)\alpha_p^L. \tag{C.0.6}$$

$$\kappa_T \approx \left[\frac{\beta}{\rho^V}\frac{M^V}{M}\left(\frac{\partial\rho^V}{\partial p}\right)_{T,\mathbf{X}} + \frac{1-\beta}{\rho^L}\frac{M^L}{M}\left(\frac{\partial\rho^L}{\partial p}\right)_{T,\mathbf{X}}\right] = \beta\kappa_T^V + (1-\beta)\kappa_T^L. \tag{C.0.7}$$

Next, application of Eq. (2.2.22) gives:

$$\kappa_S = \beta\alpha_p^V + (1-\beta)\alpha_p^L - \frac{T}{\rho}\frac{\beta^2\alpha_p^{V,2} + (1-\beta)^2\alpha_p^{L,2} + 2\beta(1-\beta)\alpha_p^V\alpha_p^L}{\beta c_p^V + (1-\beta)c_p^L}. \tag{C.0.8}$$

Elimination of all non-linear and cross terms between the phases, forces to employ the additional strong assumption:

$$\begin{aligned}\frac{T}{\rho}\frac{\beta^2\alpha_p^{V,2} + (1-\beta)^2\alpha_p^{L,2} + 2\beta(1-\beta)\alpha_p^V\alpha_p^L}{\beta c_p^V + (1-\beta)c_p^L} &\approx \left[\beta\frac{\alpha_p^{V,2}}{\rho^V c_p^V} + (1-\beta)\frac{\alpha_p^{L,2}}{\rho^L c_p^L}\right] = \\ &= \beta\underbrace{\left(\kappa_T^V - \frac{T}{\rho^V}\frac{\alpha_p^{V,2}}{c_p^V}\right)}_{\kappa_S^V = 1/(\rho^V c^{V,2})} + (1-\beta)\underbrace{\left(\kappa_T^L - \frac{T}{\rho^L}\frac{\alpha_p^{L,2}}{c_p^L}\right)}_{\kappa_S^L = 1/(\rho^L c^{L,2})} = \\ &= \beta\kappa_S^V + (1-\beta)\kappa_S^L = \frac{\beta}{\rho^V c^{V,2}} + \frac{1-\beta}{\rho^L c^{L,2}}.\end{aligned} \tag{C.0.9}$$

Hence, using Eq. (2.2.22), the following result is obtained:

$$c^2 = \frac{1}{\rho\left(\frac{\beta}{\rho^V c^{V,2}} + \frac{1-\beta}{\rho^L c^{L,2}}\right)}\,. \tag{C.0.10}$$

which is the Wood's formula [242]. With the all discussion above, the following conclusions can be drawn:

- the frozen VLE assumption still retain some important non-linearities between the phases. Not all the quantities can be written in the linear form $\Sigma = \beta\Sigma^V + (1-\beta)\Sigma^L$. This is especially true for the speed of sound;
- if the frozen speed of sound is further simplified by eliminating all non-linear terms and forcing all the intermediate quantities to behave only linearly, the Wood's equation is retrieved. In these conditions, the only information about VLE is encapsulated in the values of β, x_i and y_i. Hence, there is no surprise about the poor agreement that this correlation is known to exhibit [139].

Appendix D

ALGORITHMS FOR THE PRESENT THERMODYNAMIC MODEL

Algorithm 1 generateVLstructure(T,p,$\boldsymbol{\zeta}$,η)

1: **Inputs:** T, p, $\boldsymbol{\zeta} \leftarrow \mathbf{x}$ if $\eta = L$ or $\boldsymbol{\zeta} \leftarrow \mathbf{y}$ if $\eta = V$
2: **Compute phase molar mass:** $M^\eta = M^\eta(\boldsymbol{\zeta})$ with Eq. (2.2.11)
3: **Compute phase compressibility:** solve $Z^\eta = Z^\eta(T, p, \boldsymbol{\zeta}, \eta)$ see Appendix A
4: **Compute phase density:** $\rho^\eta = pM^\eta / Z^\eta R_u T$
5: **Compute phase energies:** $[E^\eta, H^\eta, S^\eta, G^\eta, A^\eta] = [E^\eta, H^\eta, S^\eta, G^\eta, A^\eta](T, p, \zeta)$ using Eqs. (2.2.12)–(2.2.16)
6: **Compute phase fugacity coefficient:** $\phi_i^\eta = \phi_i^\eta(T, p, \boldsymbol{\zeta}) \quad i = 1, \cdots, N_s$ using Eq. (2.2.30)
7: **Compute phase fugacity:** $f_i^\eta = f_i^\eta(T, p, \zeta)$ using $f_i^\eta = p\phi_i^\eta \zeta_i \quad i = 1, \cdots, N_s$

Algorithm 2 solveTP(T,p,$\mathbf{X}$)

1: **Inputs:** T, p, $\mathbf{X}$
2: **Solve VLE problem:** [β, $\mathbf{x}$, $\mathbf{y}$] =VLE($T, p, \mathbf{X}$) using Eqs. (2.2.36)–(2.2.37) Using Algorithm 11 (see also [49, 129])
3: **Obtain liquid mixture:** CALL generateVLstructure(T,p,$\mathbf{x}$,L) using Algorithm 1
4: **Obtain vapor mixture:** CALL generateVLstructure(T,p,$\mathbf{y}$,V) using Algorithm 1
5: **Compute mixture density:** ρ - Use Eq. (2.2.34)
6: **Compute mixture compressibility:** Z - Use Eq. (2.2.3) (Note M uses $\mathbf{X}$ here computed using Eq. (2.2.11))
7: **Compute mixture internal energy:** E - Use Eq. (2.2.35)
8: **Compute mixture additional energies:** H, S, G, A using their definitions (e.g. $H = E + pM/\rho$, $G = \beta G^V + (1-\beta)G^L$, $S = (H - G)/T$)

Algorithm 3 computeTPvariations(T,p,$\mathbf{X}$,β,$\mathbf{x}$,$\mathbf{y}$)

1: **Inputs:** T, p, $\mathbf{X}$, β, $\mathbf{x}$, $\mathbf{y}$
2: **Obtain liquid mixture:** CALL generateVLstructure(T,p,$\mathbf{x}$,L) using Algorithm 1
3: **Obtain vapor mixture:** CALL generateVLstructure(T,p,$\mathbf{y}$,V) using Algorithm 1
4: **Compute and store:** $\left(\frac{\partial \ln\phi_i^V}{\partial y_j}\right)_{T,p,\mathbf{X},\mathbf{y}_j}$, $\left(\frac{\partial \ln\phi_i^L}{\partial x_j}\right)_{T,p,\mathbf{X},\mathbf{x}_j}$ using specific EoS model
5: **Compute and store:** $\left(\frac{\partial \ln\phi_i^V}{\partial T}\right)_{p,\mathbf{X},\mathbf{y}}$, $\left(\frac{\partial \ln\phi_i^L}{\partial T}\right)_{p,\mathbf{X},\mathbf{x}}$ using specific EoS model
6: **Compute and store:** $\left(\frac{\partial \ln\phi_i^V}{\partial p}\right)_{T,\mathbf{X},\mathbf{y}}$, $\left(\frac{\partial \ln\phi_i^L}{\partial p}\right)_{T,\mathbf{X},\mathbf{x}}$ using specific EoS model
7: **Compute and store:** $\mathcal{A}_{ik}, b_{T,i}, b_{p,i}$ using Eqs. (K.0.23)–(K.0.25)
8: **Compute and store:** $\boldsymbol{\chi}_T, \boldsymbol{\chi}_p$ by inverting Eq. (K.0.21) and Eq. (K.0.22), respectively
9: **Compute:** all quantities in Eq. (2.2.39) using Eq. (K.0.3), Eq. (K.0.7), Eq. (K.0.8), Eqs. (K.0.16)–(K.0.18)
10: **Compute (Optional):** K_i coefficients derivatives using Eq. (K.0.9) and Eq. (K.0.19)
11: **Compute:** Derivatives of M^V and M^L using Eqs. (K.0.28)–(K.0.31)

Algorithm 4 computeAdditionalDerivatives(T,p,$\mathbf{X}$,β,$\mathbf{y}$,$\mathbf{x}$)

1: **Inputs:** T, p, $\mathbf{X}$, β, $\mathbf{y}$, $\mathbf{x}$
2: **Get basic derivatives:** CALL computeTPvariations(T,p,$\mathbf{X}$,β,$\mathbf{x}$,$\mathbf{y}$) Using Algorithm 3
3: **Compute:** CALL computeAdditionalPhaseDerivatives(T,p,$\mathbf{X}$,L,$\mathbf{x}$) Using Algorithm 5
4: **Compute:** CALL computeAdditionalPhaseDerivatives(T,p,$\mathbf{X}$,V,$\mathbf{y}$) Using Algorithm 5
5: **Compute:** $(\partial E/\partial T)_{p,\mathbf{X}}$ from Eq. (K.0.42)
6: **Compute:** $(\partial E/\partial p)_{T,\mathbf{X}}$ from Eq. (K.0.43)
7: **Compute:** $(\partial \rho/\partial T)_{p,\mathbf{X}}$ from Eq. (2.2.49)
8: **Compute:** $(\partial \rho/\partial p)_{T,\mathbf{X}}$ from Eq. (2.2.50)
9: **Compute:** $(\partial p/\partial T)_{\rho,\mathbf{X}}$ from Eq. (K.0.32)
10: **Compute:** $(\partial Z/\partial T)_{p,\mathbf{X}}$ from Eq. (K.0.40)
11: **Compute:** $(\partial Z/\partial p)_{T,\mathbf{X}}$ from Eq. (K.0.41)
12: **Compute:** α_p and κ_T from Eq. (2.2.21)
13: **Compute:** C_p from Eq. (2.2.38)
14: **Compute:** C_v from Eq. (2.2.25)
15: **Compute:** $\gamma = C_p/C_v$
16: **Compute:** κ_s from Eq. (2.2.22)
17: **Compute:** c from Eq. (2.2.23)

Note that the version of Algorithm 12 is specific for the case in which VLE is turned on. More in general, if an analytic solution in the form of Eq. (3.4.9) is not available, the same algorithm can be used for the single-phase system with the following exceptions:

Algorithm 5 computeAdditionalPhaseDerivatives(T,p,$\mathbf{X}$,η,$\boldsymbol{\zeta}$)

Inputs: T, p, $\mathbf{X}$, η, $\boldsymbol{\zeta}$, All other variables already computed in the phase η using Algorithm 3.
Get basic derivatives from the EoS : Compute $(\partial Z^\eta/\partial\zeta_k)_{T,p,\mathbf{X},\boldsymbol{\zeta}_k}$, $(\partial Z^\eta/\partial T)_{p,\mathbf{X},\boldsymbol{\zeta}}$, $(\partial Z^\eta/\partial p)_{T,\mathbf{X},\boldsymbol{\zeta}}$,
$(\partial\Delta E^\eta/\partial\zeta_k)_{T,p,\mathbf{X},\boldsymbol{\zeta}_k}$, $(\partial\Delta E^\eta/\partial T)_{p,\mathbf{X},\boldsymbol{\zeta}}$, $(\partial\Delta E^\eta/\partial p)_{T,\mathbf{X},\boldsymbol{\zeta}}$,
$(\partial p/\partial\rho^\eta)_{T,\mathbf{X},\boldsymbol{\zeta}}$, $(\partial p/\partial T)_{\rho^\eta,\mathbf{X},\boldsymbol{\zeta}}$,$(\partial\rho^\eta/\partial\zeta_k)_{T,p,\mathbf{X},\boldsymbol{\zeta}_k}$ Using an EoS model.
Compute: $(\partial\rho^\eta/\partial p)_{T,\mathbf{X},\boldsymbol{\zeta}}$ and $(\partial\rho^\eta/\partial T)_{p,\mathbf{X},\boldsymbol{\zeta}}$ from Eq. (K.0.37)
Compute: $(\partial\rho^\eta/\partial T)_{p,\mathbf{X}}$ using Eq. (K.0.34)
Compute: $(\partial\rho^\eta/\partial p)_{T,\mathbf{X}}$ using Eq. (K.0.35)
Compute: $(\partial Z^\eta/\partial T)_{p,\mathbf{X}}$ using Eq. (K.0.38)
Compute: $(\partial Z^\eta/\partial p)_{T,\mathbf{X}}$ using Eq. (K.0.39)
Compute: $C_v^{\eta,ig}=\sum_{j=1}^{N_s}\zeta_j C_{v,j}^{ig}$, ($C_{v,j}^{ig}$ precomputed using NASA or CHEMKIN polyomials)
Fetch from memory: E_k^{ig} (precomputed using NASA or CHEMKIN polyomials)
Compute: $(\partial E^\eta/\partial\zeta_k)_{T,p,\mathbf{X},\boldsymbol{\zeta}_k}$ from Eq. (K.0.46)
Compute: $(\partial E^\eta/\partial T)_{p,\mathbf{X},\boldsymbol{\zeta}}$ from Eq. (K.0.47)
Compute: $(\partial E^\eta/\partial p)_{T,\mathbf{X},\boldsymbol{\zeta}}$ from Eq. (K.0.48)
Compute: $(\partial E^\eta/\partial T)_{p,\mathbf{X}}$ from Eq. (K.0.44)
Compute: $(\partial E^\eta/\partial p)_{T,\mathbf{X}}$ from Eq. (K.0.45)

Algorithm 6 computePartialMolarVolume(T, p, $\mathbf{X}$, β, $\mathbf{x}$, $\mathbf{y}$)

Inputs: T, p, $\mathbf{X}$, β, $\mathbf{x}$, $\mathbf{y}$
Obtain liquid mixture: CALL generateVLstructure(T,p,$\mathbf{x}$,L) using Algorithm 1
Obtain vapor mixture: CALL generateVLstructure(T,p,$\mathbf{y}$,V) using Algorithm 1
Compute: CALL computeAdditionalPhaseDerivatives(T,p,$\mathbf{X}$,L,$\mathbf{x}$) Using Algorithm 5
Compute: CALL computeAdditionalPhaseDerivatives(T,p,$\mathbf{X}$,V,$\mathbf{y}$) Using Algorithm 5
for $i=1,N_s$ **do**
    if $i==1$ **then**
        Compute: Get matrix $\boldsymbol{\mathcal{C}}$ with Eq. (L.0.23) and compute its inverse $\boldsymbol{\mathcal{C}}^{-1}$
    end if
    Compute: Assemble vector $\mathbf{b}_N^{(i)}$ through Eq. (L.0.24)
    Compute and store: $\boldsymbol{\chi}_N^{(i)}$ by solving Eq. (L.0.25)
    Compute and store: $\delta_{ki}-\chi_{N,k}^{(i)}$ using Eq. (L.0.21)
end for
Compute: $(\partial\overline{V}^V/\partial N_k^V)_{T,p,\mathbf{N}_k^V}$ and $(\partial\overline{V}^L/\partial N_k^L)_{T,p,\mathbf{N}_k^L}$ using Eq. (L.0.4) and Eq. (L.0.5) for each k
Compute: $(\partial\overline{V}^V/\partial N_i)_{T,p,\mathbf{N}_i}$ and $(\partial\overline{V}^L/\partial N_i)_{T,p,\mathbf{N}_i}$ using Eq. (2.2.57) and Eq. (2.2.58) for each i
Compute: V_i using Eq. (2.2.53) for each i

Algorithm 7 computePartialMolarEnthalpy(T, p, $\mathbf{X}$, β, $\mathbf{x}$, $\mathbf{y}$)

1: **Inputs:** T, p, $\mathbf{X}$, β, $\mathbf{x}$, $\mathbf{y}$
2: **Compute:** CALL computePartialMolarVolume(T, p, $\mathbf{X}$, β, $\mathbf{x}$, $\mathbf{y}$) using Algorithm 6
3: **Compute:** Using $\boldsymbol{\chi}_N^{(i)}$, compute $(\partial\overline{E}^V/\partial N_i)_{T,p,\mathbf{N}_i}$ and $(\partial\overline{E}^L/\partial N_i)_{T,p,\mathbf{N}_i}$ from Eqs. (L.0.32)–(L.0.33)
4: **Compute:** Partial molar enthalpy H_i using Eq. (2.2.63)

- the solution of the Tp problem at line 9 can be removed;
- the CALL to Algorithm 4 for the derivatives can be replaced by the calculation of the single-phase derivative $(\partial\rho/\partial T)_{p,\mathbf{X}}$ using Eq. (2.2.86) and Eq. (2.2.87) as discussed in Sec. 2.2.3.2. Of course this approach will be less computationally expensive than the multi-phase algorithm.

Similarly to the PRHO problem, the solution of the ERHO problem of Algorithm 13 in case of a single-phase system also simplifies drastically since the functional dependency of the internal energy E on β is lost and $E = E(\hat{\rho}, T, \hat{\mathbf{X}})$, where $\hat{\rho}$ and $\hat{\mathbf{X}}$ are directly obtained from the conservatives at the end of the time integration step. Since $E(\hat{\rho}, T, \hat{\mathbf{X}}) = E^{ig}(T, \hat{\mathbf{X}}) + \Delta E(\hat{\rho}, T, \hat{\mathbf{X}})$ where ΔE is given by Eq. (2.2.77), the ERHO algorithm is essentially broken in two steps:

- solve $E = E(\hat{\rho}, T, \hat{\mathbf{X}})$ by iterating on T first. This assumes the same form as Eq. (3.4.10), where $F(T^n, \hat{\rho}, \hat{\mathbf{X}}) = E(T^n, \hat{\rho}, \hat{\mathbf{X}}) - \hat{E}$ and $(\partial F(T^n, \hat{\rho}, \hat{\mathbf{X}})/\partial T)_{\rho,\mathbf{X}}$ is determined using $(\partial E^{ig}/\partial T)_{\rho,\mathbf{X}} = c_v^{ig}$ and Eq. (M.2.1). That is, a single-variable iteration algorithm is used;
- compute $p = p(\hat{\rho}, \hat{T}, \hat{\mathbf{X}})$ using Eq. (2.2.67).

The above, is the same approach used for TPG mixtures.

Algorithm 8 [β, $\mathbf{x}$, $\mathbf{y}$, flag]=SSI(T,p,$\mathbf{X}$,ϵ_{VLE},N_{max},$\mathbf{K} = K_i$)

Inputs: T, p, $\mathbf{X}$, ϵ_{VLE}, N_{max}, $\mathbf{K} = K_i$
! Main loop
while $\varepsilon > \epsilon_{VLE}$ **do**
    iter = iter + 1
    ! Check on the maximum number of iterations
    if iter == N_{max} **then**
        Exit
    end if
    ! Check if this is a single phase mixture according to [129]
    if $(\sum_{i=1}^{N_s} X_i K_i - 1 \leq 0)$ **then**
        ! This mixture is pure liquid
        $\beta = 0$, $\mathbf{x} = \mathbf{X}$, $\mathbf{y} = 0$
        flag $= -1$
        Exit
    else if $(1 - \sum_{i=1}^{N_s} X_i/K_i > 0)$ **then**
        ! This mixture is pure vapor
        $\beta = 1$, $\mathbf{y} = \mathbf{X}$, $\mathbf{x} = 0$
        flag $= -1$
        Exit
    else
        ! This mixture has VLE
        Compute: β from Eq. (2.2.37) using Newton or bisection (or combined) method. See [129].
        Compute: $\mathbf{x}$ using Eq. (3.4.2)
        Compute: $\mathbf{y}$ using Eq. (3.4.3)
        flag $= 1$
    end if
    ! If VLE exists, compute fugacity and check the error
    Obtain liquid mixture: CALL generateVLstructure(T,p,$\mathbf{x}$,L) using Algorithm 1
    Obtain vapor mixture: CALL generateVLstructure(T,p,$\mathbf{y}$,V) using Algorithm 1
    Compute: Update the error according to Eq. (2.2.36): $\varepsilon = ||\ln K_i - \ln\phi_i^L + \ln\phi_i^V||$
    Compute: Update coefficients K_i for the next iteration (if it occurs): $K_i = \phi_i^L/\phi_i^V$, $i = 1, \cdots, N_s$
    Outputs: β, $\mathbf{x}$, $\mathbf{y}$, flag
end while

Algorithm 9 [**K**,nphases]=StabilityAnalysis(T,p,**X**,ϵ_{TPD},**d** = d_i,**K** = K_i)

Inputs: T, p, **X**, ϵ_{TPD}, N_{max}, d_i, K_i
$n = 0$
$\mathbf{K}^0 = \mathbf{K}$
! Run the vapor-like trial phase
$\zeta_i^V = K_i^0 X_i$
$\zeta_i^V = \zeta_i^V / \mathrm{SUM}(\zeta_\mathrm{i}^\mathrm{L})$! This normalization is required
Compute: Update $\boldsymbol{\zeta}^V$, TPD^V, nphases-V:
CALL UpdateTrialComposition(T,p,**X**,ϵ_{TPD},**d** = d_i,V,$\boldsymbol{\zeta}^V$) Using Algorithm 10

! Run the liquid-like trial phase
$\zeta_i^L = X_i / K_i^0$
$\zeta_i^L = \zeta_i^L / \mathrm{SUM}(\zeta_\mathrm{i}^\mathrm{L})$! This normalization is required
Compute: Update $\boldsymbol{\zeta}^L$, TPD^L, nphases-L:
CALL UpdateTrialComposition(T,p,**X**,ϵ_{TPD},**d** = d_i,L,$\boldsymbol{\zeta}^L$) Using Algorithm 10

! Now make the final decision based on the values of the TPD functions
if (nphases-V > 1).AND.(nphases-L > 1) **then**
    ! Both trials are unstable. Pick the one with lowest TPD function value.
    if TPD$^V <$ TPD^L **then**
        ! gas-like mixture
        Compute: Update K_i coefficients: $\mathbf{K} = \boldsymbol{\zeta}^V / \mathbf{X}$
    else
        ! liquid-like mixture
        Compute: Update K_i coefficients: $\mathbf{K} = \mathbf{X} / \boldsymbol{\zeta}^L$
    end if
    nphases = 2
else if nphases-V > 1 **then**
    ! gas-like mixture
    Compute: Update K_i coefficients: $\mathbf{K} = \boldsymbol{\zeta}^V / \mathbf{X}$
    nphases = 2
else if nphases-L > 1 **then**
    ! liquid-like mixture
    Compute: Update K_i coefficients: $\mathbf{K} = \mathbf{X} / \boldsymbol{\zeta}^L$
    nphases = 2
else
    ! This is a trivial solution. Mixture is stable as single phase.
    Compute: Update K_i coefficients with dummy values: $\mathbf{K} = 1$
    nphases = 1
end if

Algorithm 10 [$\boldsymbol{\zeta}_f$, TPD$^\eta$, nphases]=UpdateTrialComposition(T,p,$\mathbf{X}$,ϵ_{TPD},$\mathbf{d} = d_i$,$\boldsymbol{\eta}$,$\boldsymbol{\zeta}$)

Inputs: T, p, $\mathbf{X}$, ϵ_{TPD}, d_i, $\boldsymbol{\eta}$, $\boldsymbol{\zeta}$
$n = 0$
$\boldsymbol{\zeta}^0 = \boldsymbol{\zeta}$
! Main loop
while $\varepsilon > \epsilon_{TPD}$ **do**
    $n = n + 1$
    Obtain mixture at phase η: CALL generateVLstructure(T,p,$\boldsymbol{\zeta}^n$,η) using Algorithm 1
    Compute: Update trial composition using Eq. (3.4.6): $\zeta_i^{n+1} = \exp[d_i(T, P, \mathbf{X}) - \ln\phi_i^\eta(T, p, \boldsymbol{\zeta}^n)]$
    Compute: Update error $\varepsilon = ||\zeta_i^{n+1} - \zeta_i^n||$
end while
! Now compute the TPD$^\eta$ function
Compute: TPD$^\eta(T, p, \mathbf{X}, \boldsymbol{\zeta}^{n+1})$ using Eq. (3.4.4)
! Determine if this is a trivial solution
trivial =.FALSE.
if $||\boldsymbol{\zeta}^{n+1} - \mathbf{X}|| < 1e^{-5}$ **then**
    trivial =.TRUE.
end if
if (TPD$^\eta < 0$).AND.(trivial == .FALSE.) **then**
    ! VLE esists
    nphases = 2
else
    ! This is a trivial solution
    nphases = 1
end if
! Declare output
$\boldsymbol{\zeta}_f = \boldsymbol{\zeta}^{n+1}$

Algorithm 11 [β, $\mathbf{x}$, $\mathbf{y}$]=VLE(T,p,$\mathbf{X}$)

Inputs: T, p, $\mathbf{X}$
Compute: Solve single-phase state $Z = Z(T, p, \mathbf{X})$. Use min. Gibbs energy method (see Appendix A)
Compute: single-phase mixture density using $\rho = pM/ZR_uT$, $M = M(\mathbf{X})$ from Eq. (2.2.11)
Compute: single-phase mixture fugacity coefficient $\phi_i = \phi_i(T, p, \mathbf{X}) \quad i = 1, \cdots, N_s$ using Eq. (2.2.30)
Compute: $\mathbf{d} = d_i = \ln X_i + \ln\phi_i(T, P, \mathbf{X}) \quad i = 1, \cdots, N_s$
Compute: Estimate K_i coefficients for each species i, using Eq. (3.4.1)
Run SSI: for 3 steps:[β, $\mathbf{x}$, $\mathbf{y}$, flag]=SSI(T,p,$\mathbf{X}$,ϵ_{VLE},3,$\mathbf{K} = K_i$). Use Algorithm 8
Run stability analysis: [$\mathbf{K}$,nphases]=StabilityAnalysis(T,p,$\mathbf{X}$,ϵ_{TPD},$\mathbf{d} = d_i$,$\mathbf{K} = K_i$). Use Alg. 9
! The above stability test can be done even if SSI returns a single-phase system using K_i from Eq. (3.4.1)
if (flag== -1).AND.(nphases == 1) **then**
    ! both SSI and stability test agree that the system is single phase
    ! it is safe to use output from SSI
else
    ! SSI and stability analysis do not agree
    ! Run SSI again with larger N_{max} and use K_i estimation from stability analysis
    Run SSI: [β, $\mathbf{x}$, $\mathbf{y}$, flag]=SSI(T,p,$\mathbf{X}$,ϵ_{VLE},N_{max},$\mathbf{K} = K_i$). Use Algorithm 8
end if
Outputs: β, $\mathbf{x}$, $\mathbf{y}$

Algorithm 12 $[T,\ \beta,\ x,\ y]$ = solvePRHO(p,ρ,$\mathbf{X}$, N_{max}, ϵ_{PR}, ΔT_{max} T_0, p_0, λ_0)

Inputs: p, ρ, $\mathbf{X}$, N_{max}, ϵ_{PR}, ΔT_{max}, T_0
$n = 0$
! Initialize the temperature guess and the known value of density
$T^1 = T_0$
$\hat{\rho} = \rho$
! Main loop
while $(\varepsilon > \epsilon_{pr})$.AND.$(n \leq N_{max})$ **do**
    $n = n + 1$! Update iteration count
    Solve the Tp **problem (this gives** β**,** x**,** y**):** CALL solveTP(T^n,p,$\mathbf{X}$) using Algorithm 2
    ! Get all the mixture derivatives
    Compute: CALL computeAdditionalDerivatives(T,p,$\mathbf{X}$,β,y,x) using Algorithm 4
    ! Update objective function and its derivative
    Compute: $F = \rho - \hat{\rho}$, $(\partial F/\partial T)_{p,\mathbf{X}} = (\partial \rho/\partial T)_{p,\mathbf{X}}$
    Declare: $\varepsilon = F$
    ! Update unknown
    Compute: T^{n+1} using Eq. (3.4.10) and compute $\Delta T = T^{n+1} - T^n$

    Optional: ! Temperature update can be done using a line-search method
    Compute: $\lambda = \text{MIN}(\lambda_0, \text{ABS}(\Delta T_{max}/\Delta T)), \qquad \lambda_0 \in (0, 1]$
    ! Update temperature using a modified version of Eq. (3.4.10):
    Compute: $T^{n+1} = T^n - \lambda F/F'$
    ---
end while
Outputs: T, β, $\mathbf{x}$, $\mathbf{y}$

Algorithm 13 $[T,\ p,\ \beta,\ x,\ y]$ = solveERHO(E,ρ,$\mathbf{X}$, N_{max}, ϵ_{ER}, ΔT_{max}, Δp_{max}, T_0, p_0, λ_0)

Inputs: E, ρ, $\mathbf{X}$, N_{max}, ϵ_{ER}, ΔT_{max}, Δp_{max}, T_0, p_0, λ_0
$n = 0$
! Initialize the temperature and pressure guess and the known values
$T^1 = T_0$
$p^1 = p_0$
$\hat{E} = E$
$\hat{\rho} = \rho$
! Main loop
while $(\varepsilon > \epsilon_{ER})$.AND.$(n \leq N_{max})$ **do**
    $n = n + 1$! Update iteration count
    Solve the Tp **problem (this gives** β**,** x**,** y**,** E**,** ρ**):** CALL solveTP(T^n,p^n,$\mathbf{X}$) using Algorithm 2
    ! Get all the mixture derivatives
    Compute: CALL computeAdditionalDerivatives(T,p,$\mathbf{X}$,β,y,x) using Algorithm 4
    ! Update objective function and its derivative
    Compute: $F_1 = E - \hat{E}$, $(\partial F_1/\partial T)_{p,\mathbf{X}} = (\partial E/\partial T)_{p,\mathbf{X}}$, $(\partial F_1/\partial p)_{T,\mathbf{X}} = (\partial E/\partial p)_{T,\mathbf{X}}$
    Compute: $F_2 = \rho - \hat{\rho}$, $(\partial F_2/\partial T)_{p,\mathbf{X}} = (\partial \rho/\partial T)_{p,\mathbf{X}}$, $(\partial F_2/\partial p)_{T,\mathbf{X}} = (\partial \rho/\partial p)_{T,\mathbf{X}}$
    ! Assemble Jacobian and compute variations
    Compute: $\boldsymbol{\mathcal{J}}$ from Eq. (3.4.11) and compute its inverse $\boldsymbol{\mathcal{J}}^{-1}$
    Compute: $(\Delta T \quad \Delta p)^T = -\boldsymbol{\mathcal{J}}^{-1}(F_1 \quad F_2)^T$
    Declare: $\varepsilon = ||F_1^2 + F_2^2||$ or $\varepsilon = \text{ABS}(\Delta T) + \text{ABS}(\Delta p)$
    ! Update unknowns
    Compute: $T^{n+1} = T^n + \Delta T$, $p^{n+1} = p^n + \Delta p$

    Optional: ! Temperature/pressure update can be done using a line-search method
    Compute: $\lambda = \text{MIN}(\lambda_0, \text{ABS}(\Delta T_{max}/\Delta T), \text{ABS}(\Delta p_{max}/\Delta p)), \qquad \lambda_0 \in (0, 1]$
    ! Update temperature/pressure :
    Compute: $T^{n+1} = T^n - \lambda \Delta T$
    Compute: $p^{n+1} = p^n - \lambda \Delta p$
    ---
end while
Outputs: T, p, β, $\mathbf{x}$, $\mathbf{y}$

Algorithm 14 computeNumericalDerivatives(T, p, ρ, $\mathbf{X}$, $\mathbf{x}$, $\mathbf{y}$, β, ΔT_ϵ, Δp_ϵ, ϵ_s)

Inputs: T, p, $\mathbf{X}$, $\mathbf{x}$, $\mathbf{y}$, β, ΔT_ϵ, Δp_ϵ, ϵ_s
! Once the VLE problem is solved, first compute all properties that do not require derivatives
Obtain liquid mixture: CALL generateVLstructure(T,p,$\mathbf{x}$,L) using Algorithm 1
Obtain vapor mixture: CALL generateVLstructure(T,p,$\mathbf{y}$,V) using Algorithm 1
Compute mixture density: ρ - Use Eq. (2.2.34)
Compute mixture compressibility: Z - Use Eq. (2.2.3) (Note M uses $\mathbf{X}$ here computed using Eq. (2.2.11))
Compute mixture internal energy: E - Use Eq. (2.2.35)
Compute mixture additional energies: H, S, G, A using their definitions (e.g. $H = E + pM/\rho$)
! perturb the temperature forward and keep pressure constant
! define a local value of β, i.e. β^+ to check whether the perturbed state goes outside the dome
Define: $\beta^+ = 0$
Define: $\Delta T = \Delta T_\epsilon$
while $(\beta^+ = 0).\text{OR}.(\beta^+ = 1)$ **do**
    ! perturb temperature
    Compute: $T^+ = T + \Delta T$
    ! reduce the temperature in case we loop again
    Compute: $\Delta T = \Delta T/2$
    ! solve the perturbed Tp problem
    Run: CALL solveTP(T^+,p,$\mathbf{X}$) using Algorithm 2
    ! the above provides all the properties in the perturbed state $(\cdot)^+$,
    ! including a new value of β^+ for the exit condition
end while
Store: $\Delta T^+ = 2\Delta T$
! perturb the temperature backward and keep pressure constant
! define a local value of β, i.e. β^- to check whether the perturbed state goes outside the dome
Define: $\beta^- = 0$
Define: $\Delta T = \Delta T_\epsilon$
while $(\beta^- = 0).\text{OR}.(\beta^- = 1)$ **do**
    ! perturb temperature
    Compute: $T^- = T - \Delta T$
    ! reduce the temperature in case we loop again
    Compute: $\Delta T = \Delta T/2$
    ! solve the perturbed Tp problem
    Run: CALL solveTP(T^-,p,$\mathbf{X}$) using Algorithm 2
    ! the above provides all the properties in the perturbed state $(\cdot)^-$,
    ! including a new value of β^- for the exit condition
end while
Store: $\Delta T^- = -2\Delta T$
! Compute the sensor for both E and H
Compute: $S_E = \text{computeSensor}(E, E^+, E^-, \Delta T^+, \Delta T^-)$ using Eq. (3.4.15)
Compute: $S_H = \text{computeSensor}(H, H^+, H^-, \Delta T^+, \Delta T^-)$ using Eq. (3.4.15)
! Continue

Continue Algorithm 14

! Now compute the first set of derivatives
if MAX(S_E,S_H)> ϵ_s **then**
    ! Use upwind differentiation based on the last value of the perturbed β
    Declare: sensor $= -1$
    if $\beta^- > \beta$ **then**
        ! With lower T solution goes towards more gas, use backward
        Compute: $c_p = (H - H^-)/(-\Delta T^-)$
        Compute: $\alpha_p = \rho(1/\rho - 1/\rho^-)/(-\Delta T^-)$
        Compute: $(\partial\beta/\partial T)_p = (\beta - \beta^-)/(-\Delta T^-)$
        Compute: $(\partial\rho/\partial T)_p = (\rho - \rho^-)/(-\Delta T^-)$
        ! Compute everything else in the same way
    else
        Declare: sensor $= 1$
        ! With lower T solution goes towards more liquid, use forward
        Compute: $c_p = (H^+ - H)/(\Delta T^+)$
        Compute: $\alpha_p = \rho(1/\rho^+ - 1/\rho)/(\Delta T^+)$
        Compute: $(\partial\beta/\partial T)_p = (\beta^+ - \beta)/(\Delta T^+)$
        Compute: $(\partial\rho/\partial T)_p = (\rho^+ - \rho)/(\Delta T^+)$
        ! Compute everything else in the same way
    end if
else
    ! Use central differentiation
    Declare: sensor $= 0$
    Compute: $c_p = (H^+ - H^-)/(\Delta T^+ - \Delta T^-)$
    Compute: $\alpha_p = \rho(1/\rho^+ - 1/\rho^-)/(\Delta T^+ - \Delta T^-)$
    Compute: $(\partial\beta/\partial T)_p = (\beta^+ - \beta^-)/(\Delta T^+ - \Delta T^-)$
    Compute: $(\partial\rho/\partial T)_p = (\rho^+ - \rho^-)/(\Delta T^+ - \Delta T^-)$
    ! Compute everything else in the same way
end if
! perturb the pressure forward and keep temperature constant
! define a local value of β, i.e. β^+ to check whether the perturbed state goes outside the dome
Define: $\beta^+ = 0$
Define: $\Delta p = \Delta p_\epsilon$
while $(\beta^+ = 0)$.OR.$(\beta^+ = 1)$ **do**
    ! perturb pressure
    Compute: $p^+ = p + \Delta p$
    ! reduce the pressure in case we loop again
    Compute: $\Delta p = \Delta p/2$
    ! solve the perturbed Tp problem
    Run: CALL solveTP(T,p^+,**X**) using Algorithm 2
    ! the above provides all the properties in the perturbed state $(\cdot)^+$,
    ! including a new value of β^+ for the exit condition
end while
! Continue

Continue Algorithm 14

Store: $\Delta p^+ = 2\Delta p$
! perturb the pressure backward and keep temperature constant
! define a local value of β, i.e. β^- to check whether the perturbed state goes outside the dome
Define: $\beta^- = 0$
Define: $\Delta p = \Delta p_\epsilon$
while $(\beta^- = 0).\text{OR}.(\beta^- = 1)$ **do**
    ! perturb pressure
    Compute: $p^- = p - \Delta p$
    ! reduce the pressure in case we loop again
    Compute: $\Delta p = \Delta p/2$
    ! solve the perturbed Tp problem
    Run: CALL solveTP(T,p^-,$\mathbf{X}$) using Algorithm 2
    ! the above provides all the properties in the perturbed state $(\cdot)^-$,
    ! including a new value of β^- for the exit condition
end while
Store: $\Delta p^- = -2\Delta p$
! Now compute the second set of derivatives
if sensor== -1 **then**
    Compute: $\kappa_T = -\rho(1/\rho - 1/\rho^-)/(-\Delta p^-)$
    Compute: $(\partial\beta/\partial p)_T = (\beta - \beta^-)/(-\Delta p^-)$
    Compute: $(\partial\rho/\partial p)_T = (\rho - \rho^-)/(-\Delta p^-)$
    ! Compute everything else in the same way
else if sensor== 1 **then**
    Compute: $\kappa_T = -\rho(1/\rho^+ - 1/\rho)/(\Delta p^+)$
    Compute: $(\partial\beta/\partial p)_T = (\beta^+ - \beta)/(\Delta p^+)$
    Compute: $(\partial\rho/\partial p)_T = (\rho^+ - \rho)/(\Delta p^+)$
    ! Compute everything else in the same way
else if sensor== 0 **then**
    ! Use central differentiation
    Compute: $\kappa_T = -\rho(1/\rho^+ - 1/\rho^-)/(\Delta p^+ - \Delta p^-)$
    Compute: $(\partial\beta/\partial p)_T = (\beta^+ - \beta^-)/(\Delta p^+ - \Delta p^-)$
    Compute: $(\partial\rho/\partial p)_T = (\rho^+ - \rho^-)/(\Delta p^+ - \Delta p^-)$
    ! Compute everything else in the same way
end if
! Compute other derivated properties
Compute: c_v using Eq. (2.2.25) and $(\partial p/\partial T)_\rho$ using Eq. (2.2.21)
Compute: $\gamma = c_p/c_v$
Compute: κ_s using Eq. (2.2.22)
Compute: c using Eq. (2.2.23)
Compute: V_k and h_k using Eqs. (3.4.16)–(3.4.17)

Appendix E

MAXWELL CRITERION AND ANTOINE'S EQUATION

The Maxwell criterion is based on the concept of "equal area" rule, specifically designed to handle the dome region for a single species. Figure 154 shows three different isotherms computed for nitrogen within a given interval of pressure and density. The super-critical isotherm ($T = 230\,\mathrm{K}$) is essentially an hyperbola, meaning that it follows the behavior of ideal gas. The critical isotherm at $T = T_c = 126.2$ K is still monotone however is has a strong change in the first derivative at the critical point because the species switches from liquid-like to gas-like behavior. Finally, the sub-critical isotherm ($T = 115\,\mathrm{K}$) crosses the nitrogen dome and it shows not only a change in first but also second derivative. This behavior is mathematically provided by the two terms (attraction/repulsion) appearing in the EoS, however it does not represent what physically happens in the dome as a range of pressures between values A and B in Fig. 154 are allowed to satisfy the density at the same temperature. This is not true since the dome is characterized by a constant pressure, equal to the saturation value, for the given temperature crossing the two phase region. From a VLE point of view, this is the reason why the single species Tp problem is ill-posed. A complete range of densities is in fact allowed to satisfy the same values of sub-critical temperature T and the corresponding saturation pressure $p_s = p_s(T)$, creating an undefined state. In other words there is no unique density for pressure in range of p_A and p_B that satisfy the given temperature T. It is also important to point out that the EoS is not able to provide the saturation pressure, therefore, for given T and p, multiple densities (corresponding to multiple roots in Eq. (2.2.70)) can be mathematically obtained. Maxwell's idea is to exploit the concept of phase equilibrium between liquid and gas within the dome. The equilibrium condition is expressed in terms of Gibbs free energy variation:

$$dG = V dp - S dT\,. \tag{E.0.1}$$

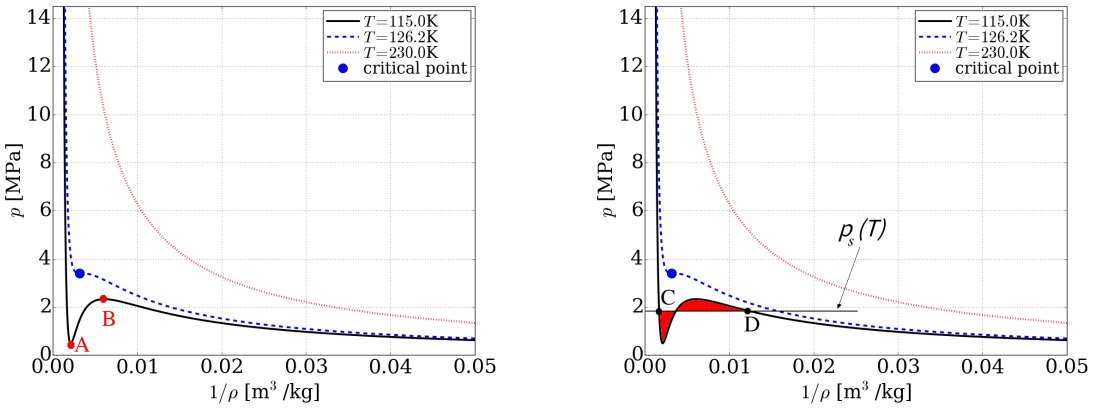

(a) (b)

Figure 154: Illustration of the Maxwell method through the "equal area" rule. (a) Three different isotherms shown for N_2: sub-critical, critical and super-critical. (b) sub-critical isotherm sliced at the corresponding saturation pressure $p_s(T)$ to create two equal areas in the VLE region.

which has to be zero across the dome to satisfy phase equilibrium. Integrating Eq. (E.0.1) along the local isotherm ($dT = 0$) the above writes (points C and D in Fig. 154(b)):

$$\int_C^D dG = \int_C^D V\,dp \qquad \rightarrow \qquad [G]_C^D = [Vp]_C^D - \int_C^D p dV\,. \tag{E.0.2}$$

Given that the Gibbs free energy variation has to be zero, the above equation becomes the definition of the Maxwell criterion:

$$p_s(V_D - V_C) = \int_C^D p dV\,. \tag{E.0.3}$$

Equation E.0.3 is true only if $p = p_s(T)$ in the integral, which geometrically corresponds to the equality of the two areas created by the saturation line on the isotherm (that is why it is called "equal area" rule). If the EoS from Eq. (2.2.67) is substituted into Eq. (E.0.3), after the integration the following expression is obtained for GCEoS:

$$p_s(V_D - V_C) = R_u T \ln\left(\frac{V_D - B_m}{V_C - B_m}\right) + \frac{A_m}{B_m(\delta_2 - \delta_1)} \ln\left[\left(\frac{V_D + B_m\delta_2}{V_C + B_m\delta_2}\right)\left(\frac{V_C + B_m\delta_1}{V_B + B_m\delta_1}\right)\right], \tag{E.0.4}$$

where $V_j = Z_j R_u T/p$ is the molar volume calculated at j condition (C or D) to close the problem. Using Eq. (E.0.4), the saturation pressure can be computed and compared to the actual value of pressure, assuming that a $T\rho$ or Tp problem are being solved. If $p > p_s$

the liquid root is chosen, otherwise the vapor root is chosen. Note, this method does not allow to solve any VLE problem inside the dome as a single phase will be always resulted. Additionally this method matches with the minimum Gibbs criterion of Appendix A for a single species.

Another (easier) method to predict the saturation pressure for a single species is the Antoine's equation. This is a more empirical relationship that can be used in the same way as the Clausius-Clapeyron equation[46].

$$\log_{10} p_c(T) = A - \frac{B}{T + C}\,. \tag{E.0.5}$$

Where T is the temperature and A, B, C are species-dependent constants, usually tuned for specific ranges of temperatures. A good list of these is given in [163].

Appendix F

OBTAIN C_1, C_2, C_3 AND C_4 FOR PR/MR-1 COMBINATION

Starting from the definition of A_m and α_i for PR/MR-1 combination (see Tab. 3 and Tab. 4):

$$
\begin{aligned}
A_m &= \sum_{i=1}^{N_s}\sum_{j=1}^{N_s} X_i X_j (1-k_{ij})\sqrt{A_i A_j}\sqrt{\alpha_i \alpha_j} = \\
&\qquad \Big\downarrow \\
&\qquad \text{Using the definition of } \alpha_i \text{ for PR in Tab. 2} \\
&= \sum_{i=1}^{N_s}\sum_{j=1}^{N_s} X_i X_j (1-k_{ij})\sqrt{A_i A_j}\left\{\left[1+f_i\left(1-\sqrt{\frac{T}{T_{c,i}}}\right)\right]^2\left[1+f_j\left(1-\sqrt{\frac{T}{T_{c,j}}}\right)\right]^2\right\}^{1/2} = \\
&= \sum_{i=1}^{N_s}\sum_{j=1}^{N_s} X_i X_j (1-k_{ij})\sqrt{A_i A_j}\left[1+f_i\left(1-\sqrt{\frac{T}{T_{c,i}}}\right)\right]\left[1+f_j\left(1-\sqrt{\frac{T}{T_{c,j}}}\right)\right] = \\
&= \sum_{i=1}^{N_s}\sum_{j=1}^{N_s} X_i X_j (1-k_{ij})\sqrt{A_i A_j}\left(1+f_i-f_i\sqrt{\frac{T}{T_{c,i}}}\right)\left(1+f_j-f_j\sqrt{\frac{T}{T_{c,j}}}\right) = \\
&= \sum_{i=1}^{N_s}\sum_{j=1}^{N_s} X_i X_j (1-k_{ij})\sqrt{A_i A_j}\left[(1+f_i+f_j+f_i f_j)-f_j(1+f_i)\sqrt{\frac{T}{T_{c,j}}}+\right. \\
&\quad \left.-f_i(1+f_j)\sqrt{\frac{T}{T_{c,i}}}+\frac{f_i f_j}{\sqrt{T_{c,i}T_{c,j}}}T\right] = \\
&= \underbrace{\sum_{i=1}^{N_s}\sum_{j=1}^{N_s} X_i X_j (1-k_{ij})\sqrt{A_i A_j}\,(1+f_i+f_j+f_i f_j)}_{=c_1} + \\
&\quad + \underbrace{\sqrt{T}}_{c_4=1/2}\underbrace{\left[-\sum_{i=1}^{N_s}\sum_{j=1}^{N_s} X_i X_j (1-k_{ij})\sqrt{A_i A_j}\frac{f_j(1+f_i)}{\sqrt{T_{c,j}}}-\sum_{i=1}^{N_s}\sum_{j=1}^{N_s} X_i X_j (1-k_{ij})\sqrt{A_i A_j}\frac{f_i(1+f_j)}{\sqrt{T_{c,i}}}\right]}_{=-\sum_{i=1}^{N_s}\sum_{j=1}^{N_s} X_i X_j (1-k_{ij})\sqrt{A_i A_j}\left[\frac{f_j(1+f_i)}{\sqrt{T_{c,j}}}+\frac{f_i(1+f_j)}{\sqrt{T_{c,i}}}\right]=c_2} + \\
&\quad + T\underbrace{\sum_{i=1}^{N_s}\sum_{j=1}^{N_s} X_i X_j (1-k_{ij})\sqrt{A_i A_j}\frac{f_i f_j}{\sqrt{T_{c,i}T_{c,j}}}}_{c_3} .
\end{aligned}
\tag{F.0.1}
$$

Appendix G

ACCESSORY DERIVATIVES FOR THE DETERMINATION OF THE FUGACITY COEFFICIENT

First, we derive the term $(\partial N^2 A_m/\partial N_i)_{\mathbf{N}_i}$. Independently of the mixing rule, the generic form of A_m can be written are $A_m = \sum_{i=1}^{N_s}\sum_{j=1}^{N_s} X_i X_j A_{ij}$, where A_{ij} is a short form to indicate any possible A_i, A_j (as well as α_i and α_j where applicable) groups for each mixing rule listed in Tab. 3. For example for MR-1 $A_{ij} = \sqrt{A_i A_j \alpha_i \alpha_j}(1-k_{ij})$ (see also Tab. 12).

$$
\begin{aligned}
\left(\frac{\partial N^2 A_m}{\partial N_i}\right)_{\mathbf{N}_i} =& \frac{\partial}{\partial N_i}\left(N^2 \sum_{i=1}^{N_s}\sum_{j=1}^{N_s} X_i X_j A_{ij}\right)_{T,\mathbf{N}_i} \overset{\text{by definition } N_i = X_i N}{\downarrow} = \\
=& \frac{\partial}{\partial N_i}\Big[N_1^2 A_{11} + N_2 N_1 A_{21} + N_3 N_1 A_{31} + \cdots + N_i N_1 A_{i1} + \cdots + N_{N_s} N_1 A_{N_s 1} + \\
& + N_1 N_2 A_{12} + N_2^2 A_{22} + N_3 N_2 A_{32} + \cdots + N_i N_2 A_{i2} + \cdots + N_{N_s} N_2 A_{N_s 2} + \\
& + N_1 N_3 A_{13} + N_2 N_3 A_{23} + N_3^2 A_{33} + \cdots + N_i N_3 A_{i3} + \cdots + N_{N_s} N_3 A_{N_s 3} + \cdots + \\
& + N_1 N_i A_{i3} + N_2 N_i A_{2i} + N_3 N_i A_{2i} + \cdots + N_i^2 A_{ii} + \cdots + N_{N_s} N_i A_{N_s i} + \cdots + \\
& + N_1 N_{N_s} A_{1N_s} + N_2 N_{N_s} A_{2N_s} + N_3 N_{N_s} A_{2N_s} + \cdots + \\
& + N_i N_{N_s} A_{iN_s} + \cdots + N_{N_s}^2 A_{N_s N_s}\Big]_{T,\mathbf{N}_i} = \\
=& N_1 A_{i1} + N_2 A_{i2} + N_3 A_{i3} + \cdots + N_{i-1} A_{i-1i-1} + \cdots + N_{i+1} A_{i+1i+1} + \cdots + N_{N_s} A_{iN_s} + \\
& + N_1 A_{1i} + N_2 A_{2i} + N_3 A_{3i} + \cdots + N_{i-1} A_{i-1i-1} + 2N_i A_{ii} + N_{i+1} A_{i+1i+1} + \\
& + \cdots + N_{N_s} A_{N_s i} = \\
=& 2\sum_{j=1} N_j A_{ji}\,. \qquad \text{(G.0.1)} \\
& \downarrow \\
& \text{since } A_{kj} = A_{jk}
\end{aligned}
$$

Regarding the term $(\partial N B_m/\partial N_i)_{\mathbf{N}_i}$ we need to differentiate depending on the mixing rule due to the fact that a unique nomenclature of B_{ij} would be inconsistent. Thus, for MR-1,

MR-2 and MR-3:

$$\left(\frac{\partial N B_m}{\partial N_i}\right)_{\mathbf{N}_i} = \frac{\partial}{\partial N_i}\left(N\sum_{j=1}^{N_s} X_j B_j\right)_{\mathbf{N}_i} =$$
$$= \frac{\partial}{\partial N_i}\left[N_1 B_1 + N_2 B_2 + N_3 B_3 + \cdots + N_i B_i + \cdots + N_{N_s} B_{N_s}\right] =$$
$$= B_i\,, \tag{G.0.2}$$

whereas for MR-4, B_m assumes the form: $B_m = \sum_{i=1}^{N_2}\sum_{j=1}^{N_2} X_i X_j B_{ij}$ similarly to the A_m form:

$$\left(\frac{\partial N B_m}{\partial N_i}\right)_{\mathbf{N}_i} = \left(\frac{\partial N^2 B_m/N}{\partial N_i}\right)_{\mathbf{N}_i} = \frac{1}{N}\left(\frac{\partial N^2 B_m}{\partial N_i}\right)_{\mathbf{N}_i} + N^2 B_m \frac{\partial}{\partial N_i}\left(\frac{1}{N}\right)_{\mathbf{N}_i} =$$
$$= \frac{1}{N}\left(\frac{\partial N^2 B_m}{\partial N_i}\right)_{\mathbf{N}_i} - \cancel{N^2}\frac{B_m}{\cancel{N^2}} \underbrace{\left(\frac{\partial N}{\partial N_i}\right)_{\mathbf{N}_i}}_{=1 \text{ from Eq. (M.3.4)}} = \frac{1}{N}\left(\frac{\partial N^2 B_m}{\partial N_i}\right)_{\mathbf{N}_i} - B_m\,.$$

Recognizing that the term in parentheses has the same formal structure of the one analyzed in Eq. (G.0.1) we conclude that:

$$\left(\frac{\partial N B_m}{\partial N_i}\right)_{\mathbf{N}_i} = \frac{1}{N} 2\sum_{j=1}^{N_s} N_j B_{ij} - B_m = 2\sum_{j=1}^{N_s} X_j B_{ji} - B_m\,. \tag{G.0.3}$$

In order to make the notation shorter, we can define a more generic symbol $\tilde{B}_i$ to indicate the derivative such that:

$$\tilde{B}_i = \left(\frac{\partial N B_m}{\partial N_i}\right)_{\mathbf{N}_i} = \begin{cases} B_i & \text{for MR-1, MR-2, MR-3} \\ \\ 2\sum_{j=1}^{N_s} X_j B_{ji} - B_m & \text{for MR-4.} \end{cases} \tag{G.0.4}$$

The derivative of Eq. (G.0.4) with respect to the generic k-th mole fraction is also used in the derivation. This is given below and defines the symbol $\hat{B}_{ik}$ used in the text:

$$\hat{B}_{ik} = \left(\frac{\partial \tilde{B}_i}{\partial X_k}\right)_{\mathbf{X}_k} = \begin{cases} \left(\dfrac{\partial B_i}{\partial X_k}\right)_{\mathbf{X}_k} = 0 & \text{for MR-1, MR-2, MR-3} \\ \\ \left[\dfrac{\partial\left(2\sum_{j=1}^{N_s} X_j B_{ji} - B_m\right)}{\partial X_k}\right]_{\mathbf{X}_k} = 2B_{ki} - \left(\dfrac{\partial B_m}{\partial X_k}\right)_{\mathbf{X}_k} & \text{for MR-4.} \end{cases} \tag{G.0.5}$$

Where $(\partial B_m/\partial X_k)_{\mathbf{X}_k}$ is given in Tab. 11.

Another important auxiliary derivative is the following (assuming the most general case in which δ_2 depends on the mixture):

$$\frac{\partial}{\partial N_i}\left(\frac{\delta_2 B_m \rho}{M}\right)_{T,\overline{V},\mathbf{N}_i} = \frac{B_m\rho}{M}\left(\frac{\partial \delta_2}{\partial N_i}\right)_{\mathbf{N}_i} + \delta_2\left[\frac{\partial (B_m\rho/M)}{\partial N_i}\right]_{T,\overline{V},\mathbf{N}_i} = \downarrow \rho/M = N/\overline{V}$$

$$= \frac{B_m\rho}{M}\underbrace{\left(\frac{\partial \delta_2}{\partial N_i}\right)_{\mathbf{N}_i}}_{\downarrow \text{Use Eq. (L.0.3) and Eq. (M.1.7)}} + \frac{\delta_2}{\overline{\overline{V}}}\underbrace{\left(\frac{\partial N B_m}{\partial N_i}\right)_{\mathbf{N}_i}}_{\text{Use the result of Eq. (G.0.4)}} =$$

$$= \frac{B_m\rho}{MN}\sum_{j=1}^{N_s}\delta_{2,j}(\delta_{ij}-X_j) + \frac{\delta_2}{\overline{\overline{V}}}\tilde{B}_i =$$

$$= \underbrace{\frac{B_m}{\overline{V}}\sum_{j=1}^{N_s}\delta_{2,j}(\delta_{ij}-X_j)}_{S_{2,i}} + \frac{\delta_2}{\overline{\overline{V}}}\tilde{B}_i = \frac{B_m}{\overline{V}}S_{2,i} + \frac{\delta_2}{\overline{\overline{V}}}\tilde{B}_i\,. \qquad \text{(G.0.6)}$$

$\downarrow \overline{V} = MN/\rho$

Similarly one obtains:

$$\frac{\partial}{\partial N_i}\left(\frac{\delta_1 B_m \rho}{M}\right)_{T,\overline{V},\mathbf{N}_i} = \frac{B_m}{\overline{V}}S_{1,i} + \frac{\delta_1}{\overline{\overline{V}}}\tilde{B}_i\,. \qquad \text{(G.0.7)}$$

Appendix H

ACCESSORY DERIVATIVES FOR THE DETERMINATION OF THE PARTIAL MOLAR QUANTITIES

One important term that is required for the determination of the partial molar enthalpy is derived below (assuming the most general case in which δ_2 depends on the mixture):

$$\left(\frac{\partial(\delta_1 B_m \rho/M)}{\partial N_i}\right)_{T,p,\mathbf{N}_i} \underset{\rho/M=1/V}{=} \left(\frac{\partial\left(\delta_1 \frac{B_m}{V}\frac{N}{N}\right)}{\partial N_i}\right)_{T,p,\mathbf{N}_i} \underset{\overline{V}=NV}{=} \left(\frac{\partial\left(\delta_1 \frac{NB_m}{\overline{V}}\right)}{\partial N_i}\right)_{T,p,\mathbf{N}_i} =$$

$$= \frac{1}{\overline{\overline{V}}}\left(\frac{\partial(\delta_1 N B_m)}{\partial N_i}\right)_{T,p,\mathbf{N}_i} + \delta_1 N B_m \frac{\partial}{\partial N_i}\left(\frac{1}{\overline{\overline{V}}}\right)_{T,p,\mathbf{N}_i} =$$

$$= \frac{1}{\overline{\overline{V}}}\left[NB_m \underbrace{\left(\frac{\partial \delta_1}{\partial N_i}\right)_{\mathbf{N}_i}}_{\text{Use Eq. (L.0.3) and Eq. (M.1.7)}} + \delta_1 \underbrace{\left(\frac{\partial N B_m}{\partial N_i}\right)_{\mathbf{N}_i}}_{\text{Use the result of Eq. (G.0.4)}} \right] - \delta_1 \frac{NB_m}{\overline{V}^2} \underbrace{\left(\frac{\partial \overline{V}}{\partial N_i}\right)_{T,p,\mathbf{N}_i}}_{=V_i} =$$

$$= \frac{1}{\overline{\overline{V}}}\left(B_m S_{1,i} + \delta_1 \tilde{B}_i\right) - \delta_1 \frac{NB_m}{\overline{V}^2} V_i = \frac{1}{\overline{\overline{V}}}\left[B_m S_{1,i} + \delta_1\left(\tilde{B}_i - B_m \frac{V_i}{V}\right)\right], \tag{H.0.1}$$

and similarly:

$$\left(\frac{\partial(\delta_2 B_m \rho/M)}{\partial N_i}\right)_{T,p,\mathbf{N}_i} = \frac{1}{\overline{\overline{V}}}\left[B_m S_{2,i} + \delta_2\left(\tilde{B}_i - B_m \frac{V_i}{V}\right)\right]. \tag{H.0.2}$$

Appendix I

FULL NEWTON METHOD FOR THE VLE PROBLEM

The starting point is again Eq. (2.2.31) written in logarithm form. The independent variables used are the so called *molar flows*, corresponding to the $v_i = \beta y_i$ variables already used in Sec. 2.2.2.2. As a result, Eq. (2.2.31) is written in the form of $g(\mathbf{v}) = 0$, where $v = \{v_i \,|\, i = 1, \cdots, N_s\}$:

$$g_i(\mathbf{v}) = \ln f_i^V - \ln f_i^L \qquad i = 1, \cdots, N_s \,. \tag{I.0.1}$$

Next, the Taylor expansion of Eq. (I.0.1) is made. In this operation, temperature, pressure and overall mixture composition (meant in terms of either mole numbers and/or mole fractions) are maintained constant:

$$\mathbf{g}(\mathbf{v}) = \mathbf{g}(\mathbf{v}^0) + \left(\frac{\partial \mathbf{g}}{\partial \mathbf{v}}\right)_{T,p,\mathbf{N}} \Delta \mathbf{v} \,. \tag{I.0.2}$$

Recognizing as $\boldsymbol{J} = J_{ij} = (\partial g_i / \partial v_j)_{T,p,\mathbf{N}}$ the Jacobian matrix, the Newton iteration method is readily obtained as:

$$\Delta \mathbf{v}^{n+1} = -\boldsymbol{J}(\mathbf{v}^n)^{-1} \mathbf{g}(\mathbf{v}^n) \,, \tag{I.0.3}$$

where $\mathbf{v}^0 = \beta \mathbf{y}^0$ is the starting guess coming from an (existing) VLE solution, i.e. either from the SSI method, or a previous time step. The Jacobian matrix elements are computed as follows:

$$J_{ij} = \left(\frac{\partial g_i}{\partial v_j}\right)_{T,p,\mathbf{N}} = \left[\left(\frac{\partial \ln f_i^V}{\partial v_j}\right)_{T,p,\mathbf{N}} - \left(\frac{\partial \ln f_i^L}{\partial v_j}\right)_{T,p,\mathbf{N}}\right] . \tag{I.0.4}$$

Given the fact that $\ln f_i^V = \ln \phi_i^V + \ln p + \ln y_i = \ln \phi_i^V + \ln p + \ln(v_i/\beta)$ and $\ln f_i^L = \ln \phi_i^L + \ln p + \ln x_i = \ln \phi_i^L + \ln p + \ln[(X_i - v_i)/(1-\beta)]$ (using $\mathbf{X} = \mathbf{v} + \mathbf{l}$), Eq. (I.0.4) can be rewritten

as:

$$J_{ij} = \left[\left(\frac{\partial \ln\phi_i^V}{\partial v_j}\right)_{T,p,\mathbf{N}} - \left(\frac{\partial \ln\phi_i^L}{\partial v_j}\right)_{T,p,\mathbf{N}}\right] + \left(\frac{\partial \ln v_i}{\partial v_j}\right)_{T,p,\mathbf{N}} - \left(\frac{\partial \ln\beta}{\partial v_j}\right)_{T,p,\mathbf{N}} + \\ - \frac{1}{X_i - v_i}\left[\cancelto{0}{\left(\frac{\partial X_i}{\partial v_j}\right)_{T,p,\mathbf{N}}} - \left(\frac{\partial v_i}{\partial v_j}\right)_{T,p,\mathbf{N}}\right] + \left(\frac{\partial \ln(1-\beta)}{\partial v_j}\right). \tag{I.0.5}$$

Using the fact that $(\partial v_i/\partial v_j) = \delta_{ij}$, $(\partial\beta/\partial v_j) = [\partial(\sum_{k=1}^{N_s} v_k)/\partial v_j] = 1$, the latter becomes:

$$J_{ij} = \left[\left(\frac{\partial \ln\phi_i^V}{\partial v_j}\right)_{T,p,\mathbf{N}} - \left(\frac{\partial \ln\phi_i^L}{\partial v_j}\right)_{T,p,\mathbf{N}}\right] + \frac{\delta_{ij}}{v_i} - \frac{1}{\beta} + \frac{\delta_{ij}}{(X_i - v_i)} - \frac{1}{1-\beta} = \\ = \left[\left(\frac{\partial \ln\phi_i^V}{\partial v_j}\right)_{T,p,\mathbf{N}} - \left(\frac{\partial \ln\phi_i^L}{\partial v_j}\right)_{T,p,\mathbf{N}}\right] + \frac{1}{\beta(1-\beta)}\left[\frac{X_i}{x_i y_i}\delta_{ij} - 1\right]. \tag{I.0.6}$$

Finally, knowing that:

$$\left(\frac{\partial \ln\phi_i^V}{\partial v_j}\right)_{T,p,\mathbf{N}} = \left(\frac{\partial \ln\phi_i^V}{\partial \beta y_j}\right)_{T,p,\mathbf{N}} = \left(\frac{\partial \ln\phi_i^V}{\partial (N^V y_j/N)}\right)_{T,p,\mathbf{N}} = N\left(\frac{\partial \ln\phi_i^V}{\partial N_j^V}\right)_{T,p,\mathbf{N}} \tag{I.0.7}$$

$$\left(\frac{\partial \ln\phi_i^L}{\partial v_j}\right)_{T,p,\mathbf{N}} = \left(\frac{\partial \ln\phi_i^L}{\partial l_j}\right)_{T,p,\mathbf{N}} \underbrace{\left(\frac{\partial l_j}{\partial v_j}\right)_{T,p,\mathbf{N}}}_{=-1} = -\left(\frac{\partial \ln\phi_i^L}{\partial (1-\beta)x_j}\right)_{T,p,\mathbf{N}} = \\ = -\left(\frac{\partial \ln\phi_i^L}{\partial N^L x_j/N}\right)_{T,p,\mathbf{N}} = -N\left(\frac{\partial \ln\phi_i^L}{\partial N_j^L}\right)_{T,p,\mathbf{N}} \tag{I.0.8}$$

Now using the result of Eq. (B.0.3):

$$N\left(\frac{\partial \ln\phi_i^V}{\partial N_j^V}\right)_{T,p,\mathbf{N}} = \frac{N}{N^V}\sum_{k=1}^{N_s}\left(\frac{\partial \ln\phi_i^V}{\partial y_k}\right)_{T,p,\mathbf{y}_k}(\delta_{kj} - y_k) = \\ = \frac{1}{\beta}\underbrace{\sum_{k=1}^{N_s}\left(\frac{\partial \ln\phi_i^V}{\partial y_k}\right)_{T,p,\mathbf{y}_k}(\delta_{kj} - y_k)}_{\Psi_{ij}^V} = \frac{\Psi_{ij}^V}{\beta}, \tag{I.0.9}$$

$$N\left(\frac{\partial \ln\phi_i^L}{\partial N_j^L}\right)_{T,p,\mathbf{N}} = \frac{N}{N^L}\sum_{k=1}^{N_s}\left(\frac{\partial \ln\phi_i^L}{\partial x_k}\right)_{T,p,\mathbf{x}_k}(\delta_{kj} - x_k) = \\ = \frac{1}{1-\beta}\underbrace{\sum_{k=1}^{N_s}\left(\frac{\partial \ln\phi_i^L}{\partial x_k}\right)_{T,p,\mathbf{x}_k}(\delta_{kj} - x_k)}_{\Psi_{ij}^L} = \frac{\Psi_{ij}^L}{1-\beta}. \tag{I.0.10}$$

Substituting the results of Eq. (I.0.9) and Eq. (I.0.10) into Eq. (I.0.6), the final form of the Jacobian is obtained:

$$J_{ij} = \frac{\Psi_{ij}^V}{\beta} + \frac{\Psi_{ij}^L}{1-\beta} + \frac{1}{\beta(1-\beta)}\left[\frac{X_i}{x_i y_i}\delta_{ij} - 1\right] = \frac{1}{\beta(1-\beta)}\left[(1-\beta)\Psi_{ij}^V + \beta\Psi_{ij}^L + \frac{X_i}{x_i y_i}\delta_{ij} - 1\right]. \tag{I.0.11}$$

Algorithm 15 summarizes the steps that are required to run the full Newton method for VLE.

Algorithm 15 [β, $\mathbf{x}$, $\mathbf{y}$]=fullNewtonVLE(T,p,$\mathbf{X}$,$\mathbf{y}$,$\mathbf{x}$,β,ϵ_{nwt})

Inputs: T, p, $\mathbf{X}$, $\mathbf{y}$, $\mathbf{x}$, β, ϵ_{nwt}
Compute: Switch to molar flows: $\mathbf{v} = \beta\mathbf{y}$
$n = 0$
while $\varepsilon > \epsilon_{nwt}$ **do**
    $n = n + 1$
    Obtain liquid mixture: CALL generateVLstructure(T,p,$\mathbf{x}$,L) using Algorithm 1
    Obtain vapor mixture: CALL generateVLstructure(T,p,$\mathbf{y}$,V) using Algorithm 1
    ! Need to assemble the Jacobian $\mathcal{J}_{ij}$
    for $i = 1, N_s$ **do**
        for $j = 1, N_s$ **do**
            $\Phi_{ij}^V = 0$
            $\Phi_{ij}^L = 0$
            ! Need to assemble Φ_{ij}^V and Φ_{ij}^L
            for $k = 1, N_s$ **do**
                $$\Phi_{ij}^V = \Phi_{ij}^V + \left(\frac{\partial \ln \phi_i^V}{\partial y_k}\right)(\delta_{jk} - y_k)$$
                $$\Phi_{ij}^L = \Phi_{ij}^L + \left(\frac{\partial \ln \phi_i^L}{\partial x_k}\right)(\delta_{jk} - x_k)$$
            end for
            Compute: $\mathcal{J}_{ij}$ using Eq. (I.0.11)
        end for
        Compute: Objective function component $g_i(\mathbf{v}) = \ln\phi_i^V - \ln\phi_i^L + \ln y_i - \ln x_i$
    end for
    Compute: Update the error $\varepsilon = ||\mathbf{g}(\mathbf{v})||$
    ! Note at this step one should put a check on β. If the system is single phase then it should exit,
    ! otherwise the Jacobian matrix becomes singular and the Newton method will produce garbage.
    Compute: Jacobian inverse $\boldsymbol{\mathcal{J}}^{-1}$
    Compute: $\Delta\mathbf{v}$ using Eq. (I.0.3)
    Compute: Update the solution
        $\mathbf{v} = \mathbf{v} + \Delta\mathbf{v}$
        $\beta = \mathrm{SUM(v_i)}$
        $y_i = v_i/\beta$
        $x_i = (X_i - v_i)/(1 - \beta)$
        $K_i = y_i/x_i$
end while
Outputs: β, $\mathbf{x}$, $\mathbf{y}$

Appendix J

SOLUTION OF THE $E\rho$ PROBLEM WITH NUMERICAL JACOBIAN

Another way to solve the $E\rho$ problem, which finds the pressure and the temperature out of the density ρ^*, internal energy e^* and composition X_k^* of a mixture, is the one suggested by [25]. We define our vector of residuals according to Eqs. (2.2.34)–(2.2.35):

$$F_1 = \frac{M}{\beta\dfrac{M^V}{\rho^V(T,p,y_k)} + (1-\beta)\dfrac{M^L}{\rho^L(T,p,x_k)}} - \rho^* = \rho - \rho^*\,, \tag{J.0.1}$$

$$F_2 = \beta E^V(T,p,y_k) + (1-\beta)E^L(T,p,x_k) - E^*\,. \tag{J.0.2}$$

Taylor expansion of the two residuals provides the following system of equations at the generic j-th iteration:

$$\begin{bmatrix} \left(\dfrac{\partial F_1}{\partial T}\right)_p & \left(\dfrac{\partial F_1}{\partial p}\right)_T \\ \left(\dfrac{\partial F_2}{\partial T}\right)_p & \left(\dfrac{\partial F_2}{\partial p}\right)_T \end{bmatrix}_{T_j,p_j} \begin{pmatrix} \Delta T \\ \Delta p \end{pmatrix}_j = - \begin{pmatrix} F_1 \\ F_2 \end{pmatrix}_j\,. \tag{J.0.3}$$

Where $\Delta T = T_{j+1} - T_j$ and $\Delta p = p_{j+1} - p_j$ for some starting values of T_0 and p_0. The Jacobian derivatives of the residuals do not have an analytic formula, thus they have to be computed numerically by using the j, j−1 and j−2 iteration history:

$$\begin{bmatrix} T(j-1)-T(j) & p(j-1)-p(j) & 0 & 0 \\ T(j-2)-T(j) & p(j-2)-p(j) & 0 & 0 \\ 0 & 0 & T(j-1)-T(j) & p(j-1)-p(j) \\ 0 & 0 & T(j-2)-T(j) & p(j-2)-p(j) \end{bmatrix} \begin{pmatrix} \left(\dfrac{\partial F_2}{\partial T}\right)_p \\ \left(\dfrac{\partial F_2}{\partial p}\right)_T \\ \left(\dfrac{\partial F_1}{\partial T}\right)_p \\ \left(\dfrac{\partial F_1}{\partial p}\right)_T \end{pmatrix}_j =$$

$$= \begin{pmatrix} F_2(j-1) - F_2(j) \\ F_2(j-2) - F_2(j) \\ F_1(j-1) - F_1(j) \\ F_1(j-2) - F_1(j) \end{pmatrix}$$

or in a more compact form:

$$\begin{pmatrix} a_{11} & a_{12} & 0 & 0 \\ a_{21} & a_{22} & 0 & 0 \\ 0 & 0 & a_{11} & a_{12} \\ 0 & 0 & a_{21} & a_{22} \end{pmatrix} \begin{bmatrix} dru_1 \\ dru_2 \\ dru_3 \\ dru_4 \end{bmatrix}_j = \begin{bmatrix} r_1 \\ r_2 \\ r_3 \\ r_4 \end{bmatrix} . \tag{J.0.4}$$

First, we construct the solution history by varying the starting values of T and p based on some input factors T_{fact} and p_{fact} such that $\Delta T \leftarrow \Delta T \cdot T_{fact}$ and $\Delta p \leftarrow \Delta p \cdot p_{fact}$. Then, the coefficients a_{ij} of Eq. (J.0.4) and the residuals differences r_1, r_2, r_3, r_4 can be computed such that the corresponding Jacobian derivatives dr_1, dr_2, dr_3, dr_4 are calculated from the subsequent iteration onwards. Then, using Eq. (J.0.3) the values of ΔT and Δp are updated, on which an additional line search can be applied. In Algorithm 16 the required steps are listed. Similarly to the $p\rho$ problem, some inputs for the $e\rho$ problem are required. For this work, $\lambda_0 = 0.9$, $T_{fact} = 0.011$, $p_{fact} = 0.12$, $\epsilon_1 = \epsilon_2 = \epsilon_3 = 0.001$, $\Delta T_0 = 10\,\mathrm{K}$, $\Delta T_{max} = 100\,\mathrm{K}$, $\Delta p_0 = 0.5\,\mathrm{MPa}$, $\Delta p_{max} = 1\,\mathrm{MPa}$.

Algorithm 16 [T, p, β, x, y, Z] = solveERHONJ(E,ρ,$\mathbf{X}$, N_{max}, ΔT_{max}, Δp_{max}, T_0, p_0, λ_0 , T_{fact}, p_{fact},ϵ_1, ϵ_2, ϵ_3, ΔT_0, Δp_0)

Inputs: E, ρ, $\mathbf{X}$, N_{max}, ϵ_{ER}, ΔT_{max}, Δp_{max}, T_0, p_0, λ_0, T_{fact}, p_{fact}, ϵ_1, ϵ_2, ϵ_3, ΔT_0, Δp_0
! Assign the target values
$E^* = E$
$\rho^* = \rho$
!Attempt single phase solution:
$E(T, \rho, \mathbf{X}) = E^{ig}(T, \mathbf{X}) + \Delta E(T, \rho, \mathbf{X})$! Using Eq. (2.2.77)
Evaluate: $|E(T, \rho^*, \mathbf{X}) - E^*| < \epsilon_1$! solved with Newton method in the form of Eq. (3.4.10)
Compute: $p = p(T, \rho^*, \mathbf{X})$ Using Eq. (2.2.67)
Solve the Tp problem (this gives β, x, y, E, ρ): CALL solveTP(T,p,$\mathbf{X}$) using Algorithm 2
Compute: $E(T, \rho, \mathbf{X}) = E^{ig}(T, \mathbf{X}) + \Delta E(T, \rho, \mathbf{X})$
if $|\rho - \rho^*| < \epsilon_1$ AND $|E - E^*| < \epsilon_2$ **then**
    Single phase solution is fine. Values of T and p are correct.
else
    ! Assign the initial guesses of T and p and their increments
    $T = T_0$, $p = p_0$
    $\Delta T = \Delta T_0$, $\Delta p = \Delta p_0$
    ! Construct the solution history
    for j=1,3 **do**
        Update: $T(j) = T$, $p(j) = p$
        Solve Tp (this gives β, x, y, E, ρ): CALL solveTP($T(j)$,$p(j)$,$\mathbf{X}$) using Algorithm 2
        ! Update residuals:
        $\varepsilon_1(j) = |\rho - \rho^*|$
        $\varepsilon_2(j) = |E - E^*|$
        Update: $T = T + \Delta T$
        Update: $p = p + \Delta p$
        Update: $\Delta T = \Delta T \cdot T_{fact}$
        Update: $\Delta p = \Delta p \cdot p_{fact}$
    end for
end if
j = 0
while $\varepsilon < \epsilon_3$ **do**
    j = j + 1
    Update T/p variations: a_{ij} Eq. (J.0.4)
    Update res. difference: r_1-r_4 Eq. (J.0.4)
    Update Jacobian: dru_1-dru_4 Eq. (J.0.4)
    Compute: $\boldsymbol{\mathcal{J}}^{-1}$! Inverse Jacobian
    Update: ΔT and Δp using Eq. (J.0.3)
    Update: $\varepsilon = |\Delta T| + |\Delta p|$! Overall error
    Compute: $\lambda = \text{MIN}(\lambda_0, \text{ABS}(\Delta T_{max}/\Delta T), \text{ABS}(\Delta p_{max}/\Delta p))$! Apply line search
    Update: $T \leftarrow T + \lambda \Delta T$, $p \leftarrow p + \lambda \Delta p$
    Solve Tp (this gives β, x, y, E, ρ): CALL solveTP(T,p,$\mathbf{X}$) using Algorithm 2
    Update: $T(j)$, $T(j-1)$, $T(j-1)$, $p(j)$, $p(j-1)$, $p(j-2)$
    Update residuals: $F_1(j)$, $F_1(j-1)$, $F_1(j-2)$, $F_2(j)$, $F_2(j-1)$, $F_2(j-2)$
end while
Compute: $Z = p\,MW/\rho R_u T$
Output: T, p, β, y_k, x_k, Z

Appendix K

MULTI-PHASE THERMODYNAMICS MATHEMATICAL DETAILS

Recalling Eq. (2.2.39), temperature derivatives are derived next. The fugacities equality of Eq. (2.2.31) is rewritten in logarithmic form, for convenience, and both sides are differentiated with respect to temperature:

$$\left(\frac{\partial \ln f_i^L}{\partial T}\right)_{p,\mathbf{X}} - \left(\frac{\partial \ln f_i^V}{\partial T}\right)_{p,\mathbf{X}} = 0\,, \qquad i = 1, \cdots, N_s\,. \tag{K.0.1}$$

Given the link between the fugacity and fugacity coefficient for each i-th species in the phase η (L or V) with composition $\boldsymbol{\zeta}$ ($\mathbf{y}$ for $\eta = \mathrm{V}$ and $\mathbf{x}$ for $\eta = \mathrm{L}$):

$$f_i^\eta = \phi_i^\eta p \zeta_i \qquad \rightarrow \qquad \ln f_i^\eta = \ln \phi_i^\eta + \ln p + \ln \zeta_i\,,$$

for the liquid phase ($\eta = L$, $\boldsymbol{\zeta} = \mathbf{x}$): $x_i = l_i/(1-\beta) = (X_i - v_i)/(1-\beta)$, hence:

$$\begin{aligned}
\left(\frac{\partial \ln f_i^L}{\partial T}\right)_{p,\mathbf{X}} =& \frac{\partial}{\partial T}\left(\ln \phi_i^L + \ln p + \ln(X_i - v_i) - \ln(1-\beta)\right)_{p,\mathbf{X}} \\
=& \left(\frac{\partial \ln \phi_i^L}{\partial T}\right)_{p,\mathbf{X}} + \cancelto{0}{\left(\frac{\partial \ln p}{\partial T}\right)_{p,\mathbf{X}}} + \left(\frac{\partial \ln(X_i - v_i)}{\partial T}\right)_{p,\mathbf{X}} - \left(\frac{\partial \ln(1-\beta)}{\partial T}\right)_{p,\mathbf{X}} \\
=& \left(\frac{\partial \ln \phi_i^L}{\partial T}\right)_{p,\mathbf{X}} - \frac{1}{X_i - v_i}\left(\frac{\partial v_i}{\partial T}\right)_{p,\mathbf{X}} + \frac{1}{1-\beta}\left(\frac{\partial \beta}{\partial T}\right)_{p,\mathbf{X}} \qquad i = 1, \cdots, N_s\,.
\end{aligned} \tag{K.0.2}$$

Using the direct link between β and v_i of Eq. (2.2.41):

$$\left(\frac{\partial \beta}{\partial T}\right)_{p,\mathbf{X}} = \frac{\partial}{\partial T}\left(\sum_{k=1}^{N_s} v_k\right)_{p,\mathbf{X}} = \sum_{k=1}^{N_s}\left(\frac{\partial v_k}{\partial T}\right)_{p,\mathbf{X}}\,. \tag{K.0.3}$$

Finally, substituting Eq. (K.0.3) into Eq. (K.0.2), one obtains for the liquid phase:

$$\begin{aligned}
\left(\frac{\partial \ln f_i^L}{\partial T}\right)_{p,\mathbf{X}} =& \left(\frac{\partial \ln \phi_i^L}{\partial T}\right)_{p,\mathbf{X}} - \frac{1}{X_i - v_i}\left(\frac{\partial v_i}{\partial T}\right)_{p,\mathbf{X}} + \frac{1}{1-\beta}\sum_{k=1}^{N_s}\left(\frac{\partial v_k}{\partial T}\right)_{p,\mathbf{X}} \\
=& \left(\frac{\partial \ln \phi_i^L}{\partial T}\right)_{p,\mathbf{X}} + \frac{1}{1-\beta}\sum_{k=1}^{N_s}\left[1 - \left(\frac{1-\beta}{X_i - v_i}\right)\delta_{ki}\right]\left(\frac{\partial v_k}{\partial T}\right)_{p,\mathbf{X}} \qquad i = 1, \cdots, N_s\,,
\end{aligned} \tag{K.0.4}$$

where δ_{ki} is the Kronecker delta. With analogous steps, one obtains for the vapor phase ($\eta = L$, $\boldsymbol{\zeta} = \mathbf{x}$):

$$\left(\frac{\partial \ln f_i^V}{\partial T}\right)_{p,\mathbf{X}} = \left(\frac{\partial \ln \phi_i^V}{\partial T}\right)_{p,\mathbf{X}} - \frac{1}{\beta}\sum_{k=1}^{N_s}\left[1 - \left(\frac{\beta}{v_i}\right)\delta_{ki}\right]\left(\frac{\partial v_k}{\partial T}\right)_{p,\mathbf{X}} \qquad i = 1, \cdots, N_s. \tag{K.0.5}$$

Substituting Eqs. (K.0.4)–(K.0.5) into Eq. (K.0.1), using Eq. (2.2.40) and rearranging, the following intermediate result is obtained in the unknowns $(\partial v_k/\partial T)_{p,\mathbf{X}}$:

$$\frac{1}{\beta(1-\beta)}\sum_{k=1}^{N_s}\left(1 - \delta_{ki}\frac{X_k}{y_k x_k}\right)\left(\frac{\partial v_k}{\partial T}\right)_{p,\mathbf{X}} = \left(\frac{\partial \ln \phi_i^V}{\partial T}\right)_{p,\mathbf{X}} - \left(\frac{\partial \ln \phi_i^L}{\partial T}\right)_{p,\mathbf{X}} \qquad i = 1, \cdots, N_s. \tag{K.0.6}$$

In addition, using the dependency between v_i, β, x_i, y_i of Eq. (2.2.40), the following derivatives can be also obtained:

$$\begin{aligned}\left(\frac{\partial y_i}{\partial T}\right)_{p,\mathbf{X},\mathbf{y}_i} &= \left(\frac{\partial v_i/\beta}{\partial T}\right)_{p,\mathbf{X},\mathbf{y}_i} = \\ &= \frac{1}{\beta^2}\left[\beta\left(\frac{\partial v_i}{\partial T}\right)_{p,\mathbf{X}} - v_i\left(\frac{\partial \beta}{\partial T}\right)_{p,\mathbf{X}}\right] = \\ &\qquad \Big\downarrow \\ &\qquad \text{Using Eq. (2.2.40) and Eq. (K.0.3)} \\ &= -\frac{y_i}{\beta}\sum_{k=1}^{N_s}\left(1 - \frac{\delta_{ik}}{y_k}\right)\left(\frac{\partial v_k}{\partial T}\right)_{p,\mathbf{X}} \qquad i = 1, \cdots, N_s\,, \end{aligned} \tag{K.0.7}$$

$$\begin{aligned}\left(\frac{\partial x_i}{\partial T}\right)_{p,\mathbf{X},\mathbf{x}_i} &= \left(\frac{\partial (X_i - v_i)/(1-\beta)}{\partial T}\right)_{p,\mathbf{X},\mathbf{x}_i} = \\ &= \frac{1}{(1-\beta)^2}\left[-(1-\beta)\left(\frac{\partial v_i}{\partial T}\right)_{p,\mathbf{X}} - (X_i - v_i)\left(\frac{\partial (1-\beta)}{\partial T}\right)_{p,\mathbf{X}}\right] = \\ &\qquad \Big\downarrow \\ &\qquad \text{Using Eq. (2.2.40) and Eq. (K.0.3)} \\ &= \frac{x_i}{1-\beta}\sum_{k=1}^{N_s}\left(1 - \frac{\delta_{ik}}{x_k}\right)\left(\frac{\partial v_k}{\partial T}\right)_{p,\mathbf{X}} \qquad i = 1, \cdots, N_s\,, \end{aligned} \tag{K.0.8}$$

where $\mathbf{y}_i = \{y_j \,|\, j = 1, \cdots, N_s,\, j \neq i\}$ and $\mathbf{x}_i = \{x_j \,|\, j = 1, \cdots, N_s,\, j \neq i\}$ have been defined. For completeness, the temperature derivative of the $K_i = y_i/x_i$ factors are also given. These can be easily constructed using Eq. (K.0.7) and Eq. (K.0.8):

$$\left(\frac{\partial K_i}{\partial T}\right)_{p,\mathbf{X}} = \frac{1}{\beta(1-\beta)x_i}\sum_{k=1}^{N_s}\left(\frac{\partial v_k}{\partial T}\right)_{p,\mathbf{X}}\left(\frac{X_i}{x_i}\delta_{ki} - y_k\right) \qquad i = 1, \cdots, N_s\,. \tag{K.0.9}$$

Next, the derivatives of the fugacity coefficients in each phase appearing in Eq. (K.0.6) need to be addressed. Since for each i-*th* specie: $\phi_i^V = \phi_i^V(T,p,\mathbf{y}(T,p,\mathbf{X}))$ and $\phi_i^L = \phi_i^L(T,p,\mathbf{x}(T,p,\mathbf{X}))$, the total differential for each quantity (in logarithmic form) writes as follows:

$$d\ln\phi_i^V = \left(\frac{\partial \ln\phi_i^V}{\partial T}\right)_{p,\mathbf{X},\mathbf{y}} dT + \left(\frac{\ln\phi_i^V}{\partial p}\right)_{T,\mathbf{X},\mathbf{y}} dp + \sum_{k=1}^{N_s}\left(\frac{\partial \ln\phi_i^V}{\partial y_k}\right)_{T,p,\mathbf{X},\mathbf{y}_k} dy_k \qquad i = 1,\cdots,N_s \tag{K.0.10}$$

$$d\ln\phi_i^L = \left(\frac{\partial \ln\phi_i^L}{\partial T}\right)_{p,\mathbf{X},\mathbf{x}} dT + \left(\frac{\ln\phi_i^L}{\partial p}\right)_{T,\mathbf{X},\mathbf{x}} dp + \sum_{k=1}^{N_s}\left(\frac{\partial \ln\phi_i^L}{\partial x_k}\right)_{T,p,\mathbf{X},\mathbf{x}_k} dx_k \qquad i = 1,\cdots,N_s\,. \tag{K.0.11}$$

As a result, in order to obtain the "total" partial derivative of the fugacity coefficient with respect to temperature, at constant pressure, one can write:

$$\left(\frac{\partial \ln\phi_i^V}{\partial T}\right)_{p,\mathbf{X}} = \left(\frac{\partial \ln\phi_i^V}{\partial T}\right)_{p,\mathbf{X},\mathbf{y}} + \sum_{k=1}^{N_s}\left(\frac{\partial \ln\phi_i^V}{\partial y_k}\right)_{T,p,\mathbf{X},\mathbf{y}_k}\left(\frac{\partial y_k}{\partial T}\right)_{p,\mathbf{X},\mathbf{y}_k} \qquad i = 1,\cdots,N_s\,, \tag{K.0.12}$$

$$\left(\frac{\partial \ln\phi_i^L}{\partial T}\right)_{p,\mathbf{X}} = \left(\frac{\partial \ln\phi_i^L}{\partial T}\right)_{p,\mathbf{X},\mathbf{x}} + \sum_{k=1}^{N_s}\left(\frac{\partial \ln\phi_i^L}{\partial x_k}\right)_{T,p,\mathbf{X},\mathbf{x}_k}\left(\frac{\partial x_k}{\partial T}\right)_{p,\mathbf{X},\mathbf{x}_k} \qquad i = 1,\cdots,N_s\,. \tag{K.0.13}$$

The above derivatives are composed of two terms, one "frozen" part, which considers the phase composition fixed as the temperature is varied and the second that takes into account this variation. By taking the difference between Eq. (K.0.12) and Eq. (K.0.13), the following second intermediate result is obtained:

$$\left(\frac{\partial \ln\phi_i^V}{\partial T}\right)_{p,\mathbf{X}} - \left(\frac{\partial \ln\phi_i^L}{\partial T}\right)_{p,\mathbf{X}} = \left(\frac{\partial \ln\phi_i^V}{\partial T}\right)_{p,\mathbf{X},\mathbf{y}} + \sum_{k=1}^{N_s}\left(\frac{\partial \ln\phi_i^V}{\partial y_k}\right)_{T,p,\mathbf{X},\mathbf{y}_k}\left(\frac{\partial y_k}{\partial T}\right)_{p,\mathbf{X},\mathbf{y}_k} +$$
$$- \left(\frac{\partial \ln\phi_i^L}{\partial T}\right)_{p,\mathbf{X},\mathbf{x}} - \sum_{k=1}^{N_s}\left(\frac{\partial \ln\phi_i^L}{\partial x_k}\right)_{T,p,\mathbf{X},\mathbf{x}_k}\left(\frac{\partial x_k}{\partial T}\right)_{p,\mathbf{X},\mathbf{x}_k} =$$

Using Eq. (K.0.7) and Eq. (K.0.8) and swap $k \leftrightarrow j$ dummy indices

$$\downarrow$$

$$= \left[\left(\frac{\partial \ln\phi_i^V}{\partial T}\right)_{p,\mathbf{X},\mathbf{y}} - \left(\frac{\partial \ln\phi_i^L}{\partial T}\right)_{p,\mathbf{X},\mathbf{x}}\right] +$$

$$+ \sum_{k=1}^{N_s}\left(\frac{\partial v_k}{\partial T}\right)_{p,\mathbf{X}} \sum_{j=1}^{N_s}\left[-\frac{y_j}{\beta}\left(\frac{\partial \ln\phi_i^V}{\partial y_j}\right)_{T,p,\mathbf{X},\mathbf{y}_j}\left(1-\frac{\delta_{kj}}{y_j}\right) - \frac{x_j}{1-\beta}\left(\frac{\partial \ln\phi_i^L}{\partial x_j}\right)_{T,p,\mathbf{X},\mathbf{x}_j}\left(1-\frac{\delta_{kj}}{x_j}\right)\right]. \tag{K.0.14}$$

Now substituting Eq. (K.0.14) into Eq. (K.0.6) and rearranging, the following formula is obtained:

$$\sum_{k=1}^{N_s}\left\{\left(1-\delta_{ki}\frac{X_k}{y_k x_k}\right) + \right.$$

$$\left. +\beta(1-\beta)\sum_{j=1}^{N_s}\left[\frac{y_j}{\beta}\left(\frac{\partial \ln\phi_i^V}{\partial y_j}\right)_{T,p,\mathbf{X},\mathbf{y}_j}\left(1-\frac{\delta_{kj}}{y_j}\right) + \frac{x_j}{1-\beta}\left(\frac{\partial \ln\phi_i^L}{\partial x_j}\right)_{T,p,\mathbf{X},\mathbf{x}_j}\left(1-\frac{\delta_{jk}}{x_j}\right)\right]\right\}\left(\frac{\partial v_k}{\partial T}\right)_{p,\mathbf{X}} =$$

$$= \beta(1-\beta)\left[\left(\frac{\partial \ln\phi_i^V}{\partial T}\right)_{p,\mathbf{X},\mathbf{y}} - \left(\frac{\partial \ln\phi_i^L}{\partial T}\right)_{p,\mathbf{X},\mathbf{x}}\right] \qquad i = 1,\cdots,N_s\,. \tag{K.0.15}$$

If analogous steps are repeated for the derivatives with respect to the pressure, the following results are obtained

$$\left(\frac{\partial \beta}{\partial p}\right)_{T,\mathbf{X}} = \sum_{k=1}^{N_s}\left(\frac{\partial v_k}{\partial p}\right)_{T,\mathbf{X}}, \tag{K.0.16}$$

$$\left(\frac{\partial y_i}{\partial p}\right)_{T,\mathbf{X},\mathbf{y}_i} = -\frac{y_i}{\beta}\sum_{k=1}^{N_s}\left(1-\frac{\delta_{ik}}{y_k}\right)\left(\frac{\partial v_k}{\partial p}\right)_{T,\mathbf{X}} \qquad i = 1,\cdots,N_s\,, \tag{K.0.17}$$

$$\left(\frac{\partial x_i}{\partial p}\right)_{T,\mathbf{X},\mathbf{x}_i} = \frac{x_i}{1-\beta}\sum_{k=1}^{N_s}\left(1-\frac{\delta_{ik}}{x_k}\right)\left(\frac{\partial v_k}{\partial p}\right)_{T,\mathbf{X}} \qquad i = 1,\cdots,N_s\,, \tag{K.0.18}$$

$$\left(\frac{\partial K_i}{\partial p}\right)_{T,\mathbf{X}} = \frac{1}{\beta(1-\beta)x_i}\sum_{k=1}^{N_s}\left(\frac{\partial v_k}{\partial p}\right)_{T,\mathbf{X}}\left(\frac{X_i}{x_i}\delta_{ki} - y_k\right) \qquad i = 1,\cdots,N_s\,. \tag{K.0.19}$$

$$\sum_{k=1}^{N_s}\left\{\left(1-\delta_{ki}\frac{X_k}{y_k x_k}\right) + \right.$$

$$\left. +\beta(1-\beta)\sum_{j=1}^{N_s}\left[\frac{y_j}{\beta}\left(\frac{\partial \ln\phi_i^V}{\partial y_j}\right)_{T,p,\mathbf{X},\mathbf{y}_j}\left(1-\frac{\delta_{kj}}{y_j}\right) + \frac{x_j}{1-\beta}\left(\frac{\partial \ln\phi_i^L}{\partial x_j}\right)_{T,p,\mathbf{X},\mathbf{x}_j}\left(1-\frac{\delta_{jk}}{x_j}\right)\right]\right\}\left(\frac{\partial v_k}{\partial p}\right)_{T,\mathbf{X}} =$$

$$= \beta(1-\beta)\left[\left(\frac{\partial \ln\phi_i^V}{\partial p}\right)_{T,\mathbf{X},\mathbf{y}} - \left(\frac{\partial \ln\phi_i^L}{\partial p}\right)_{T,\mathbf{X},\mathbf{x}}\right] \qquad i = 1,\cdots,N_s\,. \tag{K.0.20}$$

By looking at Eq. (K.0.15) and Eq. (K.0.20) one immediately realizes that both linear systems can be written in the following compact form:

$$\boldsymbol{\mathcal{A}}\boldsymbol{\chi}_T = \boldsymbol{b}_T\,, \tag{K.0.21}$$

$$\boldsymbol{\mathcal{A}}\boldsymbol{\chi}_p = \boldsymbol{b}_p\,, \tag{K.0.22}$$

where:

$$\begin{aligned}\mathcal{A}_{ik} &= \left(1 - \delta_{ki}\frac{X_k}{y_k x_k}\right) + \\ &+ \beta(1-\beta)\sum_{j=1}^{N_s}\left[\frac{y_j}{\beta}\left(\frac{\partial \ln\phi_i^V}{\partial y_j}\right)_{T,p,\mathbf{X},\mathbf{y}_j}\left(1 - \frac{\delta_{kj}}{y_j}\right) + \frac{x_j}{1-\beta}\left(\frac{\partial \ln\phi_i^L}{\partial x_j}\right)_{T,p,\mathbf{X},\mathbf{x}_j}\left(1 - \frac{\delta_{jk}}{x_j}\right)\right]\,,\end{aligned} \tag{K.0.23}$$

$$b_{T,i} = \beta(1-\beta)\left[\left(\frac{\partial \ln\phi_i^V}{\partial T}\right)_{p,\mathbf{X},\mathbf{y}} - \left(\frac{\partial \ln\phi_i^L}{\partial T}\right)_{p,\mathbf{X},\mathbf{x}}\right]\,, \tag{K.0.24}$$

$$b_{p,i} = \beta(1-\beta)\left[\left(\frac{\partial \ln\phi_i^V}{\partial p}\right)_{T,\mathbf{X},\mathbf{y}} - \left(\frac{\partial \ln\phi_i^L}{\partial p}\right)_{T,\mathbf{X},\mathbf{x}}\right]\,, \tag{K.0.25}$$

$$\chi_{T,k} = \left(\frac{\partial v_k}{\partial T}\right)_{p,\mathbf{X}}\,, \tag{K.0.26}$$

$$\chi_{p,k} = \left(\frac{\partial v_k}{\partial p}\right)_{T,\mathbf{X}}\,, \tag{K.0.27}$$

with $i,k = 1,\cdots,N_s$.

Note that $\mathcal{A}$ is the same for both systems and thus it can be assembled/inverted only once. All the fugacity coefficients (frozen) derivatives appearing in Eqs. (K.0.23)–(K.0.25) require an EoS model, thus the above formulation can be applied to any EoS that is capable to provide the fugacity and its derivatives. It is interesting to underline the fact that the v_k derivatives lead to a linear system. This is due to the effect that all species-related properties are not independent but they are linked to each other. Additional important formulas are the phase molar masses derivatives with respect to pressure and temperature.

Using similar steps one can write:

$$\left(\frac{\partial M^V}{\partial T}\right)_{p,\mathbf{X}} = \frac{\partial}{\partial T}\left(\sum_{k=1}^{N_s} y_k M_k\right)_{p,\mathbf{X}} \overset{\text{Using Eq. (2.2.40)}}{\downarrow} = \frac{1}{\beta^2}\sum_{k=1}^{N_s}\left[\left(\frac{\partial v_k}{\partial T}\right)_{p,\mathbf{X}} - v_k\left(\frac{\partial \beta}{\partial T}\right)_{p,\mathbf{X}}\right] M_k\,, \quad \text{(K.0.28)}$$

$$\left(\frac{\partial M^V}{\partial p}\right)_{T,\mathbf{X}} = \frac{\partial}{\partial p}\left(\sum_{k=1}^{N_s} y_k M_k\right)_{T,\mathbf{X}} = \frac{1}{\beta^2}\sum_{k=1}^{N_s}\left[\left(\frac{\partial v_k}{\partial p}\right)_{T,\mathbf{X}} - v_k\left(\frac{\partial \beta}{\partial p}\right)_{T,\mathbf{X}}\right] M_k\,, \quad \text{(K.0.29)}$$

$$\left(\frac{\partial M^L}{\partial T}\right)_{p,\mathbf{X}} = \frac{\partial}{\partial T}\left(\sum_{k=1}^{N_s} x_k M_k\right)_{p,\mathbf{X}} =$$

$$= \frac{1}{(1-\beta)^2}\sum_{k=1}^{N_s}\left[(X_k - v_k)\left(\frac{\partial \beta}{\partial T}\right)_{p,\mathbf{X}} - \left(\frac{\partial v_k}{\partial T}\right)_{p,\mathbf{X}}(1-\beta)\right] M_k\,, \quad \text{(K.0.30)}$$

$$\left(\frac{\partial M^L}{\partial p}\right)_{T,\mathbf{X}} = \frac{\partial}{\partial p}\left(\sum_{k=1}^{N_s} x_k M_k\right)_{T,\mathbf{X}} =$$

$$= \frac{1}{(1-\beta)^2}\sum_{k=1}^{N_s}\left[(X_k - v_k)\left(\frac{\partial \beta}{\partial p}\right)_{T,\mathbf{X}} - \left(\frac{\partial v_k}{\partial p}\right)_{T,\mathbf{X}}(1-\beta)\right] M_k\,. \quad \text{(K.0.31)}$$

Additional mixture, as well as phase-related derivatives are given below. The derivative of the pressure with respect to temperature using the link between Eq. (2.2.49) and Eq. (2.2.50):

$$\left(\frac{\partial \rho}{\partial T}\right)_{p,\mathbf{X}}\left(\frac{\partial T}{\partial p}\right)_{\rho,\mathbf{X}}\left(\frac{\partial p}{\partial \rho}\right)_{T,\mathbf{X}} = -1 \qquad \rightarrow \qquad \left(\frac{\partial p}{\partial T}\right)_{\rho,\mathbf{X}} = -\frac{\left(\frac{\partial \rho}{\partial T}\right)_{p,\mathbf{X}}}{\left(\frac{\partial \rho}{\partial p}\right)_{T,\mathbf{X}}}\,. \quad \text{(K.0.32)}$$

The above require the knowledge of the derivatives of $\rho^V = \rho^V(T,p,\mathbf{y}(T,p,\mathbf{X}))$ and $\rho^L = \rho^L(T,p,\mathbf{x}(T,p,\mathbf{X}))$. In short notation, for the generic phase $\eta = (L \,\text{or}\, \text{V})$ with molar composition $\boldsymbol{\zeta}$ one can write the total differential of $\rho^\eta = \rho^\eta(T,p,\zeta(T,p,\mathbf{X}))$:

$$d\rho^\eta = \left(\frac{\partial \rho^\eta}{\partial T}\right)_{p,\mathbf{X},\boldsymbol{\zeta}} dT + \left(\frac{\partial \rho^\eta}{\partial p}\right)_{T,\mathbf{X},\boldsymbol{\zeta}} dp + \sum_{k=1}^{N_s}\left(\frac{\partial \rho^\eta}{\partial \zeta_k}\right)_{T,p,\mathbf{X},\boldsymbol{\zeta}_k} d\zeta_k\,, \quad \text{(K.0.33)}$$

where $\boldsymbol{\zeta}_k = \{\zeta_i \,|\, i = 1,\cdots,N_s, i \neq k\}$. From Eq. (K.0.33) the "total" derivatives with respect to temperature and pressure follows:

$$\left(\frac{\partial \rho^\eta}{\partial T}\right)_{p,\mathbf{X}} = \left(\frac{\partial \rho^\eta}{\partial T}\right)_{p,\mathbf{X},\boldsymbol{\zeta}} + \sum_{k=1}^{N_s}\left(\frac{\partial \rho^\eta}{\partial \zeta_k}\right)_{T,p,\mathbf{X},\boldsymbol{\zeta}_k}\left(\frac{\partial \zeta_k}{\partial T}\right)_{p,\mathbf{X},\boldsymbol{\zeta}_k}\,, \quad \text{(K.0.34)}$$

$$\left(\frac{\partial \rho^\eta}{\partial p}\right)_{T,\mathbf{X}} = \left(\frac{\partial \rho^\eta}{\partial p}\right)_{T,\mathbf{X},\boldsymbol{\zeta}} + \sum_{k=1}^{N_s}\left(\frac{\partial \rho^\eta}{\partial \zeta_k}\right)_{T,p,\mathbf{X},\boldsymbol{\zeta}_k}\left(\frac{\partial \zeta_k}{\partial p}\right)_{T,\mathbf{X},\boldsymbol{\zeta}_k}\,. \quad \text{(K.0.35)}$$

Equations (K.0.34) and (K.0.35) require the additional derivative of the phase density with respect to the phase mole fraction. This is obtained by applying the general form of the EoS as in Eq. (2.2.3):

$$\left(\frac{\partial \rho^\eta}{\partial \zeta_k}\right)_{T,p,\mathbf{X},\boldsymbol{\zeta}_k} = \frac{p}{R_u T}\frac{M_k Z^\eta - M^\eta \left(\frac{\partial Z^\eta}{\partial \zeta_k}\right)_{T,p,\boldsymbol{\zeta}_k}}{(Z^\eta)^2}\,. \tag{K.0.36}$$

$$\downarrow$$

Use $\rho^\eta = pM^\eta/Z^\eta R_u T$ and $M^\eta = \sum_{k=1}^{N_s}\zeta_k M_k$

In the above, the (frozen) derivative $(\partial Z^\eta/\partial\zeta_k)_{T,p,\boldsymbol{\zeta}_k}$ requires a specific EoS model as well. Given the form of the EoS assumed to be explicit in pressure as in Eq. (2.2.2), a note must be made on the phase pressure/density/temperature derivatives. Particularly one can compute (without loss of generality):

$$\left(\frac{\partial \rho^\eta}{\partial p}\right)_{T,\mathbf{X},\boldsymbol{\zeta}} = \frac{1}{\left(\frac{\partial p}{\partial \rho^\eta}\right)_{T,\mathbf{X},\boldsymbol{\zeta}}}\,, \qquad \left(\frac{\partial \rho^\eta}{\partial T}\right)_{p,\mathbf{X},\boldsymbol{\zeta}} = -\frac{\left(\frac{\partial p}{\partial T}\right)_{\rho^\eta,\mathbf{X},\boldsymbol{\zeta}}}{\left(\frac{\partial p}{\partial \rho^\eta}\right)_{T,\mathbf{X},\boldsymbol{\zeta}}}\,, \tag{K.0.37}$$

$$\downarrow$$

Using $\left(\frac{\partial \rho^\eta}{\partial T}\right)_{p,\mathbf{X},\boldsymbol{\zeta}}\left(\frac{\partial T}{\partial p}\right)_{\rho^\eta,\mathbf{X},\boldsymbol{\zeta}}\left(\frac{\partial p}{\partial \rho^\eta}\right)_{T,\mathbf{X},\boldsymbol{\zeta}} = -1$

where now $(\partial p/\partial\rho^\eta)_{T,\mathbf{X},\boldsymbol{\zeta}}$ and $(\partial p/\partial T)_{\rho^\eta,\mathbf{X},\boldsymbol{\zeta}}$ can be directly computed from the EoS model. Next, the derivatives of the phase compressibilities are obtained. Using the general form of $Z^\eta = Z^\eta(T,p,\boldsymbol{\zeta}(T,p,\mathbf{X}))$ and writing the total differential one gets:

$$\left(\frac{\partial Z^\eta}{\partial T}\right)_{p,\mathbf{X}} = \left(\frac{\partial Z^\eta}{\partial T}\right)_{p,\mathbf{X},\boldsymbol{\zeta}} + \sum_{k=1}^{N_s}\left(\frac{\partial Z^\eta}{\partial \zeta_k}\right)_{T,p,\mathbf{X},\boldsymbol{\zeta}_k}\left(\frac{\partial \zeta_k}{\partial T}\right)_{p,\mathbf{X},\boldsymbol{\zeta}_k}\,, \tag{K.0.38}$$

$$\left(\frac{\partial Z^\eta}{\partial p}\right)_{T,\mathbf{X}} = \left(\frac{\partial Z^\eta}{\partial p}\right)_{T,\mathbf{X},\boldsymbol{\zeta}} + \sum_{k=1}^{N_s}\left(\frac{\partial Z^\eta}{\partial \zeta_k}\right)_{T,p,\mathbf{X},\boldsymbol{\zeta}_k}\left(\frac{\partial \zeta_k}{\partial p}\right)_{T,\mathbf{X},\boldsymbol{\zeta}_k}\,, \tag{K.0.39}$$

where $(\partial Z^\eta/\partial T)_{p,\mathbf{X},\boldsymbol{\zeta}}$ and $(\partial Z^\eta/\partial p)_{T,\mathbf{X},\boldsymbol{\zeta}}$ can be also computed from the EoS model.

On the other hand the mixture compressibility derivatives are obtained by differentiating Eq. (2.2.2):

$$\left(\frac{\partial Z}{\partial T}\right)_{p,\mathbf{X}} \overset{\text{Using } Z = pM/\rho R_u T}{\downarrow} = \frac{pM}{R_u}\frac{\partial}{\partial T}\left(\frac{1}{\rho T}\right)_{p,\mathbf{X}} = \frac{pM}{R_u}\frac{\left[\rho - T\left(\frac{\partial \rho}{\partial T}\right)_{p,\mathbf{X}}\right]}{(\rho T)^2}\,, \tag{K.0.40}$$

$$\left(\frac{\partial Z}{\partial p}\right)_{T,\mathbf{X}} = \frac{M}{R_u T}\frac{\partial}{\partial p}\left(\frac{p}{\rho}\right)_{T,\mathbf{X}} = \frac{M}{R_u T}\left[\rho - p\left(\frac{\partial \rho}{\partial p}\right)_{T,\mathbf{X}}\right]\,. \tag{K.0.41}$$

Note that the form of Eqs. (K.0.40)–(K.0.41) holds for a single phase mixture identically (that is can be used in single phase conditions too).

Finally, the last important variations to compute are the internal energy derivatives. By differentiating Eq. (2.2.35) one gets for the mixture:

$$\left(\frac{\partial E}{\partial T}\right)_{p,\mathbf{X}} = \left(\frac{\partial \beta}{\partial T}\right)_{p,\mathbf{X}} (E^V - E^L) + \beta \left(\frac{\partial E^V}{\partial T}\right)_{p,\mathbf{X}} + (1-\beta)\left(\frac{\partial E^L}{\partial T}\right)_{p,\mathbf{X}}, \tag{K.0.42}$$

$$\left(\frac{\partial E}{\partial p}\right)_{T,\mathbf{X}} = \left(\frac{\partial \beta}{\partial p}\right)_{T,\mathbf{X}} (E^V - E^L) + \beta \left(\frac{\partial E^V}{\partial p}\right)_{T,\mathbf{X}} + (1-\beta)\left(\frac{\partial E^L}{\partial p}\right)_{T,\mathbf{X}}. \tag{K.0.43}$$

On the other hand, given that $E^\eta = E^\eta(T, p, \boldsymbol{\zeta}(T, p, \mathbf{X}))$, using again the total differential, the following phase related derivatives are obtained:

$$\left(\frac{\partial E^\eta}{\partial T}\right)_{p,\mathbf{X}} = \left(\frac{\partial E^\eta}{\partial T}\right)_{p,\mathbf{X},\boldsymbol{\zeta}} + \sum_{k=1}^{N_s} \left(\frac{\partial E^\eta}{\partial \zeta_k}\right)_{T,p,\mathbf{X},\boldsymbol{\zeta}_k} \left(\frac{\partial \zeta_k}{\partial T}\right)_{p,\mathbf{X},\boldsymbol{\zeta}_k}, \tag{K.0.44}$$

$$\left(\frac{\partial E^\eta}{\partial p}\right)_{T,\mathbf{X}} = \left(\frac{\partial E^\eta}{\partial p}\right)_{T,\mathbf{X},\boldsymbol{\zeta}} + \sum_{k=1}^{N_s} \left(\frac{\partial E^\eta}{\partial \zeta_k}\right)_{T,p,\mathbf{X},\boldsymbol{\zeta}_k} \left(\frac{\partial \zeta_k}{\partial p}\right)_{T,\mathbf{X},\boldsymbol{\zeta}_k}, \tag{K.0.45}$$

where:

$$\begin{aligned}\left(\frac{\partial E^\eta}{\partial \zeta_k}\right)_{T,p,\mathbf{X},\boldsymbol{\zeta}_k} &= \frac{\partial}{\partial \zeta_k}\left(E^{\eta,ig} + \Delta E^\eta\right)_{T,p,\mathbf{X},\boldsymbol{\zeta}_k} = \frac{\partial}{\partial \zeta_k}\left(\sum_{j=1}^{N_s} \zeta_j E_j^{ig}\right)_{T,p,\mathbf{X},\boldsymbol{\zeta}_k} + \left(\frac{\partial \Delta E^\eta}{\partial \zeta_k}\right)_{T,p,\mathbf{X},\boldsymbol{\zeta}_k} = \\ &= E_k^{ig} + \left(\frac{\partial \Delta E^\eta}{\partial \zeta_k}\right)_{T,p,\mathbf{X},\boldsymbol{\zeta}_k}.\end{aligned} \tag{K.0.46}$$

$$\begin{aligned}\left(\frac{\partial E^\eta}{\partial T}\right)_{p,\mathbf{X},\boldsymbol{\zeta}} &= \frac{\partial}{\partial T}\left(E^{\eta,ig} + \Delta E^\eta\right)_{p,\mathbf{X},\boldsymbol{\zeta}} = \frac{\partial}{\partial T}\left(\sum_{j=1}^{N_s} \zeta_j E_j^{ig}\right)_{T,p,\mathbf{X},\boldsymbol{\zeta}} + \left(\frac{\partial \Delta E^\eta}{\partial T}\right)_{p,\mathbf{X},\boldsymbol{\zeta}} = \\ &= \overbrace{\sum_{j=1}^{N_s} \zeta_j \underbrace{\left(\frac{dE_j^{ig}}{dT}\right)}}^{C_v^{\eta,ig}} + \left(\frac{\partial \Delta E^\eta}{\partial T}\right)_{p,\mathbf{X},\boldsymbol{\zeta}} = C_v^{\eta,ig} + \left(\frac{\partial \Delta E^\eta}{\partial T}\right)_{p,\mathbf{X},\boldsymbol{\zeta}}.\end{aligned} \tag{K.0.47}$$

$\downarrow$

$= C_{v,j}^{ig}$. Since E_j^{ig} is only a function of T

$$\begin{aligned}\left(\frac{\partial E^\eta}{\partial p}\right)_{T,\mathbf{X},\boldsymbol{\zeta}} &= \frac{\partial}{\partial p}\left(E^{\eta,ig} + \Delta E^\eta\right)_{T,\mathbf{X},\boldsymbol{\zeta}} = \frac{\partial}{\partial p}\left(\sum_{j=1}^{N_s} \zeta_j E_j^{ig}\right)_{T,\mathbf{X},\boldsymbol{\zeta}} + \left(\frac{\partial \Delta E^\eta}{\partial p}\right)_{T,\mathbf{X},\boldsymbol{\zeta}} = \\ &= \sum_{j=1}^{N_s} \zeta_j \underbrace{\left(\frac{dE_j^{ig}}{dp}\right)}_{\to 0} + \left(\frac{\partial \Delta E^\eta}{\partial p}\right)_{T,\mathbf{X},\boldsymbol{\zeta}} = \left(\frac{\partial \Delta E^\eta}{\partial p}\right)_{T,\mathbf{X},\boldsymbol{\zeta}},\end{aligned} \tag{K.0.48}$$

where $(\partial \Delta E^{\eta}/\partial T)_{p,\mathbf{X},\boldsymbol{\zeta}}$, $(\partial \Delta E^{\eta}/\partial p)_{T,\mathbf{X},\boldsymbol{\zeta}}$ and $(\partial \Delta E^{\eta}/\partial \zeta_k)_{T,p,\mathbf{X},\boldsymbol{\zeta}_k}$ are again computed with an EoS model. In the above, $C^{ig}_{v,j}$ and E^{ig}_{j} have been used to denote the j-th species IG molar specific heat at constant volume and internal energy, respectively, while $C^{\eta,ig}_{v}$ indicated the mixture IG molar specific heat at constant volume in the phase η. Algorithm 5 in Appendix D provides the necessary steps to compute the derivatives in each phase, while Algorithm 4 provides the final steps to compute additional derivatives for the VLE mixture, up to specific heats, isothermal compressibility, isobaric expansivity and speed of sound.

Appendix L

MULTI-PHASE THERMODYNAMICS: PARTIAL MOLAR QUANTITIES

Regarding the first term of Eq. (2.2.63), using the fact that $p\overline{V}^{\eta} = \sigma Z^{\eta} R_u T$ (with σ defined in Eq. (2.2.55)), one can write for both phases:

$$\left(\frac{\partial \overline{V}^{V}}{\partial N_k^V}\right)_{T,p,\mathbf{N}_k^V} = \frac{R_u T}{p}\frac{\partial}{\partial N_k^V}\left(N^V Z^V\right)_{T,p,\mathbf{N}_k^V} = \frac{R_u T}{p}\left[Z^V \underbrace{\left(\frac{\partial N^V}{\partial N_k^V}\right)_{T,p,\mathbf{N}_k^V}}_{=1} + N^V \left(\frac{\partial Z^V}{\partial N_k^V}\right)_{T,p,\mathbf{N}_k^V}\right] =$$

$$= \frac{R_u T}{p}\left[Z^V + N^V \left(\frac{\partial Z^V}{\partial N_k^V}\right)_{T,p,\mathbf{N}_k^V}\right], \tag{L.0.1}$$

$$\left(\frac{\partial \overline{V}^{L}}{\partial N_k^L}\right)_{T,p,\mathbf{N}_k^L} = \frac{R_u T}{p}\frac{\partial}{\partial N_k^L}\left(N^L Z^L\right)_{T,p,\mathbf{N}_k^L} = \frac{R_u T}{p}\left[Z^L \underbrace{\left(\frac{\partial N^L}{\partial N_k^L}\right)_{T,p,\mathbf{N}_k^L}}_{=1} + N^L \left(\frac{\partial Z^L}{\partial N_k^L}\right)_{T,p,\mathbf{N}_k^L}\right] =$$

$$= \frac{R_u T}{p}\left[Z^L + N^L \left(\frac{\partial Z^L}{\partial N_k^L}\right)_{T,p,\mathbf{N}_k^L}\right]. \tag{L.0.2}$$

To proceed further, a conversion between a mole based derivative to a mole fraction based derivative is required. The reason for this is that some numerical simulation tools are based on mass/mole fractions and therefore having the formulas based on these is more convenient. The link between the two quantities is given by the following identity (its proof is given in Appendix B):

$$\left(\frac{\partial(\cdot)}{\partial N_j}\right)_{T,p,\mathbf{N}_j} = \sum_{k=1}^{N_s}\left(\frac{\partial(\cdot)}{\partial X_k}\right)_{T,p,\mathbf{X}_k}\frac{\delta_{kj} - X_k}{N}. \tag{L.0.3}$$

After applying Eq. (L.0.3) to the compressibility derivatives of Eq. (L.0.1) and Eq. (L.0.2) one can easily get their modified version:

$$\left(\frac{\partial \overline{V}^V}{\partial N_k^V}\right)_{T,p,\mathbf{N}_k^V} = \frac{R_u T}{p}\left[Z^V + \sum_{j=1}^{N_s}\left(\frac{\partial Z^V}{\partial y_j}\right)_{T,p,\mathbf{y}_j}(\delta_{jk} - y_j)\right], \tag{L.0.4}$$

$$\left(\frac{\partial \overline{V}^L}{\partial N_k^L}\right)_{T,p,\mathbf{N}_k^L} = \frac{R_u T}{p}\left[Z^L + \sum_{j=1}^{N_s}\left(\frac{\partial Z^L}{\partial x_j}\right)_{T,p,\mathbf{x}_j}(\delta_{jk} - x_j)\right]. \tag{L.0.5}$$

Both $(\partial Z^V/\partial y_j)_{T,p,\mathbf{y}_j}$ and $(\partial Z^V/\partial x_j)_{T,p,\mathbf{x}_j}$ can be now easily obtained from the EoS model. Next, the unknowns $(\partial \sigma_k/\partial N_i)_{T,p,\boldsymbol{\sigma}_k,\mathbf{N}_i}$ are derived. To begin, the equilibrium condition of Eq. (2.2.31) (in logarithmic form) and the continuity condition: $N_k = N_k^L + N_k^V$, $k = 1, \cdots, N_s$ are differentiated with respect to the i-*th* species mole number:

$$\left(\frac{\partial \ln f_k^L}{\partial N_i}\right)_{T,p,\mathbf{N}_i} - \left(\frac{\partial \ln f_k^V}{\partial N_i}\right)_{T,p,\mathbf{N}_i} = 0 \qquad i,k = 1,\cdots,N_s\,, \tag{L.0.6}$$

$$\left(\frac{\partial N_k^L}{\partial N_i}\right)_{T,p,\mathbf{N}_k^L,\mathbf{N}_i} + \left(\frac{\partial N_k^V}{\partial N_i}\right)_{T,p,\mathbf{N}_k^V,\mathbf{N}_i} = \left(\frac{\partial N_k}{\partial N_i}\right)_{T,p,\mathbf{N}_i} \qquad i,k = 1,\cdots,N_s\,. \tag{L.0.7}$$

Since $\ln f_k^\eta = \ln f_k^\eta(T,p,\boldsymbol{\sigma})$, application of the total differential at constant T and p and its differentiation with respect to the i-*th* species mole number produces:

$$\left(\frac{\partial \ln f_k^L}{\partial N_i}\right)_{T,p,\mathbf{N}_i} = \sum_{j=1}^{N_s}\left(\frac{\partial \ln f_k^L}{\partial N_j^L}\right)_{T,p,\mathbf{N}_j^L}\left(\frac{\partial N_j^L}{\partial N_i}\right)_{T,p,\mathbf{N}_j^L,\mathbf{N}_i}, \tag{L.0.8}$$

$$\left(\frac{\partial \ln f_k^V}{\partial N_i}\right)_{T,p,\mathbf{N}_i} = \sum_{j=1}^{N_s}\left(\frac{\partial \ln f_k^V}{\partial N_j^V}\right)_{T,p,\mathbf{N}_j^V}\left(\frac{\partial N_j^V}{\partial N_i}\right)_{T,p,\mathbf{N}_j^V,\mathbf{N}_i}. \tag{L.0.9}$$

Substituting Eq. (L.0.8) and Eq. (L.0.9) into Eq. (L.0.6) leads to:

$$\sum_{j=1}^{N_s}\left[\left(\frac{\partial \ln f_k^L}{\partial N_j^L}\right)_{T,p,\mathbf{N}_j^L}\left(\frac{\partial N_j^L}{\partial N_i}\right)_{T,p,\mathbf{N}_j^L,\mathbf{N}_i} - \left(\frac{\partial \ln f_k^V}{\partial N_j^V}\right)_{T,p,\mathbf{N}_j^V}\left(\frac{\partial N_j^V}{\partial N_i}\right)_{T,p,\mathbf{N}_j^V,\mathbf{N}_i}\right] = 0 \qquad i,k = 1,\cdots,N_s\,. \tag{L.0.10}$$

Conversion of the fugacity to its corresponding fugacity coefficient gives:

$$\ln f_k^L = \ln \phi_k^L + \ln p + \ln x_k \qquad k = 1,\cdots,N_s\,, \tag{L.0.11}$$

$$\ln f_k^V = \ln \phi_k^V + \ln p + \ln y_k \qquad k = 1,\cdots,N_s\,, \tag{L.0.12}$$

thus, by differentiating Eq. (L.0.11) and Eq. (L.0.12) by N_j^L and N_j^V, respectively, the following result is obtained:

$$\left(\frac{\partial \ln f_k^L}{\partial N_j^L}\right)_{T,p,\mathbf{N}_j^L} = \left(\frac{\partial \ln \phi_k^L}{\partial N_j^L}\right)_{T,p,\mathbf{N}_j^L} + \cancelto{0}{\left(\frac{\partial p}{\partial N_j^L}\right)_{T,p,\mathbf{N}_j^L}} + \left(\frac{\partial \ln x_k^L}{\partial N_j^L}\right)_{T,p,\mathbf{N}_j^L}, \tag{L.0.13}$$

$$\left(\frac{\partial \ln f_k^V}{\partial N_j^V}\right)_{T,p,\mathbf{N}_j^V} = \left(\frac{\partial \ln \phi_k^V}{\partial N_j^V}\right)_{T,p,\mathbf{N}_j^V} + \cancelto{0}{\left(\frac{\partial p}{\partial N_j^V}\right)_{T,p,\mathbf{N}_j^V}} + \left(\frac{\partial \ln y_k^V}{\partial N_j^V}\right)_{T,p,\mathbf{N}_j^V}. \tag{L.0.14}$$

Furthermore, by expanding the logarithm derivative in the last term of Eq. (L.0.13) and Eq. (L.0.14) and using the result of Eq. (B.0.2), Eqs. (L.0.13)–(L.0.14) can be rewritten as:

$$\left(\frac{\partial \ln f_k^L}{\partial N_j^L}\right)_{T,p,\mathbf{N}_j^L} = \left(\frac{\partial \ln \phi_k^L}{\partial N_j^L}\right)_{T,p,\mathbf{N}_j^L} + \frac{1}{x_k}\frac{\delta_{kj} - x_k}{N^L}, \tag{L.0.15}$$

$$\left(\frac{\partial \ln f_k^V}{\partial N_j^V}\right)_{T,p,\mathbf{N}_j^V} = \left(\frac{\partial \ln \phi_k^V}{\partial N_j^V}\right)_{T,p,\mathbf{N}_j^V} + \frac{1}{y_k}\frac{\delta_{kj} - y_k}{N^V}. \tag{L.0.16}$$

Also, by applying the identity of Eq. (L.0.3) to the fugacity coefficient derivatives the following additional step is obtained:

$$\left(\frac{\partial \ln \phi_k^L}{\partial N_j^L}\right)_{T,p,\mathbf{N}_j^L} = \sum_{s=1}^{N_s} \left(\frac{\ln \phi_k^L}{\partial x_s}\right)_{T,p,\mathbf{x}_s} \left(\frac{\delta_{sj} - x_s}{N^L}\right), \tag{L.0.17}$$

$$\left(\frac{\partial \ln \phi_k^V}{\partial N_j^V}\right)_{T,p,\mathbf{N}_j^V} = \sum_{s=1}^{N_s} \left(\frac{\ln \phi_k^V}{\partial y_s}\right)_{T,p,\mathbf{y}_s} \left(\frac{\delta_{sj} - y_s}{N^V}\right). \tag{L.0.18}$$

Substituting Eq. (L.0.17) and Eq. (L.0.18) into Eq. (L.0.15) and Eq. (L.0.16) and then substituting these two into Eq. (L.0.10), the following intermediate result is obtained:

$$\sum_{j=1}^{N_s} \left\{ \left[\sum_{s=1}^{N_s} \left(\frac{\partial \ln \phi_k^L}{\partial x_s}\right)_{T,p,\mathbf{x}_s} \left(\frac{\delta_{sj} - x_s}{N^L}\right) + \frac{1}{x_k}\frac{\delta_{kj} - x_k}{N^L} \right] \left(\frac{\partial N_j^L}{\partial N_i}\right)_{T,p,\mathbf{N}_j^L,\mathbf{N}_i} - \right.$$
$$\left. \left[\sum_{s=1}^{N_s} \left(\frac{\partial \ln \phi_k^V}{\partial y_s}\right)_{T,p,\mathbf{y}_s} \left(\frac{\delta_{sj} - y_s}{N^V}\right) + \frac{1}{y_k}\frac{\delta_{kj} - y_k}{N^V} \right] \left(\frac{\partial N_j^V}{\partial N_i}\right)_{T,p,\mathbf{N}_j^V,\mathbf{N}_i} \right\} = 0 \qquad i,k = 1,\cdots,N_s. \tag{L.0.19}$$

By multiplying both sides by N and recalling that $\beta = N^V/N$ and $1-\beta = N^L/N$, the previous result can be updated to the following:

$$\sum_{j=1}^{N_s}\Bigg\{\left[\sum_{s=1}^{N_s}\left(\frac{\partial \ln\phi_k^L}{\partial x_s}\right)_{T,p,\mathbf{x}_s}\left(\frac{\delta_{sj}-x_s}{1-\beta}\right)+\frac{1}{x_k}\frac{\delta_{kj}-x_k}{1-\beta}\right]\left(\frac{\partial N_j^L}{\partial N_i}\right)_{T,p,\mathbf{N}_j^L,\mathbf{N}_i} - \left[\sum_{s=1}^{N_s}\left(\frac{\partial \ln\phi_k^V}{\partial y_s}\right)_{T,p,\mathbf{y}_s}\left(\frac{\delta_{sj}-y_s}{\beta}\right)+\frac{1}{y_k}\frac{\delta_{kj}-y_k}{\beta}\right]\left(\frac{\partial N_j^V}{\partial N_i}\right)_{T,p,\mathbf{N}_j^V,\mathbf{N}_i}\Bigg\} = 0 \qquad i,k=1,\cdots,N_s\,. \tag{L.0.20}$$

Using Eq. (L.0.7) one can reduce the number of variables by expressing one set as a function of the other set. Without loss of generality, by expressing the derivatives of the liquid phase as a function of those in the vapor phase, one gets the following relationship:

$$\left(\frac{\partial N_k^L}{\partial N_i}\right)_{T,p,\mathbf{N}_k^L,\mathbf{N}_i} = \delta_{ki} - \left(\frac{\partial N_k^V}{\partial N_i}\right)_{T,p,\mathbf{N}_k^V,\mathbf{N}_i} \qquad i,k=1,\cdots,N_s\,. \tag{L.0.21}$$

Hence, using Eq. (L.0.21) into Eq. (L.0.20) and rearranging the following final result is obtained:

$$\begin{aligned}&\sum_{j=1}^{N_s}\Bigg\{\sum_{s=1}^{N_s}\left[\left(\frac{\partial \ln\phi_k^L}{\partial x_s}\right)_{T,p,\mathbf{x}_s}\left(\frac{\delta_{sj}-x_s}{1-\beta}\right)+\left(\frac{\partial \ln\phi_k^V}{\partial y_s}\right)_{T,p,\mathbf{y}_s}\left(\frac{\delta_{sj}-y_s}{\beta}\right)\right]+\\ &+\frac{1}{x_k}\frac{\delta_{kj}-x_k}{1-\beta}+\frac{1}{y_k}\frac{\delta_{kj}-y_k}{\beta}\Bigg\}\left(\frac{\partial N_j^V}{\partial N_i}\right)_{T,p,\mathbf{N}_j^V,\mathbf{N}_i} =\\ &=\sum_{j=1}^{N_s}\delta_{ji}\left\{\sum_{s=1}^{N_s}\left[\left(\frac{\partial \ln\phi_k^L}{\partial x_s}\right)_{T,p,\mathbf{x}_s}\left(\frac{\delta_{sj}-x_s}{1-\beta}\right)\right]+\frac{\delta_{ji}}{x_k}\left(\frac{\delta_{kj}-x_k}{1-\beta}\right)\right\} \qquad i,k=1,\cdots,N_s\,.\end{aligned} \tag{L.0.22}$$

Therefore by defining :

$$\mathcal{C}_{kj} = \sum_{s=1}^{N_s}\left[\left(\frac{\partial \ln\phi_k^L}{\partial x_s}\right)_{T,p,\mathbf{x}_s}\left(\frac{\delta_{sj}-x_s}{1-\beta}\right)+\left(\frac{\partial \ln\phi_k^V}{\partial y_s}\right)_{T,p,\mathbf{y}_s}\left(\frac{\delta_{sj}-y_s}{\beta}\right)\right]+\frac{1}{x_k}\frac{\delta_{kj}-x_k}{1-\beta}+\frac{1}{y_k}\frac{\delta_{kj}-y_k}{\beta}\,, \tag{L.0.23}$$

$$b_{N,k}^{(i)} = \sum_{j=1}^{N_s}\delta_{ji}\left\{\sum_{s=1}^{N_s}\left[\left(\frac{\partial \ln\phi_k^L}{\partial x_s}\right)_{T,p,\mathbf{x}_s}\left(\frac{\delta_{sj}-x_s}{1-\beta}\right)\right]+\frac{\delta_{ji}}{x_k}\left(\frac{\delta_{kj}-x_k}{1-\beta}\right)\right\}\,, \tag{L.0.24}$$

$$\chi_{N,j}^{(i)} = \left(\frac{\partial N_j^V}{\partial N_i}\right)_{T,p,\mathbf{N}_j^V,\mathbf{N}_i}\,, \tag{L.0.25}$$

the following linear system needs to be solved N_s times in the unknown vector $\boldsymbol{\chi}_N^{(i)}$:

$$\boldsymbol{\mathcal{C}}\boldsymbol{\chi}_N^{(i)} = \mathbf{b}_N^{(i)} \qquad i = 1, \cdots, N_s\,, \tag{L.0.26}$$

however, given the fact that the matrix $\boldsymbol{\mathcal{C}}$ does not depend on i, the matrix inversion itself must be done only once for all the unknowns. Algorithm 6 in Appendix D summarizes the steps to compute the partial molar volume for each species in the mixture, in case VLE occurs. If VLE does not occur, the single phase formula applies.

Using the fact that $\overline{E}^{\eta} = \overline{E}^{\eta}(T, p, \boldsymbol{\sigma})$, the total differential in compact form for both phases writes:

$$d\overline{E}^{\eta} = \left(\frac{\partial \overline{E}^{\eta}}{\partial T}\right)_{p,\boldsymbol{\sigma}} dT + \left(\frac{\partial \overline{E}^{\eta}}{\partial p}\right)_{T,\boldsymbol{\sigma}} dp + \sum_{k=1}^{N_s} \left(\frac{\partial \overline{E}^{\eta}}{\partial \sigma_k}\right)_{T,p,\boldsymbol{\sigma}_k} d\sigma_k\,. \tag{L.0.27}$$

Using the result of Eq. (L.0.27) and knowing that pressure and temperature are maintained constant, the differentiation with respect to the i-*th* species number of moles gives for both phases:

$$\overline{E}^{V} = N\beta E^{V} = N^{V} E^{V}$$

$$\left(\frac{\partial \overline{E}^{V}}{\partial N_i}\right)_{T,p,\mathbf{N}_i} \downarrow = \sum_{k=1}^{N_s} \left(\frac{\partial N^{V} E^{V}}{\partial N_k^{V}}\right)_{T,p,\mathbf{N}_k^{V}} \left(\frac{\partial N_k^{V}}{\partial N_i}\right)_{T,p,\mathbf{N}_k^{V},\mathbf{N}_i} \qquad i = 1, \cdots, N_s\,, \tag{L.0.28}$$

$$\left(\frac{\partial \overline{E}^{L}}{\partial N_i}\right)_{T,p,\mathbf{N}_i} = \sum_{k=1}^{N_s} \left(\frac{\partial N^{L} E^{L}}{\partial N_k^{L}}\right)_{T,p,\mathbf{N}_k^{L}} \left(\frac{\partial N_k^{L}}{\partial N_i}\right)_{T,p,\mathbf{N}_k^{L},\mathbf{N}_i} \qquad i = 1, \cdots, N_s. \tag{L.0.29}$$

$$\overline{E}^{L} = N(1-\beta) E^{L} = N^{L} E^{L}$$

Following the same method used for Eq. (L.0.1) and Eq. (L.0.2), the above relations can be further manipulated as follows:

$$\left(\frac{\partial \overline{E}^{V}}{\partial N_i}\right)_{T,p,\mathbf{N}_i} = \sum_{k=1}^{N_s} \left[E^{V} + N^{V} \left(\frac{\partial E^{V}}{\partial N_k^{V}}\right)_{T,p,\mathbf{N}_k^{V}}\right] \left(\frac{\partial N_k^{V}}{\partial N_i}\right)_{T,p,\mathbf{N}_k^{V},\mathbf{N}_i} \qquad i = 1, \cdots, N_s\,, \tag{L.0.30}$$

$$\left(\frac{\partial \overline{E}^{L}}{\partial N_i}\right)_{T,p,\mathbf{N}_i} = \sum_{k=1}^{N_s} \left[E^{L} + N^{L} \left(\frac{\partial E^{L}}{\partial N_k^{L}}\right)_{T,p,\mathbf{N}_k^{L}}\right] \left(\frac{\partial N_k^{L}}{\partial N_i}\right)_{T,p,\mathbf{N}_k^{L},\mathbf{N}_i} \qquad i = 1, \cdots, N_s. \tag{L.0.31}$$

Finally, application of the identity Eq. (L.0.3) on the mole number based, internal energy derivatives gives the final result:

$$\left(\frac{\partial \overline{E}^V}{\partial N_i}\right)_{T,p,\mathbf{N}_i} = \sum_{k=1}^{N_s} \left\{ E^V + \sum_{s=1}^{N_s} \left[\left(\frac{\partial E^V}{\partial y_k}\right)_{T,p,\mathbf{y}_k} (\delta_{sk} - y_s) \right] \right\} \left(\frac{\partial N_k^V}{\partial N_i}\right)_{T,p,\mathbf{N}_k^V,\mathbf{N}_i} \qquad i = 1, \cdots, N_s\,, \tag{L.0.32}$$

$$\left(\frac{\partial \overline{E}^L}{\partial N_i}\right)_{T,p,\mathbf{N}_i} = \sum_{k=1}^{N_s} \left\{ E^L + \sum_{s=1}^{N_s} \left[\left(\frac{\partial E^L}{\partial x_k}\right)_{T,p,\mathbf{x}_k} (\delta_{sk} - x_s) \right] \right\} \left(\frac{\partial N_k^L}{\partial N_i}\right)_{T,p,\mathbf{N}_k^L,\mathbf{N}_i} \qquad i = 1, \cdots, N_s. \tag{L.0.33}$$

The derivatives $(\partial E^\eta/\partial \zeta_k)_{T,p,\boldsymbol{\zeta}_k}$ are assumed to be available with the EoS model by applying Algorithm 5 and derivatives $(\partial N_k^V/\partial N_i)_{T,p,\mathbf{N}_k^V,\mathbf{N}_i}$ and $(\partial N_k^L/\partial N_i)_{T,p,\mathbf{N}_k^L,\mathbf{N}_i}$ correspond to $\boldsymbol{\chi}_N^{(i)}$ already computed with Eq. (L.0.26). Algorithm 7 in Appendix D summarizes the steps required to compute the partial molar enthalpy in the VLE region.

Appendix M

ADDITIONAL DERIVATIONS FOR THE GCEOS

M.1 Additional derivatives of the compressibility factor

Derivatives of the single-phase compressibility factor with respect to temperature, pressure and the k-th species are required. For the temperature and pressure derivatives, Eqs. (K.0.40)–(K.0.41) can be used too, however another form is also provided below. The approach is to differentiate Eq. (2.2.70) with respect to temperature and pressure such that the following relationships are obtained[1]:

$$\left(\frac{\partial Z}{\partial T}\right)_{p,\mathbf{X}} = -\frac{Z^3\left(\frac{\partial a_1}{\partial T}\right)_{p,\mathbf{X}} + Z^2\left(\frac{\partial a_2}{\partial T}\right)_{p,\mathbf{X}} + Z\left(\frac{\partial a_3}{\partial T}\right)_{p,\mathbf{X}} + \left(\frac{\partial a_4}{\partial T}\right)_{p,\mathbf{X}}}{3a_1Z^2 + 2a_2Z + a_3}, \tag{M.1.1}$$

$$\left(\frac{\partial Z}{\partial p}\right)_{T,\mathbf{X}} = -\frac{Z^3\left(\frac{\partial a_1}{\partial p}\right)_{T,\mathbf{X}} + Z^2\left(\frac{\partial a_2}{\partial p}\right)_{T,\mathbf{X}} + Z\left(\frac{\partial a_3}{\partial p}\right)_{T,\mathbf{X}} + \left(\frac{\partial a_4}{\partial p}\right)_{T,\mathbf{X}}}{3a_1Z^2 + 2a_2Z + a_3}, \tag{M.1.2}$$

[1]These derivatives, as the rest of formulas discussed in this section are intended to be applied for the generic η phase in the VLE region as well. For example $(\partial Z/\partial T)_{p,\mathbf{X}}$ of Eq. (M.1.1) must be used as $(\partial Z^\eta/\partial T)_{p,\mathbf{X},\boldsymbol{\zeta}}$ in Eq. (K.0.38) with $Z^\eta = Z^\eta(T,p,\boldsymbol{\zeta}(T,p,\mathbf{X}))$ and $\eta = L$ or V.

where the derivatives of the a_1-a_4 coefficients can be obtained from Eq. (2.2.71):

$$\begin{aligned}
\left(\frac{\partial a_1}{\partial T}\right)_{p,\mathbf{X}} &= 3T^2\frac{R_u^3}{p^3}\,,\\
\left(\frac{\partial a_2}{\partial T}\right)_{p,\mathbf{X}} &= \frac{R_u^3T^2}{p^3}\left[2\tilde{B}_m(\delta_1+\delta_2-1)-3\right]\,,\\
\left(\frac{\partial a_3}{\partial T}\right)_{p,\mathbf{X}} &= \frac{R_uB_m^2}{p}\left[\delta_1\delta_2-(\delta_1+\delta_2)\right]-2(\delta_1+\delta_2)\frac{TB_mR_u^2}{p^2}+\frac{A_mR_u}{p^2}+\frac{R_uT}{p^2}\left(\frac{\partial A_m}{\partial T}\right)_{\mathbf{X}}\,,\\
\left(\frac{\partial a_4}{\partial T}\right)_{p,\mathbf{X}} &= -\delta_1\delta_2R_u\frac{B_m^2}{p}-\frac{B_m}{p}\left(\frac{\partial A_m}{\partial T}\right)_{\mathbf{X}}\,,\\
\left(\frac{\partial a_1}{\partial p}\right)_{T,\mathbf{X}} &= -3\frac{R_u^3T^3}{p^4}\,,\\
\left(\frac{\partial a_2}{\partial p}\right)_{T,\mathbf{X}} &= \frac{R_u^3T^3}{p^4}\left[3-2\tilde{B}_m(\delta_1+\delta_2-1)\right]\,,\\
\left(\frac{\partial a_3}{\partial p}\right)_{T,\mathbf{X}} &= -\frac{R_uTB_m^2}{p^2}\left[\delta_1\delta_2-(\delta_1+\delta_2)\right]+2(\delta_1+\delta_2)\frac{B_mR_u^2T^2}{p^3}-2\frac{A_mR_uT}{p^3}\,,\\
\left(\frac{\partial a_4}{\partial p}\right)_{T,\mathbf{X}} &= \delta_1\delta_2R_uT\frac{B_m^2}{p^2}+\frac{A_mB_m}{p^2}\,.
\end{aligned} \tag{M.1.3}$$

Regarding the derivative with respect to the k-th species mole fraction, although the formal structure is the same as the ones before:

$$\left(\frac{\partial Z}{\partial X_k}\right)_{p,\mathbf{X}_k} = -\frac{Z^3\left(\frac{\partial a_1}{\partial X_k}\right)_{p,\mathbf{X}_k}+Z^2\left(\frac{\partial a_2}{\partial X_k}\right)_{p,\mathbf{X}_k}+Z\left(\frac{\partial a_3}{\partial X_k}\right)_{p,\mathbf{X}_k}+\left(\frac{\partial a_4}{\partial X_k}\right)_{p,\mathbf{X}_k}}{3a_1Z^2+2a_2Z+a_3}\,, \tag{M.1.4}$$

attention must be dedicated to the derivatives of a_1-a_4 coefficients since δ_1 and δ_2 become mixture-dependent for PR-RK EoS according to Eq. (2.2.68). For this reason, the results are provided separately. For all GCEoS except PR-RK, one obtains:

$$\begin{aligned}
\left(\frac{\partial a_1}{\partial X_k}\right)_{p,\mathbf{X}_k} &= 0\,,\\
\left(\frac{\partial a_2}{\partial X_k}\right)_{p,\mathbf{X}_k} &= \frac{R_u^2T^2}{p^2}(\delta_1+\delta_2-1)\left(\frac{\partial B_m}{\partial X_k}\right)_{\mathbf{X}_k}\,,\\
\left(\frac{\partial a_3}{\partial X_k}\right)_{p,\mathbf{X}_k} &= \frac{R_u^2T^2}{p^2}\left\{2\tilde{B}_m\left[\delta_1\delta_2-(\delta_1+\delta_2)\right]-(\delta_1+\delta_2)\right\}\left(\frac{\partial B_m}{\partial X_k}\right)_{\mathbf{X}_k}+\frac{R_uT}{p^2}\left(\frac{\partial A_m}{\partial X_k}\right)_{T,\mathbf{X}_k}\,,\\
\left(\frac{\partial a_4}{\partial X_k}\right)_{p,\mathbf{X}_k} &= -\left(2\delta_1\delta_2\frac{R_uT}{p}B_m+\frac{A_m}{p}+3\delta_1\delta_2B_m^2\right)\left(\frac{\partial B_m}{\partial X_k}\right)_{\mathbf{X}_k}-\frac{B_m}{p}\left(\frac{\partial A_m}{\partial X_k}\right)_{T,\mathbf{X}_k}\,.
\end{aligned} \tag{M.1.5}$$

On the other hand, for the PR-RK EoS, the following result is obtained:

$$
\begin{aligned}
\left(\frac{\partial a_1}{\partial X_k}\right)_{p,\mathbf{X}_k} =& 0\,,\\
\left(\frac{\partial a_2}{\partial X_k}\right)_{p,\mathbf{X}_k} =& \frac{R_u^2T^2}{p^2}(\delta_1+\delta_2-1)\left(\frac{\partial B_m}{\partial X_k}\right)_{\mathbf{X}_k} + \tilde{B}_m\left[\left(\frac{\partial \delta_1}{\partial X_k}\right)_{\mathbf{X}_k} + \left(\frac{\partial \delta_2}{\partial X_k}\right)_{\mathbf{X}_k}\right],\\
\left(\frac{\partial a_3}{\partial X_k}\right)_{p,\mathbf{X}_k} =& \frac{R_u^2T^2}{p^2}\left\{2\tilde{B}_m\left[\delta_1\delta_2-(\delta_1+\delta_2)\right]-(\delta_1+\delta_2)\right\}\left(\frac{\partial B_m}{\partial X_k}\right)_{\mathbf{X}_k} + \frac{R_uT}{p^2}\left(\frac{\partial A_m}{\partial X_k}\right)_{T,\mathbf{X}_k} +\\
&+\frac{R_uTB_m^2}{p}\left[\delta_1\left(\frac{\partial \delta_2}{\partial X_k}\right)_{\mathbf{X}_k} + \delta_2\left(\frac{\partial \delta_1}{\partial X_k}\right)_{\mathbf{X}_k} - \left(\frac{\partial \delta_1}{\partial X_k}\right)_{\mathbf{X}_k} - \left(\frac{\partial \delta_2}{\partial X_k}\right)_{\mathbf{X}_k}\right] +\\
&-\frac{R_u^2T^2B_m}{p^2}\left[\left(\frac{\partial \delta_1}{\partial X_k}\right)_{\mathbf{X}_k} + \left(\frac{\partial \delta_2}{\partial X_k}\right)_{\mathbf{X}_k}\right],\\
\left(\frac{\partial a_4}{\partial X_k}\right)_{p,\mathbf{X}_k} =& -\left(2\delta_1\delta_2\frac{R_uT}{p}B_m + \frac{A_m}{p} + 3\delta_1\delta_2B_m^2\right)\left(\frac{\partial B_m}{\partial X_k}\right)_{\mathbf{X}_k} - \frac{B_m}{p}\left(\frac{\partial A_m}{\partial X_k}\right)_{T,\mathbf{X}_k} +\\
&-\frac{R_uTB_m^2}{p}\left[\delta_1\left(\frac{\partial \delta_2}{\partial X_k}\right)_{\mathbf{X}_k} + \delta_2\left(\frac{\partial \delta_1}{\partial X_k}\right)_{\mathbf{X}_k}\right] +\\
&-B_m^3\left[\delta_1\left(\frac{\partial \delta_2}{\partial X_k}\right)_{\mathbf{X}_k} + \delta_2\left(\frac{\partial \delta_1}{\partial X_k}\right)_{\mathbf{X}_k}\right],
\end{aligned}
\tag{M.1.6}
$$

where according to Eq. (2.2.68):

$$
\begin{aligned}
\left(\frac{\partial \delta_1}{\partial X_k}\right)_{\mathbf{X}_k} &= \frac{\partial}{\partial X_k}\left(\sum_{i=1}^{N_s} X_i\delta_{1,i}\right)_{\mathbf{X}_k} = \delta_{1,k}\,,\\
\left(\frac{\partial \delta_2}{\partial X_k}\right)_{\mathbf{X}_k} &= \frac{\partial}{\partial X_k}\left(\sum_{i=1}^{N_s} X_i\delta_{2,i}\right)_{\mathbf{X}_k} = \delta_{2,k}\,.
\end{aligned}
\tag{M.1.7}
$$

M.2 Additional derivatives of the internal energy departure function

Similarly to the derivatives of Z, the derivatives of the internal energy departure function ΔE are required for the single-phase mixture (as well as in the generic phase η). These are for example used in Eqs. (K.0.46)–(K.0.48). The following results are obtained for all

GCEoS/MR:

$$\left(\frac{\partial \Delta E}{\partial T}\right)_{p,\mathbf{X}} \overset{\text{Using Eq. (2.2.82)}}{=} \begin{cases} \dfrac{\left[T\left(\dfrac{\partial A_m}{\partial T}\right)_{\mathbf{X}} - A_m\right]}{(\delta_1-\delta_2)B_m} \dfrac{\tilde{B}_m(\delta_2-\delta_1)\left[\left(\dfrac{\partial Z}{\partial T}\right)_{p,\mathbf{X}} + Z\dfrac{\tilde{B}_m}{T}\right]}{(Z+\delta_1\tilde{B}_m)(Z+\delta_2\tilde{B}_m)} + & \\ \qquad + \dfrac{T\left(\dfrac{\partial^2 A_m}{\partial T^2}\right)_{\mathbf{X}}}{(\delta_1-\delta_2)B_m}\ln\left(\dfrac{Z+\delta_1\tilde{B}_m}{Z+\delta_2\tilde{B}_m}\right) & \text{if } \delta_1,\delta_2 \neq 0 \\ \dfrac{p}{R_u Z}\left(\dfrac{\partial^2 A_m}{\partial T^2}\right)_{\mathbf{X}} - \dfrac{p}{R_u Z^2}\left[\left(\dfrac{\partial A_m}{\partial T}\right)_{\mathbf{X}} - \dfrac{A_m}{T}\right]\left[\left(\dfrac{\partial Z}{\partial T}\right)_{p,\mathbf{X}} + \dfrac{Z}{T}\right] & \text{if } \delta_1=\delta_2=0\,. \end{cases} \tag{M.2.1}$$

$$\left(\frac{\partial \Delta E}{\partial p}\right)_{T,\mathbf{X}} \overset{\text{Using Eq. (2.2.82)}}{=} \begin{cases} \dfrac{\left[T\left(\dfrac{\partial A_m}{\partial T}\right)_{\mathbf{X}} - A_m\right]}{(\delta_1-\delta_2)B_m} \dfrac{\tilde{B}_m(\delta_1-\delta_2)\left[\dfrac{Z}{p} - \left(\dfrac{\partial Z}{\partial p}\right)_{T,\mathbf{X}}\right]}{(Z+\delta_1\tilde{B}_m)(Z+\delta_2\tilde{B}_m)} & \text{if } \delta_1,\delta_2 \neq 0 \\ \dfrac{1}{R_u Z^2}\left[\left(\dfrac{\partial A_m}{\partial T}\right)_{\mathbf{X}} - \dfrac{A_m}{T}\right]\left[Z - p\left(\dfrac{\partial Z}{\partial p}\right)_{T,\mathbf{X}}\right] & \text{if } \delta_1=\delta_2=0\,. \end{cases} \tag{M.2.2}$$

$$\left(\frac{\partial \Delta E}{\partial \rho}\right)_{T,\mathbf{X}} \overset{\text{Using Eq. (2.2.79)}}{=} \begin{cases} \left[T\left(\dfrac{\partial A_m}{\partial T}\right)_{\mathbf{X}} - A_m\right] \dfrac{M}{(\delta_1 B_m\rho + M)(\delta_2 B_m\rho + M)} & \text{if } \delta_1,\delta_2 \neq 0 \\ \left[\left(\dfrac{\partial A_m}{\partial T}\right)_{\mathbf{X}} - \dfrac{A_m}{T}\right]\dfrac{1}{M} & \text{if } \delta_1=\delta_2=0\,. \end{cases} \tag{M.2.3}$$

Whereas for the mole fraction based derivative, again a distinction has to be made due to the dependency of δ_1 and δ_2 on the mixture for PR-RK EoS. For convenience, we rename

some terms appearing in Eq. (2.2.82):

$$\left(\frac{\partial \Delta E}{\partial X_k}\right)_{T,p,\mathbf{X}_k} = \begin{cases} \bar{S}\bar{T}\left(\dfrac{\partial \bar{R}}{\partial X_k}\right)_{T,p,\mathbf{X}_k} + \bar{R}\bar{T}\left(\dfrac{\partial \bar{S}}{\partial X_k}\right)_{T,p,\mathbf{X}_k} + \bar{S}\bar{R}\left(\dfrac{\partial \bar{T}}{\partial X_k}\right)_{T,p,\mathbf{X}_k} & \text{if } \delta_1, \delta_2 \neq 0 \\ \dfrac{1}{R_u Z}\left[\left(\dfrac{\partial^2 A_m}{\partial T \partial X_k}\right) - \dfrac{1}{T}\left(\dfrac{\partial A_m}{\partial X_k}\right)_{T,p,\mathbf{X}_k}\right] + & \\ \qquad -\dfrac{p}{R_u Z^2}\left(\dfrac{\partial Z}{\partial X_k}\right)_{T,p,\mathbf{X}_k}\left[\left(\dfrac{\partial A_m}{\partial T}\right)_{\mathbf{X}} - \dfrac{A_m}{T}\right] & \text{if } \delta_1 = \delta_2 = 0\,, \end{cases} \tag{M.2.4}$$

where:

$$\bar{R} = \frac{1}{(\delta_1 - \delta_2)B_m}\,,$$

$$\bar{S} = \left[T\left(\frac{\partial A_m}{\partial T}\right)_{\mathbf{X}} - A_m\right]\,,$$

$$\bar{T} = \ln\left(\frac{Z + \delta_1 \tilde{B}_m}{Z + \delta_2 \tilde{B}_m}\right)\,,$$

$$\left(\frac{\partial \bar{R}}{\partial X_k}\right)_{T,p,\mathbf{X}_k} = -\frac{(\delta_1 - \delta_2)\left(\dfrac{\partial B_m}{\partial X_k}\right)_{\mathbf{X}_k} + B_m\left[\left(\dfrac{\partial \delta_1}{\partial X_k}\right)_{\mathbf{X}_k} - \left(\dfrac{\partial \delta_2}{\partial X_k}\right)_{\mathbf{X}_k}\right]}{(\delta_1 - \delta_2)^2 B_m^2}\,,$$

$$\left(\frac{\partial \bar{S}}{\partial X_k}\right)_{T,p,\mathbf{X}_k} = T\left(\frac{\partial^2 A_m}{\partial T \partial X_k}\right) - \left(\frac{\partial A_m}{\partial X_k}\right)_{T,p,\mathbf{X}_k}\,,$$

$$\left(\frac{\partial \bar{T}}{\partial X_k}\right)_{T,p,\mathbf{X}_k} = \frac{\left[\tilde{B}_m\left(\dfrac{\partial Z}{\partial X_k}\right)_{T,p,\mathbf{X}_k} - Z\left(\dfrac{\partial \tilde{B}_m}{\partial X_k}\right)_{T,p,\mathbf{X}_k}\right](\delta_2 - \delta_1)}{(Z + \delta_1 \tilde{B}_m)(Z + \delta_2 \tilde{B}_m)} +$$

$$+ \frac{\left[\tilde{B}_m\left(\dfrac{\partial Z}{\partial X_k}\right)_{T,p,\mathbf{X}_k} - Z\left(\dfrac{\partial \tilde{B}_m}{\partial X_k}\right)_{T,p,\mathbf{X}_k}\right](\delta_2 - \delta_1) + \tilde{B}_m Z\left[\left(\dfrac{\partial \delta_1}{\partial X_k}\right)_{\mathbf{X}_k} - \left(\dfrac{\partial \delta_2}{\partial X_k}\right)_{\mathbf{X}_k}\right]}{(Z + \delta_1 \tilde{B}_m)(Z + \delta_2 \tilde{B}_m)} +$$

$$+ \frac{\tilde{B}_m^2\left[\delta_2\left(\dfrac{\partial \delta_1}{\partial X_k}\right)_{\mathbf{X}_k} - \delta_1\left(\dfrac{\partial \delta_2}{\partial X_k}\right)_{\mathbf{X}_k}\right]}{(Z + \delta_1 \tilde{B}_m)(Z + \delta_2 \tilde{B}_m)}\,,$$

$$\left(\frac{\partial \tilde{B}_m}{\partial X_k}\right)_{T,p,\mathbf{X}_k} = \frac{p}{R_u T}\left(\frac{\partial B_m}{\partial X_k}\right)_{\mathbf{X}_k}\,. \tag{M.2.5}$$

have been defined. Obviously, for EoS other than PR-RK, the derivatives $(\partial\delta_1/\partial X_k)_{\mathbf{X}_k}$ and $(\partial\delta_2/\partial X_k)_{\mathbf{X}_k}$ vanish identically.

M.3 Fugacity coefficient and its derivatives

The fugacity coefficient along with its derivatives are important quantities to compute all the variables discussed in Sec. 2.2.2. The derivation of the fugacity coefficient follows directly its definition of Eq. (2.2.30), however, attention must be given to the derivation according to the types of EoS due to the different form appearing in Eq. (2.2.84). In order to reduce the amount of algebraic steps, the fugacity coefficients for all GCEoS, except VDW are derived first and then the same quantity for VDW EoS are derived next. In the first derivation, the reader should always keep in mind the dependency of δ_1 and δ_2 on the mixture for PR-RK, which will show in additional terms for the final formula. If $\delta_1, \delta_2 \neq 0$ (all GCEoS except VDW), the first step requires to compute the extensive Helmholtz energy departure function as follows:

$$\frac{N\Delta A_{TV}}{R_u T} = -N\ln\left(\frac{M - B_m\rho}{M}\right) - \frac{N^2 A_m}{R_u T N B_m(\delta_2 - \delta_1)}\ln\left(\frac{\delta_2 B_m\rho + M}{\delta_1 B_m\rho + M}\right), \tag{M.3.1}$$

where in the second term, N^2/N has been used to represent N for later convenience. Next, the derivative of Eq. (M.3.1) with respect to the i-th mole number is performed. In this step, the extensive volume $\overline{V}$ has to be maintained constant, so the auxiliary relationship $\rho = MN/\overline{V}$ is also useful to keep in mind:

$$\begin{aligned}\frac{1}{R_u T}\left(\frac{\partial N\Delta A_{T,V}}{\partial N_i}\right)_{T,\overline{V},\mathbf{N}_i} = &\underbrace{-\left(\frac{\partial N}{\partial N_i}\right)_{\mathbf{N}_i}\ln\left(\frac{M - B_m\rho}{M}\right)}_{\text{term }(1)}\underbrace{-N\frac{\partial}{\partial N_i}\left[\ln\left(\frac{M - B_m\rho}{M}\right)\right]_{T,\overline{V},\mathbf{N}_i}}_{\text{term }(2)} + \\ &\underbrace{-\ln\left(\frac{\delta_2 B_m\rho + M}{\delta_1 B_m\rho + M}\right)\frac{\partial}{\partial N_i}\left[\frac{N^2 A_m}{N B_m R_u T(\delta_2 - \delta_1)}\right]_{T,\overline{V},\mathbf{N}_i}}_{\text{term }(3)} + \\ &\underbrace{-\frac{N^2 A_m}{N B_m R_u T(\delta_2 - \delta_1)}\frac{\partial}{\partial N_i}\left[\ln\left(\frac{\delta_2 B_m\rho + M}{\delta_1 B_m\rho + M}\right)\right]_{T,\overline{V},\mathbf{N}_i}}_{\text{term }(4)} \qquad i = 1, \cdots, N_s\,.\end{aligned} \tag{M.3.2}$$

Now each term is derived separately.

- term (1)

$$-\left(\frac{\partial N}{\partial N_i}\right)_{\mathbf{N}_i}\ln\left(\frac{M-B_m\rho}{M}\right)=-\ln\left(\frac{M-B_m\rho}{M}\right), \tag{M.3.3}$$

since:

$$\left(\frac{\partial N}{\partial N_i}\right)_{\mathbf{N}_i}=\left(\frac{\partial\sum_{j=1}^{N_s}N_j}{\partial N_i}\right)_{\mathbf{N}_i}=\left(\frac{\partial(N_1+N_2+\cdots+N_i+N_{i+1}+\cdots+N_{N_s})}{\partial N_i}\right)_{\mathbf{N}_i}=1\,. \tag{M.3.4}$$

- term (2)

$$\begin{aligned}-N\frac{\partial}{\partial N_i}\left[\ln\left(\frac{M-B_m\rho}{M}\right)\right]_{T,\overline{V},\mathbf{N}_i}=&\frac{NM}{M-B_m\rho}\left[\frac{\partial\left(B_m\rho/M\right)}{\partial N_i}\right]_{T,\overline{V},\mathbf{N}_i}\overset{\rho/M=N/\overline{V}}{=}\\ =&\frac{NM}{M-B_m\rho}\frac{\partial}{\partial N_i}\left(\frac{B_mN}{\overline{V}}\right)_{T,\overline{V},\mathbf{N}_i}=\\ =&\frac{\rho}{M-B_m\rho}\left(\frac{\partial NB_m}{\partial N_i}\right)_{T,\overline{V},\mathbf{N}_i}=\\ =&\frac{\rho\tilde{B}_i}{M-B_m\rho}\\ &\Big\downarrow\\ &\text{Using Eq. (G.0.4)}\end{aligned} \tag{M.3.5}$$

- term (3)

$$\begin{aligned}&-\ln\left(\frac{\delta_2B_m\rho+M}{\delta_1B_m\rho+M}\right)\frac{\partial}{\partial N_i}\left[\frac{N^2A_m}{NB_mR_uT(\delta_2-\delta_1)}\right]_{T,\overline{V},\mathbf{N}_i}=\\ &=-\ln\left(\frac{\delta_2B_m\rho+M}{\delta_1B_m\rho+M}\right)\frac{\left(\frac{\partial N^2A_m}{\partial N_i}\right)_{T,\mathbf{N}_i}NB_mR_uT(\delta_2-\delta_1)-N^2A_mR_uT\left[\frac{\partial(NB_m(\delta_2-\delta_1))}{\partial N_i}\right]_{\mathbf{N}_i}}{N^2B_m^2R_u^2T^2(\delta_2-\delta_1)^2},\end{aligned} \tag{M.3.6}$$

where the term in the square brackets can be rearranged as follows:

$$\left[\frac{\partial(NB_m(\delta_2-\delta_1))}{\partial N_i}\right]_{\mathbf{N}_i}=\left[(\delta_2-\delta_1)\left(\frac{\partial NB_m}{\partial N_i}\right)_{T,\overline{V},\mathbf{N}_i}+NB_m\left(\frac{\partial(\delta_2-\delta_1)}{\partial N_i}\right)_{\mathbf{N}_i}\right]. \tag{M.3.7}$$

In addition, using the identity of Eq. (L.0.3) and the result of Eq. (M.1.7) one can easily prove that:

$$\left(\frac{\partial(\delta_2-\delta_1)}{\partial N_i}\right)_{\mathbf{N}_i}=\frac{1}{N}\sum_{j=1}^{N_s}(\delta_{2,j}-\delta_{1,j})(\delta_{ij}-X_j)\,. \tag{M.3.8}$$

Using the results of Eq. (M.3.7), Eq. (M.3.8) and the results of Appendix G (particularly Eq. (G.0.1) and Eq. (G.0.4)), Eq. (M.3.6) can be recast in the following form:

$$\begin{aligned}
&-\ln\left(\frac{\delta_2 B_m\rho+M}{\delta_1 B_m\rho+M}\right)\frac{\partial}{\partial N_i}\left[\frac{N^2A_m}{NB_mR_uT(\delta_2-\delta_1)}\right]_{T,\overline{V},\mathbf{N}_i}=\\
&=-\ln\left(\frac{\delta_2 B_m\rho+M}{\delta_1 B_m\rho+M}\right)\left[\frac{2\sum_{j=1}^{N_s}X_jA_{ji}}{B_mR_uT(\delta_2-\delta_1)}-\frac{A_m\tilde{B}_i}{B_m^2R_uT(\delta_2-\delta_1)}+\right.\\
&\left.-\frac{A_mB_m\left(\sum_{j=1}^{N_s}(\delta_{2,j}-\delta_{1,j})(\delta_{ij}-X_j)\right)}{B_m^2R_uT(\delta_2-\delta_1)^2}\right]=\\
&=-\ln\left(\frac{\delta_2 B_m\rho+M}{\delta_1 B_m\rho+M}\right)\left[\frac{2\sum_{j=1}^{N_s}X_jA_{ji}}{B_mR_uT(\delta_2-\delta_1)}-\frac{A_m\tilde{B}_i}{B_m^2R_uT(\delta_2-\delta_1)}-\frac{A_mB_m(S_{2,i}-S_{1,i})}{B_m^2R_uT(\delta_2-\delta_1)^2}\right].
\end{aligned} \tag{M.3.9}$$

where:

$$S_{1,i}=\sum_{j=1}^{N_s}\delta_{1,j}(\delta_{ij}-X_j)\,, \tag{M.3.10}$$

$$S_{2,i}=\sum_{j=1}^{N_s}\delta_{2,j}(\delta_{ij}-X_j)\,, \tag{M.3.11}$$

have been defined.

- term (4)

$$\begin{aligned}
&-\frac{N^2A_m}{NB_mR_uT(\delta_2-\delta_1)}\frac{\partial}{\partial N_i}\left[\ln\left(\frac{\delta_2 B_m\rho+M}{\delta_1 B_m\rho+M}\right)\right]_{T,\overline{V},\mathbf{N}_i}=\\
&=-\frac{N^2A_m}{NB_mR_uT(\delta_2-\delta_1)}\left[\frac{\frac{\partial}{\partial N_i}\left(\delta_2\frac{B_m\rho}{M}\right)_{T,\overline{V},\mathbf{N}_i}}{\delta_2\frac{B_m\rho}{M}+1}-\frac{\frac{\partial}{\partial N_i}\left(\delta_1\frac{B_m\rho}{M}\right)_{T,\overline{V},\mathbf{N}_i}}{\delta_1\frac{B_m\rho}{M}+1}\right]=\\
&=-\frac{N^2A_m}{NB_mR_uT(\delta_2-\delta_1)}\left[\frac{M\frac{\partial}{\partial N_i}\left(\delta_2\frac{B_m\rho}{M}\right)_{T,\overline{V},\mathbf{N}_i}}{\delta_2B_m\rho+M}-\frac{M\frac{\partial}{\partial N_i}\left(\delta_1\frac{B_m\rho}{M}\right)_{T,\overline{V},\mathbf{N}_i}}{\delta_1B_m\rho+M}\right].
\end{aligned}$$

Using the results of Eq. (G.0.6) and Eq. (G.0.7) and rearranging, the following final result can be obtained:

$$
\begin{aligned}
&- \frac{N^2 A_m}{N B_m R_u T(\delta_2 - \delta_1)} \frac{\partial}{\partial N_i} \left[\ln \left(\frac{\delta_2 B_m \rho + M}{\delta_1 B_m \rho + M} \right) \right]_{T,\overline{V},\mathbf{N}_i} = \\
&= \frac{\rho A_m}{B_m R_u T(\delta_2 - \delta_1)} \left[\frac{\tilde{\Delta}_i + \tilde{B}_i M(\delta_2 - \delta_1)}{(\delta_2 B_m \rho + M)(\delta_1 B_m \rho + M)} \right] ,
\end{aligned} \tag{M.3.12}
$$

where:

$$
\tilde{\Delta}_i = B_m^2 \rho (S_{2,i}\delta_1 - S_{1,i}\delta_2) + B_m M (S_{2,i} - S_{1,i}) = \frac{B_m M}{Z} \left[\tilde{B}_m (S_{2,i}\delta_1 - S_{1,i}\delta_2) + Z(S_{2,i} - S_{1,i}) \right] . \tag{M.3.13}
$$

Using all the results from Eqs. (M.3.3)–(M.3.13), application of the definition of Eq. (2.2.30) writes:

$$
\begin{aligned}
\ln\phi_i = &- \ln \left(\frac{M - B_m \rho}{M} \right) + \frac{\rho \tilde{B}_i}{M - B_m \rho} + \\
&- \ln \left(\frac{\delta_2 B_m \rho + M}{\delta_1 B_m \rho + M} \right) \frac{A_m}{B_m R_u T(\delta_2 - \delta_1)} \left[\frac{2 \sum_{j=1}^{N_s} X_j A_{ji}}{A_m} - \frac{\tilde{B}_i}{B_m} \right] + \\
&- \frac{\rho A_m \tilde{B}_i M}{B_m R_u T(\delta_2 B_m \rho + M)(\delta_1 B_m \rho + M)} + \\
&- \ln \left(\frac{\delta_2 B_m \rho + M}{\delta_1 B_m \rho + M} \right) \frac{A_m (S_{2,i} - S_{1,i})}{B_m R_u T(\delta_2 - \delta_1)^2} + \\
&- \frac{\rho A_m \tilde{\Delta}_i}{B_m R_u T(\delta_2 - \delta_1)(\delta_2 B_m \rho + M)(\delta_1 B_m \rho + M)} - \ln Z \qquad i = 1, \cdots, N_s \, .
\end{aligned} \tag{M.3.14}
$$

Using the following identities:

$$
\frac{\rho \tilde{B}_i}{M - B_m \rho} - \frac{A_m \rho \tilde{B}_i M}{B_m R_u T(\delta_2 B_m \rho + M)(\delta_2 B_m \rho + M)} \overset{\text{Using Eq. (2.2.72)}}{=\!=\!=\!\Rightarrow} \frac{\tilde{B}_i}{B_m}(Z - 1) \, , \tag{M.3.15}
$$

$$
- \ln \left(\frac{M - B_m \rho}{M} \right) - \ln Z = -\ln \left(Z - \tilde{B}_m \right) , \tag{M.3.16}
$$

$$
\ln \left(\frac{\delta_2 B_m \rho + M}{\delta_1 B_m \rho + M} \right) = \ln \left(\frac{\delta_2 \tilde{B}_m + Z}{\delta_1 \tilde{B}_m + Z} \right) , \tag{M.3.17}
$$

Eq. (M.3.14) can be rewritten in the following form:

$$
\ln\phi_i = - \ln(Z - \tilde{B}_m) + \frac{\tilde{B}_i}{B_m}(Z - 1) - \ln \left(\frac{\delta_2 \tilde{B}_m + Z}{\delta_1 \tilde{B}_m + Z} \right) \frac{A_m}{B_m R_u T(\delta_2 - \delta_1)} \left[\frac{2 \sum_{j=1}^{N_s} X_j A_{ji}}{A_m} - \frac{\tilde{B}_i}{B_m} \right] + \tilde{\Phi}_i \, , \tag{M.3.18}
$$

where:

$$\tilde{\Phi}_i = \begin{cases} 0 & \text{for PR, RK, SRK EoS} \\ \ln\left(\dfrac{\delta_2\tilde{B}_m + Z}{\delta_1\tilde{B}_m + Z}\right)\dfrac{A_m(S_{2,i}-S_{1,i})}{B_m R_u T(\delta_2-\delta_1)^2} - \dfrac{A_m}{B_m R_u T(\delta_2-\delta_1)}\dfrac{\left(\dfrac{p}{R_u T}\right)^2}{(\delta_2\tilde{B}_m+Z)(\delta_1\tilde{B}_m+Z)}\dfrac{\tilde{\Delta}_i}{\rho}. & \text{for PR-RK EoS} \end{cases} \tag{M.3.19}$$

Similarly, for the VDW EoS we use the result of Eq. (2.2.84) corresponding to $\delta_1 = \delta_2 = 0$ to obtain the extensive Helmholtz energy departure function first:

$$\frac{N\Delta A_{TV}}{R_u T} = -N\ln\left(\frac{M - B_m\rho}{M}\right) - \frac{N^2 A_m \rho}{N R_u T M} = -N\ln\left(\frac{M - B_m\rho}{M}\right) - \frac{N^2 A_m}{\overline{V} R_u T}\,. \tag{M.3.20}$$

Next, the derivative with respect to the i-th mole number is carried out:

$$\frac{1}{R_u T}\left(\frac{\partial N\Delta A_{T,V}}{\partial N_i}\right)_{T,\overline{V},\mathbf{N}_i} = -\ln\left(\frac{M - B_m\rho}{M}\right) + \frac{\rho\tilde{B}_i}{M - B_m\rho} - \frac{2\rho\sum_{j=1}^{N_s} X_j A_{ji}}{M R_u T}\,, \tag{M.3.21}$$

such that application of Eq. (2.2.30) provides the fugacity coefficient with analogous steps are done before:

$$\ln\phi_i = -\ln(Z - \tilde{B}_m) + \frac{p}{R_u T}\frac{\tilde{B}_i}{Z - \tilde{B}_m} - \frac{2p}{Z(R_u T)^2}\sum_{j=1}^{N_s} X_j A_{ji}\,. \tag{M.3.22}$$

M.3.1 Derivative with respect to the mole fraction

As a set of useful fugacity derivatives, the i-th fugacity coefficient derivative with respect to the k-th generic mole fraction is derived first. Again due to the substantial amount of steps the derivation for all GCEoS except VDW are lumped together first and then VDW is addressed alone. For PR, RK, SRK and PR-RK, Eq. (M.3.18) is considered. For

convenience, the following terms are defined:

$$\mathcal{R}_i = \frac{\tilde{B}_i}{B_m}(Z-1)\,, \qquad \mathcal{T}_i = \mathcal{U}\,\mathcal{V}_i = \frac{A_m}{B_m R_u T(\delta_2-\delta_1)}\left[\frac{2\sum_{j=1}^{N_s} X_j A_{ji}}{A_m} - \frac{\tilde{B}_i}{B_m}\right],$$

$$\mathcal{S} = \ln(Z-\tilde{B}_m)\,, \qquad \mathcal{W} = \frac{\mathcal{X}}{\mathcal{Y}} = \frac{Z+\delta_2\tilde{B}_m}{Z+\delta_1\tilde{B}_m}\,,$$

$$\mathcal{K}_i = \frac{S_{2,i}-S_{1,i}}{\delta_2-\delta_1}\,, \qquad \mathcal{J} = \frac{\left(\frac{p}{R_u T}\right)^2}{\rho(\delta_2\tilde{B}_m+Z)(\delta_1\tilde{B}_m+Z)}\,, \tag{M.3.23}$$

thus, the derivative can be written as:

$$\left(\frac{\partial \ln\phi_i}{\partial X_k}\right)_{T,p,\mathbf{X}_k} = \frac{\partial}{\partial X_k}\left[\mathcal{R}_i - \mathcal{S} - \mathcal{T}_i \ln\mathcal{W} + \mathcal{K}_i\mathcal{U}\ln\mathcal{W} - \mathcal{U}\mathcal{J}\tilde{\Delta}_i\right]_{T,p,\mathbf{X}_k} =$$

$$= \underbrace{\left(\frac{\partial \mathcal{R}_i}{\partial X_k}\right)_{T,p,\mathbf{X}_k}}_{\text{term } (1)} - \underbrace{\left(\frac{\partial \mathcal{S}_i}{\partial X_k}\right)_{T,p,\mathbf{X}_k}}_{\text{term } (2)} - \underbrace{\left(\frac{\partial(\mathcal{T}_i\ln\mathcal{W})}{\partial X_k}\right)_{T,p,\mathbf{X}_k}}_{\text{term } (3)} + \underbrace{\left(\frac{\partial(\mathcal{K}_i\mathcal{U}\ln\mathcal{W})}{\partial X_k}\right)_{T,p,\mathbf{X}_k}}_{\text{term } (4)} - \underbrace{\left(\frac{\partial(\mathcal{U}\mathcal{J}\tilde{\Delta}_i)}{\partial X_k}\right)_{T,p,\mathbf{X}_k}}_{\text{term } (5)}\,.$$

and each term is obtained as follows:

- term (1)

$$\left(\frac{\partial \mathcal{R}_i}{\partial X_k}\right)_{T,p,\mathbf{X}_k} = \frac{\partial}{\partial X_k}\left[\frac{\tilde{B}_i}{B_m}(Z-1)\right]_{\mathbf{X}_k} = \frac{\tilde{B}_i}{B_m}\left(\frac{\partial Z}{\partial X_k}\right)_{T,p,\mathbf{X}_k} + (Z-1)\frac{\left(\frac{\partial B_i}{\partial X_k}\right)_{\mathbf{X}_k} B_m - \tilde{B}_i\left(\frac{\partial B_m}{\partial X_k}\right)_{\mathbf{X}_k}}{B_m^2} =$$

$$\downarrow \quad \text{Use Eq. (G.0.5)}$$

$$= \frac{\tilde{B}_i}{B_m}\left(\frac{\partial Z}{\partial X_k}\right)_{T,p,\mathbf{X}_k} + (Z-1)\frac{\hat{B}_{ik}B_m - \tilde{B}_i\left(\frac{\partial B_m}{\partial X_k}\right)_{\mathbf{X}_k}}{B_m^2}. \tag{M.3.24}$$

- term (2)

$$\left(\frac{\partial \mathcal{S}_i}{\partial X_k}\right)_{T,p,\mathbf{X}_k} = \frac{\partial}{\partial X_k}\left[\ln\left(Z-\tilde{B}_m\right)\right]_{T,p,\mathbf{X}_k} = \frac{1}{Z-\tilde{B}_m}\left[\left(\frac{\partial Z}{\partial X_k}\right)_{T,p,\mathbf{X}_k} - \left(\frac{\partial \tilde{B}_m}{\partial X_k}\right)_{\mathbf{X}_k}\right], \tag{M.3.25}$$

where $(\partial\tilde{B}_m/\partial X_k)_{\mathbf{X}_k}$ is given in Eq. (M.2.5).

- term (3)

$$\left(\frac{\partial(\mathcal{T}_i \ln\mathcal{W})}{\partial X_k}\right)_{T,p,\mathbf{X}_k} = \left(\frac{\partial \mathcal{T}_i}{\partial X_k}\right)_{T,p,\mathbf{X}_k} \ln\mathcal{W} + \frac{\mathcal{T}_i}{\mathcal{W}} \left(\frac{\partial \mathcal{W}}{\partial X_k}\right)_{T,p,\mathbf{X}_k} \tag{M.3.26}$$

where:

$$\left(\frac{\partial \mathcal{T}_i}{\partial X_k}\right)_{T,p,\mathbf{X}_k} = \frac{\partial}{\partial X_k}(\mathcal{U}\mathcal{V}_i)_{T,p,\mathbf{X}_k} = \left(\frac{\partial \mathcal{U}}{\partial X_k}\right)_{T,p,\mathbf{X}_k} \mathcal{V}_i + \mathcal{U}\left(\frac{\partial \mathcal{V}_i}{\partial X_k}\right)_{T,p,\mathbf{X}_k} \tag{M.3.27}$$

$$\begin{aligned}\left(\frac{\partial \mathcal{U}}{\partial X_k}\right)_{T,p,\mathbf{X}_k} =& \frac{\partial}{\partial X_k}\left[\frac{A_m}{B_m R_u T(\delta_2 - \delta_1)}\right]_{T,p,\mathbf{X}_k} = \\ =& \frac{1}{R_u T(\delta_2 - \delta_1)}\left[\frac{1}{B_m}\left(\frac{\partial A_m}{\partial X_k}\right)_{\mathbf{X}_k} - \frac{A_m}{B_m^2}\left(\frac{\partial B_m}{\partial X_k}\right)_{\mathbf{X}_k}\right] - \frac{A_m}{R_u T B_m}(\delta_{2,k} - \delta_{1,k})\,.\end{aligned} \tag{M.3.28}$$

$$\begin{aligned}\left(\frac{\partial \mathcal{V}_i}{\partial X_k}\right)_{T,p,\mathbf{X}_k} =& \frac{\partial}{\partial X_k}\left[\frac{2\sum_{j=1}^{N_s} X_j A_{ji}}{A_m} - \frac{\tilde{B}_i}{B_m}\right]_{T,p,\mathbf{X}_k} = \\ =& \frac{2A_{ki}A_m - 2\sum_{j=1}^{N_s} X_j A_{ji}\left(\frac{\partial A_m}{\partial X_k}\right)_{\mathbf{X}_k}}{A_m^2} - \frac{\hat{B}_{ik}B_m - \tilde{B}_i\left(\frac{\partial B_m}{\partial X_k}\right)_{\mathbf{X}_k}}{B_m^2}\,.\end{aligned} \tag{M.3.29}$$

$$\left(\frac{\partial \mathcal{W}}{\partial X_k}\right)_{T,p,\mathbf{X}_k} = \frac{\partial}{\partial X_k}\left(\frac{\mathcal{X}}{\mathcal{Y}}\right)_{T,p,\mathbf{X}_k} = \frac{1}{\mathcal{Y}}\left(\frac{\partial \mathcal{X}}{\partial X_k}\right)_{T,p,\mathbf{X}_k} - \frac{\mathcal{X}}{\mathcal{Y}^2}\left(\frac{\partial \mathcal{Y}}{\partial X_k}\right)_{T,p,\mathbf{X}_k}\,, \tag{M.3.30}$$

where:

$$\left(\frac{\partial \mathcal{X}}{\partial X_k}\right)_{T,p,\mathbf{X}_k} = \frac{\partial}{\partial X_k}\left(Z + \delta_2 \tilde{B}_m\right)_{T,p,\mathbf{X}_k} = \left(\frac{\partial Z}{\partial X_k}\right)_{T,p,\mathbf{X}_k} + \frac{\delta_2 p}{R_u T}\left(\frac{\partial B_m}{\partial X_k}\right)_{\mathbf{X}_k} + \tilde{B}_m \delta_{2,k}\,, \tag{M.3.31}$$

$$\left(\frac{\partial \mathcal{Y}}{\partial X_k}\right)_{T,p,\mathbf{X}_k} = \frac{\partial}{\partial X_k}\left(Z + \delta_1 \tilde{B}_m\right)_{T,p,\mathbf{X}_k} = \left(\frac{\partial Z}{\partial X_k}\right)_{T,p,\mathbf{X}_k} + \frac{\delta_1 p}{R_u T}\left(\frac{\partial B_m}{\partial X_k}\right)_{\mathbf{X}_k} + \tilde{B}_m \delta_{1,k}\,. \tag{M.3.32}$$

- term (4)

$$\left(\frac{\partial(\mathcal{K}_i \mathcal{U} \ln\mathcal{W})}{\partial X_k}\right)_{T,p,\mathbf{X}_k} = \mathcal{K}_i \frac{\mathcal{U}}{\mathcal{W}}\left(\frac{\partial \mathcal{W}}{\partial X_k}\right)_{T,p,\mathbf{X}_k} + \mathcal{K}_i\left(\frac{\partial \mathcal{U}}{\partial X_k}\right)_{T,p,\mathbf{X}_k} \ln\mathcal{W} + \mathcal{U}\ln\mathcal{W}\left(\frac{\partial \mathcal{K}_i}{\partial X_k}\right)_{T,p,\mathbf{X}_k}\,, \tag{M.3.33}$$

where:

$$\left(\frac{\partial \mathcal{K}_i}{\partial X_k}\right)_{T,p,\mathbf{X}_k} = \frac{\left[\left(\frac{\partial S_{2,i}}{\partial X_k}\right)_{\mathbf{X}_k} - \left(\frac{\partial S_{1,i}}{\partial X_k}\right)_{\mathbf{X}_k}\right](\delta_2-\delta_1) - (S_{2,i}-S_{1,i})\left[\left(\frac{\partial \delta_2}{\partial X_k}\right)_{\mathbf{X}_k} - \left(\frac{\partial \delta_1}{\partial X_k}\right)_{\mathbf{X}_k}\right]}{(\delta_2-\delta_1)^2}\,. \tag{M.3.34}$$

Given the fact that:

$$\left(\frac{\partial S_{1,i}}{\partial X_k}\right)_{\mathbf{X}_k} \overset{\text{Use Eq. (M.3.10)}}{=} \frac{\partial}{\partial X_k}\left[\sum_{j=1}^{N_s}\delta_{1,j}(\delta_{ij}-X_j)\right]_{\mathbf{X}_k} = \frac{\partial}{\partial X_k}\underbrace{\left[\sum_{j=1}^{N_s}\delta_{1,j}\delta_{ij}\right]_{\mathbf{X}_k}}_{\text{does not depend on } X_k \;\Rightarrow\; 0} - \frac{\partial}{\partial X_k}\left[\sum_{j=1}^{N_s}\delta_{1,j}X_j\right]_{\mathbf{X}_k} =$$

$$= -\sum_{j=1}^{N_s}\delta_{1,j}\left(\frac{\partial X_j}{\partial X_k}\right)_{\mathbf{X}_k} = -\sum_{j=1}^{N_s}\delta_{1,j}\delta_{jk} = -\delta_{1,k}\,, \tag{M.3.35}$$

and similarly:

$$\left(\frac{\partial S_{2,i}}{\partial X_k}\right)_{\mathbf{X}_k} = -\delta_{2,k}\,, \tag{M.3.36}$$

using Eq. (M.3.35), Eq. (M.3.36) and Eq. (M.1.7), Eq. (M.3.34) can be written in the following final form:

$$\begin{aligned}\left(\frac{\partial \mathcal{K}_i}{\partial X_k}\right)_{T,p,\mathbf{X}_k} &= \frac{-(\delta_{2,k}-\delta_{1,k})(\delta_2-\delta_1) - (S_{2,i}-S_{1,i})(\delta_{2,k}-\delta_{1,k})}{(\delta_2-\delta_1)^2} = \\ &= -(\delta_{2,k}-\delta_{1,k})\frac{(\delta_2-\delta_1)+(S_{2,i}-S_{1,i})}{(\delta_2-\delta_1)^2}\,.\end{aligned} \tag{M.3.37}$$

- term (5)

$$\left(\frac{\partial(\mathcal{U}\mathcal{J}\tilde{\Delta}_i)}{\partial X_k}\right)_{T,p,\mathbf{X}_k} = \mathcal{J}\tilde{\Delta}_i\left(\frac{\partial \mathcal{U}}{\partial X_k}\right)_{T,p,\mathbf{X}_k} + \mathcal{U}\left(\frac{\partial(\mathcal{J}\tilde{\Delta}_i)}{\partial X_k}\right)_{T,p,\mathbf{X}_k}\,. \tag{M.3.38}$$

Given the fact that:

$$\mathcal{J}\tilde{\Delta}_i = \left(\frac{p}{R_u T}\right)\underbrace{\frac{B_m}{(\delta_2\tilde{B}_m+Z)(\delta_1\tilde{B}_m+Z)}}_{\mathcal{D}}\underbrace{\left[\tilde{B}_m(S_{2,i}\delta_1 - S_{1,i}\delta_2) + Z(S_{2,i}-S_{1,i})\right]}_{\mathcal{E}}, \tag{M.3.39}$$

one can recast for simplicity:

$$\left(\frac{\partial(\mathcal{J}\tilde{\Delta}_i)}{\partial X_k}\right)_{T,p,\mathbf{X}_k} = \left(\frac{p}{R_u T}\right)\left[\mathcal{D}\left(\frac{\partial \mathcal{E}}{\partial X_k}\right)_{T,p,\mathbf{X}_k} + \mathcal{E}\left(\frac{\partial \mathcal{D}}{\partial X_k}\right)_{T,p,\mathbf{X}_k}\right], \tag{M.3.40}$$

where:

$$\left(\frac{\partial \mathcal{D}}{\partial X_k}\right)_{T,p,\mathbf{X}_k} = \frac{\left(\frac{\partial B_m}{\partial X_k}\right)_{\mathbf{X}_k}}{(\delta_2\tilde{B}_m + Z)(\delta_1\tilde{B}_m + Z)} - B_m\tilde{B}_m^2\frac{\delta_2\delta_{1,k} + \delta_1\delta_{2,k}}{(\delta_2\tilde{B}_m + Z)^2(\delta_1\tilde{B}_m + Z)^2} + \\ -B_m\left(\frac{\partial \tilde{B}_m}{\partial X_k}\right)_{T,p,\mathbf{X}_k}\frac{2\delta_1\delta_2\tilde{B}_m + Z}{(\delta_2\tilde{B}_m + Z)^2(\delta_1\tilde{B}_m + Z)^2} + \\ -B_m\left(\frac{\partial Z}{\partial X_k}\right)_{T,p,\mathbf{X}_k}\frac{\tilde{B}_m(\delta_2 + \delta_1) + 2Z}{(\delta_2\tilde{B}_m + Z)^2(\delta_1\tilde{B}_m + Z)^2} + \\ - B_m\tilde{B}_m Z\frac{\delta_{1,k} + \delta_{2,k}}{(\delta_2\tilde{B}_m + Z)^2(\delta_1\tilde{B}_m + Z)^2}\,, \tag{M.3.41}$$

and

$$\left(\frac{\partial \mathcal{E}}{\partial X_k}\right)_{T,p,\mathbf{X}_k} = \left(\frac{\partial \tilde{B}_m}{\partial X_k}\right)_{\mathbf{X}_k}(S_{2,i}\delta_1 - S_{1,i}\delta_2) + \tilde{B}_m\left[\delta_{1,k}(S_{2,i} + \delta_2) - \delta_{2,k}(S_{1,i} + \delta_1)\right] + \\ + \left(\frac{\partial Z}{\partial X_k}\right)_{T,p,\mathbf{X}_k}(S_{2,i} - S_{1,i}) + Z(\delta_{1,k} - \delta_{2,k})\,. \tag{M.3.42}$$

Obviously, if the derivatives of EoS other than PR-RK are needed, many of the above reduces to zero given the result of Eq. (M.3.19).

With an analogous approach for VDW EoS, by referring to Eq. (M.3.22) and by defining the quantities below for convenience:

$$\mathcal{R}_i = \frac{p}{R_u T}\frac{\tilde{B}_i}{Z - \tilde{B}_m}\,, \qquad \mathcal{S} = \ln(Z - \tilde{B}_m)\,, \qquad \mathcal{V}_i = -\frac{2p}{Z(R_uT)^2}\sum_{j=1}^{N_s} X_j A_{ji}\,, \tag{M.3.43}$$

one gets:

$$\left(\frac{\partial \ln\phi_i}{\partial X_k}\right)_{T,p,\mathbf{X}_k} = -\left(\frac{\partial \mathcal{S}}{\partial X_k}\right)_{T,p,\mathbf{X}_k} + \left(\frac{\partial \mathcal{R}_i}{\partial X_k}\right)_{T,p,\mathbf{X}_k} + \left(\frac{\partial \mathcal{V}_i}{\partial X_k}\right)_{T,p,\mathbf{X}_k}\,, \tag{M.3.44}$$

where each term is given below with similar derivation as done before:

$$\left(\frac{\partial \mathcal{S}}{\partial X_k}\right)_{T,p,\mathbf{X}_k} = \frac{1}{Z - \tilde{B}_m}\left[\left(\frac{\partial Z}{\partial X_k}\right)_{T,p,\mathbf{X}_k} - \left(\frac{\partial \tilde{B}_m}{\partial X_k}\right)_{\mathbf{X}_k}\right]\,, \\ \left(\frac{\partial \mathcal{R}_i}{\partial X_k}\right)_{T,p,\mathbf{X}_k} = \frac{p}{R_u T}\frac{\hat{B}_{ik}(Z - \tilde{B}_m) - \tilde{B}_i\left[\left(\frac{\partial Z}{\partial X_k}\right)_{T,p,\mathbf{X}_k} - \left(\frac{\partial \tilde{B}_m}{\partial X_k}\right)_{\mathbf{X}_k}\right]}{(Z - \tilde{B}_m)^2}\,, \\ \left(\frac{\partial \mathcal{V}_i}{\partial X_k}\right)_{T,p,\mathbf{X}_k} = \frac{2p}{(ZR_uT)^2}\left(-ZA_{ki} + \left(\frac{\partial Z}{\partial X_k}\right)_{T,p,\mathbf{X}_k}\sum_{j=1}^{N_s} A_{ji}\right)\,. \tag{M.3.45}$$

M.3.2 Derivative with respect to temperature

Following a similar strategy as in Sec. M.3.1, derivatives of the fugacity coefficient with respect to temperature are derived next. First the derivation for GCEoS except VDW is generalized and then VDW is derived independently. Once again in the derivation of the GCEoS derivatives, the most general form is provided first, obtained for the PR-RK EoS. For the remaining EoS few terms need to be canceled out according to Eq. (M.3.19).

Derivative with respect to temperature for GCEoS except VDW is obtained as follows:

$$\left(\frac{\partial \ln\phi_i}{\partial T}\right)_{p,\mathbf{X}} = \frac{\partial}{\partial T}\left[\mathcal{R}_i - \mathcal{S} - \mathcal{T}_i \ln\mathcal{W} + \mathcal{K}_i\mathcal{U}\ln\mathcal{W} - \mathcal{U}\mathcal{J}\tilde{\Delta}_i\right]_{p,\mathbf{X}_k} =$$
$$= \underbrace{\left(\frac{\partial \mathcal{R}_i}{\partial T}\right)_{p,\mathbf{X}}}_{\text{term } (1)} - \underbrace{\left(\frac{\partial \mathcal{S}_i}{\partial T}\right)_{p,\mathbf{X}}}_{\text{term } (2)} - \underbrace{\left(\frac{\partial(\mathcal{T}_i\ln\mathcal{W})}{\partial T}\right)_{p,\mathbf{X}}}_{\text{term } (3)} + \underbrace{\left(\frac{\partial(\mathcal{K}_i\mathcal{U}\ln\mathcal{W})}{\partial T}\right)_{p,\mathbf{X}}}_{\text{term } (4)} - \underbrace{\left(\frac{\partial(\mathcal{U}\mathcal{J}\tilde{\Delta}_i)}{\partial T}\right)_{p,\mathbf{X}}}_{\text{term } (5)},$$

where each term is that of Eq. (M.3.23) and is obtained independently:

- term (1)

$$\left(\frac{\partial \mathcal{R}_i}{\partial T}\right)_{p,\mathbf{X}} = \frac{\partial}{\partial T}\left[\frac{\tilde{B}_i}{B_m}(Z-1)\right]_{p,\mathbf{X}} = \frac{\tilde{B}_i}{B_m}\left(\frac{\partial Z}{\partial T}\right)_{p,\mathbf{X}}. \tag{M.3.46}$$

- term (2)

$$\left(\frac{\partial \mathcal{S}_i}{\partial T}\right)_{p,\mathbf{X}} = \frac{\partial}{\partial T}\left[\ln\left(Z-\tilde{B}_m\right)\right]_{p,\mathbf{X}} = \frac{1}{Z-\tilde{B}_m}\left[\left(\frac{\partial Z}{\partial T}\right)_{p,\mathbf{X}} + \frac{\tilde{B}_m}{T}\right]. \tag{M.3.47}$$

- term (3)

$$\left(\frac{\partial(\mathcal{T}_i\ln\mathcal{W})}{\partial T}\right)_{p,\mathbf{X}} = \left(\frac{\partial \mathcal{T}_i}{\partial T}\right)_{p,\mathcal{X}}\ln\mathcal{W} + \mathcal{T}_i\ln\mathcal{W} = \left[\left(\frac{\partial \mathcal{U}}{\partial T}\right)_{p,\mathbf{X}}\mathcal{V}_i + \mathcal{U}\left(\frac{\partial \mathcal{V}_i}{\partial T}\right)_{p,\mathbf{X}}\right]\ln\left(\frac{\mathcal{X}}{\mathcal{Y}}\right) +$$
$$+\frac{\mathcal{U}\mathcal{V}_i}{\mathcal{X}\mathcal{Y}}\left[\left(\frac{\partial \mathcal{X}}{\partial T}\right)_{p,\mathbf{X}}\mathcal{Y} - \mathcal{X}\left(\frac{\partial \mathcal{Y}}{\partial T}\right)_{p,\mathbf{X}}\right]. \tag{M.3.48}$$

where:

$$\left(\frac{\partial \mathcal{U}}{\partial T}\right)_{p,\mathbf{X}} = \frac{\partial}{\partial T}\left[\frac{A_m}{B_m R_u T(\delta_2-\delta_1)}\right]_{p,\mathbf{X}} = \frac{1}{B_m R_u(\delta_2-\delta_1)}\left[\frac{\left(\frac{\partial A_m}{\partial T}\right)_{p,\mathbf{X}} T - A_m}{T^2}\right]. \tag{M.3.49}$$

$$\left(\frac{\partial \mathcal{V}_i}{\partial T}\right)_{p,\mathbf{X}} = \frac{\partial}{\partial T}\left[\frac{2\sum_{j=1}^{N_s} X_j A_{jk}}{A_m} - \frac{\tilde{B}_i}{B_m}\right]_{p,\mathbf{X}} = \frac{\partial}{\partial T}\left[\frac{2\sum_{j=1}^{N_s} X_j A_{jk}}{A_m}\right]_{p,\mathbf{X}} - \cancelto{0}{\frac{\partial}{\partial T}\left[\frac{\tilde{B}_i}{B_m}\right]_{p,\mathbf{X}}} =$$
$$= \frac{2A_m\left(\sum_{j=1}^{N_s} X_j \frac{dA_{jk}}{dT}\right) - \left(\frac{\partial A_m}{\partial T}\right)_{\mathbf{X}}\left(2\sum_{j=1}^{N_s} X_j A_{jk}\right)}{A_m^2}, \tag{M.3.50}$$

where A_{jk} and dA_{jk}/dT are listed in Tab. 12. Finally:

$$\left[\left(\frac{\partial \mathcal{X}}{\partial T}\right)_{p,\mathbf{X}} \mathcal{Y} - \mathcal{X}\left(\frac{\partial \mathcal{Y}}{\partial T}\right)_{p,\mathbf{X}}\right] = \tilde{B}_m(\delta_1-\delta_2)\left[\left(\frac{\partial Z}{\partial T}\right)_{p,\mathbf{X}} + \frac{Z}{T}\right]. \tag{M.3.51}$$

- term (4)

$$\left(\frac{\partial(\mathcal{K}_i \mathcal{U} \ln \mathcal{W})}{\partial T}\right)_{p,\mathbf{X}} = \mathcal{U}\ln\mathcal{W}\left(\frac{\partial \mathcal{K}_i}{\partial T}\right)_{p,\mathbf{X}} + \mathcal{K}_i\left\{\left(\frac{\partial \mathcal{U}}{\partial T}\right)_{p,\mathbf{X}} \ln\left(\frac{\mathcal{X}}{\mathcal{Y}}\right) + \right.$$
$$\left. + \frac{\mathcal{U}}{\mathcal{X}\mathcal{Y}}\left[\left(\frac{\partial \mathcal{X}}{\partial T}\right)_{p,\mathbf{X}} \mathcal{Y} - \mathcal{X}\left(\frac{\partial \mathcal{Y}}{\partial T}\right)_{p,\mathbf{X}}\right]\right\}. \tag{M.3.52}$$

However the first term is zero since:

$$\left(\frac{\partial \mathcal{K}_i}{\partial T}\right)_{p,\mathbf{X}} = \frac{\partial}{\partial T}\underbrace{\left[\frac{S_{2,i}-S_{1,i}}{\delta_2-\delta_1}\right]_{p,\mathbf{X}}}_{\text{Not a function of } T} = 0. \tag{M.3.53}$$

- term (5)

$$\left(\frac{\partial(\mathcal{U}\mathcal{J}\tilde{\Delta}_i)}{\partial T}\right)_{p,\mathbf{X}} = \mathcal{U}\mathcal{J}\left(\frac{\partial \tilde{\Delta}_i}{\partial T}\right)_{p,\mathbf{X}} + \mathcal{U}\tilde{\Delta}_i\left(\frac{\partial \mathcal{J}}{\partial T}\right)_{p,\mathbf{X}} + \mathcal{J}\tilde{\Delta}_i\left(\frac{\partial \mathcal{U}}{\partial T}\right)_{p,\mathbf{X}}, \tag{M.3.54}$$

where the quantities that have not been computed so far are given:

$$\left(\frac{\partial \tilde{\Delta}_i}{\partial T}\right)_{p,\mathbf{X}} \underset{\text{Use Eq. (M.3.13)}}{=} -B_m^2 \frac{\rho}{ZT}\left(S_{2,i}\delta_1 - S_{1,i}\delta_2\right)\left[\left(\frac{\partial Z}{\partial T}\right)_{p,\mathbf{X}} + Z\right]. \tag{M.3.55}$$

$$\left(\frac{\partial \mathcal{J}}{\partial T}\right)_{p,\mathbf{X}} = \underset{\text{Use Eq. (M.3.23)}}{\downarrow} \frac{p}{R_u T^3(\delta_2\tilde{B}_m + Z)^2(\delta_1\tilde{B}_m + Z)^2}\left[\tilde{B}_m(Z(\delta_1+\delta_2)+\delta_1\delta_2)+Z^2\right]\left[\left(\frac{\partial Z}{\partial T}\right)_{p,\mathbf{X}} T - Z\right] +$$
$$-\frac{pZ}{R_u T^2(\delta_2\tilde{B}_m + Z)^2(\delta_1\tilde{B}_m + Z)^2}\left(\frac{\partial \tilde{B}_m}{\partial T}\right)_{p,\mathbf{X}}\left[2\delta_1\delta_2\tilde{B}_m + Z(\delta_1+\delta_2)\right] +$$
$$-\frac{pZ}{R_u T(\delta_2\tilde{B}_m + Z)^2(\delta_1\tilde{B}_m + Z)^2}\left(\frac{\partial Z}{\partial T}\right)_{p,\mathbf{X}}\left[\tilde{B}_m(\delta_1+\delta_2)+2Z\right], \tag{M.3.56}$$

where:

$$\left(\frac{\partial \tilde{B}_m}{\partial T}\right)_{p,\mathbf{X}} = \frac{\partial}{\partial T}\left(B_m \frac{p}{R_u T}\right)_{p,\mathbf{X}} = \frac{B_m p}{R_u}\left(-\frac{1}{T^2}\right) = -\frac{\tilde{B}_m}{T}. \tag{M.3.57}$$

Similarly, by using the definitions of Eq. (M.3.43), for the VDW EoS the following result is obtained:

$$\left(\frac{\partial \ln\phi_i}{\partial T}\right)_{p,\mathbf{X}} = -\left(\frac{\partial \mathcal{S}}{\partial T}\right)_{p,\mathbf{X}} + \left(\frac{\partial \mathcal{R}_i}{\partial T}\right)_{p,\mathbf{X}} + \left(\frac{\partial \mathcal{V}_i}{\partial T}\right)_{p,\mathbf{X}}, \tag{M.3.58}$$

where each term is given below with similar derivation as done before:

$$\left(\frac{\partial \mathcal{S}}{\partial T}\right)_{p,\mathbf{X}} = \frac{1}{Z-\tilde{B}_m}\left[\left(\frac{\partial Z}{\partial T}\right)_{p,\mathbf{X}} + \frac{\tilde{B}_m}{T}\right],$$
$$\left(\frac{\partial \mathcal{R}_i}{\partial T}\right)_{p,\mathbf{X}} = -\frac{p\tilde{B}_i}{R_u T^2(Z-\tilde{B}_m)^2}\left[Z + T\left(\frac{\partial Z}{\partial T}\right)_{p,\mathbf{X}}\right],$$
$$\left(\frac{\partial \mathcal{V}_i}{\partial T}\right)_{p,\mathbf{X}} = -\frac{2p}{(ZR_u T^2)^2}\left\{T^2 Z\sum_{j=1}^{N_s} X_j \frac{dA_{ji}}{dT} - \left[2TZ + T^2\left(\frac{\partial Z}{\partial T}\right)_{p,\mathbf{X}}\right]\sum_{j=1}^{N_s} X_j A_{ji}\right\}. \tag{M.3.59}$$

M.3.3 Derivative with respect to pressure

Derivative of the fugacity coefficient with respect to pressure is carried out in the same way as the one for temperature. For GCEoS except VDW, the general formula is first expressed as:

$$\left(\frac{\partial \ln\phi_i}{\partial p}\right)_{T,\mathbf{X}} = \frac{\partial}{\partial p}\left[\mathcal{R}_i - \mathcal{S} - \mathcal{T}_i \ln\mathcal{W} + \mathcal{K}_i\mathcal{U}\ln\mathcal{W} - \mathcal{U}\mathcal{J}\tilde{\Delta}_i\right]_{T,\mathbf{X}_k} =$$
$$= \underbrace{\left(\frac{\partial \mathcal{R}_i}{\partial p}\right)_{T,\mathbf{X}}}_{\text{term } (1)} - \underbrace{\left(\frac{\partial \mathcal{S}_i}{\partial p}\right)_{T,\mathbf{X}}}_{\text{term } (2)} - \underbrace{\left(\frac{\partial(\mathcal{T}_i \ln\mathcal{W})}{\partial p}\right)_{T,\mathbf{X}}}_{\text{term } (3)} + \underbrace{\left(\frac{\partial(\mathcal{K}_i\mathcal{U}\ln\mathcal{W})}{\partial p}\right)_{T,\mathbf{X}}}_{\text{term } (4)} - \underbrace{\left(\frac{\partial(\mathcal{U}\mathcal{J}\tilde{\Delta}_i)}{\partial p}\right)_{T,\mathbf{X}}}_{\text{term } (5)},$$

where each term is that of Eq. (M.3.23) and is obtained independently:

- term (1)

$$\left(\frac{\partial \mathcal{R}_i}{\partial p}\right)_{T,\mathbf{X}} = \frac{\partial}{\partial p}\left[\frac{\tilde{B}_i}{B_m}(Z-1)\right]_{T,\mathbf{X}} = \frac{\tilde{B}_i}{B_m}\left(\frac{\partial Z}{\partial p}\right)_{T,\mathbf{X}}. \tag{M.3.60}$$

- term (2)

$$\left(\frac{\partial \mathcal{S}_i}{\partial p}\right)_{T,\mathbf{X}} = \frac{\partial}{\partial p}\left[\ln\left(Z-\tilde{B}_m\right)\right]_{T,\mathbf{X}} = \frac{1}{Z-\tilde{B}_m}\left[\left(\frac{\partial Z}{\partial p}\right)_{T,\mathbf{X}} - \frac{\tilde{B}_m}{p}\right]. \tag{M.3.61}$$

- term (3)

$$\left(\frac{\partial(\mathcal{T}_i \ln\mathcal{W})}{\partial p}\right)_{T,\mathbf{X}} = \left(\frac{\partial \mathcal{T}_i}{\partial p}\right)_{T,\mathcal{X}} \ln\mathcal{W} + \mathcal{T}_i \ln\mathcal{W} = \left[\left(\frac{\partial \mathcal{U}}{\partial p}\right)_{T,\mathbf{X}} \mathcal{V}_i + \mathcal{U}\left(\frac{\partial \mathcal{V}_i}{\partial p}\right)_{T,\mathbf{X}}\right] \ln\left(\frac{\mathcal{X}}{\mathcal{Y}}\right) + \\ + \frac{\mathcal{U}\mathcal{V}_i}{\mathcal{X}\mathcal{Y}}\left[\left(\frac{\partial \mathcal{X}}{\partial p}\right)_{T,\mathbf{X}} \mathcal{Y} - \mathcal{X}\left(\frac{\partial \mathcal{Y}}{\partial p}\right)_{T,\mathbf{X}}\right]. \tag{M.3.62}$$

where:

$$\left(\frac{\partial \mathcal{U}}{\partial p}\right)_{T,\mathbf{X}} = \frac{\partial}{\partial p}\underbrace{\left[\frac{A_m}{B_m R_u T(\delta_2-\delta_1)}\right]_{T,\mathbf{X}}}_{\text{Does not depend on } p} = 0. \tag{M.3.63}$$

$$\left(\frac{\partial \mathcal{V}_i}{\partial p}\right)_{T,\mathbf{X}} = \frac{\partial}{\partial p}\underbrace{\left[\frac{2\sum_{j=1}^{N_s} X_j A_{jk}}{A_m} - \frac{\tilde{B}_i}{B_m}\right]_{T,\mathbf{X}}}_{\text{Does not depend on } p} = 0, \tag{M.3.64}$$

$$\left(\frac{\partial \mathcal{X}}{\partial p}\right)_{T,\mathbf{X}} = \frac{\partial}{\partial p}\left(Z+\delta_2\tilde{B}_m\right)_{T,\mathbf{X}} = \left(\frac{\partial Z}{\partial p}\right)_{T,\mathbf{X}} + \frac{\delta_2 B_m}{R_u T}, \tag{M.3.65}$$

$$\left(\frac{\partial \mathcal{Y}}{\partial p}\right)_{T,\mathbf{X}} = \frac{\partial}{\partial p}\left(Z+\delta_1\tilde{B}_m\right)_{T,\mathbf{X}} = \left(\frac{\partial Z}{\partial p}\right)_{T,\mathbf{X}} + \frac{\delta_1 B_m}{R_u T}. \tag{M.3.66}$$

- term (4)

$$\left(\frac{\partial(\mathcal{K}_i \mathcal{U}\ln\mathcal{W})}{\partial p}\right)_{T,\mathbf{X}} = \mathcal{U}\ln\mathcal{W}\left(\frac{\partial \mathcal{K}_i}{\partial p}\right)_{T,\mathbf{X}} + \mathcal{K}_i\left\{\cancelto{0}{\left(\frac{\partial \mathcal{U}}{\partial p}\right)_{T,\mathbf{X}}} \ln\left(\frac{\mathcal{X}}{\mathcal{Y}}\right) + \right. \\ \left. + \frac{\mathcal{U}}{\mathcal{X}\mathcal{Y}}\left[\left(\frac{\partial \mathcal{X}}{\partial p}\right)_{T,\mathbf{X}} \mathcal{Y} - \mathcal{X}\left(\frac{\partial \mathcal{Y}}{\partial p}\right)_{T,\mathbf{X}}\right]\right\}. \tag{M.3.67}$$

However the first term is also zero since:

$$\left(\frac{\partial \mathcal{K}_i}{\partial T}\right)_{p,\mathbf{X}} = \frac{\partial}{\partial p}\underbrace{\left[\frac{S_{2,i}-S_{1,i}}{\delta_2-\delta_1}\right]_{T,\mathbf{X}}}_{\text{Not a function of } p} = 0\,. \tag{M.3.68}$$

- term (5)

$$\left(\frac{\partial(\mathcal{U}\mathcal{J}\tilde{\Delta}_i)}{\partial p}\right)_{T,\mathbf{X}} = \mathcal{U}\mathcal{J}\left(\frac{\partial \tilde{\Delta}_i}{\partial p}\right)_{T,\mathbf{X}} + \mathcal{U}\tilde{\Delta}_i\left(\frac{\partial \mathcal{J}}{\partial p}\right)_{T,\mathbf{X}} + \mathcal{J}\tilde{\Delta}_i\cancelto{0}{\left(\frac{\partial \mathcal{U}}{\partial p}\right)_{T,\mathbf{X}}}\,, \tag{M.3.69}$$

where the quantities that have not been computed so far are given:

$$\left(\frac{\partial \tilde{\Delta}_i}{\partial p}\right)_{T,\mathbf{X}} \underset{\text{Use Eq. (M.3.13)}}{=} \frac{B_m^2 M}{Z R_u T}(S_{2,i}\delta_1 - S_{1,i}\delta_2)\left[1 - \frac{p}{Z}\left(\frac{\partial Z}{\partial p}\right)_{T,\mathbf{X}}\right]. \tag{M.3.70}$$

$$\begin{aligned}\left(\frac{\partial \mathcal{J}}{\partial p}\right)_{T,\mathbf{X}} \underset{\text{Use Eq. (M.3.23)}}{=} & \frac{\left[Z + p\left(\frac{\partial Z}{\partial p}\right)_{T,\mathbf{X}}\right]}{R_u M T(\delta_2\tilde{B}_m + Z)(\delta_1\tilde{B}_m + Z)} + \\ & - \frac{pZ}{R_u M T(\delta_2\tilde{B}_m + Z)^2(\delta_1\tilde{B}_m + Z)^2}\left\{\left[\delta_2\left(\frac{\partial \tilde{B}_m}{\partial p}\right)_{T,\mathbf{X}} + \left(\frac{\partial Z}{\partial p}\right)_{T,\mathbf{X}}\right]\left(\delta_1\tilde{B}_m + Z\right) + \right. \\ & \left. - \left(\delta_2\tilde{B}_m + Z\right)\left[\delta_1\left(\frac{\partial \tilde{B}_m}{\partial p}\right)_{T,\mathbf{X}} + \left(\frac{\partial Z}{\partial p}\right)_{T,\mathbf{X}}\right]\right\}\end{aligned} \tag{M.3.71}$$

where:

$$\left(\frac{\partial \tilde{B}_m}{\partial p}\right)_{T,\mathbf{X}} = \frac{\partial}{\partial p}\left(B_m\frac{p}{R_u T}\right)_{T,\mathbf{X}} = \frac{B_m}{R_u T} = \frac{\tilde{B}_m}{p}\,. \tag{M.3.72}$$

Similarly, by using the definitions of Eq. (M.3.43), for the VDW EoS the following result is obtained:

$$\left(\frac{\partial \ln\phi_i}{\partial p}\right)_{T,\mathbf{X}} = -\left(\frac{\partial \mathcal{S}}{\partial p}\right)_{T,\mathbf{X}} + \left(\frac{\partial \mathcal{R}_i}{\partial p}\right)_{T,\mathbf{X}} + \left(\frac{\partial \mathcal{V}_i}{\partial p}\right)_{T,\mathbf{X}}\,, \tag{M.3.73}$$

where each term is given below with similar derivation as done before:

$$\left(\frac{\partial \mathcal{S}}{\partial p}\right)_{T,\mathbf{X}} = \frac{1}{Z-\tilde{B}_m}\left[\left(\frac{\partial Z}{\partial p}\right)_{T,\mathbf{X}} - \frac{\tilde{B}_m}{p}\right],$$
$$\left(\frac{\partial \mathcal{R}_i}{\partial p}\right)_{T,\mathbf{X}} = \frac{\tilde{B}_i}{R_u T(Z-\tilde{B}_m)^2}\left[Z - p\left(\frac{\partial Z}{\partial p}\right)_{T,\mathbf{X}}\right],$$
$$\left(\frac{\partial \mathcal{V}_i}{\partial p}\right)_{T,\mathbf{X}} = -\frac{2\sum_{j=1}^{N_s} X_j A_{ji}}{(ZR_uT)^2}\left[Z - p\left(\frac{\partial Z}{\partial p}\right)_{T,\mathbf{X}}\right]. \qquad \text{(M.3.74)}$$

M.4 Partial molar quantities

Partial molar volume and enthalpy for single-phase mixtures are derived according to their definition of Eq. (2.2.28). First the partial molar volume for the i-th species in the mixture for the GCEoS is derived. This procedure requires the definition of V_i to be split in two, for convenience:

$$V_i = \left(\frac{\partial \overline{V}}{\partial N_i}\right)_{T,p,\mathbf{N}_i} = -\left(\frac{\partial \overline{V}}{\partial p}\right)_{T,\mathbf{N}}\left(\frac{\partial p}{\partial N_i}\right)_{T,\overline{V},\mathbf{N}_i}, \qquad i = 1,\cdots,N_s\,. \qquad \text{(M.4.1)}$$

$$\downarrow$$

$$\text{Using } \left(\frac{\partial \overline{V}}{\partial N_i}\right)_{T,p,\mathbf{N}_i}\left(\frac{\partial N_i}{\partial p}\right)_{T,\overline{V},\mathbf{N}_i}\left(\frac{\partial p}{\partial \overline{V}}\right)_{T,\mathbf{N}} = -1$$

The first derivative can be recast in a more convenient form as follows:

$$\left(\frac{\partial \overline{V}}{\partial p}\right)_{T,\mathbf{N}} = N\left(\frac{\partial V}{\partial p}\right)_{T,\mathbf{N}} = N\left(\frac{\partial (1/\rho)}{\partial p}\right)_{T,\mathbf{N}} = -\frac{N}{\rho^2}\left(\frac{\partial \rho}{\partial p}\right)_{T,\mathbf{N}} = -\frac{N}{\rho^2}\left(\frac{\partial \rho}{\partial p}\right)_{T,\mathbf{X}}, \qquad i = 1,\cdots,N_s \qquad \text{(M.4.2)}$$

so that Eq. (M.4.1) rewrites as:

$$V_i = \frac{N}{\rho^2}\left(\frac{\partial \rho}{\partial p}\right)_{T,\mathbf{X}}\left(\frac{\partial p}{\partial N_i}\right)_{T,\overline{V},\mathbf{N}_i}, \qquad i = 1,\cdots,N_s\,, \qquad \text{(M.4.3)}$$

where $(\partial\rho/\partial p)_{T,\mathbf{X}}$ is already available for GCEoS through its inverse computed in Eq. (2.2.87). As a result, the derivative $(\partial p/\partial N_i)_{T,\overline{V},\mathbf{N}_i}$ needs to be computed only. To begin, Eq. (2.2.67) is recast in a form that contains the number of moles N and the extensive volume $\overline{V}$:

$$p = \frac{NR_uT}{\overline{V}-NB_m} - \frac{N^2A_m}{\overline{V}^2 + (\delta_1+\delta_2)\overline{V}NB_m + \delta_1\delta_2N^2B_m^2}\,. \qquad \text{(M.4.4)}$$

$$\downarrow$$

$$\text{Use } \overline{V} = NV$$

Next, the derivative is computed. Using the results of Eq. (G.0.1), Eq. (G.0.4) and Eqs. (M.3.10)–(M.3.11) it is easy to prove that the following result is obtained:

$$\begin{aligned}\left(\frac{\partial p}{\partial N_i}\right)_{T,\overline{V},\mathbf{N}_i} =& \frac{1}{N}\frac{R_u T[(V-B_m)+\tilde{B}_i]}{(V-B_m)^2} + \\ &-\frac{1}{N}\frac{2\sum_{j=1}^{N_s} X_j A_{ji}[V^2+(\delta_1+\delta_2)VB_m+\delta_1\delta_2 B_m^2] - A_m\tilde{B}_m[V(\delta_1+\delta_2)+2B_m\delta_1\delta_2]}{[V^2+(\delta_1+\delta_2)VB_m+\delta_1\delta_2 B_m^2]^2} + \\ &+\frac{1}{N}\frac{A_m B_m[V(S_{1,i}+S_{2,i})+B_m(\delta_2 S_{1,i}+\delta_1 S_{2,i})]}{[V^2+(\delta_1+\delta_2)VB_m+\delta_1\delta_2 B_m^2]^2}, \qquad i=1,\cdots,N_s\,.\end{aligned} \tag{M.4.5}$$

It is easy to verify also that the last term in Eq. (M.4.5) vanishes identically if PR-RK EoS is not considered.

Next the partial molar enthalpy for GCEoS is derived. For convenience, the derivation is again split in two parts, that pertaining to all EoS except VDW and the one for VDW alone. Following its definition:

$$H_i = \left(\frac{\partial \overline{H}}{\partial N_i}\right)_{T,p,\mathbf{N}_i} = \left(\frac{\partial NH}{\partial N_i}\right)_{T,p,\mathbf{N}_i}, \qquad i=1,\cdots,N_s\,. \tag{M.4.6}$$

However $H = H^{ig} + \Delta H = H^{ig} + \Delta E + (Z-1)R_u T$. Using the result of Eq. (2.2.79) (for $\delta_1, \delta_2 \neq 0$) and the fact that $p\overline{V} = NZR_u T$, one gets:

$$\begin{aligned}\overline{H} =& NH = NH^{ig} + \frac{N^2}{N(\delta_1-\delta_2)B_m}\left[T\left(\frac{\partial A_m}{\partial T}\right)_{\mathbf{X}} - A_m\right]\ln\left[\frac{1+\dfrac{\delta_1 B_m\rho}{M}}{1+\dfrac{\delta_2 B_m\rho}{M}}\right] + p\overline{V} - NR_u T \\ & i=1,\cdots,N_s\,.\end{aligned} \tag{M.4.7}$$

Hence, using Eq. (M.4.7) into Eq. (M.4.6) the partial molar enthalpy is readily written as:

$$
\begin{aligned}
H_i = & \underbrace{\left(\frac{\partial N H_{ig}}{\partial N_i}\right)_{T,p,\mathbf{N}_i}}_{\text{term } (1)} + \\
& \underbrace{+\ln\left[\frac{1+\frac{\delta_1 B_m \rho}{M}}{1+\frac{\delta_2 B_m \rho}{M}}\right] \underbrace{\frac{\partial}{\partial N_i}\left\{\frac{N^2}{N(\delta_1-\delta_2)B_m}\left[T\left(\frac{\partial A_m}{\partial T}\right)_{\mathbf{X}} - A_m\right]\right\}_{T,p,\mathbf{N}_i}}_{\text{term } (2a)}}_{\text{term } (2)} + \\
& \underbrace{+\frac{N^2}{N(\delta_1-\delta_2)B_m}\left[T\left(\frac{\partial A_m}{\partial T}\right)_{\mathbf{X}} - A_m\right] \underbrace{\frac{\partial}{\partial N_i}\left\{\ln\left[\frac{1+\frac{\delta_1 B_m \rho}{M}}{1+\frac{\delta_2 B_m \rho}{M}}\right]\right\}_{T,p,\mathbf{N}_i}}_{\text{term } (3a)}}_{\text{term } (3)} + \\
& \underbrace{\left(\frac{\partial (p\overline{V})}{\partial N_i}\right)_{T,p,\mathbf{N}_i}}_{\text{term } (4)} - \underbrace{\left(\frac{\partial (N R_u T)}{\partial N_i}\right)_{T,p,\mathbf{N}_i}}_{\text{term } (5)}, \qquad i = 1, \cdots, N_s\,,
\end{aligned}
\tag{M.4.8}
$$

and each of the highlighted derivatives is further developed below:

- term (1)

$$
\left(\frac{\partial N H_{ig}}{\partial N_i}\right)_{T,p,\mathbf{N}_i} = \frac{\partial}{\partial N_i}\left(N \sum_{j=1}^{N_s} X_j H_j^{ig}\right)_{T,p,\mathbf{N}_i} = \frac{\partial}{\partial N_i}\left(\sum_{j=1}^{N_s} N_j H_j^{ig}\right)_{T,p,\mathbf{N}_i} = H_i^{ig}\,,
\tag{M.4.9}
$$

  where H_i^{ig} is the mole-based ideal gas enthalpy of the i-th species.

- term (2a)

$$\frac{\partial}{\partial N_i}\left\{\frac{N^2}{N(\delta_1-\delta_2)B_m}\left[T\left(\frac{\partial A_m}{\partial T}\right)_{\mathbf{X}}-A_m\right]\right\}_{T,p,\mathbf{N}_i}=$$
$$=\frac{\frac{\partial}{\partial N_i}\left\{N^2\left[T\left(\frac{\partial A_m}{\partial T}\right)_{\mathbf{X}}-A_m\right]\right\}_{T,p,\mathbf{N}_i}N(\delta_1-\delta_2)B_m}{N^2(\delta_1-\delta_2)^2B_m^2}+$$
$$-\frac{N^2\left[T\left(\frac{\partial A_m}{\partial T}\right)_{\mathbf{X}}-A_m\right]\frac{\partial}{\partial N_i}\left[N(\delta_1-\delta_2)B_m\right]_{T,p,\mathbf{X}}}{N^2(\delta_1-\delta_2)^2B_m^2}=$$
$$=\frac{1}{N^2(\delta_1-\delta_2)^2B_m^2}\left\{T\frac{\partial}{\partial T}\left[\left(\frac{\partial N^2A_m}{\partial N_i}\right)_{T,\mathbf{N}_i}\right]_{p,\mathbf{N}}N(\delta_1-\delta_2)B_m-N(\delta_1-\delta_2)B_m\left(\frac{\partial N^2A_m}{\partial N_i}\right)_{T,\mathbf{X}}+\right.$$
$$\left.-N^2\left[T\left(\frac{\partial A_m}{\partial T}\right)_{\mathbf{X}}-A_m\right](\delta_1-\delta_2)\left(\frac{\partial NB_m}{\partial N_i}\right)_{\mathbf{N}_i}-N^3\left[T\left(\frac{\partial A_m}{\partial T}\right)_{\mathbf{X}}-A_m\right]B_m\left(\frac{\partial(\delta_1-\delta_2)}{\partial N_i}\right)_{\mathbf{N}}\right\}. \tag{M.4.10}$$

Using the results of Eq. (G.0.1), Eq. (G.0.4), Eq. (M.3.8) and Eqs. (M.3.10)–(M.3.11), the previous result can be rewritten as follows:

$$\frac{\partial}{\partial N_i}\left\{\frac{N^2}{N(\delta_1-\delta_2)B_m}\left[T\left(\frac{\partial A_m}{\partial T}\right)_{\mathbf{X}}-A_m\right]\right\}_{T,p,\mathbf{N}_i}=$$
$$=\frac{1}{(\delta_1-\delta_2)^2B_m^2}\left\{2B_m(\delta_1-\delta_2)\left[T\sum_{j=1}^{N_s}X_j\frac{dA_{ji}}{dT}-\sum_{j=1}^{N_s}X_jA_{ji}\right]+\right.$$
$$\left.-\left[T\left(\frac{\partial A_m}{\partial T}\right)_{\mathbf{X}}-A_m\right]\left[\tilde{B}_i(\delta_1-\delta_2)+B_m(S_{1,i}-S_{2,i})\right]\right\}, \tag{M.4.11}$$

where A_{ji} and dA_{ji}/dT are given in Tab. 12.

- term (2)

  Putting together the definition of Eq. (M.4.8) and the intermediate result of Eq. (M.4.11), term 2 becomes:

$$\text{term (2)}=\ln\left[\frac{M+\delta_1B_m\rho}{M+\delta_2B_m\rho}\right]\frac{2\left[T\sum_{j=1}^{N_s}X_j\frac{dA_{ji}}{dT}-\sum_{j=1}^{N_s}X_jA_{ji}\right]}{(\delta_1-\delta_2)B_m}+$$
$$-\ln\left[\frac{M+\delta_1B_m\rho}{M+\delta_2B_m\rho}\right]\frac{1}{(\delta_1-\delta_2)^2B_m^2}\left[T\left(\frac{\partial A_m}{\partial T}\right)_{\mathbf{X}}-A_m\right]\left[\tilde{B}_i(\delta_1-\delta_2)+B_m(S_{1,i}-S_{2,i})\right]. \tag{M.4.12}$$

- term (3a)

$$\frac{\partial}{\partial N_i}\left\{\ln\left[\frac{1+\frac{\delta_1 B_m\rho}{M}}{1+\frac{\delta_2 B_m\rho}{M}}\right]\right\}_{T,p,\mathbf{N}_i} =$$

$$=\frac{1+\frac{\delta_1 B_m\rho}{M}}{1+\frac{\delta_2 B_m\rho}{M}}\frac{\left(1+\frac{\delta_2 B_m\rho}{M}\right)\frac{\partial}{\partial N_i}\left(1+\frac{\delta_2 B_m\rho}{M}\right)_{T,p,\mathbf{N}_i}-\left(1+\frac{\delta_1 B_m\rho}{M}\right)\frac{\partial}{\partial N_i}\left(1+\frac{\delta_2 B_m\rho}{M}\right)_{T,p,\mathbf{N}_i}}{\left(1+\frac{\delta_2 B_m\rho}{M}\right)^2}=$$

$$=\frac{\cancel{M+\delta_2 B_m\rho}}{M+\delta_1 B_m\rho}\frac{\left(1+\frac{\delta_2 B_m\rho}{M}\right)\left(\frac{\partial(\delta_1 B_m\rho/M)}{\partial N_i}\right)_{T,p,\mathbf{N}_i}-\left(1+\frac{\delta_1 B_m\rho}{M}\right)\left(\frac{\partial(\delta_2 B_m\rho/M)}{\partial N_i}\right)_{T,p,\mathbf{N}_i}}{\frac{1}{M^2}(M+\delta_2 B_m\rho)^{\cancel{2}}}=$$

$$=\frac{M^2}{\overline{V}(M+\delta_1 B_m\rho)(M+\delta_2 B_m\rho)}\left\{(M+\delta_2 B_m\rho)\left[B_m S_{1,i}+\delta_1\left(\tilde{B}_i-B_m\frac{V_i}{V}\right)\right]+\right.$$

$\downarrow$

Using Eq. (H.0.1) and Eq. (H.0.2)

$$\left.-(M+\delta_1 B_m\rho)\left[B_m S_{2,i}+\delta_2\left(\tilde{B}_i-B_m\frac{V_i}{V}\right)\right]\right\}=$$

$$=\frac{M^2 B_m(\delta_1-\delta_2)}{\overline{V}(M+\delta_1 B_m\rho)(M+\delta_2 B_m\rho)}\left(\frac{\tilde{B}_i}{B_m}-\frac{V_i}{V}\right)+\frac{M B_m\left[S_{1,i}(M+\delta_2 B_m\rho)-S_{2,i}(M+\delta_1 B_m\rho)\right]}{\overline{V}(M+\delta_1 B_m\rho)(M+\delta_2 B_m\rho)}$$

(M.4.13)

- term (3)

$$\text{term }(3)=\frac{N^{\cancel{2}}}{\cancel{N(\delta_1-\delta_2)B_m}}\left[T\left(\frac{\partial A_m}{\partial T}\right)_{\mathbf{X}}-A_m\right]\frac{M^2\cancel{B_m(\delta_1-\delta_2)}}{\overline{V}(M+\delta_1 B_m\rho)(M+\delta_2 B_m\rho)}\left(\frac{\tilde{B}_i}{B_m}-\frac{V_i}{V}\right)+$$

$$+\frac{N^{\cancel{2}}}{\cancel{N}(\delta_1-\delta_2)\cancel{B_m}}\left[T\left(\frac{\partial A_m}{\partial T}\right)_{\mathbf{X}}-A_m\right]\frac{M\cancel{B_m}\left[S_{1,i}(M+\delta_2 B_m\rho)-S_{2,i}(M+\delta_1 B_m\rho)\right]}{\overline{V}(M+\delta_1 B_m\rho)(M+\delta_2 B_m\rho)}=$$

$$=\frac{\rho M\left[T\left(\frac{\partial A_m}{\partial T}\right)_{\mathbf{X}}-A_m\right]\left(\frac{\tilde{B}_i}{B_m}-\frac{V_i}{V}\right)}{(M+\delta_1 B_m\rho)(M+\delta_2 B_m\rho)}+$$

$$+\frac{\rho}{(\delta_1-\delta_2)}\left[T\left(\frac{\partial A_m}{\partial T}\right)_{\mathbf{X}}-A_m\right]\frac{\left[S_{1,i}(M+\delta_2 B_m\rho)-S_{2,i}(M+\delta_1 B_m\rho)\right]}{(M+\delta_1 B_m\rho)(M+\delta_2 B_m\rho)}\,,$$

(M.4.14)

- term (4)

$$\left(\frac{\partial(p\overline{V})}{\partial N_i}\right)_{T,p,\mathbf{N}_i}=p\left(\frac{\partial\overline{V}}{\partial N_i}\right)_{T,p,\mathbf{N}_i}=pV_i\,,\tag{M.4.15}$$

- term (5)

$$\left(\frac{\partial(NR_uT)}{\partial N_i}\right)_{T,p,\mathbf{N}_i} = R_uT\left(\frac{\partial N}{\partial N_i}\right)_{\mathbf{N}_i} = R_uT\,. \tag{M.4.16}$$

Gathering together all the results, the following final version of the partial molar enthalpy for GCEoS (except VDW) is obtained:

$$\begin{aligned}
H_i =& H_i^{ig} + pV_i - R_uT + \\
&+ \ln\left[\frac{M+\delta_1 B_m\rho}{M+\delta_2 B_m\rho}\right]\frac{\left\{2T\sum_{j=1}^{N_s}X_j\frac{dA_{ji}}{dT} - 2\sum_{j=1}^{N_s}X_jA_{ji} - \left[T\left(\frac{\partial A_m}{\partial T}\right)_{\mathbf{X}} - A_m\right]\frac{\tilde{B}_i}{B_m}\right\}}{(\delta_1-\delta_2)B_m} + \\
&+ \frac{\rho M\left[T\left(\frac{\partial A_m}{\partial T}\right)_{\mathbf{X}} - A_m\right]\left(\frac{\tilde{B}_i}{B_m} - \frac{V_i}{V}\right)}{(M+\delta_1 B_m\rho)(M+\delta_2 B_m\rho)} + \\
&- \ln\left[\frac{M+\delta_1 B_m\rho}{M+\delta_2 B_m\rho}\right]\frac{(S_{1,i}-S_{2,i})}{(\delta_1-\delta_2)^2 B_m}\left[T\left(\frac{\partial A_m}{\partial T}\right)_{\mathbf{X}} - A_m\right] + \\
&+ \frac{\rho}{(\delta_1-\delta_2)}\left[T\left(\frac{\partial A_m}{\partial T}\right)_{\mathbf{X}} - A_m\right]\frac{[S_{1,i}(M+\delta_2 B_m\rho) - S_{2,i}(M+\delta_1 B_m\rho)]}{(M+\delta_1 B_m\rho)(M+\delta_2 B_m\rho)}\,, \qquad i=1,\cdots,N_s\,.
\end{aligned} \tag{M.4.17}$$

It is easy to verify that if an EoS other than PR-RK is used, the last two terms vanish to zero identically.

Finally, the partial molar enthalpy for VDW EoS is derived. Using the result of Eq. (2.2.79) (for $\delta_1 = \delta_2 = 0$) and the fact that $p\overline{V} = NZR_uT$, one gets:

$$\overline{H} = NH = NH^{ig} + \frac{N\rho}{M}\left[T\left(\frac{\partial A_m}{\partial T}\right)_{\mathbf{X}} - A_m\right] + p\overline{V} - NR_uT\,, \qquad i=1,\cdots,N_s\,. \tag{M.4.18}$$

Following similar steps as done before, it is easy to prove the following result:

$$H_i = H_i^{ig} + 2\frac{\rho}{M}\left[T\sum_{j=1}^{N_s} X_j \frac{dA_{ji}}{dT} - \sum_{j=1}^{N_s} X_j A_{ji}\right] + V_i \frac{\rho^2}{M}\left[T\left(\frac{\partial A_m}{\partial T}\right)_{\mathbf{X}} + A_m\right] + pV_i - R_u T$$

$$i = 1, \cdots, N_s\,. \tag{M.4.19}$$

Appendix N

EULER EQUATIONS FOR A GENERIC EOS

In order to derive the Euler equations (Eqs. (2.1.1)-(2.1.4) are employed with the viscous terms set to 0. First, the following generic derivatives of the internal energy are required to be derived:

$$\left(\frac{\partial e}{\partial \rho}\right)_{p,\mathbf{Y}} = \left(\frac{\partial e}{\partial \rho}\right)_{p,\mathbf{X}} = \left(\frac{\partial e}{\partial T}\right)_{p,\mathbf{X}} \left(\frac{\partial T}{\partial \rho}\right)_{p,\mathbf{X}} = \underset{e=h-p/\rho}{\downarrow}$$

$$= -\left[\left(\frac{\partial h}{\partial T}\right)_{p,\mathbf{X}} - p\frac{\partial}{\partial T}\left(\frac{1}{\rho}\right)_{p,\mathbf{X}}\right] \underbrace{\frac{1}{\rho\alpha_p}}_{\text{result of } Eq.\ (2.2.21)} =$$

$$= -\left[c_p + p \underbrace{\frac{1}{\rho^2}\left(\frac{\partial \rho}{\partial T}\right)_{p,\mathbf{X}}}_{=-\alpha_p/\rho \text{ still using } Eq.\ (2.2.21)}\right]\frac{1}{\rho\alpha_p}$$

$$= -\left[c_p - \frac{p\alpha_p}{\rho}\right]\frac{1}{\rho\alpha_p} = -\frac{c_p}{\rho\alpha_p} + \frac{p}{\rho^2} = \frac{1}{\rho}\left(\frac{p}{\rho} - \frac{c_p}{\alpha_p}\right), \tag{N.0.1}$$

$$\left(\frac{\partial e}{\partial p}\right)_{\rho,\mathbf{Y}} = \left(\frac{\partial e}{\partial p}\right)_{\rho,\mathbf{X}} = \left(\frac{\partial e}{\partial T}\right)_{\rho,\mathbf{X}} \underbrace{\left(\frac{\partial T}{\partial p}\right)_{\rho,\mathbf{X}}}_{\text{Use} Eq.\ (2.2.21)} = \frac{c_v\kappa_T}{\alpha_p} = \underset{\text{Use Eq. (2.2.24)}}{\downarrow} \frac{c_p\kappa_s}{\alpha_p} \tag{N.0.2}$$

with α_p the thermal expansion coefficient, κ_s the isentropic compressibility and κ_T the isothermal compressibility defined earlier in Sec. 2.2.1. As a result, the derivatives that contain the total energy e_T in Eqs.(2.1.1)-(2.1.4) can be recast in the following form:

$$\frac{\partial \rho e_T}{\partial t} = \rho\frac{\partial e}{\partial t} + e\frac{\partial \rho}{\partial t} + \frac{\rho}{2}\frac{\partial u_i u_i}{\partial t} + \frac{u_i u_i}{2}\frac{\partial \rho}{\partial t} \tag{N.0.3}$$

$$\frac{\partial \rho e_T u_j}{\partial x_j} = \rho u_j\frac{\partial e}{\partial x_j} + e\frac{\partial \rho u_j}{\partial x_j} + \frac{\rho u_j}{2}\frac{\partial u_i u_i}{\partial x_j} + \frac{u_i u_i}{2}\frac{\partial \rho u_j}{\partial x_j} \tag{N.0.4}$$

Using the continuity equation, the sum of the derivatives can be simplified to:

$$\frac{\partial \rho e_T}{\partial t} + \frac{\partial \rho e_T u_j}{\partial x_j} = \rho\frac{\partial e}{\partial t} + \frac{\rho}{2}\frac{\partial u_i u_i}{\partial t} + \rho u_j\frac{\partial e}{\partial x_j} + \frac{\rho u_j}{2}\frac{\partial u_i u_i}{\partial x_j} \tag{N.0.5}$$

Using the momentum equation, the kinetic energy terms can be rearranged:

$$\frac{\rho}{2}\frac{\partial u_i u_i}{\partial t} + \frac{\rho u_j}{2}\frac{\partial u_i u_i}{\partial x_j} = \rho u_i \left(\frac{\partial u_i}{\partial t} + u_j \frac{\partial u_i}{\partial x_j}\right) = -u_j \frac{\partial p}{\partial x_j} \tag{N.0.6}$$

This can be combined with the pressure term in Eq. (2.1.3):

$$-u_j \frac{\partial p}{\partial x_j} + \frac{\partial p u_j}{\partial x_j} = p\frac{\partial u_j}{\partial x_j} \tag{N.0.7}$$

This finally yields for the Euler energy equation:

$$\frac{\partial \rho e_T}{\partial t} + \frac{\partial \rho e_T u_j}{\partial x_j} = \rho \frac{\partial e}{\partial t} + \rho u_j \frac{\partial e}{\partial x_j} + p\frac{\partial u_j}{\partial x_j} = 0 \tag{N.0.8}$$

By splitting the time and space derivatives with the partial derivatives shown earlier, the following expression is obtained:

$$\left(\frac{\partial e}{\partial p}\right)_{\rho,Y_k}\left(\rho\frac{\partial p}{\partial t} + \rho u_j \frac{\partial p}{\partial x_j}\right) + \left(\frac{\partial e}{\partial \rho}\right)_{p,Y_k}\left(\rho\frac{\partial \rho}{\partial t} + \rho u_j \frac{\partial \rho}{\partial x_j}\right) \tag{N.0.9}$$

$$+ \left(\frac{\partial e}{\partial Y_k}\right)_{\rho,p,Y_l,l\neq k}\left(\rho\frac{\partial Y_k}{\partial t} + \rho u_j \frac{\partial Y_k}{\partial x_j}\right) + p\frac{\partial u_j}{\partial x_j} = 0 \tag{N.0.10}$$

Once again, this can further be simplified using conservation of mass and species:

$$\left(\frac{\partial e}{\partial p}\right)_{\rho,Y_k}\left(\rho\frac{\partial p}{\partial t} + \rho u_j \frac{\partial p}{\partial x_j}\right) - \rho^2 \frac{\partial u_j}{\partial x_j}\left(\frac{\partial e}{\partial \rho}\right)_{p,Y_k} + p\frac{\partial u_j}{\partial x_j} = 0 \tag{N.0.11}$$

Plugging in Eqs. (N.0.1) and (N.0.2):

$$\frac{\rho c_p \kappa_s}{\alpha_p}\left(\frac{\partial p}{\partial t} + u_j \frac{\partial p}{\partial x_j}\right) + \frac{\partial u_j}{\partial x_j}\left(\frac{\rho c_p}{\alpha_v} - p\right) + p\frac{\partial u_j}{\partial x_j} = 0 \tag{N.0.12}$$

$$\frac{\partial p}{\partial t} + u_j \frac{\partial p}{\partial x_j} + \frac{\partial u_j}{\partial x_j}\frac{1}{\kappa_s} = 0 \tag{N.0.13}$$

Recognizing that for any gas, $\kappa_s = 1/\rho c^2$, as written in Eq. (2.2.23), the general, EoS-independent Euler equations are recovered:

$$\frac{\partial \rho}{\partial t} + \frac{\partial \rho u_i}{\partial x_i} = 0 \tag{N.0.14}$$

$$\frac{\partial \rho u_i}{\partial t} + \frac{\partial}{\partial x_j}\left(\rho u_i u_j + p\delta_{ij}\right) = 0 \tag{N.0.15}$$

$$\frac{\partial p}{\partial t} + u_j \frac{\partial p}{\partial x_j} + \rho c^2 \frac{\partial u_j}{\partial x_j} = 0 \tag{N.0.16}$$

As one can notice, this form is suitable for any kind of EoS and particularly for VLE as well which can be considered as another advanced EoS model.

Appendix O

THERMODYNAMIC AND TRANSPORT SPECIES PROPERTIES USED IN THIS WORK

The database of the species constants used in the present work are given in the following table. These are found either in [163, 149] or on NIST website.

Table 35: List of species-dependent properties used in the present work: T_c critical temperature, p_c critical pressure, ω acentric factor, V_c critical volume, Σ_v Fuller parameter (used in Eq. (2.3.22)) and molecular weight.

Species	T_c [K]	p_c [MPa]	ω [-]	V_c $[m^3/kmol]$	Σ_v [-]	MW [kg/kmol]
CH_4	190.56	4.599	0.008	$98.6{\cdot}10^{-3}$	25.14	16.04
N_2	126.2	3.395	0.0039	$8.9{\cdot}10^{-2}$	18.5	28.01
O_2	154.58	5.053	0.00222	$77.37{\cdot}10^{-3}$	16.3	31.99
C_6H_{14}	507.82	3.034	0.299	$36.95{\cdot}10^{-2}$	127.74	86.17
H_2	33.19	1.315	-0.214	$6.64{\cdot}10^{-2}$	6.12	2.01
H_2S	373.4	8.963	0.009	$98.0{\cdot}10^{-3}$	27.52	34.08
H_2O	647.14	22.06	0.334	$55.95{\cdot}10^{-3}$	13.1	18.01
CO_2	304.12	7.374	0.225	$94.07{\cdot}10^{-3}$	26.9	44.01
Ar	150.86	4.898	-0.002	$74.57{\cdot}10^{-3}$	16.2	39.94
C_2H_4	282.4	5.040	0.089	$130.4{\cdot}10^{-3}$	41.04	28.05
n-$C_{12}H_{26}$	658.1	1.82	0.574	$74.8{\cdot}10^{-2}$	107.22	170.34
C_2H_6	305.32	4.872	0.099	$145.5{\cdot}10^{-3}$	45.66	30.07
C_3H_8	369.83	4.248	0.152	$200.0{\cdot}10^{-3}$	66.18	44.09
i-C_4H_{10}	407.85	3.647	0.186	$26.27{\cdot}10^{-2}$	127.74	58.12
n-C_4H_{10}	425.16	3.796	0.200	$25.50{\cdot}10^{-2}$	107.22	58.12
i-C_5H_{12}	469.7	3.375	0.252	$31.10{\cdot}10^{-2}$	107.22	72.14
n-C_5H_{12}	433.75	3.199	0.197	$30.32{\cdot}10^{-2}$	107.22	72.14
C_7H_{16}	540.3	2.736	0.349	$432.0{\cdot}10^{-3}$	148.26	100.21
C_8H_{18}	568.7	2.490	0.399	$49.20{\cdot}10^{-2}$	148.24	114.23
C_7H_8	591.75	4.108	0.264	$31.60{\cdot}10^{-2}$	148.26	92.14

Appendix P

DETERMINATION OF TML DIMENSIONS

The TML dimensions used in Sec. 5.3 are determined in a similar manner are done by [134] and are summarized below. With fixed Mach number Ma, Reynolds number Re_0 and operating pressure p, the top and bottom stream-wise velocities u_T and u_B are defined as follows:

$$\begin{aligned} u_\mathrm{T} &= -\frac{2\,Ma\,c_\mathrm{T}}{1+\dfrac{c_\mathrm{T}}{c_\mathrm{B}}\sqrt{\dfrac{\rho_\mathrm{T}Z_\mathrm{T}}{\rho_\mathrm{B}Z_\mathrm{B}}}}\,, \\ u_\mathrm{B} &= -u_\mathrm{T}\sqrt{\frac{\rho_\mathrm{T}Z_\mathrm{T}}{\rho_\mathrm{B}Z_\mathrm{B}}}\,. \end{aligned} \tag{P.0.1}$$

Where subscripts T and B refer to the top and bottom stream properties, respectively (see also Tab. 28). Next, by defining the following quantities:

$$\begin{aligned} \Delta u &= u_\mathrm{T} - u_\mathrm{B}\,, \\ \rho_0 &= \frac{\rho_\mathrm{T}+\rho_\mathrm{B}}{2}\,, \\ \mu_0 &= \frac{\mu_\mathrm{T}+\mu_\mathrm{B}}{2}\,, \end{aligned} \tag{P.0.2}$$

the vorticity thickness is defined as [134]:

$$\delta_{\omega,0} = \frac{Re_0\mu_0}{\rho_0\,|\Delta u|}\,. \tag{P.0.3}$$

Finally, the domain lengths are defined as:

$$\begin{aligned} L_x &= \lambda_0\delta_{\omega,0}\,, \\ L_y &= 3\lambda_0\delta_{\omega,0}\,, \\ L_z &= \lambda_0\delta_{\omega,0}\,. \end{aligned} \tag{P.0.4}$$

Where $\lambda_0 = 7.29$ is a factor associated to the first-mode unstable wavelength [134]. In addition to the properties already listed in Tab. 28, the properties listed in Tab. 36 are obtained

Table 36: Additional input conditions for Case 1 to Case 3 for the TML. These, along with those listed in Tab. 28 are used to determine the TML dimensions according to Eqs. (P.0.1)–(P.0.4).

Case 1: $c_\mathrm{T} = 176.675\,\mathrm{m/s}$, $\mu_\mathrm{T} = 1.955 \cdot 10^{-5}\,\mathrm{Pa \cdot s}$
Case 2: $c_\mathrm{T} = 151.692\,\mathrm{m/s}$, $\mu_\mathrm{T} = 2.418 \cdot 10^{-5}\,\mathrm{Pa \cdot s}$
Case 3: $c_\mathrm{T} = 317.020\,\mathrm{m/s}$, $\mu_\mathrm{T} = 7.398 \cdot 10^{-5}\,\mathrm{Pa \cdot s}$
All cases: $c_\mathrm{B} = 356.281\,\mathrm{m/s}$, $\mu_\mathrm{B} = 1.796 \cdot 10^{-5}\,\mathrm{Pa \cdot s}$

for the free-stream conditions, using the PR EoS. Finally, the expression to compute the momentum thickness is given:

$$\delta_m = \frac{1}{(\Theta_\mathrm{T} - \Theta_\mathrm{B})^2} \int_{-\infty}^{+\infty} (\Theta_\mathrm{B} - \langle \rho u \rangle)(\langle \rho u \rangle - \Theta_\mathrm{T})\, \mathrm{d}y \tag{P.0.5}$$

where:

$$\begin{aligned} \Theta_\mathrm{T} &= \frac{1}{L_x} \int_{-L_x/2}^{L_x/2} \rho u(x, y = 3L_y/2) \mathrm{d}y\,, \\ \Theta_\mathrm{B} &= \frac{1}{L_x} \int_{-L_x/2}^{L_x/2} \rho u(x, y = -3L_y/2) \mathrm{d}y\,, \\ \langle \rho u \rangle\,(y) &= \frac{1}{L_x} \int_{-L_x/2}^{L_x/2} \rho u(x, y) \mathrm{d}x\,. \end{aligned} \tag{P.0.6}$$

Of course, the above are to be computed for any given time instant of the simulation.

Appendix Q

ADDITIONAL RESULTS

In this Appendix, any additional result that is not directly important for the main body is added. The reason for this appendix is to create a repository of results that sometimes may result redundant/repetitive in the main body, however they are still useful, for example validation purposes.

Q.1 Results for the 1D N_2/C_6H_{14} contact advection

Figures 155 and 156 show the relevant variables of the N_2/C_6H_{14} one-dimensional advection discussed in Sec. 5.1. In this particular case, the figures illustrate the grid dependency of the properties when the fully-analytical PRHO problem is used to reconstruct the temperature at the cell interface, before the call to the approximate Riemann solver. As discussed in Sec. 3.3, in fact, the cell-interface temperature can be determined by imposing the "match condition" on the compressibilities between the whole mixture and the two phases, if they occur. This condition is mathematically provided by Eq. (3.3.2). As these pictures illustrate, the mixture properties do not "sense" the difference between the FC and the QC scheme for sufficiently refined grids [226]. Moreover, these trends match those computed with the fully numerical PRHO problem showed in Figs. (92)–(93), providing validation of the consistency and correctness between the two approaches.

Q.2 Results for the 2D blob/shock interaction

Figure 157 shows the time-dependent scatter plot of the thermodynamic state obtained for $Y_{N_2} \in [0.1\ 0.9]$ at the four instants considered in Fig. 97. As the comparison can be immediately done along with Fig. 158, the shock/bubble interaction simulated with the fully analytical PRHO model for cell-interface temperature reconstruction is formally identical to that simulated with the fully numerical model. The shock increases both temperature

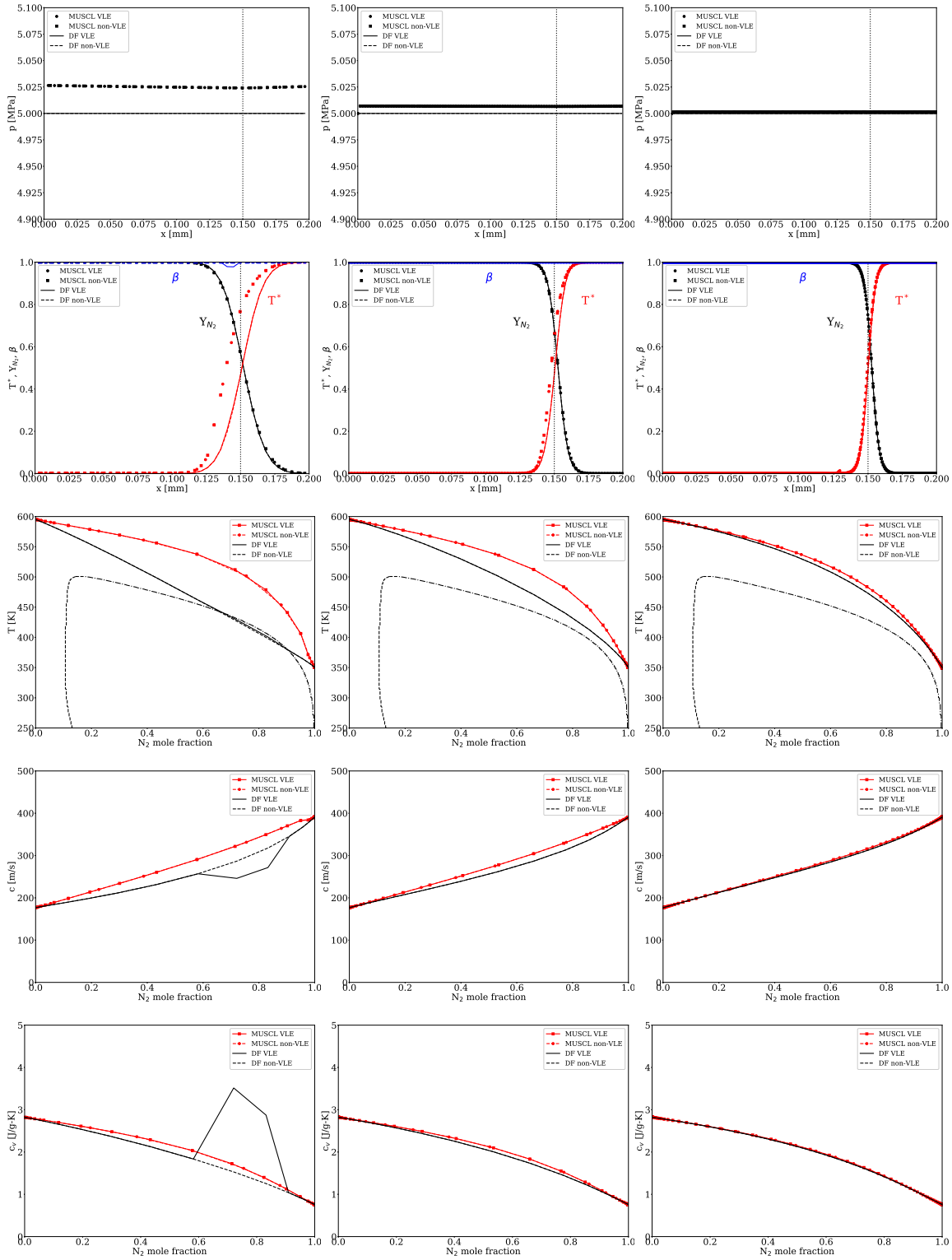

(m) $N = 128$ (n) $N = 1024$ (o) $N = 8192$

Figure 155: Sequence of pressure p, phase fraction β, reduced temperature T*, nitrogen mass fraction Y_{N_2}, mixing temperature T, speed of sound c and specific heat at constant volume c_v for case 1 obtained with the fully-analytical PRHO model for the temperature interface reconstruction. Sensitivity analysis on numerical scheme, thermodynamics and resolution is shown.

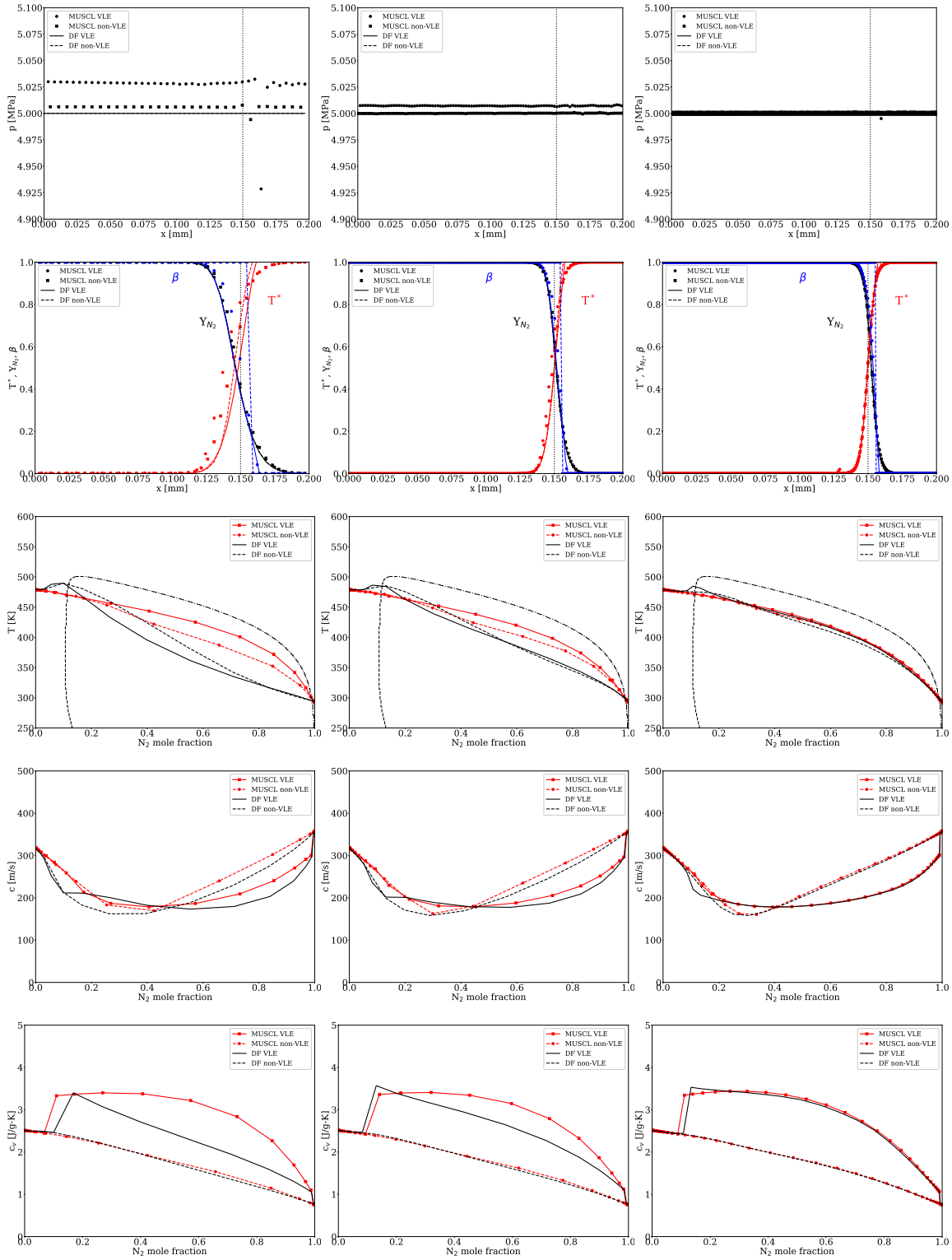

(m) $N = 128$ (n) $N = 1024$ (o) $N = 8192$

Figure 156: Sequence of pressure p, phase fraction β, reduced temperature T*, nitrogen mass fraction Y_{N_2}, mixing temperature T, speed of sound c and specific heat at constant volume c_v for case 2 obtained with the fully-analytical PRHO model for the temperature interface reconstruction. Sensitivity analysis on numerical scheme, thermodynamics and resolution is shown.

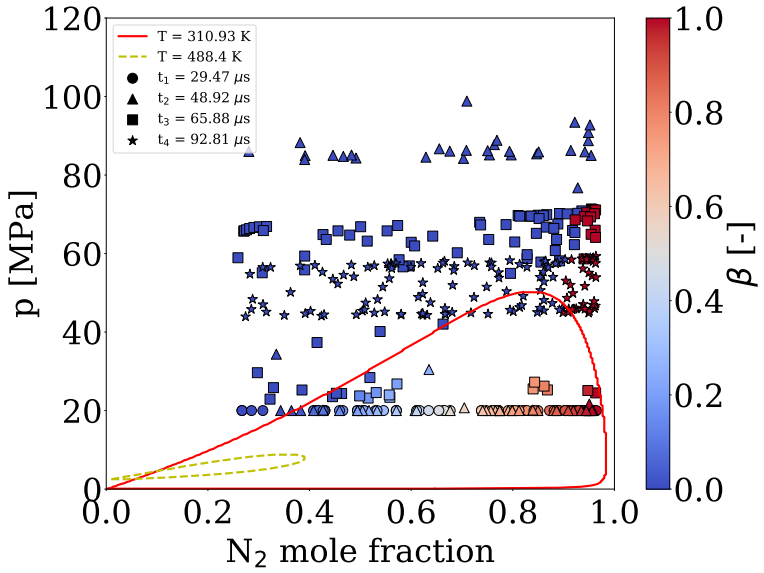

Figure 157: Representation of the bubble interface thermodynamic state during the four time instants analyzed. Symbols correspond to the different times and they are colored based on the local value of the phase fraction β. VLE domes at $T = 310.93$ K and $T = 488.4$ K are directly taken from Fig. 54. Symbols are scattered from the initial raw data with an interval of 7 to improve picture readability. This picture refers to the simulation run with the fully analytical PRHO model for temperature interface reconstruction.

and pressure of the bubble interface initially located within the VLE dome with the result to obtain a single-phase state. The main thermodynamic (mean and standard deviation) variables are displayed in Fig. 159 in analogy with Fig. 100, for which identical conclusions can be formulated.

Q.3 Results for the 3D non-reacting TML

Additional results for the non-reacting TML of Sec. 5.3.2 are listed here. These represent the comparison of the non-VLE results obtained for Case 3 according to Tab. 29. The goal is to prove the equivalence of the PRHO problem method (analytical vs numerical) even in the non-VLE case (for the VLE case was already proven in Sec. 5.3.2).

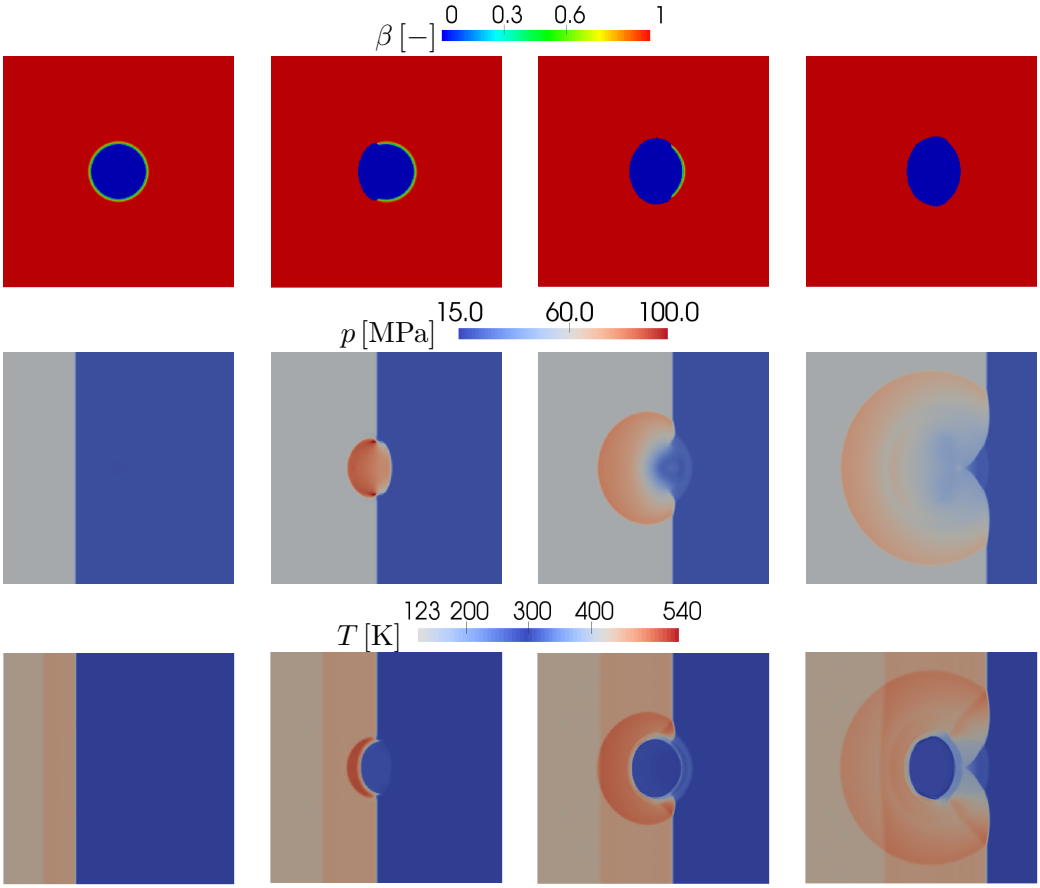

(a) $t = t_1$ (b) $t = t_2$ (c) $t = t_3$ (d) $t = t_4$

Figure 158: Time sequence contour snapshots of phase fraction β, pressure p and temperature T. This picture refers to the simulation run with the fully analytical PRHO model for temperature interface reconstruction.

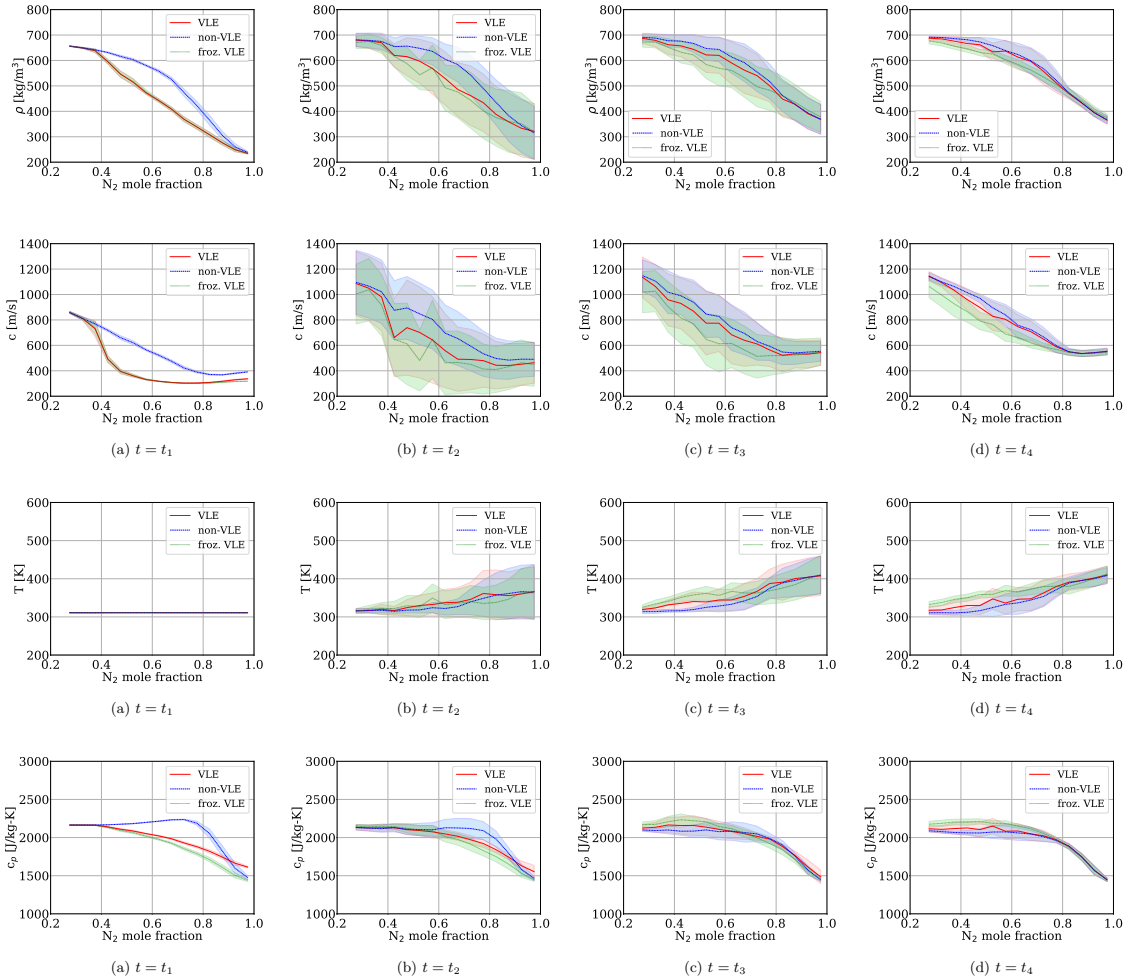

(a) $t = t_1$ (b) $t = t_2$ (c) $t = t_3$ (d) $t = t_4$

(a) $t = t_1$ (b) $t = t_2$ (c) $t = t_3$ (d) $t = t_4$

(a) $t = t_1$ (b) $t = t_2$ (c) $t = t_3$ (d) $t = t_4$

Figure 159: From top to bottom: density, speed of sound, temperature and specific heat at constant pressure sequence conditional averages (with shaded) standard deviations for the four time instants. The results are for the VLE, non-VLE and frozen VLE models. This picture refers to the simulation run with the fully analytical PRHO model for temperature interface reconstruction.

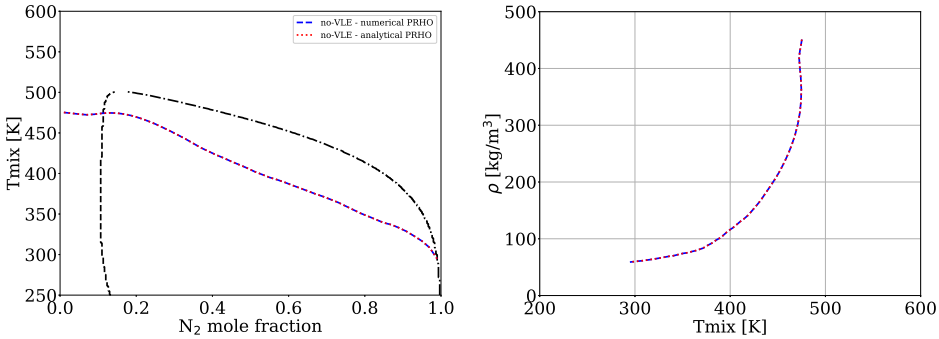

(a) Mixing temperature

(b) Density

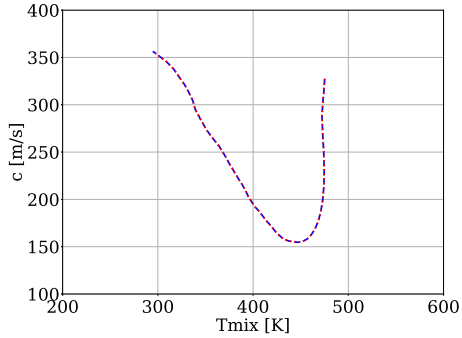

(c) Speed of sound

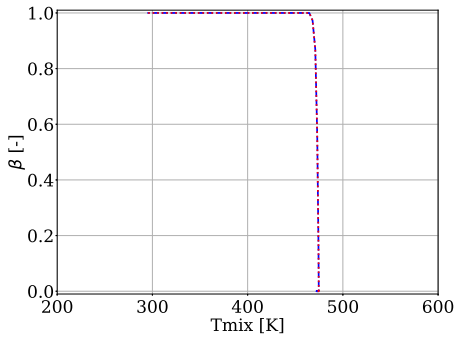

(d) phase frac.

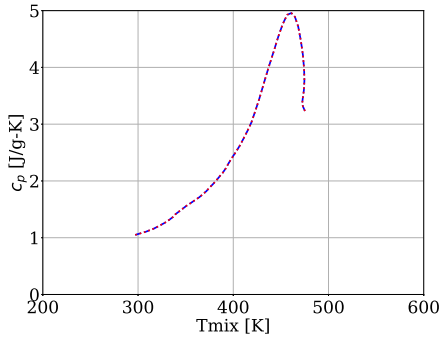

(e) Spec. heat const. pres.

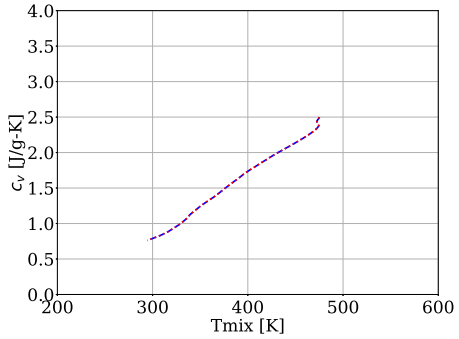

(f) Spec. heat const. vol.

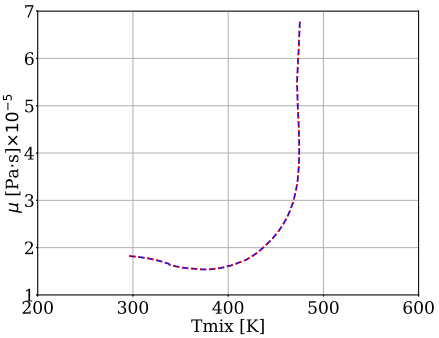

(g) Dynamic viscosity

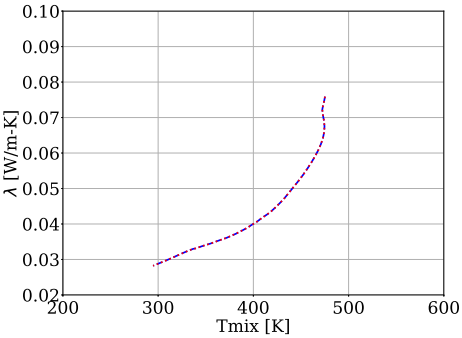

(h) Thermal conductivity

Figure 160: Relevant properties computed along the mixing lines for the hybrid 64^3 case 3 of Fig. 105 with the non-VLE model and different PRHO model for temperature reconstruction. Mixture properties are showed along the mixing line. Similarly to what explained for Fig. 110, the $\beta \in (0, 1)$ values are artificially obtained because of the time- and conditional-average operation.

Q.4 Results for the 2D non-reacting SML

Additional results for the 2D SML are reported below, for clarity. Particularly Fig. 161 and Fig. 162 refer to the reference line position across the vortex leading and trailing edges, respectively that have been used for both the VLE and non-VLE simulation to understand the different vortex dynamics that ultimately causes a difference in the macroscopic mixing. Next, key results of the mixture properties extracted along this reference abscissa are illustrated in Fig. 163 and Fig. 163 for the trailing edge case.

Next, joint PDFs are given in Fig. 165 and Fig. 166 for the VLE and non-VLE case, respectively. The Lewis number profile along the same abscissa is given in Fig. 167. For a detail explanation about these pictures and their correlation with the leading edge case, the reader is referred to Sec. 5.4.1.

Regarding the statistics, various properties are plotted against the axial location at several x/h ratios, where h is the splitter plate height. According to the discussion made in Sec. 5.4.1, the shear layer is thicker in the VLE case.

Q.5 Results for the 1D diffusion flame for kinetics verification

Figure 173 shows the one-dimensional diffusion flame temperature and major species profiles obtained for the CH_4/O_2 diffusion flame at 13.3 MPa for a strain rate value of $\xi = 50\ s^{-1}$.

Q.6 Results for the reacting 3D TML

Additional results for the 3D reacting TML are showed in Figs. (174)–(179). In the first sequence: Figs. (174)–(178), the TML flow field is analyzed along the XZ plane with relevant variables. As observed in Figs. (138)–(142), VLE is formed in two separate regions, the

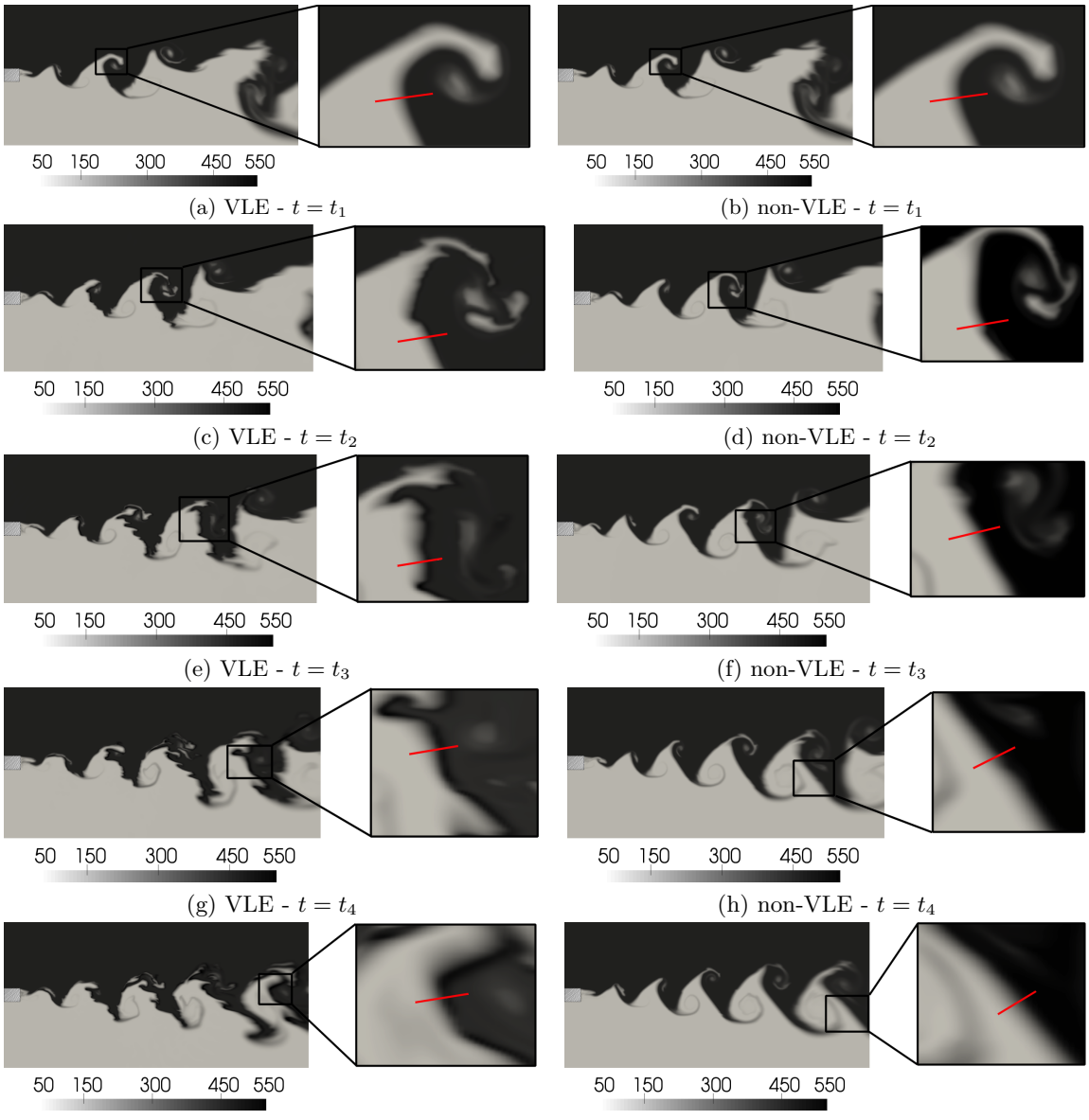

(a) VLE - $t = t_1$ (b) non-VLE - $t = t_1$

(c) VLE - $t = t_2$ (d) non-VLE - $t = t_2$

(e) VLE - $t = t_3$ (f) non-VLE - $t = t_3$

(g) VLE - $t = t_4$ (h) non-VLE - $t = t_4$

(i) VLE - $t = t_5$ (j) non-VLE - $t = t_5$

Figure 161: Identification of the reference line taken to study the vortex leading edge.

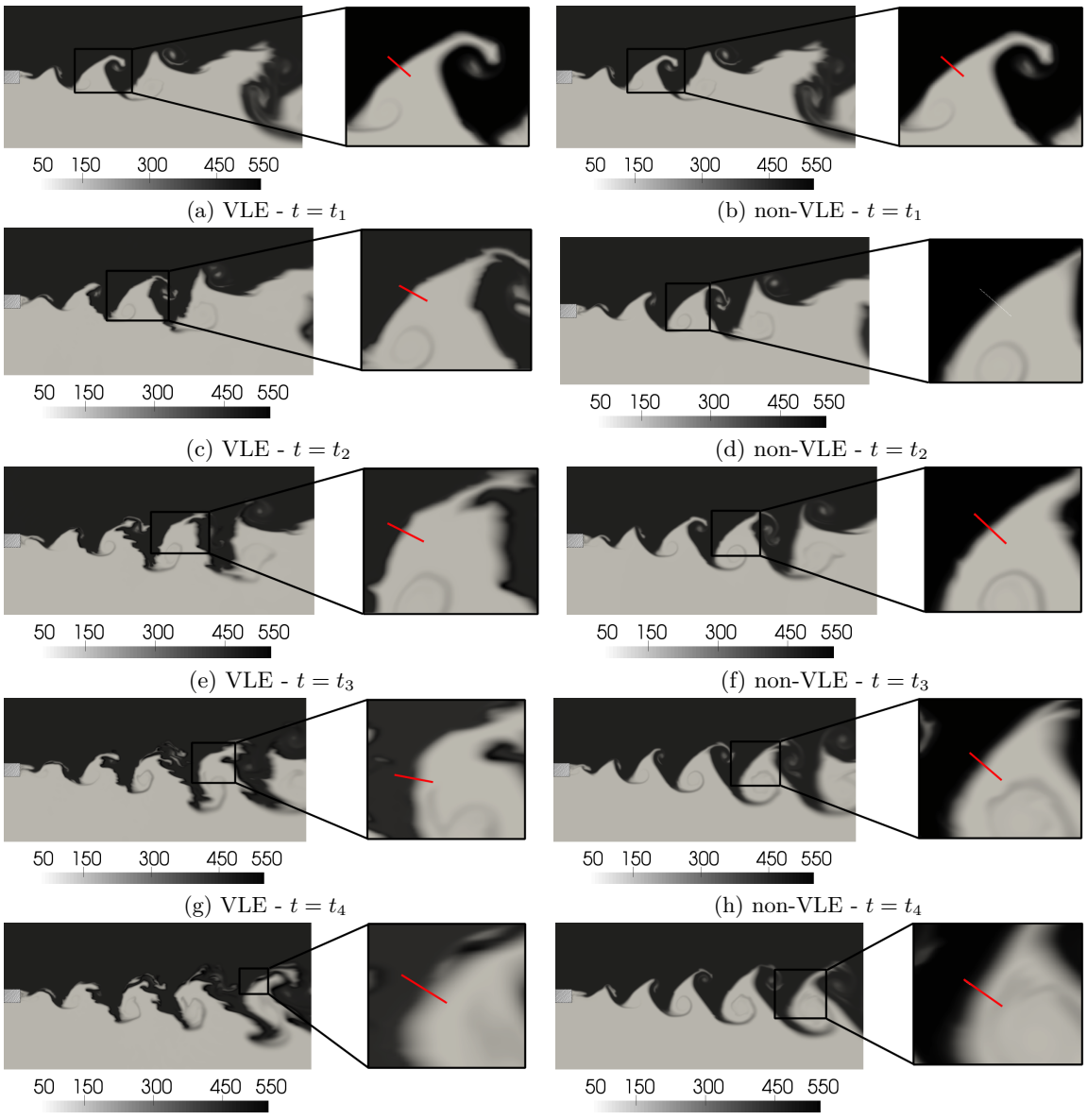

(a) VLE - $t = t_1$ (b) non-VLE - $t = t_1$

(c) VLE - $t = t_2$ (d) non-VLE - $t = t_2$

(e) VLE - $t = t_3$ (f) non-VLE - $t = t_3$

(g) VLE - $t = t_4$ (h) non-VLE - $t = t_4$

(i) VLE - $t = t_5$ (j) non-VLE - $t = t_5$

Figure 162: Identification of the reference line taken to study the vortex trailing edge.

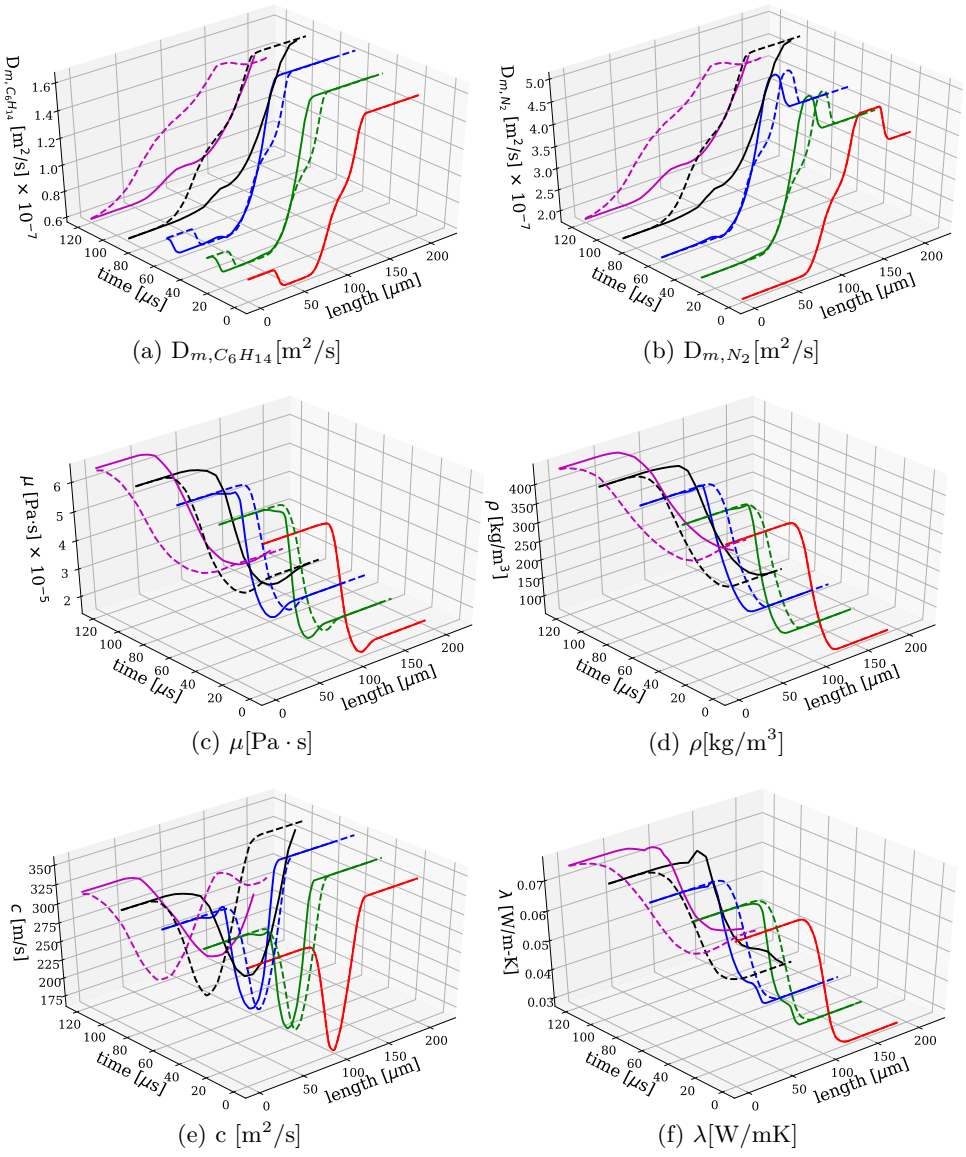

Figure 163: First set of properties collected across the reference abscissa s at the vortex trailing edge (*cf.* Fig. 162) for both simulations: (a) C_6H_{14} mass diffusion coefficient, (b) N_2 mass diffusion coefficient, (c) dynamic viscosity, (d) density, (c) speed of sound and (d) thermal conductivity. Colors refer to the time instant (indicated on the axis). Solid lines indicate the VLE solution, while dashed lines indicate the non-VLE solution.

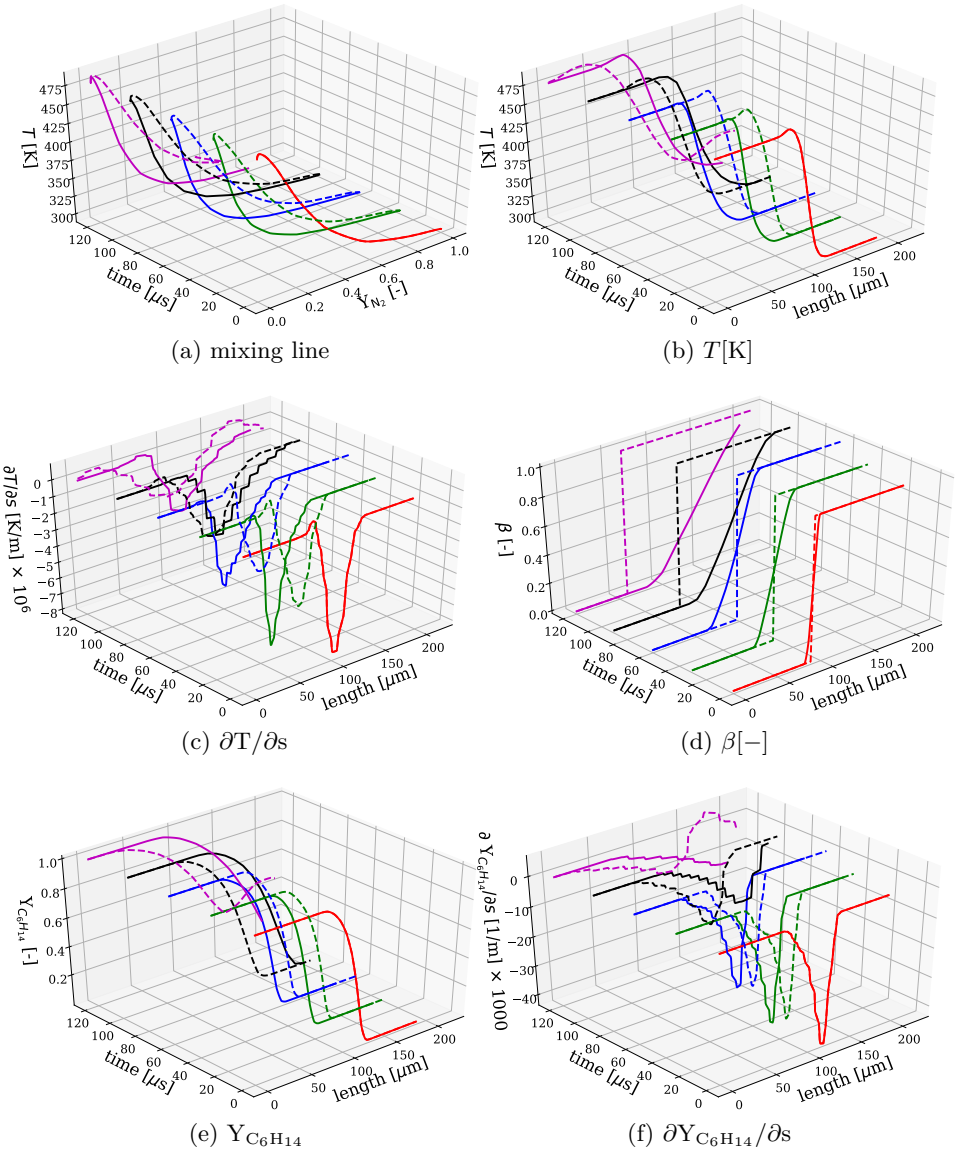

(a) mixing line (b) T[K]

(c) ∂T/∂s (d) $\beta[-]$

(e) $Y_{C_6H_{14}}$ (f) $\partial Y_{C_6H_{14}}/\partial$s

Figure 164: Second set of properties collected across the reference abscissa s at the vortex trailing edge (*cf.* Fig. 162) for both simulations: (a) temperature vs N_2 mass fraction (mixing line), (b) temperature, (c) temperature gradient, (d) phase fraction, (c) C_6H_{14} distribution (d) C_6H_{14} gradient. Colors refer to the time instant (indicated on the axis). Solid lines indicate the VLE solution, while dashed lines indicate the non-VLE solution.

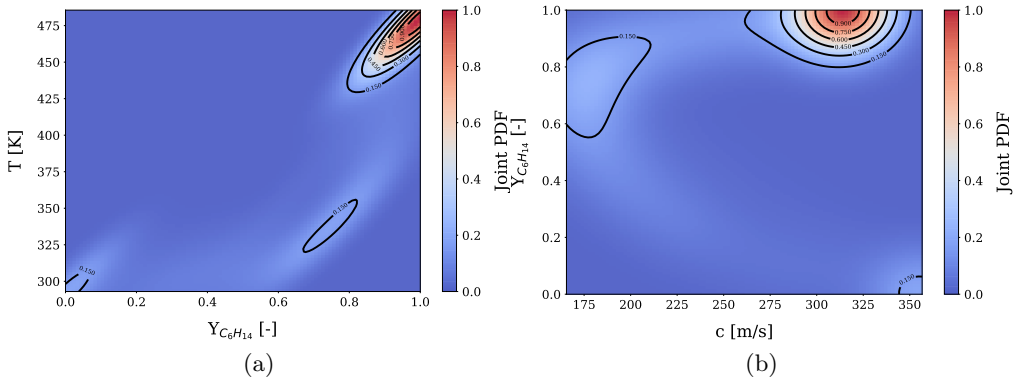

Figure 165: Joint PDF between (a) n-hexane mass fraction and temperature and (b) speed of sound and temperature. Data refers to the line segment extracted for the VLE simulation at vortex trailing edge.

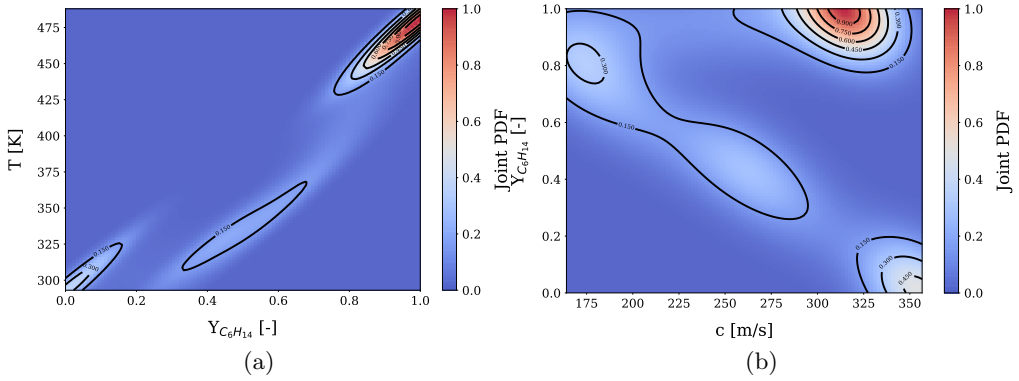

Figure 166: Joint PDF between (a) n-hexane mass fraction and temperature and (b) speed of sound and temperature. Data refers to the line segment extracted for the non-VLE simulation at vortex trailing edge.

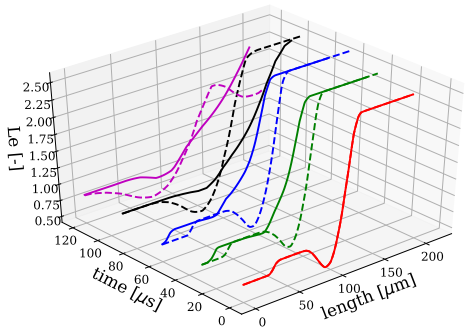

Figure 167: Lewis number calculated across the reference abscissa s at the vortex trailing edge (*cf.* Fig. 162).

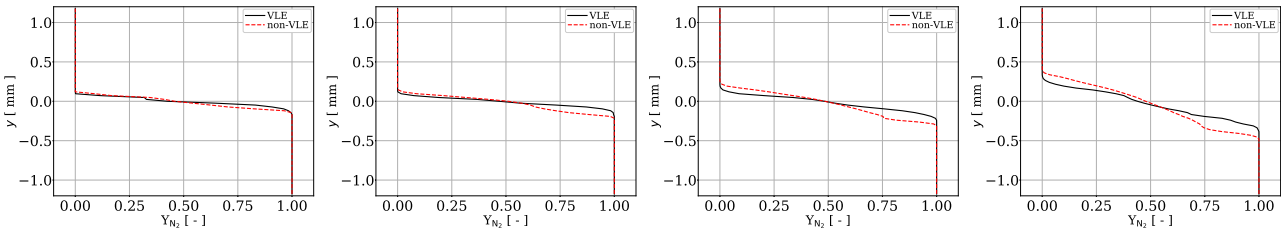

(a) $x/h = 0.5$ (b) $x/h = 1.0$ (c) $x/h = 2.0$ (d) $x/h = 4.0$

Figure 168: N_2 mass fractions profiles extracted at several x locations downstream the SML.

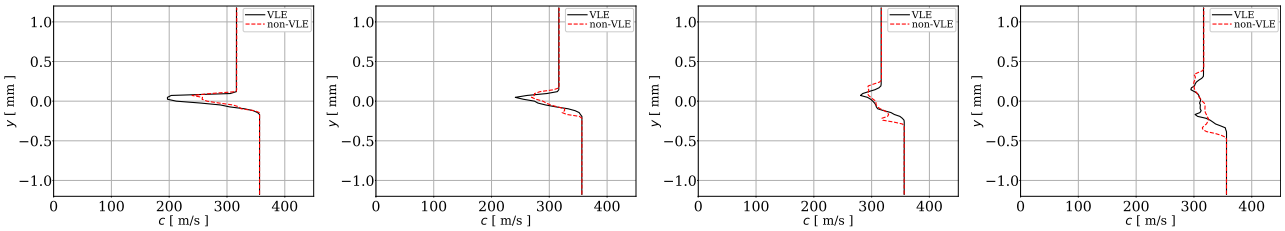

(a) $x/h = 0.5$ (b) $x/h = 1.0$ (c) $x/h = 2.0$ (d) $x/h = 4.0$

Figure 169: Speed of sound profiles extracted at several x locations downstream the SML.

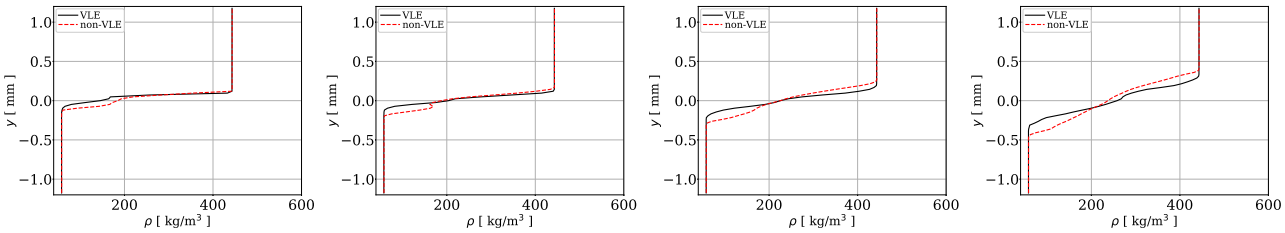

(a) $x/h = 0.5$ (b) $x/h = 1.0$ (c) $x/h = 2.0$ (d) $x/h = 4.0$

Figure 170: Density profiles extracted at several x locations downstream the SML.

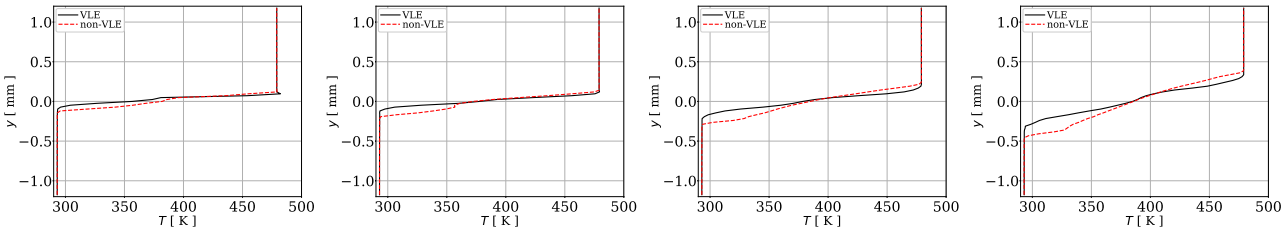

(a) $x/h = 0.5$ (b) $x/h = 1.0$ (c) $x/h = 2.0$ (d) $x/h = 4.0$

Figure 171: Temperature profiles extracted at several x locations downstream the SML.

(TOP) region mainly characterized by a mixing between oxygen, water and minor amount of carbon dioxide, and a (BOTTOM) region, mainly formed by methane and water. As discussed for the YZ plane, these VLE regions have a minor impact on the flow field variables because the phase fraction is very close to one. On the other hand, Fig. 179 displays the VLE diagrams of the TOP VLE region displayed in the temperature-oxygen mass

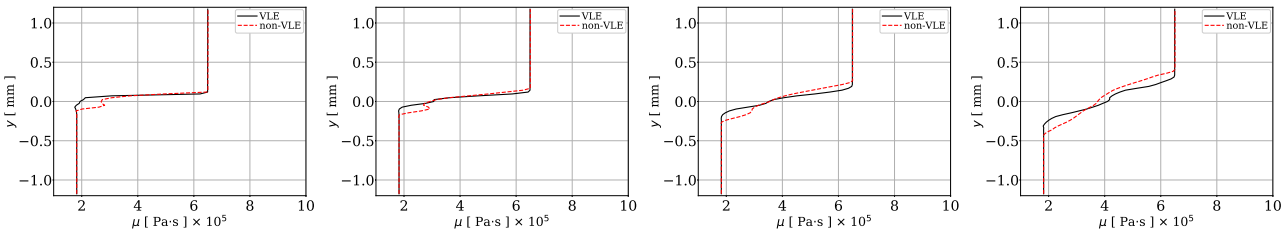

(a) $x/h = 0.5$ (b) $x/h = 1.0$ (c) $x/h = 2.0$ (d) $x/h = 4.0$

Figure 172: Dynamic viscosity profiles extracted at several x locations downstream the SML.

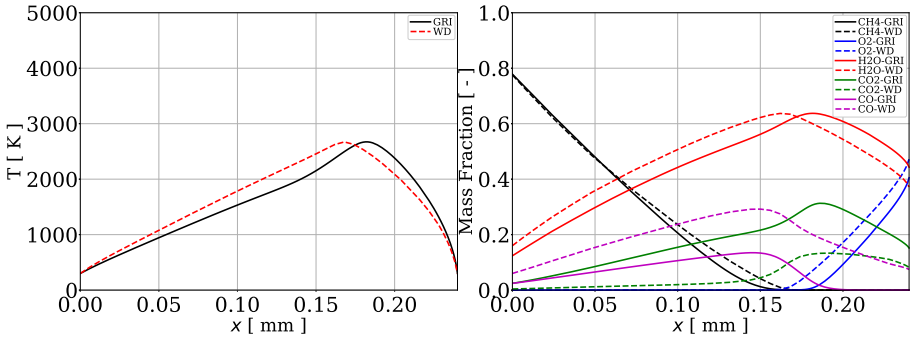

(a) Temperature at $\xi = 50$ s^{-1} (b) Major species at $\xi = 50$ s^{-1}

Figure 173: One-dimensional laminar diffusion flame at 13.3 MPa between CH_4 and O_2 for a strain rate of $\xi = 50$ s^{-1}. (a) Temperature and (b) major species distribution across the flame width.

fraction diagram, parametrized by the amount of CO_2. As discussed in Sec. 5.5.5, the VLE distribution of the data is well represented by the 0D mixing models, which indicate how the state falls in the two-phase region.

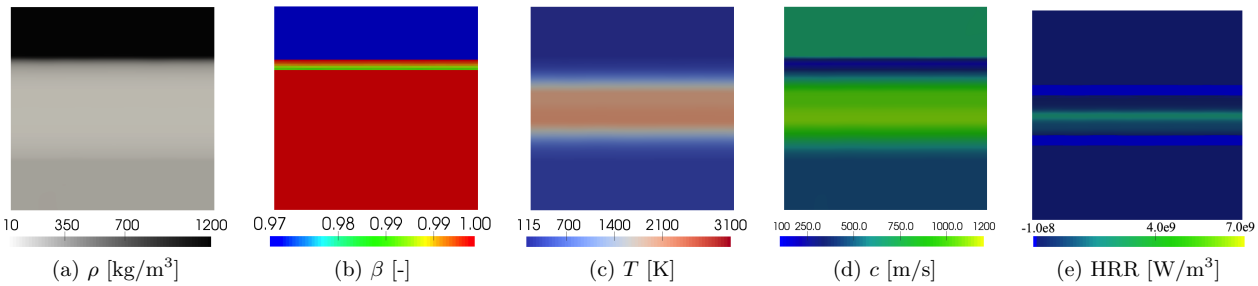

(a) ρ [kg/m^3] (b) β [-] (c) T [K] (d) c [m/s] (e) HRR [W/m^3]

(f) ρ [kg/m^3] (g) β [-] (h) T [K] (i) c [m/s] (j) HRR [W/m^3]

Figure 174: Relevant field variables obtained for the VLE (top) and non-VLE (bottom) solutions on plane XZ at time $t_1 = 0.21\,\mu$s .

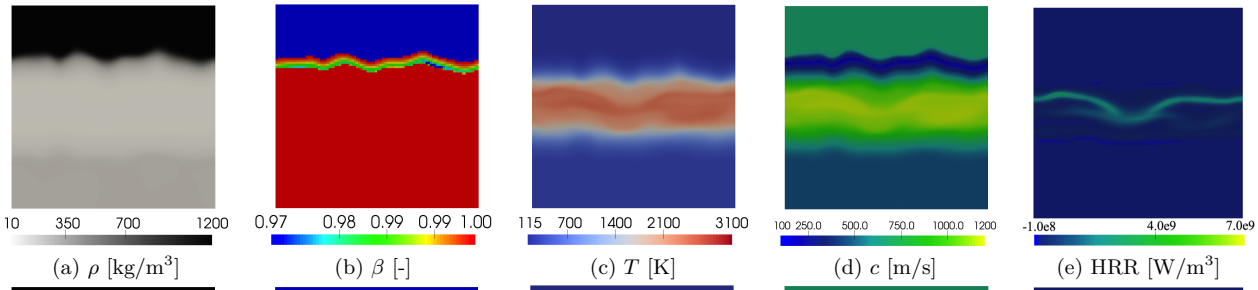

(a) ρ [kg/m^3] (b) β [-] (c) T [K] (d) c [m/s] (e) HRR [W/m^3]

(f) ρ [kg/m^3] (g) β [-] (h) T [K] (i) c [m/s] (j) HRR [W/m^3]

Figure 175: Relevant field variables obtained for the VLE (top) and non-VLE (bottom) solutions on plane XZ at time $t_2 = 10.18\,\mu$s .

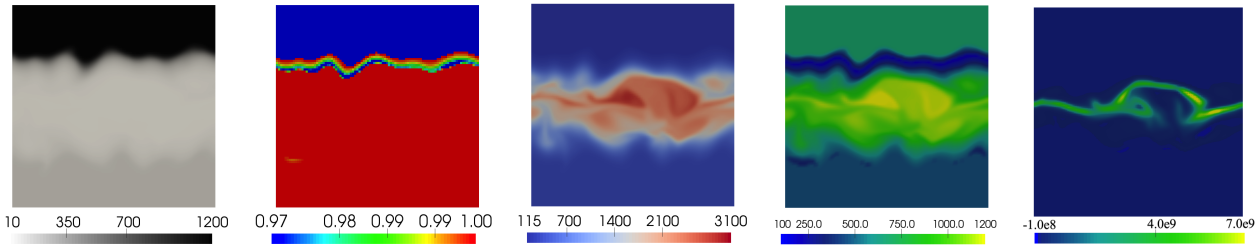

(a) ρ [kg/m^3] (b) β [-] (c) T [K] (d) c [m/s] (e) HRR [W/m^3]

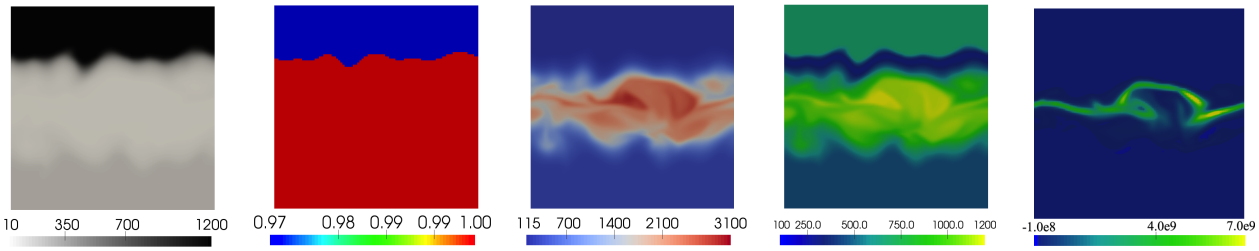

(f) ρ [kg/m^3] (g) β [-] (h) T [K] (i) c [m/s] (j) HRR [W/m^3]

Figure 176: Relevant field variables obtained for the VLE (top) and non-VLE (bottom) solutions on plane XZ at time $t_3 = 19.30\,\mu$s .

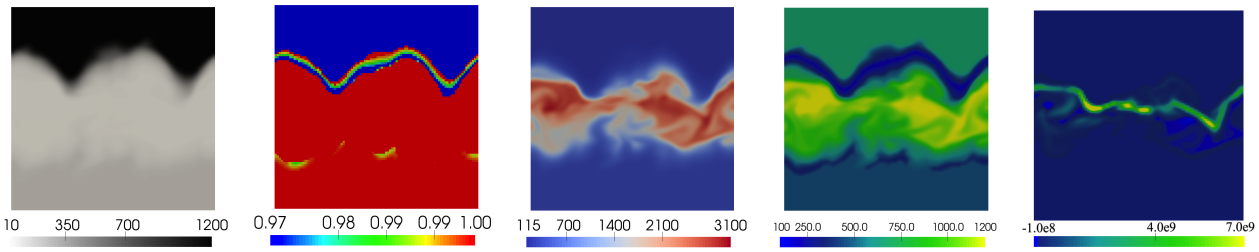

(a) ρ [kg/m^3] (b) β [-] (c) T [K] (d) c [m/s] (e) HRR [W/m^3]

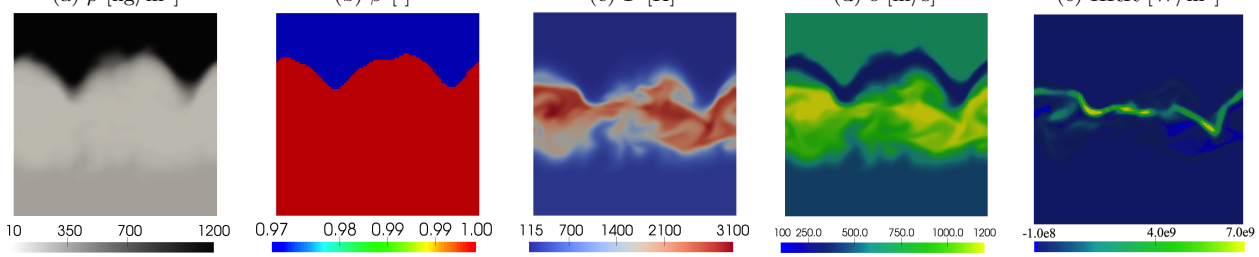

(f) ρ [kg/m^3] (g) β [-] (h) T [K] (i) c [m/s] (j) HRR [W/m^3]

Figure 177: Relevant field variables obtained for the VLE (top) and non-VLE (bottom) solutions on plane XZ at time $t_4 = 28.22\,\mu$s .

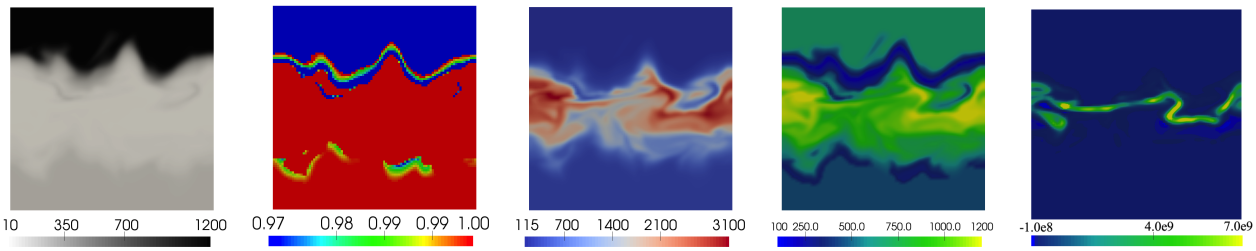

(a) ρ [kg/m^3] (b) β [-] (c) T [K] (d) c [m/s] (e) HRR [W/m^3]

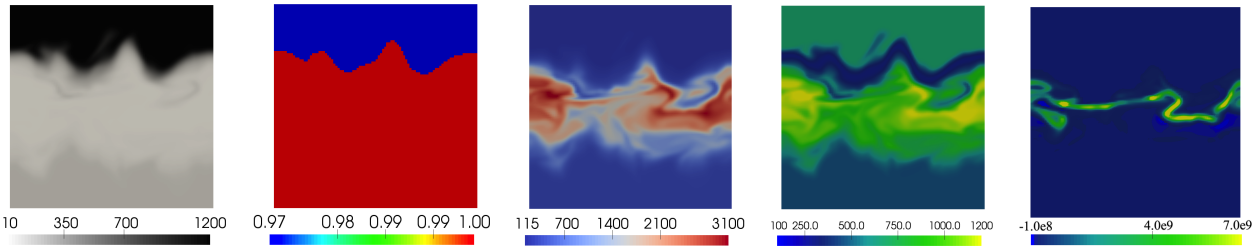

(f) ρ [kg/m^3] (g) β [-] (h) T [K] (i) c [m/s] (j) HRR [W/m^3]

Figure 178: Relevant field variables obtained for the VLE (top) and non-VLE (bottom) solutions on plane XZ at time $t_5 = 37.09\,\mu$s .

Q.7 Results for the reacting 2D SML

Figure 180 shows additional comparison of the iso-density lines of 350 kg/m^2 evaluated at two different time instants. The comparison between the two thermodynamic models indicate that only local, minor differences exist and the overall vortex structure is retained.

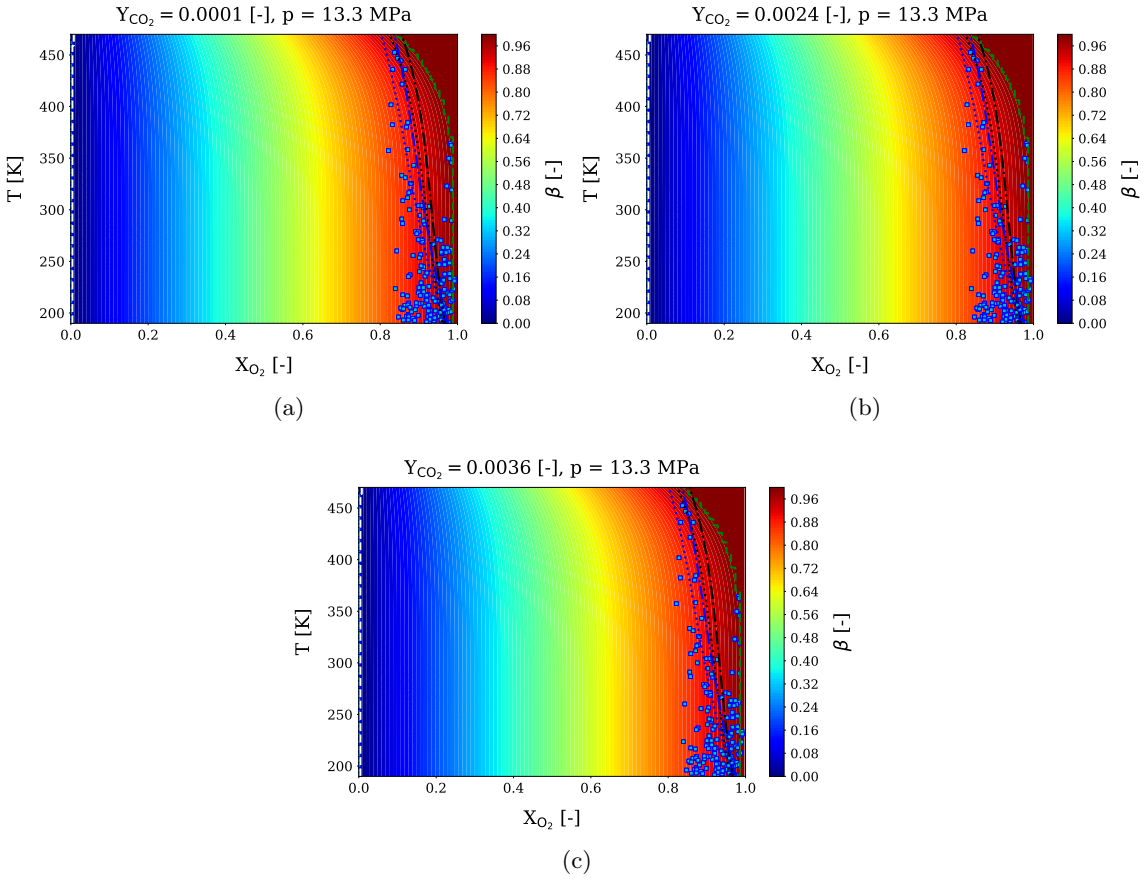

Figure 179: Temperature-Oxygen mole fraction diagram for the top side of the TML for (a) $Y_{CO_2} = 0.0001$, (b) $Y_{CO_2} = 0.0024$ and (c) $Y_{CO_2} = 0.0036$. The color map refers to the phase fraction field as the amount of oxygen and temperature are varied. Dew line is represented with a white dashed line at approximately constant $X_{O_2} = 0.00379$. Bubble line is represented with a green dashed curve on the right side of the picture (*cf.* the value of the β field). Blue and black lines indicate the isochoric and adiabatic mixing models. Specifically: blue line (. . .) indicates the isochoric mixing with $T_{H_2O} = T_{CO_2} = 2000$ K, black line (. . .) indicates the adiabatic mixing with $T_{H_2O} = T_{CO_2} = 2000$ K, blue line (.-) indicates the isochoric mixing with $T_{H_2O} = T_{CO_2} = 2500$ K, black line (.-) indicates the adiabatic mixing with $T_{H_2O} = T_{CO_2} = 2500$ K. In all cases the initial oxygen temperature is set to 115 K. Squared blue symbols refer to the data directly extracted from the TML.

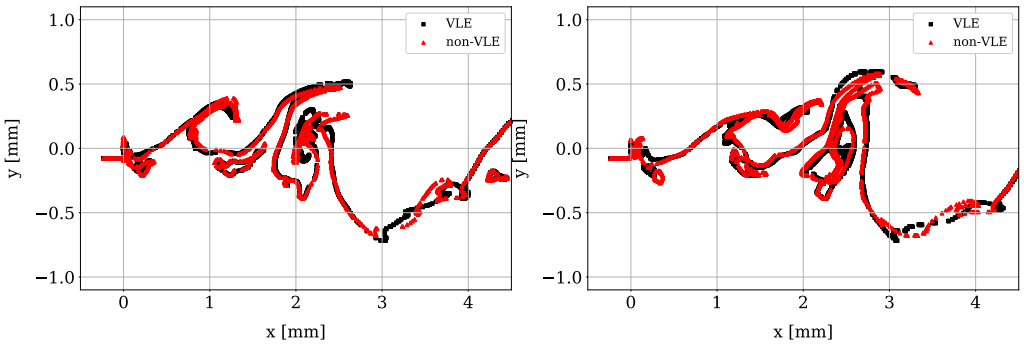

(a) $\rho = 350$ [kg/m^3]- $t = 42.5\,\mu s$ (b) $\rho = 350$ [kg/m^3]- $t = 51\,\mu s$

Figure 180: Iso-density (top) at 350 kg/m^2 comparison between the two thermodynamic models at two different time instants.

Appendix R

WIDOM LINE LOCUS FOR THE GCEOS

The pseudo-boiling line or Widom line is commonly identified as the locus of points in the phase diagram where the single component, or the mixture crosses the pseudo-phase from compressible liquid to super-critical fluid or vice-versa. Methematically, this is defined as the locus of points where the specific heat at constant pressure peaks [95]. In this appendix, this condition is formally derived for the GCEoS. The starting point is the definition of the specific heat at constant pressure through Eq. (2.2.25), which is re-proposed here in a slightly different form, for convenience:

$$C_p = C_v + \frac{TM}{\rho^2}\frac{\left(\frac{\partial p}{\partial T}\right)^2_{\rho,\mathbf{X}}}{\left(\frac{\partial p}{\partial \rho}\right)_{T,\mathbf{X}}} = C_v + \frac{Z^2 R_u^2 T^3}{p^2 M}\frac{\left(\frac{\partial p}{\partial T}\right)^2_{\rho,\mathbf{X}}}{\left(\frac{\partial p}{\partial \rho}\right)_{T,\mathbf{X}}} = C_v + \Omega\,. \tag{R.0.1}$$

where $(\partial p/\partial T)_{\rho,\mathbf{X}}$ and $(\partial p/\partial \rho)_{T,\mathbf{X}}$ are expressed in Eq. (2.2.86) and Eq. (2.2.87), respectively. Substituting Eq. (2.2.86) and Eq. (2.2.87), the expression of the Ω factor is obtained after manipulations:

$$\begin{aligned}\Omega = R_u &\frac{(ZT+\delta_1\overline{B}_m)^2(ZT+\delta_2\overline{B}_m)^2 + \frac{p^2}{R_u^4}\left(\frac{dA_m}{dT}\right)^2_{\mathbf{X}}(ZT-\overline{B}_m)^2}{(ZT+\delta_1\overline{B}_m)^2(ZT+\delta_2\overline{B}_m)^2 - \frac{A_m p}{R_u^2 T}(ZT-\overline{B}_m)^2\left[2ZT+(\delta_1+\delta_2)\overline{B}_m\right]} + \\ - R_u &\frac{\frac{2p}{R_u^2}\left(\frac{dA_m}{dT}\right)_{\mathbf{X}}(ZT-\overline{B}_m)(ZT+\delta_2\overline{B}_m)(ZT+\delta_1\overline{B}_m)}{(ZT+\delta_1\overline{B}_m)^2(ZT+\delta_2\overline{B}_m)^2 - \frac{A_m p}{R_u^2 T}(ZT-\overline{B}_m)^2\left[2ZT+(\delta_1+\delta_2)\overline{B}_m\right]} = R_u\frac{\mathcal{F}}{\mathcal{G}}\,,\end{aligned} \tag{R.0.2}$$

where $\overline{B}_m = B_m p/R_u$ has been defined. For convenience, the numerator and the denominator of Eq. (R.0.2) are also defined as $\mathcal{F}$ and $\mathcal{G}$, respectively. Now by following the definition, the Widom line corresponds to the locus of the T, p, $\mathbf{X}$ points such that:

$$\left(\frac{\partial C_p}{\partial T}\right)_{p,\mathbf{X}} = 0 = \left(\frac{\partial C_v}{\partial T}\right)_{p,\mathbf{X}} + \left(\frac{\partial \Omega}{\partial T}\right)_{p,\mathbf{X}} = \left(\frac{\partial C_v}{\partial T}\right)_{p,\mathbf{X}} + \frac{R_u}{\mathcal{G}^2}\left[\left(\frac{\partial \mathcal{F}}{\partial T}\right)_{p,\mathbf{X}}\mathcal{G} - \left(\frac{\partial \mathcal{G}}{\partial T}\right)_{p,\mathbf{X}}\mathcal{F}\right]. \tag{R.0.3}$$

After some lengthy manipulations one can show that:

$$\left(\frac{\partial \mathcal{F}}{\partial T}\right)_{p,\mathbf{X}} = 2\left(\frac{\partial ZT}{\partial T}\right)_{p,\mathbf{X}}\left[(ZT+\delta_1\overline{B}_m)(ZT+\delta_2\overline{B}_m)^2+(ZT+\delta_2\overline{B}_m)(ZT+\delta_1\overline{B}_m)^2\right]+$$
$$+2\left[\left(\frac{d^2A_m}{dT^2}\right)_{p,\mathbf{X}}(ZT-\overline{B}_m)+\left(\frac{dA_m}{dT}_{p,\mathbf{X}}\right)\left(\frac{\partial ZT}{\partial T}\right)_{p,\mathbf{X}}\right]\times$$
$$\times\left[\frac{p^2}{R_u^4}\left(\frac{dA_m}{dT}\right)_{p,\mathbf{X}}(ZT-\overline{B}_m)-\frac{p}{R_u^2}(ZT+\delta_2\overline{B}_m)(ZT+\delta_1\overline{B}_m)\right]+$$
$$-2\frac{p}{R_u^2}\left(\frac{dA_m}{dT}\right)_{p,\mathbf{X}}\left(\frac{\partial ZT}{\partial T}\right)_{p,\mathbf{X}}(ZT-\overline{B}_m)[2ZT+(\delta_1+\delta_2)\overline{B}_m]\,, \tag{R.0.4}$$

$$\left(\frac{\partial \mathcal{G}}{\partial T}\right)_{p,\mathbf{X}} = 2\left(\frac{\partial ZT}{\partial T}\right)_{p,\mathbf{X}}(ZT+\delta_1\overline{B}_m)(ZT+\delta_2\overline{B}_m)[2ZT+(\delta_1+\delta_2)\overline{B}_m]+$$
$$-\frac{p(ZT-\overline{B}_m)}{R_u^2T}\left\{\left[\left(\frac{dA_m}{dT}\right)_{p,\mathbf{X}}-\frac{A_m}{T}\right](ZT-\overline{B}_m)[2ZT+(\delta_1+\delta_2)\overline{B}_m]+\right.$$
$$\left.+2A_m\left(\frac{\partial ZT}{\partial T}\right)_{p,\mathbf{X}}[3ZT+(\delta_1+\delta_2-1)\overline{B}_m]\right\}. \tag{R.0.5}$$

In both Eq. (R.0.4) and Eq. (R.0.5) the additional auxiliary derivative is required:

$$\left(\frac{\partial ZT}{\partial T}\right)_{p,\mathbf{X}} = \left[Z+T\left(\frac{\partial Z}{\partial T}\right)_{p,\mathbf{X}}\right], \tag{R.0.6}$$

where $(\partial Z/\partial T)_{p,\mathbf{X}}$ has been given in Eq. (M.1.1).

Finally, the derivatives of the specific heat at constant volume are given:

$$\left(\frac{\partial C_v}{\partial T}\right)_{p,\mathbf{X}} = \left(\frac{\partial C_v^{ig}}{\partial T}\right)_{p,\mathbf{X}}+$$
$$+\frac{1}{(\delta_1-\delta_2)B_m}\left\{\ln\left(\frac{ZT+\delta_1\overline{B}_m}{ZT+\delta_2\overline{B}_m}\right)\left[\left(\frac{d^2A_m}{dT^2}\right)_{p,\mathbf{X}}+T\left(\frac{d^2A_m}{dT^3}\right)_{p,\mathbf{X}}\right]+\right.$$
$$\left.-T\left(\frac{d^2A_m}{dT^2}\right)_{p,\mathbf{X}}\left(\frac{\partial ZT}{\partial T}\right)_{p,\mathbf{X}}\frac{(\delta_1-\delta_2)\overline{B}_m}{(ZT+\delta_1\overline{B}_m)(ZT+\delta_2\overline{B}_m)}\right\}, \tag{R.0.7}$$

$$\left(\frac{dC_v^{ig}}{dT}\right)_{p,\mathbf{X}} = \frac{d}{dT}\left(\sum_{i=1}^{N_s}X_iC_{v,i}^{ig}\right)_{p,\mathbf{X}} = \sum_{i=1}^{N_s}X_i\left(\frac{dC_{v,i}^{ig}}{dT}\right)_{p,\mathbf{X}}. \tag{R.0.8}$$

Depending on whether the Chemkin [80] (Eq. (R.0.9)) or NASA [123](Eq. (R.0.10)) polynomials are used for the determination of the specific heats, the following two formulas

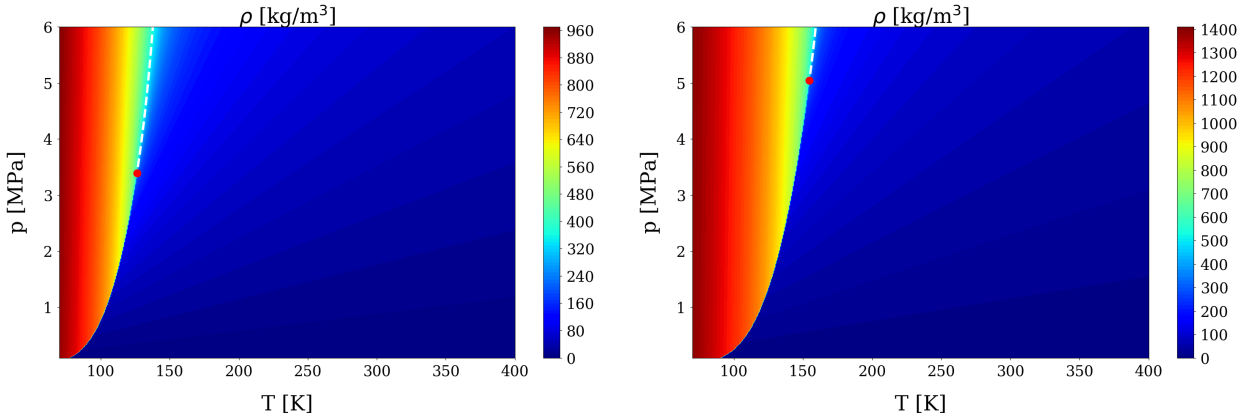

(a) N_2

(b) O_2

(c) CH_4

Figure 181: Two dimensional density color maps for (a) N_2, (b) O_2 and (c) CH_4 displaying the Widom line in dashed white color departing from the species critical point (red dot).

apply for the temperature derivative of the species' specific heat at constant volume.

$$\frac{dC_{v,i}^{ig}}{dT} = R_u(\alpha_2 + 2\alpha_3 T + 3\alpha_4 T^2 + 4\alpha_5 T^3) \tag{R.0.9}$$

$$\frac{dC_{v,i}^{ig}}{dT} = R_u(-2\beta_1 T^{-3} - \beta_2 T^{-2} + \beta_4 + 2\beta_5 T + 3\beta_6 T^2 + 4\beta_7 T^3) \tag{R.0.10}$$

$$\tag{R.0.11}$$

where α_i and β_i represent the species-dependent coefficients that can be found in the Chemkin [80] or NASA [123] databases, respectively.

If Eq. (R.0.3) is solved in temperature for given pressure and composition, the Widom line locus can be plotted for a given species or mixture. To illustrate this procedure, Fig. 181 shows the density color maps for nitrogen, oxygen and methane along with the Widom line departing from the critical point.

REFERENCES

[1] Abgrall, R. and Karni, S., "Computations of compressible multifluids," *J. Comp. Phys.*, vol. 169, no. 2, pp. 594–623, 2001.

[2] Abraham, F., *Homogeneous nucleation theory*, vol. 263. Elsevier, 1974.

[3] Abudour, A. M., Mohammad, S. A., Robinson, R. L., and Gasem, K. A., "Volume-translated peng-robinson equation of state for liquid densities of diverse binary mixtures," *Fluid Ph. Equil.*, vol. 349, pp. 37–55, 2013.

[4] Andersen, J., Rasmussen, C., Giselsson, T., and Glarborg, P., "Global combustion mechanisms for use in cfd modeling under oxy-fuel conditions," *Energy & Fuels*, vol. 23, no. 3, pp. 1379–1389, 2009.

[5] Anderson, D., Tannehill, J., and Pletcher, R., *Computational fluid mechanics and heat transfer*. Taylor & Francis, 2016.

[6] Aursand, P., Hammer, M., Munkejord, S., and Wilhelmsen, O., "Pipeline transport of co2 mixtures: models for transient simulation," *Int. J. of Greenhouse Gas Ctrl.*, vol. 15, pp. 174–185, 2013.

[7] Baab, S., Förster, F., Lamanna, G., and Weigand, B., "Speed of sound measurements and mixing characterization of underexpanded fuel jets with supercritical reservoir condition using laser-induced thermal acoustics," *Exp. in Fluids*, vol. 57, no. 11, p. 172, 2016.

[8] Balchandani, S., Mandal, B., and Dharaskar, S., "Measurements and modeling of vapor liquid equilibrium of co2 in amine activatedimidazolium ionic liquid solvents," *Fluid Ph. Equil.*, vol. tba, pp. 1–54, 2020.

[9] Banuti, D. and Bellan, J., "Inter-species molecular attraction effect in the development of a two-species mixing layer," in *AIAA 2020-1155*, pp. 1–13, 2020.

[10] Banuti, D., "Crossing the widom-line–supercritical pseudo-boiling," *J. Sup. F.*, vol. 98, pp. 12–16, 2015.

[11] Banuti, D., Raju, M., and Ihme, M., "Similarity law for widom lines and coexistence lines," *Physical Review E*, vol. 95, no. 5, p. 052120, 2017.

[12] Bellan, J., "Future challenges in the modelling and simulations of high-pressure flows," *Combust. Sci. Technol.*, pp. 1–20, 2020.

[13] Benedict, M., Webb, G., and Rubin, L., "An empirical equation for thermodynamic properties of light hydrocarbons and their mixtures i. methane, ethane, propane and n-butane," *The J. of Chem. Phys.*, vol. 8, no. 4, pp. 334–345, 1940.

[14] Berche, B., Henkel, M., and Kenna, R., "Critical phenomena: 150 years since Cagniard de la Tour," vol. 1, 2009.

[15] Billet, G. and Abgrall, R., "An adaptive shock-capturing algorithm for solving unsteady reactive flows," *Comp. and Fluids*, vol. 32, no. 10, pp. 1473–1495, 2003.

[16] Binotti, M., Astolfi, M., Campanari, S., Manzolini, G., and Silva, P., "Preliminary assessment of sco2 cycles for power generation in csp solar tower plants," *Applied energy*, vol. 204, pp. 1007–1017, 2017.

[17] Bird, R., "Viewpoints on transport phenomena," *Korean J. of Chem. Eng.*, vol. 15, no. 2, p. 105, 1998.

[18] Blanco, S., Rivas, C., Bravo, R., Fernandez, J., Artal, M., and Velasco, I., "Discussion of the influence of co and ch4 in co2 transport, injection, and storage for ccs technology," *Env. sci. & tech.*, vol. 48, no. 18, pp. 10984–10992, 2014.

[19] Borghesi, G. and Bellan, J., "Models for the large eddy simulation equations to describe multi-species mixing occuring at supercritical pressure," *Int. J. of Energetic Materials and Chem. Prop.*, vol. 13, no. 5, 2014.

[20] Brown, P., Byrne, G., and Hindmarsh, A., "Vode: A variable-coefficient ode solver," *SIAM journal on scientific and statistical computing*, vol. 10, no. 5, pp. 1038–1051, 1989.

[21] Buffett, B. A., "The thermal state of earth's core," *Science*, vol. 299, no. 5613, pp. 1675–1677, 2003.

[22] Cahn, J. and Hilliard, J., "Free energy of a nonuniform system. i. interfacial free energy," *The J. of chem. phy.*, vol. 28, no. 2, pp. 258–267, 1958.

[23] Candel, S., Juniper, M., Singla, G., Scouflaire, P., and Rolon, C., "Structure and dynamics of cryogenic flames at supercritical pressure," *Combust. Sci. Technol.*, vol. 178, no. 1-3, pp. 161–192, 2006.

[24] Carrero-Mantilla, J. and Llano-Restrepo, M., "Vapor-liquid equilibria of the binary mixtures nitrogen+ methane, nitrogen+ ethane and nitrogen+ carbon dioxide, and the ternary mixture nitrogen+ methane+ ethane from gibbs-ensemble molecular simulation," *Fluid Ph. Equil.*, vol. 208, no. 1, pp. 155–169, 2003.

[25] Castier, M., "Solution of the isochoric–isoenergetic flash problem by direct entropy maximization," *Fluid Ph. Equil.*, vol. 276, no. 1, pp. 7–17, 2009.

[26] Castier, M., "Thermodynamic speed of sound in multiphase systems," *Fluid Ph. Equil.*, vol. 306, no. 2, pp. 204–211, 2011.

[27] Castiglioni, G. and Bellan, J., "On models for predicting thermodynamic regimes in high-pressure turbulent mixing and combustion of multispecies mixtures," *J. Fluid Mech.*, vol. 843, pp. 536–574, 2018.

[28] Chehroudi, B., "Recent experimental efforts on high-pressure supercritical injection for liquid rockets and their implications," *Int. J. of Aer. Eng.*, vol. 2012, 2012.

[29] Chehroudi, B., Talley, D., and Coy, E., "Visual characteristics and initial growth rates of round cryogenic jets at subcritical and supercritical pressures," *Phys. of Fluids*, vol. 14, no. 2, pp. 850–861, 2002.

[30] Chueh, P. and Prausnitz, J., "Vapor-liquid equilibria at high pressures: Calculation of critical temperatures, volumes, and pressures of nonpolar mixtures," *AIChE Journal*, vol. 13, no. 6, pp. 1107–1113, 1967.

[31] Chung, T., Ajlan, M., Lee, L., and Starling, K., "Generalized multiparameter correlation for nonpolar and polar fluid transport properties," *Ind. & Eng. Chem. Res.*, vol. 27, no. 4, pp. 671–679, 1988.

[32] Chung, W., Ma, P., and Ihme, M., "Examination of diesel spray combustion in supercritical ambient fluid using large-eddy simulations," *Int. J. of Eng. Res.*, vol. 21, no. 1, pp. 122–133, 2020.

[33] Cismondi, M. and Mollerup, J., "Development and application of a three-parameter rk–pr equation of state," *Fluid Ph. Equil.*, vol. 232, no. 1, pp. 74–89, 2005.

[34] Congiunti, A. and Bruno, C., "Supercritical combustion properties," in *AIAA 2003-478*, p. 478, 2003.

[35] Coogan, S., Gao, X., McClung, A., and Sun, W., "Evaluation of kinetic mechanisms for direct fired supercritical oxy-combustion of natural gas," in *ASME Turbo Expo 2016*, American Society of Mechanical Engineers Digital Collection, 2016.

[36] Dahms, R., "Understanding the breakdown of classic two-phase theory and spray atomization at engine-relevant conditions," *Phys. of Fluids*, vol. 28, no. 4, p. 042108, 2016.

[37] Dahms, R. and Oefelein, J., "On the transition between two-phase and single-phase interface dynamics in multicomponent fluids at supercritical pressures," *Phys. of Fluids*, vol. 25, no. 9, p. 092103, 2013.

[38] Dahms, R. and Oefelein, J., "Non-equilibrium gas–liquid interface dynamics in high-pressure liquid injection systems," *Proc. Combust. Inst.*, vol. 35, no. 2, pp. 1587–1594, 2015.

[39] Darmofal, D., Moinier, P., and Giles, M., "Eigenmode analysis of boundary conditions for the one-dimensional preconditioned euler equations," *J. Comp. Phys.*, vol. 160, no. 1, pp. 369–384, 2000.

[40] Davis, S., "Simplified second-order godunov-type methods," *SIAM J. on Sci. and Stat. Comp.*, vol. 9, no. 3, pp. 445–473, 1988.

[41] de La Tour, C., "Exposé de quelques résultats obtenus par l'action combinée de la chaleur et de la compression sur certains liquides, tels que l'eau, l'alcool, l'éther sulfurique et l'essence de pétrole rectifiée," *Ann. chim. phys*, vol. 21, no. 2, p. 127, 1822.

[42] Debenedetti, P., "Homogeneous nucleation in supercritical fluids," *AIChE Journal*, vol. 36, no. 9, pp. 1289–1298, 1990.

[43] Denbigh, K., *The principles of chemical equilibrium: with applications in chemistry and chemical engineering*. Camb. Univ. Press, 1981.

[44] Edwards, J., Franklin, R., and Liou, M.-S., "Low-diffusion flux-splitting methods for real fluid flows with phase transitions," *AIAA J.*, vol. 38, no. 9, pp. 1624–1633, 2000.

[45] Eliosa-Jiménez, G., Silva-Oliver, G., García-Sánchez, F., and de Ita de la Torre, A., "High-pressure vapor-liquid equilibria in the nitrogen + n-hexane system," *J. of Chem. and Eng. Data*, vol. 52, no. 2, pp. 395–404, 2007.

[46] Elliott, J. and Lira, C., *Introductory chemical engineering thermodynamics*, vol. 184. Prentice Hall PTR Upper Saddle River, NJ, 1999.

[47] F., W., *Viscous Fluid Flow*. Tata McGraw Hill, 2011.

[48] Fathi, M. and Hickel, S., "Rapid multi-component phase-split calculations using volume functions and reduction methods," *arXiv preprint arXiv:2001.06285*, 2020.

[49] Firoozabadi, A., *Thermodynamics and applications in hydrocarbon energy production*. McGraw-Hill Education New York, 2016.

[50] Franzelli, B., Riber, E., Gicquel, L. Y. M., and Poinsot, T., "Large eddy simulation of combustion instabilities in a lean partially premixed swirled flame," *Combust. Flame*, vol. 159, pp. 621–637, 2012.

[51] Frassoldati, A., Cuoci, A., Faravelli, T., Ranzi, E., Candusso, C., and Tolazzi, D., "Simplified kinetic schemes for oxy-fuel combustion," in *1st Int. conf. on sustainable fossil fuels for future energy*, pp. 6–10, 2009.

[52] Fuller, E., Schettler, P., and Giddings, J., "New method for prediction of binary gas-phase diffusion coefficients," *Ind. & Eng. Chem.*, vol. 58, no. 5, pp. 18–27, 1966.

[53] Gao, X., Yang, S., and Sun, W., "A global pathway selection algorithm for the reduction of detailed chemical kinetic mechanisms," *Combust. Flame*, vol. 167, pp. 238–247, 2016.

[54] Génin, F., *Study of compressible turbulent flows in supersonic environment by large-eddy simulation*. PhD thesis, Georgia Institute of Technology, 2012.

[55] Génin, F. and Menon, S., "Dynamics of sonic jet injection into supersonic crossflow," *J. of Turb.*, vol. 11, pp. 1–30, 2010.

[56] Gernert, J., Jäger, A., and Span, R., "Calculation of phase equilibria for multicomponent mixtures using highly accurate helmholtz energy equations of state," *Fluid Ph. Equil.*, vol. 375, pp. 209–218, 2014.

[57] Giovangigli, V., Matuszewski, L., and Dupoirieux, F., "Detailed modeling of planar transcritical h2–o2–n2 flames," *Combust. Theory Modelling*, vol. 15, no. 2, pp. 141–182, 2011.

[58] Groves, T., Bishnoi, P., and Wallbridge, J., "Decompression wave velocities in natural gases in pipe lines," *The Canadian J. of Chem.l Eng.*, vol. 56, no. 6, pp. 664–668, 1978.

[59] Guezennec, N., Masquelet, M., and Menon, S., "Large eddy simulation of flame-turbulence interactions in a LOX-CH_4 shear coaxial injector," *AIAA 2012-1267*, 2012.

[60] Gunston, B., *Jane's aero-engines*. Jane's Information Group, 2001.

[61] Habiballah, M., Orain, M., Grisch, F., Vingert, L., and Gicquel, P., "Experimental studies of high-pressure cryogenic flames on the mascotte facility," *Combust. Sci. Technol.*, vol. 178, no. 1-3, pp. 101–128, 2006.

[62] Haile, J., Johnston, I., Mallinckrodt, A., and McKay, S., "Molecular dynamics simulation: elementary methods," *Computers in Physics*, vol. 7, no. 6, pp. 625–625, 1993.

[63] Harstad, K. and Bellan, J., "Mixing rules for multicomponent mixture mass diffusion coefficients and thermal diffusion factors," *The J. of Chem. Phys.*, vol. 120, no. 12, pp. 5664–5673, 2004.

[64] Harstad, K., Miller, R., and Bellan, J., "Efficient high-pressure state equations," *AIChE J.*, vol. 43, no. 6, pp. 1605–1610, 1997.

[65] Harten, A., Lax, P., and Van Leer, B., "On upstream differencing and godunov-type schemes for hyperbolic conservation laws," *SIAM review*, vol. 25, no. 1, pp. 35–61, 1983.

[66] Haugen, K., Firoozabadi, A., and Sun, L., "Efficient and robust three-phase split computations," *AIChE J.*, vol. 57, no. 9, pp. 2555–2565, 2011.

[67] Heidemann, R. and Khalil, A., "The calculation of critical points," *AIChE journal*, vol. 26, no. 5, pp. 769–779, 1980.

[68] Heywood, J., "Combustion engine fundamentals," *1ª Edição. Estados Unidos*, 1988.

[69] Hill, P. and Peterson, C., "Mechanics and thermodynamics of propulsion," *Reading, MA, Addison-Wesley Publishing Co., 1992, 764 p.*, 1992.

[70] Hirschfelder, J., Curtiss, C., Bird, R., and Mayer, M., *Molecular theory of gases and liquids*, vol. 165. Wiley New York, 1964.

[71] Hobold, G. and da Silva, A., "A generalized multifluid optimal pressure for heat exchangers operating with supercritical fluid," *Num. Heat Transf.*, vol. 72, no. 5, pp. 345–354, 2017.

[72] Hoteit, H. and Firoozabadi, A., "Simple phase stability-testing algorithm in the reduction method," *AIChE journal*, vol. 52, no. 8, pp. 2909–2920, 2006.

[73] Hughes, K., Turányi, T., Clague, A., and Pilling, M., "Development and testing of a comprehensive chemical mechanism for the oxidation of methane," *Int. J. of Chem. Kin.*, vol. 33, no. 9, pp. 513–538, 2001.

[74] Iwai, Y., Itoh, M., Morisawa, Y., Suzuki, S., Cusano, D., and Harris, M., "Development approach to the combustor of gas turbine for oxy-fuel, supercritical co2 cycle," in *ASME Turbo Expo 2015: Turbine Technical Conference and Exposition*, American Society of Mechanical Engineers Digital Collection, 2015.

[75] Jacobsen, R. and Stewart, R., "Thermodynamic properties of nitrogen including liquid and vapor phases from 63k to 2000k with pressures to 10,000 bar," *J. of Phys. and Chem. Ref. Data*, vol. 2, no. 4, pp. 757–922, 1973.

[76] Jensen, R., Dodson, H., and Claflin, S., "Lox/hydrocarbon combustion instability investigation," 1989.

[77] Jindrová, T. and Mikyška, J., "General algorithm for multiphase equilibria calculation at given volume, temperature, and moles," *Fluid Ph. Equil.*, vol. 393, pp. 7–25, 2015.

[78] Jones, W. and Lindstedt, R., "Global reaction schemes for hydrocarbon combustion," *Combust. Flame*, vol. 73, no. 3, pp. 233–249, 1988.

[79] Kawai, S., Terashima, H., and Negishi, H., "A robust and accurate numerical method for transcritical turbulent flows at supercritical pressure with an arbitrary equation of state," *J. Comp. Phys.*, vol. 300, pp. 116–135, 2015.

[80] Kee, R., Rupley, F., and Miller, J., "The chemkin thermodynamic data base," *From Web*, 1990.

[81] Keizer, J., "Statistical thermodynamics of nonequilibrium processes," *Verlag New-York Inc.–1987.–608 p*, 1987.

[82] Kim, S., Choi, H., and Kim, Y., "Thermodynamic modeling based on a generalized cubic equation of state for kerosene/lox rocket combustion," *Combust. Flame*, vol. 159, no. 3, pp. 1351–1365, 2012.

[83] Knudsen, E., Doran, E., Mittal, V., Meng, J., and Spurlock, W., "Compressible eulerian needle-to-target large eddy simulations of a diesel fuel injector," *Proc. Combust. Inst.*, vol. 36, no. 2, pp. 2459–2466, 2017.

[84] Kogekar, G., Karakaya, C., Liskovich, G., Oehlschlaeger, M., DeCaluwe, S., and Kee, R. J., "Impact of non-ideal behavior on ignition delay and chemical kinetics in high-pressure shock tube reactors," *Combust. Flame*, vol. 189, pp. 1–11, 2018.

[85] Kouremenos, D., "The normal shock waves of real gases and the generalized isentropic exponents," *Forschung im Ingenieurwesen A*, vol. 52, no. 1, pp. 23–31, 1986.

[86] Kraichnan, R. H., "Diffusion by a random velocity field," *Phys. of Fluids*, vol. 13, no. 1, pp. 22–31, 1970.

[87] Kruger, C. and Vincenti, W., "Introduction to physical gas dynamics," *John Wlley & Sons*, 1965.

[88] Królikowska, M., Romańska, K., Paduszyński, K., and Skonieczny, M., "The study on the influence of glycols on the vapor pressure, density and dynamicviscosity of lithium bromide aqueous solution," *Fluid Ph. Equil.*, vol. tba, pp. 1–41, 2020.

[89] Lacaze, G., Misdariis, A., Ruiz, A., and Oefelein, J., "Analysis of high-pressure diesel fuel injection processes using les with real-fluid thermodynamics and transport," *Proc. Combust. Inst.*, vol. 35, no. 2, pp. 1603–1611, 2015.

[90] Lacaze, G. and Oefelein, J., "Modeling of high density gradient flows at supercritical pressures," *AIAA 2013-3717*, 2013.

[91] Lacaze, G., Ruiz, A., Thomas, S., and Oefelein, J. C., "Robust treatment of thermodynamic nonlineari-ties in the simulation of transcritical flows," *SIAM 16th International Conference on Numerical Combustion, Orlando, FL.*, 2017.

[92] Lacaze, G., Schmitt, T., Ruiz, A., and Oefelein, J., "Comparison of energy-, pressure-and enthalpy-based approaches for modeling supercritical flows," *Comp. and Fluids*, 2019.

[93] Lafon, P., Meng, H., Yang, V., and Habiballah, M., "Vaporization of liquid oxygen (lox) droplets in hydrogen and water environments under sub-and supercritical conditions," *Combust. Sci. Technol.*, vol. 180, no. 1, pp. 1–26, 2007.

[94] Lamarre, E. and Melville, W., "Instrumentation for the measurement of sound speed near the ocean surface," *J. of Atm. and Ocean. Tech.*, vol. 12, no. 2, pp. 317–329, 1995.

[95] Lamorgese, A., Ambrosini, W., and Mauri, R., "Widom line prediction by the soave–redlich–kwong and peng–robinson equations of state," *The Journal of Supercritical Fluids*, vol. 133, pp. 367–371, 2018.

[96] Lapenna, P. and Creta, F., "Mixing under transcritical conditions: an a-priori study using direct numerical simulation," *J. Sup. F.*, 2017.

[97] Lapenna, P. and Creta, F., "Direct numerical simulation of transcritical jets at moderate reynolds number," *AIAA J.*, vol. 57, no. 6, pp. 2254–2263, 2019.

[98] Lebonnois, S. and Schubert, G., "The deep atmosphere of venus and the possible role of density-driven separation of co 2 and n 2," *Nature Geoscience*, vol. 10, no. 7, pp. 473–477, 2017.

[99] Leonardi, M., Nasuti, F., and Onofri, M., "Basic analysis of a lox/methane expander bleed engine," *EUCASS 2017*, 2017.

[100] Li, H., *Thermodynamic properties of CO2 mixtures and their applications in advanced power cycles with CO2 capture processes*. PhD thesis, Royal Institute of Technology, 2008.

[101] Li, Z. and Firoozabadi, A., "General strategy for stability testing and phase-split calculation in two and three phases," *SPE J.*, vol. 17, no. 04, pp. 1–096, 2012.

[102] Li, Z. and Firoozabadi, A., "Initialization of phase fractions in rachford–rice equations for robust and efficient three-phase split calculation," *Fluid Ph. Equil.*, vol. 332, pp. 21–27, 2012.

[103] Lin, K.-C., Cox-Stouffer, S., and Jackson, T., "Structures and phase transition processes of supercritical methane/ethylene mixtures injected into a subcritical environment," *Combust. Sci. Technol.*, vol. 178, no. 1-3, pp. 129–160, 2006.

[104] Lopez-Echeverry, J., Reif-Acherman, S., and Araujo-Lopez, E., "Peng-robinson equation of state: 40 years through cubics," *Fluid Ph. Equil.*, vol. 447, pp. 39–71, 2017.

[105] Lou, H. and Miller, R., "On ternary species mixing and combustion in isotropic turbulence at high pressure," *Phys. of Fluids*, vol. 16, no. 5, pp. 1423–1438, 2004.

[106] Lu, C., Jin, Z., and Li, H., "A two-phase flash algorithm with the consideration of capillary pressure at specified mole numbers, volume and temperature," *Fluid Ph. Equil.*, vol. 485, pp. 67–82, 2019.

[107] Ma, P., *Modeling of turbulent mixing and combustion at transcritical conditions*. PhD thesis, Stanford University, 2018. https://stacks.stanford.edu/file/druid:xb567kv4007/thesis-augmented.pdf.

[108] Ma, P., Lv, Y., and Ihme, M., "An entropy-stable hybrid scheme for simulations of transcritical real-fluid flows," *J. Comp. Phys.*, vol. 340, pp. 330–357, 2017.

[109] Ma, P., Wu, H., Banuti, D., and Ihme, M., "On the numerical behavior of diffuse-interface methods for transcritical real-fluids simulations," *Int. J. of Multiph. Fl.*, 2019.

[110] Ma, P., Wu, H., Jaravel, T., Bravo, L., and Ihme, M., "Large-eddy simulations of transcritical injection and auto-ignition using diffuse-interface method and finite-rate chemistry," *Proc. Combust. Inst.*, vol. 37, no. 3, pp. 3303–3310, 2019.

[111] MacCormack, R., *Numerical computation of compressible and viscous flow*. AIAA, 2014.

[112] Mahle, I., Sesterhenn, J., and Friedrich, R., "Turbulent mixing in temporal compressible shear layers involving detailed diffusion processes," *J. of Turb.*, no. 8, p. N1, 2007.

[113] Manin, J., Bardi, M., Pickett, L., Dahms, R., and Oefelein, J., "Microscopic investigation of the atomization and mixing processes of diesel sprays injected into high pressure and temperature environments," *Fuel*, vol. 134, pp. 531–543, 2014.

[114] Masquelet, M., *Large-eddy simulations of high-pressure shear coaxial flows relevant for H2/O2 rocket engines*. PhD thesis, Georgia Institute of Technology, 2012. https://smartech.gatech.edu/handle/1853/47522.

[115] Masquelet, M., Guezennec, N., and Menon, S., "Numerical studies of mixing and flame-turbulence interactions in shear coaxial injector flows under trans-critical conditions," *AIAA 2012-1269*, 2012.

[116] Masquelet, M., Menon, S., Jin, Y., and Friedrich, R., "Simulation of unsteady combustion in a LOX-GH2 fueled rocket engine," *Aer. Sci. Tech.*, vol. 13, no. 8, pp. 466–474, 2009.

[117] Matheis, J. and Hickel, S., "Multi-component vapor-liquid equilibrium model for les and application to ecn spray a," *Center for Turb. Research*, 2016.

[118] Matheis, J. and Hickel, S., "Multi-component vapor-liquid equilibrium model for LES of high-pressure fuel injection and application to ecn spray a," *Int. J. of Multiph. Fl.*, vol. 99, pp. 294–311, 2018.

[119] Matheis, J., Müller, H., Lenz, C., Pfitzner, M., and Hickel, S., "Volume translation methods for real-gas computational fluid dynamics simulations," *J. Sup. F.*, vol. 107, pp. 422–432, 2016.

[120] Mayer, W., Schik, A. H., Vielle, B., Chauveau, C., Gökalp, I., Talley, D., and Woodward, R., "Atomization and breakup of cryogenic propellants under high-pressure subcritical and supercritical conditions," *J. Prop. Pow.*, vol. 14, no. 5, pp. 835–842, 1998.

[121] Mayer, W. and Smith, J., "Fundamentals of supercritical mixing and combustion of cryogenic propellants," *Liquid Rocket Thrust Chambers: Aspects of Modeling, Analysis and Design*, vol. 200, 2004.

[122] Mayer, W. and Tamura, H., "Propellant injection in a liquid oxygen/gaseous hydrogen rocket engine," *J. Prop. Pow.*, vol. 12, no. 6, pp. 1137–1147, 1996.

[123] McBride, B., Zehe, M., and Gordon, S., "Nasa glenn coefficients for calculating thermodynamic properties of individual species," 2002.

[124] McMillan, P. and Stanley, H., "Going supercritical," *Nature Physics*, vol. 6, no. 7, pp. 479–480, 2010.

[125] Meng, H. and Yang, V., "A unified treatment of general fluid thermodynamics and its application to a preconditioning scheme," *J. Comp. Phys.*, vol. 189, no. 1, pp. 277–304, 2003.

[126] Michelsen, M., "The isothermal flash problem. part i. stability," *Fluid Ph. Equil.*, vol. 9, no. 1, pp. 1–19, 1982.

[127] Michelsen, M., "The isothermal flash problem. part ii. phase-split calculation," *Fluid Ph. Equil.*, vol. 9, no. 1, pp. 21–40, 1982.

[128] Michelsen, M., "State function based flash specifications," *Fluid Ph. Equil.*, vol. 158, pp. 617–626, 1999.

[129] Michelsen, M. and Mollerup, J., "Thermodynamic models: fundamental and computational aspects," 2007.

[130] Milan, P., Wang, X., Hickey, J.-P., Li, Y., and Yang, V., "Accelerating numerical simulations of supercritical fluid flows using deep neural networks," in *AIAA 2020-1157*, pp. 1–12, 2020.

[131] Miller, R. and Lou, H., "Effects of oret and dufour diffusion on conditional expectations in isotropic turbulent mixing at supercritical pressure," in *APS Division of Fluid Dynamics Meeting Abstracts*, 2000.

[132] Miller, R. and Bellan, J., "Direct numerical simulation of a confined three-dimensional gas mixing layer with one evaporating hydrocarbon-droplet-laden stream," *J. Fluid Mech.*, vol. 384, pp. 293–338, 1999.

[133] Miller, R. and Bellan, J., "Direct numerical simulation and subgrid analysis of a transitional droplet laden mixing layer," *Phys. of Fluids*, vol. 12, no. 3, pp. 650–671, 2000.

[134] Miller, R., Harstad, K., and Bellan, J., "Direct numerical simulations of supercritical fluid mixing layers applied to heptane–nitrogen," *J. Fluid Mech.*, vol. 436, pp. 1–39, 2001.

[135] Mills, J., Boatz, J., and Langhoff, P., "Quantum-mechanical definition of atoms and their mutual interactions in born-oppenheimer molecules," *Phys. Rev. A*, vol. 98, no. 1, p. 012506, 2018.

[136] Müller, H., Niedermeier, C., Matheis, J., Pfitzner, M., and Hickel, S., "Large-eddy simulation of nitrogen injection at trans-and supercritical conditions," *Phys. of Fluids*, vol. 28, no. 1, p. 015102, 2016.

[137] Müller, H., Pfitzner, M., Matheis, J., and Hickel, S., "Large-eddy simulation of coaxial ln2/gh2 injection at trans-and supercritical conditions," *J. Prop. Pow.*, 2015.

[138] Nichita, D., Gomez, S., and Luna, E., "Multiphase equilibria calculation by direct minimization of gibbs free energy with a global optimization method," *Comp. & Chem. Eng.*, vol. 26, no. 12, pp. 1703–1724, 2002.

[139] Nichita, D., Khalid, P., and Broseta, D., "Calculation of isentropic compressibility and sound velocity in two-phase fluids," *Fluid Ph. Equil.*, vol. 291, no. 1, pp. 95–102, 2010.

[140] Oefelein, J., Lacaze, G., Dahms, R., Ruiz, A., and Misdariis, A., "Effects of real-fluid thermodynamics on high-pressure fuel injection processes," *SAE Int. J. of Engines*, vol. 7, no. 3, pp. 1125–1136, 2014.

[141] Oefelein, J. and Yang, V., "Modeling high-pressure mixing and combustion processes in liquid rocket engines," *J. Prop. Pow.*, vol. 14, no. 5, 1998.

[142] Oefelin, J. and Yang, V., "Analysis of transcritical spray phenomena in turbulent mixing layers," *AIAA 96-0085*, p. 85, 1996.

[143] Okong'o, N. and Bellan, J., "Consistent boundary conditions for multicomponent real gas mixtures based on characteristic waves," *Journal of Computational Physics*, vol. 176, pp. 330–344, 2002.

[144] Okong'o, N. and Bellan, J., "Perturbation and initial reynolds number effects on transition attainment of supercritical, binary, temporal mixing layers," *Comp. and Fluids*, vol. 33, no. 8, pp. 1023–1046, 2004.

[145] Okongó, N., Harstad, K., and Bellan, J., "Direct numerical simulations of o/h temporal mixing layers under supercritical conditions," *AIAA J.*, vol. 40, no. 5, pp. 914–926, 2002.

[146] Okong'o, N. and Bellan, J., "Direct numerical simulation of a transitional supercritical binary mixing layer: heptane and nitrogen," *J. Fluid Mech.*, vol. 464, pp. 1–34, 2002.

[147] Oschwald, M., Schik, A., Klar, M., and Mayer, W., "Investigation of coaxial ln2/gh2-injection at supercritical pressure by spontaneous raman scattering," *AIAA 1999-2887*, no. 99-2887, 1999.

[148] Oschwald, M., Smith, J., Branam, R., Hussong, J., Schik, A., Chehroudi, B., and Talley, D., "Injection of fluids into supercritical environments," *Combust. Sci. Technol.*, vol. 178, no. 1-3, pp. 49–100, 2006.

[149] Palle, S., *On real gas and molecular transport effects in high pressure mixing and combustion*. PhD thesis, Clemson University, 2006.

[150] Palle, S. and Miller, R., "Analysis of high-pressure hydrogen, methane, and heptane laminar diffusion flames: thermal diffusion factor modeling," *Combust. Flame*, vol. 151, no. 4, pp. 581–600, 2007.

[151] Pantano, C., Saurel, R., and Schmitt, T., "An oscillation free shock-capturing method for compressible van der waals supercritical fluid flows," *J. Comp. Phys.*, vol. 335, pp. 780–811, 2017.

[152] Papon, P., Leblond, J., and Meijer, P., *Physics of Phase Transitions*. Springer, 2002.

[153] Pelletier, M., Schmitt, T., and Ducruix, S., "A multifluid taylor-galerkin methodology for the simulation of compressible multicomponent separate two-phase flows from subcritical to supercritical states," *Comp. and Fluids*, p. 104588, 2020.

[154] Peng, D-Y.and Robinson, D., "A new two-constant equation of state," *Ind. & Eng. Chem. Fund.*, vol. 15, no. 1, pp. 59–64, 1976.

[155] Peters, N., *Turbulent Combustion*. Cambridge University Press, 2000.

[156] Petersen, E. and Hanson, R., "Reduced kinetics mechanisms for ram accelerator combustion," *Journal of Propulsion and power*, vol. 15, no. 4, pp. 591–600, 1999.

[157] Petit, X., Ribert, G., and Domingo, P., "Framework for real-gas compressible reacting flows with tabulated thermochemistry," *J. Sup. F.*, vol. 101, pp. 1–16, 2015.

[158] Petit, X., Ribert, G., Lartigue, G., and Domingo, P., "Large-eddy simulation of supercritical fluid injection," *J. Sup. F.*, vol. 84, pp. 61–73, 2013.

[159] Picard, D. and Bishnoi, P., "Calculation of the thermodynamic sound velocity in two-phase multicomponent fluids," *Int. J. of Multiph. Fl.*, vol. 13, no. 3, pp. 295–308, 1987.

[160] Pitzer, K., "The volumetric and thermodynamic properties of fluids. i. theoretical basis and virial coefficients1," *J. of the Amer. Chem. Soc.*, vol. 77, no. 13, pp. 3427–3433, 1955.

[161] Pizzarelli, M., Nasuti, F., Paciorri, R., and Onofri, M., "Numerical analysis of three-dimensional flow of supercritical fluid in cooling channels," *AIAA journal*, vol. 47, no. 11, pp. 2534–2543, 2009.

[162] Poinsot, T. and Veynante, D., *Theoretical and Numerical Combustion*. http://elearning.cerfacs.fr/, 3rd ed., 2012.

[163] Poling, B. E., Prausnitz, J., and O'connell, J. P., *The properties of gases and liquids*, vol. 5. Mcgraw-hill New York, 2001.

[164] Poston, R. and McKetta, J., "Vapor-liquid equilibrium in the n-hexane-nitrogen system.," *J. of Chem. and Eng. Data*, vol. 11, no. 3, pp. 364–365, 1966.

[165] Poursadegh, F., Lacey, J., Brear, M., and Gordon, R., "On the fuel spray transition to dense fluid mixing at reciprocating engine conditions," *Energy & Fuels*, vol. 31, no. 6, pp. 6445–6454, 2017.

[166] Prakash, S., Raman, V., Lietz, C., Hargus, W., and Schumaker, S., "High fidelity simulations of a methane-oxygen rotating detonation rocket engine," *AIAA 2020-0689*, pp. 1–17, 2020.

[167] Prausnitz, J. and Gunn, R., "Volumetric properties of nonpolar gaseous mixtures," *AIChE Journal*, vol. 4, no. 4, pp. 430–435, 1958.

[168] Qiu, L. and Reitz, R., "Simulation of supercritical fuel injection with condensation," *I. J. of Heat Mass Transfer*, vol. 79, pp. 1070–1086, 2014.

[169] Qiu, L. and Reitz, R., "An investigation of thermodynamic states during high-pressure fuel injection using equilibrium thermodynamics," *Int. J. of Multiph. Fl.*, vol. 72, pp. 24–38, 2015.

[170] Qiu, L., Wang, Y., Jiao, Q., Wang, H., and Reitz, R., "Development of a thermodynamically consistent, robust and efficient phase equilibrium solver and its validations," *Fuel*, vol. 115, pp. 1–16, 2014.

[171] Qiu, L., Wang, Y., and Reitz, R., "On regular and retrograde condensation in multiphase compressible flows," *Int. J. of Multiph. Fl.*, vol. 64, pp. 85–96, 2014.

[172] Rachedi, R., Crook, L., and Sojka, P., "An experimental study of swirling supercritical hydrocarbon fuel jets," *J. of Eng. for Gas Turb. and Pow.*, vol. 132, no. 8, 2010.

[173] Rahmani, F., Weathers, T., Hosangadi, A., and Chiew, Y., "A non-equilibrium molecular dynamics study of subcritical, supercritical and transcritical mixing of liquid-gas systems," *Chem. Eng. Sci.*, vol. 214, p. 115424, 2020.

[174] Raju, M., Banuti, D., Ma, P., and Ihme, M., "Widom lines in binary mixtures of supercritical fluids," *Scientific reports*, vol. 7, no. 1, pp. 1–10, 2017.

[175] Raju, M., Govindaraju, P., van Duin, A., and Ihme, M., "Atomistic and continuum scale modeling of functionalized graphyne membranes for water desalination," *Nanoscale*, vol. 10, no. 8, pp. 3969–3980, 2018.

[176] Ream, A., *Creating reduced order methane-air combustion mechanisms that satisfy the differential entropy inequality*. PhD thesis, Texas A& M Univ., 2015.

[177] Redlich, O. and Kwong, J., "On the thermodynamics of solutions. v. an equation of state. fugacities of gaseous solutions.," *Chemical reviews*, vol. 44, no. 1, pp. 233–244, 1949.

[178] Riazi, M. and Whitson, C., "Estimating diffusion coefficients of dense fluids," *Ind. & Eng. Chem. Res.*, vol. 32, no. 12, pp. 3081–3088, 1993.

[179] Ribert, G., Domingo, P., and Petit, X., "Simulation of high-pressure methane flames," *AIAA 2016-1935*, p. 1935, 2016.

[180] Ribert, G., Domingo, P., and Vervisch, L., "Analysis of sub-grid scale modeling of the ideal-gas equation of state in hydrogen–oxygen premixed flames," *Proc. Combust. Inst.*, vol. 37, no. 2, pp. 2345–2351, 2019.

[181] Ribert, G., Zong, N., Yang, V., Pons, L., Darabiha, N., and Candel, S., "Counterflow diffusion flames of general fluids: Oxygen/hydrogen mixtures," *Combust. Flame*, vol. 154, no. 3, pp. 319–330, 2008.

[182] Riggs, D., *Lecture 09: generalized compressibility chart*, 2019.

[183] Roa, M. and Talley, D., "Wave dynamic mechanisms in coaxial hydrogen/liquid-oxygen jet flames," *J. Prop. Pow.*, pp. 1–13, 2018.

[184] Rodriguez, C., Rokni, H., Koukouvinis, P., Gupta, A., and Gavaises, M., "Complex multicomponent real-fluid thermodynamic model for high-pressure diesel fuel injection," *Fuel*, vol. 257, p. 115888, 2019.

[185] Rodriguez, C., Vidal, A., Koukouvinis, P., Gavaises, M., and McHugh, M., "Simulation of transcritical fluid jets using the pc-saft eos," *J. Comp. Phys.*, vol. 374, pp. 444–468, 2018.

[186] Roy, A., Joly, C., and Segal, C., "Disintegrating supercritical jets in a subcritical environment," *J. Fluid Mech.*, vol. 717, pp. 193–202, 2013.

[187] Roy, A. and Segal, C., "Experimental study of fluid jet mixing at supercritical conditions," *J. Prop. Pow.*, vol. 26, no. 6, p. 1205, 2010.

[188] Ruiz, A., Lacaze, G., Oefelein, J., Mari, R., Cuenot, B., Selle, L., and Poinsot, T., "Numerical benchmark for high-reynolds-number supercritical flows with large density gradients," *AIAA J.*, 2015.

[189] Sadus, R., "Calculating critical transitions of fluid mixtures: theory vs. experiment," *AIChE journal*, vol. 40, no. 8, pp. 1376–1403, 1994.

[190] Sanchez, C., Gil, I., and Rodriguez, G., "Fluid phase equilibria for the isoamyl acetate production by reactive distillation," *Fluid Ph. Equil.*, vol. tba, pp. 1–30, 2020.

[191] Schmitt, T., "Large-eddy simulations of the mascotte test cases operating at supercritical pressure," *Flow Turb. Combust.*, pp. 1–31, 2020.

[192] Schmitt, T., Méry, Y., Boileau, M., and Candel, S., "Large-eddy simulation of oxygen/methane flames under transcritical conditions," *Proc. Combust. Inst.*, vol. 33, no. 1, pp. 1383–1390, 2011.

[193] Schmitt, T., Selle, L., Ruiz, A., and Cuenot, B., "Large-eddy simulation of supercritical-pressure round jets," *AIAA J.*, vol. 48, no. 9, pp. 2133–2144, 2010.

[194] Schonfeld, T. and Rudgyard, M., "Steady and unsteady flow simulations using the hybrid flow solver avbp," *AIAA J.*, vol. 37, no. 11, pp. 1378–1385, 1999.

[195] Sciacovelli, L. and Bellan, J., "The influence of the chemical composition representation according to the number of species during mixing in high-pressure turbulent flows," *J. Fluid Mech.*, vol. 863, pp. 293–340, 2019.

[196] Segal, C. and Polikhov, S., "Subcritical to supercritical mixing," *Phys. of Fluids*, vol. 20, no. 5, p. 052101, 2008.

[197] Selle, L., Okong'o, N., Bellan, J., and Harstad, K., "Modelling of subgrid-scale phenomena in supercritical transitional mixing layers: an a priori study," *J. Fluid Mech.*, vol. 593, pp. 57–91, 2007.

[198] Seyf, J. and Asgari, M., "Correlation and prediction of small to large sizedpharmaceuticals solubility, and crystallization in binary and ternary mixed solvents using the uniquac-sac model," *Fluid Ph. Equil.*, vol. tba, pp. 1–25, 2020.

[199] Shojaeian, A. and Fatoorehchi, H., "Modeling solubility of refrigerants in ionic liquids using peng robinson-two state equation of state," *Fluid Ph. Equil.*, vol. 486, pp. 80–90, 2019.

[200] Simeoni, G., Bryk, T., Gorelli, F., Krisch, M., Ruocco, G., S., M., and Scopigno, T., "The widom line as the crossover between liquid-like and gas-like behaviour in supercritical fluids," *Nature Physics*, vol. 6, no. 7, pp. 503–507, 2010.

[201] Singla, G., Scouflaire, P., Rolon, C., and Candel, S., "Transcritical oxygen/-transcritical or supercritical methane combustion," *Proc. Combust. Inst.*, vol. 30, no. 2, pp. 2921–2928, 2005.

[202] Sirignano, W. A., *Fluid dynamics and transport of droplets and sprays*. Cam. univ. press, 1999.

[203] Skaugen, G., Kolsaker, K., Walnum, H., and Wilhelmsen, O., "A flexible and robust modelling framework for multi-stream heat exchangers," *Comp. & Chem. Eng.*, vol. 49, pp. 95–104, 2013.

[204] Slavinskaya, N. and Haidn, O., "Reduced chemical model for high presure methane combustion with pah formation," in *AIAA 2008-1012*, pp. 1–14, 2008.

[205] Smejkal, T. and Mikyška, J., "Phase stability testing and phase equilibrium calculation at specified internal energy, volume, and moles," *Fluid Ph. Equil.*, vol. 431, pp. 82–96, 2017.

[206] Smith, G., Golden, D., Frenklach, M., Moriarty, N. W., Eiteneer, B., Goldenberg, M., Bowman, C. T., Hanson, R. K., Song, S., Gardiner, W. C., Lissianski, V. V., and Qin, Z., "GRI-Mech 3.0," `http://www.me.berkeley.edu/gri_mech/`.

[207] Soave, G., "Equilibrium constants from a modified redlich-kwong equation of state," *Chem. Eng. Sci.*, vol. 27, no. 6, pp. 1197–1203, 1972.

[208] Star, A., Edwards, J., Lin, K.-C., Cox-Stouffer, S., and Jackson, T., "Numerical simulation of injection of supercritical ethylene into nitrogen," *J. Prop. Pow.*, vol. 22, no. 4, pp. 809–819, 2006.

[209] Stechmann, D. P., *Experimental study of high-pressure rotating detonation combustion in rocket environments*. PhD thesis, Purdue University, 2017.

[210] Stępczyńska-Drygas, K., Łukowicz, H., and Dykas, S., "Calculation of an advanced ultra-supercritical power unit with co2 capture installation," *Energy conv. and manag.*, vol. 74, pp. 201–208, 2013.

[211] Stiel, L. and Thodos, G., "Force constants for polar substances: their prediction from critical properties," *AICHE journal*, vol. 10, no. 2, pp. 266–269, 1964.

[212] Su, W., Zhao, L., and Deng, S., "Recent advances in modeling the vapor-liquid equilibrium of mixed working fluids," *Fluid Ph. Equil.*, vol. 432, pp. 28–44, 2017.

[213] Sutton, G. and Biblarz, O., *Rocket propulsion elements*. John Wiley & Sons, 2017.

[214] Takahashi, S., "Preparation of a generalized chart for the diffusion coefficients of gases at high pressures," *J. of Chem. Eng. of Japan*, vol. 7, no. 6, pp. 417–420, 1975.

[215] Takahashi, S. and Hongo, M., "Diffusion coefficients of gases at high pressures in the co2-c2h4 system," *J. of Chem. Eng. of Japan*, vol. 15, no. 1, pp. 57–59, 1982.

[216] Terashima, H. and Koshi, M., "Approach for simulating gas–liquid-like flows under supercritical pressures using a high-order central differencing scheme," *J. Comp. Phys.*, vol. 231, no. 20, pp. 6907–6923, 2012.

[217] Thompson, W., Zollweg, J., and Gabis, D., "Vapor-liquid equilibrium thermodynamics of n2+ ch4: model and titan applications," *Icarus*, vol. 97, no. 2, pp. 187–199, 1992.

[218] Thorade, M. and Saadat, A., "Helmholtzmedia—a fluid properties library," in *Proceedings of the 9th International MODELICA Conference; September 3-5; 2012; Munich; Germany*, no. 076, pp. 63–70, Linköping University Electronic Press, 2012.

[219] Thorade, M. and Saadat, A., "Partial derivatives of thermodynamic state properties for dynamic simulation," *Env. Earth Sci.*, vol. 70, no. 8, pp. 3497–3503, 2013.

[220] Toro, E., *Riemann solvers and numerical methods for fluid dynamics: a practical introduction*. Springer Science & Business Media, 2013.

[221] Tramecourt, N., Menon, S., and Amaya, J., "Les of supercritical combustion in a gas turbine engine," *AIAA 2004-3381*, pp. 1–11, 2004.

[222] Trappehl, G. and Knapp, H., "Vapour-liquid equilibria in the ternary mixtures n2-ch4-c2h6 and n2-c2h6-c3h8," *Cryogenics*, vol. 27, no. 12, pp. 696–716, 1987.

[223] Traxinger, C., Banholzer, M., and Pfitzner, M., "Real-gas effects and phase separation in underexpanded jets at engine-relevant conditions," in *AIAA 2018-1815*, 2018.

[224] Traxinger, C., Müller, H., Pfitzner, M., Baab, S., Lamanna, G., Weigand, B., Matheis, J., Stemmer, C., Adams, N. A., and Hickel, S., "Experimental and numerical investigation of phase separation due to multi-component mixing at high-pressure conditions," *arXiv:1706.03923*, 2017.

[225] Traxinger, C., Zips, J., and Pfitzner, M., "Single-phase instability in non-premixed flames under liquid rocket engine relevant conditions," *J. Prop. Pow.*, vol. 35, no. 4, pp. 675–689, 2019.

[226] Tudisco, P. and Menon, S., "Numerical investigations of phase-separation during multi-component mixing at super-critical conditions," *Flow Turb. Combust.*, vol. 104, no. 2, pp. 693–724, 2019.

[227] Tudisco, P. and Menon, S., "Analytical framework for real-gas mixtures with phase-equilibrlium thermodynamics," *J. Sup. F.*, vol. tba, no. tba, pp. 1–47, 2020. doi:10.1016/j.supflu.2020.104929.

[228] Turns, S., "An introduction to combustion: concepts and applications," 2018.

[229] Urbano, A., Selle, L., Staffelbach, G., Cuenot, B., Schmitt, T., Ducruix, S., and Candel, S., "Exploration of combustion instability triggering using large eddy simulation of a multiple injector liquid rocket engine," *Combust. Flame*, vol. 169, pp. 129–140, 2016.

[230] Van Der Waals, J. and Rowlinson, J., *On the continuity of the gaseous and liquid states*. Courier Corporation, 2004.

[231] Van Konynenburg, P. and Scott, R., "Critical lines and phase equilibria in binary van der waals mixtures," *Phil. Trans. of the Royal Soc. of London. Series A, Math. and Phys. Sci.*, vol. 298, no. 1442, pp. 495–540, 1980.

[232] Van Leer, B., "Towards the ultimate conservative difference scheme. v. a second-order sequel to godunov's method," *J. Comp. Phys.*, vol. 32, no. 1, pp. 101–136, 1979.

[233] Vasudevan, S., *Thermal diffusion coefficient modeling for high pressure combustion simulations*. PhD thesis, Clemson University, 2007.

[234] Vishnyakov, A., Weathers, T., Hosangadi, A., and Chiew, Y., "Molecular models for phase equilibria of alkanes with air components and combustion products ii. alkane–oxygen mixtures," *Fluid Ph. Equil.*, p. 112650, 2020.

[235] Wang, X., Huo, H., Unnikrishnan, U., and Yang, V., "A systematic approach to high-fidelity modeling and efficient simulation of supercritical fluid mixing and combustion," *Combust. Flame*, vol. 195, pp. 203–215, 2018.

[236] Wang, X., Huo, H., Wang, Y., and Yang, V., "Comprehensive study of cryogenic fluid dynamics of swirl injectors at supercritical conditions," *AIAA J.*, pp. 3109–3119, 2017.

[237] Weathers, T., Vishnyakov, A., Chiew, Y., and Hosangadi, A., "Characterizing thermodynamic properties of pure components and binary mixtures at rocket conditions using molecular dynamics," *AIAA 2019-1284*, pp. 1–15, 2019.

[238] Wehrfritz, A., Kaario, O., Vuorinen, V., and Somers, B., "Large eddy simulation of n-dodecane spray flames using flamelet generated manifolds," *Combust. Flame*, vol. 167, pp. 113–131, 2016.

[239] Westbrook, C. and Dryer, F., "Simplified reaction mechanisms for the oxidation of hydrocarbon fuels in flames," *Combust. Sci. Technol.*, vol. 27, no. 1-2, pp. 31–43, 1981.

[240] Wilhelmsen, O., Aasen, A., Skaugen, G., Aursand, P., Austegard, A., Aursand, E., Gjennestad, M., Lund, H., Linga, G., and Hammer, M., "Thermodynamic modeling with equations of state: present challenges with established methods," *Ind. & Eng. Chem. Res.*, vol. 56, no. 13, pp. 3503–3515, 2017.

[241] Wilhelmsen, O., Skaugen, G., Hammer, M., Wahl, P., and Morud, J., "Time efficient solution of phase equilibria in dynamic and distributed systems with differential algebraic equation solvers," *Ind. & Eng. Chem. Res.*, vol. 52, no. 5, pp. 2130–2140, 2013.

[242] Wood, A. and Lindsay, R., "A textbook of sound," *Physics Today*, vol. 9, p. 37, 1956.

[243] Woodward, R. and Talley, D., "Raman imaging of transcritical cryogenic propellants," *AIAA 96-0468*, p. 468, 1996.

[244] Yao, M., Hickey, J., Ma, P., and Ihme, M., "Molecular diffusion and phase stability in high-pressure combustion," *Combust. Flame*, vol. 210, pp. 302–314, 2019.

[245] Yi, P., Yang, S., Habchi, C., and Lugo, R., "A multicomponent real-fluid fully compressible four-equation model for two-phase flow with phase change," *Phys. of Fluids*, vol. 31, no. 2, p. 026102, 2019.

[246] Yorizane, M., Yoshimura, S., Masuoka, H., and Yoshida, H., "Thermal conductivities of binary gas mixtures at high pressures: nitrogen-oxygen, nitrogen-argon, carbon dioxide-argon, and carbon dioxide-methane," *Ind.& Eng. Chem. Fund.*, vol. 22, no. 4, pp. 458–463, 1983.

[247] Younglove, B. and Ely, J., "Thermophysical properties of fluids. ii. methane, ethane, propane, isobutane, and normal butane," *J. of Phys. and Chem. Ref. Data*, vol. 16, no. 4, pp. 577–798, 1987.

[248] Zong, N. and Yang, V., "Cryogenic fluid dynamics of pressure swirl injectors at supercritical conditions," *Phys. of Fluids*, vol. 20, no. 5, p. 056103, 2008.

VITA

Principio Tudisco was born on October 9th, 1987 in Venosa (Italy), the town were the famous Latin poet Orazio was born. He attended the "Liceo Scientifico - Federico II di Svevia" in Melfi, a town close to Venosa where he met his wife Arianna. After earning the Space Engineering and a Space-Transportation Systems Master degrees at "La Sapienza", University or Rome, and earned an internship in Munich at "Airbus - Space and Defense", he decided to continue his studies for a Doctoral degree at Georgia Tech, where he joined the CCL in 2014 under the supervision of Prof. Menon. During this time at GT he worked on many different projects, became father of Vittoria and married his love Arianna. After his Doctoral degree, they are expected to move to LA to continue their life and have many more adventures.